

PERYLENE DIIMIDE-BASED MATERIALS FOR ORGANIC ELECTRONICS AND  
OPTICAL LIMITING APPLICATIONS

A Dissertation  
Presented to  
The Academic Faculty

By

Chun Huang

In Partial Fulfillment  
Of the Requirements for the Degree  
Doctor of Philosophy in the School of  
Chemistry and Biochemistry

Georgia Institute of Technology

December 2010

Copyright 2010 by Chun Huang

PERYLENE DIIMIDE-BASED MATERIALS FOR ORGANIC ELECTRONICS AND  
OPTICAL LIMITING APPLICATIONS

Approved By:

Dr. Seth R. Marder, Advisor  
School of Chemistry and Biochemistry  
*Georgia Institute of Technology*

Dr. Jean-Luc Brédas  
School of Chemistry and Biochemistry  
*Georgia Institute of Technology*

Dr. Laren Tolbert  
School of Chemistry and Biochemistry  
*Georgia Institute of Technology*

Dr. David M. Collard  
School of Chemistry and Biochemistry  
*Georgia Institute of Technology*

Dr. Bernard Kippelen  
School of Electrical and Computer  
Engineering  
*Georgia Institute of Technology*

Date Approved: August 17, 2010

致我敬爱的父母和亲爱的严容  
*To my Parents and Yanrong*

## ACKNOWLEDGEMENTS

First and foremost, I would like to express my sincerest appreciation to my research advisor, Dr. Seth R. Marder, for his guidance, encouragement, and trust on me. He has been always very supportive and understanding whenever I need his help for my research work at Georgia Institute of Technology. What I have learned from Seth in these years is not only about science but also for personal life in general.

I would like to thank Dr. Stephen Barlow for his help throughout these years. Besides research advices, both Seth and Steve are also my patient and helpful English teachers showing me how to express my ideas correctly with English. Especially, it was Dr. Barlow who spent a tremendous amount of time proofreading my thesis and made it read like English. I am also grateful to the time and effort provided by Mr. Anthony Giordano and Dr. Matthew Sartin in proofreading and editing parts of this thesis.

This thesis is a product from the collaborating research from several research groups. I appreciate Dr. Bernard Kippelen and his group members, including Mr. William J. Potscavage *Jr.*, Dr. Shree P. Tiwari, Dr. Yinghua Zhou, Dr. Hyeunseok Cheun and Mr. Sinan M. Suctu for their efforts on device fabrication and analysis. I am thankful to Dr. Joe W. Perry and his group members, Dr. Matthew M. Sartin, Dr. Nisan Siegel, and Mr. Matteo Cozzuol, for helping in obtaining the transient absorption data, 2PA spectra, and optical limiting response for Chapter 5 and 6. I would like to thank Dr. Elisa Riedo and Dr. Debin Wang for the KPFM analysis. Last but not least, I thank Dr. James Durrant and Dr. Safa Shoaee in Imperial College (London) for their contribution in Chapter 4. I also appreciate the help of using instruments in different groups at Georgia Tech, specifically, Matthew R. Kincer in the Backham group for obtaining some GPC data, Wei Long in the



Jones group for some TGA analysis, and, Jasmeet Kaur in the Shofner group for some DSC analysis. I also would like to thank all of my committee members for providing their valuable suggestions to this thesis.

I would like to show my appreciation to all the current and past group members in the Marder group for their help during these years. Without them, this work will not be going on so smoothly. Especially, I thank Dr. Yadong Zhang, Dr. Susan A. Odom, Dr. Zesheng An, Dr. Richard Mason Jr. and Dr. Xuan Zhang for providing some starting materials and Mr. Anthony Giordano and Dr. Soo Young Kim for some AFM analysis. I also want to thank Dr. Stephen Barlow, Dr. Simon Jones, and Dr. Mariacristina Rumi for participating my Marderization sessions and their suggestions on my research over the years. I also want to thank Ms. Marsha D. Lamb, Ms. Carmen Rivera, and Miss Veronique Brédas; they make my life in the Marder group much easier.

I would like to give my deepest appreciation to my parents for their support all the time even though they might not understand much of my research since 2002. Without the love, care, and, support from my parents, I would not be who I am today. At the end, I would like to express my special appreciation to my wife, Yanrong Shi, for her selfless support and the happiness she brings to everyday of our life. Yanrong is the reason for our wonderful life every day.

## TABLE OF CONTENTS

ACKNOWLEDGEMENTS.....	IV
LIST OF FIGURES .....	X
LIST OF TABLES .....	XX
LIST OF SCHEMES.....	XXI
LIST OF ABBREVIATIONS.....	XXII
SUMMARY.....	XXIII
 <b>Chapter 1. Introduction of Perylene Diimides</b>	
1.1 The use of perylene diimides as pigments in industry .....	1
1.2 Preparation of PDI derivatives.....	4
1.2.1 Preparation of PDIs with substituents on the imide positions .....	4
1.2.2 Preparation of PDIs with various substituents on the bay positions.....	11
1.2.3 Preparation of PDIs with various substituents on the other positions .....	11
1.3 Physical properties of PDIs .....	16
1.3.1 Optical properties of PDIs .....	16
1.3.2 Redox properties of PDIs.....	23
1.3.3 Molecular packing of PDIs in the solid state.....	25
1.3.4 Photo-induced electron transfer in PDIs .....	28
1.3.4.1 Photo-induced electron transfer in porphyrin-PDI systems .....	31
1.3.4.2 Photo-induced electron transfer in other donor-PDI systems .....	33
1.4 Application of PDI dyes in organic electronics and optics.....	35
1.4.1 PDIs as electron-transport materials in OFETs .....	48
1.4.2 PDIs as acceptors and photo-sensitizers for solar cells .....	54
1.5 Research goals and organization of the thesis .....	61
1.5.1 Research goals and design strategies .....	61
1.5.2 Thesis organization .....	62
1.6 References.....	64

## Chapter 2. Perylene Diimide-based Side-chain Polynorbornenes for Organic Electronic Applications

2.1	Introduction.....	71
2.2	Syntheses of the homopolymers .....	78
2.3	Optical properties of the PDIs.....	83
2.4	Redox properties of the monomers .....	87
2.5	Powder XRD of the homopolymers .....	89
2.6	Thermal properties of the homopolymers.....	91
2.7	OFET and OPV performance of the PDI homopolymers.....	93
2.8	Morphology studies of the P3HT/PDI HP blends.....	98
2.9	Conclusions.....	100
2.10	Experimental section.....	101
2.11	References.....	121

## Chapter 3 Diblock Copolynorbornenes with Perylene Diimide and Oligothiophene Side-groups for Organic Photovoltaics

3.1	Introduction.....	124
3.2	Polymerization kinetics of the C11PDI monomer .....	133
3.3	Synthesis of the OT-based monomer and homopolymers .....	134
3.4	Absorption and redox properties of the OT-based materials .....	139
3.5	Device evaluation of the OT-based homopolymers.....	142
3.6	Synthesis and optical properties of the block copolymers.....	143
3.7	Thermal properties of the copolymers .....	148
3.8	Solar-cell performance for the block copolymers.....	149
3.9	Morphology study of the copolymers .....	153
3.10	Conclusions.....	154
3.11	Experimental section.....	155
3.12	References.....	167

## Chapter 4. Perylene Diimide-based Acceptors with Various Electron Affinities and Miscibility with P3HT and Their Influence on the Yields of Charge Photo-generation in Donor/Acceptor Blends

4.1	Introduction.....	171
4.2	Synthesis and redox properties of PDI <sub>X</sub> (X = A to F) derivatives .....	175
4.3	Optical properties of P3HT:PDI <sub>X</sub> (X = A to F) blends .....	177
4.4	Transient absorption of P3HT:PDI <sub>X</sub> (X= A to F) blends.....	180
4.5	Morphology study and solar cells of P3HT:PDI <sub>D</sub> blends .....	182
4.6	Synthesis of new PDI <sub>X</sub> (X= G to I) materials .....	186
4.7	Optical and electrochemical properties of new PDI <sub>X</sub> (X= G to I) .....	189
4.8	Transient absorption of the P3HT:PDI <sub>X</sub> (X= G to I) blends.....	192
4.9	Morphology study and solar cellperformance of the P3HT:PDI <sub>X</sub> (X = G to I and D) blends .....	193
4.10	Conclusions.....	195
4.11	Experimental section.....	196
4.12	Reference .....	207

## Chapter 5. Photo-induced Charge Transfer and Optical Limiting in Dyads Composed of Two-photon Absorbing Donors and A Perylene Diimide Acceptor

5.1	Introduction.....	209
5.2	Synthesis and thermal properties of the dyads and model compounds .....	218
5.3	Optical properties of the dyads and model compounds .....	223
5.4	Redox properties of the dyads and model compounds .....	232
5.5	Transient absorption.....	234
5.6	Optical limiting .....	237
5.7	Conclusions.....	239
5.8	Experimental section.....	240
5.9	References.....	252

## Chapter 6. Photo-induced Electron Transfer and Optical Limiting in Poly(carbazole-alt-2,7-fluorene)s Bearing Perylene Diimides as Pendant Acceptors

6.1	Introduction.....	255
6.2	Syntheses of the PDI-grafted monomers and polymers.....	262
6.3	Thermal properties of the materials .....	264
6.4	Linear absorption and emission of the materials in solution .....	266
6.5	Redox properties of the materials .....	271
6.6	Transient absorption of the polymers .....	273
6.7	Non-linear absorption and optical limiting.....	278
6.8	D–A type PCF with 4-nitrophenyl-based acceptor for optical limiting.....	280
6.9	Conclusions.....	285
6.10	Experimental section.....	286
6.11	References.....	300

## Chapter 7. Conclusions and outlook

7.1	Conclusionsand outlook.....	303
7.2	References.....	313

## LIST OF FIGURES

Figure 1.1	The chemical structures for PTCDA (left) and respective perylene diimides without bay-substitutions.....	1
Figure 1.2	The chemical structures of three widely used PDI-based industry pigments. ....	2
Figure 1.3	The frontier orbitals (HOMO and LUMO) of perylene diimides....	10
Figure 1.4	The UV-Vis absorption and emission spectra of a perylene diimide in toluene..	18
Figure 1.5	The concentration-dependent UV-Vis absorption of the perylene diimide in MCH.....	20
Figure 1.6	The concentration-dependent emission of the perylene diimide in toluene.....	21
Figure 1.7	PDI anion(s) absorption in ethanol ( $1 \times 10^{-4}$ mol/L tetramethylammonium hydroxide) obtained by controlled reduction with $H_2$ in the presence of Pt. The concentration for neutral PDI was 5.4 pM.....	22
Figure 1.8	The bond length (left, in Å) and $\pi$ - $\pi$ stacking of Pigment Red 179 (right) in crystal.....	26
Figure 1.9	Metal-coordination-directed (left) and hydrogen-bonding-directed (right) self-assembly in forming perylene diimide based supramolecules.....	27
Figure 1.10	Photo-induced charge transfer between donor and acceptor (PDI) in forming $D^+$ -PDI $^-$ : (a) electron transfer from excited donor to PDI; (b) electron-transfer from donor to excited PDI. The blue balls represent electrons. ....	28
Figure 1.11	Relationship between free energy ( $\Delta G_{CT}$ ) and nuclear motion for diabatic exergonic electron transfer (Figure adapted from Dr. Jing Wang in the Marder group). ....	29
Figure 1.12	The chemical structure of porphyrin-PDI-porphyrin. ....	31
Figure 1.13	The chemical structures of tetrakis(perylenediimide) substituted zinc tetraphenylporphyrin (2) and the model compound (3).....	32
Figure 1.14	The chemical structures of several non-porphyrin donor-PDI derivatives for forming photo-induced charge-separated states.....	34
Figure 1.15	Schematic representations of two widely used OFET geometries: Top-contact OFET (left); bottom-contact OFET (right).....	35
Figure 1.16	Typical $I$ - $V$ curves of an OFET device: (a) output curve at different constant $V_G$ and (b) transfer curve at a constant $V_{SD}$ (Figure adapted from Dr. Xuan Zhang of the Marder's group).....	36

Figure 1.17	The energy diagram of various charge carrier transport according to a given electrode material. The charge preference is dependent on the injection barrier from the organic materials to the respective metal electrode, and ambipolar materials exhibit a relatively small injection barrier from the metal electrode for both hole and electron. ....	39
Figure 1.18	Schematic of frontier molecular orbitals (HOMO and LUMO) at a D/A interface, showing steps in the photovoltaic process. Ionization potential (IP) and electron affinity (EA) are depicted for the donor and acceptor, respectively .....	41
Figure 1.19	Energy state diagram for free charge formation in a donor/acceptor (D/A) system via a bound CT state following photo-excitation (Figure adapted from Dr Shoaee in Imperial College (London)).....	42
Figure 1.20	Schematic illustration of an OPV device: bilayer solar cell (top), BHJ solar cell (middle), and ordered heterojunction cells (bottom) (This figure was adapted from Dr. Xuan Zhang in the Marder group). ....	44
Figure 1.21	Typical $J-V$ curves in an OPV device under dark (dotted line) and under illumination (solid line). <sup>33</sup> (b) Equivalent circuit used to model solar cells, where $R_s$ is the series resistances, $R_p$ is the shunt resistance.....	46
Figure 1.22	The chemical structures of the some PDI derivatives for OFET applications. ....	49
Figure 1.23	The chemical structures of the PDI derivatives with substitutions in the bay positions as electron-transport materials. ....	50
Figure 1.24	The chemical structures of solution-processable PDI materials as electron-transport materials.....	53
Figure 1.25	The chemical structures of PV, CuPc, pentacene, and rebrene.....	55
Figure 1.26	PDI-based materials for solution processable solar cells. ....	56
Figure 1.27	PDI-based diblock copolymers for OPV applications.....	59
Figure 1.28	Conjugated PDI-based polymers with D-A connection on the PDI bay positions.....	61
Figure 1.29	Some PDI materials as photo-sensitizers for DSSCs .....	61
Figure 2.1	Grubbs initiators and the mechanism for ruthenium-based ROMP. ....	77
Figure 2.2	The chemical structures of the PDI-grafted polynorbornenes .....	78
Figure 2.3	The UV-Vis absorption spectra of the monomers: N-PDI (black), C7 PDI (red), and C11 PDI (blue) (left) and respective homopolymers: N-PDI HP (black), C7 PDI HP (red), and C11 PDI HP (blue) (right) in chloroform .....	87

Figure 2.4	The UV-Vis absorption spectra of spin-casted films of N-PDI HP (black), C7 PDI HP (red), and C11 PDI HP (blue) on glass, using 10 mg/mL polymer solution in toluene at 1000 rpm for 1 minute.....	87
Figure 2.5	The emission spectra of C11PDI (red) and C11PDI HP (black) in CH <sub>2</sub> Cl <sub>2</sub> . In both cases, the sample was excited at 490 nm and the emission intensity has been normalized to the same absorbance at the excitation wavelength.....	88
Figure 2.6	The cyclic voltammograms of N-PDI (black), C7PDI (red), and C11PDI (blue) in CH <sub>2</sub> Cl <sub>2</sub> , 0.1 M [ <i>n</i> -Bu <sub>4</sub> N][PF <sub>6</sub> ], with scan rate = 50 mV s <sup>-1</sup> , with ferrocene as an internal reference. ....	90
Figure 2.7	Power XRD of N-PDI HP (black), C7PDI HP (red), and C11PDI HP (blue) with a Cu Ka source ( $\lambda = 1.5406 \text{ \AA}$ ) in continuous scan mode with a step of 0.02° (Data were collected by Dr Soo Young Kim in the Marder group). ....	92
Figure 2.8	TGA traces (left) and DSC (right) traces for the second heating process of the N-PDI HP (black), C7 PDI HP (red), and C11 PDI HP (blue) with a heating rate of 5 °C/min under N <sub>2</sub> . ....	93
Figure 2.9	General OFET device structure for these homopolymers (Figure was adapted from Dr. Shree Tiwari in the Kippelen group) ....	95
Figure 2.10	OFET device characteristics for C11PDI HP after annealing at 200 °C (Figures were adapted from Dr. Shree Tiwari in the Kippelen group). ....	96
Figure 2.11	General solar cell structure for the homopolymer/P3HT blends (figure was adapted from William Potscavage Jr. in the Kippelen group).....	98
Figure 2.12	The films absorption spectra of C11PDI HP/P3HT (black) and C7PDI HP/P3HT (red) on PEDOT : PSS-coated ITO. These films were prepared in a way similar to real solar cell fabrication. ....	98
Figure 2.13	The <i>I-V</i> characteristics of the solar cells for P3HT:C11PDI HP blend and IPCE curves for the HP/P3HT blends (Figures were adapted from Mr. William Potscavage Jr. in the Kippelen group) ....	99
Figure 2.14	The topography (left two) and surface potential (right two) images for P3HT:C11PDI HP (top two) and P3HT:C7PDI HP (bottom two) by KPFM. Here, major topographical hills lead to dark areas and thus low surface potential in the SP images, especially for P3HT:C7PDI HP blend (KPFM images were collected by Dr. Debin Wang in the Riedo group). ....	101
Figure 3.1	Schematic illustration of D/A BHJ solar cell, with a magnified area showing the bicontinuous morphology of the active layer .....	125
Figure 3.2	Schematic representation of a diblock copolymer; (b) lamellar phase morphology depicting arrangement of polymer chains; (c) partial list of phases formed by diblock copolymers in the bulk .....	127



Figure 3.3	The chemical structures for the diblock copoly(3-alkylthiophene)s and P3HT. 130
Figure 3.4	The chemical structures of the Thelakkat copolymers with PDI and triphenylamine moieties (left). TEM images of the thin film cross section for one copolymer and respective homopolymers blend (right)..... 130
Figure 3.5	Designed PDI-OT diblock copolymers and estimated energy diagrams of the PDI and OT monomers..... 132
Figure 3.6	Kinetics of the polymerization of C11PDI monomer (left) and its molecular weight and polydispersity – [Monomer]/[Catalyst] relationship (right)..... 134
Figure 3.7	TGA traces (left) and DSC traces (right) for the OT-based homopolymers..... 138
Figure 3.8	The UV-Vis absorption spectra of the OT-based materials..... 139
Figure 3.9	Power XRD of 5T HP (black) and 6T HP (red) with a Cu Ka source ( $\lambda = 1.5406 \text{ \AA}$ ) in a continuous scan mode with a step of $0.02^\circ$ (The data were collected by Dr. Doo Young Kim in the Marder group)..... 140
Figure 3.10	The cyclic voltammetry curve of 5T (black) and 6T (red) in $\text{CH}_2\text{Cl}_2$ , 0.1 M [ <i>n</i> -Bu <sub>4</sub> N][PF <sub>6</sub> ], with scan rate = $50 \text{ mVs}^{-1}$ , with FeCp <sub>2</sub> as an internal reference .... 142
Figure 3.11	The chemical structures of the PDI-grafted block copolymers..... 145
Figure 3.12	The UV-Vis absorption spectra of the copolymers in $\text{CHCl}_3$ solution (left) and in films (right). The films were prepared via spin-coating using 5mg/mL toluene solution at a spin rate of 500 rpm for 1 minute on glass substrates..... 147
Figure 3.13	Thin-film emission spectra of the copolymers and C11PDI HP and 5T / 6T HP controls on ITO substrates. All polymer films were excited at 450 nm (Figure adapted from Dr. Safa Shoaee in the Durrant group)..... 147
Figure 3.14	TGA traces (left) and DSC traces (right) for the second heating process of PDI-5T CPA (black), PDI-5T CPB (red), and PDI-6T CPA (green) with a heating rate of $5^\circ\text{C}/\text{min}$ under nitrogen atmosphere..... 149
Figure 3.15	The IPCE curves of solar cells from the PDI-5T copolymers (A and B) and the blends of C11PDI HP and 5T HP (1:1 and 2:1 weight ratio) (Figure was adapted from Mr. William Potscavage Jr. in the Kippelen group)..... 152
Figure 3.16	The transient absorption decay of the copolymer films after photoexcitation (similar films as the active layers in solar cells) under nitrogen (excited at 466 nm, probed at 720 nm.) (Figure was adapted from Dr. Safa Shoaee in the Durrant group)..... 152
Figure 3.17	The TEM images for PDI-5T CPA and PDI-5T CPB (Figures were adapted from Dr. Safa Shoaee in the Durrant group)..... 154
Figure 4.1	The energy level diagram of a donor/acceptor interface showing a simplified viewpoint of photo-excitation of an electron into the donor LUMO (with

	efficiency $\eta_{\text{ABS}}$ ), followed by exciton dissociation via electron-transfer into the acceptor LUMO ( $\eta_{\text{DISS(EX)}}$ ) and migration of the separated charges away from the interface. It also illustrates the potential for electron transfer initially to generate a coulombically bound CT state that also requires dissociation ( $\eta_{\text{DISS(CT)}}$ ) before free charge carriers can be collected (This figure was adapted from Dr. Safa Shoaee in the Durrant group).....	172
Figure 4.2	The chemical structures of PCBM, PDI2 and various polythiophenes with different IP and Es for the study of efficiency of charge photo-generation process and $G_{\text{CS}}$ relationship.....	173
Figure 4.3	The transient absorption signal measured at 1 $\mu\text{s}$ of various polythiophene: PDI <sub>2</sub> (blue) or polythiophene: PCBM (red) (1:1 weight ratio) blend films plotted against $-\Delta G_{\text{CS}}$ , estimated as $E_{\text{S}} - (\text{IP}_{\text{D}} - \text{EA}_{\text{A}})$ . The transient signal has been corrected for variation in the absorbance at the excitation wavelength (500 nm) and PL quenching. $\lambda_{\text{probe}} = 700 \text{ nm}$ at $50 \mu\text{Jcm}^{-2}$ (This figure was adapted from Dr. Safa Shoaee in the Durrant group).....	174
Figure 4.4	The chemical structures of PDI <sub>X</sub> (X = A to F) derivatives.....	175
Figure 4.5	The cyclic voltammograms of PDI <sub>X</sub> (X = A to F) in $\text{CH}_2\text{Cl}_2$ , 0.1 M [ <i>n</i> -Bu <sub>4</sub> N][PF <sub>6</sub> ], with a scan rate = $50 \text{ mVs}^{-1}$ for each material. FeCp <sub>2</sub> was used as an internal reference .....	176
Figure 4.6	The absorption and photoluminescence spectra measured for the following pristine P3HT film and blend films of PDI <sub>X</sub> :P3HT (X = A to F, 1:1 weight ratio) spin-cast from chloroform solution at 1000 rpm for 1 minute. The PL spectra were measured using 500 nm excitation and adjusted to the same absorbance at the excitation wavelength (These figures were adapted from Dr Safa Shoaee in the Durrant group).....	179
Figure 4.7	The absorption and photoluminescence spectra measured for the following pristine and blend films: PDI <sub>D</sub> , P3HT, and (1:1) P3HT:PDI <sub>D</sub> . The PL spectra were measured using 500 nm excitation, and the intensities were normalized according to the absorbance (This figure was adapted from Dr Safa Shoaee in the Durrant group) .....	179
Figure 4.8	The transient absorption decay (left) for P3HT:PDI <sub>X</sub> (X = A –F and 2) in a N <sub>2</sub> environment, probed at 700 nm, with $\lambda_{\text{exc}} = 520 \text{ nm}$ at $50 \mu\text{Jcm}^{-2}$ . Spectrum of P3HT:PDI <sub>D</sub> at 1 $\mu\text{s}$ under N <sub>2</sub> using $\lambda_{\text{exc}} = 520 \text{ nm}$ at $50 \mu\text{Jcm}^{-2}$ (right) (These figures were adapted from Dr Safa Shoaee in the Durrant group).....	182
Figure 4.9	The transient absorbance signal measured at 1 $\mu\text{s}$ of various P3HT:PDI <sub>X</sub> (1:1 weight ratio) blend films with P3HT plotted against $-\Delta G_{\text{CS}}$ , estimated as $E_{\text{S}} - (\text{IP}_{\text{D}} - \text{EA}_{\text{A}})$ . The transient signal has been corrected for variation in optical absorbance at the excitation wavelength (500 nm) and PL quenching. $\lambda_{\text{prb}} = 700 \text{ nm}$ at $50 \mu\text{Jcm}^{-2}$ (This figure was adapted from Dr Safa Shoaee in the Durrant group) .....	182

Figure 4.10	The AFM images of P3HT:PDI <sub>D</sub> (1:1 weight ratio) blend films. The films were prepared via spin-casting from 20 mg/mL chlorobenzene solution on PEDOT:PSS coated ITO with spin rate of 700 rpm for 1 minute (The images were collected by Dr. Debin Wang in the Riedo group).....	184
Figure 4.11	The TEM micrographs of P3HT:PDI <sub>D</sub> (left) film (expanded region, centre: crystallisation of PDI <sub>D</sub> lattice) and P3HT:PDI <sub>I</sub> (right) <sup>6</sup> (This figure was adapted from Dr. Safa Shoaee in the Durrant group).....	184
Figure 4.12	The DSC traces for PDI <sub>D</sub> and P3HT:PDI <sub>D</sub> (sample prepared from 1:1 weight ratio blend in CHCl <sub>3</sub> solution) under nitrogen.....	186
Figure 4.13	The chemical structure of PDI-based materials with oligo-3-hexyl-thiophenes moieties .....	187
Figure 4.14	The UV-Vis absorption spectra of PDI <sub>X</sub> (X = G to I) and PDI <sub>D</sub> in dilute chloroform solution with concentration of <i>ca.</i> $1 \times 10^{-5}$ mol/L.....	189
Figure 4.15	The thin-film UV-Vis absorption of P3HT:PDI <sub>X</sub> (X = G to I, and D, 1:1 weight ratio, 5 mg/mL) on glass, spin-casted from chlorobenzene solution with a rate of 1000 rpm for 1 minute.....	191
Figure 4.16	The cyclic voltammograms of PDI <sub>D</sub> (blue), PDI <sub>G</sub> (green), PDI <sub>H</sub> (red), and PDI <sub>I</sub> (black) in CH <sub>2</sub> Cl <sub>2</sub> (0.1 M [ <i>n</i> -Bu <sub>4</sub> N][PF <sub>6</sub> ]), with scan rate = 50 mV s <sup>-1</sup> for each material using FeCp <sub>2</sub> as an internal reference. ....	191
Figure 4.17	The transient absorption decay for P3HT:PDI <sub>X</sub> (X = G to I, and D) in N <sub>2</sub> environment, monitored at 700 nm, with $\lambda_{\text{exc}} = 520$ nm at 50 $\mu\text{Jcm}^{-2}$ (This figure was adapted from Dr Safa Shoaee in the Durrant group).....	193
Figure 4.18	The AFM (topography) images of P3HT:PDI <sub>X</sub> (X = G to I, and D, 1:1 weight ratio) on ITO substrates. The films were prepared via spin-casting from 20 mg/mL chlorobenzene solution on PEDOT:PSS coated ITOs at the rate of 1000 rpm for 1 minute .....	194
Figure 5.1	The Jablonski diagram for two-photon and one-photon absorption and the 1PA, 2PA, and emission spectra of an example 2PA dye.....	215
Figure 5.2	The Jablonski diagram for 2PA-induced charge-transfer .....	215
Figure 5.3	The 2PA cross-sections of some D- $\pi$ -D type quadrupolar chromophores .....	216
Figure 5.4	The chemical structures of the phenylene-linked (1) and hexylene-linked (2) dyads and the respective model compounds.....	217
Figure 5.5	Mechanism for 2PA-induced charge-transfer & optical limiting in the dyads. .	218
Figure 5.6	The TGA traces (left) for Dyad 1 (black), Dyad 2 (red), PDI model (green) and Donor model compound (blue) under N <sub>2</sub> flow with a 5K/min heating rate for each material. DSC (right) curves for Dyad 1 (black), Dyad 2 (red), PDI model	

	(green) and Donor model (blue) with heating rate of 5 K/min under N <sub>2</sub> flow in the second cycle .....	222
Figure 5.7	The UV-Vis absorption spectra of the dyads and model compound: Dyad 1 (black), Dyad 2 (red), PDI model (green) and donor model (blue) in toluene with concentration of <i>ca.</i> $1 \times 10^{-5}$ mol/L .....	224
Figure 5.8	The emission spectra of the dyads and model compounds: Dyad 1 (black), Dyad 2 (red), PDI model (green) and donor model (blue) in Toluene with concentration of $1 \times 10^{-6}$ mol/L. The Donor model and dyads are excited at 390 nm while the PDI model is excited at 490 nm.....	225
Figure 5.9	The excitation spectra (blue) of 2 $\mu$ M Dyad 1 (left) and Dyad 2 (right) in toluene with a fixed emission wavelength at 579 nm, overlaid with their respective absorption spectra (black) show that the dual emission observed for both dyads in the emission spectra is a result of energy transfer (Excitation spectra were collected by Dr Matthew Sartin in the Perry group) .....	225
Figure 5.10	The radical-ion absorption of the model compounds: cation of Donor model in dichloromethane (black) and PDI model anion in THF (red). Both spectra were taken under nitrogen atmosphere. The inserted plot is the absorption spectrum of cation of Donor model plot in energy form. A large excess PDI or Donor model was used to ensure the generation of mono ion only .....	228
Figure 5.11	The neutral Donor model absorption spectrum (black) and the absorption spectra of Donor model with various amount (tris( <i>p</i> -bromophenyl)aminium hexachloroantimonatemixture) in CH <sub>2</sub> Cl <sub>2</sub> .....	229
Figure 5.12	The neutral Dyad 1 (left) and Dyad 2 (right) absorption (black) and the absorption of dyads with different amounts of oxidation reagent (tris( <i>p</i> -bromophenyl)aminium hexachloroantimonatemixture) in dichloromethane ....	230
Figure 5.13	The radical-anion absorption spectra of the Dyad 1 (black) and Dyad 2 (red) via chemical reduction using cobaltocene in THF. The radical anions were generated in a nitrogen-flow glove-box and the absorption spectra were taken under nitrogen atmosphere .....	230
Figure 5.14	The 2PA spectra of Dyad 1 (black), Dyad 2 (red), Donor model (blue), and PDI model (green) prepared at 100 $\mu$ M in toluene. The difference between the dyad spectra and the 2PA spectrum of the donor and acceptor could result from overestimation of the quantum yield of the dyads, due to direct excitation of the acceptor in the one-photon fluorescence spectra. Additionally, the uncertainty in the dyad cross-section is $\sim 40\%$ , due to the large uncertainty in dyad quantum yields. The uncertainty in the model compound-cross-section is $\sim 15\%$ (2PA spectra were collected by Dr. Nisan Siegel in the Perry group). .....	231
Figure 5.15	The cyclic voltammograms of Dyad 1 (black), Dyad 2 (red), PDI model (green) and donor model (blue), in CH <sub>2</sub> Cl <sub>2</sub> (0.1 M [ <i>n</i> -Bu <sub>4</sub> N][PF <sub>6</sub> ]), with a scan rate = 50 mV s <sup>-1</sup> for each material, using FeCp <sub>2</sub> as an internal reference.....	233

Figure 5.16	The ss-pulse transient absorption spectra for (a) Donor model (blue) and PDI model (green) in toluene with excitation at absorption maximum; (b) 34 $\mu$ M Dyad 1; and (c) 37 $\mu$ M Dyad 2 in toluene, at various time after photo-excitation at 390 nm with 2.7 $\mu$ J/pulse with OD of the dyads at $\sim 0.35$ in a 2 mm cuvette under nitrogen atmosphere (The spectra were collected by Dr. Matthew Sartin in the Perry group) .....	235
Figure 5.17	The Nanosecond pulse transient absorption decay following excitation at 355 nm (OD = 0.11) of 2 $\mu$ M Dyad 1 in toluene using 900 $\mu$ J/pulse. The initial 10 ns “bleach” is due to scattered laser light. The red lines are fit lines (The data were collected by Dr. Matthew Sartin in the Perry group) .....	236
Figure 5.18	The nanosecond OL of 2 mM solutions of Dyad 1 (black), Dyad 2 (green), and Donor model (red) in toluene at various pump wavelengths focused in an f/5 geometry onto the middle of a 1 cm pathlength cell: 700 nm (left), 750 nm (center), and 800 nm (right) (The data were collected by Dr. Matthew Sartin in the Perry group). .....	238
Figure 5.19	Concentration dependence of peak absorption coefficients at 700, 750, and 800 nm for the Dyads and PDI model.....	239
Figure 6.1	The Jablonski diagram (left) for RSA-based optical limiting processes through either singlet- or triplet-excited-state absorption. Electronic absorption (right) of bis[tri-(n-hexyl)siloxy]SnPc: ground-state absorption (solid line) and triplet state absorption (data points linked by line).....	256
Figure 6.2	Two published PDI-based “double-cable” polycarbazole copolymers .....	259
Figure 6.3	The chemical structures of PDI grafted polymers and the model compounds ..	260
Figure 6.4	The mechanism for optical-limiting response for PDI-grafted PCFs.....	261
Figure 6.5	The chemical structure of 4-nitrophenyl grafted polymer .....	261
Figure 6.6	The TGA traces (left) and DSC (right) traces of the polymer in nitrogen atmosphere.....	266
Figure 6.7	The linear absorption spectra of the polymers in diluted toluene solution.....	268
Figure 6.8	A) The absorption spectra of the PDI-grafted polymers in highly concentrated toluene solutions. The band peaked at 920 nm for polymer 2 is tentatively attributed to ground-state intermolecular or intramolecular charge-transfer complexes; B) molar absorptivity of the PDI-grafted polymers in highly concentrated toluene solution at different wavelengths .....	269
Figure 6.9	The emission spectra of the PDI grafted polymers and respective model compounds. Polymer 1 and 2 as well as the respective model polymer were excited at 375 nm. The PDI model emission spectrum was collected using excitation at 490 nm .....	269

Figure 6.10	The excitation spectra (blue) of Polymer 1 (black) and (b) Polymer 2 (red) in toluene with a fixed emission wavelength at 620 nm ..... 270
Figure 6.11	The polaron absorption of the model polymers, Polymer 1 model (red) and Polymer 2 model (black), in CH <sub>2</sub> Cl <sub>2</sub> and the PDI model radical-anion absorption (blue) in THF ..... 271
Figure 6.12	The cyclic voltammograms of polymer films drop-cast from ~ 2 mg/mL CHCl <sub>3</sub> solution onto a Pt working electrode in acetonitrile with 0.1 M tetra- <i>n</i> -butylammonium hexafluorophosphate, except for PDI model, for which the CV was performed in solution. Potential was scanned at a rate of 50 mV/s ..... 272
Figure 6.13	The femtosecond transient absorption of Polymer 1 (top left) and Polymer 2 (top right) in toluene excited at 530 nm. Transient absorption of Polymer 1 (bottom left) and Polymer 2 (bottom right) in toluene following excitation at 350 nm. All samples were prepared at ~30 μM (in PDI units) in toluene in a 2 mm cuvette to yield an OD near 0.3 at the excitation wavelength (Transient absorption spectra were collected by Dr Matthew M. Sartin in the Perry group) ..... 274
Figure 6.14	The femtosecond laser pulse transient absorption of Polymer 1 model (left) and Polymer 2 model (right) in toluene excited at 350 nm with OD of <i>ca.</i> 0.3. (Transient absorption spectra were collected by Dr. Matthew M. Sartin in the Perry group)..... 275
Figure 6.15	The nanosecond transient absorption decay of Polymer 1 model (left, probe at NIR) and Polymer 2 model (right, probe at 715 nm) in toluene excited at 355 nm with OD of <i>ca.</i> 0.2. (Transient absorption spectra were collected by Dr. Matthew M. Sartin in the Perry group)..... 276
Figure 6.16	Proposed energy level diagram showing the lowest excited singlet states of PFP and nonaggregated PDI, of the aggregates (PDI) <sub>n</sub> , and that of the charge-transfer state. The arrows show the processes that might occur upon photo-excitation of PCF or PDI. .... 277
Figure 6.17	Optical limiting of 680 nm, 6 ns pulses focused in f/5 geometry onto samples of Polymer 1 and 2 in toluene, and the respective polymer model compounds mixed with PDI model in toluene, in a nitrogen-purged 2 mm cell (Optical limiting behavior was measured by Dr. Matthew M. Sartin in the Perry group)..... 279
Figure 6.18	The 2PA spectra of the Polymer models, Polymer 1 model (red) and Polymer 2 model (black) in 100 μM solution in toluene (2PA spectra were collected by Dr. Nisan Siegel in the Perry group)..... 280
Figure 6.19	The linear absorption of Polymer-NO <sub>2</sub> in diluted toluene solution..... 282
Figure 6.20	The femtosecond transient absorption spectra of Polymer-NO <sub>2</sub> (left) and Nanosecond transient absorption decay at 770 nm of Polymer-NO <sub>2</sub> (right) in toluene excited at 355 nm (Transient absorption spectra were collected by Dr. Matthew M. Sartin in the Perry group) ..... 283

Figure 6.21	Optical limiting 6 ns pulses focused in an f/5 geometry onto samples of Polymer-NO <sub>2</sub> (red) and Polymer 1 model (black) of 13 mg/mL in toluene in a N <sub>2</sub> purged, 2 mm cell. (Optical limiting behavior was measured by Dr. Matthew M. Sartin in the Perry group) .....	285
Figure 7.1	Some possible “3D-PDI” type materials .....	307
Figure 7.2	Other PDI-based materials worth of investigation on blend photo-physics .....	309

## LIST OF TABLES

Table 1.1	The optical properties of some perylene diimide dyes.....	19
Table 1.2	Redox properties of some PDI dyes.....	23
Table 1.3	p-n Heterojunction solar cell performance containing PDI-based acceptors. ....	56
Table 2.1	Summary of synthetic yields, molecular weight, the thermal properties (TGA and DSC), and EAs and IPs for the homopolymers. ....	93
Table 2.2	Summary of OFET device characteristics for the homopolymers (Data were collected by Dr. Shree Tiwari in the Kippelen group) .....	94
Table 2.3	Summary of solar cell characteristics for the homopolymers (Data were collected by Mr. William Potscavage <i>Jr.</i> in the Kippelen group).....	98
Table 3.1	Summary of the device performance from 5T HP or 6T HP/C <sub>60</sub> bilayer cells (Data were collected by Mr. William Potscavage <i>Jr.</i> in the Kippelen group) ..	143
Table 3.2	Summary of thermal properties of the copolymers.....	148
Table 3.3	Summary of solar cell characteristics for the copolymers or homopolymer blends in device geometry of ITO/PEDOT:PSS/polymer(s)/Al (Data were collected by Mr. William Potscavage <i>Jr.</i> in the Kippelen group) .....	153
Table 4.1	The Properties of the P3HT:PDI <sub>x</sub> blends (Some data were collected by Dr Safa Shoaee in the Durrant group).....	180
Table 4.2	Summary of the electrochemical behaviour of PDI <sub>x</sub> (X = G to I) and PDI <sub>D</sub> .....	192
Table 4.3	Summary of the solar cell performance of P3HT:PDI <sub>x</sub> (X = G to I and D) (Data were collected by Mr. William Potscavage <i>Jr.</i> in the Kippelen group) .....	195
Table 5.1	Summary for the linear optical properties for dyads and models in solution and thermal properties .....	226
Table 5.2	Electrochemical half-wave potentials (V) for dyads and model compounds vs. FeCp <sub>2</sub> <sup>+0</sup> in CH <sub>2</sub> Cl <sub>2</sub> (0.1 M [ <sup>n</sup> Bu <sub>4</sub> N][PF <sub>6</sub> ]) with a scan rate of 50 mV s <sup>-1</sup> for each material.....	234
Table 5.3	Summary of the optical limiting performance of the materials (The data were collected by Dr. Matthew Sartin in the Perry group) .....	238
Table 6.1	Polymerization results and thermal properties of the polymers.....	266
Table 6.2	Summary of the optical and electrochemical behaviors of the polymers.....	272



## LIST OF SCHEMES

Scheme 1.1	The preparation of PDIs with various substituents on the imide positions.....	5
Scheme 1.2	The preparation of PDIs with various substituents on the imide positions.....	6
Scheme 1.3	The two methods for the preparation of asymmetrical PDIs with different substituents on each imide position.....	9
Scheme 1.4	The preparation of PDIs with various substituents in the bay positions.....	13
Scheme 1.5	The preparation of PDIs with substitution on the 2,5,8,11-positions. ....	14
Scheme 2.1	The synthetic scheme for the two PDI homopolymers.....	81
Scheme 2.2	The synthetic scheme for the N-PDI homopolymer.....	83
Scheme 3.1	The synthetic scheme for the 5T and 6T monomers .....	136
Scheme 3.2	The synthetic scheme for the 5T and 6T homopolymers .....	136
Scheme 3.3	The synthetic scheme for the PDI-5T copolymers:.....	146
Scheme 3.4	The synthetic scheme for the PDI-6T copolymer: PDI-6T CPA .....	143
Scheme 4.1	The synthetic scheme for the PDI <sub>X</sub> (X = A to F) materials .....	177
Scheme 4.2	The synthetic scheme for the three new PDI materials .....	188
Scheme 5.1	The synthetic scheme for the dibromo-compounds .....	220
Scheme 5.2	The synthetic scheme for the dyads and donor model compound .....	221
Scheme 6.1	The synthetic scheme for the PDI-grafted monomers and respective polymers and the model materials. ....	265
Scheme 6.2	The synthetic scheme for the new polymer with 4-nitrophenyl pendants.. .....	281

## LIST OF ABBREVIATIONS

1PA	One-Photon Absorption
2PA	Two-Photon Absorption
CT	Charge-Transfer
Cp	Cyclopentadienyl
CS	Charge-Teparation
DCC	N,N'-Dicyclohexylcarbodiimide
DMAP	4-(Dimethylamino)pyridine
DMF	Dimethylformamide
DMAc	Dimethylacetamide
DSC	Differential Scanning Calorimetry
EA	Electron Affinity
FOM	Figure of Merit
GPC	Gel Permeation Chromatography
HOMO	Highest Occupied Molecular Orbital
HRMS	High Resolution Mass Spectrometry
IP	Ionization Potential
LUMO	Lowest Unoccupied Molecular Orbital
$M_n$	Number-average molecular weight
$M_w$	Weight-average molecular weight
NBS	N-bromosuccinimide
NIR	Near Infrared
NLO	Nonlinear Optical
NMR	Nuclear Magnetic Resonance
OD	Optical Density
P3HT	Poly(3-hexylthiophene)
PCz	Polycarbazole
PCBM	Phenyl-C61-butyric acid methyl ester
PDI	Perylene Diimide
PEDOT:PSS	Poly(3,4-ethylenedioxythiophene):poly(styrenesulfonate)
PL	Photoluminescence
PPV	Polyphenylenevinylene
ROMP	Ring Opening Metathesis Polymerization
TGA	Thermogravimetric Analysis
THF	Tetrahydrofuran
UV-Vis	Ultraviolet-Visible

Other abbreviations and symbols are explained in the text.

## SUMMARY

This dissertation described the investigation of the synthesis and characterization of new perylene diimide (PDI)-based photonic and electronic materials. In the first part of this thesis, PDI-based polynorbornenes, including PDI-grafted homopolymers and block-copolymers (BCPs) were designed, synthesized and characterized as alternative acceptors for fullerene derivatives in organic solar cells. It was found that the PDI pendants on the polymer side-chains affect  $\pi$ - $\pi$  stacking with the neighboring PDIs, which has implications for the use of these materials for organic field-effect transistors (OFETs) and organic photovoltaic devices (OPVs). It should also be noted that the performance of solar cell based on the PDI-grafted polynorbornenes was poor, like most other solar cells using PDI acceptors. One of the major reasons could be the challenge in controlling the molecular alignment of the PDI-based materials, which leads to much lower electron mobilities in films compared to devices with fullerene-based acceptors. One of the PDI-grafted BCPs showed much better OPV performance compared to the other BCPs and respective homopolymer blends, presumably due to favorable morphology. In the second part of this thesis, the photo-induced charge-separation in blends of poly-3-hexylthiophene (P3HT) and various PDI derivatives have also been studied. Probing of long-lived photo-generated PDI radical anions and P3HT polarons provided insight on these photo-induced processes, including the relationship between the yields of charge photo-generation and energy difference between the first singlet excited state of P3HT and final charge-separated states. In the third part of this thesis, the use of photo-generated PDI radical-anion absorption was shown to be effective for optical limiting of nanosecond

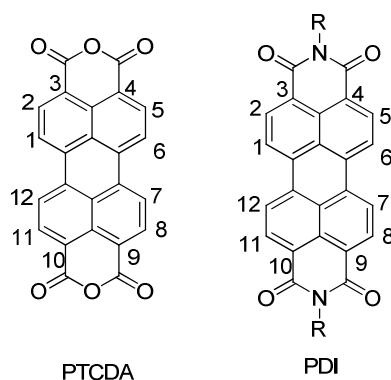
laser pulses between 650 – 800 nm. In Chapter 5, an effective approach for two-photon absorption (2PA)-induced optical limiting using donor-PDI dyads through which donors and acceptors can be independently chosen to maximize optical suppression at particular wavelengths has been demonstrated. This finding could be extended to other donor/acceptor pairs for optical suppression in other spectrum region. In Chapter 6, conjugated polymers with PDI pendants and poly(carbazole-*alt*-2,7-fluorene) main-chains were synthesized for optical limiting using the photo-generated PDI radical anion via PDI aggregate excitation and/or 2PA from the polymer backbones. It was also found that nitro-phenyl group or similar derivatives could be good candidates to incorporate into those donor-conjugated polymers, which have significant overlap between their 2PA band and respective polaron absorptions for 2PA-induced optical limiting.

# CHAPTER 1

## INTRODUCTION OF PERYLENE DIIMIDES

### 1.1 The use of perylene diimides as pigments in industry

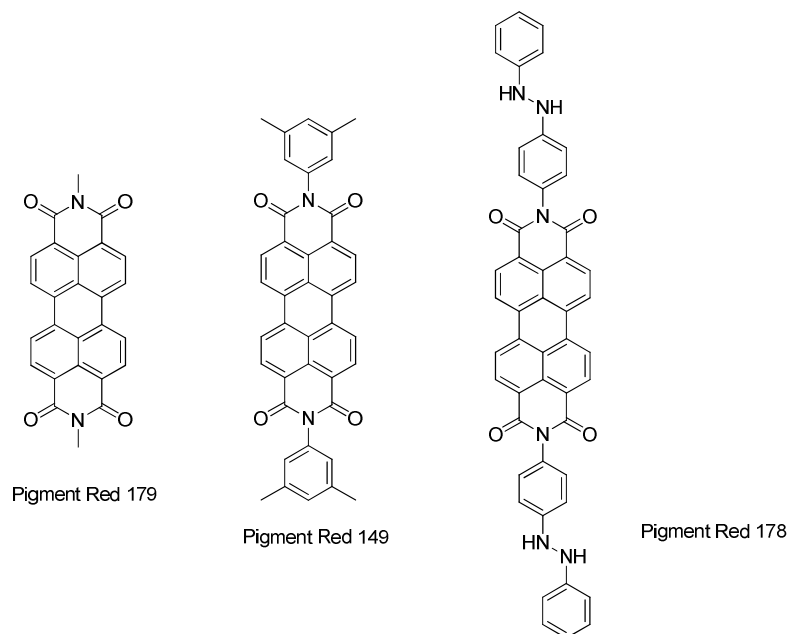
Perylene-3,4,9,10-tetracarboxylic acid diimide derivatives, also known as perylene diimides, or PDIs, are colorants that have been extensively studied as industrial dyes and pigments. Perylene-3,4,9,10-tetracarboxylic dianhydride (PTCDA), which is commonly considered as the parent compound of this class of dyes, was first described in 1912.<sup>1</sup> As shown in Figure 1.1, various perylene diimide dyes with different chemical and physical properties could be obtained via modification of the substituents on the imide (the R groups) or bay (the 1, 6, 7, 12 position on the core aromatic scaffold) positions.



**Figure 1.1. The chemical structures for PTCDA (left) and respective perylene diimides without bay-substitutions.**

A series of perylene diimides emerged (peryene dimethylimides, also named Pigment Red 179, was first reported in 1913), which were initially used exclusively for industrial purposes as pigments following the ground-breaking work of Harmon Colors in describing the conversion of vat dyes to pigments. As a group of high performance

pigments, perylene diimides exist in a wide range of colors from red to violet, and even shades of black.<sup>2</sup> In addition, these molecules exhibit excellent migration stability in plastics, easy over-coating when used as paints, chemically inert, superior thermal stability, and excellent light and weather stability.<sup>1,3</sup>



**Figure 1.2. The chemical structures of three widely used PDI-based industry pigments.**

Several perylene diimide derivatives, such as Pigment Red 179, Pigment Red 178, and Pigment Red 149 (as shown in Figure 1.2), have thus found their way into industrial scale production and applications since 1950.<sup>1</sup> Pigment Red 149 is a yellow shade red, while Pigment Red 178 and Pigment Red 179 are of blue shades because of different molecular packing of these pigments in the solid state.<sup>1,3</sup> From an economic point of view, the use of PDI-based pigments in those disposable articles is somewhat limited, due to the relatively high cost of these materials as pigments.<sup>1</sup> Today, PDI-based pigments are found predominately in fiber applications or in other high-grade industrial paints, where

their cost is outweighed by the high quality and/or durability of the colors, particularly in carpet fibers and automobile industry.<sup>1,3</sup>

Yet, while perylene diimides are important industrial pigments, they also combine a strong absorption in the visible region with almost unity fluorescence quantum yields, high photochemical stability, and many other interesting chemical and physical properties. These properties allow perylene diimides to be used as outstanding materials for many other new applications.<sup>3-13</sup> For example, perylene diimides feature a relatively low reduction potential (*ca.* -1.0 V and -1.2 V vs the ferrocene/ferrocenium ( $\text{FeCp}_2^{+/0}$ ) redox couple for the first and second half-wave reduction potentials, respectively), which enables their use as electron acceptors for organic electronics and other related research.<sup>3-4,7-8,13-17</sup> Up to this point in time, perylene monoimide and perylene diimide derivatives have been utilized in various electronic and optical applications, such as organic field-effect transistors (OFETs),<sup>13-14,16,18-20</sup> fluorescent solar collectors,<sup>21</sup> electrophotographic devices,<sup>22</sup> dye lasers,<sup>9-10</sup> organic photovoltaic cells (OPVs),<sup>16,23-25</sup> and optical power limiters (OPLs),<sup>26</sup> because of their appealing physical, optical, and electronic properties.

In addition to application-directed research in fields such as OFETs and OPVs, functionalized perylene diimides have also been extensively studied in fundamental research on photo-induced energy- and electron-transfer processes because of their easily identifiable excited-state and anion absorption.<sup>3,5,27-31</sup> Such research not only provides details for understanding complex energy- and electron-transfer reaction but also benefits many related research areas. In particular, researchers in the field of OPVs have benefited from studies of photo-induced charge-transfer involving PDI-based acceptors, which is a key step in the overall photovoltaic process.<sup>32-34</sup>

Recently, research attention has increasingly focused on using perylene diimides as active semiconducting materials in the field of organic electronics. Perylene diimides are still one of the most promising electron-transport materials available to date with a low electron affinity (EA,  $\sim -3.9$  eV for unmodified PDIs, closed to C<sub>60</sub> and its derivatives), the potential for good molecular ordering in the solid state, and facile chemical functionalization as compared to fullerene-based acceptors.<sup>3,24,35</sup> These features make PDI-type materials promising candidates for applications in *n*-channel OFETs.<sup>4</sup> In addition, based on their unique combination of optical and redox properties and thermal- as well as photo-stability, PDI-based materials have also been widely investigated within fields such as optical limiting and OPVs.<sup>22,24,26</sup>

The major research effort in this thesis focuses on utilizing the optical and electronic properties of functionalized perylene diimides for applications of OPVs and optical limiting via fine tuning of the molecular structures and properties. A review of the material syntheses, physical properties, and the various applications of perylene diimide derivatives are given in this chapter.

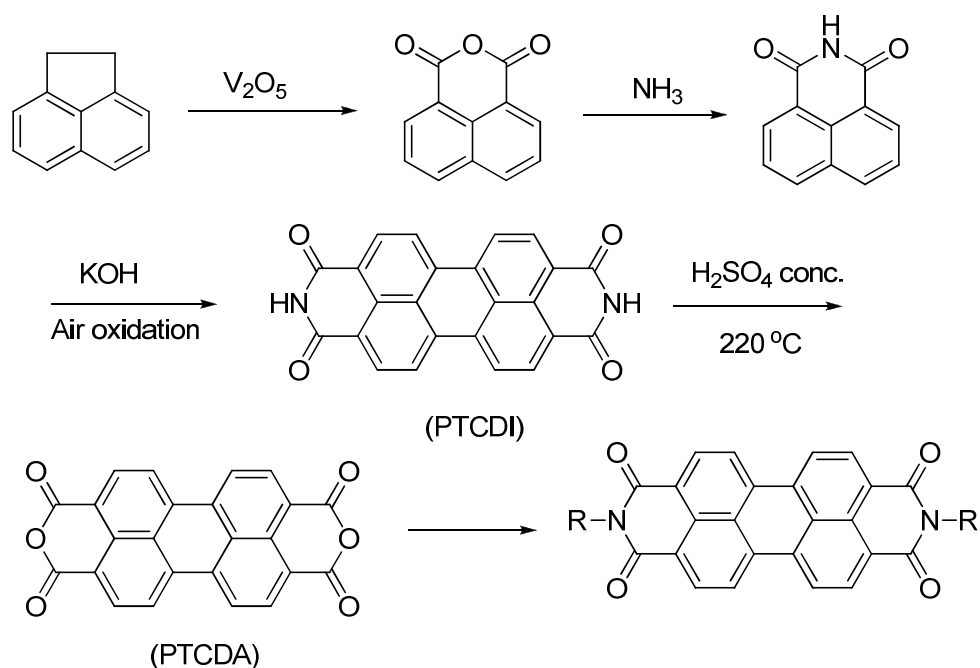
## **1.2 Preparation of PDI derivatives**

### **1.2.1 Preparation of PDIs with substituents on the imide positions**

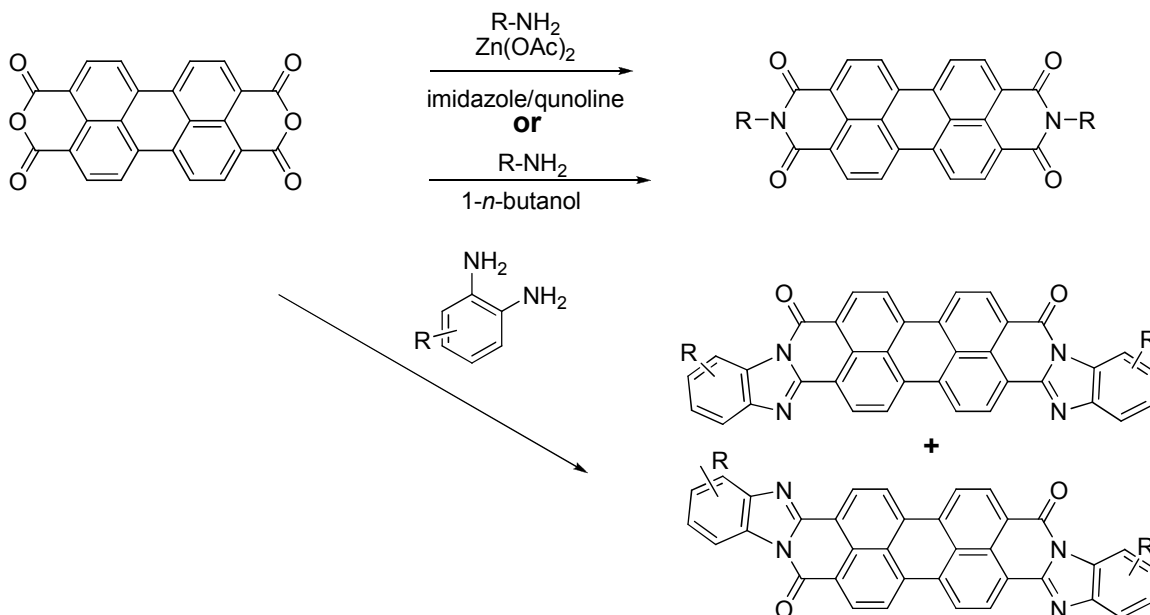
In both the research laboratory and the industrial setting, the primary starting material for synthesizing perylene diimide derivatives is PTCDA. The condensation reaction between PTCDA and an alkyl amine or an aniline results in the formation of respective perylene diimide derivatives in high yield.<sup>1,3</sup> As shown in Scheme 1.1, the industrial scale synthesis of PTCDA starts from the oxidation of acenaphthene by air to give naphthalic anhydride, which is subsequently treated with ammonia to provide 1,8-



naphthalene dicarboxylic acid imide. Perylene,3,4,9,10-tetracarboxylic diimide (PTCDI) is obtained by fusing 1,8-naphthalene dicarboxylic imide with caustic alkali, for instance in potassium hydride at 190 to 220 °C, followed by air oxidation of the molten reaction mixture. PTCDA is then synthesized by hydrolyses of the PTCDI solid with concentrated sulfuric acid at ~ 220 °C. In the dye and pigment industries, insoluble and symmetrical organic perylene diimides with high melting points can be easily obtained in high isolated yields from the reactions between PTCDA and various aliphatic amines or aromatic aniline.<sup>1</sup> For example, most insoluble perylene diimide dyes, such as Pigment Red 179, Pigment Red 178, and Pigment Red 149, have yields over 90% in industrial scale synthesis via PTCDA and respective amines and aniline.<sup>1</sup>



**Scheme 1.1. The preparation of PDIs with various substituents on the imide positions.**



**Scheme 1.2. The preparation of PDIs with various substituents on the imide positions.**

Other than the need to prepare insoluble and high melting point PDI-based dyes for the pigment industry, most current research on perylene diimides is related to organic electronics, photo-induced processes, and supramolecular organization, which requires PDIs with reasonable solubility in common solvents.<sup>3</sup> Consequently, synthetic methods in making highly soluble perylene diimides were developed, and there are currently two different strategies that have proved to be successful. The most common method of preparing symmetrical perylene diimides was first described by Langhals and coworkers in the 1990s. They improved the solubility of PDI dyes by incorporating solubilizing substituents, such as branching alkyl groups at the PDI imide positions.<sup>36</sup> The other, synthetically more elaborate, strategy is to incorporate substituents, such as phenyl groups, at the “bay-positions” of the PDI aromatic cores (*i.e.* 1,6 position or 1,7 positions) to break the strong  $\pi$ – $\pi$  interactions of these chromophores for better solubility in

common organic solvents.<sup>3,35</sup> Water-soluble perylene diimides were also reported recently by incorporating water-soluble substituents, including Newkome-type carboxylates,<sup>37</sup> phosphate surfactants,<sup>38</sup> and other polar but uncharged moieties, such as polyglycerol dendrons<sup>39</sup> and cyclodextrin,<sup>40</sup> in the imide positions using the strategy similar to that described by Langhals.

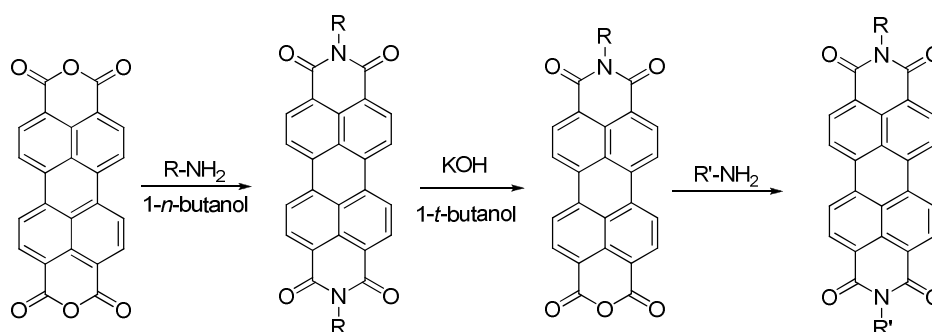
As shown in Scheme 1.2, there are several methods to obtain soluble perylene diimide dyes by attaching substituents to their imide positions. The most common procedure in synthesizing symmetrical PDI derivatives is the condensation reaction of PTCDA with aromatic aniline and aliphatic primary amines in high boiling point solvents such as imidazole or quinioline (boiling point > 160 °C) with ~ 10 to 30% molar ratio anhydrous Zn(OAc)<sub>2</sub> as catalyst. The isolated yields of these reactions approach 95% for most cases, with relatively simple purification procedures.<sup>3,35-36</sup> Another important method for symmetrical PDI synthesis is treating PTCDA (or more reactive PTCDA-type starting materials with aromatic core dibromo- or tetrachloro-substitutions) with reactive amines in hot alcohol (such as *n*-butanol), carboxylic acid (such as acetic acid and propionic acid), or mixtures of alcohol and water with isolated yields over 90%.<sup>35</sup> Compared to the first synthetic method, the latter is more suitable for preparing dibromo- or tetrachloro-aromatic-bay-substituted PDIs, since there are fewer side reactions, such as nucleophilic substitution at the halogenated PTCDAs, which results in replacement of the halogen atoms.<sup>35</sup> Furthermore, it has been found that perylene benzoimidazole derivatives can also be obtained via the similar condensation reaction between PTCDA and respective *o*-phenylenediamine derivatives in good to excellent isolated yields. Generally, a mixture of two regioisomers can be obtained in the synthesis of benzoimidazole

derivatives and the separation of the isomers is challenging using common purification methods, such as column chromatography and recrystallization.<sup>35</sup>

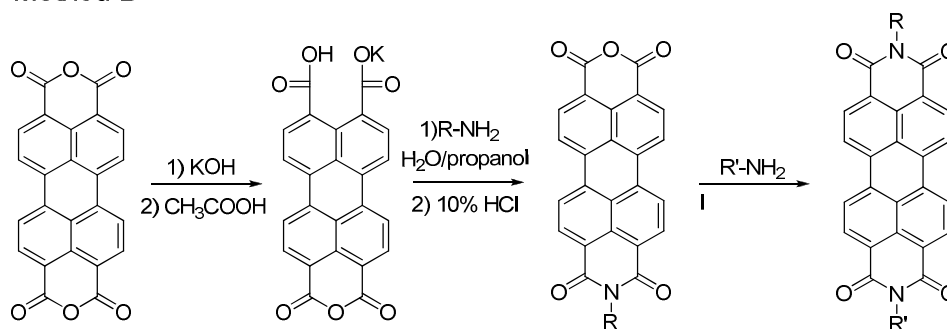
Asymmetrically substituted perylene diimides with different substituents on each imide position have also been reported recently. Attempts at one-pot formation of asymmetrically substituted perylene diimides by performing the reaction with either simultaneous or sequential addition of two different amines are usually unsuccessful because of the small differences in reactivity of the amines with PTCDA. Typically, only traces of the desired products are observed, with the dominant species being the respective symmetrical PDI-based materials.<sup>35</sup> There are currently two general methods to synthesize PDI derivatives with different substituents on the imide positions via multistep organic synthesis.<sup>35</sup> As shown in Scheme 1.3, the first synthetic method for asymmetrical substituted perylene diimides actually starts from preparing the respective symmetrical PDI dyes. Hydrolysis of symmetrical perylene diimides gives the respective perylene monoimide monoanhydride compounds in ~ 50% yield. Further imidization reaction of the perylene monoimide monoanhydride derivative with a second amine or aniline is used to introduce the other substituent in creating the desired asymmetrical perylene diimides. It is worth mentioning that it is challenging to synthesize a perylene monoanhydride monoimide compound directly from PTCDA with respective primary amine because it is hard to ensure that the condensation reaction occurs at only one site. Generally, symmetrical perylene diimides are always the dominant products even when only one equivalent or less of the primary amine is added to the reaction mixture. The synthesis of perylene imide benzimidazole was also reported using this method.<sup>41</sup> Another practical approach for asymmetrical PDI synthesis was first described by Tam-

Chan and coworkers,<sup>42</sup> wherein the target asymmetrical PDI dyes were prepared via the perylene monoanhydride salt from the hydrolysis of PTCDA, followed by further functionalization reactions such as imidizations, as shown in Scheme 1.3. In this thesis, the first synthetic method was chosen in preparing the symmetrical PDI-based dyes for further modification because of the higher yield and easier purifications.

#### Method A



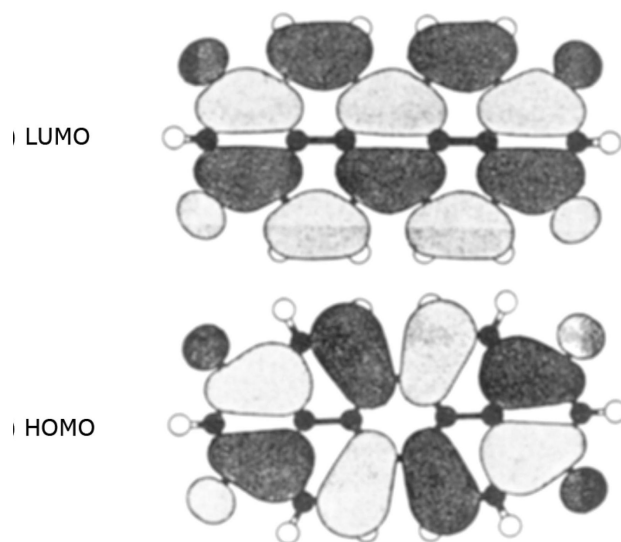
#### Method B



**Scheme 1.3. The two methods for the preparation of asymmetrical PDIs with different substituents on each imide position.**

The perylene diimides obtained from the above synthetic approaches by incorporation of different substituents on each imide position usually exhibit indistinguishable absorption and emission properties from the respective symmetrical

perylene diimides, particularly in solution at low concentrations when the molecular aggregation is limited. This is because the nodes in the highest occupied molecular orbital (HOMO) and lowest unoccupied molecular orbital (LUMO) at the imide positions of perylene diimides reduce the electronic coupling between PDI aromatic cores and imide substituents to a minimum, as shown in Figure 1.3.<sup>3,35</sup> It should be noted that the major electronic effect from the imide group will be only inductive in nature. As a result there is little change in the electronic properties of perylene diimides with various imide substituents (*ca.* < 0.1 eV change on PDI's LUMO upon switching from phenyl to perfluorophenyl on the imide positions).<sup>20</sup> It is beneficial to be able to control the solubility as well as the molecular packing in the solid state of the materials by incorporating different side-chains at the PDI imide positions without significantly changing their optical and electronic properties.<sup>3,35</sup>



**Figure 1.3. The frontier orbitals (HOMO and LUMO) of perylene diimides.<sup>2-3</sup> Reprinted with permission from ref 2. Copyright 1994 American Chemical Society.**

### 1.2.2 Preparation of PDIs with various substituents on the bay positions

Another method for synthesizing highly soluble perylene diimides is to introduce functional groups in the “bay-region” of PDI aromatic cores. The chemistry of introducing substituents in the bay-position of perylene diimides was first developed by Seybold and coworkers at BASF in the late 1980s.<sup>3,43</sup> According to this first report, four phenoxy groups were incorporated onto the tetrachloro-bay-substituted perylene diimide via nucleophilic substitution to replace chlorine atoms in the PDI bay positions (as shown in Scheme 1.4). Recently, the synthesis of tetrafluoro-bay-substituted perylene diimides were synthesized in reasonable yields from the respective tetrachloro-bay-substituted starting materials, as reported by Würthner and coworkers.<sup>44-45</sup> However, the introduction of many other nucleophiles on the PDI’s aromatic scaffolds proved to be difficult and successful cases were rare. Although the procedure for four fold chlorination of PTCDA had already been known since 1985,<sup>46</sup> only recently was it discovered that the bromination of PTCDA could afford dibromo-bay-substituted PTCDA, which could be further converted into dibromo-substituted perylene diimides.<sup>47</sup> However, the crude product mixture obtained from the bromination reaction is more complicated than that of the chlorination of PTCDA, since one- and three-fold bromination products, as well as significant amounts (~ 10 – 20%) of a second dibromo-substituted regioisomer (1, 6-dibromo-PDI), are formed. Furthermore, each dibromo-bay-substituted PDI regioisomer from the latter dibromo-PTCDAs cannot be easily purified from the product mixture and is only detectable using high field (> 400 MHz) proton NMR spectroscopy.<sup>3,48</sup>

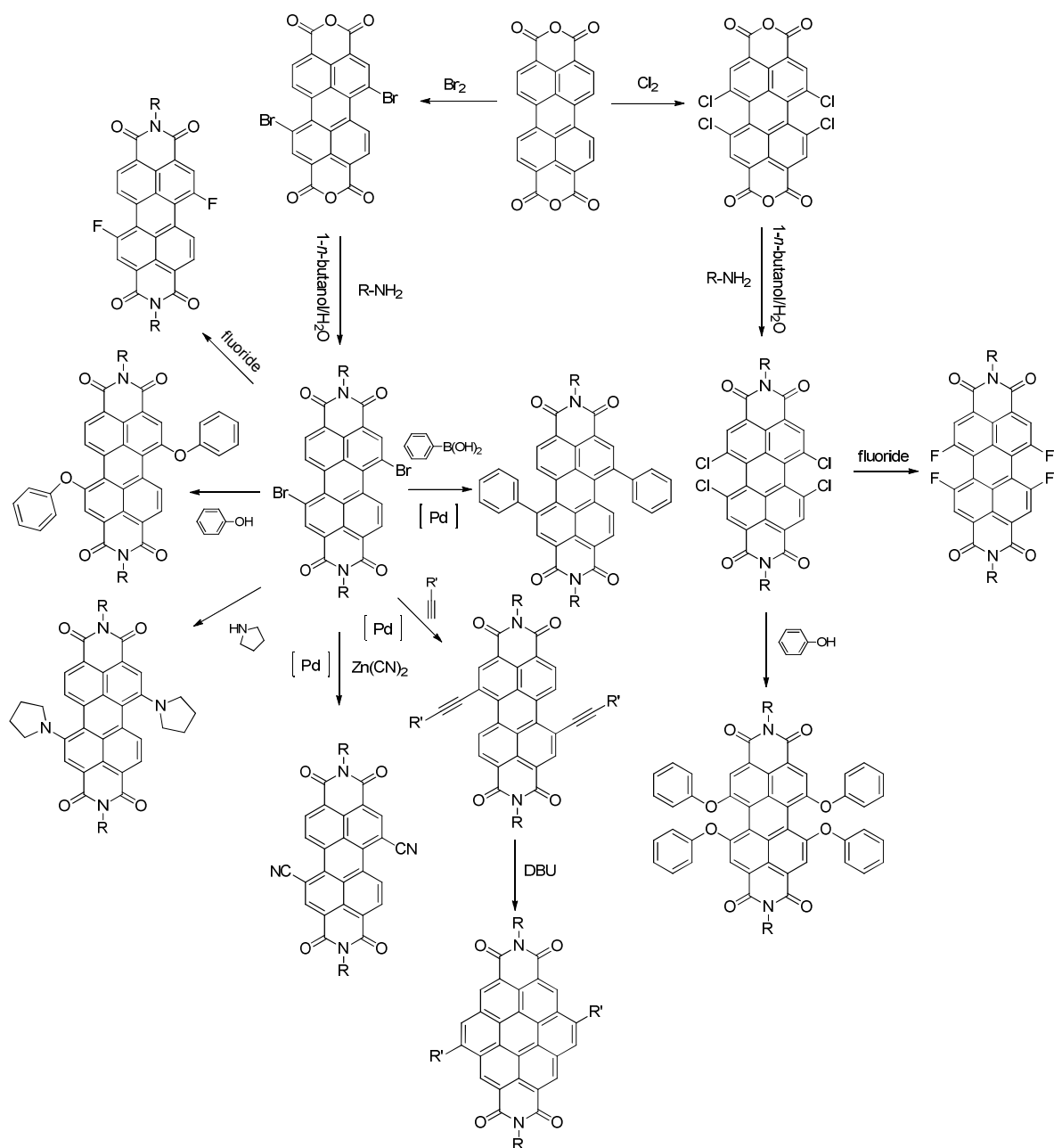
### 1.2.3 Preparation of PDIs with various substituents on the other positions

Recently, it was also discovered that facile, direct bromination of perylene diimides under controlled conditions is possible, although mono-, di-, and tribrominated PDIs are also obtained, with two isomers of the dibrominated PDIs. Harsh reaction conditions, such as heating (*ca.* 60 °C), allows the bromination to go on to exclusively affording the bay-dibromo-substituted PDIs as the dominant products with good yields and shorter reaction time, but this does not yield a higher ratio of the 1,7 dibromo-substituted isomer.<sup>49</sup> Only very recently, it was reported that some isomerically pure 1,7-dibromo-substituted perylene diimides could be obtained after multiple recrystallizations with low isolated yields by Würthner and coworkers.<sup>3,48</sup>

Replacement of the halogen atoms in aromatic cores via nucleophilic substitution on these dibromo-bay-substituted or tetrachloro-bay-substituted perylene diimides is relatively straightforward, and generally products can be isolated in relatively high yields. Currently, fluoride, cyanide, thiophenol, alcohol, phenol, and amine based nucleophiles have been coupled to the perylene diimide cores, leading to various PDI derivatives with interesting optical and electronic features (as shown in Scheme 1.4), because of the direct electronic coupling between the new substituents and the perylene diimide cores.<sup>3,19,36,50</sup> Moreover, transition-metal catalytic C-C coupling reactions, such as Suzuki coupling,<sup>51-52</sup> Stille coupling,<sup>16,53</sup> and Sonogashira coupling,<sup>29,54</sup> have been applied in preparing functionalized perylene diimides from the bay-dibromo-substituted perylene diimides. Isomers of some of these new developed dyes can be separated via column chromatography if bulky substituents, such as triphenylsilane acetylene, are incorporated.<sup>19</sup> Furthermore, from the PDI-based acetylenic derivatives prepared through Sonogashira synthesis, corenene diimide derivatives, with extended conjugated scaffold

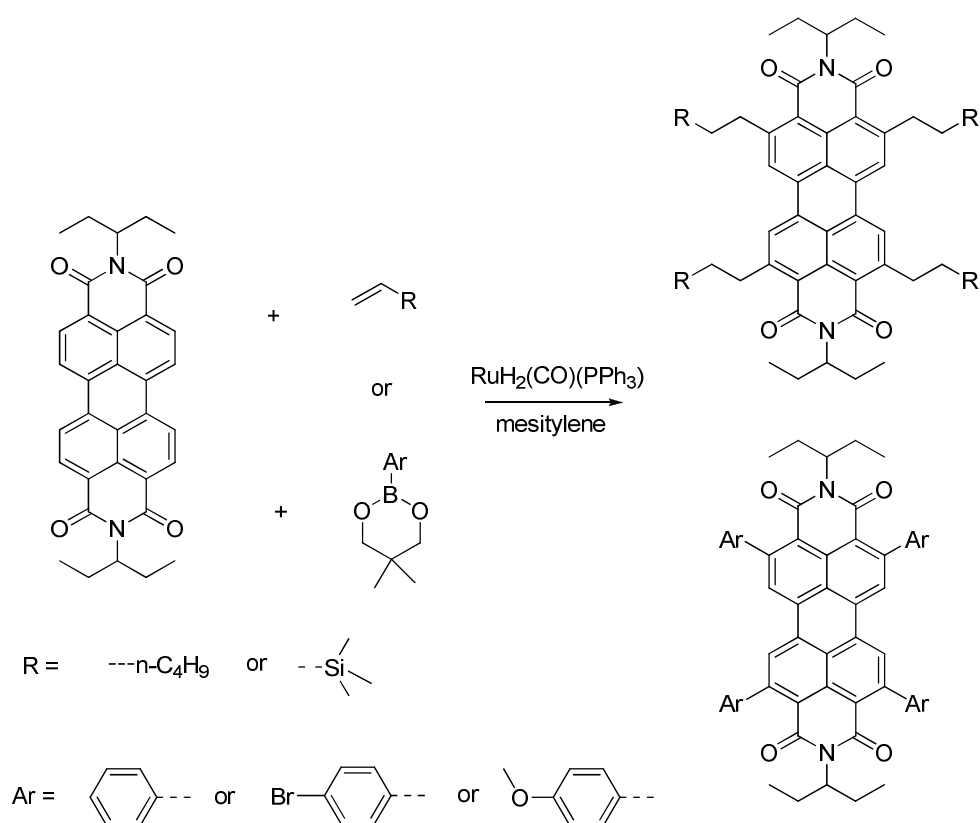


as compared to respective PDI dyes, can be synthesized via simple reactions, as described by Müllen and coworkers.<sup>54-55</sup>



**Scheme 1.4.** The preparation of PDIs with various substituents in the bay positions.

On the other hand, a synthetic procedure for 2,5,8,11-substituted perylene diimides has been unavailable until very recently. Ru-catalyzed C-H bond activation is effective for direct arylation<sup>56</sup> or alkylation<sup>57</sup> of perylene diimides at 2,5,8,11-positions, as illustrated in Scheme 1.5. Introduction of alkyl groups at PDI's 2,5,8,11-positions significantly enhances their solid state emission as well as their solubility in organic solvents without causing any serious distortion of the PDI core.<sup>57</sup> Both electron-rich and electron-deficient aryl groups can be incorporated in perylene diimides with satisfactory yields. The electronic nature of aryl substituents has a significant impact on their optical and electrochemical properties, because the HOMO and LUMO levels are substantially influenced by the aryl substituents at PID's 2,5,8,11-positions.<sup>56</sup>



**Scheme 1.5. The preparation of PDIs with substitution on the 2,5,8,11-positions.**

More recently, 1,2,5,6,7,8,11,12-octachloroperylene-3,4:9,10-tetracarboxylic diimide was obtained as an orange solid by chlorination of perylene-3,4:9,10-tetracarboxylic diimide in chlorosulfonic acid at 80 °C in high yield. However, due to the limited solubility of this material, multiple recrystallizations in N-methylpyrrolidone (NMP) and acetic acid, followed by gradient sublimation, are required to ensure sufficient purity for OFET applications.<sup>58</sup>

The solubility of PDI derivatives strongly depends on the substituents on the imide positions and/or in the bay positions. It was found that perylene diimides with long di-swallowtails<sup>59</sup> or *ortho*-substituted phenyl groups<sup>60</sup> as the two *N*-terminal groups typically showed good solubility. The usual explanation for this observation is that the bulky substituents are forced out of the molecular plane of the chromophore, thereby hampering the face-to-face  $\pi$ - $\pi$  stacking of the PDI molecules, thereby increasing the solubility of these molecules.<sup>3,59-60</sup> Similarly, substituents on the aromatic bay-region could lead to a propeller-like twisting of the two naphthalene half units in PDI-based materials. This has also been found to be an efficient way to prevent the face-to-face  $\pi$ - $\pi$  stacking and improve the solubility of PDI materials. In general, the incorporation of bulky groups on the bay positions could result in an increase of several orders-of-magnitude in the solubility of the perylene diimides.<sup>61</sup> For example, 1,(6)7-dibromo-substituted *N,N'*-dioctyl-perylene 3,4,9,10-tetracarboxylic acid diimide shows reasonable solubility in common organic solvents while the non-bay-brominated analogue is insoluble in most organic solvents. It is worth noting that halogenated solvents such as chloroform, chlorobenzene, and dichloromethane seem to be good organic solvents for common PDI derivatives at room temperature. The ability to work with soluble PDI

materials allows for them to be used in the fabrication organic electronic devices by solution processing.

### **1.3 Physical properties of PDIs**

PDI derivatives exhibit a combination of interesting absorption, emission, redox, and other physical properties, which has results in significant research on these materials for various applications, including OPVs and OFETs.<sup>3,24</sup> A short review about some of these physical properties and the respective potential applications of perylene diimide derivatives is given as follows. Reviews about PDI-based materials can also be found in the literature.<sup>3,24,35</sup>

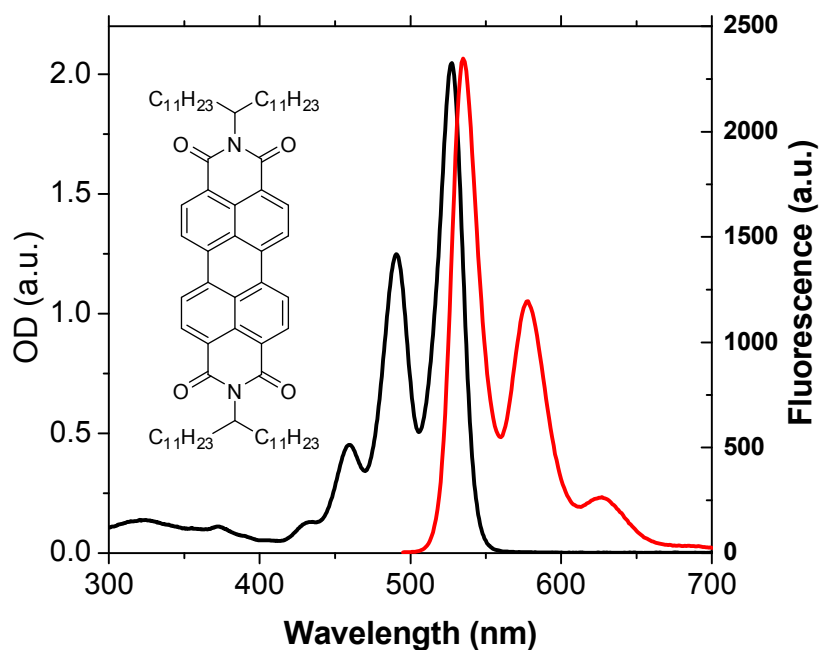
#### **1.3.1 Optical properties of PDIs**

Most PDI-based chromophores are red solids with high melting points and excellent photo- and thermal-stability. However, PDI-based pigments with orange, maroon, bluish black, and even black color are also known due to, in some cases very pronounced aggregation effects, leading to the observed variation in solid absorption spectra.<sup>1-3</sup> In general, perylene diimides are considered as a group of excellent organic dyes with large absorption extinction coefficients at visible wavelengths (400 – 600 nm), almost unity fluorescence quantum yields, and long singlet-excited-state life-times (approximately 4 ns in common organic solvents).<sup>3,24,35</sup>

Typical perylene diimide type absorption and emission spectra are shown in Figure 1.4, and the optical properties of some PDI dyes in common organic solvents are summarized in Table 1.1. Generally, perylene diimides are characterized by a vibronically structured band with strong absorption in the visible region between 400 to 550 nm, and they exhibit a strong yellow-green fluorescence as a mirror image of the

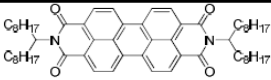

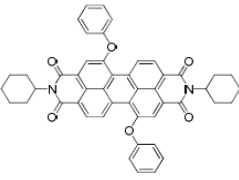
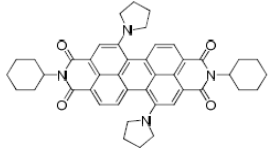
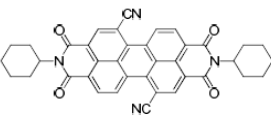
absorption in common organic solvents.<sup>3</sup> It has been reported that the electronic transitions for unsubstituted perylene diimides are predominantly HOMO to LUMO transitions.<sup>3</sup> The absorbance of the (0,0) vibronic transition at  $\sim 527$  nm and the (0,1) vibronic band at  $\sim 490$  nm for free PDI molecules in solution shows the relationship as  $(0,0)/(0,1) > 1.6$ , though molecular aggregation of PDI dyes causes a significant decrease in this value.<sup>3,62</sup> Similar phenomena are also observed in the emission spectra for perylene diimides in solution. Generally, a change of less than 5 nm in the absorption and emission maximum can be observed by changing the *N*-terminal groups (examples are shown in Table 1.1). In contrast, substituents on the aromatic core bay-positions show a much more obvious effect on the absorption and emission spectra of perylene diimides as expected, due to the stronger electronic coupling between the PDIs'  $\pi$ -orbital and the substituents on the aromatic bay region. For example, two phenoxy substituents on the PDIs' bay positions result in  $\sim 20$  nm and 40 nm bathochromic shifts in the absorption and emission maximum ( $\lambda_{\text{absm}}$  and  $\lambda_{\text{emm}}$ ), respectively, compared to that of the unsubstituted PDI dyes and the color of the fluorescence changes to orange.<sup>3,63</sup> More pronounced spectral changes occur upon substitution of the aromatic cores with electron donors such as pyrrolidino groups, which affords PDI derivatives with a dark-green color both in the solid state and solution, due to the bathochromic shift over 150 nm. Only weak emission can be observed in the near infrared (NIR) region. Because such a large spectral shift is associated with the amino to PDI internal charge-transfer (ICT) character, some solvatochromism is observed for these PDI derivatives, and their fluorescence quantum yields (QY = 35%, in toluene) are largely decreased.<sup>3,19,64</sup> In contrast, limited spectral changes and solvatochromism effect are observed if electron-withdrawing substituents

(like F, Cl, Br, and CN) are incorporated into perylene diimides in the bay position because inductive effect of such  $\sigma$ -acceptors in general will lower both the LUMO and HOMO levels in similar manner and there is no obvious ICT present in these systems.<sup>3,44,48,50</sup> Usually, there are several nanometer red-shifts of the  $\lambda_{\text{absm}}$  and  $\lambda_{\text{emm}}$  for these compounds because the  $\sigma$ -acceptors stabilized the LUMO slightly more than the HOMO, consequently narrowing the energy gap, probably due to be more pronounced electron coupling between the PDI LUMO to the attached acceptors. Moreover, limited change in the FQY was commonly observed for PDIs with electron-withdrawing substituents on the bay positions.



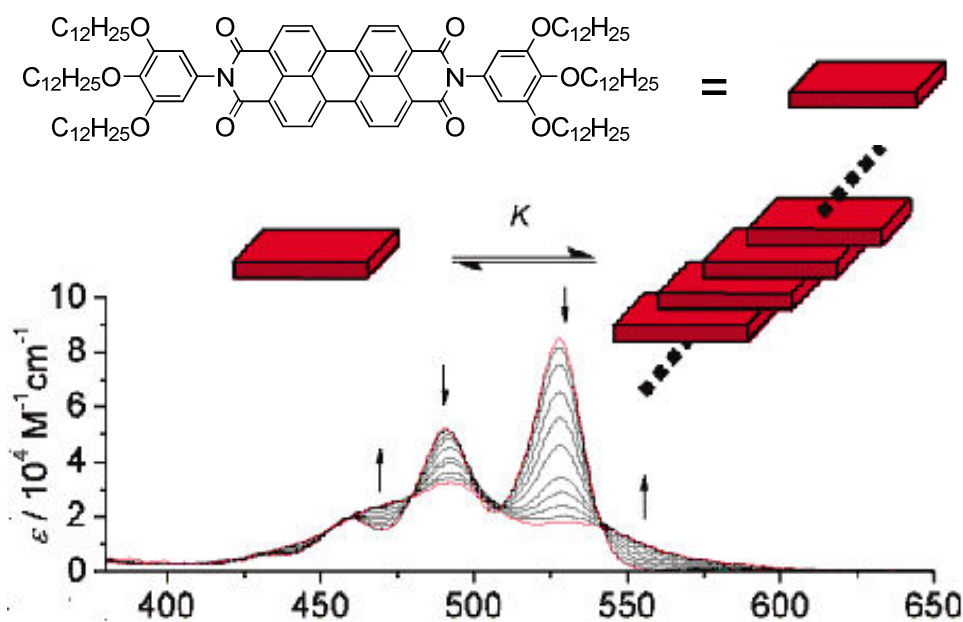
**Figure 1.4.** The UV-Vis absorption and emission spectra of a perylene diimide in toluene.

**Table 1.1. The optical properties of some perylene diimide dyes.**

Materials	$\lambda_{\max}^{\text{abs}}$ (nm)	$\epsilon$ ( $\text{M}^{-1}\text{cm}^{-1}$ )	$\lambda_{\max}^{\text{em}}$ (nm)	<i>QY</i>
 (in $\text{CH}_2\text{Cl}_2$ )	526	88000	533	100%
 (in $\text{CH}_2\text{Cl}_2$ )	526	94000	537	100%
 (in toluene)	549	55000	578	100%
 (in toluene)	686	46000	721	35%
 (in toluene)	530	47000	545	100%

In addition, optical properties of PDI-based dyes are highly dependent upon concentration and environmental conditions, such as solvent polarity and temperature.<sup>3</sup> For example, aggregation between the aromatic scaffolds in higher concentration ( $> 10^{-4}$  mol/L) solutions results in a large bathochromic shift and broader absorption, with a tail absorption that extends into the NIR for PDI derivatives.<sup>3</sup> As shown in Figure 1.5, the

concentration-dependent (concentration range  $10^{-7}$  to  $10^{-5}$  mol/L) UV-Vis absorption of the perylene diimide dyes in a low-polarity solvent such as methylcyclohexane (MCH) revealed significant changes of the absorption spectra upon changing the concentration. The strong aggregation caused by  $\pi$ - $\pi$  interactions led to an almost complete loss of fine structure in the absorption spectra.<sup>3,65</sup> For better solvents, such as  $\text{CHCl}_3$ , the dependence of PDI's aggregation on concentration was not as pronounced; no obvious PDI-aggregation is observed, as indicated by absorption spectroscopy, with concentrations up to  $10^{-5}$  mol/L for most cases.<sup>3</sup>

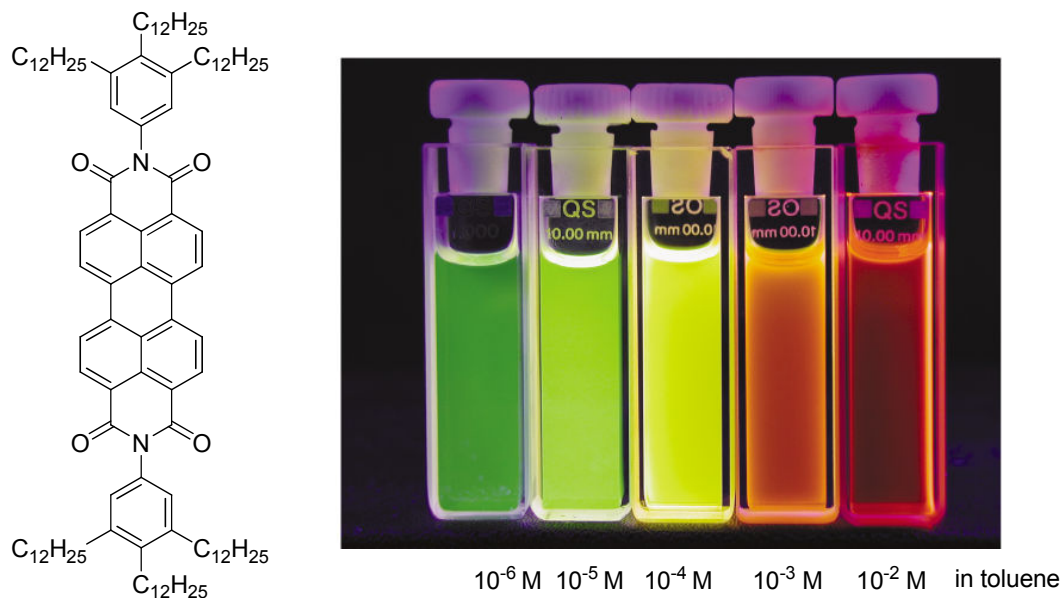


**Figure 1.5.** The concentration-dependent UV-Vis absorption of the perylene diimide in MCH.<sup>3,65</sup> Reproduced by permission of the Royal Society of Chemistry.

Similar observations were found for PDI's emission spectra as a function of increasing concentration. The behavior of a perylene diimide in toluene is shown in Figure 1.6. More aggregate-type emission and decreased fluorescence quantum yields



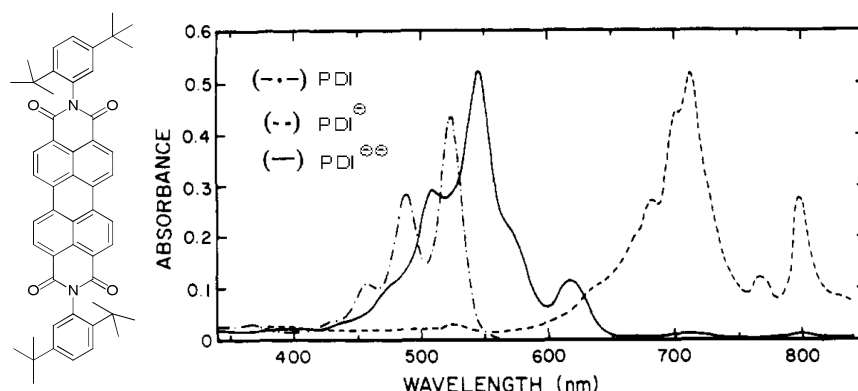
were observed with increasing dye concentration in toluene (concentration range  $10^{-6}$  to  $10^{-2}$  mol/L).<sup>3,63</sup> The aggregation of PDI-based dyes have been widely studied and used for applications such as supramolecular organization.<sup>3</sup>



**Figure 1.6. The concentration-dependent emission of the perylene diimide in toluene.**<sup>3,63</sup> Reproduced by permission of the Royal Society of Chemistry.

As mentioned earlier, functionalized perylene diimides are often used for fundamental photo-induced charge-transfer studies because of the easily identified PDI radical anion(s) absorption spectra in the Vis-NIR region.<sup>66</sup> The absorption from a perylene diimide and its respective chemically generated anions are shown in Figure 1.7. The value of the absorption coefficient for the PDI radical anion at 713 nm is *ca.*  $1.0 \times 10^5 \text{ M}^{-1}\text{cm}^{-1}$ , while the dianion shows an absorption coefficient of *ca.*  $1.0 \times 10^5 \text{ M}^{-1}\text{cm}^{-1}$  peaked at 546 nm. Substituents at the imide positions show limited effect on the anion absorption spectra while substituents at the bay region cause considerable change in the

shape and peak positions. These effects are similar to the substituents effects on the neutral PDI compounds.<sup>29,64</sup> The distinct features of these absorptions make it easy to determine the rate of each electron-transfer reaction in functionalized PDIs. Photo-induced intermolecular charge-transfer between PDI-based acceptors and other electron donors, such as polythiophenes, or intramolecular charge transferred within those PDI-based donor-acceptor type materials have been extensively studied using transient absorption spectroscopy.<sup>3,6,19,27</sup> This research provides not only insight into photo-induced charge-transfer process of PDI-based materials, but also valuable information for other technological applications, such as OPVs and optical limiting, where the photo-physical processes following photo-excitation play an important role.

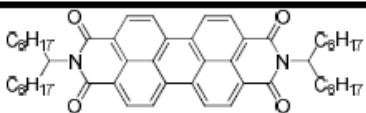
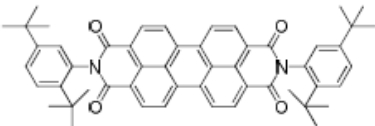
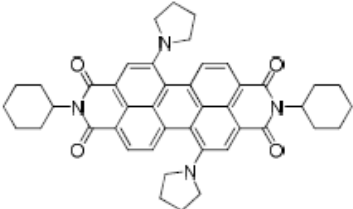
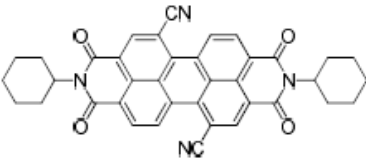


**Figure 1.7.** PDI anion(s) absorption in ethanol ( $1 \times 10^{-4}$  mol/L tetramethylammonium hydroxide) obtained by controlled reduction with  $H_2$  in the presence of Pt. The concentration for neutral PDI was 5.4 pM.<sup>66</sup> Reprinted with permission from ref 66. Copyright 1994 American Chemical Society.

### 1.3.2 Redox properties of PDIs

The electrochemical properties of perylene diimide derivatives have been widely investigated by different research groups, and some electrochemical data (referenced to  $Fe(Cp)_2^{+/0}$ ) for PDI-based materials is summarized in Table 1.2.<sup>3,50,64,67-68</sup>

**Table 1.2. Redox properties of some PDI dyes.**<sup>3,50,64,67-68</sup>

Materials	$E_{\text{red}}(\text{PDI}^{2-/1-})$ (V)	$E_{\text{red}}(\text{PDI}^{1-/0})$ (V)	$E_{\text{ox}}(\text{PDI}^{0/1+})$ (V)
 (in CH <sub>3</sub> CN)	-1.21	-0.98	+1.21
 (in CH <sub>3</sub> CN)	-1.15	-0.93	+1.25
 (in PrCN)	-1.46	-1.28	+0.16
 (in PrCN)	-0.92	-0.59	N.A.

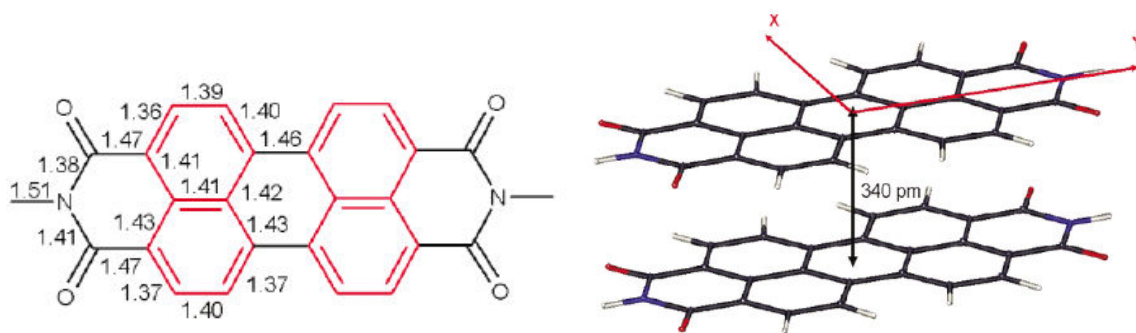
Perylene diimides without modification of their core bay-region are good electron acceptors, and they are quite easily reduced and rather difficult oxidized in solution. For most unsubstituted perylene diimides, two reversible reduction waves and one reversible oxidation wave (*ca.* -1.0 V and -1.2 V vs.  $\text{Fe}(\text{Cp})_2^{+/0}$ , respectively) can be observed if

appropriate organic solvents are chosen.<sup>3</sup> Generally, perylene diimides exhibit a first reduction potential comparable to that of C<sub>60</sub> and its derivatives, which makes them attractive acceptors for replacing fullerene derivatives in photovoltaic applications with their relatively lower cost in comparison to C<sub>60</sub>-based acceptors, as well as better light-harvesting and ease of chemical modification.<sup>3,68</sup> As was the case for their optical behavior, relatively small effects on the redox properties of perylene diimides in solution (in general less than 100 mV on the reduction and oxidation half-wave potential) are observed from variation of the substituents at the imide positions.<sup>3,20</sup> However, the substituents in the core bay-area have pronounced effects on the redox potentials.<sup>3,8,14,52</sup> For example, perylene diimides with cyano or fluoro substituents in the bay positions are over 0.3 V more easily reduced and have a much higher oxidation potential than unmodified PDI-based compounds.<sup>3,50</sup> This change in the redox properties is primarily due to the inductive effect from the electron withdrawing groups, which could stabilize the perylene diimides by lowering the energy of both the HOMOs and LUMOs to a similar extent. However, with electron donating pyrrolidino groups at the bay-positions, a quasi-reversible oxidation wave can be observed, and the reduction potential of the material becomes ~ 0.3 V more negative, due to the electron donating effect of the amino moieties.<sup>3,64,67</sup> PDI derivatives with conjugated substituents in the bay positions are generally somewhat more readily reduced compared to unsubstituted perylene diimides regardless of whether  $\pi$ -donor or  $\pi$ -acceptor groups are attached.<sup>29</sup> This is probably due to the extension of conjugation as conjugated substituents are incorporated in their core bay-positions.<sup>29</sup>

It appears that since the substituents at imide position show only limited effect on optical and redox properties of perylene diimides, various functional groups have been attached to the imide positions in order to tune the solubility and molecular packing in the solid state, while their PDI-based remains largely unaffected. On the other hand, efforts on preparing perylene diimides with various optical and electrical characteristics have been carried out by introducing functional groups at the bay-positions of perylene diimides.<sup>3,50,64,67,69-70</sup> Currently, both approaches have been found to be effective in improving the device performance of PDI-based OFETs and OPVs.<sup>16,25,53,71</sup>

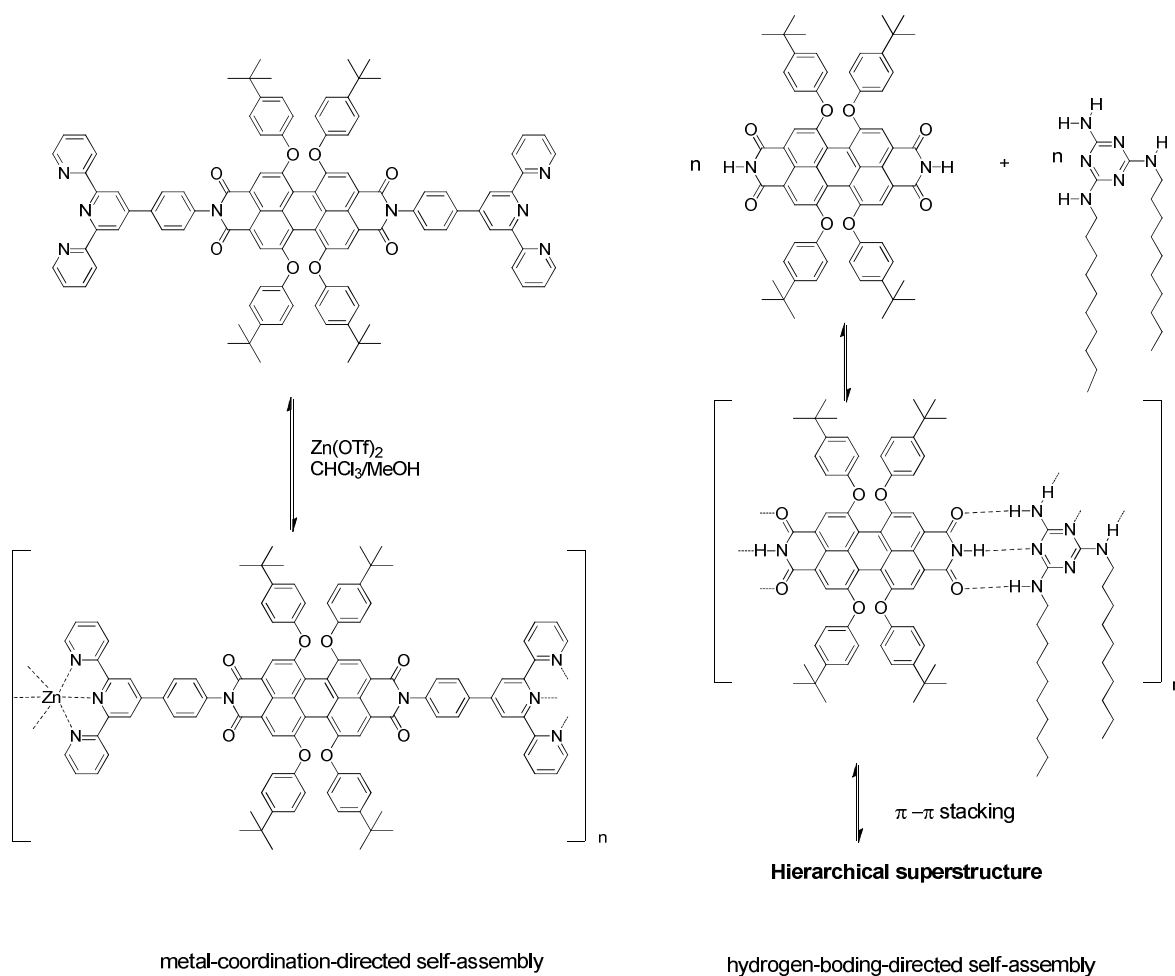
### **1.3.3 Molecular packing of PDIs in the solid state.**

The molecular packing behavior of perylene diimides in the solid state has been extensively studied since the early 1980's for the purpose of controlling the pigment colors for industrial applications.<sup>1-3</sup> Perylene diimide crystal structures often reveal flat  $\pi$ -systems with parallel orientation of the chromophores at an inter-plane distance of  $\sim 3.4$  Å (as illustrated in Figure 1.8), which is quite similar to the layer-to-layer distance in graphite.<sup>3,18,72-73</sup> Substituents at the imide position can significantly affect the stacking distance (the longitudinal and transverse offset between the neighboring perylene diimides in the solid states), which influences the intermolecular interactions of the  $\pi$ -systems in the crystal lattice, results in perylene diimide powders of various colors, from red to dark.<sup>3,74</sup> On the other hand, substituents at the bay-positions could cause distortion of the flat  $\pi$ -systems due to the steric strain; this is considered an effective way to prevent significant  $\pi$ - $\pi$  stacking interactions for perylene diimides both in solution or the solid states.



**Figure 1.8.** The bond length (left, in Å) and  $\pi$ - $\pi$  stacking of Pigment Red 179 (right) in crystal.<sup>3</sup> Reproduced by permission of the Royal Society of Chemistry.

Another area of increasing interest focuses on the molecular packing behavior of PDI derivatives upon supramolecular organization in order to form functional molecular architectures.<sup>3,75-76</sup> New materials with interesting optical and electrical properties have been demonstrated by leading scientists in the field, including Müllen, Würthner, and Meijer via control of the spatial organization of PDI dyes using molecular self-assembly techniques.<sup>2-3,75,77-80</sup> Examples of metal-coordination-directed and hydrogen-bonding-directed self-assembly in forming PDI-based nano- and meso-scopic supramolecular structures are shown in Figure 1.9.<sup>3,78,81-82</sup> Currently, different kinds of appealing nano-structures or larger objects have become accessible by functionalized perylene diimides using self-assembly techniques. The simplicity of such an approach for constructing various size architectures is attractive with less need for time-consuming, multi-step organic synthesis. However, since this thesis focuses on the applications of functional perylene diimides on organic electronics and optical power limiting, an in depth discussion of the supramolecular organization of PDI-based dyes will not be given here.

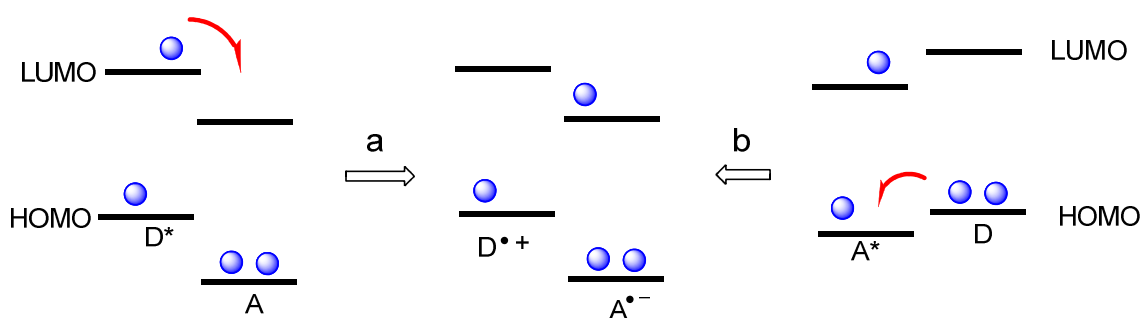


**Figure 1.9. Metal-coordination-directed (left) and hydrogen-bonding-directed (right) self-assembly in forming perylene diimide based supramolecules.<sup>3</sup>**

### 1.3.4 Photo-induced electron transfer in perylene diimides

PDI-based materials can engage in a variety of excited-state electron-transfer reactions, primarily as acceptors, as illustrated in Figure 1.10. Functionalized donor – acceptor (D – A) type perylene diimide derivatives have attracted much research effort on their PICT processes, since their easily identified radical-ion absorption spectra can be utilized to monitor the charge-transfer processes following photo-excitation.<sup>83</sup>

In general for D–A type molecules, the thermodynamics and kinetics of the electron-transfer reactions have been extensively studied and many of these features can be described by the Rehm-Weller equation,<sup>84</sup> the change in Gibbs free energy during the charge separation, and by Marcus' theory<sup>85-88</sup> for the electron transfer rate.



**Figure 1.10. Photo-induced charge transfer between donor and acceptor (PDI) in forming  $D^{\bullet+}$ -PDI $^{\bullet-}$  : (a) electron transfer from excited donor to PDI; (b) electron transfer from donor to excited PDI. The blue balls represent electrons.**

The Rehm-Weller equation (Eq 1.1) provides an estimated driving force ( $\Delta G_{CT}$ ) for the photo-induced charge-transfer process in molecular D–A systems, by summing terms describing the thermal-energy of an excited-state redox reaction and the Coulomb term accounting for finite distance between positive and negative charges.  $E_{coul}$  (a positive value) is the Coulombic stabilization energy that is often neglected based on the assumption of the formation of solvent-separated free ions.  $E_{(0,0)}$  is the energy of the relaxed first singlet excited state.  $E^{1/2}_{(D/D^{\bullet+})}$  is electrochemical half-wave potential corresponding to the oxidation process in the electron donor.  $E^{1/2}_{(A^{\bullet-}/A)}$  is electrochemical half-wave potential corresponding to the reduction process in the electron acceptor.  $[E^{1/2}_{(D/D^{\bullet+})} - E^{1/2}_{(A^{\bullet-}/A)}]$  is related to the energy gap between the HOMO of the donor and



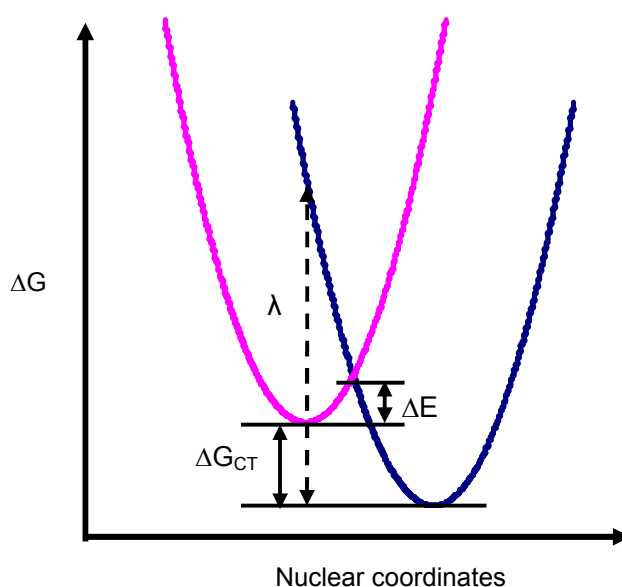
the LUMO of the acceptor. For any given D–A conjugate, electron transfer over longer distances is energetically less favored due to the decrease of  $E_{\text{coul}}$  and the free energy for charge separation becomes more exergonic when the polarity ( $\epsilon_s$ ) of the solvent increases since  $E_{\text{coul}}$  is more positive.<sup>84</sup>

$$\Delta G_{\text{CT}} = e[E^{1/2}_{(\text{D/D}^+\bullet)} - E^{1/2}_{(\text{A}\bullet/\text{A})}] - E_{(0,0)} - E_{\text{coul}} \quad \text{Eq 1.1}$$

Marcus' theory describes the kinetics of nonadiabatic electron-transfer reactions as shown in Eq 1.2 and Eq 1.3 and Figure 1.11, where  $k_{\text{CT}}$  is the rate of electron-transfer in terms of the free-energy barrier  $\Delta G_{\text{CT}}$  for electron transfer, the reorganization energy  $\lambda$ , and the electronic coupling  $V_{\text{DA}}$  between donor and acceptor in the excited state.<sup>85-88</sup>

$$k_{\text{CT}} \propto V_{\text{DA}}^2 \exp[-(\Delta G_{\text{CT}} + \lambda)^2 / (4 \lambda k_{\text{b}}T)] \quad \text{Eq 1.2}$$

$$\Delta E = (\Delta G_{\text{CT}} + \lambda)^2 / 4 \lambda \quad \text{Eq 1.3}$$



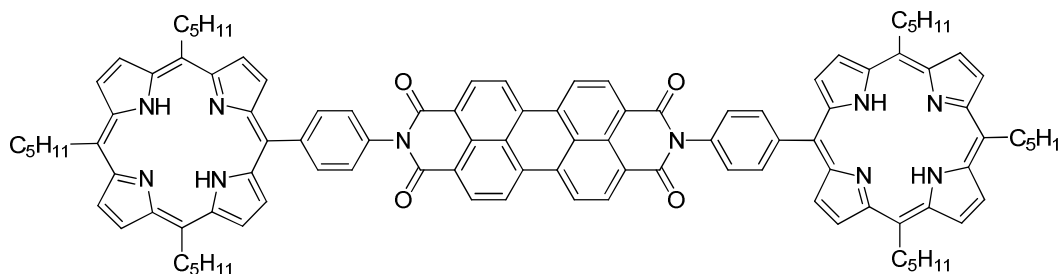
**Figure 1.11. Relationship between free energy ( $\Delta G_{\text{CT}}$ ) and nuclear motion for diabatic exergonic electron transfer (Figure adapted from Dr. Jing Wang in the Marder group).**

Marcus' theory, in particular Equation 1.2, indicates that when the driving force for electron transfer increases, the activation energy barrier is lowered and, hence, the electron transfer rate rises until the reorganization energy ( $\lambda$ ), which is the energy required for all structural adjustments needed for A and D to assume the configuration required for electron transfer, equals the change in free energy for charge separation (where,  $\lambda = -\Delta G_{CT}$ ). At this point the maximum electron-transfer rate is obtained. However, beyond this point, a further increase in the free energy change results in an increase in the activation energy and, hence, the electron-transfer reaction will become slower. The prediction implies that there are three regions for electron transfer: the 'normal' region, where the change in free energy for electron transfer is less than the reorganization energy ( $-\Delta G_{CT} < \lambda$ ), the optimal region ( $-\Delta G_{CT} = \lambda$ ), and the 'inverted' region, where the change in free energy is larger ( $-\Delta G_{CT} > \lambda$ ). The distance and orientation of the donor and acceptor are of major importance for electron-transfer rate. The most important parameter to the  $k_{CS}$  is the electronic coupling  $V_{DA}$ , which decreases exponentially with increasing center to center distance for the D–A system in the electron-transfer reaction.<sup>85-88</sup>

#### 1.3.4.1 Photo-induced electron transfer in porphyrin-PDI systems.

The porphyrin-PDI systems are the most well studied photo-induced charge-transfer systems, having been extensively studied by Wasielewski and Lindsey in the 1990s.<sup>27-28,67,79,89</sup> Figure 1.12 shows the first donor-acceptor-donor (D – A – D) compound **1** containing a PDI and two porphyrin moieties reported by Wasielewski and coworkers in 1992.<sup>27</sup> Photo-excitation of **1** at 585 nm (pumping porphyrin) results in the

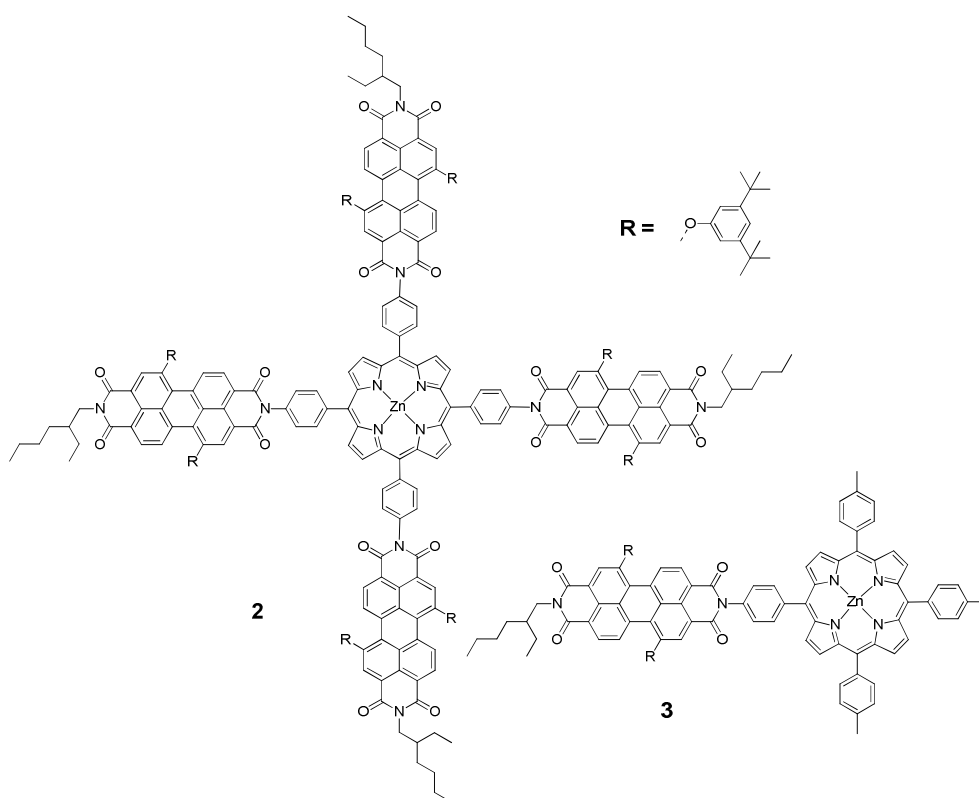
formation of a  $D^+-A^--D$  charge-separated state with a rate of  $k_{CS,1} = 1.1 \times 10^{11} \text{ s}^{-1}$ , which subsequently undergoes a charge recombination with a rate of  $k_{CR,1} = 9.1 \times 10^9 \text{ s}^{-1}$  according to the growth and decay of the PDI radical-anion absorption peaked at *ca.* 713 nm observed via transient absorption spectroscopy. It is worth noting that further excitation of this molecule with much higher intensity irradiation at 580 nm could excite both porphyrin units in the D–A–D triad and result in the formation of a  $D^+-A^{2-}-D^+$  doubly charge-separated state, with the appearance of PDI-based dianion absorption peaks at *ca.* 546 nm in transient absorption spectra. Much slower electron-transfer ( $k_{CS,2} = 5.6 \times 10^9 \text{ s}^{-1}$ ) as well as charge-recombination rate ( $k_{CR,2} = 2.2 \times 10^8 \text{ s}^{-1}$ ) were found during the forming of  $D^+-A^{2-}-D^+$  as compared to the formation of the  $D^+-A^--D$  species through photo-excitation of porphyrin.



**Figure 1.12. The chemical structure of porphyrins-perylene diimide-porphyrins.**<sup>27</sup>

Tetrakis(peryene diimide) substituted zinc tetraphenylporphyrin **2** (as shown in Figure 1.13) exhibits interesting optical properties with respect to its photo-induced charge-transfer processes, as these molecules can self-assemble into nanoparticles with an average of 12 close packed molecules in each nanoparticle (**(2)**<sub>12</sub>).<sup>79</sup> The photo-induced charge-transfer processes in these (**2**)<sub>12</sub> occur in toluene with near unity

efficiency and a rate of  $k_{CS} = 3.1 \times 10^{11} \text{ s}^{-1}$ , while the separated charges recombine with  $k_{CR} = 1.4 \times 10^8 \text{ s}^{-1}$ . As compared with the model compound **3**, faster (4 times) charge-transfer as well as slower (1.4 times) charge-recombination were obtained in the nanoparticle (**2**)<sub>12</sub>. The transient absorption spectra of the reduced PDI species in (**2**)<sub>12</sub> are substantially broadened and decreased in peak intensity as compared with those in the spectrum of **3** in the region of PDI radical anion absorption. It was suggested that this might be due to delocalization of the negative charge from PDI<sup>•-</sup> onto the other PDI units in (**2**)<sub>12</sub> that were within the van der Waals distances.<sup>79</sup> It is worth noting that the formation of (PDI)<sub>n</sub><sup>-</sup> in stabilizing the charge-separated state could potentially be explored for other applications such as OPVs and optical power limiting.

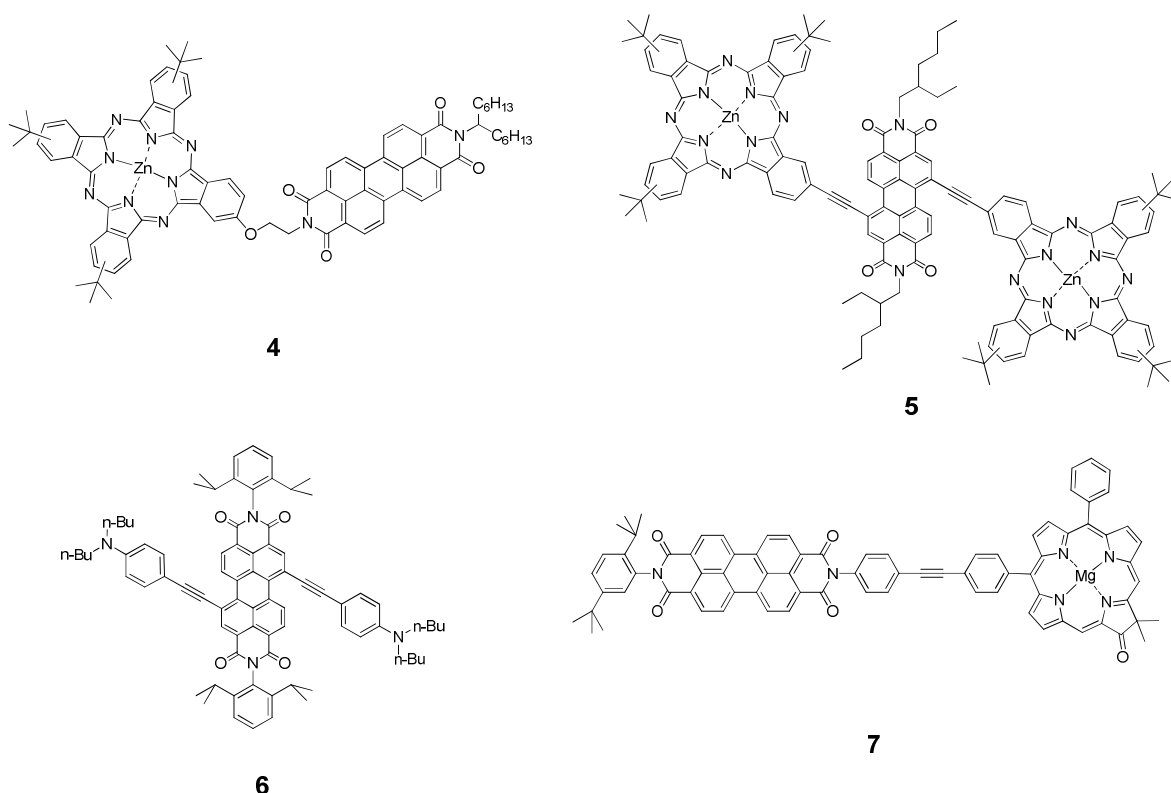


**Figure.1.13.** The chemical structures of tetrakis(peryene diimide) substituted zinc tetraphenylporphyrin (compound **2**) and the model compound (**3**).<sup>79</sup>

#### 1.3.4.2 Photo-induced electron transfer in other donor-PDI systems

Photo-induced processes of donor-PDI systems other than porphyrin-PDI conjugates have also been well studied. As shown in Figure 1.14, it was found that photo-excitation of a zinc phthalocyanine-PDI (**4**) dyad<sup>31</sup> afforded the triplet excited state without fluorescence emission, whereas the addition of  $\text{Mg}^{2+}$  to the photo-excited **4** resulted in formation of a very long-lived (up to 240  $\mu\text{s}$ ) charge-separated state ( $\text{ZnPc}^+-\text{PDI}^-/\text{Mg}^{2+}$ ) in which the PDI radical anion is believed to form a complex with  $\text{Mg}^{2+}$  ( $\text{ZnPc}^+-\text{PDI}^-/\text{Mg}^{2+}$ ) in solution. The absorption band due to the  $\text{ZnPc}^+-\text{PDI}^-/\text{Mg}^{2+}$  complex ( $\lambda_{\text{max}} = \text{ca. } 500 \text{ nm and } 550 \text{ nm}$ ) is significantly shifted from that of PDI radical anion ( $\lambda_{\text{max}} = \text{ca. } 720 \text{ nm}$ ) due to the complex formation with  $\text{Mg}^{2+}$ .<sup>31</sup> The reason for forming  $\text{ZnPc}^+-\text{PDI}^-/\text{Mg}^{2+}$  is that this charge-transfer complex is lower in energy than the triplet state ( $\text{ZnPc}-^3\text{PDI}^*$ ). The quantum yield of the charge-separated state ( $\text{ZnPc}^+-\text{PDI}^-/\text{Mg}^{2+}$ ) was determined as 72%.<sup>31</sup> However, photo-excitation of the close coupled phthalocyanine-PDI-phthalocyanine triad (**5**) through an ethylene spacer on the bay region of perylene diimide produces a charge-separated state with life-time at nanosecond timescale. There is no evidence for forming PDI triplet state (triplet-triplet (T-T) absorption spectrum of PDIs have  $\lambda_{\text{max}}$  at *ca.* 500 nm<sup>70</sup>) according to the transient absorption spectra in this case. Another type of donor-PDI compound (**6**) with strong electronic coupling between the triphenyl amine-based donor and the PDI moiety also indicates fast charge transfer (within 10 ps) as well as nanosecond lived charge-separated states following photo-excitation.<sup>29</sup> Efficient photo-induced charge transfer also occurs in PDI-(Mg)oxochlorin (PDI-MgO, **7**) with the yield of oxochlorin-to-PDI electron transfer in high overall yield (> 90%) in toluene or benzonitrile. The charge-separated state for **7**

has a lifetime of  $> 1$  ns in both toluene and benzonitrile. The pathway for generating  $\text{PDI}^- - \text{MgO}^+$  from the excited PDI moiety involves both hole transfer and energy transfer to the oxochlorin, followed by electron transfer from the resulting  $\text{MgO}^*$  to PDI, because energy of  $\text{PDI}^- - \text{MgO}^+$  is well below that of  $\text{MgO}^*$ . The yield of MgO-to-perylene electron-transfer rises to 70% in toluene and to 85% in more polar benzonitrile.<sup>90-91</sup>



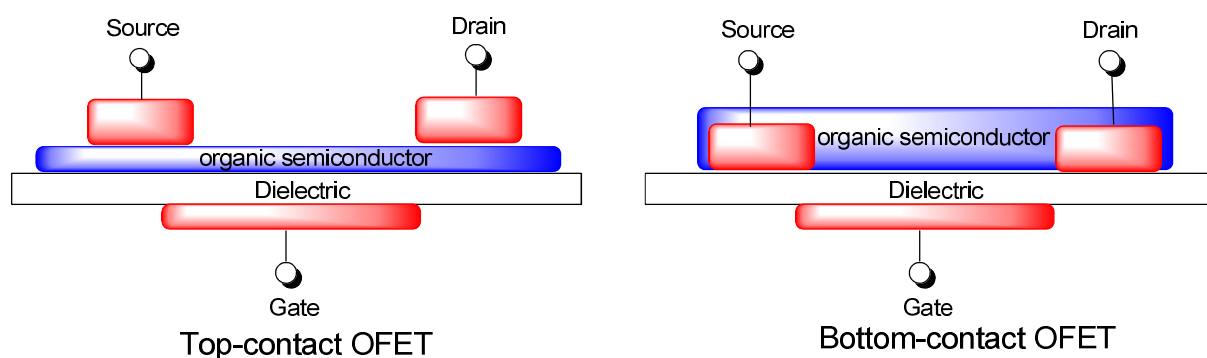
**Figure 1.14. The chemical structures of several non-porphyrin donor-PDI derivatives for forming photo-induced charge-separated states.**

In general, the photo-excitation of these donor-PDI systems generates relatively long-lived charge-separated states, with PDI radical anions and/or dianions showing strong absorption band peaks at  $\sim 720$  nm and/or  $\sim 550$  nm, respectively. Because perylene diimides without chemical modification at the aromatic bay positions exhibit high linear

transparency in the NIR range, these photo-generated ions could potentially be applied to optical limiting applications in the PDIs' radical anion absorption spectroscopic range if appropriate molecular donors are chosen in building up the donor-PDI conjugates.<sup>92-94</sup>

#### 1.4 Application of PDI dyes in organic electronics (OFETs and OPVs)

PDI-based materials, with small optical band-gaps ( $\sim 2.2$  eV),<sup>3,35</sup> low-lying LUMO levels (*ca.* -3.9 eV),<sup>3,8,14</sup> high electron mobilities ( $> 1$  cm<sup>2</sup>V<sup>-1</sup>s<sup>-1</sup>),<sup>7-8,16</sup> good molecular ordering in thin films,<sup>3,7,72-73</sup> high molar absorption coefficients ( $\sim 1 \times 10^5$  M<sup>-1</sup>cm<sup>-1</sup>),<sup>3,35</sup> and facile chemical functionalization at both imide and bay positions,<sup>3,35</sup> show potential as promising electron-transport materials and/or organic acceptors in organic electronics, especially for OFET and OPV applications.<sup>3,24,95</sup>



**Figure 1.15. Schematic representations of two widely used OFET geometries: Top-contact OFET (left); bottom-contact OFET (right).**

OFETs are a type of thin-film transistors (TFTs) with organic semiconductors as the active layers, analogous to conventional silicon-based metal-oxide-semiconductor thin-film transistors (MOSTFTs).<sup>96</sup> OFETs rely on an electric field to control the

conductivity of the charge-carrier channel. The most commonly used transistor device geometry for an OFET device (as shown in Figure 1.15) is the bottom gate with top-contact drain and source electrodes, similar to the well-studied silicon-based MOSTFTs. These generally show higher performance over other device geometries because of their smaller contact resistance compared with bottom-contact MOSTFTs, which can have lower fabrication costs.<sup>4</sup> It is believed that OFETs can offer a suitable low-cost building-block for flexible and large-area electronic applications, such as organic-based displays, RF-ID tags, smart cards, and sensors in the near future.<sup>4,96-99</sup>

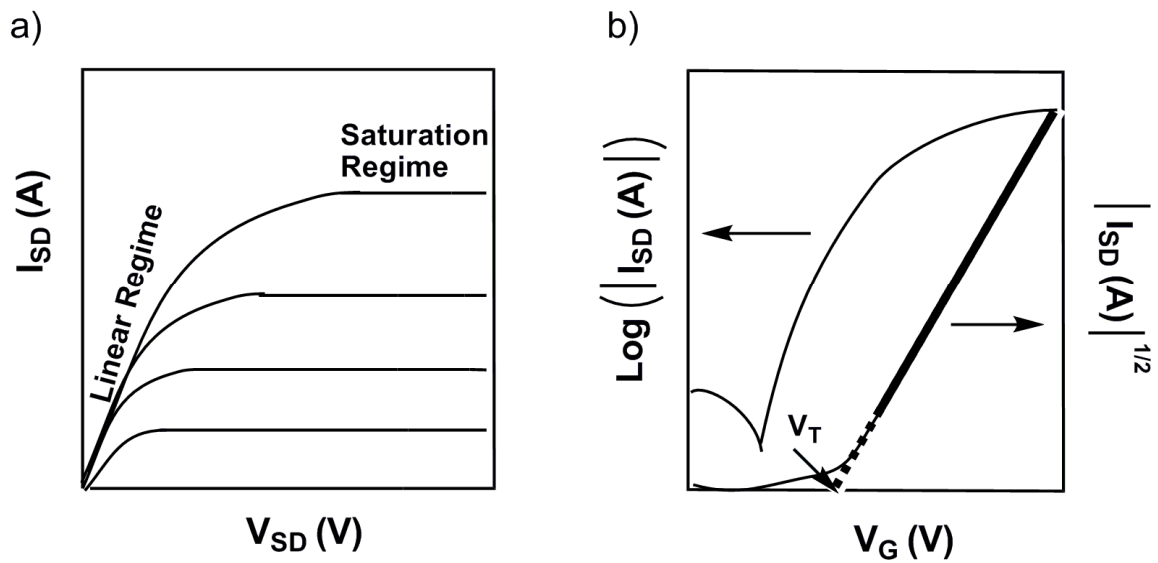


Figure 1.16, Typical  $I$ - $V$  curves of an OFET device: (a) output curve at different constant  $V_G$  and (b) transfer curve at a constant  $V_{SD}$  (Figure adapted from Dr. Xuan Zhang of the Marder's group).<sup>100</sup>



$$I_{SD} = \frac{W}{L} \mu C \left[ (V_G - V_T) V_{SD} - \frac{1}{2} V_{SD}^2 \right] \quad \text{Eq 1.4}$$

$$I_{SD,linear} = \frac{W}{L} \mu C (V_G - V_T) V_{SD} \quad \text{Eq 1.5}$$

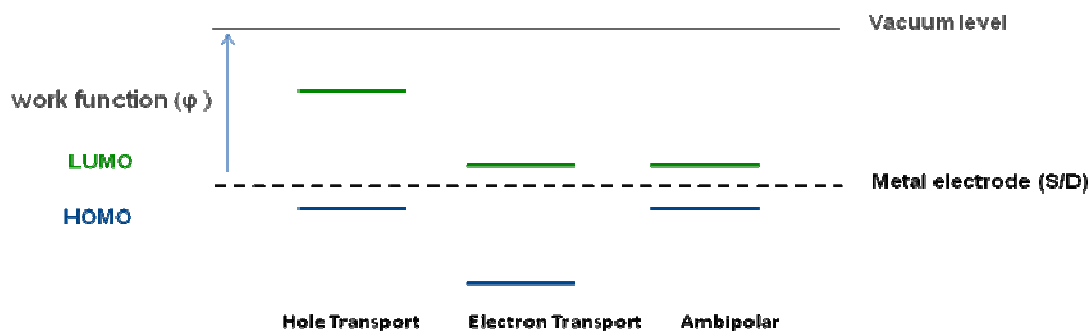
$$I_{SD,Sat} = \frac{W}{2L} \mu C (V_G - V_T)^2 \quad \text{Eq 1.6}$$

In the device “off” state, without applied gate bias, there is only limited current flow between the source and drain electrodes in an OFET device when it is operated. In the “on” state, as voltage is applied to the gate electrode, electron or holes can be injected from source/drain electrodes and accumulate at the semiconductor-dielectric interface forming the active channel, which results in increasing source-drain current.<sup>4</sup> The most critical characteristics of organic semiconductors in OFETs are the charge-carrier mobility (hole, electron, or both in so-called ambipolar devices) and the  $I_{on}/I_{off}$  ratio. The current between the source and drain electrodes ( $I_{SD}$ ) under a given  $V_G$  can be expressed in terms gate voltage ( $V_G$ ), current ( $I_{SD}$ ) and voltage ( $V_{SD}$ ) between the source and drain electrodes, threshold gate voltage ( $V_T$ , voltage at which the current starts to rise), and capacitance density (capacitance per unit area) of the gate dielectric ( $C$ ) as Equation 1.4. Here,  $W$  and  $L$  are the width and length of the devices. Equation 1.4 can also be simplified in the linear regime ( $|V_{SD}| \ll |V_G - V_T|$ ) and saturated regime ( $|V_{SD}| > |V_G - V_T|$ ), as described in Equations 1.5 and 1.6, respectively. The  $I_{on}/I_{off}$  is the ratio of the maximum  $I_{DS}$  (“on” current) value to the minimum  $I_{DS}$  (“off” current) value, obtained from transfer characteristics plotted on a logarithmic scale ( as Figure 1.16). The ratio characterizes the ability of the device to switch a signal from “on” to “off”.<sup>96</sup> The  $I_{on}/I_{off}$

ratio can also be a useful indicator of purity, because high extrinsic doping levels in the semiconductor normally lead to high off current. A typical I-V response for an OFET device is shown in Figure 1.16a. Figure 1.16b shows the transfer characteristic in the saturated regime of a transistor, i.e.,  $I_{SD}$  vs.  $V_G$  at a constant  $V_{SD}$ . It is usually plotted as a logarithmic plot of  $I_{SD}$  vs.  $V_G$  and as a linear plot of the square root of  $I_{SD}$ . Important parameters for an OFET device ( $I_{on}/I_{off}$ ,  $V_T$  and  $\mu$ ) can be extracted from the transfer curve.  $I_{on}/I_{off}$  can be obtained from the logarithmic plot according to Eq. 1.6;  $V_T$  can be obtained by extrapolating the linear fit to zero; the field-effect mobility can be extracted from the slope of the linear plot.  $V_T$  can be obtained by extrapolating the linear fit to zero. It is also worth noting that low values (ideally close to zero) of  $V_T$  are highly desired for low power consumption in real device applications.<sup>4</sup>

Organic semiconductors are, in principle, expected to show ambipolar transport characteristics with both hole and electron conductivities when employed as the active layer in an OFET. In practice, the majority OFETs reported to date show p-type characters. OFETs based on organic materials with low electron affinity (electron affinity defined as the energy change when an electron is added to the neutral species to form a negative ion), such as perylene diimides and  $C_{60}$  derivatives, show electron transport properties. OFETs using electron donors as the active materials, like polythiophenes, typically exhibit hole transport character. Only a limited number of materials can perform both processes simultaneously in OFETs. One of the reasons is the fact that in most organic semiconductors the HOMO-LUMO gap is sufficiently large that, at best, only one of the frontier orbitals (either HOMO or LUMO) is accessible for charge injection from a given electrode material, since charge preference is dependent on the injection

barrier from the organic materials to metal electrode, as shown in Figure 1.17. Another factor that promotes unbalanced transport is the selectivity of the trapping of injected carriers in the devices. In many cases, negative charge carriers (electrons) are more readily trapped than their positive counterpart (holes) in OFETs by the hydroxyl groups at the semiconductor–dielectric (like SiO<sub>2</sub>) interface or other trapping sites.<sup>4,101</sup> As a result, most organic transistors show only hole transport characteristics and recent achievements in hole transport materials have fulfilled many of the requirements ( $\mu > 0.1 \text{ cm}^2\text{V}^{-1}\text{s}^{-1}$  with  $I_{\text{on}}/I_{\text{off}} > 10^5$ ) for diverse applications.<sup>4,95,97,102</sup> On the other hand, the development of electron transport materials needed for complementary circuits continues to present challenges, such as low electron mobilities, instability in air, poor solubility for efficient film-casting and large energy barriers for electron injection.<sup>4,95,97,102</sup> Research efforts on exploring new high-performance electron transport materials, as well as ambipolar materials, are essential for further development of organic electronics.

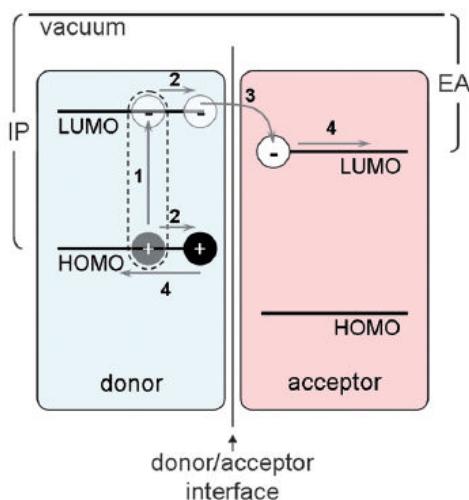


**Figure 1.17.** The energy diagram of various charge carrier transport according to a given electrode material. The charge preference is dependent on the injection barrier from the organic materials to the respective metal electrode, and ambipolar materials exhibit a relatively small injection barrier from the metal electrode for both hole and electron.

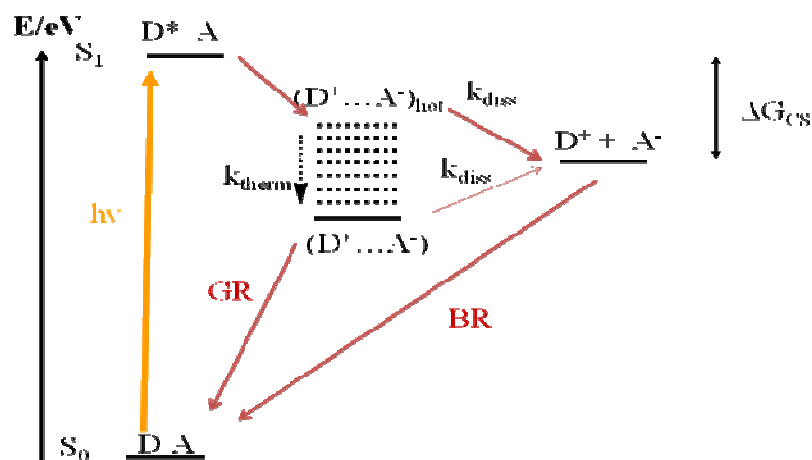
Photovoltaic science and technology is related to the processes of converting solar energy directly into electricity. Solar energy is expected to be one of the clean alternative

energy sources to fossil fuels in the near future.<sup>103</sup> Organic photovoltaic systems, using organic semiconductors as the active materials (light-harvesting and charge-transport materials), are potentially a cost-effective and lightweight solar energy conversion platform as compared to their inorganic counterparts.<sup>32-34,104-105</sup> In inorganic semiconducting materials, such as silicon, excitons (the coulomb-correlated electron-hole pairs with no net charge) are generally bound weakly ( $< 0.01$  eV), so that ambient thermal energy ( $kT = ca. 0.025$  eV) is sufficient to achieve the charge separation. However, the photo-generated excitons in organic semiconductors are typically strongly coulombically bound, with energies of hundreds of meV, *i.e.*, much greater than thermal energy at ambient temperature, meaning efficient charge separation cannot be achieved in a single organic material. For the organic solar cells using the donor/acceptor heterojunction for charge dissociation, it is believed that a minimum energy difference of  $> 0.3$  eV is required for the LUMO or the HOMO offset between the donor and acceptor materials to overcome such an “exciton-binding” energy for an efficient photovoltaic process in organic D/A interface.<sup>32-34,105-106</sup> Organic solar cells may not compete with silicon-based solar cells in device performance, due to their limitations in light harvesting ability, charge carrier mobility, as well as the thermal- and photo-stability over silicon. However, large-area organic solar cells may be manufactured more cheaply with low energy cost using possible wet-processing methods, such as ink-jet printing or blade-coating. As shown in Figure 1.18, the process of converting solar energy into electricity using OPVs can be schematically described by the following several steps: absorption of a photon by the light-harvesting material, which leads to the formation of an exciton (the bound electron/hole pair); exciton diffusion from the bulk materials to the

D/A interface for charge dissociation; and free charge transport within the active layer to the respective electrodes for charge-carrier collection.<sup>32,105</sup> Figure 1.19 shows the free charge formation in a D/A system via a  $(D^+ \cdots A^-)$  CT state. The initially formed bound CT state  $(D^+ \cdots A^-)_{\text{hot}}$  can either undergo thermalisation ( $k_{\text{therm}}$ ) to lower energy CT states or dissociation ( $k_{\text{diss}}$ ) into the free charge carriers  $D^+ + A^-$  (charge-separated (CS) state), which can then contribute to the device current and make such photovoltaic processes much more complicated, as shown in Figure 1.18. Separated charge-carriers can recombine either by geminate (GR) or bimolecular (BR) recombination, and BR recombination is likely to proceed via reformation of interfacial CS states.<sup>30,107</sup> The energy difference between the CS state and the first singlet state ( $S_1$ ),  $\Delta G_{\text{CS}}$ , as shown in Figure 1.19, is considered the driving force for charge-separation, which is essentially the free energy loss in the photovoltaic process. More detailed discussion about dependence of the yield of charge photo-generation on  $\Delta G_{\text{CS}}$  will be given in Chapter 4.



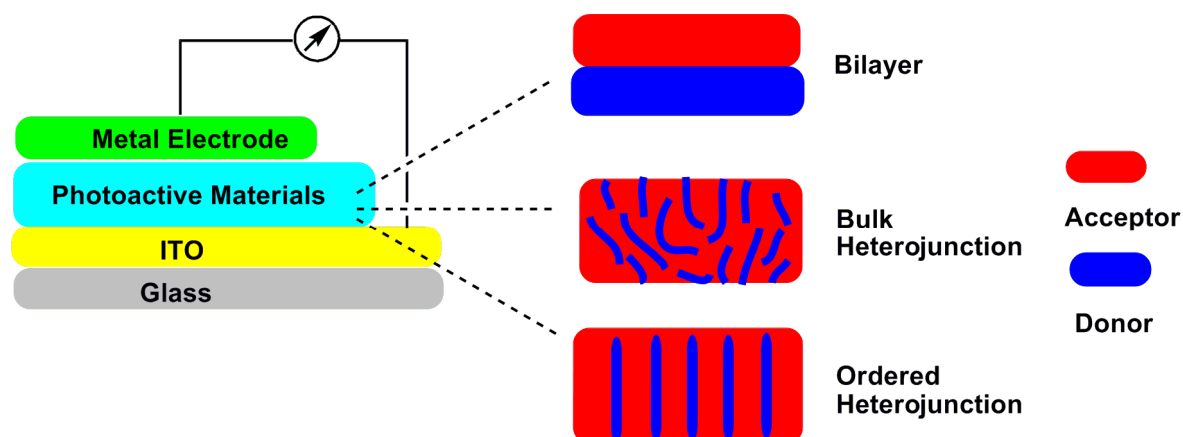
**Figure 1.18.** Schematic of frontier molecular orbitals (HOMO and LUMO) at a D/A interface, showing steps in the photovoltaic process. Ionization potential (IP) and electron affinity (EA) are depicted for the donor and acceptor, respectively.<sup>105</sup> Reproduced by permission of the Royal Society of Chemistry.



**Figure 1.19. Energy state diagram for free charge formation in a donor/acceptor (D/A) system via a bound CT state following photo-excitation (Figure adapted from Dr Shoaee in Imperial College (London)).**

A typical organic solar cell consists of a thin film(s) of organic semiconductor(s) sandwiched between two electrodes. Commonly used architectures of OPV devices are shown in Figure 1.20. There are two major architectures for single-cell-based OPVs: bilayer solar cells (in which donor and acceptor materials are sequentially stacked on top of each other as active layer) and bulk hetero-junction solar cells (BHJs, in which a blend of a donor and an acceptor material is the active layer). Bilayer solar cells are more closely analogous to conventional silicon-based solar cells. These devices benefit from the separated charge carriers transporting layers that ensure transport pathway to the correct electrode for each charge carrier type and give the separated charge carriers limited chance to recombine with their counterparts. One of the drawbacks for this device is that the limited exciton diffusion length (the lifetime of excitons is only on the order of ps – ns, resulting in maximum diffusion distances around 10 nm<sup>105,108</sup>) in organic semiconductors normally limits the thickness and light-harvesting ability of respective

devices for highly efficient solar cells.<sup>104,109</sup> In contrast, one of the merits for BHJ solar cells is the large D/A interface area if the molecular mixing occurs on a scale length that allows most generated excitons to reach the D/A interface for charge dissociation before decay, for which the thickness and light-harvesting issues are less serious.<sup>33-34,110</sup> However, such blends exhibit significant structural disorder, relying on random phase separation of the components. In most cases, these molecular domains are too large (cause excitonic loss) or too small (leading to facile charge recombination) in size, which lowers the overall OPV device performance.<sup>105</sup> Currently, more research effort on OPVs are directed towards the BHJ-type solar cells, since they potentially could provide cost-effective devices through a wet-processing method. It has been proposed by Fréchet<sup>34</sup> that the ideal bulk-heterojunction solar cell should have a continuous composite of donor and acceptor materials with a mean domain size of the order of the exciton diffusion length (typically  $< ca. 10\text{ nm}$ <sup>105</sup>). Hence, the photo-generated excitons could diffuse efficiently to the D/A interface before decay, for efficient charge separation.<sup>33-34</sup> However, a number of variables, including choice of donor and acceptor, the donor-acceptor weight ratio, and the solvent and post-treatment, can dramatically affect the morphology, making device optimization challenging. In addition, based on these two basic device structures, new solar cell device architectures, such as tandem solar cells<sup>111-112</sup> and inverted organic solar cells<sup>113-114</sup> have also been investigated, which benefit the overall organic solar cell research either on more efficient energy conversion or facile device fabrication process.



**Figure 1.20. Schematic illustration of an OPV device: bilayer solar cell (top), BHJ solar cell (middle), and ordered heterojunction cells (bottom) (This figure was adapted from Dr. Xuan Zhang in the Marder group).**

Currently, power conversion efficiencies (PCEs) of organic solar cells have so far been limited to approximately 8% with the Solarmer polymer blends in small area device ( $< 0.1 \text{ cm}^2$ ),<sup>115-116</sup> while PCEs have been demonstrated to exceed 20% for Si-based solar cells, 15% for thin film inorganic cells, and 11% for dye-sensitized solar cells.<sup>105</sup> However, further research attention on OPVs could potentially leads to increased PCEs comparable to other photovoltaic technologies. In the long term, OPV technologies might make a significant contribution to the photovoltaic conversion of solar energy, as long as there is a major investment in research into new, more efficient ( $> 10\%$ ), and long-lasting organic materials, as well as more reliable and cost effective large-area device fabrication methods.

While from an economic perspective, the cost/watt is a critical metric for evaluating competing energy generating technologies, from a scientific perspective, the device power conversion efficiency, is the most important characteristic when evaluating



an organic solar cell. The PCE is defined according to Eq 1.7 and Eq 1.8, where  $V_{OC}$  is the open circuit voltage (the voltage when the current equals zero),  $J_{SC}$  is the short circuit current density (the current density under zero bias),  $P_{out}$  is the output power for the solar cell under irradiation,  $P_{in}$  is the incident light power density on the solar cells, and FF is the fill factor defined as the ratio of power density ( $J_{max} \times V_{max}$ ) at maximum output power divided by ( $V_{OC} \times J_{SC}$ ). FF is directly affected by the values of the cells series and shunt resistances of the cells, as shown in Figure 1.21b. Increasing the shunt resistance ( $R_p$ ) and decreasing the series resistance ( $R_s$ ) could lead to larger FF and push the device  $P_{out}$  towards its theoretical maximum.  $J_{max}$  and  $V_{max}$  are the current density and voltage at the maximum output power point (that is, the point at which the product of  $J_{max}$  and  $V_{max}$  reaches its maximum value), respectively. A typical current-voltage curve for an OPV cell is shown in Figure 1.21.<sup>34</sup> In the dark, a typical diode-type  $J$ - $V$  response with limited current flows in the reverse bias direction ( $V < 0$ ) can be recorded. As the cell is illuminated, the  $J$ - $V$  curve is ideally shifted down at all potentials because of the additional photocurrent, and power is generated in the devices.

$$\eta = \frac{P_{out}}{P_{in}} = FF \frac{J_{SC} V_{OC}}{P_{in}} \quad \text{Eq 1.7}$$

$$FF = \frac{J_{max} V_{max}}{J_{SC} V_{OC}} \quad \text{Eq 1.8}$$

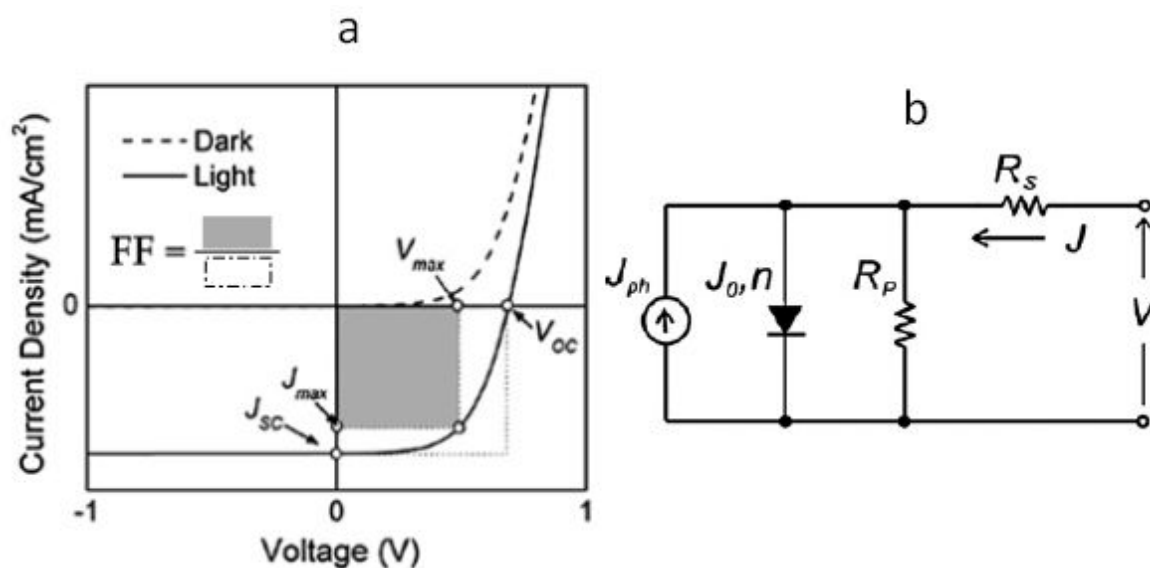


Figure 1.21. (a) Typical  $J$ - $V$  curves in an OPV device under dark (dotted line) and under illumination (solid line).<sup>34</sup> (b) Equivalent circuit used to model solar cells, where  $R_s$  is the series resistances,  $R_p$  is the shunt resistance.<sup>32</sup>

Since the active layer(s) in an organic solar cell requires two components, an electron acceptor and an electron donor, efforts on developing both promising hole-transport and electron-transport materials with good light-harvesting ability have been carried on over the years. For high performance BHJ type solar cells, semiconducting materials are required to have high charge-carrier mobility in the solid state, favorable energy-level matching for charge separation at the D/A interface, relatively low energy bandgap and high molar absorption coefficients for more efficient solar-light-harvesting, and reasonable solubility for wet processing.<sup>33-34</sup> Exploration of hole-transport materials (donors) for OPV purposes has been more successful than research on electron-transport materials (acceptors). Important representatives of donor-type semiconducting polymers are (i) derivatives of phenylene vinylene backbones like poly[2-methoxy-5-(3,7-dimethyloctyloxy)-1,4-phenylenevinylene] (MDMOPPV), (ii) derivatives of

polythiophenes such as poly(3-hexylthiophene) (P3HT), and (iii) low bandgap conjugated polymers with alternating electron donor and acceptor moieties (D–A type polymer) such as poly(2,7-carbazole-*alt*-benzothiadiazole). Current state-of-the-art devices of this nature have active layers of blended conjugated polymers (typically P3HT) and fullerene derivatives, and they reach solar-light-to-electricity conversion efficiencies of *ca.* 5%<sup>117-118</sup> and, more recently, 6.7% in a tandem cell.<sup>112</sup> D – A type polymer–fullerene-based solar cells, with the advantage of better light harvesting, show PCEs approaching 8% using the donor materials from Solarmer Energy Inc. in a blend with [6,6]-phenyl-C<sub>71</sub>butyric acid methyl ester (PC<sub>71</sub>BM).<sup>115-116</sup> On the other hand, progress on the development of acceptor materials for solar cell application is relatively limited. Fullerenes, including their soluble derivatives, are still the only group of materials that show promising performance benchmarks (PCE > 5%), in spite of their relatively high cost and limited light-harvesting ability across the solar spectrum. Thus, while most current solar cells devices without fullerene derivatives have relatively poor performance, developing other electron-transport materials as alternative organic acceptors in order to compete with fullerene derivatives for high performance solar cells as well as lower cost and easy processing is highly desirable and could be beneficial in approaching the 10% PCE goal for organic solar cells.

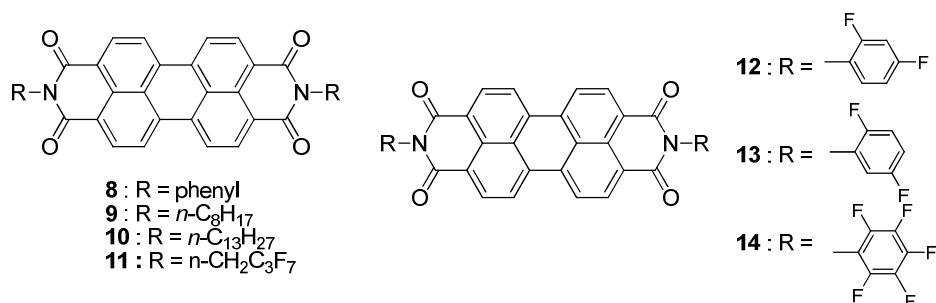
#### **1.4.1 PDIs as electron-transport materials in OFETs**

With the low lying LUMOs and the possibility for highly ordered  $\pi$ -packing ability in the solid state, perylene diimides have been utilized as electron-transport materials for decades. There are various methods for testing the electron mobilities of PDI derivatives including time-of-flight (TOF),<sup>119-121</sup> space-charge limited-current

(SCLC),<sup>122</sup> and n-channel OFETs measurements.<sup>4</sup> In TOF and SCLC experiment geometries, charge transport is typically measured perpendicular to the substrate. In OFET devices, charge carrier mobilities parallel to the substrate are measured. Charge-carrier mobilities of the same material obtained from devices with different geometry and fabricating method could be significantly different due to the anisotropic nature of molecular packing and charge-carrier hopping in thin films from organic materials.

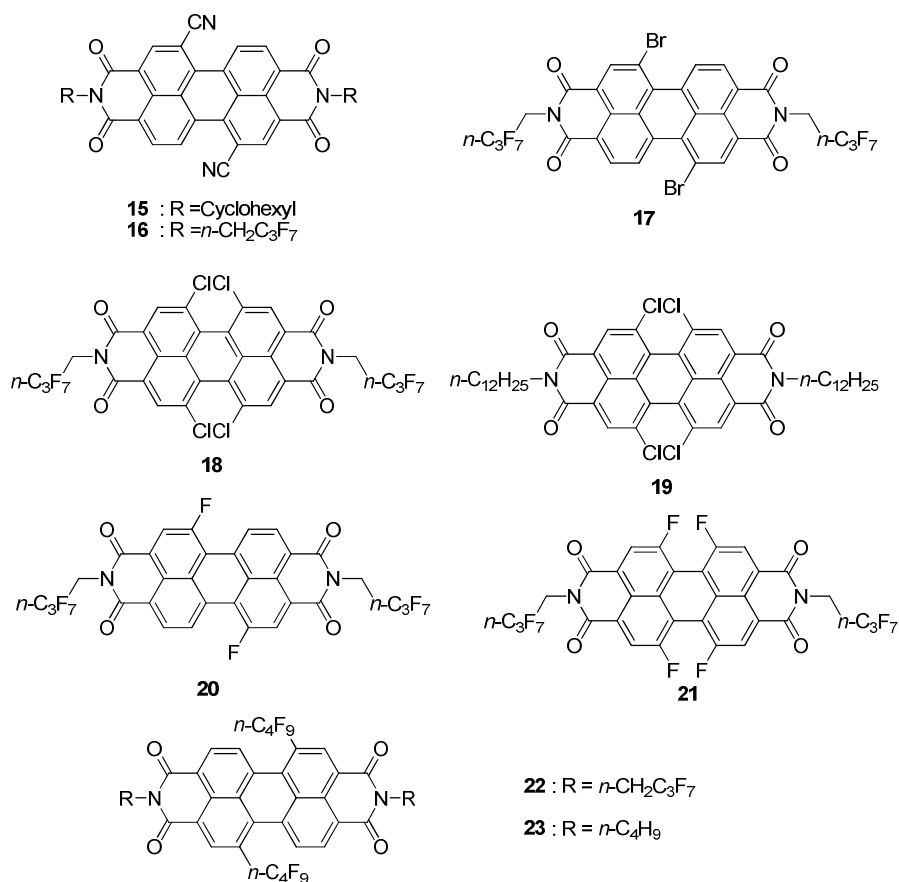
PTCDA-based vacuum-deposited n-channel field-effect transistors were first fabricated by Ostrick and co-workers. The measured electron mobilities in bottom-contact devices were found to be  $10^{-4} \text{ cm}^2\text{V}^{-1}\text{s}^{-1}$  when the devices were operated in vacuum.<sup>123</sup> As shown in Figure 22, PDI-based transistors with electron mobilities of  $10^{-5} \text{ cm}^2\text{V}^{-1}\text{s}^{-1}$  were first demonstrated by Horowitz and co-workers in 1996 using vacuum-deposited **8** as the active material.<sup>124</sup> Alkyl substituted perylene diimides (**9** and **10** in Figure 1.22)<sup>125-126</sup> were also investigated as electron-transport materials in OFETs. Malenfant and co-workers reported that bottom-contact devices using films from vacuum-deposited **9** (substrate temperature was kept at 50 °C) showed electron mobilities of  $0.6 \text{ cm}^2\text{V}^{-1}\text{s}^{-1}$  with  $I_{\text{on}}/I_{\text{off}} > 10^5$  in vacuum. However, these devices need to be operated at very high voltage, and their threshold voltage was found to be around 75 V. An electron mobility of  $2.1 \text{ cm}^2\text{V}^{-1}\text{s}^{-1}$  with  $I_{\text{on}}/I_{\text{off}} = 4.2 \times 10^5$  was recently reported for devices based on **10** by Tatemichi and co-workers. It was claimed that the high electron mobilities could be ascribed to improvement of the crystallinity of **10** in films after thermal annealing at 140 °C.<sup>125</sup> Recently, Oh and co-workers utilized the fluoroalkyl-substituted PDI **11** in vacuum-deposited OFETs. The electron mobilities of these devices were as high as  $0.72 \text{ cm}^2\text{V}^{-1}\text{s}^{-1}$  in vacuum and  $0.51 \text{ cm}^2\text{V}^{-1}\text{s}^{-1}$  in air by using

octadecyltrichlorosilane (OTS) treated SiO<sub>2</sub> as the dielectric layer. There was no obvious change in  $I_{\text{on}}/I_{\text{off}}$  ( $\sim 10^6$ ) for transistors measured in vacuum and air.<sup>17</sup>



**Figure 1.22.** The chemical structures of the some PDI derivatives for OFET applications.

N,N'-Perfluorophenyl-substituted perylene diimide (**14**) and related compounds (**12** and **13**) developed by Chen and co-workers were demonstrated to be good, air-stable materials in n-channel OFETs. The electron mobilities of these devices based on **12**, **13**, and **14** were found to be 0.011, 0.026 and 0.042 cm<sup>2</sup>V<sup>-1</sup>s<sup>-1</sup>, respectively, for OFETs measured in ambient atmosphere. These values were reduced by only 5 to 25% as compared to the electron mobilities measured in vacuum. Since there are only limited difference in the LUMOs of these fluorinated-PDI-based materials as compared to their nonfluorinated counterparts, the improved air stability of the OFETs could be attributed to the better molecular packing of the fluorinated-PDIs in vacuum-deposited films, in which the fluorinated substituents could effectively prevent the penetration of oxygen and water.<sup>20</sup>



**Figure 1.23.** The chemical structures of the PDI derivatives with substitutions in the bay positions as electron-transport materials.

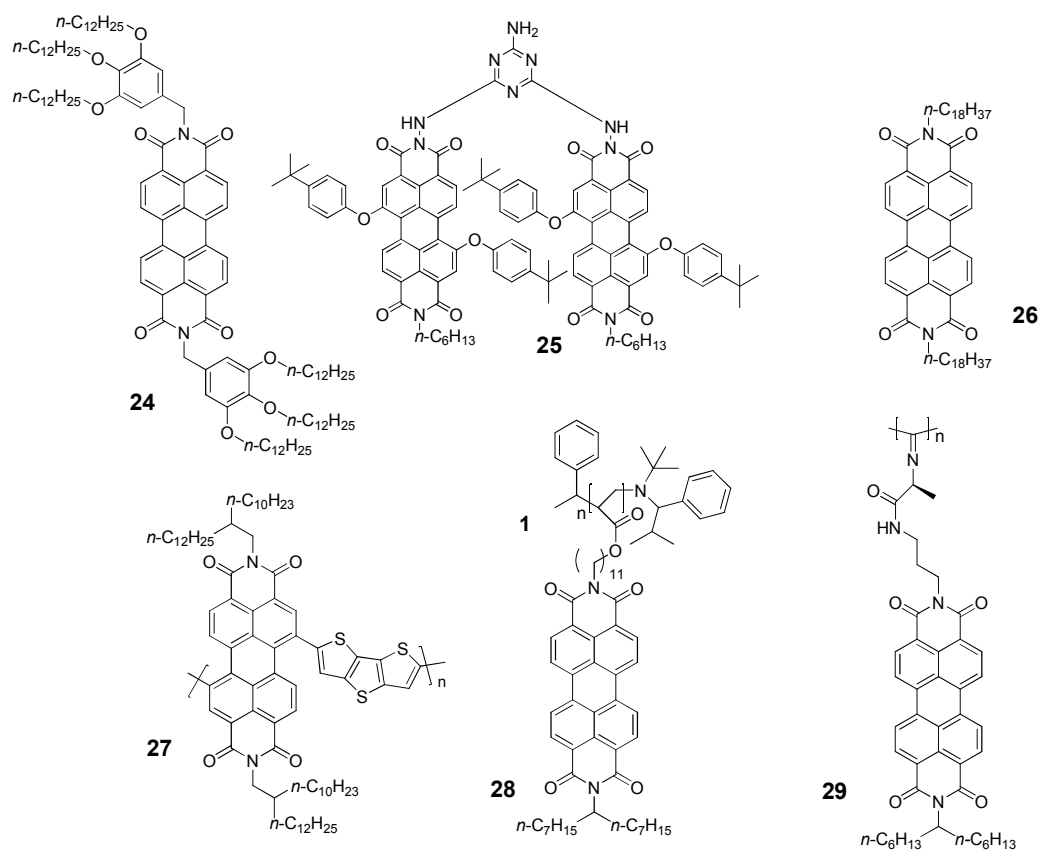
Perylene diimides with substitutions in the aromatic bay position have also been studied as active materials in n-channel OFETs. Biscyano-substituted perylene diimides (**15** and **16**, in Figure 1.23) developed by Jones and co-workers exhibit considerably lower LUMOs and high solubility. The electron mobilities in top-contact devices were found to be 0.1 and 0.64  $\text{cm}^2\text{V}^{-1}\text{s}^{-1}$  with  $I_{\text{on}}/I_{\text{off}} = \sim 10^5$  for the vacuum-deposited films from **15** and **16**, respectively, in ambient atmosphere. Top-contact devices fabricated from drop-cast films were also found to be air stable and exhibited mobilities of  $10^{-3}$  to  $10^{-5} \text{ cm}^2\text{V}^{-1}\text{s}^{-1}$ .<sup>8,14</sup> PDI-based materials **17** and **18**, with bromo- or chloro-substitutions in

the bay positions, were investigated by the same group, recently. It was found that devices of these materials operated in ambient atmosphere showed similar performance as those operated in vacuum, although the electron mobilities ( $\sim 10^{-4}$ – $10^{-5}$   $\text{cm}^2\text{V}^{-1}\text{s}^{-1}$ ) were low because of the non planarity of PDI cores and consequently poor  $\pi - \pi$  stacking.<sup>4,127</sup> However, another tetrachloro-substituted perylene diimide (**19**) was found via pulse-radiolysis time-resolved microwave conductivity technique (PR-TRMC) to have a charge-carrier mobility of  $0.14 \text{ cm}^2\text{V}^{-1}\text{s}^{-1}$ ,<sup>128</sup> which indicates that these types of materials might still be good candidates for transistor applications, if the film morphology could be well controlled.<sup>129</sup> Furthermore, in order to reduce the torsions from the substituents in the bay positions, materials with two or four smaller fluorine substituents of perylene diimides were developed. The electron mobilities of vacuum deposited films from **20** and **21** were found to be  $0.34$  and  $0.031 \text{ cm}^2\text{V}^{-1}\text{s}^{-1}$  with  $I_{\text{on}}/I_{\text{off}} > 10^5$  in ambient atmosphere. The higher mobility from the device containing **20** could be attributed to the less reduced torsion on the perylene diimide aromatic core.<sup>44-45</sup> Recently, perylene diimides (**22** and **23**) with perfluoralkyl chains in the bay positions were developed by Li and co-workers, and **23** showed electron mobilities up to  $0.052 \text{ cm}^2\text{V}^{-1}\text{s}^{-1}$  with  $I_{\text{on}}/I_{\text{off}} = 8 \times 10^6$  in ambient condition. It is worth mentioning that there was nearly no change of the mobility and  $I_{\text{on}}/I_{\text{off}}$  compared to the data measured in vacuum for **23**. The electron mobility of **22** was only  $0.005 \text{ cm}^2\text{V}^{-1}\text{s}^{-1}$  with  $I_{\text{on}}/I_{\text{off}} = 4 \times 10^3$ . However, the turn-on voltage for devices from **22** was  $4.7 \text{ V}$ , which was 10 times lower than those devices from **23**.<sup>15</sup>

Recently, research interest has focused on developing wet-processing perylene diimides with high electron mobility. Liquid-crystalline (LC) type material **26** was found to exhibit charge mobility of  $0.1 \text{ cm}^2\text{V}^{-1}\text{s}^{-1}$  in the liquid crystalline phase (*ca.*  $220^\circ\text{C}$ ),

and a charge-carrier mobility as high as  $0.2 \text{ cm}^2\text{V}^{-1}\text{s}^{-1}$  in the crystalline phase using PR-TRMC.<sup>130</sup> In 2005, room temperature LC material **24** was reported to exhibit electron mobilities as high as  $1.3 \text{ cm}^2\text{V}^{-1}\text{s}^{-1}$  under ambient atmosphere using the steady-state SCLC technique. This electron mobility is actually higher than that of amorphous silicon. However, the electron mobilities of the material measured via other techniques were low, as control of the PDI molecular alignment is challenging for **24** in thin films.<sup>7</sup> Also, field-effect transistors using highly ordered Langmuir – Blodgett (LB) films from compound **25** were fabricated and studied by Wang and co-workers. Within the top-contact devices, the molecules kept face-face configuration in films, and the electron mobilities went up to  $0.05 \text{ cm}^2\text{V}^{-1}\text{s}^{-1}$  with  $I_{\text{on}}/I_{\text{off}} > 10^3$ .<sup>131</sup> Very recently, a PDI-based D–A type conjugated polymer **27** was investigated as an electron-transport material in OFETs. The spin-coating films of the polymer were found to exhibit electron mobilities as high as  $0.013 \text{ cm}^2\text{V}^{-1}\text{s}^{-1}$  with  $I_{\text{on}}/I_{\text{off}} > 10^4$  in top-contact OFETs under nitrogen. The electron mobility of this material is among the highest value reported in conjugated polymers to date.<sup>16</sup> Side chain polymers (**28** and **29**) with PDI-pendants have also been investigated as electron transporting materials in OFET devices. Electron mobilities of  $1.2 \times 10^{-3} \text{ cm}^2\text{V}^{-1}\text{s}^{-1}$  with  $I_{\text{on}}/I_{\text{off}} > 10^4$  were reported for polymer **28** when thermal-annealing at  $210^\circ\text{C}$  for 60 minutes was performed on the spin-casted films in bottom-contact OFETs. Similar device performance was achieved when the devices from **29** were measured at 360 K in a top-contact device, which may be ascribed to the better intermolecular electron hopping upon thermal treatment.<sup>132-133</sup>





**Figure 1.24. The chemical structures of solution-processable PDI materials.**

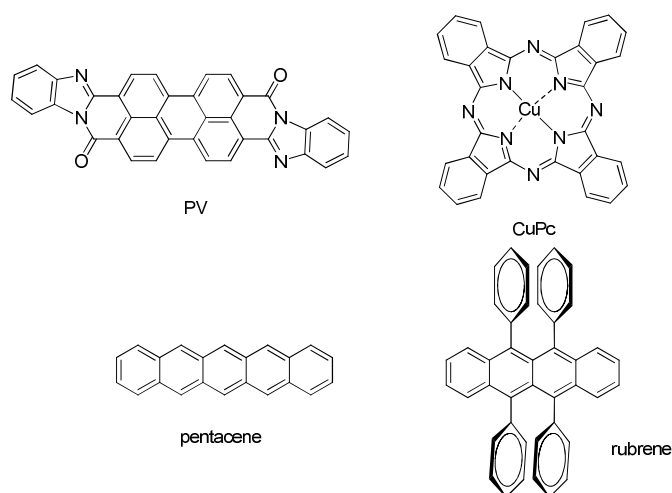
Over the years, great progress has been made in research on PDI-based materials for OFETs. However, the modest performance from transistors based on solution processable PDI materials actually limits their application in organic electronics. Research in order to further explore high performance wet-processable perylene diimides is highly desirable.

#### 1.4.2 PDIs as acceptors and photo-sensitizers in solar cell devices

Recently, perylene diimide derivatives have been extensively studied as electron acceptors for OPV applications because of their relatively low cost as compared to many other organic acceptors, good thermal- and photo-chemical stability, low electron affinity,

and intense light absorption in visible range.<sup>24,35</sup> Also, compared with the fullerene derivatives, PDI-based materials are more easily functionalized via chemical modification on the imide and/or bay positions to optimize the physical and chemical properties of the dyes.<sup>3,24</sup> The first organic solar cells, which were reported by Tang in 1986, in fact utilized a PDI derivative (PV) as the acceptor and Cu phthalocyanine (CuPc) as donor (as shown in Figure 1.25) in a p-n bilayer cell (ITO/CuPc/PV/Ag). The PCEs of the devices are approaching 1%.<sup>104</sup> Since that time, phthalocyanine and PDI derivatives have been commonly used in thin-film organic solar cells with phthalocyanines performing as p-type, hole-transport materials and PDI derivatives working as the electron-transport acceptors. Recently, following Tang's basic device structure, external PCEs of 2.4% have been demonstrated within a thin cell geometry where the incident photons make multiple passes through the light absorbing organic films to avoid exciton diffusion length/optical absorption length mismatch.<sup>134</sup> In this devices, the incorporating of an exciton-blocking layer (bathocuproine, also known as BCP)<sup>134</sup> between the organic layers and the metal cathode is essential to prevents damage due to cathode evaporation<sup>135</sup> and eliminates parasitic exciton quenching at the PDI/cathode interface.<sup>136</sup> Inverted bilayer organic solar cells with a structure consisting of an n-type insoluble PV layer with a spin-cast p-type-conjugated polymer, such as (poly(2-methoxy-5-(28-ethylhexyloxy)-1,4-phenylenevinylene)(MEH-PPV) and (poly(phenylimino-1,4-phenylene-1,2-ethenylene- 2,5-dihexyloxy-1,4-phenylene-1,2-ethenylene-1,4-phenylene) (PPAV-HH-PPV) on top of the acceptor layer show PCEs of *ca.* 0.4%.<sup>137</sup> Further ITO and Au electrodes were modified with In and PEDOT:PSS, respectively, leading to a smoother contact faciling electron transport and a utilization of the wide range of

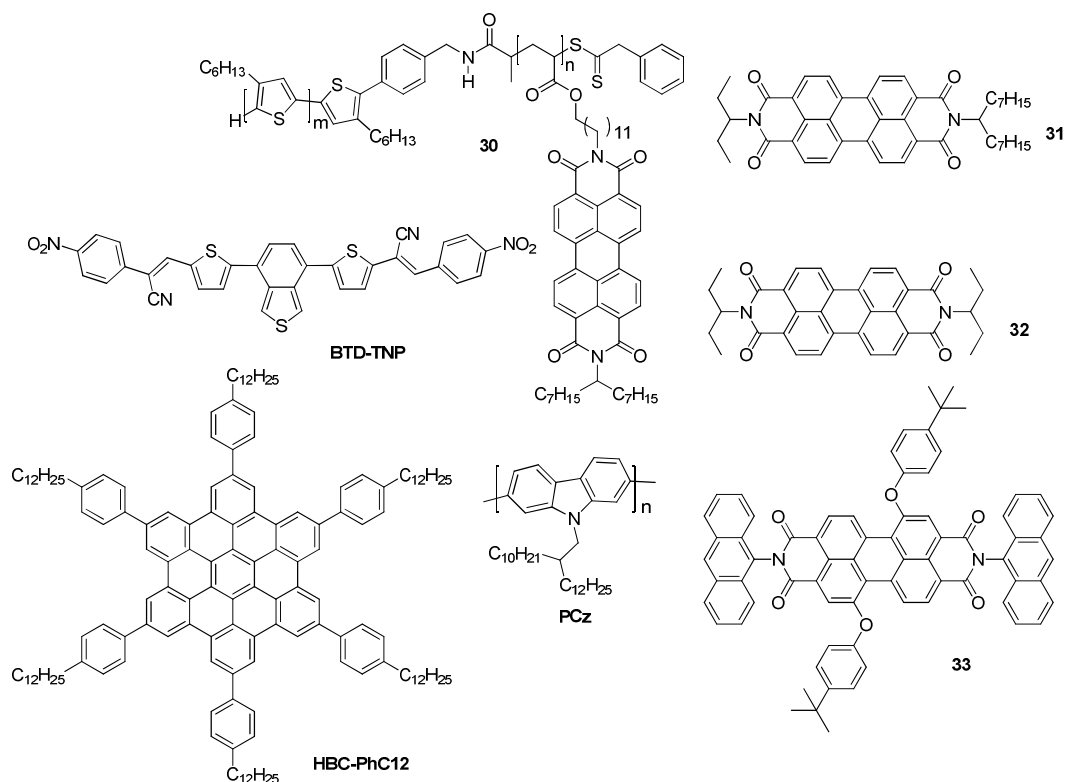
absorption by exciton confinement. Thus, the photovoltaic properties of the solar cells produced by the combination of those methods have been remarkably improved and give cells with PCEs approaching 2%.<sup>137</sup> Bilayer organic solar cells containing PDI-based acceptors and organic small molecular donors such as pentacene<sup>138</sup> and rubrene<sup>139</sup> can afford PCEs up to 2%. Some of these achievements are summarized in Table 1.3.



**Figure 1.25.** The chemical structures of the PV, CuPc, pentacene, and rubrene.

**Table 1.3.** p-n Heterojunction solar cell performance containing PDI-based acceptors.<sup>104,134,137-138,140-141</sup>

Devices	$V_{oc}$ (V)	$J_{sc}$ (mA/cm <sup>2</sup> )	$FF$	PCE (%)
ITO/CuPc/PV/Ag	0.45	2.3	0.65	1.0
ITO/DMP/CuPc/Ag	0.54	0.94	0.48	0.29
ITO/DMP/CuPc/Ag	0.53	1.61	0.43	0.63
ITO/DMP/CuPc/Ag	0.31	1.71	0.41	1.21
ITO/CuPc/PV/BCP/Ag	N.A.	N.A.	0.54	2.4
ITO/PEDOT/13/pentacene/BCP/Al	0.40	5.0	0.64	1.6
ITO/PV/MEH-PPV/Au	0.56	2.4	0.29	0.40
ITO/PV/PPAV-HH-PPV/Au	0.48	2.5	0.28	0.33



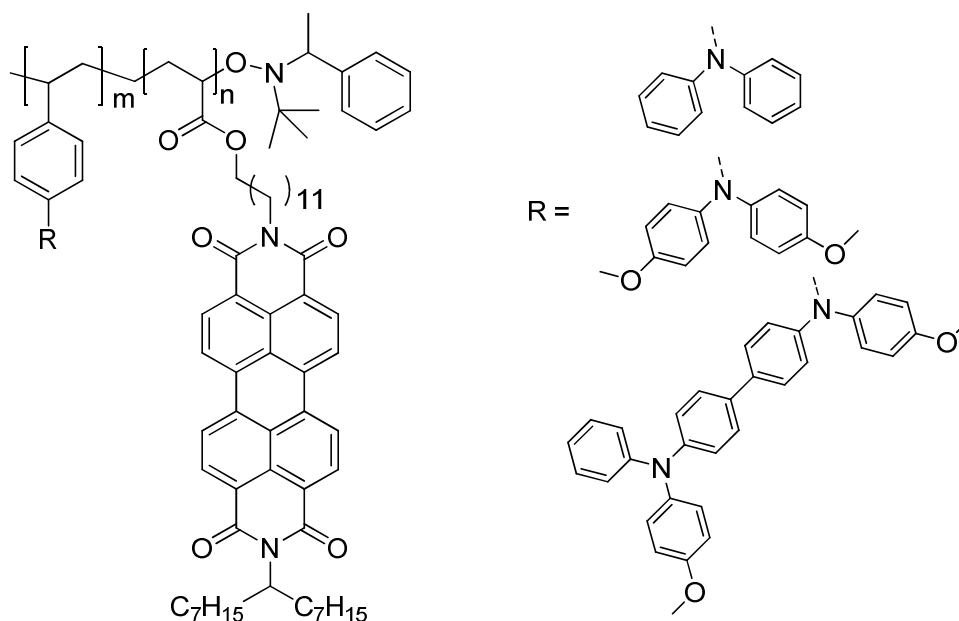
**Figure 1.26. PDI-based materials for solution processable solar cells.**

Compared to the bilayer solar cells, limited progress has been achieved on PDI-based BHJ solar cells, this is possibly due to the formation of micrometer-sized (or even larger) PDI-based aggregates in the blend films, leading to incomplete exciton dissociation.<sup>24</sup> Solar cells comprised of blends of perylene diimides and P3HT exhibit low PCEs, (typically below 0.05%). Recently, by using asymmetric PDI derivatives (**31**), PCEs as high as 0.37% have been demonstrated using the P3HT:PDI blend, probably because fewer PDI aggregates formed. Device performance can be further enhanced in the presence of the compatibilizer (**30**) with optimized devices showing an efficiency of 0.55% because smaller size PDI domains were formed in the active layer.<sup>71</sup> Müllen and coworkers found that device efficiency could be largely improved under illumination with

solar light for PDI-based solar cells as P3HT was replaced with a poly(2,7-carbazaole)-based donor (PCz, as shown in Figure 1.26).<sup>142</sup> The best photovoltaic device exhibits high external quantum efficiency (EQE) of 16% at 490 nm, with PCEs over 0.6% under AM 1.5 irradiation. This is one of the best reported PCE and EQE values for solar cells using polymer/PDI blends, though they are still much lower than those devices using polymer/PCBM blend. The morphology of PCz:**32** blend films studied by SEM showed the formation of favorable phase separation, which is important in obtaining high efficiency.<sup>142</sup> Using a blend of discotic liquid-crystal HBC-PhC12 (as shown in Figure 1.26) with **32** produces thin-films with vertically segregated HBC-PhC12 and **32** domains, with large interfacial surface areas, resulting in solar cells with external quantum efficiencies greater than 34% near 490 nm, with PCE *ca.* 2%.<sup>23</sup> Very recently, a blend of **33** and a D–A type small molecular donor (BTD-TNP as shown in Figure 1.26) was shown to give overall device PCEs of 2.85%.<sup>143</sup> The much higher  $J_{SC}$  ( $6.6 \text{ mAcm}^{-2}$ ) of these devices as compared to other PDI-based solar cells results from the contribution of exciton generation by both donor and acceptor components used in these BHJ solar cells, as well as the balanced charge transport in the devices (*ca.*  $1.0 \times 10^{-4} \text{ cm}^2 \text{V}^{-1} \text{s}^{-1}$  for electron and  $4.6 \times 10^{-4} \text{ cm}^2 \text{V}^{-1} \text{s}^{-1}$  for hole, which are comparable to the charge carrier mobilities for those high-efficiency BHJ solar cells based on P3HT:PCBM<sup>144</sup> blend).<sup>143</sup>

One recent promising approach for solar cell devices is to use self-organizing or supramolecular materials to control the thin-film nanomorphology of the photoactive layer.<sup>105</sup> The self-assembly of a block-copolymer (BCP) in which block A contains an electron donor and block B contains an electron acceptor could undergo microphase separation, which could, in principle, produce a highly regular nanometer-scale structure

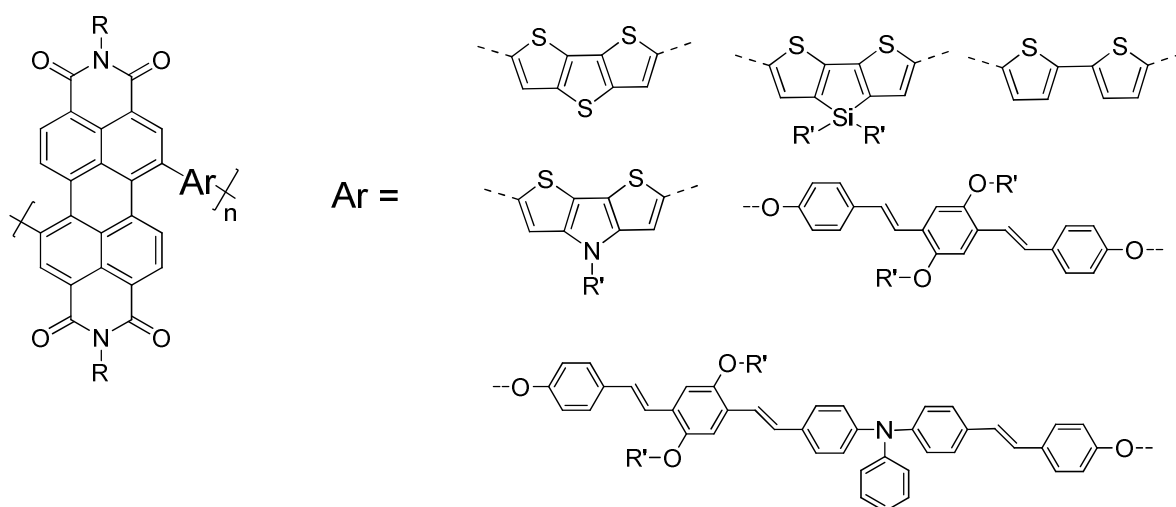
of idealized morphology spontaneously during film preparation.<sup>105</sup> Thelakkat and coworkers reported the using of D–A diblock copolymers (as shown in Figure 1.27), carrying PDIs and triphenylamines as electron-transport and hole-transport moieties, respectively, to realize stable nanometer-scale microphase-separation in the active layers. These produced an increase in the device efficiencies by an order of magnitude compared with the blend films from the two homopolymers, and solar cells using these BCPs show PCEs of 0.3%.<sup>18,110,132,145</sup> Periodic, nanometer-scale morphology was also successfully accomplished using the P3HT-block-PDI copolymers (**30** and materials with similar structures) as the active layer in solar cells with PCEs over 0.5%.<sup>146-147</sup> The state-of-the-art using this approach displays attractive properties, including phase-separation of donor and acceptor block components on length scales commensurate with exciton diffusion lengths, an ability to self-assemble into a range of different morphologies, and construction of an all-in-one molecule that can also include additional components for functional enhancement, such as dyes for expanding solar spectra absorption. However, the overall power conversion efficiencies of the devices with current diblock-copolymers are still far from satisfactory ( $\eta < 1\%$ ). So, further effort toward developing better D–A diblock or multiblock copolymers with matching D/A energy levels, high charge mobilities, and good solar spectrum coverage is of interest. Furthermore, a more detailed understanding of the parameters controlling charge transfer and migration in these self-organizing block copolymer systems might facilitate the rational design and synthesis of new D–A type materials and morphology control required for high-performance OPV devices as a result.



**Figure 1.27. PDI-based diblock copolymers for OPV applications.**

Recently, research on using PDI-donor-based conjugated polymers connected at the perylene 1,6(7)-bay positions for solar cell applications have also been carried on in different research groups.<sup>16,53,148-150</sup> The introduction of electron donor moieties such as dithienothiophene (DTT),<sup>16,150</sup> dithienopyrrole (DTP),<sup>53</sup> bithiophene,<sup>151</sup> oligo-phenylene vinylene,<sup>148</sup> dithienosilole (DTS)<sup>152</sup> and triphenyl amine type donor<sup>148</sup> into the bay areas of perylene diimides (Figure 1.28) enhanced the solubility of polymers and dramatically quenched the fluorescence. Additionally, the electron mobilities of these kinds of polymers are approaching  $0.1 \text{ cm}^2 \text{V}^{-1} \text{s}^{-1}$  in OFETs. Photovoltaic devices using these types of polymers in blends with appropriate polythiophene-based donor polymers or other D–A type polymers exhibit PCE approaching 1.5%.<sup>16,25,152</sup> One limitation these kinds of D–A polymers for better solar energy conversion is that these materials contribute little for light-harvesting in solar cells. For example, an EQE wavelength plot of a photovoltaic

device based on a BHJ cells from DTT-PDI polymer/polythiophene blend is close to the absorption spectrum of the polythiophene itself, with little contribution from the lower energy absorptions of the PDI-based materials. This may be because of the ultra fast photo-induced intramolecular charge transfer and charge recombination in the DTT-PDI polymer, suggested by the transient absorption spectra, which shortens the DTT-PDI exciton life-time (several hundred picoseconds), reducing the number of excitons that diffuse to the D/A interface for charge dissociation.<sup>153</sup> Further development for new PDI-donor-based conjugated polymers or other kinds arylene diimide based D – A type conjugated polymers are centered around practical approaches for high performance electron-transport polymers for OPV and OFET applications.

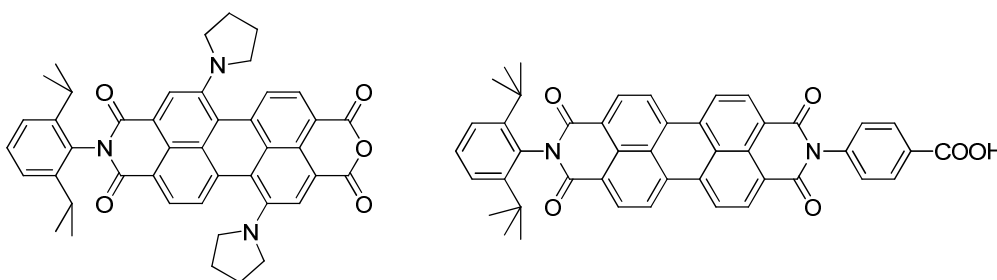


**Figure 1.28. Conjugated PDI-based polymers with D-A connection on the PDI bay positions.**

Recently, PDI-based light-harvesting materials (as shown in Figure 1.29) were also used in dye-sensitized solar cells (DSSCs, also known as Grätzel cells)<sup>154</sup> with varying



binding groups (like carboxylic acid or anhydride), as well as different bulk inorganic semiconductors.<sup>155-156</sup> The best reported DSSCs utilizing PDI-based photosensitive dyes for device gave power conversion efficiencies over 2.5% with an impressive fill factor value (FF = 0.63).<sup>156</sup> Since DSSCs follow a different mechanism from OPVs, in depth discussion on using PDI-based dyes for DSSC application will not be given here.



**Figure 1.29. Some PDI materials as photo-sensitizers for DSSCs.**

Ever since Tang's demonstration of organic solar cells with PDI derivatives as the acceptor, research attentions have been focused on using PDI-based dyes as active materials in solar cells as well as in OFETs. Despite for the promising performance of those vacuum-deposited devices, devices fabricated via a wet-process exhibit limited performance. This had been speculated for the poor film morphology and low charge mobility, perhaps due to anisotropy in solution-process thin-films from these PDI-based semiconductors. Further research targeting perylene diimides solving these existing problems with improving solar cell performance could be valuable for both fundamental research and real OPV applications in the near future.

## **1.5 Research goals and organization of the thesis**

### **1.5.1 Research goals and design strategies.**

The aim of this thesis is to develop new PDI-based conjugated materials and understand their structure-property relationships to better meet the needs of applications in organic electronics and optical limiting. In the first part of this thesis, the development of functionalized perylene diimide is described primarily for OPV applications. In the first projects, the synthesis, properties, and solar cell performance of PDI-based homopolynorbornenes and diblock copolynorbornenes were investigated. Also, perylene diimide derivatives with various substituents were developed to improve their mixing with polythiophenes, and the solar cell performance of these blends was studied. In the second part of this thesis, perylene diimide radical anion absorption was utilized for one-photon- or two-photon-induced optical limiting in the spectral range of the perylene diimide radical-anion absorption of new PDI-donor conjugates, such as molecular dyads and donor conjugated polymers with perylene diimide pendants. A variety of PDI-based conjugated materials (polymers and molecular dyads) have been synthesized, characterized, and investigated for electronic or optic applications.

### **1.5.2 Organization of the thesis**

The remainder of the thesis contains the following four chapters.

Chapter 2 describes research on various PDI-grafted polynorbornenes. It includes a short introduction to PDI-based organic solar cells, the design and synthesis of the target polymers, their physical properties, and applications for organic electronics.

Chapter 3 concerns research on using PDI-based diblock-copolymers for organic solar cell applications. It contains an introduction to using block copolymers for electronic application, the design and synthesis of target perylene diimide

/oligothiophenes diblockcopolymers, studies of their physical properties, thin film morphologies, and solar cell performance.

Chapter 4 is concerned with improving PDI-based solar cell performance by attaching functional groups to perylene diimide molecules. It includes a literature review on the promising photophysics of perylene diimide/polythiophene blend, the design and synthesis of the target molecules, and studies of the photophysics and solar cells in blend films with polythiophenes.

Chapter 5 describes 2PA-induced optical limiting using photo-generated perylene diimide radical anions. It covers a short introduction to 2PA-induced optical limiting, the design and synthesis of the target dyads, and studies of the photophysics and optical limiting applications between 700 – 800 nm.

Chapter 6 describes the optical limiting application on using perylene diimide – donor, double-cable conjugated polymers. It contains an introduction to double-cable conjugated polymers and reverse saturable absorption (RSA) induced optical limiting, the design and synthesis of the target acceptor-grafted “double cable” conjugated polymers, research on the synthesis of the target acceptor-grafted double-cable conjugated polymers, research on their physical properties, the photophysics, and optical limiting applications.

Chapter 7 summarizes the major findings from the research described in this thesis and suggests future directions that may lead to further improvement in OPV and optical limiting materials with PDI moieties.

## 1.6 Reference

- (1) Herbst, W.; Hunger, K. *Industrial Organic Pigments (Second Completely Revised Edition)*; Weinheim, 1997.
- (2) Kazmaier, P. M.; Hoffmann, R. *J. Am. Chem. Soc.* **1994**, *116*, 9684-9691.
- (3) Würthner, F. *Chem. Commun.* **2004**, 1564-1579.
- (4) Bao, Z.; Locklin, J. *Organic Field-Effect Transistors*; CRC Press, 2006.
- (5) Serin, J. M.; Brousmiche, D. W.; Fréchet, J. M. J. *Chem. Commun.* **2002**, 2605-2607.
- (6) Gronheid, R.; Hofkens, J.; Kohn, F.; Weil, T.; Reuther, E.; Müllen, K.; Schryver, F. C. D. *J. Am. Chem. Soc.* **2002**, *124*, 2418-2419.
- (7) An, Z.; Yu, J.; Jones, S. C.; Barlow, S.; Yoo, S.; Domercq, B.; Prins, P.; Siebbeles, L. D. A.; Kippelen, B.; Marder, S. R. *Adv. Mater.* **2005**, *17*, 2580-2583.
- (8) Jones, B. A.; Facchetti, A.; Wasielewski, M. R.; Marks, T. J. *J. Am. Chem. Soc.* **2007**, *129*, 15259-15278.
- (9) Sadrai, M.; Bird, G. R. *Opt. Commun.* **1984**, *51*, 62-64.
- (10) Ford, W. E.; Kamat, P. V. *J. Phys. Chem.* **1987**, *91*, 6373-6380.
- (11) Seybold, G.; Wagenblast, G. *Dyes and Pigments* **1989**, *11*, 303-317.
- (12) Weil, T.; Wiesler, U. M.; Herrmann, A.; Bauer, R.; Hofkens, J.; Schryver, F. C. D.; Müllen, K. *J. Am. Chem. Soc.* **2001**, *123*, 8101-8108.
- (13) Ahrens, M. J.; Fuller, M. J.; Wasielewski, M. R. *Chem. Mater.* **2003**, *15*, 2684-2686.
- (14) Jones, B. A.; Ahrens, M. J.; Yoon, M.-H.; Facchetti, A.; Marks, T. J.; Wasielewski, M. R. *Angew. Chem. Int. Ed.* **2004**, *43*, 6363-6366.
- (15) Li, Y.; Tan, L.; Wang, Z.; Qian, H.; Shi, Y.; Hu, W. *Org. Lett.* **2008**, *10*, 529-532.
- (16) Zhan, X.; Tan, Z. A.; Domercq, B.; An, Z.; Zhang, X.; Barlow, S.; Li, Y.; Zhu, D.; Kippelen, B.; Marder, S. R. *J. Am. Chem. Soc.* **2007**, *129*, 7246-7247.
- (17) Oh, J. H.; Liu, S.; Bao, Z.; Schmidt, R.; Würthner, F. *Appl. Phys. Lett.* **2007**, *91*, 212107.
- (18) Lindner, S. M.; Kaufmann, N.; Thelakkat, M. *Org. Electr.* **2007**, *8*, 69-75.
- (19) Jimnez, n. J.; Spnig, F.; Rodríguez-Morgade, M. S.; Ohkubo, K.; Fukuzumi, S.; Guldi, D. M.; Torres, T. *Org. Lett.* **2007**, *9*, 2481-2484.
- (20) Chen, H. Z.; Ling, M. M.; Mo, X.; Shi, M. M.; Wang, M.; Bao, Z. *Chem. Mater.* **2007**, *19*, 816-824.
- (21) Gvishi, R.; Reisfeld, R.; Burshtein, Z. *Chem. Phys. Lett.* **1993**, *213*, 338-344.
- (22) Law, K. Y. *Chem. Rev.* **1993**, *93*, 449-486.
- (23) Schmidt-Mende, L.; Fechtenkötter, A.; Müllen, K.; Moons, E.; Friend, R. H.; MacKenzie, J. D. *Science* **2001**, *293*, 1119-1122.
- (24) Wang, H.; Peng, B.; Wei, W. *Progress Chem.* **2008**, *20*, 1751-1760.
- (25) Tan, Z. A.; Zhou, E.; Zhan, X.; Wang, X.; Li, Y.; Barlow, S.; Marder, S. R. *Appl. Phys. Lett.* **2008**, *93*, 073309.
- (26) Belfield, K. D. B., M. V.; Hernandez, F. E.; Przhonska, O. V. *J. J. Phys. Chem. C* **2008**, *112*, 5618-5622.

- (27) O'Neil, M. P.; Niemczyk, M. P.; Svec, W. A.; Gosztola, D.; L.Gaines, G.; Wasielewski, M. R. *Science* **1992**, *257*, 63-65.
- (28) Prathapan, S.; Yang, S. I.; Seth, J.; Miller, M. A.; Bocian, D. F.; Holten, D.; Lindsey, J. S. *J. Phys. Chem. B* **2001**, *105*.
- (29) An, Z. S.; Odom, S. A.; Kelley, R. F.; Huang, C.; Zhang, X.; Barlow, S.; Padilha, L. A.; Fu, J.; Webster, S.; Hagan, D. J.; Van Stryland, E. W.; Wasielewski, M. R.; Marder, S. R. *J. Phys. Chem. A* **2009**, *113*, 5585-5593.
- (30) Shoaee, S. A., Z.; Zhang, X.; Barlow, S.; Marder, S. R.; Duffy, W.; Heeney, M.; McCulloch, I.; Durrant, J. R. *Chem. Commun.* **2009**, 5445-5447.
- (31) Fukuzumi, S.; Ohkubo, K.; Ortiz, J.; Gutierrez, A. M.; Fernandez-Lazaro, F.; Sastre-Santos, A. *Chem. Commun.*, **2005**, 3814-3816.
- (32) Kippelen, B.; Brédas, J. L. *Energy Environ. Sci.* **2009**, *2*, 251-261.
- (33) Günes, S.; Neugebauer, H.; Sariciftci, N. S. *Chem. Rev.* **2007**, *107*, 1324-1338.
- (34) Thompson, B. C.; Fréchet, J. M. J. *Angew. Chem. Int. Ed.* **2008**, *47*, 58-77.
- (35) Nagao, Y. *Progress Org. Chem.* **1997**, *31*, 43-49.
- (36) Langhals, H. *Heterocycles* **1995**, *40*, 477-500.
- (37) Huang, Y.; Yan, Y.; Smarsly, B. M.; Wei, Z.; Faul, C. F. J. *J. Mater. Chem.* **2009**, *19*.
- (38) Backes, C.; Schmidt, C.; Hauke, F.; Böttcher, C.; Hirsch, A. *J. Am. Chem. Soc.* **2009**, *131*, 2172-2173.
- (39) Heek, T.; Fasting, C.; Rest, C.; Zhang, X.; Würthner, F.; Haag, R. *Chem. Commun.* **2010**, *46*, 188-1886.
- (40) Liu, Y.; Wang, K.-R.; Guo, D.-S.; Jiang, B.-P. *Adv. Funct. Mater.* **2009**, *19*, 2230-2235.
- (41) Wicklein, A.; Kohn, P.; Ghazaryan, L.; Thurn-Albrecht, T.; Thelakkat, M. *Chem. Commun.* **2010**, *46*, 2328-2230.
- (42) Iverson, I. K.; Tam-Chang, S.-W. *J. Am. Chem. Soc.* **1999**, *121*, 5801-5802.
- (43) Seybold, G.; Wagenblast, G. *Dyes and Pigments* **1989**, *11*, 303-317.
- (44) Schmidt, R.; Ling, M. M.; Oh, J. H.; Winkler, M.; Könnemann, M.; Bao, Z.; Würthner, F. *Adv. Mater.* **2007**, 3692-3695.
- (45) Würthner, F.; Osswald, P.; Schmidt, R.; Kaiser, T. E.; Mansikkama, H.; Könnemann, M. *Org. Lett.* **2006**, *8*, 3765-3768.
- (46) Iden, R.; Seybold, G. In *Ger. Pat. Appl.*, 1985; Vol. DE 3434059 A1.
- (47) Böhm, A.; Arms, H.; Henning, G.; Blaschka, P. In *Ger. Pat. Appl.*, 1997; Vol. DE 19547209 A1.
- (48) Würthner, F.; Stepanenko, V.; Chen, Z.; Saha-Moller, C. R.; Kocher, N.; Stalke, D. *J. Org. Chem.* **2004**, *69*, 7933-7939.
- (49) Rajasingh, P.; Cohen, R.; Shirman, E.; Shimon, L. J. W.; Rybtchinsk, B. *J. Org. Chem.* **2007**, *72*, 5973-5979.
- (50) Ahrens, M. J.; Fuller, M. J.; Wasielewski, M. R. *Chem. Mater.* **2003**, *15*, 2684-2686.
- (51) Qiu, W.; Chen, S.; Sun, X.; Liu, Y.; Zhu, D. *Org. Lett.* **2006**, *8*, 867-870.

- (52) Sivamurugan, V.; Kazlauskas, K.; Jursenas, S.; Gruodis, A.; Simokaitiene, J.; Grazulevicius, J. V.; Valiyaveettil, S. *J. Phys. Chem. B* **2010**, *114*, 1782-1789.
- (53) Zhan, X.; Tan, Z. A.; Zhou, E.; Li, Y.; Misra, R.; Grant, A.; Domercq, B.; Zhang, X.-H.; An, Z.; Zhang, X.; Barlow, S.; Kippelen, B.; Marder, S. R. *J. Mater. Chem.* **2009**, *19*, 5794-5803.
- (54) Rohr, U.; Kohl, C.; Müllen, K.; Craats, A. v. d.; Warman, J. *J. Mater. Chem.* **2001**, *11*, 1789-1799.
- (55) Rohr, U.; Schlichting, P.; Böhm, A.; Gross, M.; Meerholz, K.; Bräuchle, C.; Müllen, K. *Angew. Chem. Int. Ed.* **1998**, *37*, 1434-1437.
- (56) Nakazono, S.; Easwaramoorthi, S.; Kim, D.; Shinokubo, H.; Osuka, A. *Org. Lett.* **2009**, *11*, 5426-5429.
- (57) Nakazono, S.; Imazaki, Y.; Yoo, H.; Yang, J.; Sasamori, T.; Tokitoh, N.; Cedric, T.; Kageyama, H.; Kim, D.; Shinokubo, H.; Osuka, A. *Chem. Eur. J.* **2009**, *15*, 7530-7533.
- (58) Gsänger, M.; Oh, J. H.; Könemann, M.; Höffken, H. W.; Krause, A.-M.; Bao, Z.; Würthner, F. *Angew. Chem. Int. Ed.* **2010**, *49*, 740-743.
- (59) Wescott, L. D.; Mattern, D. L. *J. Org. Chem.* **2003**, *68*, 10058-10066.
- (60) Rademacher, A.; Märkle, S.; Langhals, H. *Chem. Ber.* **1982**, *115*, 2927-2934.
- (61) Würthner, F.; Sautter, A.; Schilling, J. *J. Org. Chem.* **2002**, *67*, 3037-3044.
- (62) Gómez, R.; Veldman, D.; Blanco, R.; Seoane, C.; Segura, J. L.; Janssen, R. A. J. *Macromolecules* **2007**, *40*, 2760-2772.
- (63) Würthner, F.; Thalacker, C.; Diele, S.; Tschierske, C. *Chem. Eur. J.* **2001**, *7*, 2245-2253.
- (64) Zhao, Y.; Wasielewski, M. R. *Tetrahedron Lett.* **1999**, *40*, 7047-7050.
- (65) Würthner, F.; Thalacker, C.; Diele, S.; Tschierske, C. *Chem. Eur. J.* **2001**, *7*, 2245-2253.
- (66) Ford, W. E.; Hiratsuka, H.; Kamat, P. V. *J. Phys. Chem.* **1989**, *93*, 6692-6696.
- (67) Lukas, A. S.; Zhao, Y.; Miller, S. E.; Wasielewski, M. R. *J. Phys. Chem. B* **2002**, *106*, 1299-1306.
- (68) Salbeck, J.; Kunkely, H.; Langhals, H.; Saalfrank, R. W.; Daub, J. *Chimia* **1989**, *43*, 6-9.
- (69) Langhals, H.; Karolinb, J.; Johansson, L. *J. Chem. Soc., Faraday Trans.* **1998**, *94*, 2919-2922.
- (70) Ford, W. E.; Kamat, P. V. *J. Phys. Chem.* **1987**, *6373-6380*, 6373-6380.
- (71) Rajaram, S.; Armstrong, P. B.; Kim, B. J.; Fércet, J. M. J. *Chem. Mater.* **2009**, *21*, 1775-1777.
- (72) Hädicke, E.; Graser, F. *Acta Crystallogr., Sect. C* **1986**, *42*, 195-198.
- (73) Hädicke, E.; Graser, F. *Acta Crystallogr., Sect. C* **1986**, *42*, 189-195.
- (74) Zugenmaier, P.; Duff, J.; Bluhm, T. L. *Cryst. Res. Technol* **2000**, *35*, 1095-1115.
- (75) Sijibesma, R. P.; Meijer, E. W. *Chem. Commun.* **2003**, 5-16.
- (76) Wang, W.; Han, J. J.; Wang, L.-Q.; Li, L.-S.; Shaw, W. J.; Li, A. D. Q. *Nano Lett.* **2003**, *3*, 455-458.

- (77) You, C. C.; Würthner, F. *J. Am. Chem. Soc.* **2003**, *125*, 9716-9725.
- (78) Würthner, F.; Thalacker, C.; Sautter, A. *Adv. Mater.* **1999**, *11*, 754-758.
- (79) van der Boom, T.; Hayes, R. T.; Zhao, Y.; Bushard, P. J.; Weiss, E. A.; Wasielewski, M. R. *J. Am. Chem. Soc.* **2002**, *124*, 9582-9590.
- (80) Wang, W.; Wan, W.; Zhou, H. H.; Niu, S. Q.; Li, A. D. Q. *J. Am. Chem. Soc.* **2003**, *125*, 5245-5249.
- (81) Dobrawa, R.; Kurth, D. G.; Würthner, F. *Polymer Preprints* **2004**, *45*, 378-379.
- (82) Dobrawa, R.; Würthner, F. *Chem. Commun.* **2002**, 1878-1879.
- (83) Neuteboom, E. E. *Ph.D thesis* **2004**, Technische Universiteit Eindhoven.
- (84) Rehm, D.; Weller, A. *Isr. J. Chem.* **1970**, *8*, 258-262.
- (85) Marcus, R. A. *J. Chem. Phys.* **1956**, *24*, 966-978.
- (86) Marcus, R. A. *Can. J. Chem.* **1959**, *37*, 155-163.
- (87) Marcus, R. A. *Angew. Chem. Int. Ed.* **1993**, *32*, 1111-1121.
- (88) Marcus, R. A. *Rev. Mod. Phys.* **1993**, *65*, 599-610.
- (89) Kelley, R. F.; Shin, W. S.; Rybtchinski, B.; Sinks, L. E.; Wasielewski, M. R. *J. Am. Chem. Soc.* **2007**, *129*, 3173-3181.
- (90) Muthukumar, K.; Loewe, R. S.; Kirmaier, C.; Hindin, E.; Schwartz, J. K.; Sazanovich, I. V.; Diers, J. R.; Bocian, D. F.; Holten, D.; Lindsey, J. S. *J. Phys. Chem. B* **2003**, *107*, 3431-3442.
- (91) Kirmaier, C.; Hindin, E.; K., J.; Schwartz, J. S.; Sazanovich, I. V.; Diers, J. R.; Muthukumar, K.; Taniguchi, M.; Bocian, D. F.; Lindsey, J. S.; Holten, D. *J. Phys. Chem. B* **2003**, *107*, 3443-3454.
- (92) Cha, M.; Sariciftci, N. S.; Heeger, A. J.; Hummelen, J. C.; Wudl, F. *Appl. Phys. Lett.* **1995**, *67*, 3850-3852.
- (93) Spangler, C. W. *J. Mater. Chem.* **1999**, *9*, 2013-2020.
- (94) Chi, S.-H.; Hales, J. M.; Cozzuol, M.; Ochoa, C.; Fitzpatrick, M.; Perry, J. W. *Opt. Lett.* **2009**, *17*, 22062-22072.
- (95) Coropceanu, V.; Cornil, J.; Filho, D. A. d. S.; Olivier, Y.; Silbey, R.; Brédas, J.-L. *Chem. Rev.* **2007**, *107*, 926-952.
- (96) Zhang, X.-H. *Ph.D thesis* **2009**, Georgia Institute of Technology.
- (97) Arias, A. C.; MacKenzie, J. D.; McCulloch, I.; Rivnay, J.; Salleo, A. *Chem. Rev.* **2010**, *110*, 3-24.
- (98) Gelinck, G. H.; Huitema, H. E. A.; Van Veenendaal, E.; Cantatore, E.; Schrijnemakers, L.; Van der Putten, J.; Geuns, T. C. T.; Beenhakkers, M.; Giesbers, J. B.; Huisman, B. H.; Meijer, E. J.; Benito, E. M.; Touwslager, F. J.; Marsman, A. W.; Van Rens, B. J. E.; De Leeuw, D. M. *Nat. Mater.* **2004**, *3*, 106-110.
- (99) Shirota, Y.; Kageyama, H. *Chem. Rev.* **2007**, *107*, 953-1010.
- (100) Zhang, X. *Ph.D Thesis* **2009**, Georgia Institute of Technology.
- (101) Chua, L.-L.; Zaumseil, J.; Chang, J.-F.; Ou, E. C.-W.; Ho, P. K.-H.; Sirringhaus, H.; Friend, R. H. *Nature* **2005**, *34*, 194-199.
- (102) Anthony, J. E. *Chem. Rev.* **2006**, *106*, 5028-5048.
- (103) Hovel, H. *Semiconductors & Semimetals, Volume II, Solar Cells*; Academic Press, N. Y., 1975.
- (104) Tang, C. W. *Appl. Phys. Lett.* **1986**, *48*, 183-185.

- (105) Darling, S. B. *Energy Environ. Sci.* **2009**, 2, 1266-1273.
- (106) Brabec, C. J.; Sariciftci, N. S.; Hummelen, J. C. *Adv. Funct. Mater.* **2001**, 11, 15-26.
- (107) Ohkita, H. C., S.; Astuti, Y.; Duffy, W.; Tierney, S.; Zhang, W.; Heeney, M.; McCulloch, I.; Nelson, J.; Bradley, D. D. C.; Durrant, J. R. *J. Am. Chem. Soc.* **2008**, 130, 3030-3042.
- (108) Knupfer, M. *Appl. Phys. A: Mater. Sci. Process.* **2003**, 77, 623-626.
- (109) Heremans, P.; Cheyins, D.; Rand, B. P. *Acc. Chem. Res.* **2009**, 42, 1740-1747.
- (110) Lindner, S. M.; Huttner, S.; Chiche, A.; Thelakkat, M.; G. Krausch, A. *Angew. Chem., Int. Ed.* **2006**, 45, 3364-3368.
- (111) Sista, S.; Hong, Z.; Park, M.-H.; Xu, Z.; Yang, Y. *Adv. Mater.* **2010**, 22, 77-80.
- (112) Kim, J. Y.; Lee, K.; Coates, N. E.; Moses, D.; Nguyen, T.-Q.; Dante, M.; Heeger, A. J. *Science* **2007**, 317, 222-225.
- (113) Waldauf, C.; Morana, M.; Denk, P.; Schilinsky, P.; Coakley, K.; Choulis, S. A.; Brabec, C. J. *Appl. Phys. Lett.* **2006**, 89, 233517
- (114) Haua, S. K.; Yip, H.-L.; Zou, J.; Jen, A. K.-Y. *Org. Electr.* **2009**, 10, 1401-1407.
- (115) Liang, Y. Y.; Wu, Y.; Feng, D. Q.; Tsai, S. T.; Son, H. J.; Li, G.; Yu, L. P. *J. Am. Chem. Soc.* **2009**, 131, 56-57.
- (116) Liang, Y.; Feng, D.; Wu, Y.; Tsai, S.-T.; Li, G.; Ray, C.; Yu, L. *J. Am. Chem. Soc.* **2009**, 131, 7792-7799.
- (117) Ma, W.; Yang, C.; Gong, X.; Lee, K.; Heeger, A. J. *Adv. Funct. Mater.* **2005**, 15, 1617-1622.
- (118) Reyes-Reyes, M.; Kim, K.; Carroll, D. L. *Appl. Phys. Lett.* **2005**, 87, 083506.
- (119) Haber, K. S.; Albercht, A. C. *J. Phys. Chem.* **1984**, 88.
- (120) Kepler, R. G. *Phys. Rev.* **1960**, 119, 1226-1229.
- (121) Leblanc, O. H. *J. Chem. Phys.* **1960**, 33, 626-626.
- (122) Lampert, M. A., Mark, P. *Current injection in solids; Academic Press, New York*, , 1970.
- (123) Ostrick, J. R.; Dodabalapur, A.; Torsi, L.; Lovinger, A. J.; Kwock, E. W.; Miller, T. M.; Galvin, M.; Berggren, M.; Katz, H. E. *J. Appl. Phys.* **1997**, 81, 6804-6808.
- (124) Horowitz, G. K., F.; Spearman, P.; Fichou, D.; Nogues, C.; Pan, X.; Garnier, F. *Adv. Mater.* **1996**, 8, 242-244.
- (125) Tatemichi, S.; Ichikawa, M.; Koyama, T.; Taniguchi, Y. *Appl. Phys. Lett.* **2006**, 89, 112108.
- (126) Malenfant, P. R. L.; Dimitrakopoulos, C. D.; Gelorme, J. D.; Kosbar, L. L.; Graham, T. O.; Curioni, A.; Andreoni, W. *Appl. Phys. Lett.* **2002**, 80, 2517-1519.
- (127) Scholz, M.; Schmidt, R.; Krause, S.; Schöll, A.; Reinert, F.; Würthner, F. *Appl. Phys. A: Mater. Sci. Process.* **2009**, 95, 285-290.
- (128) Warman, J. M.; Haas, M. P. d.; Dicker, G.; Grozema, F. C.; Pirijs, J.; Debije, M. G. *Chem. Mater.* **2004**, 16.



- (129) Chen, Z.; Debije, M. G.; Debaerdemaeker, T.; Osswald, P.; Wurthner, F. *ChemPhysChem* **2004**, *5*, 137-140.
- (130) Struijk, C. W.; Sieval, A. B.; Dakhorst, J. E. J.; Dijk, M. v.; Kimkes, P.; Koehorst, R. B. M.; Donker, H.; Schaafsma, T. J.; Picken, S. J.; Craats, A. M. v. d.; Warman, J. M.; Zuilhof, H.; Sudhltter, E. J. R. *J. Am. Chem. Soc.* **2000**, *122*, 11057-11066.
- (131) Wang, Y.; Chen, Y.; Li, R.; Wang, S.; Su, W.; Ma, P.; Wasielewski, M. R.; Li, X.; Jiang, J. *Langmuir* **2007**, *23*, 5836-5842.
- (132) Hüttner, S.; Sommer, M.; Thelakkat, M. *Appl. Phys. Lett.* **2008**, *92*, 093302.
- (133) Finlayson, C. E.; Friend, R. H.; Otten, M. B. J.; Schwartz, E.; Cornelissen, J. J. L. M.; Nolte, R. J. M.; Rowan, A. E.; Samorì, P.; Palermo, V.; Liscio, A.; Kalina Peneva; Müllen, K.; Beljonne, S. T. *Adv. Funct. Mater.* **2008**, *18*, 1-9.
- (134) Peumans, P.; Bulovic, V.; Forrest, S. R. *Appl. Phys. Lett.* **2000**, *19*, 2650-2652.
- (135) Arbour, C.; Armstrong, N. R.; Brina, R.; Collins, G.; Danziger, J.; J.-P. Dodelet; Lee, P.; Nebesny, K. W.; Pankow, J.; Waite, S. *Mol. Cryst. Liq. Cryst.* **1990**, *183*, 307-320.
- (136) Hirose, Y.; Kahn, A.; Aristov, V.; Soukiassian, P.; Bulovic, V.; Forrest, S. R. *Phys. Rev. B* **1996**, *54*, 13748-13758.
- (137) Nakamura, J.-I.; Yokoe, C.; Murataa, K. *J. Appl. Phys.* **2004**, *96*, 6878-6884.
- (138) Pandey, A. K.; Dabos-Seignon, S.; Nunzia, J.-M. *Appl. Phys. Lett.* **2006**, *89*, 113506.
- (139) Pandey, A. K.; Nunzi, J. M. *Appl. Phys. Lett.* **2007**, *90*, 263508.
- (140) Hiramoto, M.; Fujiwara, H.; Yokoyama, M. *J. Appl. Phys.* **1992**, *72*, 3781-3787.
- (141) Whitlock, J. B.; Panayotatos, P.; Sharma, G. D.; Cox, M. D.; Sauers, R. R.; Bird, G. R. *Opt. Eng.* **1993**, *32*, 1921-1934.
- (142) Li, J. L.; Dierschke, F.; Wu, J. S.; Grimsdale, A. C.; Müllen, K. *J. Mater. Chem.* **2006**, *16*, 96-100.
- (143) Sharma, G. D.; P.Balraju; Mikroyannidis, J. A.; MinasM.Stylianakis *Sol. Energy Mater. Sol. Cells* **2009**, *93*, 2025-2028.
- (144) Chirvase, D.; Chiguvare, Z.; Knipper, M.; Parisi, J.; Dyakonov, V.; Hummelen, J. C. *Synth. Met.* **2003**, *138*, 299-304.
- (145) Sommer, M.; Lindner, S. M.; M, T. *Adv. Funct. Mater.* **2007**, *17*, 1493-1500.
- (146) Sommer, M.; Lang, A. S.; Thelakkat, M. *Angew. Chem. Int. Ed.* **2008**, *47*, 7901-7904.
- (147) Zhang, Q.; Cirpan, A.; Russell, T. P.; Emrick, T. *Macromolecules* **2009**, *42*, 1079-1082.
- (148) Liu, Y.; Yang, C.; Li, Y.; Li, Y.; Wang, S.; Zhuang, J.; Liu, H.; Wang, N.; He, X.; Li, Y.; Zhu, D. *Macromolecules* **2005**, *38*, 716-721.
- (149) Liu, Y.; Wang, N.; Li, Y.; Liu, H.; Li, Y.; Xiao, J.; Xu, X.; Huang, C.; Cui, S.; Zhu, D. *Macromolecules* **2005**, *38*, 4880-4887.

- (150) Tan, Z. a.; Zhou, E.; Zhan, X.; Wang, X.; Li, Y.; Barlow, S.; Marder, S. R. *Appl. Phys. Lett.* **2008**, *93*, 073309.
- (151) Chen, Z. H.; Zheng, Y.; Yan, H.; Facchetti, A. *J. Am. Chem. Soc.* **2009**, *131*, 8-9.
- (152) Hou, J.; Zhang, S.; Chen, T. L.; Yang, Y. *Chem. Commun.* **2008**, 6034-6036.
- (153) Huang, J.; Wu, Y.; Fu, H.; Zhan, X.; Yao, J.; Barlow, S.; Marder, S. R. *J. Phys. Chem. A* **2009**, *113*, 5039-5046.
- (154) O'Regan, B.; Grätzel, M. *Nature* **1991**, *353*, 737-740.
- (155) Tian, H.; Liu, P.-H.; Zhu, W.; Gao, E.; Wua, D.-J.; Cai, S. *Chem. Commun.* **2000**, *10*, 2708-2715.
- (156) Shibano, Y.; Umeyama, T.; Matano, Y.; Imahori, H. *Org. Lett.* **2007**, *9*, 1971-1974.

## CHAPTER 2

### PERYLENE DIIMIDE-BASED SIDE-CHAIN POLYNORBORNENES FOR ORGANIC ELECTRONIC APPLICATIONS

#### 2.1 Introduction

As discussed in Chapter 1, perylene diimides (also known as PDIs) are among the most promising electron acceptors for organic-based electronic devices to date because of their intrinsic chemical and physical properties, including relatively small electron affinity, high electron mobilities, and high molar absorption coefficients (*ca.*  $1 \times 10^5 \text{ M}^{-1} \text{ cm}^{-1}$ ) in the UV-Vis range.<sup>1-2</sup> It is believed that the rigid, aromatic, fused-ring aromatic scaffold of the electron accepting PDI cores can enhance  $\pi$ - $\pi$  intermolecular interactions, which leads to high electron mobilities in devices.<sup>3-4</sup> Recently, field-effect electron mobilities as high as  $2.1 \text{ cm}^2 \text{ V}^{-1} \text{ s}^{-1}$  with decent  $I_{\text{on}}/I_{\text{off}}$  ( $4.2 \times 10^5$ ) have been reported using PDI-based small molecules in vacuum-deposited organic field-effect transistors (OFETs). Recently, air stable vacuum-deposited n-channel OFETs with excellent performance have been demonstrated using aromatic-bay-modified PDIs.<sup>3-5</sup> Furthermore, because of their relatively small optical band-gaps (*ca.* 2.0 eV) and high molar extinction coefficients, perylene diimides show strong absorption between 450 – 600 nm, which comprises a significant part of the solar spectrum. This is complimentary to the absorption spectra of widely used donors such as oligothiophenes (OTs), metallophthalocyanines (MPc), pentacene, and other materials. These properties are potentially advantageous for organic photovoltaics (OPVs), especially as compared to the most commonly used acceptor, phenyl-C<sub>61</sub>-butyric-acid-methyl ester (PCBM), making

perylene diimides potential acceptor candidates for organic solar cell applications, due to their high electron affinity, which is similar to that of PCBM ( $\sim -3.9$  eV). Vacuum-deposited bilayer organic solar cells containing PDI-based acceptors and small molecule donors, such as pentacene,<sup>6</sup> rubrene,<sup>7</sup> and CuPc,<sup>8</sup> can exhibit power conversion efficiencies (PCEs) up to 2%. More examples of the successful use and promising device performance of perylene diimides as electron-transport materials in OFETs and acceptors in OPVs have been described earlier, in Chapter 1. In contrast, solution-process organic electronic devices based on perylene diimides currently show relatively poor performance, with general electron mobilities smaller than  $1 \times 10^{-4} \text{ cm}^2\text{V}^{-1}\text{s}^{-1}$  in OFETs and PCEs lower than 0.1% in blends with donor polymers such as poly-3-hexyl-thiophene (P3HT) in bulk heterojunction (BHJ) solar cells.<sup>9</sup> The low electron mobilities of these OFETs have been attributed to poor PDI molecular alignment. However, poor phase-segregation and larger PDI-rich aggregates of up to tens of micrometers have been found in PDI-based solution-processed solar cells.<sup>2,10</sup> Recently, it was found that chemical modification of the imide and/or bay positions of perylene diimides could result in much better film morphology and considerably improve the performance of PDI-based electronic devices. This inspired further exploration of PDI-based small-molecule and polymeric materials with controlled film morphology.<sup>11-17</sup> Among these candidates, PDI-based polymeric materials with considerable solubility have demonstrated their potential as high-performance electron-transport materials for wet-processing OFETs and OPVs,<sup>14-16</sup> making further research efforts focusing on developing new, solution-process PDI-based polymers highly desirable.

There are currently two major approaches to synthesize PDI-based polymers for organic electronic devices. The first one is incorporating the aromatic scaffold of perylene diimide into conjugated polymer chains via connection at the 1,(6)7-bay-positions of PDI derivatives via palladium catalyzed polycondensation reactions such as a Suzuki coupling, Stille coupling, or Sonogashira coupling with aromatic diboron, ditin, and diacetylene reagents respectively. Donor–acceptor (D–A) type polymers with alternating PDI and electron donor moieties such as dithienothiophene,<sup>15</sup> dithienopyrrole,<sup>16,18</sup> dithienosilole,<sup>13</sup> oligothiophenes,<sup>19-20</sup> and oligo(p-phenylene ethylene)<sup>21</sup> have been extensively studied for applications in organic electronics. Generally, these types of materials show smaller optical band gap and dramatic fluorescence quenching due to intrachain donor-to-PDI electron transfer, as well as enhanced solubility due to the propeller-like twisting of the two naphthalene half units in PDI moieties as compared to the bay-unsubstituted perylene diimides. The electron mobilities of such polymers are higher than  $0.01 \text{ cm}^2\text{V}^{-1}\text{s}^{-1}$  in OFETs.<sup>15,19</sup> Solution-process solar cells based on the blends of such polymers with appropriate donor polymers have exhibited PCEs as high as 1.5%.<sup>13-15</sup>

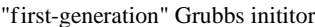
A second, recent approach for practical device applications involves using polymers with a stable and electronically inert backbone and PDI pendants in the polymer side chains.<sup>2,22-25</sup> This side-chain PDI-polymer approach has the potential to combine the desirable electronic and optical properties of the small-molecule perylene diimides, such as low lying LUMOs and good light-harvesting ability, with the mechanical strength and film-forming properties of the polymer main chain.<sup>26-27</sup> Currently, several PDI-grafted polymers have been reported bearing various main-chain

scaffolds such as polyisocyanodipeptides,<sup>22</sup> polyacrylates,<sup>23-24</sup> and polycarbazoles<sup>28</sup> for applications in organic electronic devices. To date, the device performance of these side-chain polymers has been generally much poorer compared to those main-chain PDI-based conjugated polymers described earlier. However, since diblock copolymers with PDI pendants in one polymer block offer the possibility of controlling and stabilizing nanometer-scale phase-segregation within the active layer and dramatically increasing the solar cell<sup>23</sup> and OFET<sup>29</sup> performance. Research on further exploring new side-chain PDI-based polymers with various main-chain structures and side-chain pendants will be interesting and might increase the likelihood of achieving high performance, cost-effective, OPV and OFET devices.<sup>22-25,29</sup>

The polynorbornene backbone could be a good choice for developing such kinds of grafting functional polymers for electronic applications because of its flexibility, relative chemical inertness, high optical transparency at visible-NIR wavelengths, and ease of preparation via ring-opening metathesis polymerization (ROMP) from norbornene and various derivatives.<sup>30</sup> More importantly, the “living” characteristic nature of ruthenium-complex-initiated ROMP, first described by Grubbs, allows the fine-tuning of the polymeric structures and molecular weight, which potentially could be used to build up D–A type block copolymers with desirable properties (also see Chapter 3). The high polymerization yields and good chemical stability of both the monomers and polymers for polynorbornenes over other system such as styrenes and acrylates are also potential advantages for practical applications.<sup>30</sup> Furthermore, functionalized polynorbornenes can often be readily solution-processed and have been used as key components in optoelectronic devices.<sup>26-27,31-34</sup> For example, Weck and coworkers

reported the synthesis of a series of norbornene-based copolymers with iridium- and/or platinum-complexes and their use in highly efficient electrophosphorescent light-emitting diodes.<sup>26,31-32</sup> Recently, oligothiophene-based polynorbornenes were developed and used in electronic devices by Ng and coworkers.<sup>33-34</sup>

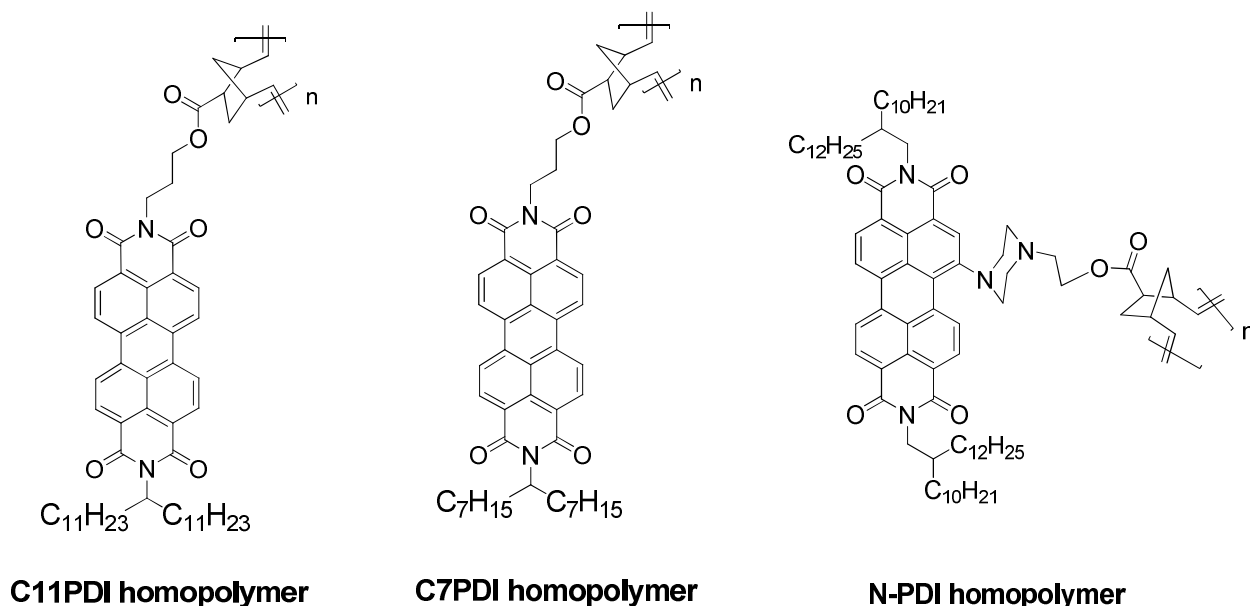
Ruthenium-complex-based ROMP is a promising polymerization method for both laboratory and industrial scale synthesis.<sup>30</sup> The driving force for such a polymerization is the relief of ring strain in cyclic olefins including norbornenes. Previous research shows that Grubbs initiators (or Grubbs catalysts, as they are usually described in olefin metathesis reactions) are tolerant to a wide range of functional groups on monomers and solvents, which makes these catalysts extraordinarily versatile in synthesis. The “first generation” Grubbs initiator is a relatively stable compound in air, and as such, it is not required to perform the polymerization under highly strict air- and water- free conditions. The “second-generation” Grubbs initiator shows much higher activity, but it is oxygen and water sensitive and thus should be handled under an inert atmosphere, such as a nitrogen glove-box or on schlenk line. Furthermore, the “first-generation” Grubbs initiator has been discovered to initiate ‘living’ ROMP with a moderate polymerization rate for common norbornenes.<sup>30</sup> Hence, the “first-generation” Grubbs initiator is used in growing the homo-polynorbornene chains with perylene diimide pendants in this chapter, as well as the D-A type diblock copolymers with grafted PDIs and oligothiophenes (OTs) in Chapter 3.



A simplified schematic of the ruthenium-complex-based ROMP mechanism is illustrated in Figure 2.1. In the initiation step, the ruthenium-complex initiator attacks the double bond in the ring of monomer to generate a highly strained metalloacyclobutane intermediate. The ring then opens to initiate the polymerization with a new metal-carbene and a terminal double bond. Then, the chain grows with the insertion of the next monomers to produce linear polymer chains.<sup>30</sup> As the driving force for the ROMP is the relief of ring strain and the initiation and chain propagation steps shown in Figure 2.1 are essentially irreversible for efficient polymerization. Hence, olefins such as cyclohexenes or benzene with little or no ring strain cannot be polymerized because there is no thermodynamic preference for polymers versus respective monomers. Strained cyclic olefins, such as norbornene, cyclopentene, and their derivatives, have sufficient ring



strain to make this process possible. Monomers based on norbornene derivatives are especially popular, as they can be readily synthesized from Diels-Alder reactions with cyclopentadiene. It is worth noting that only unsubstituted double bonds can be easily ring-opened using Grubbs initiators, and it is very difficult to metathesize or ROMP tri- and tetra-substituted olefins.



**Figure 2.2.** The chemical structures of the PDI-grafted polynorbornenes.

In this chapter, the incorporation of various PDI derivatives onto the side-chains of polynorbornenes, as shown in Figure 2.2, is described, along with the investigation of these materials as electron-transport materials for organic electronic applications, including OFETs and OPVs. First of all, aromatic-bay-unmodified perylene diimides, **C7PDI homopolymer (HP)** and **C11PDI HP**, with different side-chains on the N-

terminal were synthesized to investigate the effect of the choice of different end-swallow-tails on device performance. Also, a polynorbornene bearing PDI pendants with electron-donating amino moiety in the aromatic bay position was prepared. The attachment of the amino donor to the bay position is expected to red-shift the PDI absorption for better coverage of solar spectrum due to the possible amino to PDI internal charge-transfer (ICT) character in **N-PDI HP**.<sup>35</sup> Furthermore, the investigation of these three homopolymers could also benefit the selection of the PDI building blocks for the PDI-OT-based diblock copolymers research described in Chapter 3.

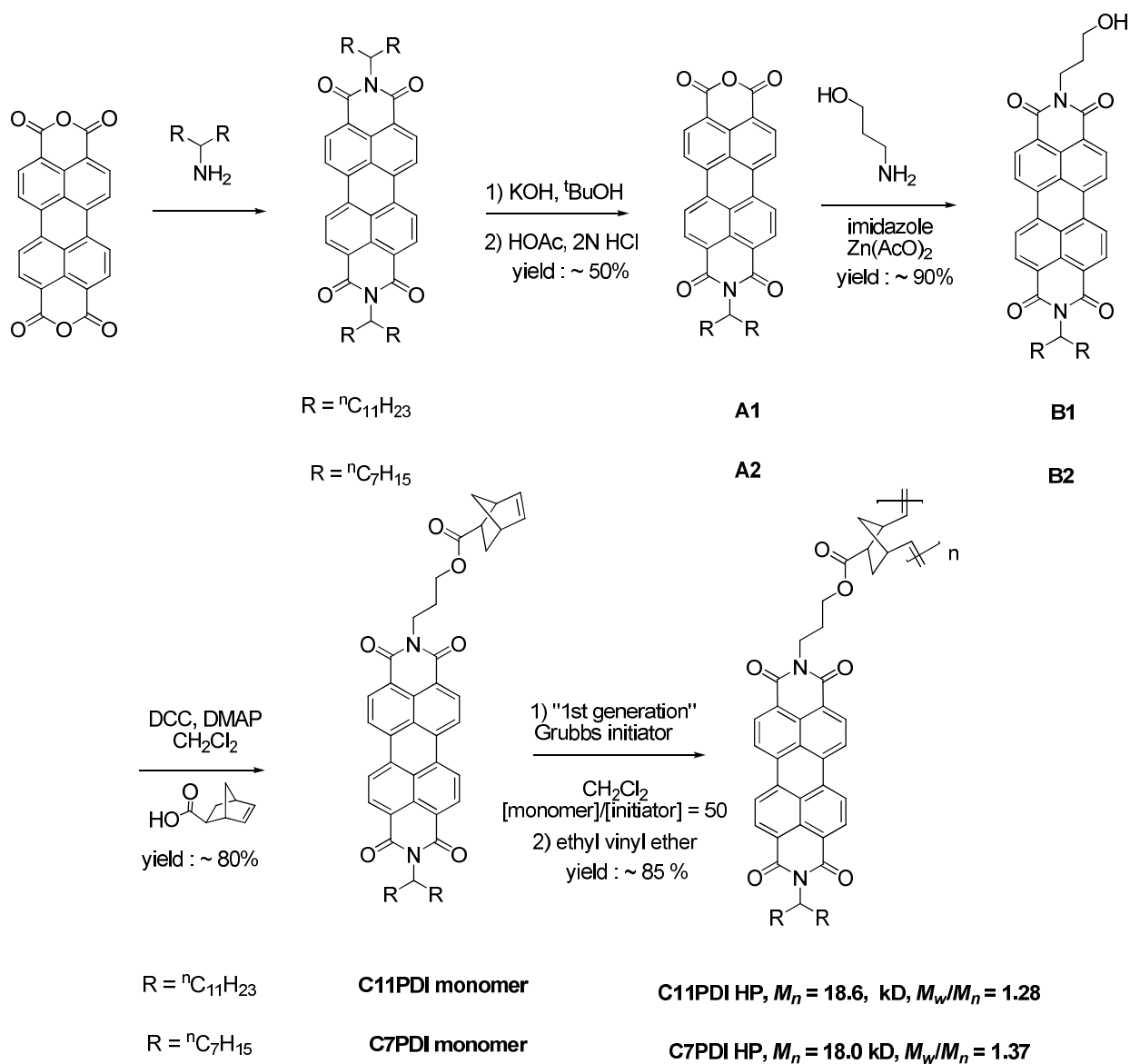
## 2.2 Synthesis of the homopolymers

The syntheses of the two bay-unmodified-PDI-grafted homopolymers (**C7PDI HP** and **C11PDI HP**) with different N-terminal swallow-tail side-chains and respective monomers (**C11PDI** or **C7PDI**) are shown in Scheme 2.1. The synthesis route started from the imidization reaction of perylene-3,4,9,10-tetracarboxylic dianhydride (PTCDA) with respective primary amine bearing different swallow-tails, following the literature procedure, which offered respective perylene diimides with high isolated yields.<sup>36</sup> The following hydrolysis of the symmetrical perylene diimides (**C11C11PDI** and **C7C7PDI**) gave the perylene monoimide monoanhydride compounds (**A1** and **A2**) in ~ 50% yields.<sup>37</sup> Further imidization reactions between **A1** or **A2** with large excess 3-aminopropan-1-ol afforded compound **B1** or **B2**, which had an alcohol group for further functionalization in good yields (between 75 to 90%). Dicyclohexylcarbodiimide/4-(dimethylamino)pyridine (DCC/DMAP) assisted coupling reactions between the pure exo-isomer of bicyclo[2.2.1]hept-5-ene-2-carboxylic acid and **B1** or **B2** at ambient

temperature were then applied to incorporate the norbornene moiety as a polymerizable group, yielding the PDI-grafted monomers (**C11PDI** or **C7PDI**) in isolated yields over 80%. The N-terminal swallow-tails in the monomers affords good solubility and allows for ruthenium-complex-assisted ROMP in dichloromethane. It is also worth noting that these two PDI-based monomers are quite stable and no obvious change was observed in their proton NMR and UV-Vis absorption spectra with storage at ambient conditions for over two years.

The polymerizations of the two bay-unmodified-PDI-based monomers (**C11PDI** and **C7PDI**) were carried out using 0.5 mol/L monomer and 0.01 mol/L initiator in dichloromethane at ambient temperature under nitrogen atmosphere on a Schlenk line.<sup>26-27,32</sup> The “first-generation” Grubbs initiator was utilized in the polymer synthesis because of its “living” nature and easy control of polymerization, which will be more important for the synthesis of the block copolymers discussed in Chapter 3.<sup>38</sup> Thin layer chromatography (TLC) is a suitable method to monitor the polymerization, since the polymers stay at the baseline while the respective monomers can move using chloroform as eluent for both cases. The red color and the strong yellow/yellow-orange color emission from the materials make this method quite sensitive. Ethyl vinyl ether was used to quench the polymerization by removing the attached ruthenium-based alkylidene from the polymer chains after TLC indicated that all the PDI-based monomer was consumed.<sup>30,32</sup> These two homopolymers were purified using multiple precipitations by addition of the high concentration polymer solutions in good solvents, such as dichloromethane and chloroform, to poor solvents such as methanol. Subsequent Soxhlet extraction using methanol and acetone was used to further purify the polymers. The

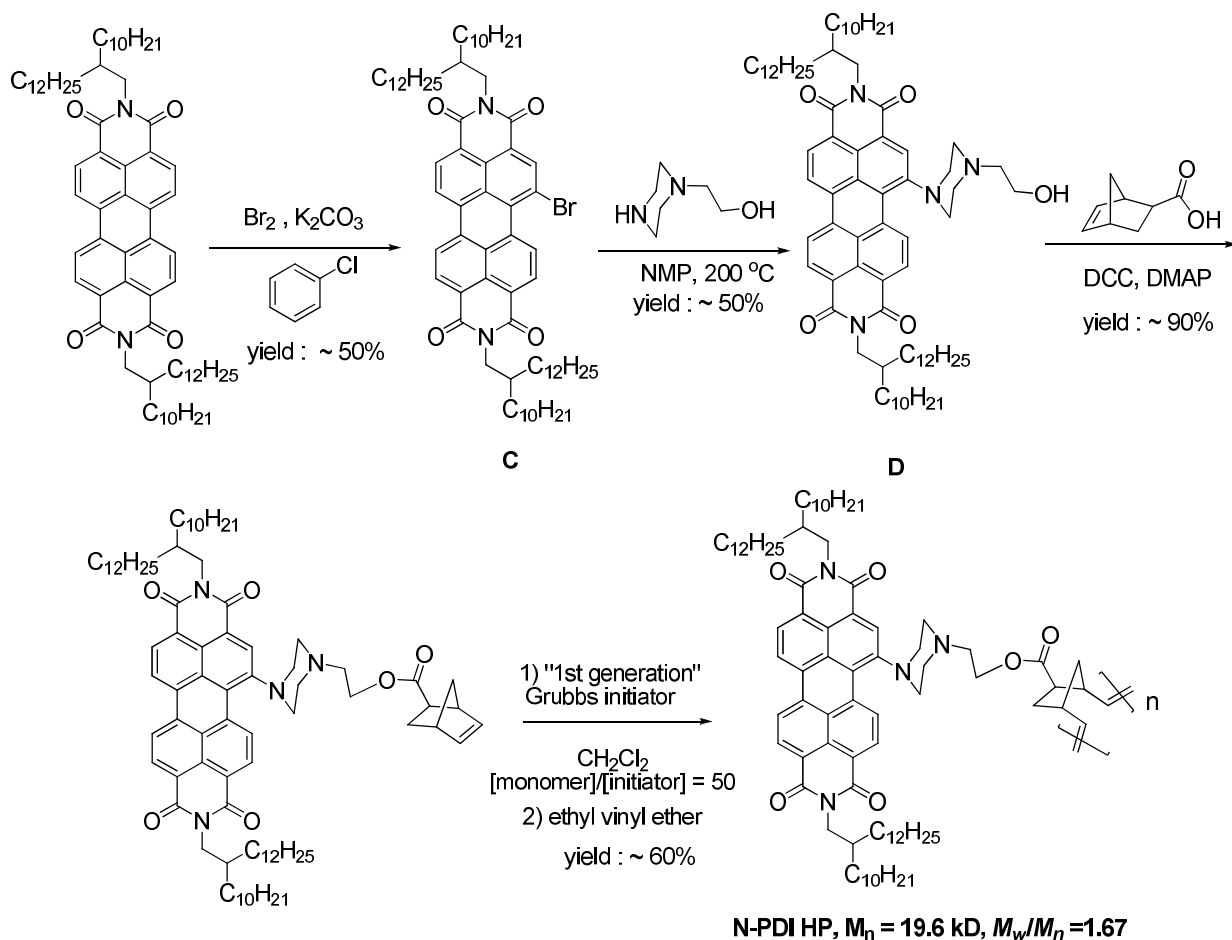
isolated yields for the polymers were around 85% with relatively narrow molecular weight distributions. The value  $M_n = 18.5$  kD and polydispersity ( $M_w/M_n$ ) = 1.3 and  $M_n = 18.0$  kD and  $M_w/M_n = 1.3$  were estimated according to GPC (toluene) results for **C11PDI HP** and **C7PDI HP**, respectively. These observed molecular weights are smaller than the ideal molecular weight (*ca.* 40 kD) assuming “living” ROMP occurs in our cases. This is presumably because the conformations of the PDI-grafted polymer-chains are different from the polystyrene standard for GPC analysis. It should be noted that different molecular weights for **C11PDI HP** were obtained using GPC with different solvents. For example,  $M_n$  for **C11PDI HP** was found to be 16.9, 18.5, and 66.5 kD, with similar  $M_w/M_n$  values obtained in tetrahydrofuran (THF), toluene, and chloroform based GPC respectively. Furthermore, a nearly linear relationship was found for  $M_n$  (based on GPC (THF)) versus the ratio of [monomer]/[initiator], for [monomer]/[initiator] ratios up to ~ 70 : 1 for different **C11PDI**-based homopolymers. The small variations in the polydispersity (1.1 – 1.3), suggest that a well-controlled ROMP occurs during **C11PDI HP** synthesis. Because of the long swallow-tail side-chains on the N-terminal of the PDI pendants, these two PDI-based homopolymers are highly soluble (> 30 mg/mL) in common organic solvents, including toluene, dichloromethane, chloroform, and THF, which makes the preparation of high-quality thin films from **C11PDI HP** and **C7PDI HP** relatively straightforward.



**Scheme 2.1.** The synthetic scheme for the two PDI homopolymers.

As shown in Scheme 2.2, the synthesis of the **N-PDI HP** started from the monobromination of the symmetrical perylene diimide<sup>39</sup> via modification of a procedure described in the literature.<sup>40</sup> The nucleophilic replacement of the bromine substituent on the PDI-bay position of compound **C** with 2-(piperazin-1-yl)ethanol in NMP solvent

afforded the corresponding unsymmetrical derivative **D** in a moderate yield (relatively low compared to that for similar reactions reported in the literature).<sup>35</sup> Interestingly, based on UV-Vis absorption spectra of the reaction mixture, a longer reaction time (*ca.* 3 hours instead of 1.5 hours) leads to lower yield of **D** and the formation of respective PDI without bay substituent. This phenomenon was described earlier in literature, and the mechanism for this conversion is still unclear.<sup>35</sup> The DCC/DMAP-based coupling reaction was then utilized to synthesize the new monomers (**N-PDI**) at ambient temperature with a yield around 90%. Similar polymerizations were carried out on monomer **N-PDI** to give **N-PDI HP** with lower yield (60%) after multiple precipitations along with Soxhlet washing with hot methanol and acetone. It is worth noting that size-exclusion chromatography (SEC) over cross-linked polystyrene beads is required to remove the very small amount of **N-PDI** monomer residue (< 5 % and which was not detectable in the <sup>1</sup>H NMR spectrum) that was present after the Soxhlet extraction. This polymer has a much broader molecular weight distribution ( $M_w/M_n = 1.7$ ) than those for the previous two bay-unmodified-PDI-based homopolymers with  $M_n = 19.6$  kD, estimated from GPC (toluene). Similarly, this  $M_n$  is lower than the expected molecular weight (60 kD) presumably due to similar reason as that for **C7PDI HP** and **C11PDI HP**. **N-PDI HP** shows excellent solubility in common organic solvents, such as toluene (~ 40 mg/mL), dichloromethane, chloroform, and THF, which makes it a potential candidate for wet-process electronics devices.



**Scheme 2.2.** The synthetic scheme for the N-PDI homopolymer.

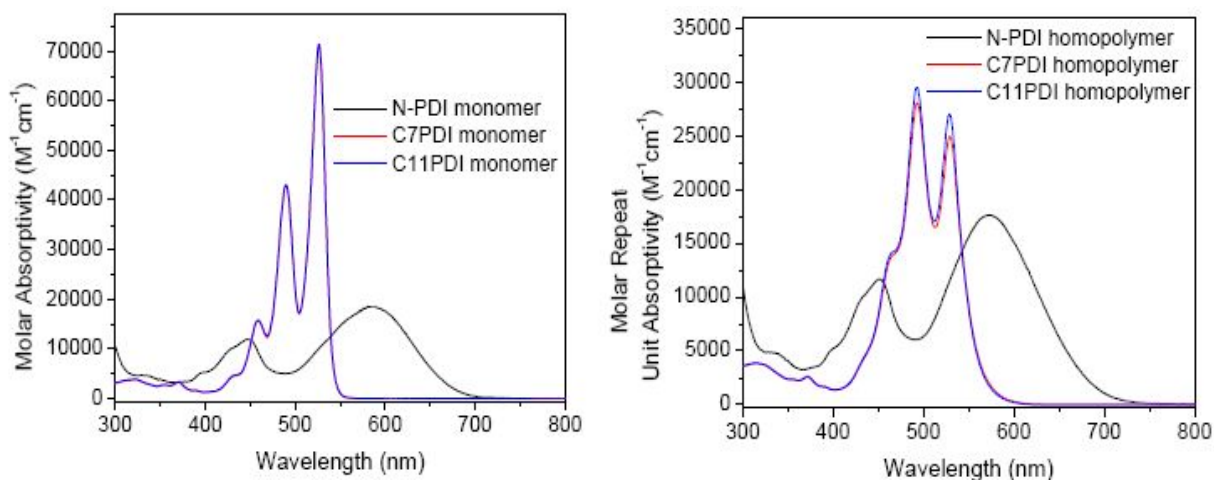
### 2.3 Optical properties of the PDIs

The UV-Vis absorption spectra of these three homopolymers and corresponding monomers in dilute chloroform solution (*ca.*  $1 \times 10^{-5}$  mol/L) are shown in Figure 2.3. The near superposition the absorption spectra of the **C7PDI** and **C11PDI** monomers can be attributed to their high degree of chemical similarity. The distinct four-peaked absorption spectral pattern with a vibrational progression of about  $1400 \text{ cm}^{-1}$  in the visible region

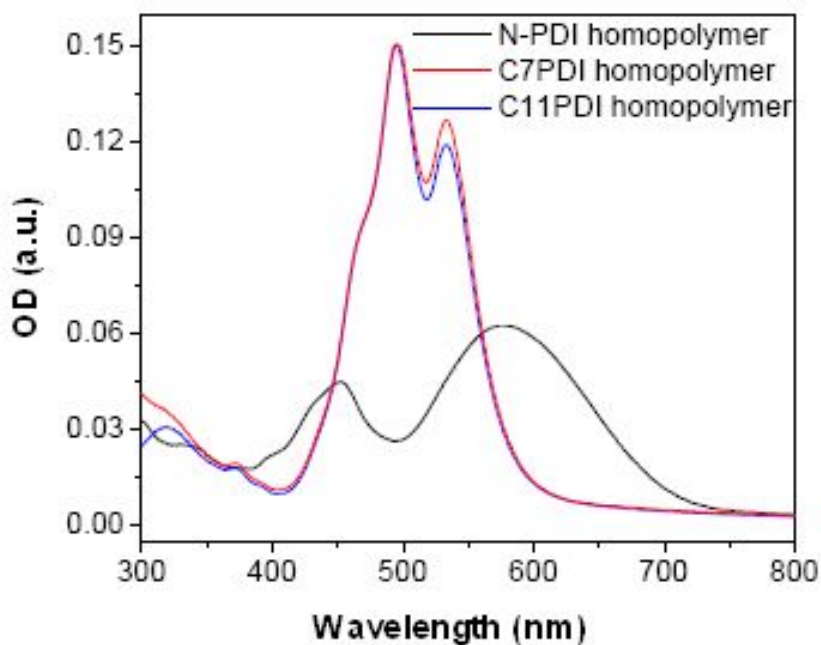
was observed for both monomers.<sup>41</sup> Here, electronic transition that peaked at 490 nm is assigned to the (0,1) transition, and the one that peaked at 527 nm corresponds to the (0,0) transition.<sup>41</sup> In dilute chloroform solution, the absorbance ratios from the two transitions ((0,0)/(0,1)) are 1.66 for both monomers, which indicates free-PDI-type absorption in solution and limited molecular aggregation between the PDI units at this concentration (*ca.*  $1 \times 10^{-5}$  mol/L).<sup>41-42</sup> The PDI-based peak extinction coefficients of the two PDI homopolymers are much lower than those for respective monomers at similar dye concentration. Also, the observed smaller (0,0)/(0,1) values, 0.89 and 0.91, respectively, for **C7PDI HP** and **C11PDI HP**, suggest much more aggregation of PDI units on the polymer side-chain even in dilute solution, as compared with the monomers, and there appears to be slightly more PDI-aggregation in **C7PDI HP** than the other polymer with the relatively smaller (0,0)/(0,1) value.<sup>42-43</sup> Even more aggregate-PDI-type absorption was observed for these homopolymers in thin films (spin-coated on glass from 10 mg/mL toluene solution with rate of 1000 rpm for 1 minute) with smaller (0,0)/(0,1) values. Because of the electron-donating amino moiety attached at the PDI-bay position, both **N-PDI** and **N-PDI HP** show ICT type absorption characteristics with significantly red-shifted and broader absorptions, and without the fine vibronic structure in the UV-Vis spectra compared observed in the **C7PDI**- and **C11PDI**-based materials.<sup>35</sup> Also, much lower peak extinction coefficients were observed relative to perylene diimides without aromatic bay substituent(s), which is similar to what has been observed in literature.<sup>35</sup> The broader absorption spectra of the **N-PDI**-based materials potentially could provide better solar spectrum coverage for OPV applications.<sup>2,44-45</sup> However, the similarity of the absorption spectra between the **N-PDI** monomer and **N-PDI HP** suggests limited  $\pi$ - $\pi$



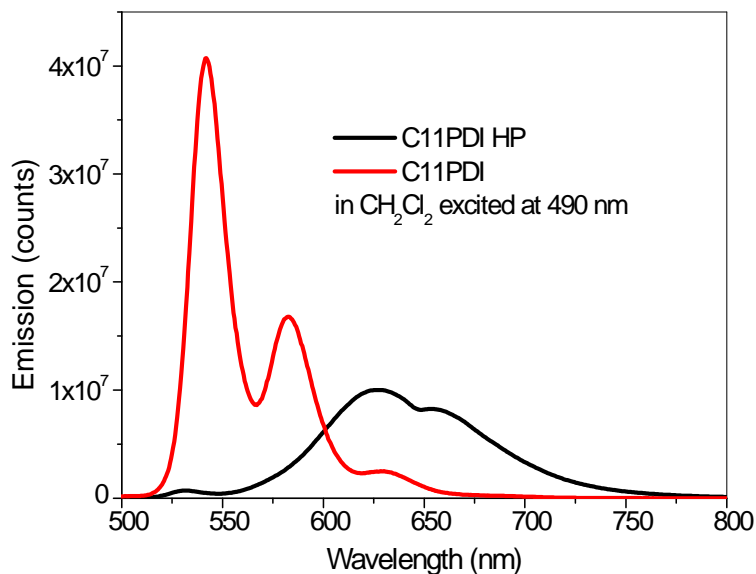
stacking of the repeat units on the **N-PDI HP** side chain. Such poor packing for **N-PDI** units might be attributed to the torsion caused by the bay substitutions, which force the twisting of the two naphthalene half units on **N-PDI HP**. Similar phenomena have been observed earlier for bay-tetrachloro-substituted or bay-dibromo-substituted PDIs.<sup>46-48</sup> In addition, only limited differences in the absorption spectra were found between the thin-film and solution of **N-PDI HP**, which suggests only a small degree of aggregation between the perylene units, even in the solid state. The optical band gaps for the monomers, **C7PDI**, **C11PDI**, and **N-PDI**, are 2.25, 2.25, and 1.76 eV, while those for homopolymers, **C7PDI HP**, **C11PDI HP**, and **N-PDI HP**, are 2.03, 2.03, and 1.66 eV, respectively. This was estimated from the onsets of the lower optical band in the solution absorption spectra according to  $E_{\text{gap}}(\text{optical}) = 1240/\lambda_{\text{onset}}$ . The emission spectra of the **C11PDI** monomer and **C11PDI HP** at low concentration ( $\sim 1 \times 10^{-6}$  mol/L) are shown in Figure 2.5. The fluorescence peaks obtained for **C11PDI** monomer in both dichloromethane and toluene are mirror images of the respective absorption bands in the same solvents.<sup>1,41,49</sup> On the other hand, the emission spectrum for **C11PDI HP** loses the fine vibronic fine structure and exhibits a *ca.* 100 nm red-shift on the emission maximum, which suggests aggregate-type PDIs on the homopolymer side-chain.<sup>49</sup> This is consistent with the observation of the absorption spectra changing upon going from the **C11PDI** monomer to **C11PDI HP**. Similar emission behaviors were observed for **C7PDI** and **C7PDI HP**. However, no detectable emission was observed for **N-PDI** and **N-PDI HP** in toluene solution.



**Figure 2.3.** The UV-Vis absorption spectra of the monomers: N-PDI (black), C7PDI (red), and C11PDI (blue) (left) and respective homopolymers: N-PDI HP (black), C7PDI HP (red), and C11PDI HP (blue) (right) in chloroform.



**Figure 2.4.** The UV-Vis absorption of spin-casted films of N-PDI HP (black), C7 PDI HP (red), and C11 PDI HP (blue) on glass, using 10 mg/mL polymer solution in toluene at 1000 rpm for 1 minute.



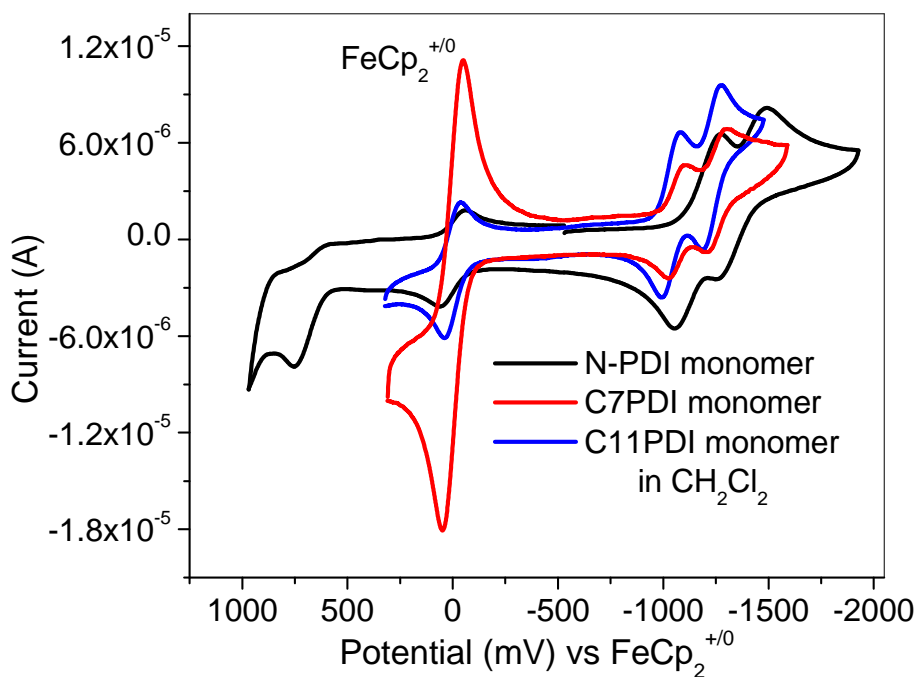
**Figure 2.5.** The emission spectra of C11PDI (red) and C11PDI HP (black) in CH<sub>2</sub>Cl<sub>2</sub>. In both cases, the sample was excited at 490 nm and the emission intensity has been normalized to the same absorbance at the excitation wavelength.

## 2.4 Redox properties of the monomers

The redox properties of the homopolymers were estimated via cyclic voltammetry (CV) measurements of the respective monomers in anhydrous dichloromethane with ferrocene (FeCp<sub>2</sub>) as an internal reference (Figure 2.6). The half-wave potential ( $E_{1/2}$ ) values (defined as  $(E_{pa} + E_{pc})/2$ , where  $E_{pa}$  and  $E_{pc}$  are peak oxidation and reduction potentials, respectively) of monomers **C7PDI**, **C11PDI**, and **N-PDI**, are -1.04, -1.03, and -1.14 V for the first reduction and -1.26, -1.24, and -1.37 V at the second reduction vs. FeCp<sub>2</sub><sup>+0</sup> redox couple. The reductions for all three monomers were found to be reversible by cyclic voltammetry at scan rates of 50 mVs<sup>-1</sup>, exhibiting  $I_{pa}/I_{pc}$  (the ratio of the peak currents of the oxidative and reductive waves) values of *ca.* 1. The similarities in the electrochemical properties of the **C11PDI** and **C7 PDI** could be attributed to similarities

in their chemical structures. **N-PDI** is slightly less readily reduced compared with **C11PDI** and **C7 PDI** ( $\sim 0.1$  V), which is consistent with the earlier observations in the literature of a small change (*ca.* 0.3 V) in the reduction potential of 1,(6)7-bispyrrolidine-substituted-PDI compared to PDI without the bay-substituent.<sup>35</sup> However, the half-wave reduction potential indicates that it is still a sufficient electron acceptor for OPV cells involving blends with typical donor materials such as P3HT.<sup>9</sup> An EC-type (reversible electron transfer followed by a rapid chemical decomposition) molecular oxidation peak was observed for **N-PDI** at  $E_{1/2}^{+/0} = \sim 0.64$  V vs.  $\text{FcCp}_2^{+/0}$ . An “electrochemical gap” of 1.78 eV, estimated from the redox potentials for **N-PDI**, is close to its optical bandgap (1.76 eV) obtained from the absorption onset in chloroform. This may indicate that the energetic stabilization by strong solvation of ionic species in the CV measurements (at least in 0.1 M solutions of tetra-*n*-butylammonium hexafluorophosphate in dry dichloromethane) is similar to that of the “exciton-binding energy” of the excited-state. No oxidation peaks were observed for **C7PDI** and **C11PDI** in dichloromethane. The first electrochemical half-wave reduction potentials  $E_{1/2}^{0/-}$  were used to estimate the electron affinity (EA) with  $\text{EA} = -e (E_{1/2}^{0/-} + 4.8 \text{ V})$  based on the ionization potential (IP) of 4.8 eV for solid state ferrocene with respect to the vacuum level.<sup>50</sup> Here, the EAs for **C7PDI**, **C11PDI**, and **N-PDI** are -3.8 eV, -3.8 eV, and -3.7 eV, respectively. Their IPs are estimated from the optical bandgaps and EA values to be 6.0, 6.0, and 5.4 eV respectively for **C7PDI**, **C11PDI**, and **N-PDI**, according to  $\text{IP} = -(\text{EA} - E_{\text{gap}})$ . Here, the IP and EA values for these polymers, especially for the ones without PDI-bay-substituents, are comparable to those fullerene-based acceptors including PCBM, while their better light-

harvesting ability in visible range over PCBM suggests their potential advantage as acceptors for solar cell applications.

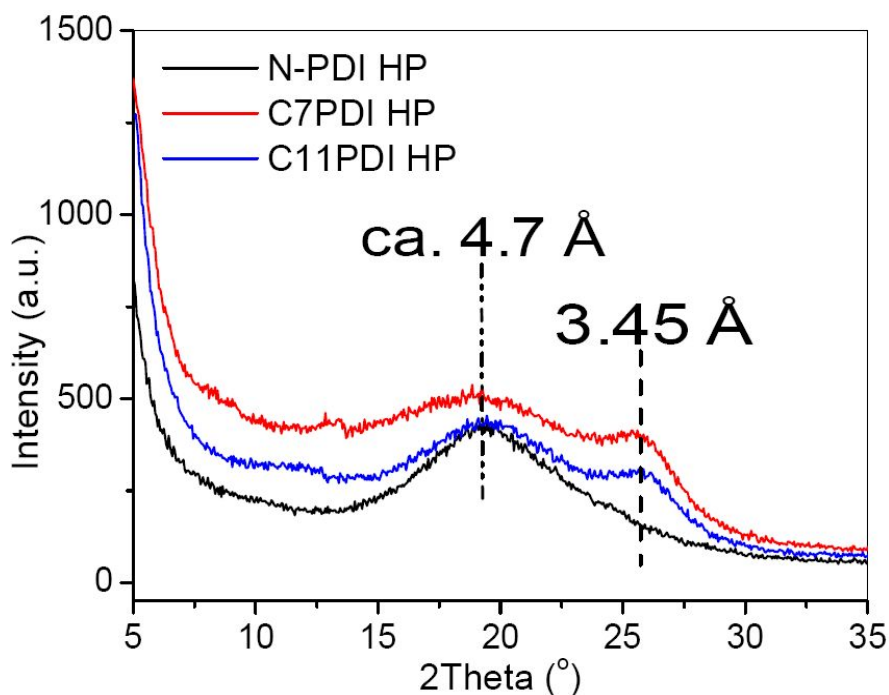


**Figure 2.6.** The cyclic voltammograms of N-PDI (black), C7PDI (red), and C11PDI (blue) in  $\text{CH}_2\text{Cl}_2$ , 0.1 M  $[n\text{-Bu}_4\text{N}][\text{PF}_6]$ , with scan rate =  $50 \text{ mV s}^{-1}$ , with ferrocene as an internal reference.

## 2.5 Powder XRD of the homopolymers

X-ray diffraction (XRD) is a powerful technique for obtaining information on the molecular packing and crystallinity of organic/polymer materials in crystals, powders, or even thin-films. As previously shown in Figures 2.3, 2.4, and 2.5, the absorption and emission spectra of **C11PDI** and **C7PDI** in solution are significantly different from the respective homopolymers in dilute solution and solid states. This may be attributable to

the strong intermolecular interactions, such as  $\pi$ - $\pi$  stacking, between the individual PDI pendants in the polymer side-chains. On the other hand, no obvious absorption change was observed for **N-PDI**-based materials from the monomer to the polymer, which indicated limited molecular  $\pi$ - $\pi$  stacking for the perylene segments in the polymer chains. Powder XRD measurements on these homopolymers were carried out to further confirm the assumption. As shown in Figure 2.6, in the diffraction angle,  $2\theta$ , range of  $15 - 20^\circ$ , all three polymers show a broad peak correlated to a d-spacing of  $4.7 \text{ \AA}$ , according to the Bragg equation  $n\lambda = 2d\sin\theta$ . This could be assigned to the halo peak and is attributed to the characteristic of the amorphous phase probably due to the polynorbornene or alkyl chains stacking.<sup>29</sup> Furthermore, for the **C7PDI** and **C11PDI HP**, a peak at *ca*  $26^\circ$  corresponding to a d-spacing of  $3.45 \text{ \AA}$  was observed in the XRD spectra, which is rather close to the reported  $\pi$ - $\pi$  stacking distances of PDI-based materials in small molecules or polymer side-chains.<sup>1,29</sup> This agrees with the aggregate-type PDI UV-Vis absorption spectra of these two polymers. In contrast, there is no obvious peak correlated to  $\pi$ - $\pi$  stacking d-spacing found in the powder XRD of **N-PDI HP**. The low degree of PDI-type aggregation in **N-PDI HP** is, therefore, perhaps attributable to the twisting of the PDI molecular plane caused by the substituent (the secondary amino group) in the bay position, which causes a propeller-like twisting of the two naphthalene half units in PDI, and prevents face-to-face  $\pi$ - $\pi$  stacking, as discussed earlier.<sup>1,48</sup> Attempts to obtain the XRD patterns for thin films on silicon wafers from these three homopolymers failed, presumably because of the low film quality on silicon substrates from either spin-coating or drop-casting from various solvents including chlorobenzene and toluene.

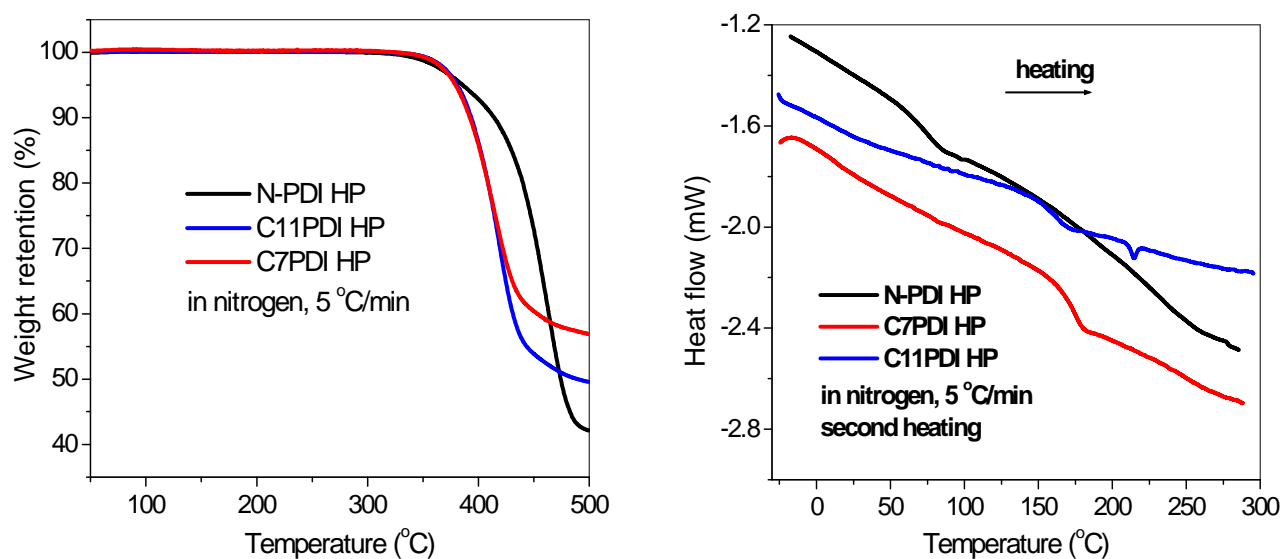


**Figure 2.7.** Power XRD of N-PDI HP (black), C7PDI HP (red), and C11PDI HP (blue) with a Cu Ka source ( $\lambda = 1.5406 \text{ \AA}$ ) in continuous scan mode with a step of  $0.02^\circ$  (Data were collected by Dr Soo Young Kim in the Marder group).

## 2.6 Thermal properties of the homopolymers

As revealed in Figure 2.8, all three homopolymers exhibited good thermal stability, the decomposition temperatures ( $T_d$ ), defined as that at which 5% weight loss is observed are found to be *ca.*  $380^\circ\text{C}$ , under nitrogen atmosphere, as determined by thermogravimetric analysis (TGA) heating from room temperature to  $500^\circ\text{C}$  at a heating rate of  $5^\circ\text{C}/\text{min}$ . The thermal behavior of these polymers was recorded through differential scanning calorimetry (DSC) analysis over the temperature range from  $-30$  to  $300^\circ\text{C}$  under nitrogen atmosphere. The DSC trace of the second heating with a heating rate of  $5^\circ\text{C}/\text{min}$  are shown in Figure 2.8 and reveal glass transition temperatures ( $T_g$ ) of  $171$ ,  $159$ , and  $76^\circ\text{C}$ , for **C7PDI HP**, **C11PDI HP**, and **N-PDI HP**, respectively. The

much lower  $T_g$  of **N-PDI HP** as compared to the other two homopolymers is consistent with the limited  $\pi$ - $\pi$  stacking interaction of the PDI moieties on the **N-PDI HP** side-chain observed in their absorption spectra and powder XRD. The slightly lower  $T_g$  of **C11PDI HP** over **C7PDI HP** may be attributed to the longer N-terminal swallow-tail side-chain on the PDI pendants. There is a small melting transition at 223 °C in the DSC trace of **C11PDI HP**, which suggests a low degree of crystallinity presented for this polymer in the solid state. There is no obvious melting transition observed for **C7PDI HP** and **N-PDI HP** in the DSC trace. The good thermal-stability as well as the relatively high  $T_g$  (>150 °C), are both positive aspects for using **C7PDI HP** and **C11PDI HP** in organic electronic devices, including OFETs and OPVs.



**Figure 2.8.** TGA traces (left) and DSC (right) traces for the second heating process of the **N-PDI HP** (black), **C7 PDI HP** (red), and **C11 PDI HP** (blue) with a heating rate of 5 °C/min under  $N_2$ .



**Table 2.1. Summary of synthetic yield, molecular weight, the thermal properties (TGA and DSC), and EAs and IPs for the homopolymers.**

Polymer	Yield	$M_n$	$M_w / M_n$	$T_d(^{\circ}\text{C})$	$T_g(^{\circ}\text{C})$	EA (eV) <sup>a</sup>	IP(eV) <sup>a</sup>
<b>C11PDI HP</b>	85%	18.6 k	1.3	385	159	-3.8	6.0
<b>C7PDI HP</b>	93%	18.1 k	1.3	386	171	-3.8	6.0
<b>N-PDI HP</b>	57%	19.6 k	1.7	380	76	-3.7	5.4

a : EA =  $-e (E_{1/2}^{0/-} + 4.8 \text{ V})$  and IP =  $-(\text{EA} - E_{\text{gap}}(\text{optical}))$

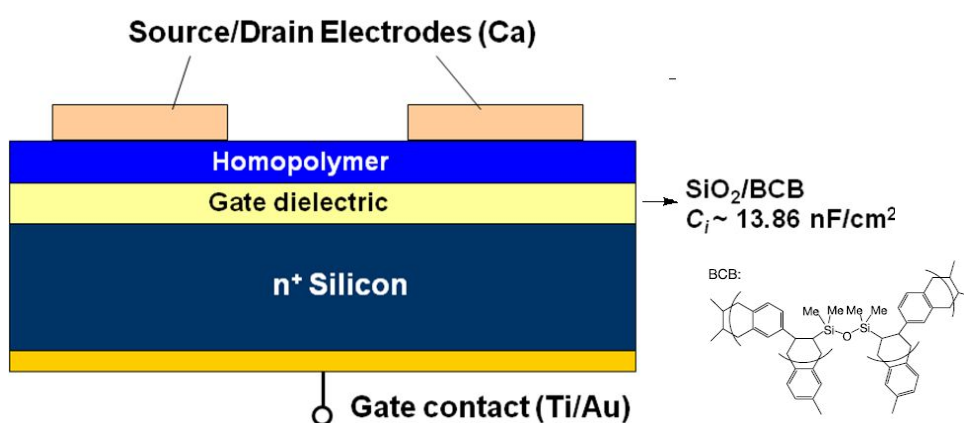
## 2.7 OFET and solar cell device performance for the three homopolymers

OFET devices containing the PDI-based polymers as the solution-processed active layer were fabricated by Dr. Shree Tiwari in the Kippelen group using top-contact configuration (as shown in Figure 2.9), using calcium electrodes to investigate their field-effect electron mobilities. Here, a hydroxyl-free gate dielectric material, bis(benzocyclobutene) derivative (BCB), was used to limit the number of electron-trapping sites in the organic/dielectric interface.<sup>51</sup> The device performances are summarized in Table 2.2 and the device characteristics were shown in Figure 2.10. The pristine **C11PDI HP** and **C7PDI HP** films showed electron mobilities of  $7.8 \times 10^{-6}$  and  $1.8 \times 10^{-5} \text{ cm}^2\text{V}^{-1}\text{s}^{-1}$ , respectively; these electron mobilities were improved to  $2.7 \times 10^{-5}$  and  $4.9 \times 10^{-5} \text{ cm}^2\text{V}^{-1}\text{s}^{-1}$  by annealing the transistors at 200 °C for 1 hour in a nitrogen glove-box. The current on/off ratios of the devices are on the order of  $10^2$ , and thermal annealing shows only small effects on the on/off ratios. A slight decrease in device performance was observed with further annealing at 250 °C for another hour for the devices. **C7PDI HP** shows slightly better electron-transport ability than **C11PDI HP** in OFETs, perhaps because of the shorter N-terminus swallow-tail substitution. Thermal

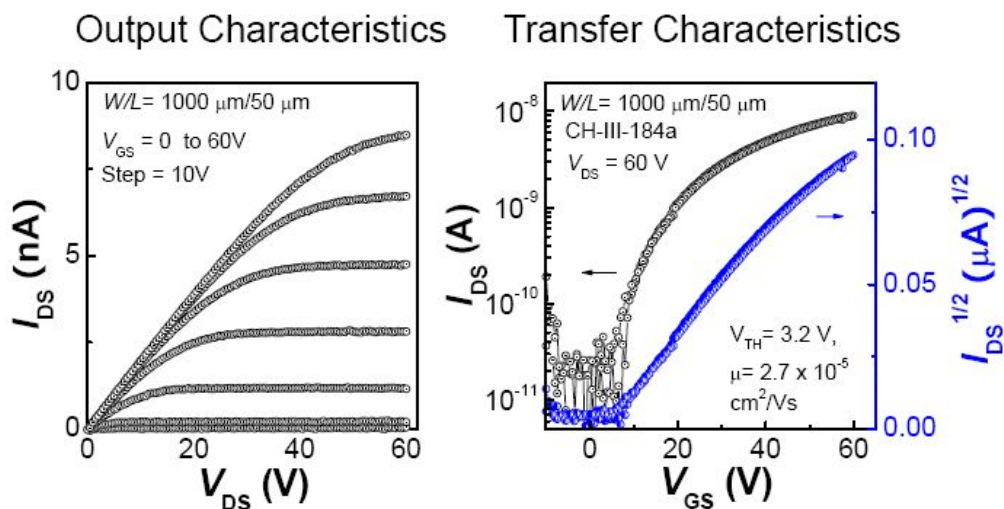
treatments of the homopolymer films above their glass transition temperatures help to improve the electron mobilities, probably due to better molecular ordering during the annealing process. No detectable field-effect electron mobility was observed from devices based on **N-PDI HP** in a similar device geometry with either pristine or annealed films. This may be attributed to the low aggregation of the perylene repeat units on the polymer chain, which is similar to the earlier observation of a decrease in electron mobility of tetraochloro-bay-substituted-PDI (*ca.*  $1 \times 10^{-5} \text{ cm}^2 \text{ V}^{-1} \text{ s}^{-1}$ ) compared with PDI without bay-substitutions ( $> 10^{-2} \text{ cm}^2 \text{ V}^{-1} \text{ s}^{-1}$ ) in vacuum-deposited devices.<sup>52</sup>

**Table 2.2. Summaries of OFET device characteristics for the homopolymers (Data were collected by Dr. Shree Tiwari in the Kippelen group).**

Polymer	Pristine film			Annealed at 200 °C for 1 h			Annealed at 200 °C for 1 h then annealed 250 °C for 1 h		
	$\mu_e (\text{cm}^2 \text{ V}^{-1} \text{ s}^{-1})$	$V_{th} (\text{V})$	$I_{on}/I_{off}$	$\mu_e (\text{cm}^2 \text{ V}^{-1} \text{ s}^{-1})$	$V_{th} (\text{V})$	$I_{on}/I_{off}$	$\mu_e (\text{cm}^2 \text{ V}^{-1} \text{ s}^{-1})$	$V_{th} (\text{V})$	$I_{on}/I_{off}$
<b>C11PDI HP</b>	$7.8 \times 10^{-6}$	1.0	$2 \times 10^2$	$2.7 \times 10^{-5}$	3.2	$4 \times 10^2$	$1.2 \times 10^{-5}$	2.5	$3 \times 10^2$
<b>C7PDI HP</b>	$1.8 \times 10^{-5}$	3.9	$3 \times 10^2$	$4.9 \times 10^{-5}$	3.4	$6 \times 10^2$	$2.5 \times 10^{-5}$	4.0	$4 \times 10^2$
<b>N-PDI HP</b>	No detectable electron mobilities were observed								



**Figure 2.9. General OFET device structure for these homopolymers (Figure was adapted from Dr. Shree Tiwari in the Kippelen group).**



**Figure 2.10.** OFET device characteristics for C11PDI HP after annealing at 200 °C (Figures were adapted from Dr. Shree Tiwari in the Kippelen group).

Bulk heterojunction organic photovoltaic devices were constructed using a 1:1 weight ratio of P3HT:homopolymer blends by Mr. William Potscavage *Jr.* in the Kippelen group, and the device performances are summarized in Table 2.3. For the devices with average active layer thicknesses of  $\sim 100 \text{ nm}$ , P3HT:C11PDI HP cells show better performance compared with the other two blend systems, with short-circuit current ( $J_{SC}$ ) and PCEs up to  $1.8 \pm 0.1 \text{ mA}/\text{cm}^2$  and  $0.38 \pm 0.01\%$ , respectively. Measurements of the incident photon-to-current efficiency (IPCE, Figure 2.13) show much higher energy conversion in the whole spectral range than the other two systems, and the IPCE is over  $\sim 10\%$  between 500 – 600 nm for devices from P3HT:C11PDI HP blend. The much lower  $J_{SC}$  and PCE for P3HT:N-PDI HP blend compared with the other two blends might be attributed to the low electron mobility originating from the low aggregation of the perylene repeat units of this material. The expansion of the

absorption spectrum for **N-PDI HP** does not benefit the PCE in devices here. Limited contribution from the lower energy absorptions of the **N-PDI HP** was observed according to IPCE wavelength plot and lower IPCE over the whole UV-Vis spectra range were obtained against the other two polymer blends. Despite the low  $V_{OC}$  from P3HT:**N-PDI HP** (0.44 V), the  $V_{OC}$  from devices based on P3HT:**C11PDI HP** and P3HT:**C7PDI HP** are similar to those of many other organic solar cells, the PCEs of these devices are primarily limited by the  $J_{SC}$  and fill factor ( $FF$ ). The low electron mobility of these materials might be a major reason for the small  $J_{SC}$ , though other factors including film morphologies and charge photo-generation yields might also play import roles. Furthermore, the low electron mobilities of the PDI-based polymers could result in charge accumulation and inefficient charge collection, while the possible unbalanced charge carrier mobilities (P3HTs show hole mobility = *ca.*  $10^{-3}$  to  $10^{-4}$   $\text{cm}^2\text{V}^{-1}\text{s}^{-1}$  in P3HT:PCBM blend)<sup>45</sup> could decrease the  $FF$  and overall PCEs of BHJ devices by promoting charge recombination.<sup>53-54</sup> Annealing of the devices at 125 °C for 30 minutes was tested, but this thermal treatment led to a slight decrease in all of the performance parameters. The higher  $J_{SC}$  and IPCE of devices from P3HT:**C11PDI HP** blend might be attributed to more favourable nanomorphology, considering the P3HT:homopolymer blend films showed similar UV-Vis absorption, and **C7PDI HP** showed slightly higher electron mobility over **C11PDI HP** in OFET devices. It is worth noting that 0.38% has been among the top reported PCEs for those P3HT:PDI BHJ devices to date,<sup>55-56</sup> especially for those device with 1:1 donor to acceptor weight ratio, although it is still a quite low PCE value relative to BHJ solar cells with other acceptors, such as fullerene derivatives.

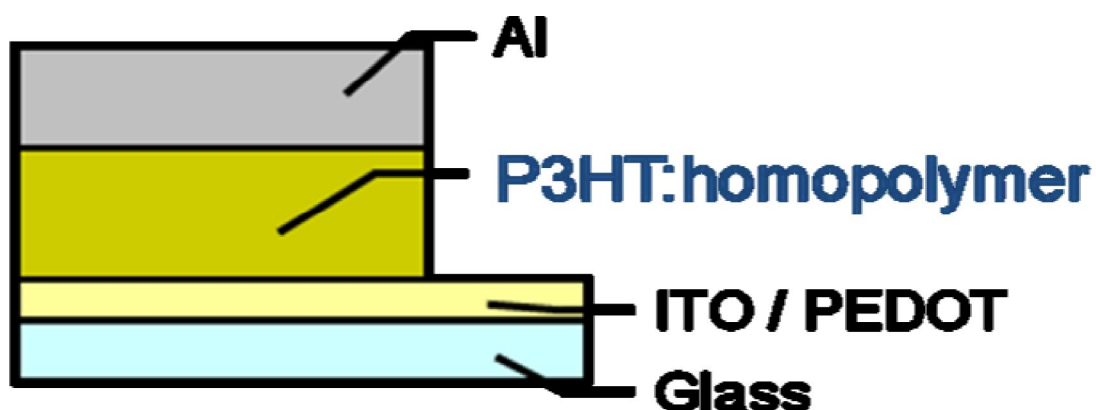


Figure 2.11. General solar cell structure for the homopolymer/P3HT blends (figure was adapted from William Potscavage Jr. in the Kippelen group).

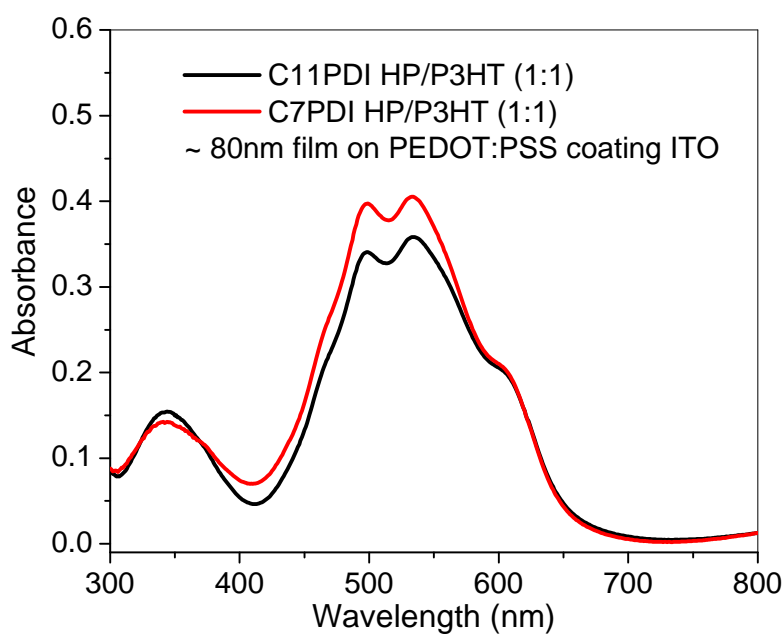
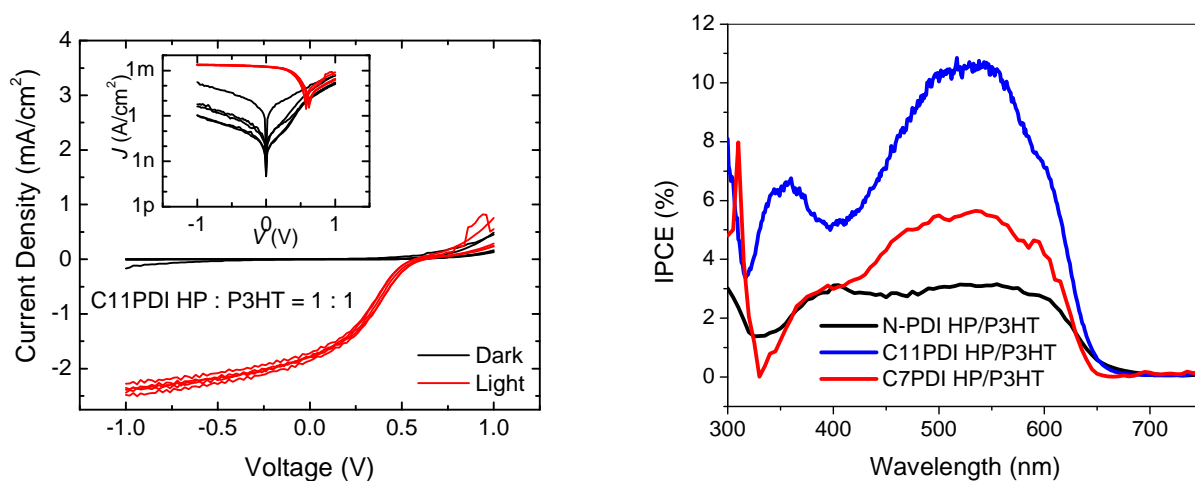


Figure 2.12. The films absorption spectra of C11PDI HP/P3HT (black) and C7PDI HP/P3HT (red) on PEDOT : PSS-coated ITO. These films were prepared in a way similar to real solar cell fabrication.

**Table 2.3. Summary of solar cell characteristics for the homopolymers (Data were collected by Mr. William Potscavage Jr. in the Kippelen group).**

Polymer	$V_{OC}$ (mV)	$J_{SC}$ (mA/cm <sup>2</sup> )	$FF$	PCE(%)
<b>P3HT: C11PDI HP (1 : 1)</b>	$603 \pm 28$	$1.9 \pm 0.1$	$0.31 \pm 0.01$	$0.38 \pm 0.01$
<b>P3HT: C7PDI HP (1 : 1)</b>	$619 \pm 3$	$0.85 \pm 0.02$	$0.31 \pm 0.01$	$0.20 \pm 0.01$
<b>P3HT: N-PDI HP (1 : 1)</b>	$441 \pm 13$	$0.20 \pm 0.01$	$0.32 \pm 0.01$	$0.04 \pm 0.01$



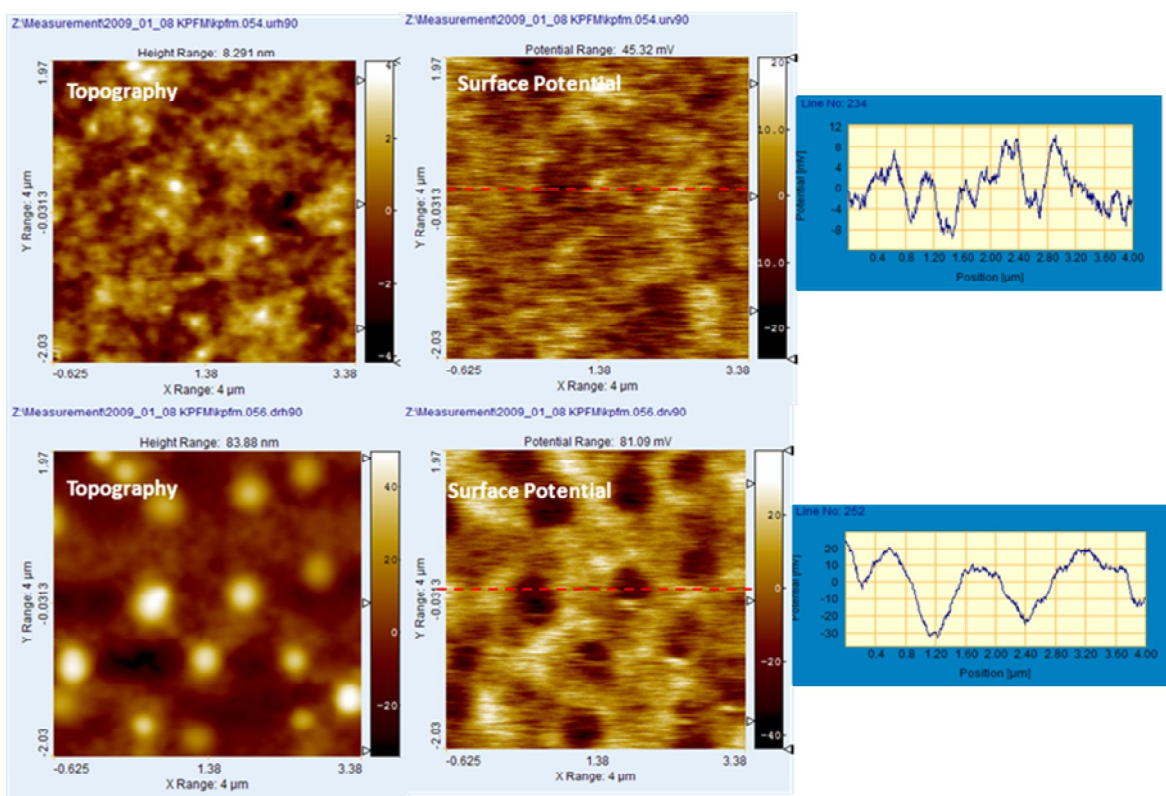
**Figure 2.13. The  $I$ - $V$  characteristics of the solar cells for P3HT:C11PDI HP blend and IPCE curves for the HP/P3HT blends (Figures were adapted from Mr. William Potscavage Jr. in the Kippelen group).**

## 2.8 Morphology studies of the P3HT/PDI HP blends

Recently, Kelvin probe force microscopy<sup>57</sup> (KPFM) has been extensively employed to characterize organic transistors<sup>58</sup> and solar cells.<sup>59</sup> KPFM is a contactless atomic force microscope (AFM) technique that measures the height variations on the sample surface while employing the electrostatic force between sample and tip to yield electric surface potential (SP) images. The SP images of a sample can, to a first

approximation, be considered the work function of the sample by taking into account the effects due to the surface polarizability as well as band bending.<sup>59</sup> Hence, KPFM could potentially offer useful phase-segregation information about the D-A blend regarding the difference in work functions for the donor rich and acceptor rich domains.<sup>59</sup> KPFM was applied to study the morphology of **PDI HP/P3HT** (1:1, weight ratio) blend films by Dr. Debin Wang in the Riedo group. As shown in the topography images of Figure 2.14, **C11PDI HP/P3HT** blend films (prepared under similar condition as for real devices) show much smoother surfaces (average roughness = 1.5 nm) over that from **C7PDI HP/P3HT** films (average roughness = 15 nm). A thin film morphology with isolated islands was obtained in the **C7PDI HP/P3HT** blend, probably due to the PDI-based aggregation, which was previously observed in other PDI/donor polymer blend films.<sup>60</sup> Regarding to the SP images, **C11PDI HP/P3HT** blend films show phase separation with domain sizes of 300 – 400 nm, while the domain size for the **C7PDI HP/P3HT** blend films is upwards of ~1  $\mu\text{m}$ . The much smaller phase separation domain size for **C11PDI HP/P3HT** blend film could potentially lead to a larger D/A interface, which might consequently result in higher photo-current and PCEs in solar cell devices. This is consistent with the higher  $J_{\text{SC}}$  and better solar cell performance found for the **C11PDI HP/P3HT** blend relative to the **C7PDI HP/P3HT** blend. Thermal annealing at 125 °C for 30 minutes (of similar annealing conditions for the respective solar cells) under nitrogen did not result in obvious changes of the film morphology. It should be noted that the KPFM images shown here only provide information about lateral phase separation at the surface, and information about phase separation in the bulk of the film is unclear. A

transmission electron microscopy (TEM) image of the cross-section of the films might provide the bulk morphology information, although we do not have this expertise.



**Figure 2.14.** The topography (left two) and surface potential (right two) images for P3HT:C11PDI HP (top two) and P3HT:C7PDI HP (bottom two) by KPFM. Here, major topographical hills lead to dark areas and thus low surface potential in the SP images, especially for P3HT:C7PDI HP blend (KPFM images were collected by Dr. Debin Wang in the Riedo group).

## 2.9 Conclusions

A series of PDI-grafted homopolynorbornenes have been synthesized, characterized and investigated as electron-transport materials in OFETs and acceptors in



BHJ-based solar cells. It was found that the PDI pendants tended to  $\pi$ - $\pi$  aggregate with other nearby PDI units in **C11PDI HP** and **C7PDI HP**, even in dilute solution, with large changes in the absorption and emission spectra on going from the monomer to polymer. Such  $\pi$ - $\pi$  stacking in polymer side-chains could be largely suppressed by the incorporation of functional groups in the bay positions. However, this resulted in poor OFET and OPV performance for **N-PDI HP**, despite the fact that it showed a broader and more red-shifted absorption spectrum relative to those of **C11PDI HP** and **C7PDI HP**. The OFETs based on **C11PDI HP** and **C7PDI HP** gave electron mobility of up to *ca.*  $5 \times 10^{-5} \text{ cm}^2 \text{ V}^{-1} \text{ s}^{-1}$  after thermal annealing. In the solar cells made from the P3HT:PDI HP blends, devices based on **C11PDI HP** exhibited moderate performance with a PCE up to  $0.38 \pm 0.01\%$  without optimization. This value is among the highest reported PCEs for PDI/P3HT blends. The study of P3HT:PDI HP blends with KPSM indicates more favorable morphology from P3HT:**C11PDI HP** blends over P3HT:**C7PDI HP** blends, including a much smoother surface and possible small domain size. This may provide useful information for further design of donor–acceptor type diblock copolymers with PDI-based pendants. In summary, the current study indicates that **C11PDI HP** blended with P3HT shows better performance in solar cells than the other two polymers. **C11PDI** will be chosen as the building block in preparing the D–A type diblock copolymers shown in Chapter 3.

## 2.10 Experimental section

**General:** Most organic and inorganic chemicals in this chapter were obtained from Aldrich, Alfa Aesar, and TCI and used without further purification. 1-Undecyl-

dodecylamine,<sup>61</sup> 8-aminopentadecane,<sup>61</sup> and pure *exo*-isomer of bicyclo[2.2.1]hept-5-ene-2-carboxylic acid<sup>62</sup> were synthesized via literature procedures or from Solvay. The <sup>1</sup>H and <sup>13</sup>C NMR spectra were collected on a Bruker 400 MHz or a Bruker 500 MHz spectrometer. Mass spectra were measured on an Applied Biosystems 4700 Proteomics Analyzer using MALDI mode. Elemental analyses (for C, H, N elements in this Chapter) were carried out by Atlantic Microlab using a LECO 932 CHNS elemental analyzer. Solution (chloroform) and thin film UV-Vis absorption spectra were recorded on a Varian Cary 500 UV/Vis/near-IR spectrophotometer while solution (toluene) emission spectra were recorded with a Shimadzu FP-5301PC spectrofluorometer. Electrochemical measurements were carried out under nitrogen in deoxygenated 0.1 M solutions of tetra-*n*-butylammonium hexafluorophosphate in dry dichloromethane using a computer-controlled BAS 100B electrochemical analyzer, a glassy-carbon working electrode, a platinum-wire auxiliary electrode, and an Ag wire anodized with AgCl as a pseudo-reference electrode. The cyclic voltammetry was performed using a scan rate of 50 mV/s. The potentials were referenced to FeCp<sub>2</sub><sup>+0</sup> redox couple by using ferrocene as an internal standard. TGA measurements were performed on an NETZSCH STA 449C analyzer under a nitrogen flow of 40 mL/min with a heating rate of 5 °C/min. DSC measurements were performed on a TA Instruments DSC Q200 analyzer under a nitrogen flow of 50 mL/min with a heating rate of 5 °C/min. Powder XRD data was collected on a Scintag X1 diffractometer with a Cu K $\alpha$  source ( $\lambda = 1.5406 \text{ \AA}$ ) in a continuous scan mode with a step size of 0.02°.

KPFM was carried out with a two-pass lift mode procedure using a Veeco Multimode IV AFM by Dr. Debin Wang in the Riedo group. The surface topography is

obtained by generic tapping mode scan in the first pass and the surface potential is measured on the second pass. On the first pass (main scan), the cantilever was mechanically vibrated near its resonant frequency by a small piezoelectric oscillator. On the second pass (interleave scan), the tip ascends to a constant lift scan height (20 nm); the tapping mode excitation oscillator is turned off and an oscillating AC voltage is applied directly to the probe tip. A lock-in amplifier and a servo feedback unit were used to track the cantilever oscillation at the resonant frequency and record the contact potential. Nanoworld SCM-PIT probes were selected for EFM and KPFM operation. The mechanical properties (force constant  $k = 2.8$  N/m and resonance frequency  $f = 75$  kHz) and the special Pt/Ir5 coating of probes are optimized for electrostatic force application. The typical tip radius of curvature is less than 25 nm.

OFET devices were fabricated by Dr. Shree Tiwari in the Kippelen group on heavily doped n-type silicon substrates (resistivity  $< 0.005$   $\Omega$ cm, with wafer thickness of  $\sim 500$   $\mu$ m from Silicon Quest Int., also serves as gate electrodes) with 200 nm thick thermally grown SiO<sub>2</sub> as the gate dielectric, in top-contact configuration. Ti/Au (10 nm/100 nm) metallization on the backside of the substrate was performed to enhance the gate electrical contact. Firstly, the substrates were cleaned by O<sub>2</sub> plasma for three minutes, to ensure the film adhesion by increase the hydrophilicity of the SiO<sub>2</sub> surface. The SiO<sub>2</sub> dielectric surface was then passivated with a thin buffer layer of bisbenzocyclobutene (BCB) (Cyclotene<sup>TM</sup>, Dow Chemicals), to provide a high-quality hydroxyl-free interface. The BCB was dissolved in 1,3,5-trimethylbenzene (TMB) with a weight ratio of 1 : 20 and spin-coated at 3000 rpm for 1 minute to provide a very thin, uniform layer (thickness was not measured, final capacitance density was measured). The samples were annealed

at 250 °C for 1 hour inside a nitrogen glove-box for thermal-cross-linking. The total capacitance density ( $C_{OX}$ ) was measured using parallel-plate capacitors as 13.86 nF/cm<sup>2</sup>. A thin layer of organic materials was formed on the substrates by spin coating at 1000 rpm for 60 seconds from a solution prepared in chlorobenzene (15 mg/mL). The devices were never exposed to ambient environment in the process. Calcium (*ca.* 150 nm) electrodes were deposited through a shadow mask to act as source and drain electrodes.

Solar cells were fabricated by Mr. William Potscavage *Jr.*, in the Kippelen group, by blending one of the homopolymers with P3HT (Rieke Metals, 4002-E). Solutions of a PDI polymer and P3HT were made in chlorobenzene (1 : 1 weight ratio, 20 mg/mL) for each of the polymers. ITO-coated glasses (Colorado Concept Coatings LLC) with a sheet resistivity of *ca.* 15  $\Omega$ /sq. were used as the substrates for the solar cells. The substrates were cleaned in an ultrasonic bath of detergent water, rinsed with deionized water, and then cleaned in sequential ultrasonic baths of deionized water, acetone, and isopropanol. Nitrogen was used to dry the substrates after each of the last three baths. A 300-nm-thick layer of SiO<sub>x</sub> was deposited on the cleaned ITOs by e-beam deposition (AXXIS, Kurt J. Lesker) to pattern the anode. Next, the substrates were ultrasonicated in isopropanol for 15 minutes, blown dry with nitrogen, and air-plasma treated for 2 minutes. A hole-conducting layer of PEDOT : PSS (poly(3,4-ethylenedioxythiophene) : poly(styrenesulfonate), CLEVIOS P VP AI 4083, H. C. Starck) was filtered through a 0.45- $\mu$ m-pore PVDF filter and spin coated on the substrates at 5000 rpm for 1 minute, and the substrates were annealed at 140 °C for 10 minutes in ambient atmosphere. After loading into a nitrogen-filled glove box, films of the polymer mixtures were deposited on the substrates by spin coating for 1 minute at speeds of 1000 – 1500 rpm for the mixture.

All solutions were filtered through 0.2- $\mu$ m-pore PTFE filters prior to spin coating. The substrates were then loaded into a vacuum thermal evaporation system (SPECTROS, Kurt J. Lesker) connected to the glove box, and  $\sim 200$  nm of Al was deposited through a shadow mask at a rate of  $1 - 3 \text{ \AA/s}$  and a base pressure of  $\sim 7 \times 10^{-8}$  Torr to define the cathodes. The completed devices were transferred in a sealed container to another nitrogen-filled glove box for electrical measurements. Current-voltage characteristics were measured using a source meter (2400, Keithley) controlled by a LabVIEW program. When testing the solar cells under illumination, filtered light from a 175 W Xenon lamp (ASB-XE-175EX, CVI) was used as a broadband light source with an irradiance of  $\sim 72 \text{ mW/cm}^2$  to simulate sunlight. A monochromator and calibrated photodiode were used to measure IPCE.

Solar cells were fabricated by Mr. William Potscavage *Jr.*, in the Kippelen group, by blending one of the homopolymers with P3HT (Rieke Metals, 4002-E). Solutions of a PDI polymer and P3HT were made in chlorobenzene (1 : 1 weight ratio, 20 mg/mL) for each of the polymers. ITO-coated glasses (Colorado Concept Coatings LLC) with a sheet resistivity of *ca.* 15  $\Omega/\text{sq.}$  were used as the substrates for the solar cells. The substrates were cleaned in an ultrasonic bath of detergent water, rinsed with deionized water, and then cleaned in sequential ultrasonic baths of deionized water, acetone, and isopropanol. Nitrogen was used to dry the substrates after each of the last three baths. A 300-nm-thick layer of  $\text{SiO}_x$  was deposited on the cleaned ITOs by e-beam deposition (AXXIS, Kurt J. Lesker) to pattern the anode. Next, the substrates were ultrasonicated in isopropanol for 15 minutes, blown dry with nitrogen, and air-plasma treated for 2 minutes. A hole-conducting layer of PEDOT : PSS (poly(3,4-ethylenedioxythiophene) :

poly(styrenesulfonate), CLEVIOS P VP AI 4083, H. C. Starck) was filtered through a 0.45- $\mu\text{m}$ -pore PVDF filter and spin coated on the substrates at 5000 rpm for 1 minute, and the substrates were annealed at 140 °C for 10 minutes in ambient atmosphere. After loading into a nitrogen-filled glove box, films of the polymer mixtures were deposited on the substrates by spin coating for 1 minute at speeds of 1000 – 1500 rpm for the mixture. All solutions were filtered through 0.2- $\mu\text{m}$ -pore PTFE filters prior to spin coating. The substrates were then loaded into a vacuum thermal evaporation system (SPECTROS, Kurt J. Lesker) connected to the glove box, and  $\sim 200$  nm of Al was deposited through a shadow mask at a rate of 1 – 3  $\text{\AA}/\text{s}$  and a base pressure of  $\sim 7 \times 10^{-8}$  Torr to define the cathodes. The completed devices were transferred in a sealed container to another nitrogen-filled glove box for electrical measurements. Current-voltage characteristics were measured using a source meter (2400, Keithley) controlled by a LabVIEW program. When testing the solar cells under illumination, filtered light from a 175 W Xenon lamp (ASB-XE-175EX, CVI) was used as a broadband light source with an irradiance of  $\sim 72$   $\text{mW}/\text{cm}^2$  to simulate sunlight. A monochromator and calibrated photodiode were used to measure IPCE.

Solar cells were fabricated by Mr. William Potscavage *Jr.*, in the Kippelen group, by blending one of the homopolymers with P3HT (Rieke Metals, 4002-E). Solutions of a PDI polymer and P3HT were made in chlorobenzene (1 : 1 weight ratio, 20 mg/mL) for each of the polymers. ITO-coated glasses (Colorado Concept Coatings LLC) with a sheet resistivity of *ca.* 15  $\Omega/\text{sq.}$  were used as the substrates for the solar cells. The substrates were cleaned in an ultrasonic bath of detergent water, rinsed with deionized water, and then cleaned in sequential ultrasonic baths of deionized water, acetone, and isopropanol.

Nitrogen was used to dry the substrates after each of the last three baths. A 300-nm-thick layer of SiO<sub>x</sub> was deposited on the cleaned ITOs by e-beam deposition (AXXIS, Kurt J. Lesker) to pattern the anode. Next, the substrates were ultrasonicated in isopropanol for 15 minutes, blown dry with nitrogen, and air-plasma treated for 2 minutes. A hole-conducting layer of PEDOT : PSS (poly(3,4-ethylenedioxythiophene) : poly(styrenesulfonate), CLEVIOS P VP AI 4083, H. C. Starck) was filtered through a 0.45-μm-pore PVDF filter and spin coated on the substrates at 5000 rpm for 1 minute, and the substrates were annealed at 140 °C for 10 minutes in ambient atmosphere. After loading into a nitrogen-filled glove box, films of the polymer mixtures were deposited on the substrates by spin coating for 1 minute at speeds of 1000 – 1500 rpm for the mixture. All solutions were filtered through 0.2-μm-pore PTFE filters prior to spin coating. The substrates were then loaded into a vacuum thermal evaporation system (SPECTROS, Kurt J. Lesker) connected to the glove box, and ~200 nm of Al was deposited through a shadow mask at a rate of 1 – 3 Å/s and a base pressure of  $\sim 7 \times 10^{-8}$  Torr to define the cathodes. The completed devices were transferred in a sealed container to another nitrogen-filled glove box for electrical measurements. Current-voltage characteristics were measured using a source meter (2400, Keithley) controlled by a LabVIEW program. When testing the solar cells under illumination, filtered light from a 175 W Xenon lamp (ASB-XE-175EX, CVI) was used as a broadband light source with an irradiance of  $\sim 72$  mW/cm<sup>2</sup> to simulate sunlight. A monochromator and calibrated photodiode were used to measure IPCE.

Solar cells were fabricated by Mr. William Potscavage *Jr.*, in the Kippelen group, by blending one of the homopolymers with P3HT (Rieke Metals, 4002-E). Solutions of a

PDI polymer and P3HT were made in chlorobenzene (1 : 1 weight ratio, 20 mg/mL) for each of the polymers. ITO-coated glasses (Colorado Concept Coatings LLC) with a sheet resistivity of *ca.* 15  $\Omega$ /sq. were used as the substrates for the solar cells. The substrates were cleaned in an ultrasonic bath of detergent water, rinsed with deionized water, and then cleaned in sequential ultrasonic baths of deionized water, acetone, and isopropanol. Nitrogen was used to dry the substrates after each of the last three baths. A 300-nm-thick layer of SiO<sub>x</sub> was deposited on the cleaned ITOs by e-beam deposition (AXXIS, Kurt J. Lesker) to pattern the anode. Next, the substrates were ultrasonicated in isopropanol for 15 minutes, blown dry with nitrogen, and air-plasma treated for 2 minutes. A hole-conducting layer of PEDOT : PSS (poly(3,4-ethylenedioxythiophene) : poly(styrenesulfonate), CLEVIOS P VP AI 4083, H. C. Starck) was filtered through a 0.45- $\mu$ m-pore PVDF filter and spin coated on the substrates at 5000 rpm for 1 minute, and the substrates were annealed at 140 °C for 10 minutes in ambient atmosphere. After loading into a nitrogen-filled glove box, films of the polymer mixtures were deposited on the substrates by spin coating for 1 minute at speeds of 1000 – 1500 rpm for the mixture. All solutions were filtered through 0.2- $\mu$ m-pore PTFE filters prior to spin coating. The substrates were then loaded into a vacuum thermal evaporation system (SPECTROS, Kurt J. Lesker) connected to the glove box, and ~200 nm of Al was deposited through a shadow mask at a rate of 1 – 3 Å/s and a base pressure of  $\sim 7 \times 10^{-8}$  Torr to define the cathodes. The completed devices were transferred in a sealed container to another nitrogen-filled glove box for electrical measurements. Current-voltage characteristics were measured using a source meter (2400, Keithley) controlled by a LabVIEW program. When testing the solar cells under illumination, filtered light from a 175 W Xenon lamp



(ASB-XE-175EX, CVI) was used as a broadband light source with an irradiance of  $\sim 72$  mW/cm<sup>2</sup> to simulate sunlight. A monochromator and calibrated photodiode were used to measure IPCE.

***N,N'*-Bis(1-undecyl-dodecyl)-perylene-3,4,9,10-tetracarboxylic diimide:**<sup>63</sup> A mixture of perylene-3,4,9,10-tetracarboxydianhydride (6.0 g, 15 mmol), 1-undecyl-dodecylamine (12 g, 35 mmol), zinc acetate (1.6 g, 8.7 mmol), and imidazole (70 g) were heated at 180 °C for 5 h before it was allowed to cool to room temperature and treated with 2 N aqueous HCl (400 mL). The mixture was then extracted with chloroform (2  $\times$  200 mL). The organic phase was washed with water (3  $\times$  100 mL) and dried over MgSO<sub>4</sub>. The solvent was then removed under reduced pressure and the residue was purified by flash column chromatography on silica gel, using CHCl<sub>3</sub> / hexane (1:1 and then 2:1) as eluent to give the desired product as a red solid (12 g, 77%). <sup>1</sup>H NMR (500 MHz, CDCl<sub>3</sub>):  $\delta$  8.64 (m, 8H), 5.18 (m, 2H), 2.22 (m, 4H), 1.86 (m, 4H), 1.4–1.1 (m, 72H), 0.80 (t,  $J$  = 6.6 Hz, 12H). The <sup>1</sup>H NMR spectrum of this product is consistent with that reported in the literature.<sup>63</sup>

***N,N'*-Bis(1-heptyloctyl) perylene-3,4,9,10-tetracarboxylic diimide:**<sup>64</sup> A mixture of perylene-3,4,9,10-tetracarboxydianhydride (6.6 g, 17 mmol), 8-aminopentadecane (10 g, 43 mmol), zinc acetate (1.6 g, 8.7 mmol) and imidazole (70 g) were heated at 180 °C for 5 h before it was allowed to cool to room temperature and treated with 2 N aqueous HCl (400 mL). The mixture was then extracted with chloroform (2 $\times$  200 mL). The organic phase was washed with water (3  $\times$  100 mL) and dried over MgSO<sub>4</sub>. The solvent was then removed under reduced pressure and the residue was purified by flash column

chromatography on silica gel, using CHCl<sub>3</sub> / hexane (1:1 and then 2:1) as eluent to give the desired product as a red solid (10 g, 73%). <sup>1</sup>H NMR (500 MHz, CDCl<sub>3</sub>): δ 8.59–8.63 (m, 4H), 8.50–8.52 (d, *J* = 8.0 Hz, 4H), 5.18–5.23 (m, 2H), 2.22–2.29 (m, 4H), 1.88–1.92 (m, 4H), 1.25–1.38 (m, 40H), 0.82 (t, *J* = 6.6 Hz, 12H). The <sup>1</sup>H NMR spectrum of the product is consistent with that reported in the literature.<sup>64</sup>

***N*-(1-Undecyl-dodecyl)-perylene-3,4-dicarboxylicmonoanhydride-9,10**

**dicarboxylicmonoimide (A1):**<sup>63</sup> *N,N'*-Bis(1-undecyl-dodecyl)-perylene-3,4,9,10-tetracarboxylic diimide (1.0 g, 1.0 mmol), potassium hydroxide (powder, 0.19 g, 3.4 mmol) in *tert*-butanol (18 mL) were heated to 120 °C and maintained at this temperature for 50 min under nitrogen. After the solution was cooled to *ca.* 100°C, it was treated with acetic acid (17 mL) and 2 N aqueous HCl (10 mL). The resultant mixture was stirred at room temperature overnight and then extracted with chloroform (100 mL). The organic layer was washed sequentially with water (2 × 20 mL), 0.5 N aqueous NaHCO<sub>3</sub> (20 mL), and water (20 mL) in sequence. The mixture was dried over MgSO<sub>4</sub>, and the solvent was removed under reduced pressure. The residue was purified by flash chromatography on silica gel eluted with CHCl<sub>3</sub>. **A1** was obtained as a red solid (0.33 g, 48%). <sup>1</sup>H NMR (500 MHz, CDCl<sub>3</sub>): δ : 8.72–8.66 (m, 8H), 5.18 (m, 1H), 2.25 (m, 2H), 1.88 (m, 2H), 1.35–1.29 (m, 36H), 0.82 (t, *J* = 6.3 Hz, 6H). Anal. Calcd for C<sub>47</sub>H<sub>55</sub>NO<sub>5</sub>: : C, 79.07; H, 7.76; N, 1.96. Found: C, 78.86; H, 7.79; N, 1.94. The <sup>1</sup>H NMR spectrum of which is consistent with that reported in the literature.<sup>63</sup>

***N*-(1-Heptyloctyl)-perylene-3,4-dicarboxylicmonoanhydride-9,10**

**dicarboxylicmonoimide (A2):**<sup>64</sup> *N,N'*-Bis(1-heptyloctyl) perylene-3,4,9,10-tetracarboxylic diimide (3.2 g, 4.0 mmol), potassium hydroxide (0.55 g, 8.4 mmol) in

*tert*-butanol (90 mL) were heated to 120 °C and maintained at this temperature for 50 min under nitrogen. After the solution was cooled to *ca.* 80 °C, it was treated with acetic acid (72 mL) and 2 N aqueous HCl (50 mL). The resultant mixture was stirred at room temperature overnight and then extracted with chloroform (100 mL). The organic layer was washed with water (2 × 40 mL), 0.5 N aqueous NaHCO<sub>3</sub> (40 mL), and water (2 × 40 mL) in sequence. The mixture was dried over MgSO<sub>4</sub> and filtered, and the solvent was removed under reduced pressure. The residue was purified by flash chromatography on silica gel eluted with CHCl<sub>3</sub>. **A2** was obtained as a red solid (1.4 g, 59%). <sup>1</sup>H NMR (500 MHz, CDCl<sub>3</sub>): δ 8.69–8.50 (m, 8H), 5.18 (m, 1H), 2.24 (m, 2H), 1.86 (m, 2H), 1.34–1.20 (m, 20H), 0.81 (t, *J* = 6.5 Hz, 6H). The <sup>1</sup>H NMR spectrum is consistent with that reported in the literature.<sup>64</sup>

**Compound B1:** Compound **A1** (0.30 g, 0.42 mmol), 3-amino-propanol (0.30 g, 4.0 mmol), anhydrous zinc acetate (0.080 mg, 0.43 mol), and imidazole (2.0 g) were heated under N<sub>2</sub> at 180 °C for 3 h before the mixture was cooled down to around 130 °C and treated with 2 N aqueous HCl (50 mL). The resultant red precipitate was filtered and washed with 2 N aqueous HCl (10 mL), water (2 × 20 mL), and methanol (3 × 20 mL) in sequence. The red solid was then heated in methanol (30 mL) for 1 h at reflux and filtered when it was hot to provide pure **B1** as a red solid (0.30 g, 92 %). <sup>1</sup>H NMR (300 MHz, CDCl<sub>3</sub>): δ 8.70–8.60 (m, 8H), 5.15 (m, 1H), 4.38 (t, *J* = 6.6 Hz, 2H), 3.62 (t, *J* = 5.4 Hz, 2H), 2.23 (m, 2H), 2.00 (m, 2H), 1.84 (m, 2H), 1.51–1.16 (m, 36H), 0.82 (t, *J* = 6.6 Hz, 6H), (the alcohol proton was not observed). <sup>13</sup>C{<sup>1</sup>H}NMR (125 MHz, CDCl<sub>3</sub>): δ 164.4, 163.8, 163.3, 134.8, 133.8, 131.6, 131.4, 130.8, 129.3, 129.2, 126.2, 126.0, 124.1, 123.3, 123.1, 122.7, 122.5, 58.9, 54.8, 37.0, 32.3, 31.8, 30.9, 29.5, 29.4, 29.2, 26.9, 22.6, 14.0

(the observation of three carbonyl carbon resonances and two more aromatic carbon peaks is consistent with previous work on perylene diimides using similar swallow-tailed *N*-substituents and has been attributed to restricted rotation about the N—C<sub>alkyl</sub> bonds. Three alkyl carbons were not observed, presumably due to overlap).<sup>65</sup> HRMS (FAB) calcd for C<sub>50</sub>H<sub>62</sub>N<sub>2</sub>O<sub>5</sub>: 770.4659 Found: 770.4662. Anal. Calcd for C<sub>50</sub>H<sub>62</sub>N<sub>2</sub>O<sub>5</sub>: C, 77.89; H, 8.10; N, 3.63. Found: C, 77.91; H, 8.27; N, 3.71.

**Compound B2:** Compound **A2** (1.20 g, 2.00 mmol), 3-amino-propanol (1.50 g, 20.0 mmol), anhydrous zinc acetate (0.500, 2.74 mmol), and imidazole (20 g) were heated under N<sub>2</sub> at 180 °C for 3 h before the mixture was cooled down to around 130 °C and treated with 2 N aqueous HCl (50 mL). The resulted red precipitate was filtered and washed with 2 N aqueous HCl (40 mL), water (2 × 50 mL), and methanol (3 × 30 mL) in sequence. The resultant solid was then dissolved in 50 mL CHCl<sub>3</sub> and passed through a short silica gel plug eluted with CHCl<sub>3</sub> and then CHCl<sub>3</sub>/ methanol (10:1) to provide pure **B1** as a red solid after solvent removal (0.92 g, 70%). <sup>1</sup>H NMR (500 MHz, CDCl<sub>3</sub>): δ 8.70-8.62 (m, 8H), 5.18 (m, 1H), 4.39 (t, *J* = 6.0 Hz, 2H), 3.63 (m, 2H) 3.03 (t, *J* = 6.0 Hz, 2H), 2.26 (m, 2H), 2.04 (m, 2H), 1.87 (m, 2H), 1.51-1.16 (m, 18H), 0.82 (t, *J* = 6.5 Hz, 6H) (the alcohol proton was not observed). <sup>13</sup>C{<sup>1</sup>H} NMR (125 MHz, CDCl<sub>3</sub>): δ 164.5, 164.0, 163.5, 134.9, 134.0, 131.8, 131.6, 131.0, 129.4, 129.3, 126.3, 126.2, 124.2, 123.5, 123.2, 122.9, 122.6, 59.1, 54.9, 37.1, 32.4, 31.8, 31.0, 29.6, 29.3, 27.1, 22.7, 14.2. (the observation of three carbonyl carbon resonances and two more aromatic carbon peaks is consistent with previous work on perylene diimides using similar swallow-tailed *N*-substituents, and it has been attributed to restricted rotation about the N—C<sub>alkyl</sub>

bonds).<sup>65</sup> HRMS (MALDI) calcd for C<sub>42</sub>H<sub>46</sub>N<sub>2</sub>O<sub>5</sub>: 658.34; Found: 658.35. Anal. Calcd for C<sub>42</sub>H<sub>46</sub>N<sub>2</sub>O<sub>5</sub>: C, 76.57; H, 7.04; N, 4.25. Found: C, 76.30; H, 7.18; N, 4.16.

**C11PDI monomer:** Compound **B1** (0.45 g, 0.58 mmol) and exo-bicyclo[2.2.1]hept-5-ene-2-carboxylic acid (0.15 g, 1.1 mmol) were dissolved in dichloromethane (10.0 mL) in a 25 mL round-bottomed flask under N<sub>2</sub>. Dicyclohexylcarbodiimide (186 mg, 0.9 mmol) and 4-(dimethylamino)pyridine (11 mg, 0.09 mmol) in methylene chloride (3.0 mL) were added in one portion. The reaction mixture was stirred overnight at room temperature under N<sub>2</sub> before it was poured into a short silica gel plug and eluted with CHCl<sub>3</sub>. The solvent was then removed under reduced pressure and the residul was purified with silica gel column chromatography using CH<sub>2</sub>Cl<sub>2</sub>/ethyl acetate (50:1) as eluent. After the solvent was removed under reduced pressure, **C11PDI monomer** was obtained as a red solid. (0.38 g, 74 %). <sup>1</sup>H NMR (500 MHz, CDCl<sub>3</sub>): δ 8.66–8.57 (m, 8H), 6.08 (dd, *J*<sub>1</sub> = 5.5 Hz, *J*<sub>2</sub> = 3.0 Hz, 1H), 6.01 (dd, *J*<sub>1</sub> = 5.5 Hz, *J*<sub>2</sub> = 3.0 Hz, 1H), 5.16 (m, 1H), 4.34 (t, *J* = 7.0 Hz, 2H), 4.24 (td, *J*<sub>1</sub> = 6.0 Hz, *J*<sub>2</sub> = 2.0 Hz, 2H), 3.03 (s, 1H), 2.87 (s, 1H), 2.25–2.12 (m, 5H), 1.93–1.89 (m, 1H), 1.86–1.82 (m, 2H), 1.34–1.17 (m, 39H), 0.83 (t, *J* = 7.0 Hz, 6H). <sup>13</sup>C{<sup>1</sup>H} NMR (125 MHz, CDCl<sub>3</sub>): δ 176.2, 164.5, 163.4, 163.2, 138.5, 138.0, 135.7, 134.6, 134.1, 131.7, 131.3, 131.0, 129.4, 129.2, 126.3, 126.2, 124.0, 123.3, 123.0, 122.9, 122.8, 62.4, 54.8, 46.6, 46.4, 43.1, 41.6, 37.8, 32.3, 31.9, 30.3, 29.7, 29.6, 29.5, 29.3, 27.4, 27.0, 22.6, 14.1 (the observation of four carbonyl carbon resonances and three more aromatic carbon peaks is consistent with previous work on perylene diimides using similar swallow-tailed *N*-substituents, and it has been attributed to restricted rotation about the N—C<sub>alkyl</sub> bonds. Three alkyl carbons were not observed, presumably due to overlap).<sup>65</sup> HRMS (MALDI) calcd for C<sub>58</sub>H<sub>70</sub>N<sub>2</sub>O<sub>6</sub>: 890.5234; Found: 890.5109

(MALDI). Anal. Calcd for  $C_{58}H_{70}N_2O_6$ : C, 78.17; H, 7.92; N, 3.40; Found: C, 78.32; H, 7.99; N, 3.18. UV-visible absorption (chloroform)  $\lambda_{\max}(\epsilon)$ : 459 ( $1.59 \times 10^4$ ), 490 ( $4.32 \times 10^4$ ), 527 ( $7.14 \times 10^4$ ) nm ( $M^{-1}cm^{-1}$ ).

**C7PDI monomer**: Compound **B2** (0.85 g, 1.28 mmol) and exo-bicyclo[2.2.1]hept-5-ene-2-carboxylic acid (0.60 g, 4.1 mmol) were dissolved in dichloromethane (30 mL) in a 50 mL round-bottomed flask under  $N_2$ . Dicyclohexylcarbodiimide (0.40 g, 1.9 mmol) and 4-(dimethylamino)pyridine (0.030 mg, 0.27 mmol) in dichloromethane (3.0 mL) were added in one portion. The reaction mixture was stirred overnight at room temperature under  $N_2$  before it was poured into a short silica gel plug and eluted with chloroform. The solvent was then removed under reduced pressure and the residul was purified with silica gel column chromatography using  $CH_2Cl_2$ /ethyl acetate (30:1) as eluent. After the solvent was removed under reduced pressure, **C7PDI monomer** was obtained as a red solid. (0.88 g, 88 %).  $^1H$  NMR (500 MHz,  $CDCl_3$ ):  $\delta$ : 8.63–8.54 (m, 8H), 6.06 (m, 1H), 6.00 (m, 1H), 5.17 (m, 1H), 4.33 (t,  $J = 7.0$  Hz, 2H), 4.23 (t,  $J = 6.0$  Hz, 2H), 3.02 (s, 1H), 2.86 (s, 1H), 2.21–2.12 (m, 5H), 1.93–1.82 (m, 3H), 1.52–1.17 (m, 23H), 0.81 (t,  $J = 7.0$  Hz, 6H).  $^{13}C\{^1H\}$  NMR: (125 MHz,  $CDCl_3$ ),  $\delta$  176.1, 164.4, 163.3, 163.1, 138.0, 135.6, 134.5, 134.0, 131.6, 131.2, 131.1, 130.9, 129.3, 129.1, 126.2, 126.1, 124.0, 123.2, 122.8, 122.7, 62.3, 54.7, 46.5, 46.3, 43.0, 41.5, 37.7, 32.3, 31.7, 30.2, 29.4, 29.1, 27.3, 26.9, 22.5, 14.0 (the observation of four carbonyl carbon resonances and three more aromatic carbon peaks is consistent with previous work on perylene diimides using similar swallow-tailed *N*-substituents, and it has been attributed to restricted rotation about the  $N-C_{alkyl}$  bonds. Three alkyl carbons were not observed, presumably due to overlap).<sup>65</sup> HRMS (MALDI) calcd for  $C_{50}H_{54}N_2O_6$ : 778.3981; Found: 778.3687. Anal. Calcd for  $C_{50}H_{54}N_2O_6$ : C,

77.09; H, 6.99; N, 3.60, Found: C, 77.06; H, 7.14; N, 3.61. UV-visible absorption (chloroform)  $\lambda_{\text{max}}(\epsilon)$ : 459 ( $1.59 \times 10^4$ ), 490 ( $4.32 \times 10^4$ ), 527 ( $7.14 \times 10^4$ ) nm ( $\text{M}^{-1}\text{cm}^{-1}$ ).

**C11PDI HP:** **C11PDI** monomer (700 mg, 0.77 mmol) was dissolved in anhydrous dichloromethane (15 mL) under  $\text{N}_2$ , the “first generation” Grubbs initiator (12.6 mg, 0.015 mmol) in 1 mL methylene chloride was then added in one portion. The reaction mixture was stirred for another 5 h until all the monomers were consumed (monitored with TLC), and then ethyl vinyl ether (0.2 mL) was added. The reaction mixture was stirred for another 5 h before it was added to methanol (200 mL) dropwise; the red precipitate was filtered, washed with methanol, and dried under vacuum. The resultant solid was then dissolved in 25 mL dichloromethane and added to 200 mL methanol dropwise. The precipitate was filtered, washed with methanol, and dried under vacuum. The red solid was then washed with hot methanol in a Soxhlet apparatus for 6 h, and then with hot acetone overnight. Finally,  $\text{CHCl}_3$  was used to extract the materials for 5 h. Most of the solvent was removed under vacuum and the residue was precipitated into 200 mL methanol dropwise. After filtration, **C11PDI HP** was achieved as a red solid (590 mg, 85 %). GPC (toluene):  $M_n = 18.6$  kD,  $M_w/M_n = 1.3$ .  $^1\text{H}$  NMR (500 MHz,  $\text{CDCl}_3$ ):  $\delta$  8.5–7.5 (m, 8nH), 5.6–5.0 (m, 3nH), 4.5–4.0 (sb, 4nH), 3.0–1.5 (m, 10nH), 1.34–1.17 (m, 39nH), 0.83 (sb, 6nH). Anal. Calcd for  $(\text{C}_{58}\text{H}_{70}\text{N}_2\text{O}_6)_n$ : C, 78.17; H, 7.91; N, 3.13; Found: C, 77.78; H, 7.92; N, 3.17. UV-visible absorption (chloroform)  $\lambda_{\text{max}}(\epsilon)$ : 464 ( $1.42 \times 10^4$ ), 492 ( $2.95 \times 10^4$ ), 529 ( $2.69 \times 10^4$ ) nm ( $\text{M}^{-1}\text{cm}^{-1}$ ).

**C7PDI HP:** **C7PDI** monomer (500 mg, 0.641 mmol) was dissolved in anhydrous methylene chloride (12 mL) under  $\text{N}_2$ , the “first generation” Grubbs initiator (10.5 mg, 0.0128 mmol) in 1 mL methylene chloride was then added in one portion. The reaction

mixture was kept stirred for another 5 hours until all the monomers were consumed (monitored with TLC), and ethyl vinyl ether (0.2 mL) was added. The reaction mixture was then stirred for another 5 hours before it was added to methanol (200 mL), dropwise, and the red precipitate was filtered, washed with methanol, and dried under vacuum. The resultant solid was then dissolved in 25 mL dichloromethane and added to 200 mL methanol, dropwise. The precipitate was filtered, washed with methanol, and dried under vacuum. The red solid was then washed with hot methanol in a Soxhlet apparatus for 6 hours, and then with hot acetone overnight. Finally, chloroform was used to extract the materials for 5 hours. Most of the solvent was removed under vacuum, and the residue was precipitated into 200 mL methanol dropwise. **C7PDI HP** was achieved as a red solid via filtration (467 mg, 93%). GPC (toluene):  $M_n = 18.0$  kD,  $M_w/M_n = 1.3$ .  $^1\text{H}$  NMR (500 MHz,  $\text{CDCl}_3$ ):  $\delta$  8.5–7.5 (m, 8nH), 5.6–5.0 (m, 3nH), 4.5–4.0 (sb, 4nH), 3.5–1.5 (m, 10nH), 1.34–1.17 (m, 23nH), 0.83 (sb, 6nH). Anal. Calcd for  $(\text{C}_{58}\text{H}_{70}\text{N}_2\text{O}_6)_n$ : C, 77.09; H, 6.99; N, 3.60; Found: C, 77.65; H, 7.00; N, 3.56. UV-visible absorption (chloroform)  $\lambda_{\text{max}}(\epsilon)$ : 464 ( $1.39 \times 10^4$ ), 493 ( $2.80 \times 10^4$ ), 529 ( $2.50 \times 10^4$ ) nm ( $\text{M}^{-1}\text{cm}^{-1}$ ).

***N,N'*-Bis(2-decyl-tetradecyl)-perylene-3,4:9,10-tetracarboxydimide:** Perylene-3,4,9,10-tetracarboxydianhydride (4.0 g, 10 mmol), 2-decyl-tetradecylamine (17.0 g, 48.0 mmol) and imidazole (31 g) were combined in a round-bottomed flask with an air condenser, and the reaction flask was immersed in an oil bath at 160 °C for 3 h after which the reaction flask was removed from the oil bath. After it was cooled to room temperature, 2 N HCl aqueous (400 mL) was added. The reaction mixture was extracted with  $\text{CHCl}_3$ , dried over  $\text{MgSO}_4$ , and filtered. The solvent was removed by rotary evaporation, and the residue was purified by column chromatography, eluted with  $\text{CHCl}_3$ ,



yielding the desired product as a red solid (10.4 g, 98%)  $^1\text{H}$  NMR (500 MHz,  $\text{CDCl}_3$ )  $\delta$  8.52 (d,  $J = 8.0$  Hz, 4H), 8.38 (d,  $J = 8.0$ , 4H), 4.09 (d,  $J = 7.5$  Hz, 4H), 1.97 (m, 2H), 1.5–1.0 (m, 80H), 0.83 (m, 12H).  $^{13}\text{C}\{^1\text{H}\}$  NMR (125 MHz,  $\text{CDCl}_3$ )  $\delta$  163.5, 134.2, 131.2, 129.2, 126.1, 123.2, 122.8, 44.7, 36.6, 31.9, 31.7, 30.1, 29.69, 29.66, 29.65, 29.4, 26.5, 22.7, 14.1 (12 alkyl carbons missing, presumably due to overlap). HRMS (FAB) calcd for  $\text{C}_{72}\text{H}_{106}\text{N}_2\text{O}_4$ : 1062.8153. Found: 1062.8167. Anal. Calcd. for  $\text{C}_{72}\text{H}_{114}\text{N}_2\text{O}_4$ : C, 80.69; H, 10.72; N, 2.61. Found: C, 81.33; H, 10.02; N, 2.68.

**(*N,N'*-Bis(2'-decyltetradecanyl)-1-bromo-perylene-3,4,9,10-tetracarboxylic diimide)**

**(C):** *N,N'*-Bis(2-decyl-tetradecyl)-perylene-3,4,9,10-tetracarboxydimide (6.0 g, 5.6 mmol), potassium carbonate (4.0 g, 29 mmol) and chlorobenzene (80 mL) were mixed in a 200 mL round-bottomed flask equipped with a condenser. Bromine (4.8 mL, 93 mmol) in chlorobenzene (10 mL) was then added dropwise. The reaction mixture was heated to 60 °C overnight. It was then cooled to room temperature and poured into saturated  $\text{Na}_2\text{S}_2\text{O}_3$  aqueous solution (500 mL). The mixture was then extracted with  $\text{CHCl}_3$  (2  $\times$  200 mL); the organic phase was washed with water (2  $\times$  100 mL) and dried over  $\text{Na}_2\text{SO}_4$ . After the solvent was removed, the residue was purified using column chromatography on silica gel, with  $\text{CHCl}_3$  / hexane (1 : 1) as the eluent. After the solvent was removed under reduced pressure, compound **C** was obtained as a red solid (2.7 g, 42%).  $^1\text{H}$  NMR (500 MHz,  $\text{CDCl}_3$ ):  $\delta$  9.62 (d,  $J = 8.0$  Hz, 1H), 8.72 (s, 1H), 8.51 (m, 3H), 8.36 (m, 2H), 4.09 (d,  $J = 7.0$  Hz, 2H), 4.06 (d,  $J = 7.0$  Hz, 2H), 1.95 (m, 2H), 1.5–1.1 (m, 80H), 0.82 (m, 12H).  $^{13}\text{C}\{^1\text{H}\}$  NMR (125 MHz,  $\text{CDCl}_3$ ):  $\delta$  163.5, 163.2, 163.1, 162.3, 138.9, 133.5, 133.1, 133.0, 130.8, 130.3, 128.5, 128.3, 127.9, 127.6, 126.6, 123.5, 123.4, 123.3, 122.92, 122.7, 122.5, 120.9, 44.79, 44.72, 36.63, 36.58, 31.9, 31.7, 30.1, 30.0, 29.7, 29.6 (2 close

peaks), 29.6, 29.4, 26.5 (2 close peaks), 22.7, 14.1 (two aryl carbon peaks and 31 alkyl carbon peaks were not observed, presumably due to overlap). HRMS (MALDI) calcd for  $C_{72}H_{105}BrN_2O$  ( $M^+$ ): 1140.728, found: 1140.734. Anal. Calcd for  $C_{72}H_{105}BrN_2O$ : C, 75.69; H, 9.26; N, 2.45. Found : C, 75.77; H, 9.26; N, 2.50.

**Compound D:** *N,N'*-Bis(2'-decyltetradecanyl)-1-bromo-perylene-3,4,9,10-tetracarboxylic diimide (1.0 g 0.90 mmol) and 2-(piperazin-1-yl) ethanol (1.2 g, 9.3 mmol) were heated in N-methylpyrrolidone (30 mL) at 200 °C for 1.5 hours under nitrogen. The reaction mixture was cooled to room temperature and chloroform (200 mL) was added. The organic phase was then washed with water ( $6 \times 100$  mL) and dried over  $Na_2SO_4$ . The solvent was then removed under reduced pressure, and the residue was passed through a short silica gel plug with  $CHCl_3$  and then  $CHCl_3$ /methanol (10: 1) to collect the band of black color. The solvent was then removed under reduced pressure and the residue was dried under vacuum. The solid was then run through a short silica plug again to give nearly pure product. After the removal of the solvent, compound **D** was achieved as a black solid. (0.50 g, 47%).  $^1H$  NMR (400 MHz,  $CD_2Cl_2$ ):  $\delta$  9.87 (d,  $J = 8.7$  Hz, 1H), 8.67–8.52 (m, 6H), 4.14 (t,  $J = 6.4$  Hz, 4H), 3.68 (sb, 2H), 3.50 (d,  $J = 8.4$  Hz, 2H), 3.15 (t,  $J = 11.2$  Hz, 2H), 2.97 (d,  $J = 11.2$  Hz, 2H), 2.71–2.66 (m, 4H), 2.57 (m, 1H), 1.99 (sb, 2H), 1.31–1.90 (m, 80H), 0.85 (m, 12H). HRMS (MALDI) calcd for  $C_{78}H_{118}N_4O_5$ : 1190.91, Found: 1191.94. ( $M+1$ ) This compound was used for next step reaction without further purification.

**N-PDI monomer:** Compound **C** (0.50 g, 42 mmol) and exo-bicyclo[2.2.1]hept-5-ene-2-carboxylic acid (0.30 g, 2.1 mmol) were dissolved in methylene chloride (10 mL) in a 50 mL round-bottomed flask under nitrogen. Dicyclohexylcarbodiimide (21 mg, 1.0

mmol) and 4-(dimethylamino)pyridine (15 mg, 0.14 mmol) in methylene chloride (2.0 mL) were added in one portion. The reaction mixture was stirred overnight at room temperature under N<sub>2</sub>. It was poured to a short silica gel plug and eluted with CHCl<sub>3</sub> and then CHCl<sub>3</sub> / ethyl acetate (6 : 1) and the black band was collected. The solvent was then removed under reduced pressure to give **N-PDI monomer** as a black solid (0.51 g, 92 %).

<sup>1</sup>H NMR (500 MHz, CDCl<sub>3</sub>):  $\delta$  9.91 (d,  $J$  = 8.5 Hz, 1H), 8.64 (t,  $J$  = 8.0 Hz, 2H), 8.54–8.49 (m, 4H), 6.14–6.12 (m, 1H), 6.11–6.09 (m, 1H), 4.31–4.24 (m, 2H), 4.14 (t,  $J$  = 8.0 Hz, 4H), 3.46 (db,  $J$  = 8.5 Hz, 2H), 3.12 (tb,  $J$  = 10 Hz, 2H), 3.05 (s, 1H), 2.96–2.92 (m, 4H), 2.77 (t,  $J$  = 5.5 Hz, 2H), 2.66–2.64 (mb, 2H), 2.26 (m, 1H) 2.01–1.91 (m, 4H), 1.39–1.19 (m, 80H) 0.85–0.81 (m, 12H). <sup>13</sup>C{<sup>1</sup>H} NMR (125 MHz, CD<sub>2</sub>Cl<sub>2</sub>):  $\delta$  176.2, 164.1, 163.9, 152.0, 138.4, 136.0, 135.8, 134.8, 134.2, 131.4, 131.0, 129.4, 129.2, 128.9, 127.3, 124.9, 124.0, 123.21, 122.84, 122.0, 115.8, 108.4, 101.5, 99.1, 89.9, 88.3, 84.8, 83.6, 80.1, 76.2, 73.7, 71.5, 69.9, 68.3, 61.8, 57.1, 51.7, 48.9, 47.0, 46.7, 44.9, 44.8, 43.5, 42.1, 39.3, 37.0, 32.3, 32.1, 30.7, 30.4 (3 peaks), 30.1, 30.0, 29.7, 26.9, 23.0, 18.7, 14.2 (13 alkyl carbon peaks were not observed, presumably due to overlap). HRMS (MALDI) calcd for C<sub>86</sub>H<sub>126</sub>N<sub>4</sub>O<sub>6</sub>: 1310.97. Found: 1311.95 (M + 1). Anal. Calcd for C<sub>86</sub>H<sub>126</sub>N<sub>4</sub>O<sub>6</sub>: C, 78.73; H, 9.68; N, 4.27; Found : C, 78.49; H, 9.75; N, 4.20. UV-visible absorption (chloroform)  $\lambda_{\text{max}}(\epsilon)$ : 451 (1.20  $\times 10^4$ ), 585 (1.87  $\times 10^4$ ) nm (M<sup>-1</sup>cm<sup>-1</sup>).

**N-PDI homopolymer:** **C11PDI** monomer (394 mg, 0.300 mmol) was dissolved in anhydrous dichloromethane (10.0 mL) under N<sub>2</sub>, and the “first-generation” Grubbs initiator (4.9 mg, 0.006 mmol) in dichloromethane (1 mL) was then added in one portion. The reaction mixture was kept stirred for another 5 h until all the monomers were consumed (monitored with TLC) and ethyl vinyl ether (0.2 mL) was added. The reaction

mixture was stirred for another 5 hours before it was added to methanol (150 mL), dropwise, and the black precipitate was filtered, washed with methanol, and dried under vacuum. The resultant solid was then dissolved in dichloromethane (5 mL) and added to methanol (200 mL) dropwise. The precipitate was filtered, washed with methanol, and dried under vacuum. The red solid was then washed with hot methanol in a Soxhlet set-up for 6 h, and then with hot acetone overnight. Finally,  $\text{CHCl}_3$  was used to extract the materials for 5 h. Most of the solvent was removed under vacuum, and the residue was precipitated into methanol (200 mL) dropwise. After filtration, the black solid was dissolved in THF and size-exclusion chromatography column (S-X1 Biobeads, 1.2 meter long, ~ 6 cm in diameter) was used to purify the polymer with THF as eluent. The first black band was collected and the solvent was removed. The resultant solid was dissolved in  $\text{CHCl}_3$  (4 mL) and added to methanol (120 mL) dropwise, and the black solid was then filtered and dried under vacuum to give **N-PDI HP** as a black solid (221 mg, yield: 57%). GPC (toluene):  $M_n = 19.6$  k,  $M_w/M_n = 1.7$ .  $^1\text{H}$  NMR (500 MHz,  $\text{CDCl}_3$ ):  $\delta$  9.5 (sb, 1nH), 8.5–7.0 (m, 6nH), 5.0 (sb, 2nH), 4.5–3.7 (m, 6nH), 3.2–1.5 (m, 18nH), 1.5–1.0 (m, 80nH), 0.83 (sb, 12nH). Anal. Calcd for  $(\text{C}_{86}\text{H}_{126}\text{N}_4\text{O}_6)_n$ : C, 78.73; H, 9.68; N, 4.27; Found: C, 78.52; H, 9.83; N, 4.27. UV-visible absorption (chloroform)  $\lambda_{\text{max}}(\epsilon)$ : 451 ( $1.16 \times 10^4$ ), 572 ( $1.76 \times 10^4$ ) nm ( $\text{M}^{-1}\text{cm}^{-1}$ ).

## 2.10 References

- (1) Würthner, F. *Chem. Commun.* **2004**, 1564-1579.
- (2) Wang, H.; Peng, B.; Wei, W. *Progress Chem.* **2008**, *20*, 1751-1760.
- (3) Jones, B. A.; Facchetti, A.; Wasielewski, M. R.; Marks, T. J. *J. Am. Chem. Soc.* **2007**, *129*, 15259-15278.
- (4) Jones, B. A.; Ahrens, M. J.; Yoon, M.-H.; Facchetti, A.; Marks, T. J.; Wasielewski, M. R. *Angew. Chem. Int. Ed.* **2004**, *43*, 6363-6366.
- (5) Tatemichi, S.; Ichikawa, M.; Koyama, T.; Taniguchi, Y. *Appl. Phys. Lett.* **2006**, *89*, 112108.
- (6) Pandey, A. K.; Dabos-Seignon, S.; Nunzia, J.-M. *Appl. Phys. Lett.* **2006**, *89*, 113506.
- (7) Pandey, A. K.; Nunzi, J. M. *Appl. Phys. Lett.* **2007**, *90*, 263508.
- (8) Peumans, P.; Bulovic, V.; Forrest, S. R. *Appl. Phys. Lett.* **2000**, *19*, 2650-2652.
- (9) Shin, W. S.; Jeong, H.-H.; Kim, M.-K.; Jin, S.-H.; Kim, M.-R.; Lee, J.-K.; Lee, J. W.; Gal, Y.-S. *J. Mater. Chem.* **2006**, *16*, 384-390.
- (10) Dittmer, J. J.; Marseglia, E. A.; Friend, R. H. *Adv. Mater.* **2000**, *12*, 1270-1274.
- (11) Bao, Z.; Locklin, J. *Organic Field-Effect Transistors*; CRC Press, 2006.
- (12) Chen, H. Z.; Ling, M. M.; Mo, X.; Shi, M. M.; Wang, M.; Bao, Z. *Chem. Mater.* **2007**, *19*, 816-824.
- (13) Hou, J.; Zhang, S.; Chen, T. L.; Yang, Y. *Chem. Commun.* **2008**, 6034-6036.
- (14) Tan, Z. A.; Zhou, E.; Zhan, X.; Wang, X.; Li, Y.; Barlow, S.; Marder, S. R. *Appl. Phys. Lett.* **2008**, *93*, 073309.
- (15) Zhan, X.; Tan, Z. A.; Domercq, B.; An, Z.; Zhang, X.; Barlow, S.; Li, Y.; Zhu, D.; Kippelen, B.; Marder, S. R. *J. Am. Chem. Soc.* **2007**, *129*, 7246-7247.
- (16) Zhan, X.; Tan, Z. A.; Zhou, E.; Li, Y.; Misra, R.; Grant, A.; Domercq, B.; Zhang, X.-H.; An, Z.; Zhang, X.; Barlow, S.; Kippelen, B.; Marder, S. R. *J. Mater. Chem.* **2009**, *19*, 5794-5803.
- (17) Sharma, G. D.; P. Balraju; Mikroyannidis, J. A.; Stylianakis, M. M. *Sol. Energy Mater. Sol. Cells* **93**, 2025-2028.
- (18) Zhou, E.; Tajima, K.; Yang, C.; Hashimoto, K. *J. Mater. Chem.* **2010**, *20*, 2362 - 2368.
- (19) Chen, Z.; Zheng, Y.; Yan, H.; Facchetti, A. *J. Am. Chem. Soc.* **2009**, *131*, 8-9.
- (20) Huo, L.; Zhou, Y.; Li, Y. *Macromol. Rapid Commun.* **2008**, *29*, 1444-1448.
- (21) Wang, R.; Pu, K. Y.; Qin, C. Y.; Peng, B.; Huang, W.; Wei, W. *Acta Polym. Sin.* **2008**, *10*, 967-973.
- (22) Finlayson, C. E.; Friend, R. H.; Otten, M. B. J.; Schwartz, E.; Cornelissen, J. J. L. M.; Nolte, R. J. M.; Rowan, A. E.; Samori, P.; Palermo, V.; Liscio, A.; Kalina Peneva; Müllen, K.; Beljonne, S. T. *Adv. Funct. Mater* **2008**, *18*, 1-9.

- (23) Lindner, S. M.; ttner, S. H.; Chiche, A.; Thelakkat, M.; G. Krausch, A. *Angew. Chem., Int. Ed.* **2006**, *45*, 3364-3368.
- (24) Sommer, M.; Lang, A. S.; Thelakkat, M. *Angew. Chem. Int. Ed.* **2008**, *47*, 7901-7904.
- (25) Zhang, Q.; Cirpan, A.; Russell, T. P.; Emrick, T. *Macromolecules* **2009**, *42*, 1079-1082.
- (26) Feng, K.; Zuniga, C.; Zhang, Y.-D.; Kim, D.; Barlow, S.; Marder, S. R.; Brédas, J. L.; Weck, M. *Macromolecules* **2009**, *42*, 6855-6864.
- (27) Kimyonok, A.; Domercq, B.; Haldi, A.; Cho, J.-Y.; Carlise, J. R.; Wang, X.-Y.; Hayden, L. E.; Jones, S. C.; Barlow, S.; Marder, S. R.; Kippelen, B.; Weck, M. *Chem. Mater.* **2007**, *19*, 5602-5608.
- (28) Yuan, M.-C.; Su, M.-H.; Chiu, M.-Y.; Wei, K.-H. *J. Polym. Sci. Part A: Polym. Chem.* **2010**, *48*, 1298-1309.
- (29) Lindner, S. M.; Kaufmann, N.; Thelakkat, M. *Org. Electr.* **2007**, *8*, 69-75.
- (30) Trnka, T. M.; Grubbs, R. H. *Acc. Chem. Res.* **2001**, *34*, 18-29.
- (31) Haldi, A.; Kimyonok, A.; Domercq, B.; Hayden, L. E.; Jones, S. C.; MardeR, S. R.; Weck, M.; Kippelen, B. *Adv. Funct. Mater.* **2008**, *18*, 3056-3062.
- (32) Cho, J.-Y.; Domercq, B.; Barlow, S.; Suponitsky, K. Y.; Li, J.; Timofeeva, T. V.; Jones, S. C.; Hayden, L. E.; Kimyonok, A.; South, C. R.; Weck, M.; Kippelen, B.; Marder, S. R. *Organometallics* **2007**, *26*, 4816-4829.
- (33) Zhao, C. C.; Zhang, Y.; Wang, C. W.; Rothberg, L.; Ng, M. K. *Org. Lett.* **2006**, *8*, 1585-1588.
- (34) Zhao, C. C.; Zhang, Y.; Pan, S. L.; Rothberg, L.; Ng, M. K. *Macromolecules* **2007**, *40*, 1816-1823.
- (35) Zhao, Y.; Wasielewski, M. R. *Tetrahedron Lett.* **1999**, *40*, 7047-7050.
- (36) Nagao, Y. *Progress Org. Chem.* **1997**, *31*, 43-49.
- (37) Tauber, M. J.; Kelley, R. F.; Giaimo, J. M.; Rybtchinski, B.; Wasielewski, M. R. *J. Am. Chem. Soc.* **2006**, *128*, 1782-1783.
- (38) Trnka, T. M.; Grubbs, R. H. *Acc. Chem. Res.* **2001**, *34*, 18-29.
- (39) Odom, S. A.; Webster, S.; Padilha, L. A.; Peceli, D.; Hu, H.; Nootz, G.; Chung, S.-J.; Ohira, S.; Matichak, J. D.; Przhonska, O. V.; Kachkovski, A. D.; Barlow, S.; Brédas, J.-L.; Anderson, H. L.; Hagan, D. J.; Stryland, V.; W., E.; Marder, S. R. *J. Am. Chem. Soc.* **2009**, 7510-7511.
- (40) Rajasingh, P.; Cohen, R.; Shirman, E.; Shimon, L. J. W.; Rybtchinsk, B. *J. Org. Chem* **2007**, *72*, 5973-5979.
- (41) Ford, W. E.; Kamat, P. V. *J. Phys. Chem.* **1987**, *91*, 6373-6380.
- (42) Gómez, R.; Veldman, D.; Blanco, R.; Seoane, C.; Segura, J. L.; Janssen, R. A. J. *Macromolecules* **2007**, *40*, 2760-2772.
- (43) Ford, W. E. *J. Photochem.* **1987**, *37*, 189-204.
- (44) Günes, S.; Neugebauer, H.; Sariciftci, N. S. *Chem. Rev.* **2007**, *107*, 1324-1338.
- (45) Thompson, B. C.; Fréchet, J. M. J. *Angew. Chem. Int. Ed.* **2008**, *47*, 58-77.
- (46) Würthner, F.; Stepanenko, V.; Chen, Z. J.; Saha-Möller, C. R.; Kocher, N.; Stalke, D. *J. Org. Chem.* **2004**, *69*, 7933-7936.

- (47) Chen, Z.; Debije, M. G.; Debaerdemaeker, T.; Osswald, P.; Würthner, F. *ChemPhysChem* **2004**, *5*, 137-140.
- (48) Gsänger, M.; Oh, J. H.; Könemann, M.; Höffken, H. W.; Krause, A.-M.; Bao, Z.; Würthner, F. *Angew. Chem. Int. Ed.* **2010**, *49*, 740-743.
- (49) Würthner, F.; Thalacker, C.; Diele, S.; Tschierske, C. *Chem. Eur. J.* **2001**, *7*, 2245-2253.
- (50) Thelakkat, M.; Schmidt, H.-W. *Adv. Mater.* **1998**, *10*, 219-223.
- (51) Chua, L.-L.; Zaumseil, J.; Chang, J.-F.; Ou, E. C.-W.; Ho, P. K.-H.; Sirringhaus, H.; Friend, R. H. *Nature* **2005**, *34*, 194-199.
- (52) Scholz, M.; Schmidt, R.; Krause, S.; Schöll, A.; Reinert, F.; Würthner, F. *Appl. Phys. A: Mater. Sci. Process.* **2009**, 95.
- (53) Koster, L. J. A.; Mihailetschi, V. D.; Blom, P. W. M. *Appl. Phys. Lett.* **2006**, *88*, 052104.
- (54) Peumans, P.; Forrest, S. R. *Chem. Phys. Lett.* **2004**, *398*, 27-31.
- (55) Li, J. L.; Dierschke, F.; Wu, J. S.; Grimsdale, A. C.; Müllen, K. *J. Mater. Chem.* **2006**, *16*, 96-100.
- (56) Finlayson, C. E.; Friend, R. H.; Otten, M. B. J.; Schwartz, E.; Cornelissen, J. J. L. M.; Nolte, R. J. M.; Rowan, A. E.; Samori, P.; Palermo, V.; Liscio, A.; Kalina Peneva; Mülllen, K.; Trapani, S.; Beljonne, D. *Adv. Funct. Mater.* **2008**, *18*, 1-9.
- (57) Palermo, V.; Palma; Samorì, P. *Adv. Mater.* **2006**, *18*, **145 - 164**.
- (58) Chiesa, M.; Burgi, L.; Kim, J. S.; Shikler, R.; Friend, R. H.; Sirringhaus, H. *Nano Lett.* **2005**, *5*, 559-563.
- (59) Palermo, V.; Otten, M. B. J.; Liscio, A.; Schwartz, E.; de Witte, P. A. J.; Castriciano, M. A.; Wienk, M. M.; Nolde, F.; Luca, G. D.; Jeroen J. L. M. Cornelissen; Janssen, R. A. J.; Ilen, K. M.; Rowan, A. E.; Nolte, R. J. M.; Samorì, P. *J. Am. Chem. Soc.* **2008**, *130*, 14605-14614.
- (60) Shoaee, S. A., Z.; Zhang, X.; Barlow, S.; Marder, S. R.; Duffy, W.; Heeney, M.; McCulloch, I.; Durrant, J. R. *Chem. Commun.* **2009**, 5445-5447.
- (61) Sugandhi, E. W.; Falkinham, J. O.; Gandour, R. D. *Bioorg. Med. Chem.* **2007**, *15*, 3842-3853.
- (62) Lakshmipathi, P.; Crevisy, C.; Gree, R. *J. Comb. Chem.* **2002**, *4*, 612-621.
- (63) Kelley, R. F.; Shin, W. S.; Rybtchinski, B.; Sinks, L. E.; Wasielewski, M. R. *J. Am. Chem. Soc.* **2007**, *129*, 3173-3181.
- (64) Rajaram, S.; Armstrong, P. B.; Kim, B. J.; Fréchet, J. M. J. *Chem. Mater.* **2009**, *21*, 1775-1777.
- (65) Wescott, L. D.; Mattern, D. L. *J. Org. Chem.* **2003**, *68*, 10058-10066.

## CHAPTER 3

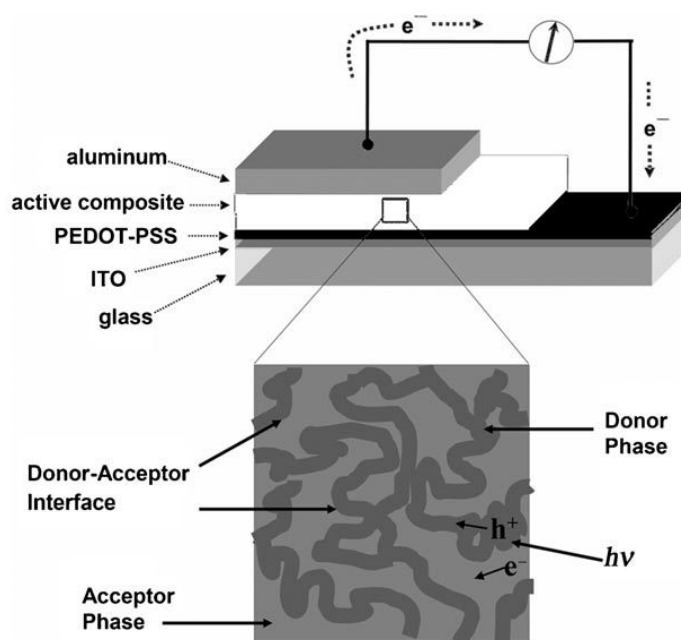
# DIBLOCK COPOLYNORBORNANES WITH PERYLENE DIIMIDE AND OLIGOTHIOPHENE SIDE-GROUPS FOR ORGANIC PHOTOVOLTAICS

### 3.1 Introduction

As discussed in the previous chapters, thin-film organic solar cells have lower light to electricity conversion compared to their best inorganic counterparts.<sup>1-2</sup> Excitonic loss is one of the issues that severely limits the power conversion efficiencies (PCEs) of organic solar cells.<sup>1</sup> In the organic photovoltaic (OPV) process, only the excitons generated within a 10 nm distance (typical exciton diffusion length for organic semiconductors) of the donor/acceptor (D/A) interface could be efficiently dissociated into free charge carriers.<sup>1</sup> Thus, it was proposed by Fréchet that the ideal bulk-heterojunction (BHJ) solar cell should have an ordered and bicontinuous composite of donor and acceptor materials with favorable domain size, as shown in Figure 3.1.<sup>1</sup> Ideally, the donor and acceptor components should phase-segregate during the film preparation into domains with suitable size (approximately 10 nm) and favorable morphology, resulting in less excitonic loss and effective charge transport through continuous pathways to respective electrodes.<sup>1-4</sup> Furthermore, from a practical application standpoint, the active layers should be prepared via a cost-effective process and could ideally self-assemble into the most favorable morphology with a minimal use of external treatments, as well as having long-term stability. Recently, solar cells with PCEs of approximately 5% have been achieved by optimizing the thin-film morphologies of the poly(3-



hexylthiophene)/[6,6]-phenyl C<sub>61</sub>-butyric acid methyl ester (P3HT/PCBM) blend via thermal or solvent annealing post-treatments on the active films in addition to many other processes.<sup>5-7</sup> Similar optimizations have also been applied to other D/A blends, such as the poly[2-methoxy-5-(3,7-dimethyloctyloxy)-1,4-phenylene-*alt*-(vinylene)](MDMO-PPV)/PCBM blend, for better solar cell performance.<sup>1</sup>



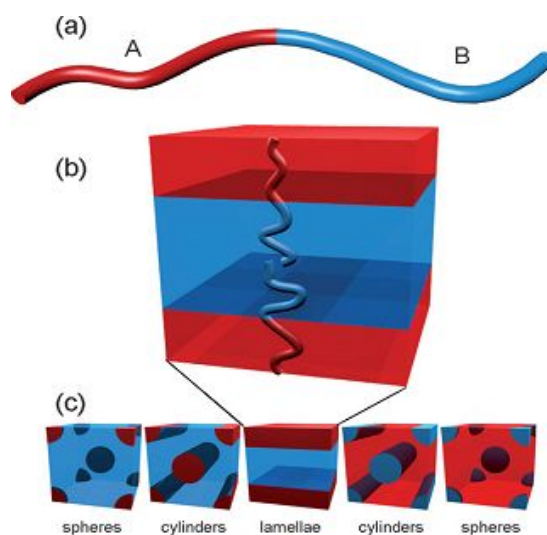
**Figure 3.1.** Schematic illustration of D/A BHJ solar cell, with a magnified area showing the bicontinuous morphology of the active layer.<sup>1</sup> Figure reproduced according to ref 1 by permission of the Wiley-VCH Verlag GmbH & Co. KGaA.

Currently, it is clear that good film morphology is essential for realizing high performance organic solar cells, although the relationship between the film morphology and device performance is not yet fully understood. It is still quite challenging to obtain favorable morphologies for D/A blends. Generally, the active layer morphology depends on the interplay between a number of intrinsic and extrinsic variables, including: the

crystallinity and relative miscibility of the two materials, choice of donor and acceptor for energetic matching, the D/A blending weight ratio, selection of solvents and additives, and the post-treatments applied to the films. Any one of these factors could dramatically affect the thin-film morphology and thus the solar cell performances, which makes the optimization of BHJ cells using polymer blends challenging.<sup>1-2</sup> At this time, most solution-processed BHJ solar cells that consist of D/A mixtures do not exhibit well defined morphologies because either such devices commonly rely on random phase-separation of blending components, or the morphologies that developed through specific techniques, such as thermal annealing and lithography-based techniques, are not stable on sufficient timescales or are not cost effective for practical applications.<sup>1</sup> Hence, thermodynamically stable nanostructure BHJs that can be obtained through a spontaneous self-assembly process with defined charge percolation pathways and suitable domain sizes are highly desirable for organic solar cells.<sup>1-2</sup>

A recent approach utilizing block copolymers (BCPs) as the active material(s) in solar cells is considered as a reliable method in obtaining such favorable nanostructures spontaneously during polymer film preparation. Furthermore, promising results based on BCP-type materials for organic electronics have been demonstrated.<sup>2,8-11</sup> BCPs are macromolecules comprised of two or more polymer blocks covalently bound to one another. Among this class of copolymers, diblock copolymers are the most common materials with polymeric block A and block B attached to the end of each other, as illustrated in Figure 3.2a.<sup>12-13</sup> In general, the incompatibility between each polymer block in BCPs drives a phase separation in the solid state while the covalent bond between the polymer blocks in the macromolecular chain can prohibit the bulk phase-separation,

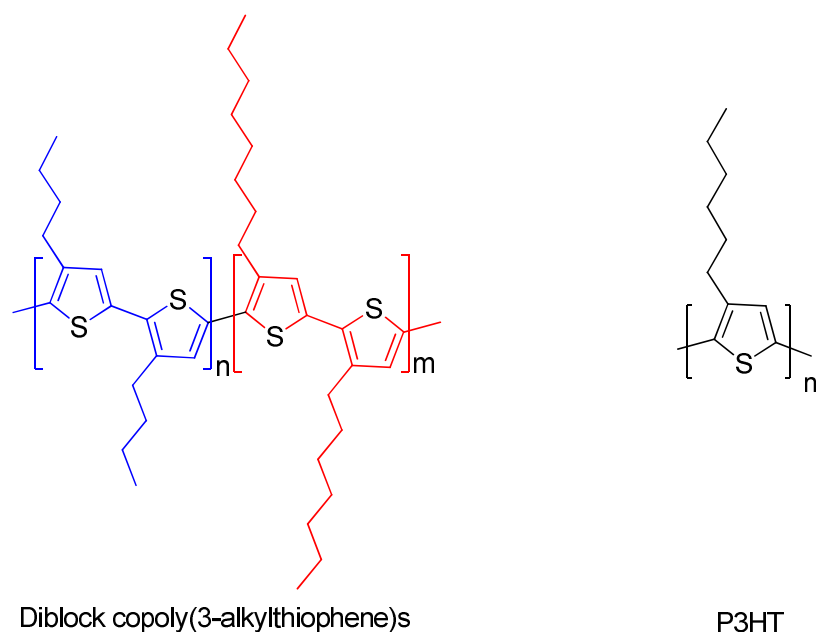
normally observed in simple polymer blends, and lead to micro-phase-segregation with domains in nanometer size regime.<sup>12</sup> The most frequently observed diblock morphologies are body-centered cubic spheres, hexagonally packed cylinders, and lamellae, as shown in Figure 3.2c.<sup>2,13</sup> Furthermore, other more complex geometries have also been reported depending on the block to block interaction and the ratio of block lengths using BCPs.<sup>2,13</sup> Hence, such a self-assembly process for BCPs containing an electron-donor block and an electron-acceptor block could, in principle, direct the desired morphologies and be applied in obtaining the micro-phase-segregation with donor and/or acceptor rich domains with favorable domain size.<sup>2</sup> Dramatic OPV device performance improvements have been observed using such kind of BCPs as active materials, compared to devices with physical D/A blends of respective homopolymers, because of the spontaneous micro-phase-segregation in the BCP-based films.<sup>9</sup>



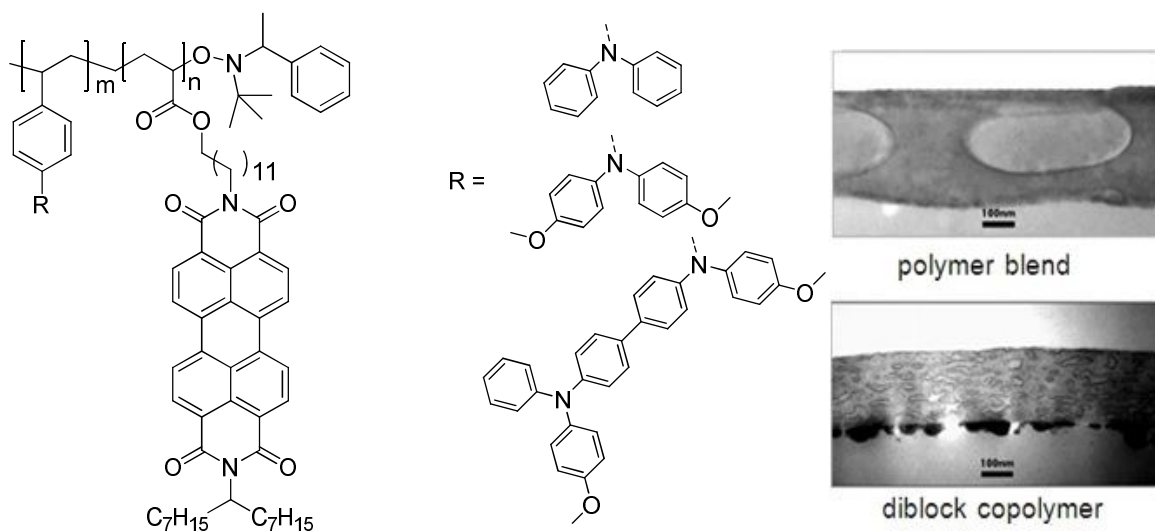
**Figure 3.2.** (a) Schematic representation of a diblock copolymer; (b) lamellar phase morphology depicting arrangement of polymer chains; (c) partial list of phases formed by diblock copolymers in the bulk.<sup>2</sup> Reproduced by permission of the Royal Society of Chemistry and Elsevier Limited.

There are three major categories of diblock copolymers used for OPVs currently: the rod–rod BCPs, rod–coil BCPs, and coil–coil BCPs (the names refer to the rigidity of the polymer backbones for each block).<sup>2</sup> The rod–rod BCPs generally consist of varying length conjugated blocks with functional side groups attached, which present a number of challenges, especially for those D/A type rod–rod BCPs, in terms of synthesis and self-assembly process. The rod–rod BCPs also show relatively limited potential for practical applications.<sup>14-16</sup> However, a recent study of diblock copoly(3-alkylthiophene)s (Figure 3.3) with PCBM blends showed that the crystalline-type diblock copoly(3-alkylthiophene) could substantially enhance the photovoltaic properties compared to the parent P3HT donor.<sup>17-18</sup> Importantly, the synthesis for such diblock copoly(3-alkylthiophene)s is quite straightforward.<sup>17-18</sup> On the other hand, rod–coil BCPs are more commonly used as active materials in organic electronics. Hazdiiioannou and coworkers reported such kind of copolymers with a rigid poly(phenylenevinylene) (PPV) block and a flexible coil polystyrene block with grafted fullerenes, which demonstrated the potential of using rod–coil BCPs to improve photovoltaic performance with self-assembled periodic nanostructures.<sup>19-21</sup> Another rod–coil material system recently studied by several groups is the BCP comprised of a conjugated P3HT block and a polyacrylates-based coil block with perylene diimide (PDI) pendants.<sup>11,22</sup> These materials, which form highly crystalline domains in spin-casted films, favorable for both exciton dissociation and charge-carrier transport, exhibit PCEs approaching 0.6% in single-polymer devices.<sup>11</sup> Polymers of this type could also serve as compatibilizers and considerably enhance the device performance of P3HT:PDI blend in BHJ cells.<sup>23</sup> The PCE improvement could be attributed to the formation of smaller size PDI domains in the active layer with the compatibilizer as

compared to the simple polymer blends according to the morphology studies.<sup>23</sup> It has also been reported that a copolynorbornene with a rigid P3HT-based block and coil PCBM block could be used to stabilize thin-film morphologies of the P3HT:PCBM blends against destructive thermal phase segregation, which may also be a feasible strategy to improve device stability.<sup>24</sup> Research on using coil-coil BCPs with each block functionalized with particular side groups are attracting intense research attention for OPV applications due to relative ease of synthesis and facile self-assembly behavior relative to those containing rod polymer blocks.<sup>2</sup> As shown in Figure 3.4, Thelakkat and coworkers demonstrated this approach using copolymers with various triphenylamines and PDI moieties as the donor and acceptor blocks, respectively, as active materials in solar cells.<sup>8-9,25</sup> Periodic nanometer-scale morphologies were formed in these BCP films, and solar cells using these materials show PCEs of about 0.3%.<sup>8-9</sup> It is worth noting that the PCEs of the BCP-based devices are several times higher than those using simple polymer blends of the respective homopolymers as the active layer. It could be attributed to more favorable micro-phase-segregation formed by the BCPs over the polymer blends.<sup>9</sup> Hence, although the absolute PCEs of the these devices based on the Thelakkat copolymers were still considerably lower than the best state-of-the-art OPV cells using fullerene-based acceptors, the studies provided a proof-of-principle clearly showing that the concept of nanostructured BHJ devices based on BCPs is potentially useful for OPV applications. Research on developing D/A block copolymers with matching D/A energy levels, high charge-carrier mobilities, balance hole and electron transport in films, and good solar spectrum coverage are essential and may increase the likelihood for high performance (PCEs > 10%), cost-effective OPV systems.



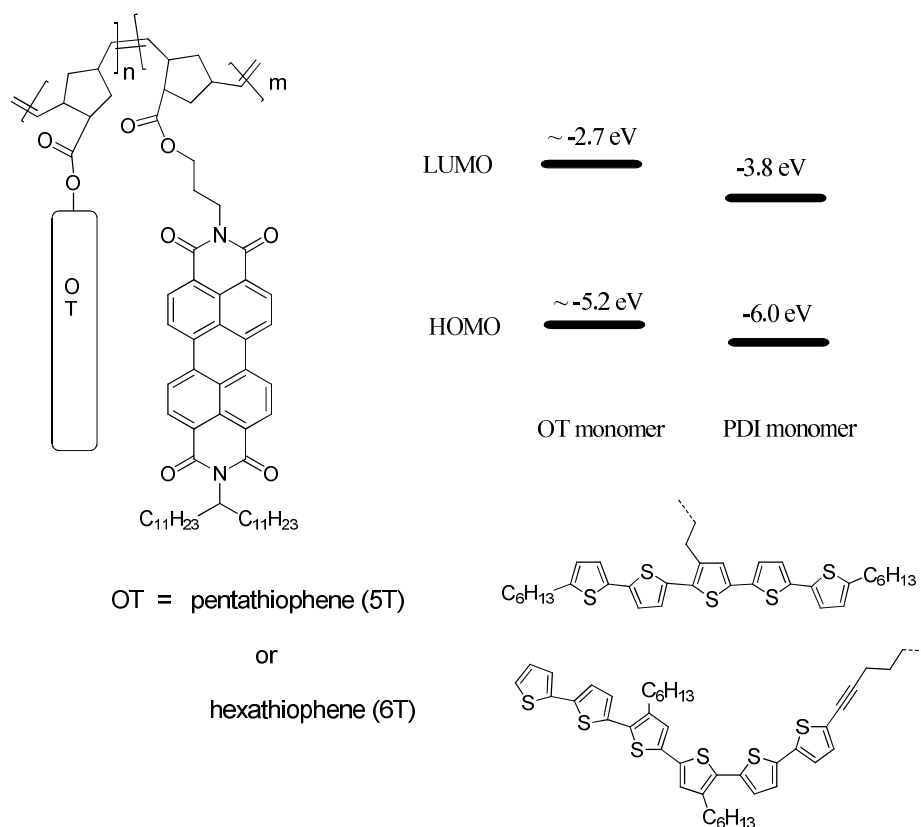
**Figure 3.3.** The chemical structures for the diblock copoly(3-alkylthiophene)s and P3HT.



**Figure 3.4.** The chemical structures of the Thelakkat copolymers with PDI and triphenylamine moieties (left) and TEM images for the cross-section of the films in real devices from a diblock copolymer and respective homopolymer blends.<sup>9</sup> Figure reproduced according to ref 9 by permission of the Wiley-VCH Verlag GmbH & Co. KGaA.

This chapter discusses the studies of PDI and oligothiophenes (OTs) grafted coil-coil diblock copolynorbornenes, adapted from the basic idea of the Thelakkat copolymers, that were designed and synthesized for OPV applications, as illustrated in Figure 3.5. Here, the PDI moiety was incorporated as the acceptor in the BCPs because of their potential advantages for OPV applications, including low-lying LUMO and high electron mobility (as described in the previous chapters).<sup>26-31</sup> As discussed in Chapter 2, **C11PDI HP** was found to give better solar cell performance in the blends with P3HT as compared to the other two PDI-grafted polymers. Hence, **C11PDI** monomer was selected to build up the PDI-block in the BCPs. OT moieties were utilized in this BCPs study due to their relatively high hole mobilities and electron donating nature, according to the aforementioned studies, as well as their UV-Vis absorption, which complements that of PDIs in the visible range of the solar spectrum.<sup>32-34</sup> Furthermore, the device open-circuit voltage ( $V_{OC}$ ) within organic solar cells can be influenced by the energy offset ( $I_g$ ) between the HOMO of the donors and the LUMO of the acceptors and larger  $I_g$  could generally lead to higher  $V_{OC}$  in organic solar cells.<sup>4,35-37</sup> Hence, the relatively large  $I_g$  (> 1.0 eV) in these PDI-OT BCPs could potentially result in high- $V_{OC}$  solar cells (> 0.8 V). Aside from the difference in conjugation length of the aromatic cores for the **5T** and **6T** building blocks, the linkage position on the **6T** to the polymer is on the end rather than on the center as for the **5T** derivative. Hence, different packing behavior of these BCPs in thin-films was expected, which could result in various film morphologies, charge-carrier mobilities, and device performance for the respective BCP-based solar cells. Ring-opening metathesis polymerizations (ROMP)<sup>38</sup> were applied to synthesize the PDI and OT grafted polynorbornene-based BCPs since it has been demonstrated to be a powerful technique in

achieving “living” polymerization, as discussed in Chapter 2 with “first generation” Grubbs initiator. This living polymerization technique is the key step in preparing coil-coil BCPs in this chapter. Furthermore, functionalized polynorbornenes can often be readily solution-processed and have been successfully used as key components in light-emitting diodes,<sup>39-41</sup> as described in Chapter 2, suggesting the potential use of polynorbornenes in OPV devices. Moreover, by varying the donor/PDI ratios and copolymer architectures (random, block, or more complicated structures), material properties and film morphologies might be fine-tuned for high performance organic photovoltaic cells.



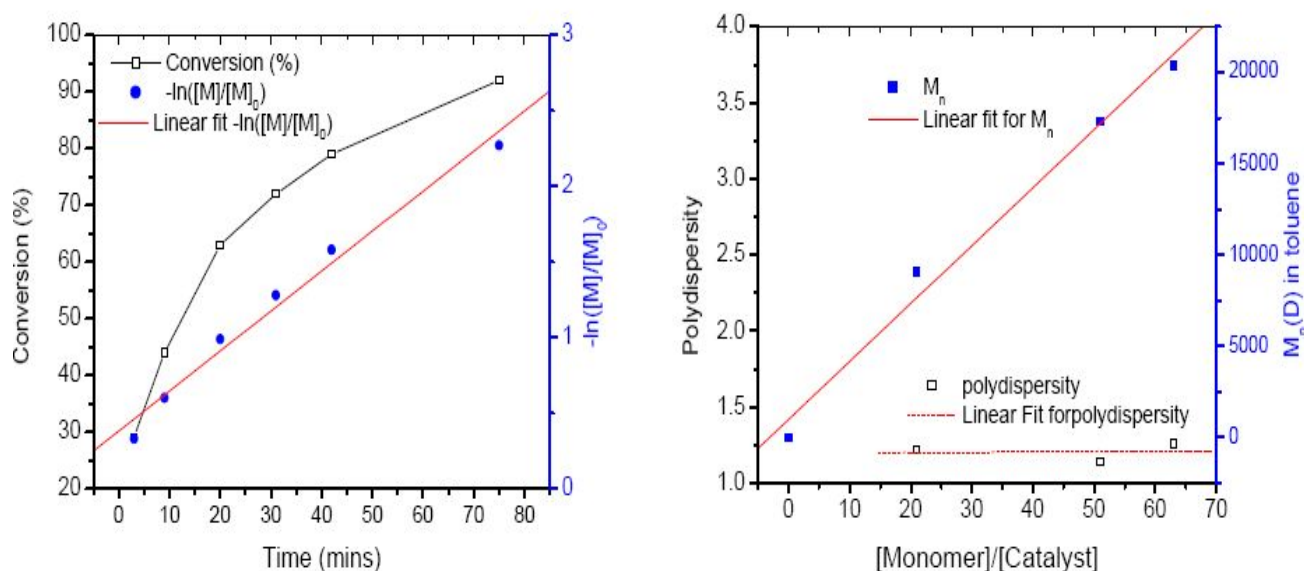
**Figure 3.5.** Designed PDI-OT diblock copolymers and estimated energy diagrams of the PDI and OT monomers.



### 3.2 Polymerization kinetics of the C11PDI monomer

In order to obtain a diblock copolymer, the polymerization of the first polymeric block, at least, has to be “living”. The kinetics of the polymerization of the **C11PDI** monomer with the “first generation” Grubbs initiator in  $\text{CDCl}_3$  under similar condition as those used for bulk polymer synthesis was monitored using  $^1\text{H}$  NMR spectroscopy with particular focus on the integration of the characteristic aromatic proton in the monomer and polymer (as shown in Figure 3.6). An approximately first-order polymerization was observed according to the curves of  $-\ln([M]/[M]_0)$  versus time. It needs to be pointed out that there could be quite large error for the  $-\ln([M]/[M]_0)$  value at conversion below 10% and over 90% because of the difficulties in obtaining accurate  $^1\text{H}$  NMR integrations. Moreover, a nearly linear increase of the molecular weight, as well as small polydispersity ( $M_w/M_n$ ) change (*ca.* 1.1 – 1.3), were obtained for **C11PDI HP** with different molecular weight as the [monomer]/[initiator] ratio increased from 10 to 70. These observations suggest the polymerization of **C11PDI** monomer might be controlled and could be utilized to prepare the PDI-based “macroinitiator” for the respective BCP synthesis using the “first generation” Grubbs initiator. This PDI-based “macroinitiator”, with a metal-carbene at the end of the macromolecular chain, could then initiate the polymerization of additional monomers, such as the OT grafted monomers, to build up the next block, and thus make the desired linear-D–A-BCPs. According to the monomer conversion versus time curves, shown in Figure 3.6, the polymerization of **C11PDI** monomer (0.5 mol/L in dichloromethane with 2% “first generation” Grubbs initiator) can be completed in 3 to 4 hours at room temperature (> 95% conversion after 120 minutes) under nitrogen

atmosphere. Subsequently, the electron rich monomer (**5T** or **6T** monomer) could be added in for the donor-based polymer block synthesis.

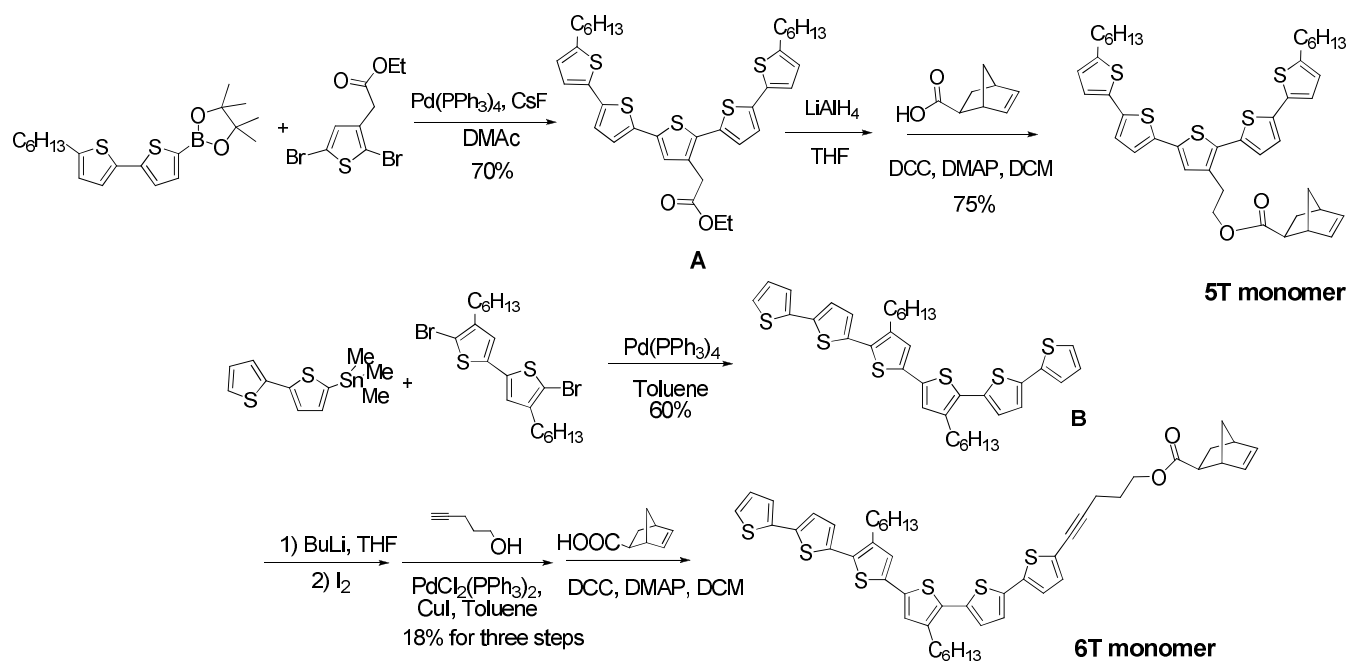


**Figure 3.6.** Kinetics of the polymerization of C11PDI monomer (left) and its molecular weight and polydispersity – [Monomer]/[Catalyst] relationship (right).

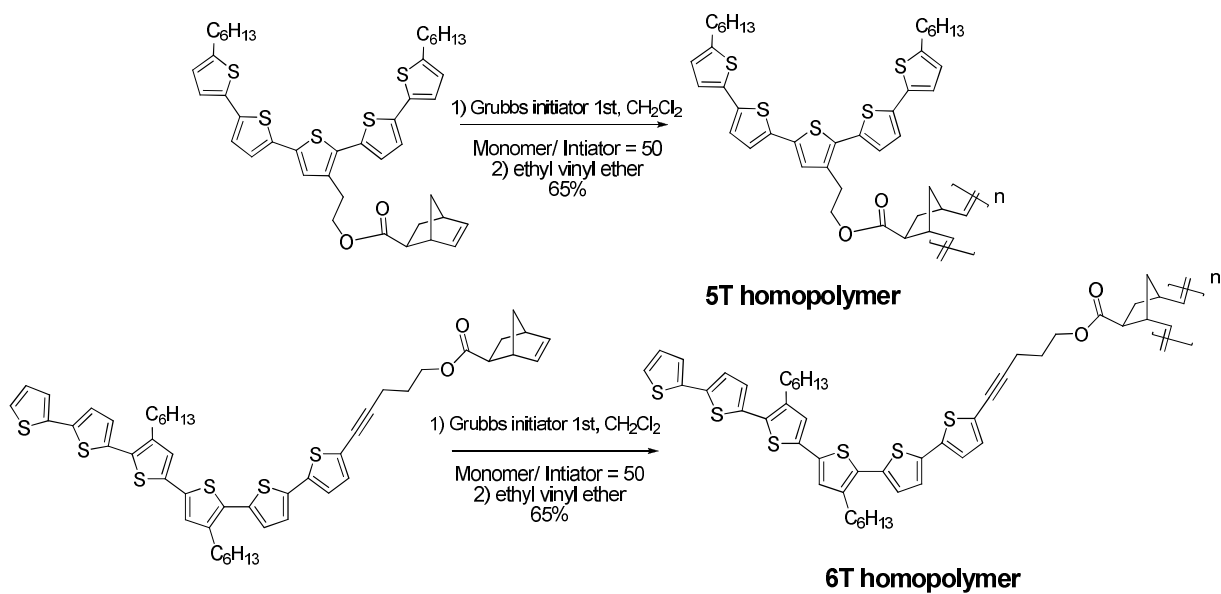
### 3.3 Synthesis of the OT-based monomer and homopolymers

As shown in Scheme 3.1, the **5T** monomer and **6T** monomers were designed and synthesized for the electron donating block in BCPs, and their respective homopolymers (with theoretical degree of polymerization of 50) were also synthesized. The **5T** and **6T** monomers with ester linkers between the oligothiophene moieties and the norbornene-based polymerizable groups were synthesized using straightforward synthetic routes. Compound **A** was synthesized via a Suzuki coupling reaction between 5'-hexyl-2,2'-bithiophene-5-boronic acid pinacol ester and ethyl 2,5-dibromothiophene-3-acetate<sup>42-43</sup> with  $\text{Pd}(\text{PPh}_3)_4$  as a catalyst. Here, because of the ester group in the starting materials and

compound **A**, water- and base-free Suzuki coupling reaction with cesium fluoride as a co-catalyst and anhydrous dimethylacetamide as solvent were used to obtain the desired product.<sup>44</sup> The ester group in compound **A** was then converted into an alcohol functionality using  $\text{LiAlH}_4$  as a reducing agent. The resulting product was then reacted with *exo*-bicyclo[2.2.1]hept-5-ene-2-carboxylic acid<sup>45</sup> in the presence of a mixture of dicyclohexylcarbodiimide (DCC)/*p*-dimethylaminopyridine (DMAP) to afford **5T** monomer with a total yield of around 75% in two steps. The synthesis of **6T** monomer started from the synthesis of the hexathiophene-based compound **B** via a Stille coupling reaction between 5-trimethylstannyl-2,2'-dithienyl<sup>46</sup> and 5,5'-dibromo-4,4'-dihexyl-2,2'-bithiophene<sup>47</sup> with  $\text{Pd}(\text{PPh}_3)_4$  as a catalyst. As shown in Scheme 3.2, the three step synthesis, including an iodination, a Sonogashira coupling, and a DCC/DMAP-assisted coupling, for the **6T** monomer gave a relatively low yield (~ 18% for three steps). The crystallization process for the obtaining pure **6T** monomer is quite slow (more than one month in ethanol at -20 °C). Obviously, it required much more effort to obtain pure **6T** monomer relative to the **5T** monomer. The low yield and tedious purification for **6T** monomer limits the practical use for the respective homopolymer and/or copolymers in organic electronics. The chemical structure and purity of the monomers and intermediates were confirmed using NMR spectroscopy, mass spectroscopy, and elemental analysis. Both monomers are quite soluble in common organic solvents including toluene, dichloromethane, THF, and chloroform (> 20 mg/mL in dichloromethane).



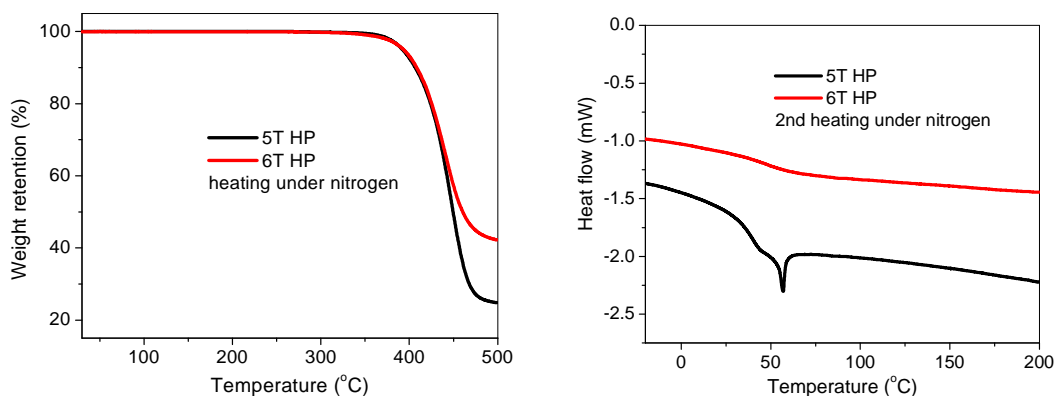
**Scheme 3.1.** The synthesis of the 5T and 6T monomers.



**Scheme 3.2.** The synthesis of the 5T and 6T homopolymers.

The polymerizations of the two OT-based monomers were carried out in dichloromethane using the same concentration (0.5 mol/L for each monomer and 0.01 mol/L for the initiator) at ambient temperature under nitrogen atmosphere on a Schlenk line. These conditions are similar to those used for the ROMP of the PDI monomers described in Chapter 2.<sup>38</sup> The expected degree of polymerization will be 50, assuming “living” polymerizations for these monomers. Thin layer chromatography (TLC) was used to monitor the polymerization since the OT-based homopolymers stay at the baseline while the two respective monomers move using chloroform as the eluent. Ethyl vinyl ether was applied to quench the polymerization by removing the attached ruthenium-based alkylidene from the polymer-chain ends when all of the monomers had been consumed according to TLC.<sup>38</sup> These two OT-based homopolymers were purified using multiple precipitations by addition of the high concentration polymer solutions in good solvents, such as dichloromethane and chloroform, to poor solvents such as methanol or methanol/water mixture. Subsequent Soxhlet extraction using methanol and acetone was used to further purify the polymers. The isolated yields for the polymers were around 65% with broader molecular weight distributions than those of the PDI-based HPs discussed in Chapter 2. The value of  $M_n = 23.6$  kD,  $M_w/M_n = 1.4$  and  $M_n = 28.7$  kD and  $M_w/M_n = 1.9$  were estimated according to GPC (THF) results for **5T HP** and **6T HP**, respectively. The reason for the quite broad  $M_w/M_n$  value of **6T HP** is not clear. It should be noted that the large polydispersity of **6T HP** suggested that the **6T** monomer might not polymerize in a “living” manner, which could affect the synthesis of BCPs using **6T** monomer. Furthermore, the observed molecular weights for **5T HP** and **6T HP** are lower than the ideal target molecular weights (35 – 40 kD), which is similar to that for

the PDI-based HPs and may presumably be attributed to the possible conformation difference between the OT-based polymers and the polystyrene standard for GPC analysis. Both polymers show excellent solubility in common organic solvents, such as chloroform, toluene, chlorobenzene, and dichloromethane (> 100 mg/mL for both **5T HP** and **6T HP** in chlorobenzene).

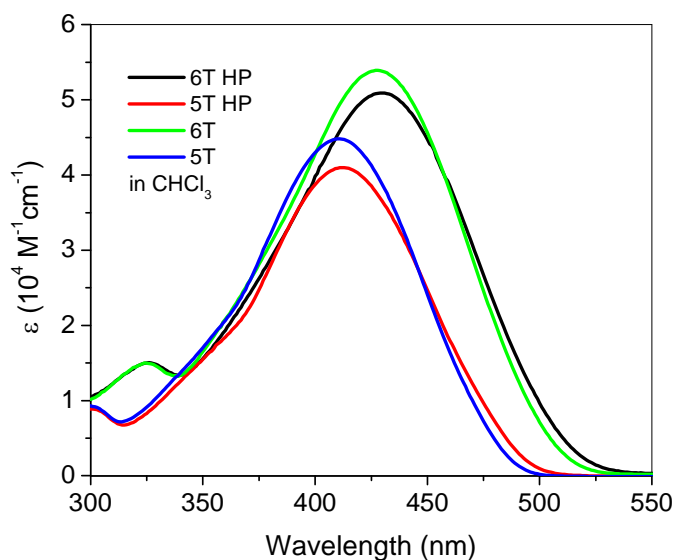


**Figure 3.7. The TGA traces (left) and DSC traces (right) for the OT-based homopolymers.**

These two OT-based homopolymers exhibit good thermal stability with the decomposition temperatures ( $T_d$ ), defined as that at which 5% weight loss is observed to be around 395 °C under nitrogen flow according to thermogravimetric analysis (TGA) heating from room temperature to 500 °C with a heating rate of 5 °C/min. The thermal behavior of these polymers were examined by differential scanning calorimetry (DSC) analysis within the temperature range from -30 to 200 °C under nitrogen atmosphere. The DSC traces of the second heating with a heating rate of 5 °C/min are shown in Figure 3.7 and reveal glass transition temperatures ( $T_g$ ) of 38 and 51 °C, for **5T HP** and **6T HP**, respectively. There is also a weak melting transition for **5T HP** at 58 °C immediately following its glass transition.

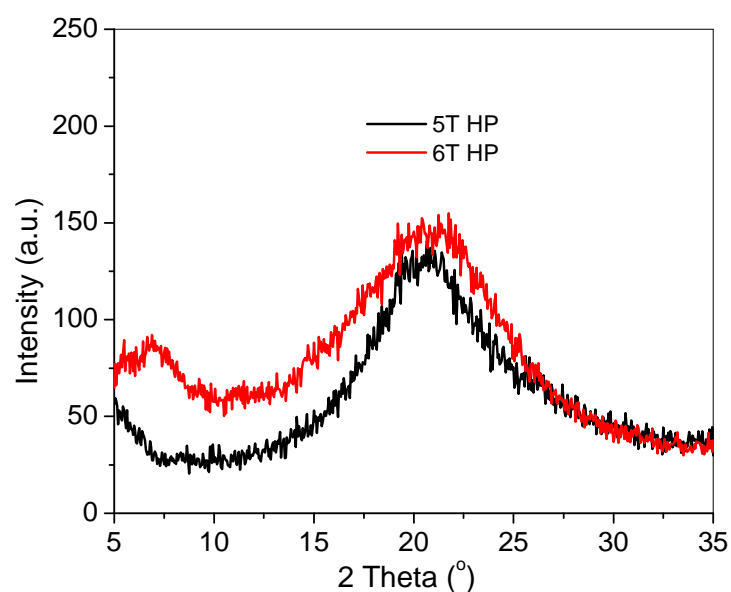
### 3.4 Absorption and redox properties of the OT-based materials

The UV-Vis absorption spectra of the two OT-based homopolymers and corresponding monomers in chloroform solution (*ca.*  $5 \times 10^{-6}$  mol/L according to respective OT concentration) are shown in Figure 3.8. Both polymers exhibit intense absorption in the range between 350 – 500 nm, while the **6T**-based materials show slightly broader absorption and larger peak extinction coefficients. The optical band gap for **5T HP** (2.45 eV according the absorption onset) is slightly larger than that for the **6T HP** (2.29 eV) presumably due to the longer conjugation length for the **6T** moieties in the polymer; a similar observation was made for the respective monomers. Only small absorption changes in absorption maxima and spectra shape were observed between the monomer and respective homopolymer, suggesting limited aggregation of the OT moieties on the polymer backbone for both homopolymers.



Scheme 3.8. The UV-Vis absorption spectra of the OT-based materials

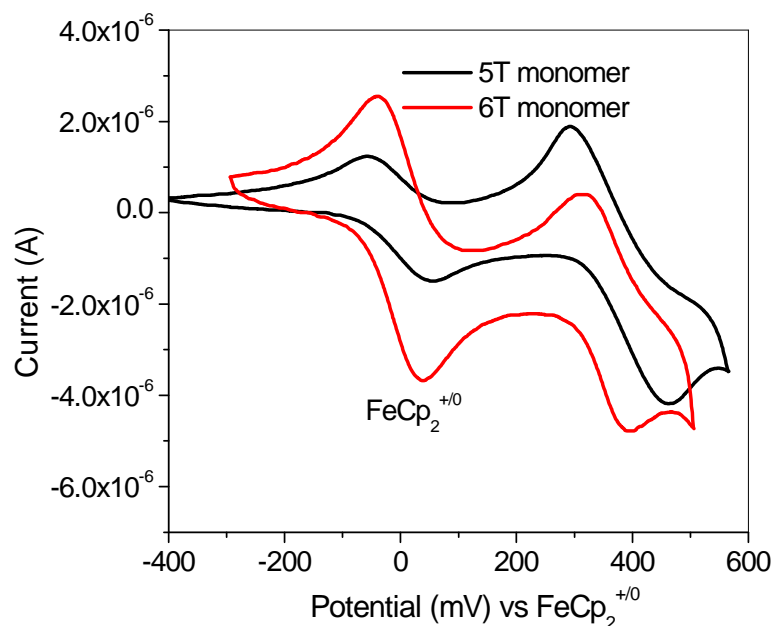
The assumption of a low-degree of  $\pi$ - $\pi$  stacking between the OT moieties on polymer chains was further confirmed by the powder XRD measurements on these homopolymers. Both polymers show a broad peak, at a diffraction angle,  $2\theta$ , of around  $20^\circ$ , corresponding to a d-spacing of  $4.7 \text{ \AA}$ , according to Bragg equation  $n\lambda = 2d\sin\theta$ . This feature appears to be “halo” feature, typically for an amorphous material and could be assigned to polynorbornenes or alkyl chains stacking in these two homopolymers. Similar XRD data for PDI-based HPs were discussed earlier in Chapter 2. No obvious d-spacing correlated to  $\pi$ - $\pi$  stacking was observed for both OT-based polymers, consistent with the limited change for monomer and polymer absorption spectra.



**Figure 3.9.** Power XRD of 5T HP (black) and 6T HP (red) with a Cu Ka source ( $\lambda = 1.5406 \text{ \AA}$ ) in a continuous scan mode with a step of  $0.02^\circ$  (The data were collected by Dr. Doo Young Kim in the Marder group).



The redox properties of the OT-based homopolymers were estimated via cyclic voltammetry (CV) measurements of the respective monomers in anhydrous dichloromethane with ferrocene ( $\text{FeCp}_2$ ) as an internal reference (Figure 3.10). The half-wave potential ( $E_{1/2}$ ) values (defined as  $(E_{pa} + E_{pc})/2$ , where  $E_{pa}$  and  $E_{pc}$  are peak oxidation and reduction potentials, respectively) of monomers **5T** and **6T**, are 0.38 and 0.35 V for the first oxidation versus  $\text{FeCp}_2^{+/0}$  redox couple, respectively. The oxidation for these monomers were found to be reversible, exhibiting  $I_{pa}/I_{pc}$  (the ratio of the peak currents of the oxidative and reductive waves) values of *ca.* 1, which was similar to that for the  $\text{FeCp}_2^{+/0}$  redox couple. **5T** is slightly less readily oxidized compared with **6T** ( $\sim 0.03$  V), which could be attributed to the longer conjugation length in the **6T** monomer. The ionization potentials (IPs) for **5T** and **6T** were both estimated to be *ca.* 5.2 eV based on assuming an IP value of 4.8 eV for solid state ferrocene.<sup>48</sup> The electron affinity (EA) values for **5T** and **6T** are estimated from the optical bandgaps and IP values to be -2.7 and -2.9 eV respectively according to  $\text{EA} = -(\text{IP} - E_{\text{gap}})$ . The fairly large offset (1.4 eV) between the HOMO energy (-5.2 eV, defined as -IP) for OT materials and LUMO energy of **C11PDI** (-3.8 eV, estimated as EA) could potentially result in solar cells using PDI-OT-based BCPs with large  $V_{\text{OC}}$ . Furthermore, the large energy offsets between the LUMOs (*ca.* 1.1 eV) or HOMOs (*ca.* 0.8 eV) of the OT- and PDI-based materials suggests sufficient driving force for dissociation of both donor- and acceptor-based excitons at the D/A interface. It is worth mentioning that these values are somewhat too large according to what is believed to be the minimum requirement (0.3 – 0.5 eV) for effective exciton-dissociation and could therefore lead to undesirable thermal-energy loss during the overall photovoltaic process.<sup>1</sup>



**Figure 3.10.** The cyclic voltammetry curve of **5T** (black) and **6T** (red) in  $\text{CH}_2\text{Cl}_2$ , 0.1 M [*n*- $\text{Bu}_4\text{N}$ ][ $\text{PF}_6$ ], with scan rate =  $50 \text{ mVs}^{-1}$ , with  $\text{FeCp}_2$  as an internal reference.

### 3.5 Device evaluation of the OT-based homopolymers

Bilayer solar cell devices using spin-casted **5T HP** or **6T HP** film as the donor layer, vacuum deposited  $\text{C}_{60}$  (45 nm) as the acceptor layer, and bathocuproine (BCP, 8 nm) on the top of the  $\text{C}_{60}$  layer were fabricated and characterized by Mr. William Potscavage Jr. in the Kippelen group. The film thickness of the donor layer played an important role in the solar cell performance, as summarized in Table 3.1. The devices with 20 nm thick **5T HP** film show PCE of *ca.* 0.19 % with  $J_{\text{SC}} = 1.2 \text{ mA/cm}^2$  while similar devices with 25 nm thick **5T HP** film show a dramatic decrease in overall PCEs and  $J_{\text{SC}}$ . The relationship between the film thickness and PCEs of the **6T HP**/ $\text{C}_{60}$  cells are similar to those **5T HP**/ $\text{C}_{60}$  solar cells, though the device efficiencies of the **6T HP**/ $\text{C}_{60}$  system were found to be 3 times as high as that of devices using **5T HP**. Devices with maximum efficiency of

0.48% were obtained with **6T HP** film of 10 – 15 nm thickness. These PCEs are comparable to unoptimized P3HT/C<sub>60</sub>-based bilayer cells.<sup>49</sup> For devices with **5T/6T HPs**, the major contribution of the device efficiency increase is from the enhancement of  $J_{SC}$ . OFET devices based on the homopolymer films were also fabricated using the top-contact geometry via solution-process using gold-based source and drain electrodes by Dr. Shree Tiwari in the Kippelen group. However, no detectable hole mobilities were obtained for either homopolymers, which might be attributed to the poor  $\pi$ - $\pi$  stacking between the OT moieties on the polymer side-chain (similar to **N-PDI HP** described earlier).

**Table 3.1. Summaries of the device performance from 5T HP or 6T HP/C<sub>60</sub> bilayer cells (Data were collected by Mr. William Potscavage Jr. in the Kippelen group).**

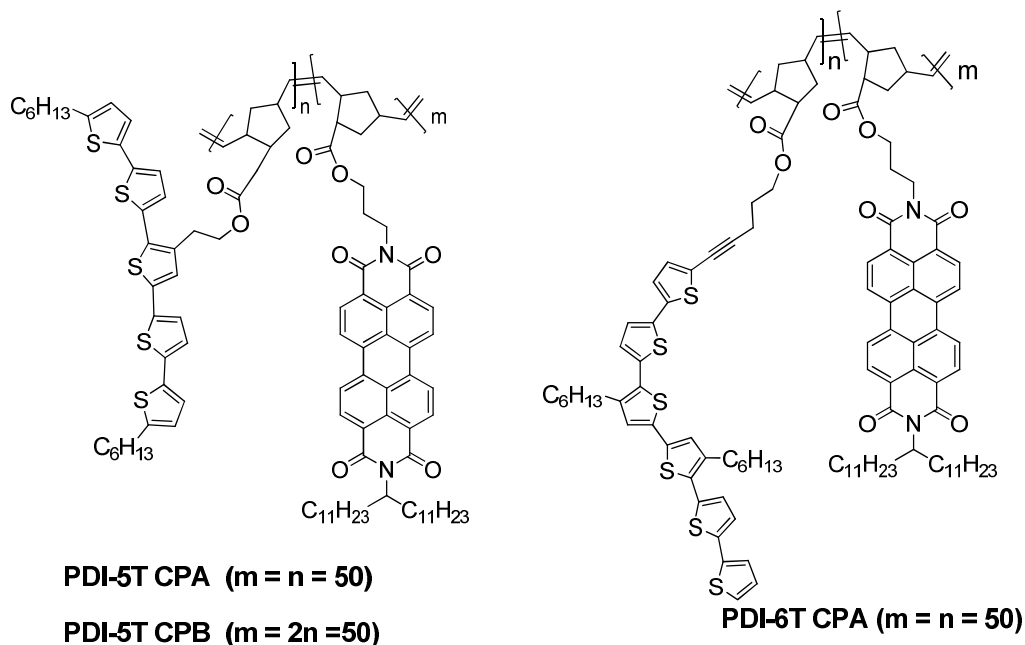
Devices	$V_{oc}$ (mV)	$J_{sc}$ (mA/cm <sup>2</sup> )	FF	PCEs (%)
<b>25 nm 5T HP</b>	557 ± 12	0.30 ± 0.12	0.17 ± 0.00	0.03 ± 0.01
<b>15-20 nm 5T HP</b>	593 ± 10	1.2 ± 0.1	0.17 ± 0.00	0.19 ± 0.01
<b>30-40 nm 6T HP</b>	688 ± 18	1.13 ± 0.11	0.19 ± 0.01	0.18 ± 0.03
<b>20 nm 6T HP</b>	703 ± 44	1.81 ± 0.10	0.23 ± 0.01	0.36 ± 0.03
<b>10-15 nm 6T HP</b>	675 ± 9	2.30 ± 0.08	0.25 ± 0.01	0.48 ± 0.04

### 3.6 Synthesis and optical properties of the block copolymers

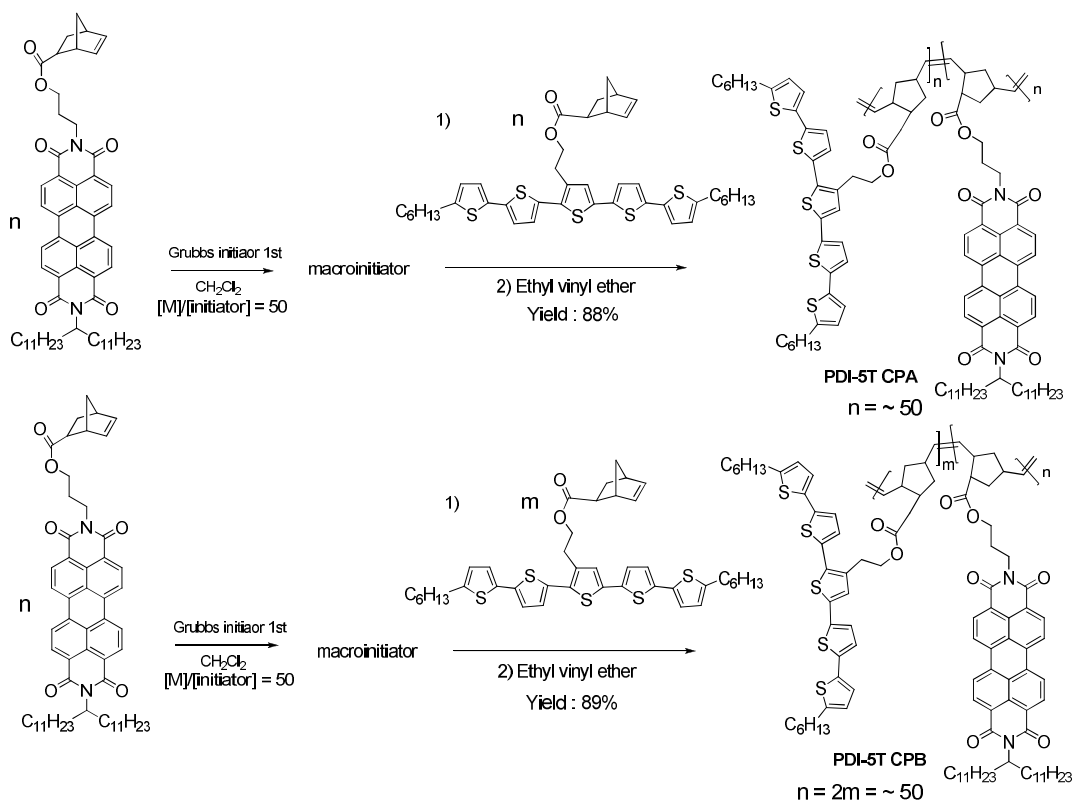
As illustrated in scheme 3.3, the synthesis of the BCPs containing **C11PDI** and **5T** monomers were carried out in dichloromethane (**C11PDI** monomer concentration: 0.5 mol/L and initiator concentration: 0.01 mol/L). This condition for making the PDI-based “macroinitiator” is similar to the synthesis for the PDI-based homopolymerization described in Chapter 2. The “first-generation” Grubbs initiator was utilized in the BCP synthesis because of its “living” nature and relatively simple handling requirement.<sup>38</sup>

After the consumption of **C11PDI** monomer (monitored using TLC as described earlier), the formed PDI-based “macroinitiator” was used to initiate the polymerization of the **5T** monomer by adding a certain amount of **5T** monomer into the reaction mixture. After the consumption of the **5T** monomer (monitored using TLC), ethyl vinyl ether was used to quench the polymerization by removing the attached ruthenium-based alkylidene from the polymer-chain ends. These two homopolymers, with different **5T** block length (theoretical degree of polymerization are 50 and 25 for the **5T** monomer), were purified using multiple precipitations by addition of the high concentration polymer solutions in good solvents, such as dichloromethane and chloroform, to poor solvents such as methanol. Subsequent Soxhlet extraction using methanol and acetone was used to further purify the polymers. The isolated yields for the PDI-5T BCPs were over 85% with relatively broad molecular weight distributions over the PDI- and **5T**-based homopolymers. A similar polymerization was carried out to obtain **PDI-6T CPA** with theoretical degree of polymerization of 50 for **PDI**-monomer and 50 for **6T**-monomer in a yield of 82%, as shown in Scheme 3.4. The GPC results suggest that diblock copolymers, **PDI-5T CPA**, **PDI-5T CPB**, and **PDI-6T CPA**, are obtained with increased molecular weight and  $M_w/M_n$  compared to those of the **PDI**-based “macroinitiator”. The values of  $M_n = 15$  kD and  $M_w/M_n = 1.3$  were estimated according to GPC (THF) results for the **PDI**-based “macroinitiators”, while  $M_n = 30, 22,$  and  $26$  kD along with  $M_w/M_n = 1.9, 1.7,$  and  $1.7$ , respectively for **PDI-5T CPA**, **PDI-5T CPB**, and **PDI-6T CPA** were obtained from the same GPC. The molecular weights of the copolymers are smaller than the ideal molecular weight assuming the occurring of the “living” type ROMP in the BCP synthesis, probably due to similar reasons as for the homopolymers. It is worth noting

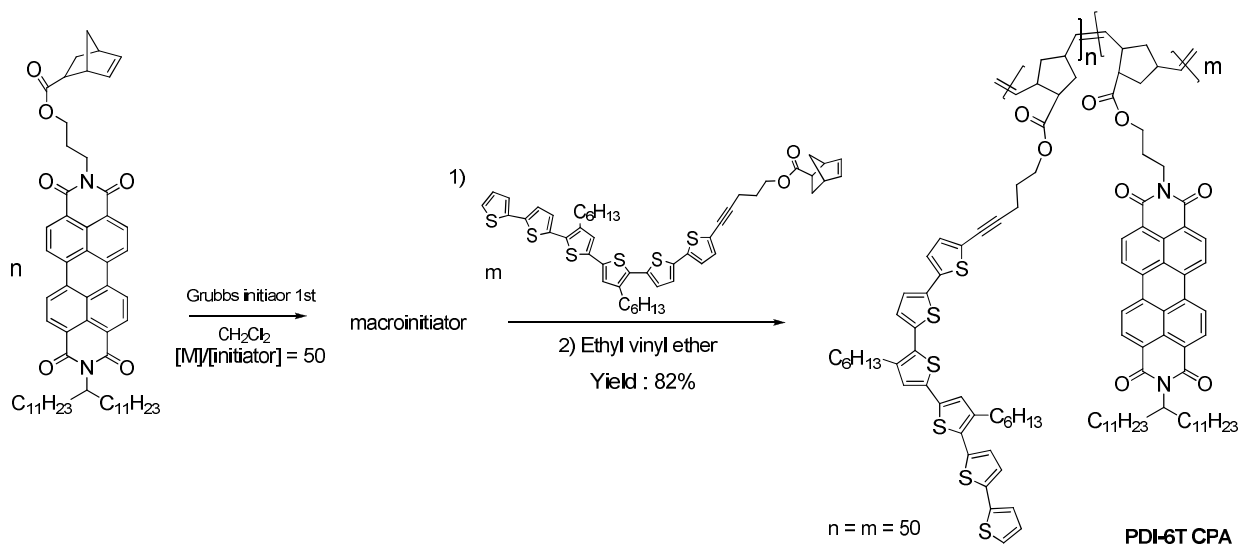
that the molecular weight increase in **PDI-5T CPA** and **PDI-5T CPB** has good correlation with the theoretical increase in **5T**-based block length, suggesting a “living” polymerization of the second block during the BCP synthesis. The  $^1\text{H}$  NMR integration, the UV-Vis absorption in  $\text{CHCl}_3$  and films (Figure 3.12), and elemental analysis results suggest that the actual molar ratio of each monomer in the BCPs, **PDI-5T CPA**, **PDI-5T CPB**, and **PDI-6T CPA**, are good in agreement with that calculated from the corresponding feed ratio in the polymerization. Broad absorption spectra, from 300 – 600 nm, with both OT and PDI characteristic bands were observed for all three copolymers in solution and as a film on glass. Furthermore, strong photoluminescence (PL) quenching (> 95 %) relative to **C11PDI HP** and **5T/6T HP** controls was observed from the spin-casted polymer films on ITO substrates (Figure 3.13), indicating that efficient electron transfer occurs in quenching the **OT** or **PDI** excitons.



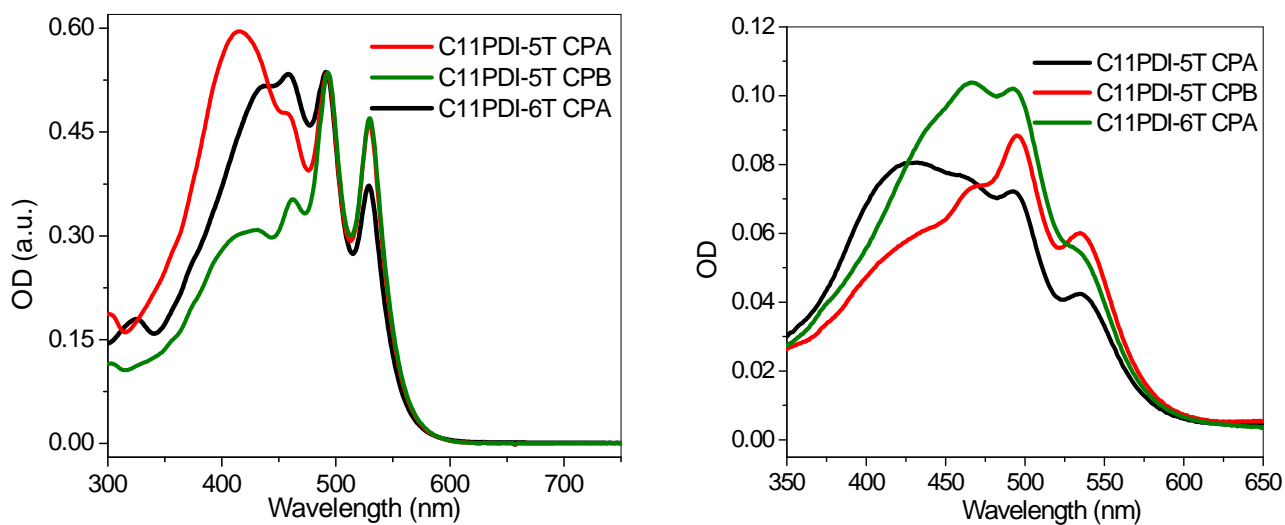
**Figure 3.11. The chemical structures of the copolymers.**



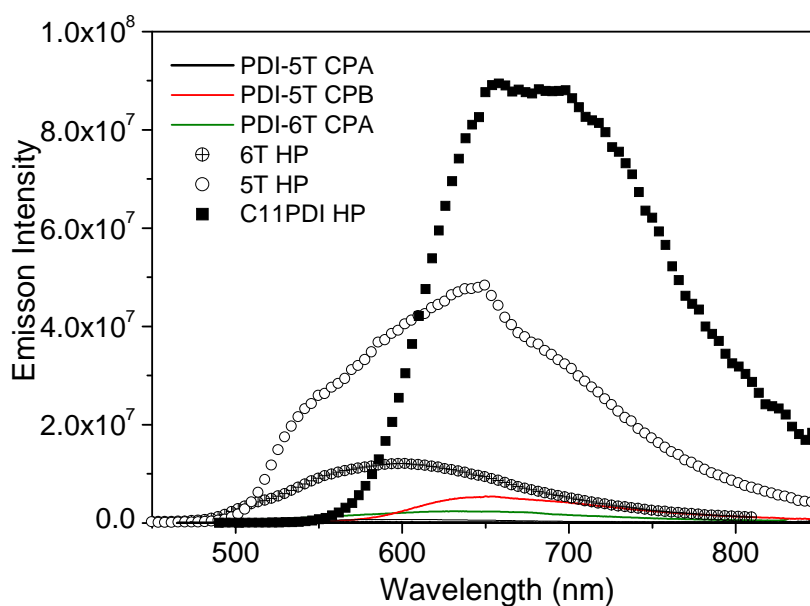
**Scheme 3.3.** The synthetic scheme for the PDI-5T copolymers: PDI-5T CPA and PDI-5T CPB.



**Scheme 3.4.** The synthetic scheme for the PDI-6T copolymer: PDI-6T CPA.



**Figure 3.12.** The UV-Vis absorption spectra of the copolymers in  $\text{CHCl}_3$  solution (left) and in films (right). The films were prepared via spin-coating using 5mg/mL toluene solution at a spin rate of 500 rpm for 1 minute on glass substrates.



**Figure 3.13.** Thin-film emission spectra of the copolymers and C11PDI HP and 5T / 6T HP controls on ITO substrates. All polymer films were excited at 450 nm (This figure was adapted from Dr. Safa Shoaee in the Durrant group).

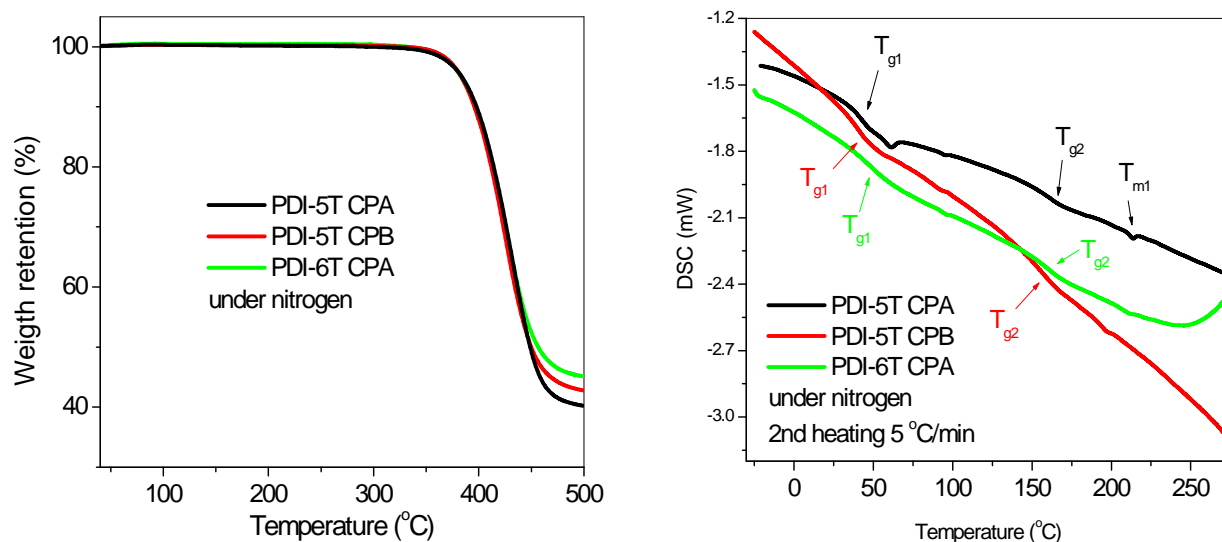
### 3.7 Thermal properties of the copolymers

As revealed in Figure 3.14, all three **PDI-OT** BCPs exhibits good thermal stability, the decomposition temperatures ( $T_d$ ), defined as that at which 5% weight loss is observed are found to be *ca.* 385 °C, under nitrogen atmosphere, as determined by thermogravimetric analysis (TGA) heating from room temperature to 500 °C at a heating rate of 5 °C/. The  $T_d$  of the copolymers is quite similar to that of **C11PDI HP** and around 10 °C lower than the **OT**-based homopolymers, indicating that such thermal degradation probably occurs on the PDI-based block first during the TGA analysis. The thermal behaviors of these copolymers were recorded through differential scanning calorimetry (DSC) analysis within the temperature range from -30 to 300 °C under nitrogen atmosphere. The DSC traces of the second heating with a heating rate of 5 °C/min are shown in Figure 3.15. All three **PDI-OT** copolymers showed features similar to those of the corresponding homopolymers, **C11PDI HP**, **5T HP**, and **6T HP**, which further supports the formation of respective BCPs during synthesis. The thermal properties of these diblock copolymers are summarized in Table 3.2.

**Table 3.2. Summary of thermal properties of the copolymers.**

Polymer	$T_d$ (°C)	$T_m$ (°C)	$T_g$ (°C)
<b>PDI-5T CPA</b>	385	61, 213	44, 160
<b>PDI-5T CPB</b>	385	N.A.	42, 158
<b>PDI-6T CPA</b>	385	N.A.	51, 158
<b>C11PDI HP</b>	385	223	159
<b>5T HP</b>	395	58	38
<b>6T HP</b>	395	N.A.	51





**Figure 3.14.** TGA traces (left) and DSC traces (right) for the second heating process of **PDI-5T CPA** (black), **PDI-5T CPB** (red), and **PDI-6T CPA** (green) with a heating rate of 5 °C/min under nitrogen atmosphere.

### 3.8 Solar-cell performance for the block copolymers

Solar cells were constructed by Mr. William Potscavage *Jr.* in the Kippelen group using a ITO/PEDOT:PSS/polymer(s)/Al configuration to evaluate the solar cell performance the copolymers and respective material blends; the respective device performances are summarized in Table 3.3. All of the solar cells shown here gave limited performance and the PCEs of these devices are primarily limited by the  $J_{SC}$  and fill factor ( $FF$ ). The low charge mobility of the copolymers might be a major reason for the small  $J_{SC}$  since the respective homopolymers have low mobility in OFET devices (**C11PDI HP** showed electron mobilities of  $\sim 10^{-5} \text{ cm}^2 \text{ V}^{-1} \text{ s}^{-1}$  and **5T HP** and **6T HP** exhibited no hole mobilities in OFETs). Of course, other factors including the poor light-harvesting ability and morphologies of the films might play import roles in the limited photo current as

well.<sup>1</sup> Furthermore, unbalanced charge transport in **PDI-5T** and **PDI-6T** copolymers could result in charge accumulation and inefficient charge collection resulting in a decreased *FF* and overall PCE by promoting the possibility of charge recombination.<sup>1</sup> The  $V_{OC}$  of the devices from **PDI-5T CPA** and **PDI-5T CPB** is up to 0.8 V which can be attributed to the relatively larger  $I_g$  (*ca.* 1.4 eV). The large  $V_{OC}$  of solar cells from the three BCPs could be considered as an advantage for OPV applications although these polymers do not harvest much light beyond 550 nm and exhibit quite poor device performance. It should be pointed out that the solar cell devices from **PDI-5T CPA** had PCEs three times higher than those from **PDI-5T CPB** and the blend film from **C11PDI HP** and **5T HP** (PCEs = 0.15% for **PDI-5T CPA**) because of their much larger  $J_{SC}$ , respectively. Measurements of the incident photon-to-current efficiency (IPCE) show much higher energy conversion in the whole spectra range than the other two systems and the maximum IPCE is over ~ 7% between 300 – 600 nm for devices from **PDI-5T CPA**, as shown in Figure 3.16. The higher IPCE for devices from **PDI-5T CPA** might be attributed to more favorable micro-phase-separation in the films as compared to **PDI-5T CPB** and homopolymer blends as the chemical composite of the materials are similar. The similar shape of IPCE curves (Figure 3.15), with respective BCP film absorption spectra (Figure 3.13), suggests both donor- and acceptor-based excitons could contribute to the photo current. In **PDI-5T CPB**, the shorter **5T** block might limit its ability to form favorable micro-phase separation in films as seen with **PDI-5T CPA**. A possible reason for low PCEs of **PDI-5T CPB** may be relatively unbalanced charge-transport ability due to the lower ratio of **5T** moieties. Solar cells for **PDI-6T CPA** gave PCEs of 0.04% with  $V_{OC} = 512$  mV and  $J_{SC} = 0.17$  mAcm<sup>-2</sup>, the PCEs of which are similar to those from **PDI-**

**5T CPB** and homopolymer blends from **C11PDI HP** and **5T HP**. The transient absorption, performed in the Durrant group in Imperial College (London), of the copolymer films exhibited micro- to millisecond long-lived PDI anion absorption at 720 nm after photo-excitation at 466 nm, as illustrated in Figure 3.16. The oxygen-independent decay dynamics are consistent with the assignment to ion rather than triplet absorption. Here, the magnitude of the PDI anion absorption<sup>50-52</sup> at 720 nm at a time delay of 1  $\mu$ s (corresponding to the time delay used in previous studies of D/A blend films and approximating to the typical timescale for charge collection in such D/A blend devices).<sup>53-54</sup> These  $\Delta OD$  signal intensities at 1  $\mu$ s are also summarized in Table 3.3. Here, a greater than two-fold increase for  $\Delta OD$  at 1  $\mu$ s related to the yielding of free charge was observed for **PDI-5T CPA** film relative to films from **PDI-5T CPB** and **PDI-6T CPA**. It should be noted that there is a good correlation between the PCEs and  $J_{SC}$  with  $\Delta OD$  at 1  $\mu$ s (related to the yield of charge photo-generation). According to the transient absorption decay of the copolymer films, larger  $\Delta OD$  leads to devices with higher PCEs. Furthermore, the values of  $\Delta OD$  at 1  $\mu$ s from **PDI-5T CPA** films are more than 5 times smaller than in P3HT/PDI blends reported in the literature or the system shown in Chapter 4.<sup>53</sup> This suggests that a key performance limitation of these solar cells is the low yield of charge photo-generation. However, given the low yields of charge photo-generation, the  $J_{SC}$  in the devices from **PDI-5T CPA** is reasonable compared to P3HT/PDI blends shown in literature and Chapter 4, suggesting that the percolation pathway, perhaps due to more favorable micro-phase-segregation in films, might be presented for facilitating charge collection.

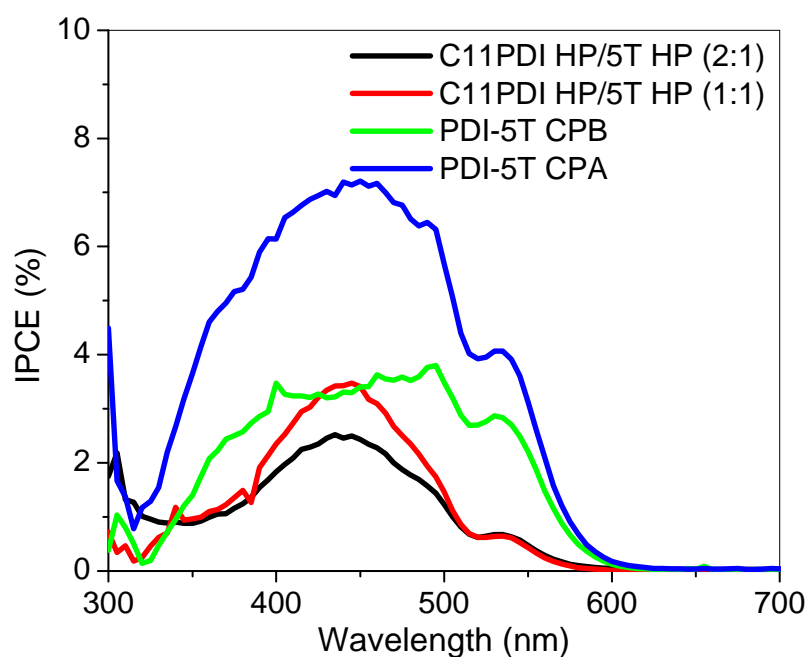


Figure 3.15. IPCE curves of solar cells from the PDI-5T copolymers (A and B) and the blends of C11PDI HP and 5T HP (1:1 and 2:1 weight ratio) (Figure was adapted from Mr. William Potscavage Jr. in the Kippelen group).

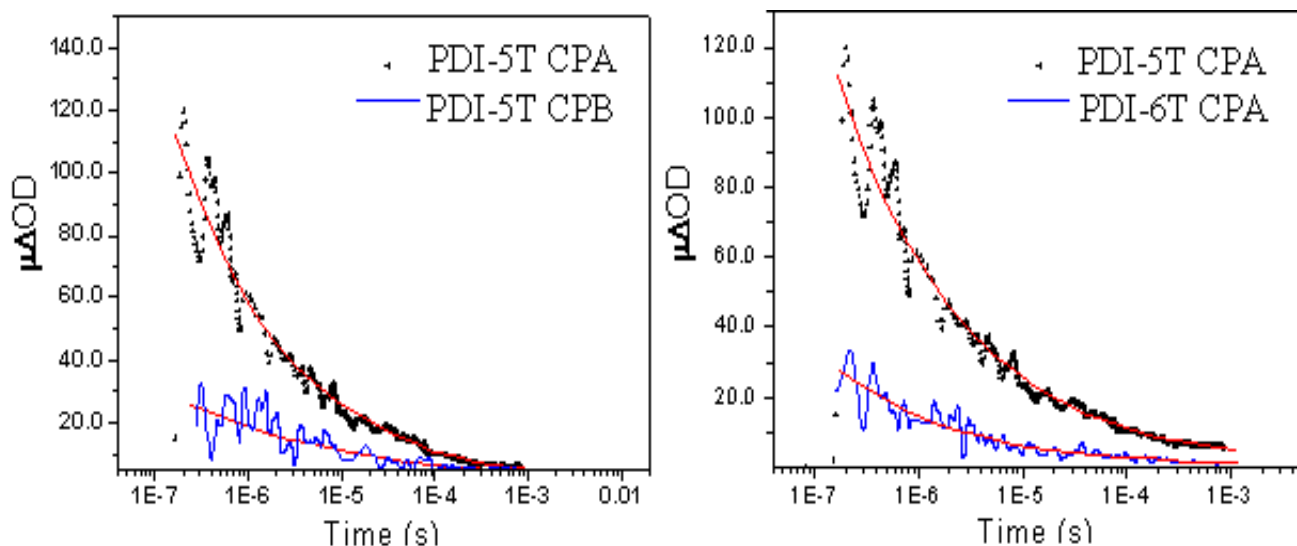


Figure 3.16. Transient absorption decay of the copolymer films after photoexcitation (similar films as the active layers in solar cells) under nitrogen (excited at 466 nm, probed at 720 nm.) (Figure was adapted from Dr. Safa Shoaee in the Durrant group).

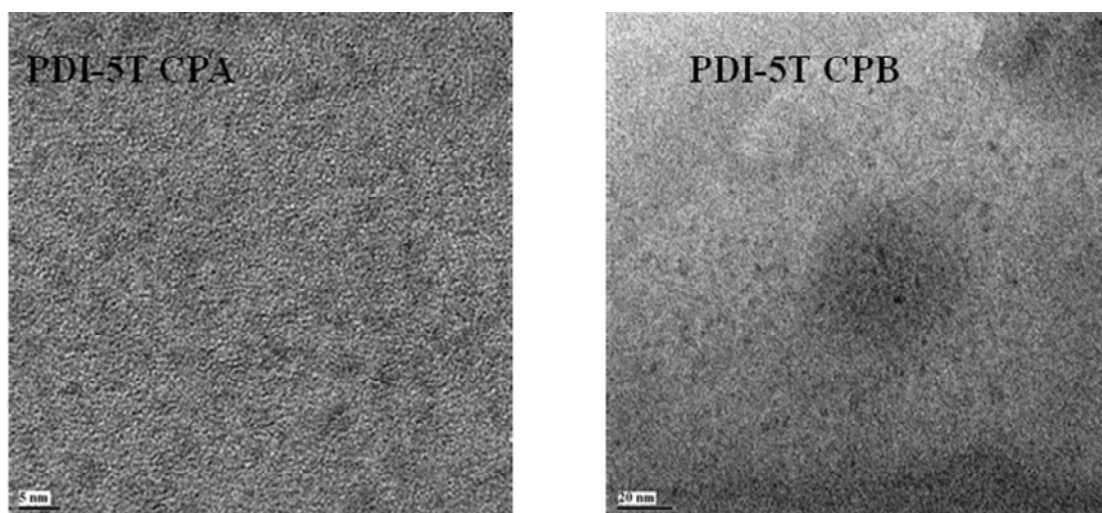
**Table 3.3. Summary of solar cell characteristics for the copolymers or homopolymer blends in device geometry of ITO/PEDOT:PSS/polymer(s)/Al (Data were collected by Mr. William Potscavage Jr. in the Kippelen group).**

Copolymers or polymer blends	$V_{OC}$ (mV)	$J_{SC}$ (mA/cm <sup>2</sup> )	$FF$	PCE(%)	$\mu AOD$ (1 $\mu$ s)
<b>PDI-5T CPA</b>	862 $\pm$ 12	0.42 $\pm$ 0.02	0.30 $\pm$ 0.00	0.15 $\pm$ 0.01	50
<b>PDI-5T CPB</b>	800 $\pm$ 51	0.16 $\pm$ 0.02	0.26 $\pm$ 0.00	0.05 $\pm$ 0.01	20
<b>C11PDI HP/5T HP = 1 : 1</b> (weight ratio)	723 $\pm$ 223	0.17 $\pm$ 0.01	0.31 $\pm$ 0.02	0.05 $\pm$ 0.02	N.A.
<b>C11PDI HP/5T HP = 2 : 1</b> (weight ratio)	770 $\pm$ 22	0.14 $\pm$ 0.01	0.32 $\pm$ 0.01	0.05 $\pm$ 0.01	N.A.
<b>PDI-6T CPA</b>	512 $\pm$ 15	0.20 $\pm$ 0.04	0.28 $\pm$ 0.01	0.04 $\pm$ 0.01	14

### 3.9 Morphology study of the copolymers

Transmission electron microscopy (TEM) was performed, by Dr. Safa Shoaee in the Durrant group at Imperial College (London), to study the phase-segregation of the copolymer films. For these experiments, RuO<sub>4</sub> was used to stain the sample to provide better contrast for different domains. The darker regions of the images correspond to the regions of PDI-rich domain stained with RuO<sub>4</sub>, as claimed in the earlier research.<sup>9,22</sup> Here, since the PEDOT:PSS layer is water soluble, thin composite films of the copolymers on top of the PEDOT:PSS layer were removed from their PEDOT:PSS coated ITO substrates onto the surface of water and transferred to a 300 mesh TEM carbon coated copper grids and stained with RuO<sub>4</sub>.<sup>9,25</sup> However, according to the TEM images shown in Figure 3.17, no obvious nanometer-scale phase-segregation was observed in these samples. However, since RuO<sub>4</sub> can stain only the surface of the copolymer films, the TEM images shown here

do not give information about the phase separation in the bulk, which might give totally different morphologies as that on the surface. Further TEM analysis on the film cross-section might be necessary for better understanding of the phase segregation in the bulk films and its relationship to the overall device performance.



**Figure 3.17. TEM images for PDI-5T CPA and PDI-5T CPB (These images were adapted from Dr. Safa Shoaee in the Durrant group).**

### 3.10 Conclusions

A series of **PDI-OT**-based diblock copolynorbornenes have been synthesized, characterized, and investigated as active materials in organic solar cells. It was observed in solution and in films that the block copolymers show broad absorption spectra, from 300 to 600 nm, with both **OT** and **PDI** characteristic bands. Strong PL quenching (> 95 %) compared to **C11PDI HP** and **5T/6T HP** of the spin-casting polymer films suggests efficient electron transfer occurs in quenching the excited states of **OT** or **PDI**. In solar cells, **PDI-5T CPA** (PCE = 0.15%, and  $J_{SC} = 0.42 \text{ mA/cm}^2$ ) show much higher

PCEs and  $J_{SC}$  over the other two copolymers and the respective **C11PDI HP/5T HP** blend. There is good correlation between the PCEs and  $J_{SC}$  of the solar cells from these copolymers with the yield of charge photo-generation according to the copolymer film transient absorption decay (larger yield of charge photo-generation is related to devices with higher PCEs). Furthermore, the relatively low yields of charge photo-generation might be the key reason for the poor device performance from these polymers. No obvious micro-phase-segregation was observed on the surface of the copolymer films via TEM techniques.

### 3.11 Experimental section

**General:** Most organic and inorganic chemicals in this chapter were obtained from Aldrich, Alfa Aesar, and TCI and used without further purification. The pure *exo*-isomer of bicyclo [2.2.1]hept-5-ene-2-carboxylic acid were synthesized via literature procedures or from Solvay. The  $^1\text{H}$  and  $^{13}\text{C}$  NMR spectra were collected on a Bruker 400 MHz or a Bruker 500 MHz spectrometer. Mass spectra were measured on an Applied Biosystems 4700 Proteomics Analyzer using MALDI mode. Elemental analyses (for C, H, N, S elements in this Chapter) were carried out by Atlantic Microlab using a LECO 932 CHNS elemental analyzer. Solution (chloroform) and thin film UV-Vis absorption spectra were recorded on a Varian Cary 500 UV/Vis/near-IR spectrophotometer while solution (toluene) emission spectra were recorded with a Shimadzu FP-5301PC spectrofluorometer. Electrochemical measurements were carried out under nitrogen in deoxygenated 0.1 M solutions of tetra-*n*-butylammonium hexafluorophosphate in dry dichloromethane using a computer-controlled BAS 100B electrochemical analyzer, a

glassy-carbon working electrode, a platinum-wire auxiliary electrode, and an Ag wire anodized with AgCl as a pseudo-reference electrode at a scan rate of 50 mV/s. The potentials were referenced to  $\text{FeCp}_2^{+/0}$  redox couple by using ferrocene as an internal standard. TGA measurements were performed on an NETZSCH STA 449C analyzer under a nitrogen flow of 40 mL/min with a heating rate of 5 °C/min. DSC measurements were performed on a TA Instruments DSC Q200 analyzer under a nitrogen flow of 50 mL/min with a heating rate of 5 °C/min. Powder XRD data was collected on a Scintag X1 diffractometer with a Cu K $\alpha$  source ( $\lambda = 1.5406 \text{ \AA}$ ) in a continuous scan mode with a step size of 0.02°.

BHJ solar cells were fabricated by Mr. William Postcavage *Jr.* in the Kippelen group using the BCPs or the blend of **C11PDI HP** and **5T HP**. Solution of a block copolymer or polymer blend was made in chlorobenzene (20 mg/mL). ITO-coated glasses (Colorado Concept Coatings LLC) with a sheet resistivity of  $\sim 15 \text{ }\Omega/\text{sq}$  were used as the substrates for the solar cells. The substrates were cleaned in an ultrasonic bath with detergent water, rinsed with deionized water, and then cleaned in sequential ultrasonic baths with deionized water, acetone, and isopropanol. Nitrogen was used to dry the substrates after each of the last three baths. A 300-nm-thick layer of  $\text{SiO}_x$  was deposited on the cleaned ITOs by e-beam deposition (AXXIS, Kurt J. Lesker) to pattern the anode. Next, the substrates were ultrasonicated in isopropanol for 15 minutes, blown dry with nitrogen, and air-plasma treated for 2 minutes. A hole-conducting layer of PEDOT : PSS (CLEVIOS P VP AI 4083, H. C. Starck) was filtered through a 0.45- $\mu\text{m}$ -pore PVDF filter and spin coated on the substrates at 5000 rpm for 1 minute, and the substrates were annealed at 140 °C for 10 minutes in ambient atmosphere. After loading into a nitrogen-



filled glove box, films of the polymer mixtures were deposited on the substrates by spin coating for 1 minute at speeds of 1000 – 1500 rpm for the mixture. All solutions were filtered through 0.2- $\mu$ m-pore PTFE filters prior to spin coating. The substrates were then loaded into a vacuum thermal evaporation system (SPECTROS, Kurt J. Lesker) connected to the glove box, and *ca.* 200 nm of Al was deposited through a shadow mask at a rate of 1 – 3  $\text{\AA}/\text{s}$  and a base pressure of *ca.*  $7 \times 10^{-8}$  Torr to define the cathodes. The completed devices were transferred in a sealed container to another nitrogen-filled glove box for electrical measurements. Current-voltage characteristics were measured using a source meter (2400, Keithley) controlled by a LabVIEW program. When testing the solar cells under illumination, filtered light from a 175 W Xenon lamp (ASB-XE-175EX, CVI) was used as a broadband light source with an irradiance of  $\sim 72 \text{ mW}/\text{cm}^2$  to simulate sunlight. A monochromator and calibrated photodiode were used to measure IPCE. Bilayer Solar cells were fabricated by Mr. William Postcavage *Jr.* in the Kippelen group by spin coating a layer of OT HP as the donor and depositing  $\text{C}_{60}$  as the acceptor on top. First, a 15 mg/mL solution of OT HP in chlorobenzene was made and stirred for several hours in a nitrogen-filled glove box. ITO-coated glass (Colorado Concept Coatings LLC) with a sheet resistivity of *ca.*  $15 \text{ }\Omega/\text{sq.}$  was used as the substrates for the solar cells. The substrates were cleaned in an ultrasonic bath of detergent water, rinsed with deionized water, and then cleaned in sequential ultrasonic baths of deionized water, acetone, and isopropanol. Nitrogen was used to dry the substrates after each of the last three baths. A 300-nm-thick layer of  $\text{SiO}_x$  was deposited on the cleaned ITO by e-beam deposition (AXXIS, Kurt J. Lesker) to pattern the anode. Next, the substrates were ultrasonicated in isopropanol for 10 minutes, blown dry with nitrogen, and air-plasma treated for 3 min. A

hole-conducting layer of PEDOT : PSS was filtered through 0.45- $\mu$ m-pore PVDF filters and spin coated on several of the substrates at 5,000 rpm for 1 min, and the PEDOT-coated substrates were annealed at 140 °C for 10 min in atmosphere. After loading into a nitrogen-filled glove box, films of OT HP were deposited on the substrates with and without PEDOT : PSS by spin coating for 1 min at 1,000, 2,000, 4,000, and 8,000 rpm. The solution was filtered through 0.2- $\mu$ m-pore PTFE filters prior to spin coating. The substrates were then loaded into a vacuum thermal evaporation system (SPECTROS, Kurt J. Lesker) connected to the glove box, and 45 nm of C<sub>60</sub>, 8 nm of bathocuproine, and 200 nm of Al were deposited on top of the polymer films through shadow masks at a base pressure of *ca.*  $3 \times 10^{-8}$  Torr. The C<sub>60</sub> (Alfa Aesar) and bathocuproine (TCI America) were purified with zone sublimation prior to use. The completed devices were transferred in a sealed container to another nitrogen-filled glove box for electrical measurements in similar way as described earlier.

Transient absorption decays were measured by Dr. Safa Shoaee in the Durant group in Imperial College (London) by exciting the sample films, under nitrogen atmosphere, with a dye laser (Photon Technology International Inc., GL-301). The excitation wavelength used was 466 nm for all blends, with pump intensities of *ca.* 30  $\mu$ Jcm<sup>-2</sup> and a repetition frequency of 4 Hz. A 100 W quartz halogen lamp (Bentham, IL 1) with a stabilized power supply (Bentham, 605) was used as a probe light source, with a typical probe wavelength of 720 nm. The probe light passing through the sample film was detected with a silicon photodiode (Hamamatsu Photonics, S1722-01). Signal from the photodiode was pre-amplified and sent to the main amplification system with an electronic band-pass filter (Costronics Electronics). The amplified signal was collected

with a digital oscilloscope (Tektronics, TDS220), which was synchronized with a trigger signal of the pump laser pulse from a photodiode (Thorlabs Inc., DET210). To reduce stray light, scattered light and sample emission, two monochromators and appropriate optical cut-off filters were placed before and after the sample.

**Compound A:** 5'-Hexyl-2,2'-bithiophene-5-boronic acid pinacol ester (1.2 g, 3.2 mmol), ethyl 2,5-dibromothiophene-3-acetate (0.42 g, 1.3 mmol), Pd(PPh<sub>3</sub>)<sub>4</sub> (30 mg, 26 μmol), and CsF (0.61g, 6 mmol) were refluxed in anhydrous dimethylacetamide (15 mL) under nitrogen overnight in a two-neck round-bottomed flask. After the reaction was cooled to room temperature, most of the solvent was removed by vacuum distillation. The residue was dissolved in toluene (100 mL) and washed with water (3 × 20 mL). The organic phase was dried over MgSO<sub>4</sub> and the solvent was removed under vacuum. The residue was passed through a short silica gel plug eluted with hexane, toluene/hexane (4 : 1), and then toluene to give compound **A** as yellow solid after the solvent was removed under vacuum (0.81 g, 51%). <sup>1</sup>H NMR (500 MHz, CD<sub>2</sub>Cl<sub>2</sub>): δ 7.11–7.09 (m, 4H), 7.03–7.01 (m, 3H), 6.72 (s, 2H), 4.21 (q, *J* = 7.0 Hz, 2H), 3.76 (s, 2H), 2.82 (t, *J* = 7.5 Hz, 4H), 1.70 (q, *J* = 7.0 Hz, 4H), 1.39–1.27 (m, 16H); <sup>13</sup>C{<sup>1</sup>H} NMR (125 MHz, CD<sub>2</sub>Cl<sub>2</sub>): δ 170.9, 146.6, 146.5, 138.9, 137.6, 135.0, 135.6, 134.4, 133.3, 132.2, 131.7, 127.7, 127.1, 125.4, 124.9, 124.0, 123.9, 61.5, 35.4, 32.0, 30.5, 30.1, 29.1, 23.0, 14.4, 14.2. (Four aromatic and one alkyl carbon resonances were not observed, presumably due to overlap): HRMS(EI) Calcd for C<sub>36</sub>H<sub>42</sub>O<sub>2</sub>S<sub>5</sub>: 666.1788. Found: 666.1753. Anal. Calcd for C<sub>36</sub>H<sub>42</sub>O<sub>2</sub>S<sub>5</sub>: C, 64.82; H, 6.35; S, 24.04. Found: C, 64.56; H, 6.39; S, 23.96.

**5T Monomer:** Compound **A** (0.80 g, 1.2 mmol) in THF (20 mL) was added dropwise to the mixture of lithium aluminum hydride (0.38 g, 10 mmol) and THF (10 mL) at 0 °C . The mixture was warmed up to room temperature slowly and kept stirring at room temperature for another 2 h. Water (2 mL) was added dropwise and the resultant white precipitate was removed by filtration. The solvent of the filtrate was removed and the residue was dissolved in chloroform (50 mL) and washed with water (3 × 20 mL). The organic phase was dried over Na<sub>2</sub>SO<sub>4</sub> and the solvent was removed under vacuum to give a yellow solid (0.71 g). This yellow solid was used for reaction without further purification. The yellow solid (0.71 g) and exo-bicyclo[2.2.1]hept-5-ene-2-carboxylic acid (0.44 g, 3.2 mmol) were charged to a two-neck round-bottomed flask and dissolved in dichloromethane (25 mL) under nitrogen. A mixture of dicyclohexylcarbodiimide (0.27 g, 1.4 mmol) and 4-(dimethylamino)pyridine (22 mg, 0.18 mmol) in dichloromethane (5 mL) was then added in the flask in one portion. The mixture was stirred overnight under nitrogen at room temperature before it was passed through a short silica gel pad eluted with chloroform. The solvent was then removed under vacuum to give the **5T Monomer** as a yellow solid (0.60 g, 71%). <sup>1</sup>H NMR (500 MHz, CD<sub>2</sub>Cl<sub>2</sub>): δ 7.08 (m, 4H), 7.03 (m, 3H), 6.72 (s, 2H), 6.12–6.09 (m, 2H), 4.37 (m, 2H), 3.14 (t, *J* = 6.0 Hz, 2H), 2.99 (s, 1H), 2.88 (s, 1H), 2.81 (m, 4H), 2.21 (m, 1H), 1.89 (m, 1H), 1.71 (m, 4H), 1.51 (m, 16H), 0.90 (m, 6H). <sup>13</sup>C{<sup>1</sup>H} NMR (125 MHz, CD<sub>2</sub>Cl<sub>2</sub>): δ 176.3, 146.1, 137.2, 136.1, 135.9, 135.2, 133.7, 131.5, 127.3, 126.8, 125.4, 124.7, 124.0, 123.6, 64.1, 47.0, 46.7, 43.5, 42.1, 31.9, 30.7, 30.5, 29.1, 23.0, 14.2 (9 aromatic carbons and 7 alkyl resonances were not observed, presumably due to overlap). HRMS(EI) Calcd for

$C_{42}H_{48}O_2S_5$ : 744.2258. Found: 744.2242. Anal. Calcd for  $C_{42}H_{48}O_2S_5$ : C, 67.70; H, 6.49; S, 21.52. Found: C, 67.67; H, 6.63; S, 21.32.

**5T HP: 5T monomer** (225 mg, 0.301 mmol) was dissolved in dichloromethane (10 mL) under nitrogen, and then the “first generation” Grubbs initiator (4.0 mg, 0.0060 mmol) in dichloromethane (1 mL) was added in one portion. The mixture was then kept stirred for another 5 h. Then, ethyl vinyl ether (0.2 mL) was added in one portion and the mixture was stirred for another 4 h at room temperature. The mixture was added to methanol (200 mL) dropwise and the resultant yellow precipitate was filtered, washed with methanol (50 mL) and hexane (50 mL) in a sequence, and dried under vacuum. The resultant yellow solid was then washed with hot methanol for 6 h and hot acetone overnight in a Soxhlet apparatus and then chloroform to extract the polymer for 5 h. Most of the solvent was removed under vacuum and the residue was precipitated into methanol/Water = 10 :1 (200 mL). **5T HP** was obtained as a yellow solid after filtration (136 mg, 65%). GPC (THF):  $M_n$  = 23.6 kD,  $M_w/M_n$  = 1.4.  $^1H$  NMR (500 MHz,  $CD_2Cl_2$ ):  $\delta$  7.02 (sb, 7nH), 6.74 (sb, 2nH), 5.10 (mb, 2nH), 4.42 (sb, 2nH), 3.1–2.3 (m, 9nH), 1.9–1.3 (m, 20nH), 0.85 (sb, 6nH). Anal. Calcd for  $(C_{42}H_{48}O_2S_5)_n$ : C, 67.70; H, 6.49; S, 21.52. Found: C, 67.52; H, 6.41; S, 21.24.

Compound **B**: 5-Trimethylstannyl-2,2'-dithienyl (2.2 g, 60 mmol), 5,5'-dibromo-4,4'-dihexyl-2,2'-bithiophene (1.20 g, 25 mmol),  $Pd(PPh_3)_4$  (20 mg, 0.017 mmol) were refluxed in toluene (30 mL) under nitrogen overnight in a two-neck round-bottomed flask with condenser. After the reaction was cooled to room temperature, the reaction mixture was washed with water ( $3 \times 20$  mL) and dried over  $MgSO_4$ . The solvent was then

removed under vacuum and the residue was recrystallized in heptane twice to give compound **B** as an orange solid (1.0 g, 63%).  $^1\text{H}$  NMR (500 MHz,  $\text{CD}_2\text{Cl}_2$ ):  $\delta$  7.28 (d,  $J$  = 1.0 Hz, 2H), 7.27 (d,  $J$  = 1.0 Hz, 2H), 7.22 (d,  $J$  = 1.0 Hz, 2H), 7.16–7.04 (m, 6H), 2.79 (t,  $J$  = 7.5 Hz, 4H), 1.70 (pentet,  $J$  = 7.5 Hz, 4H), 1.44–1.41 (m, 4H), 1.35–1.32 (m, 8H), 0.90 (t,  $J$  = 7.0 Hz, 6H).  $^{13}\text{C}\{^1\text{H}\}$  NMR (125 MHz,  $\text{CD}_2\text{Cl}_2$ ):  $\delta$  141.2, 137.4, 137.3, 135.2, 135.1, 129.8, 128.4, 127.1, 126.8, 125.0, 124.4, 124.1, 32.0, 30.8, 29.8, 29.6, 23.0, 14.2. HRMS (FAB) Calcd for  $\text{C}_{36}\text{H}_{38}\text{S}_6$ : 662.129. Found: 662.128. Anal. Calcd for  $\text{C}_{36}\text{H}_{38}\text{S}_6$ : C, 65.21; H, 5.78; Found: C, 65.16; H, 5.74.

**6T monomer:** Compound **B** (1.32 g 2.00 mmol) was dissolved in anhydrous THF (30 mL) under nitrogen and the mixture was cooled to  $-78\text{ }^\circ\text{C}$  followed by the addition of 0.2 mL TMEDA. After the mixture was stirred for 10 min at this temperature, *n*-butyl lithium in hexane (2.3 mol/L, 0.89 mL, 2.0 mmol) was added through syringe slowly. The reaction mixture was kept stirring at  $-78\text{ }^\circ\text{C}$  for 1 h before it was warmed to room temperature slowly. After the mixture was stirred at room temperature for 30 min, it was cooled down to  $-78\text{ }^\circ\text{C}$  and iodine (0.504 g, 2.00 mmol) in THF (5 mL) was added in one portion. The mixture was warmed up to room temperature and kept stirring overnight. The solvent was then removed under vacuum and the residue was passed through a short silica gel plug with hexane as the eluent. The solvent was removed under vacuum and the residue together with CuI (5 mg, 0.03 mmol),  $\text{PdCl}_2(\text{PPh}_3)_2$  (20 mg, 0.030 mmol), were charged to a two-neck round-bottomed flask. The reaction system was evacuated/refilled with nitrogen three times and triethylamine (5 mL), toluene (20 mL), and 4-pentyn-1-ol (1 mL) were added via syringe. The mixture was then stirred at  $80\text{ }^\circ\text{C}$  overnight under

nitrogen before it was cooled to room temperature, washed with water, and dried over  $\text{MgSO}_4$ . After the solvent was removed under vacuum, the residue was purified on a silica gel column with hexane/ethyl acetate (3 : 1). A yellow oil was obtained when the solvent was removed, which was dissolved in dichloromethane (10 mL) with exo-bicyclo[2.2.1]hept-5-ene-2-carboxylic acid (0.30 g, 2.2 mmol) under nitrogen. Then, a mixture of dicyclohexylcarbodiimide (0.20 g, 0.97 mmol) and 4-(dimethylamino)pyridine (15 mg, 0.12 mmol) in dichloromethane (3 mL) was added in one portion and the mixture was stirred overnight at room temperature. The reaction mixture was passed through a short silica gel plug eluted with chloroform. After the solvent was removed, the residue was refluxed in 15 mL ethanol for 30 minutes and stored for one month at  $-20\text{ }^\circ\text{C}$ . **6T monomer** was achieved as an orange solid after filtration (0.31 g, 18%).  $^1\text{H}$  NMR (500 MHz,  $\text{CD}_2\text{Cl}_2$ ):  $\delta$  7.32 (dd,  $J_1 = 4.0\text{ Hz}$ ,  $J_2 = 1.0\text{ Hz}$ , 1H), 7.27 (dd,  $J_1 = 3.5\text{ Hz}$ ,  $J_2 = 1.0\text{ Hz}$ , 1H), 7.21 (d,  $J = 4.0\text{ Hz}$ , 1H), 7.19 (d,  $J = 4.0\text{ Hz}$ , 1H), 7.11-6.16 (m, 7H), 4.26 (t,  $J = 6.5\text{ Hz}$ , 2H), 3.08 (s, 1H), 2.95 (s, 1H), 2.83–2.80 (m, 4H) 2.63 (t,  $J = 7.0\text{ Hz}$ , 2H), 2.29-2.27 (m, 1H), 2.00–1.94 (m, 3H), 1.75–1.69 (m, 4H), 1.54–1.25 (m, 17H), 0.95 (t,  $J = 7.0\text{ Hz}$ , 6H).  $^{13}\text{C}\{^1\text{H}\}$  NMR (125 MHz,  $\text{CD}_2\text{Cl}_2$ ):  $\delta$  176.3, 141.3, 141.2, 138.4, 137.6, 137.4, 137.3, 136.7, 136.1, 135.7, 135.2 (2 peaks) 135.0, 132.6, 129.8, 129.6, 128.3, 127.1 (2 close peaks), 126.7, 125.1, 124.8, 124.4, 124.1, 123.6, 123.1, 94.9, 74.3, 63.4, 47.0, 46.7, 43.5, 42.1, 32.0, 30.8 (2 peaks) 30.7, 30.1, 29.9, 29.8, 29.6, 28.1, 23.0, 17.0, 14.2. (One aromatic carbone and three alkyl carbons were not observed, presumably due to overlap). HRMS (FAB) Calcd for  $\text{C}_{49}\text{H}_{52}\text{O}_2\text{S}_6$ : 864.2291. Found: 864.2278. Anal. Calcd for  $\text{C}_{49}\text{H}_{52}\text{O}_2\text{S}_6$ : C, 68.01; H, 6.06; S, 22.23, Found : C, 68.03; H, 6.03; S, 22.41.

**6T homopolymer:** **6T monomer** (240 mg, 0.277 mmol) was dissolved in dichloromethane (10 mL) under nitrogen, and the “first generation” Grubbs initiator (4.5 mg, 0.0055 mmol) in dichloromethane (2 mL) was added. The mixture was then kept stirring for 5 h. Then, ethyl vinyl ether (0.2 mL) was added in one portion and the mixture was stirred for another 4 h at room temperature. It was added to methanol (125 mL) dropwise and the yellow precipitate was filtered, washed with methanol (50 mL) and dried under vacuum after filtration. The resultant yellow solid was then washed with hot methanol for 4 h and hot acetone overnight in a Soxhlet apparatus, then with chloroform to extract the polymer for 5h. Most of the solvent was removed under vacuum and the residue was precipitated in to methanol (200 mL). **6T HP** was obtained as an orange solid after filtration (151 mg, 63 %). GPC (THF) :  $M_n = 28.7$  kD,  $M_w/M_n = 1.9$ .  $^1\text{H}$  NMR (500 MHz,  $\text{CD}_2\text{Cl}_2$ ):  $\delta$  7.2–6.9 (mb, 11nH), 5.5–5.0 (m, 2nH), 4.14 (sb, 2nH), 2.6–2.5 (m, 5nH), 1.9–1.6 (m, 3nH), 1.6–1.3 (m, 23nH), 0.87 (sb, 6nH). Anal. Calcd for  $(\text{C}_{49}\text{H}_{52}\text{O}_2\text{S}_6)_n$ : C, 68.01; H, 6.06; S, 22.23. Found: C, 67.81; H, 6.12; S, 22.13.

**PDI-5T CPA:** **C11PDI** monomer (330 mg, 0.371 mmol) was dissolved in anhydrous dichloromethane (9.0 mL) under  $\text{N}_2$ , the “first generation” Grubbs initiator (6.1 mg, 0.0075 mmol) in dichloromethane (1.0 mL) was then added in one portion. The reaction mixture was kept stirring for 6 h until all **C11PDI** monomers had been consumed (monitored by TLC) and **5T monomer** (276 mg, 0.371 mmol) in dichloromethane (5.0 mL) was then added and the mixture was stirred overnight at room temperature before the addition of ethyl vinyl ether (0.2 mL). It was kept stirring for another 5 h and added to methanol (200 mL) dropwise. The red precipitate was filtered, washed with methanol, and dried under vacuum. The resultant solid was then dissolved in chloroform (10 mL)



and precipitated out in methanol (200 mL) again. The red solid was then washed with hot methanol for 6 h and hot acetone overnight in a Soxhlet apparatus. Finally,  $\text{CHCl}_3$  was used to extract the materials for 5 h in a Soxhlet apparatus. Most solvent was removed under vacuum and the residue was precipitated into methanol (200 mL) dropwise. After filtration, **PDI-5T CPA** was achieved as a red solid (0.54 g, 82%). GPC (THF):  $M_n = 30.6 \text{ k}$ ,  $M_w/M_n = 1.96$ .  $^1\text{H}$  NMR (500 MHz,  $\text{CDCl}_3$ ):  $\delta$  8.5–6.5 (m, 17nH), 5.7–5.0 (m, 5nH), 4.5–4.0 (mb, 6nH), 3.5–1.0 (m, 78nH), 0.85 (sb, 12nH). Anal. Calcd for  $(\text{C}_{100}\text{H}_{118}\text{N}_2\text{O}_8\text{S}_5)_n$ : C, 73.40; H, 7.27; N, 1.70; Found : C, 72.75; H, 7.45; N, 1.71.

**PDI-5T CPB:** **C11PDI** monomer (400 mg, 0.449 mmol) was dissolved in anhydrous dichloromethane (9.0 mL) under  $\text{N}_2$ , the “first generation” Grubbs initiator (7.3mg, 0.0090 mmol) in dichloromethane (1.0 mL) was added in one portion. The reaction mixture was kept stirring for 6 h until all **C11PDI** monomers had been consumed (monitored by TLC) and **5T monomer** (166 mg, 0.224 mmol) in dichloromethane (4.0 mL) was then added and the mixture was stirred overnight at room temperature before the addition of ethyl vinyl ether (0.2 mL). It was kept stirring for another 5 h before it was added to methanol (200 mL) dropwise; the red precipitate was filtered, washed with methanol, and dried under vacuum. The resultant solid was then dissolved in chloroform (10 mL) and precipitated out from methanol (200 mL) again. The red solid was then washed with hot methanol for 6 h and hot acetone overnight in a Soxhlet apparatus for 6 h. Finally,  $\text{CHCl}_3$  was used to extract the materials for 5 h in a Soxhlet apparatus. Most solvent was removed under vacuum and the residue was precipitated into methanol (200 mL) dropwise. After filtration, **PDI-5T CPB** was achieved as a red solid (0.50 g, 89%). GPC (THF):  $M_n = 21.5 \text{ k}$ ,  $M_w/M_n = 1.67$ .  $^1\text{H}$  NMR (500 MHz,  $\text{CDCl}_3$ ):  $\delta$  8.5–6.5 (m,

25nH), 5.6–5.0 (m, 8nH), 4.5–4.0 (mb, 10nH), 3.5–1.0 (m, 127nH), 0.85 (sb, 18nH).

Anal. Calcd for  $[(C_{42}H_{48}O_2S_5)_n \cdot (C_{58}H_{70}N_2O_6)_{2n}]$ : C, 75.08; H, 7.50; N, 2.22; Found: C, 75.33; H, 7.55; N, 2.23.

**PDI-6T CPA: C11PDI** monomer (330 mg, 0.371 mmol) was dissolved in anhydrous dichloromethane (12.0 mL) under  $N_2$ , the “first generation” Grubbs initiator (6.1 mg, 0.0075 mmol) in dichloromethane (1.0 mL) was added in one portion. The reaction mixture was kept stirring for 6 h until all **C11PDI** monomers had been consumed (monitored by TLC) and **6T monomer** (320 mg, 0.371 mmol) in dichloromethane (5.0 mL) was then added and the mixture was stirred overnight at room temperature before the addition of ethyl vinyl ether (0.2 mL). It was kept stirring for another 5 h before it was added to methanol (200 mL) dropwise; the red precipitate was filtered, washed with methanol, and dried under vacuum. The resultant solid was then dissolved in chloroform (10 mL) and precipitated out from methanol (200 mL) again. The red solid was then washed with hot methanol for 8 h and hot acetone overnight in a Soxhlet apparatus. Finally,  $CHCl_3$  was used to extract the materials for 5 h in a Soxhlet apparatus. Most solvent was removed under vacuum and the residue was precipitated into methanol (200 mL) dropwise. After filtration, **PDI-6T CPA** was achieved as a red solid (0.52 g, 80%). GPC (THF):  $M_n = 26.0$  kD,  $M_w/M_n = 1.69$ .  $^1H$  NMR (500 MHz,  $CDCl_3$ ):  $\delta$  8.2–6.8 (m, 19nH), 5.7–5.0 (m, 5nH), 4.5–4.0 (mb, 6nH), 3.5–1.0 (m, 80nH), 0.86 (sb, 12nH). Anal. Calcd for  $(C_{107}H_{122}N_2O_8S_6)_n$ : C, 73.16; H, 7.00; N, 1.59; S, 10.95; Found: C, 73.18; H, 6.92; N, 1.80; S, 10.66.

### 3.12 References

- (1) Thompson, B. C.; Fréchet, J. M. J. *Angew. Chem. Int. Ed.* **2008**, *47*, 58-77.
- (2) Darling, S. B. *Energy Environ. Sci.* **2009**, *2*, 1266-1273.
- (3) Günes, S.; Neugebauer, H.; Sariciftci, N. S. *Chem. Rev.* **2007**, *107*, 1324-1338.
- (4) Kippelen, B.; Brédas, J. L. *Energy Environ. Sci.* **2009**, *2*, 251-261.
- (5) Ma, W.; Yang, C.; Gong, X.; Lee, K.; Heeger, A. J. *Adv. Funct. Mater.* **2005**, *15*, 1617-1622.
- (6) Reyes-Reyes, M.; Kim, K.; Carroll, D. L. *Appl. Phys. Lett.* **2005**, *87*, 083506.
- (7) Zhao, Y.; Xie, Z.; Qu, Y.; Geng, Y.; Wang, L. *Appl. Phys. Lett.* **2007**, *90*, 043504.
- (8) Sommer, M.; Lindner, S. M.; Thelakkat, M. *Adv. Funct. Mater.* **2007**, *17*, 1493-1500.
- (9) Lindner, S. M.; ttner, S. H.; Chiche, A.; Thelakkat, M.; Krausch, G. *Angew. Chem., Int. Ed.* **2006**, *45*, 3364-3368.
- (10) Hüttner, S.; Sommer, M.; Thelakkat, M. *Appl. Phys. Lett.* **2008**, *92*, 093302.
- (11) Zhang, Q.; Cirpan, A.; Russell, T. P.; Emrick, T. *Macromolecules* **2009**, *42*, 1079-1082.
- (12) Segalman, R. A. *Mater. Sci. Eng.*, **2005**, *48*, 191-226.
- (13) Darling, S. B. *Prog. Polym. Sci.* **2007**, *32*, 1152-1204.
- (14) Scherf, U.; Gütacker, A.; Koenen, N. *Acc. Chem. Res.* **2008**, *41*, 1086-1097.
- (15) Ohshimizu, K.; Ueda, M. *Macromolecules* **2008**, *41*, 5289-5294.
- (16) Tu, G.; Li, H.; Forster, M.; Heiderhoff, R.; Balk, L. J.; Scherf, U. C. *Macromolecules* **2006**, *39*, 4327-4331.
- (17) Ren, G. Q.; Wu, P. T.; Jenekhe, S. A. *Chem. Mater.* **2010**, *22*, 2020-2026.
- (18) Wu, P. T.; Ren, G. Q.; Jenekhe, S. A. *Macromolecules* **2010**, *7*, 3306-3313
- (19) Stalmach, U.; B. de Boer, C.; C. Videlot; van Hutten, P. F.; Hadziioannou, G. *J. Am. Chem. Soc.* **2000**, *122*, 5464-5472.
- (20) van der Veen, M. H.; de Boer, B.; Stalmach, U.; van de Wetering, K. I.; Hadziioannou, G. *Macromolecules* **2004**, *37*, 3673-3684.
- (21) Barrau, S.; Heiser, T.; Richard, F.; Brochon, C.; Ngov, C.; van de Wetering, K.; Hadziioannou, G.; Anokhin, D. V.; Ivanov, D. A. *Macromolecules* **2008**, *41*, 2701-2710.
- (22) Sommer, M.; Lang, A. S.; Thelakkat, M. *Angew. Chem. Int. Ed.* **2008**, *47*, 7901-7904.
- (23) Rajaram, S.; Armstrong, P. B.; Kim, B. J.; Fréchet, J. M. J. *Chem. Mater.* **2009**, *21*, 1775-1777.
- (24) Sivula, K.; Ball, Z. T.; Watanabe, N.; Fréchet, J. M. J. *Adv. Mater.* **2006**, *18*, 206-210.
- (25) Lindner, S. M.; Kaufmann, N.; Thelakkat, M. *Org. Electr.* **2007**, *8*, 69-75.

- (26) Jones, B. A.; Facchetti, A.; Wasielewski, M. R.; Marks, T. J. *J. Am. Chem. Soc.* **2007**, *129*, 15259-15278.
- (27) Jones, B. A.; Ahrens, M. J.; Yoon, M.-H.; Facchetti, A.; Marks, T. J.; Wasielewski, M. R. *Angew. Chem. Int. Ed.* **2004**, *43*, 6363-6366.
- (28) Würthner, F. *Chem. Commun.* **2004**, 1564-1579.
- (29) Nagao, Y. *Progress Org. Chem.* **1997**, *31*, 43-49.
- (30) Wang, H.; Peng, B.; Wei, W. *Progress Chem.* **2008**, *20*, 1751-1760.
- (31) An, Z.; Yu, J.; Jones, S. C.; Barlow, S.; Yoo, S.; Domercq, B.; Prins, P.; Siebbeles, L. D. A.; Kippelen, B.; Marder, S. R. *Adv. Mater.* **2005**, *17*, 2580-2583.
- (32) Zhao, C. C.; Zhang, Y.; Wang, C. W.; Rothberg, L.; Ng, M. K. *Org. Lett.* **2006**, *8*, 1585-1588.
- (33) Zhao, C. C.; Zhang, Y.; Pan, S. L.; Rothberg, L.; Ng, M. K. *Macromolecules* **2007**, *40*, 1816-1823.
- (34) Bao, Z.; Locklin, J. *Organic Field-Effect Transistors*; CRC Press, 2006.
- (35) Potscavage, W. J.; Sharma, A.; Kippelen, B. *Acc. Chem. Res.* **2009**, *42*, 1758-1767.
- (36) Mutolo, K. L.; Mayo, E. I.; Rand, B. P.; Forrest, S. R.; Thompson, M. E. *J. Am. Chem. Soc.* **2006**, *128*, 8108-8109.
- (37) Gadisa, A.; Svensson, M.; Andersson, M. R.; Inganäs, O. *Appl. Phys. Lett.* **2004**, *84*, 1609-1611.
- (38) Trnka, T. M.; Grubbs, R. H. *Acc. Chem. Res.* **2001**, *34*, 18-29.
- (39) Cho, J.-Y.; Domercq, B.; Barlow, S.; Sponitsky, K. Y.; Li, J.; Timofeeva, T. V.; Jones, S. C.; Hayden, L. E.; Kimyonok, A.; South, C. R.; Weck, M.; Kippelen, B.; Marder, S. R. *Organometallics* **2007**, *26*, 4816-4829.
- (40) Feng, K.; Zuniga, C.; Zhang, Y.-D.; Kim, D.; Barlow, S.; Marder, S. R.; Brédas, J. L.; Weck, M. *Macromolecules* **2009**, *42*, 6855-6864.
- (41) Kimyonok, A.; Domercq, B.; Haldi, A.; Cho, J.-Y.; Carlise, J. R.; Wang, X.-Y.; Hayden, L. E.; Jones, S. C.; Barlow, S.; Marder, S. R.; Kippelen, B.; Weck, M. *Chem. Mater.* **2007**, *19*, 5602-5608.
- (42) Loewe, R. S.; McCullough, R. D. *Polymer* **1999**, *40*, 852-853.
- (43) Taranekekar, P.; Fulghum, T.; Baba, A.; Patton, D.; Advincula, R. *Langmuir* **2007**, *23*, 908-917.
- (44) Brookins, R. N.; Schanze, K. S.; Reynolds, J. R. *Macromolecules* **2007**, *40*, 3524-3526.
- (45) Lakshmipathi, P.; Crevisy, C.; Gree, R. *J. Comb. Chem.* **2002**, *4*, 612-621.
- (46) Bilge, A.; Zen, A.; Forster, M.; Li, H.; Galbrecht, F.; Nehls, B. S.; Farrell, T.; Neher, D.; Scherf, U. *J. Mater. Chem.* **2006**, *16*, 3177-3182.
- (47) Takahashi, M.; Masui, K.; Sekiguchi, H.; Kobayashi, N.; Mori, A.; Funahashi, M.; Tamaoki, N. *J. Am. Chem. Soc.* **2006**, *128*, 10930-10933.
- (48) Thelakkat, M.; Schmidt, H.-W. *Adv. Mater.* **1998**, *10*, 219-223.
- (49) Geise, A.; Fan, B.; Benmansour, H.; Castro, F.; Heier, J.; Keller, B.; Mayerhofer, K. E.; Nuesch, F.; Hany, R. *Sol. Energy Mater. Sol. Cells* **2008**, *92*, 464-473.
- (50) Ford, W. E.; Hiratsuka, H.; Kamat, P. V. *J. Phys. Chem.* **1989**, *93*, 6692-6696.

- (51) Tauber, M. J.; Kelley, R. F.; Giaimo, J. M.; Rybtchinski, B.; Wasielewski, M. R. *J. Am. Chem. Soc.* **2006**, *128*, 1782-1783.
- (52) O'Neil, M. P.; Niemczyk, M. P.; Svec, W. A.; Gosztola, D.; L.Gaines, G.; Wasielewski, M. R. *Science* **1992**, *257*, 63-65.
- (53) Shoaee, S.; An, Z.; Zhang, X.; Barlow, S.; Marder, S. R.; Duffy, W.; Heeney, M.; McCulloch, I.; Durrant, J. R. *Chem. Commun.* **2009**, 5445-5447.
- (54) Ohkita, H. C., S.; Astuti, Y.; Duffy, W.; Tierney, S.; Zhang, W.; Heeney, M.; McCulloch, I.; Nelson, J.; Bradley, D. D. C.; Durrant, J. R. *J. Am. Chem. Soc.* **2008**, *130*, 3030-3042.

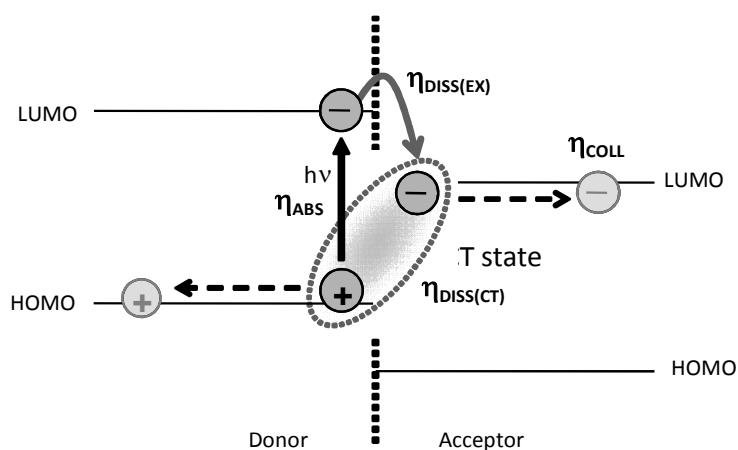
## CHAPTER 4

### PERYLENE DIIMIDE-BASED ACCEPTORS WITH VARIOUS ELECTRON AFFINITIES AND MISCIBILITY WITH P3HT AND THEIR INFLUENCE ON THE YIELDS OF CHARGE PHOTO-GENERATION IN DONOR/ACCEPTOR BLENDS

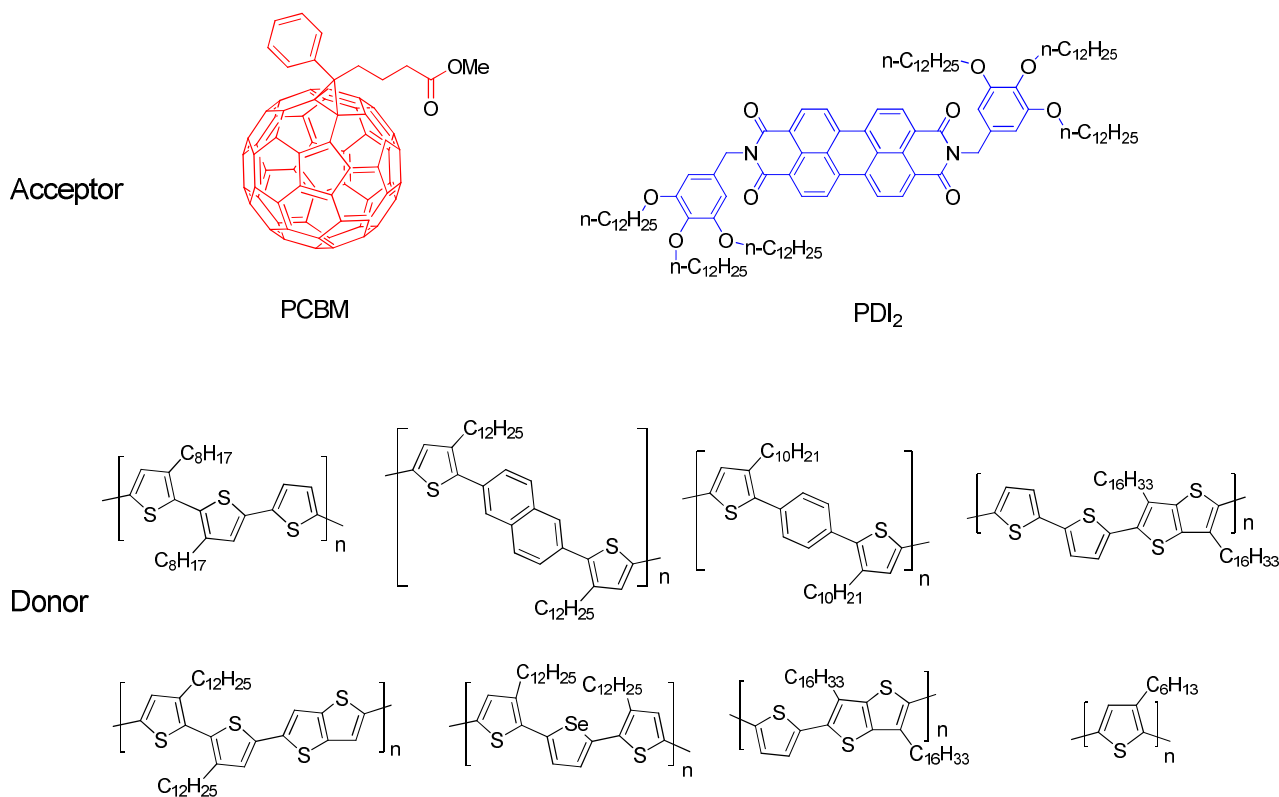
#### 4.1 Introduction

Organic donor/acceptor (D/A) blends have been drawing an increasing amount of attention for solar cell applications,<sup>1-3</sup> and the state-of-the-art solar cells using D/A blend as the active materials in bulk-heterojunction (BHJ) cells have power conversion efficiencies (PCEs) approaching 8%.<sup>4-5</sup> Organic photovoltaic (OPV) processes are based on photo-induced charge separation at the D/A interface following photo-excitation of the light-harvesting materials, as illustrated in Figure 4.1. The efficiency of such a charge-separation process is determined by the population of excitons that reach the D/A interface to generate charge-transfer (CT) states after photo-excitation. The yields of charge-transfer state generation is denoted  $\eta_{DISS(EX)}$ , and the yields of charge dissociation of these CT states is denoted as  $\eta_{DISS(CT)}$ . The combination of  $\eta_{DISS(EX)}$  and  $\eta_{DISS(CT)}$  are crucial factor affecting the charge photo-generation yield, and thus the photocurrent and overall PCEs of the solar cells.<sup>6-7</sup> The yields of the charge photo-generation (the sum of  $\eta_{DISS(EX)}$  and  $\eta_{DISS(CT)}$ ) in organic D/A blend films have been reported to depend on a range of variables, one of which is the free-energy difference driving charge-separation<sup>6-7</sup> ( $\Delta G_{CS}$ , which can be estimated from the difference between electron affinity of the acceptor ( $EA_A$ ), ionization potential of the donor ( $IP_D$ ), and the lowest singlet state of light-harvesting material ( $E_s$ ), according to  $\Delta G_{CS} = E_s - (IP_D + EA_A)$ ). Such a free-energy difference,  $\Delta G_{CS}$ , is essentially the thermal-energy loss in the photovoltaic process associated with photo-generated charges.<sup>6-7</sup> It was

previously found that the yield of charge photo-generation for a series of polythiophenes (as shown in Figure 4.2), including poly-3-hexylthiophenes (P3HT), blended with phenyl-C<sub>61</sub>-butyric acid methyl ester (PCBM), is highly dependent on  $\Delta G_{CS}$ ,<sup>1,7</sup> which might be related to the relative energy of the CT state and the triplet states in such blends. If the CT state is lower in energy than the triplet-states (as in the case of P3HT and PCBM with large  $\Delta G_{CS}$ ) the CT state can lead to free charge carriers. However, if the CT state is higher in energy than the available triplet states, intersystem crossing could occur from the CT state and lead to the generation of triplet-states rather than free charges.<sup>1,8-9</sup> According to transient absorption measurements of photo-generated free charges ( $\Delta OD$  measured at a time delay of 1  $\mu$ s after excitation), a relatively large  $\Delta G_{CS}$  (0.9 eV) was required to drive efficient charge-separation in the blend films of polythiophene/PCBM and thus to achieve efficient solar cells, as illustrated in Figure 4.3.



**Figure 4.1.** The energy level diagram of a donor/acceptor interface showing a simplified viewpoint of photo-excitation of an electron into the donor LUMO (with efficiency  $\eta_{ABS}$ ), followed by exciton dissociation via electron-transfer into the acceptor LUMO ( $\eta_{DISS(EX)}$ ) and migration of the separated charges away from the interface. It also illustrates the potential for electron transfer initially to generate a coulombically bound CT state that also requires dissociation ( $\eta_{DISS(CT)}$ ) before free charge carriers can be collected (This figure was adapted from Dr. Safa Shoaee in the Durrant group).

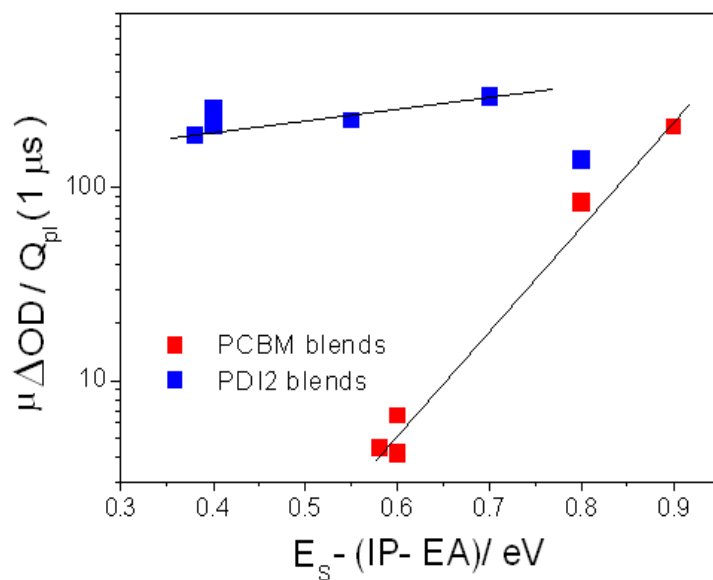


**Figure 4.2. The chemical structures of PCBM, PDI<sub>2</sub> and various polythiophenes with different IP and Es for the study of efficiency of charge photo-generation process and  $G_{CS}$  relationship.**

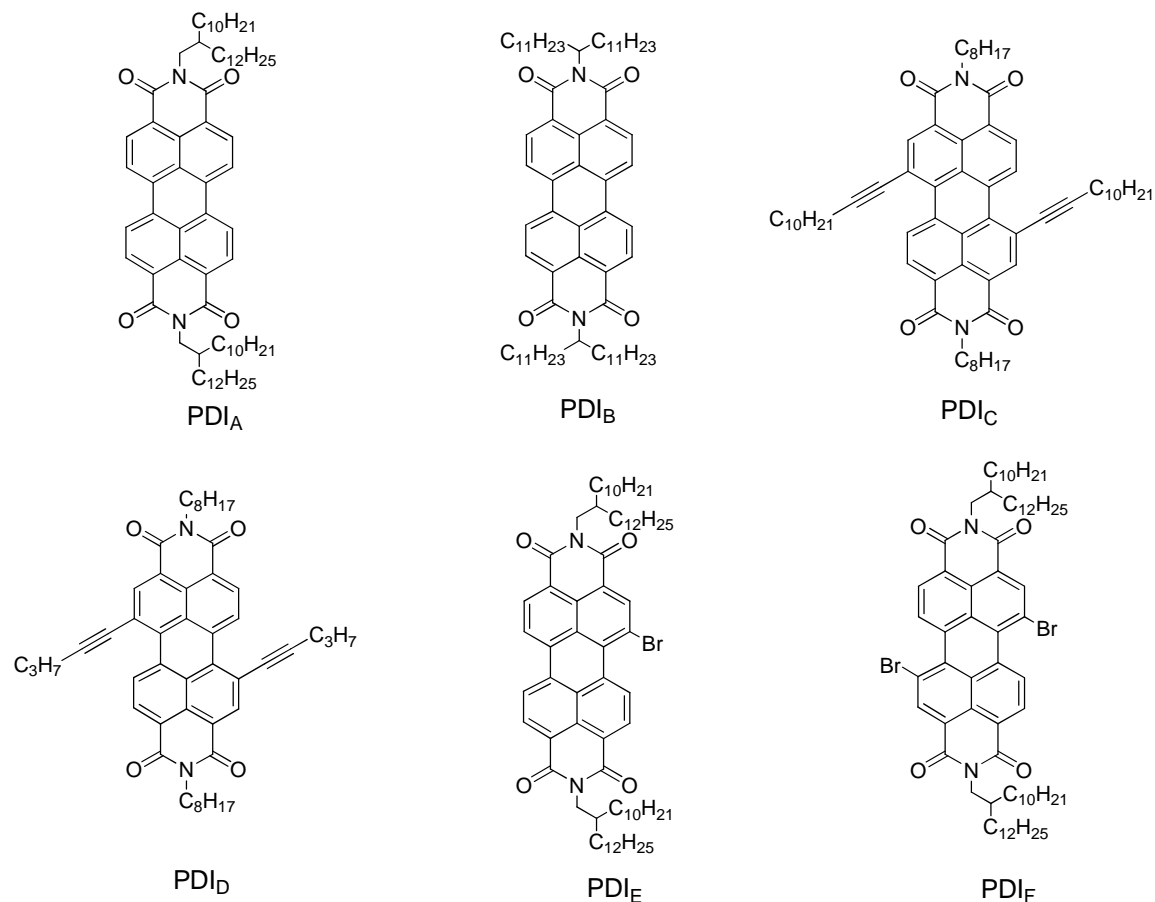
Perylene diimides (also known as PDIs) are attractive electron acceptors for studies of charge photo-generation in D/A blends because of their well-defined and intense radical anion absorption, together with their electron-accepting nature. Detailed examples regarding the successful use of PDI-based acceptors in OPVs and their respective device performances have been described earlier in Chapters 1 through 3. Recently, a comparison study of charge photo-generation between polythiophene:PCBM blends and the respective polythiophene:PDI<sub>2</sub> blends was reported.<sup>6</sup> It was observed that for equivalent values of  $\Delta G_{CS}$ , the polythiophene:PDI<sub>2</sub> films could offer higher charge-generation efficiency, and



that their yields of dissociated charges (as estimated from transient absorption spectra at 1  $\mu$ s at 910 nm) showed much less dependence upon  $\Delta G_{CS}$  compared with the polythiophene:PCBM blends, as shown in Figure 4.3. Hence, even with their limited solar cell performance compared to polythiophene:PCBM based solar cells, which may be due to unfavorable phase-separation and poor charge carrier collection, the higher yields of charge photo-generation in polythiophene:PDI<sub>2</sub> system inspire further research using PDIs as alternative acceptors to PCBM for D/A-based BHJ cells. As shown in Figure 4.4, this thesis aims to explore the synthesis of a series of PDI derivatives (PDI<sub>x</sub>, X = A to F) with different substituents on imide- and/or bay-positions and various EA. The photo-physical studies in these P3HT:PDI<sub>x</sub> (X = A to F) blends could show the role of PDI-based acceptors on charge photo-generation in D/A blend films.



**Figure 4.3.** The transient absorption signal measured at 1  $\mu$ s of various polythiophene: PDI<sub>2</sub> (blue) or polythiophene: PCBM (red) (1:1 weight ratio) blend films plotted against  $-\Delta G_{CS}$ , estimated as  $E_s - (IP_D - EA_A)$ . The transient signal has been corrected for variation in the absorbance at the excitation wavelength (500 nm) and PL quenching,  $\lambda_{probe} = 700$  nm at 50  $\mu Jcm^{-2}$  (This figure was adapted from Dr. Safa Shoaee in the Durrant group).

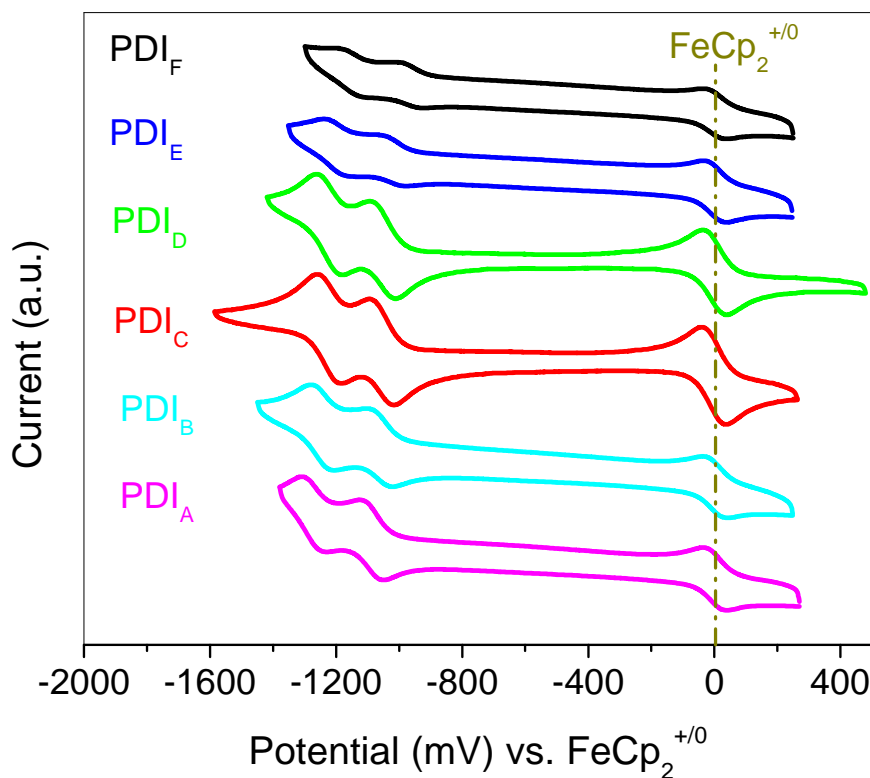


**Figure 4.4.** The chemical structures of PDI<sub>X</sub> (X = A to F) derivatives.

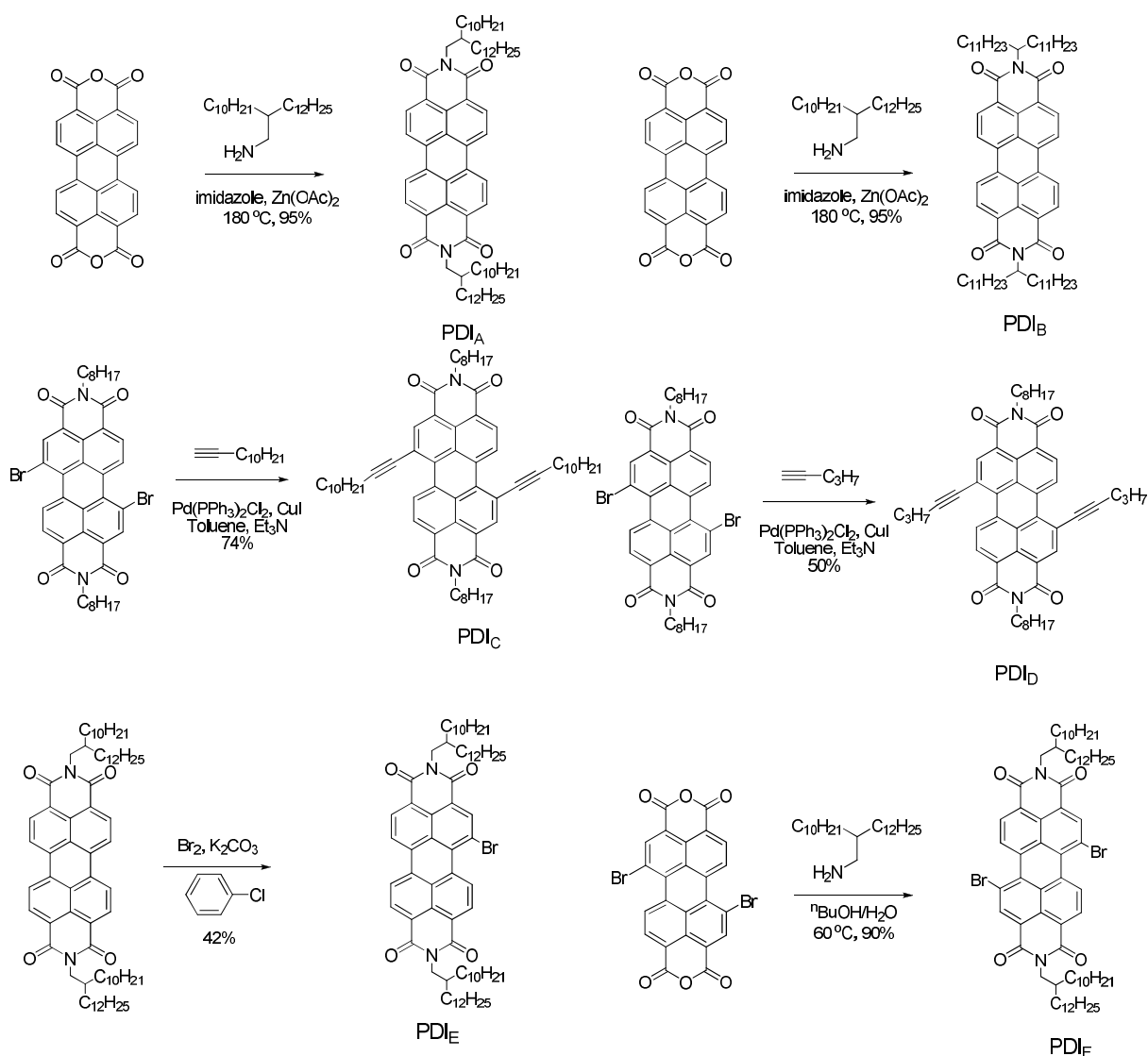
## 4.2 Synthesis and redox properties of PDI<sub>X</sub> (X = A to F) derivatives

Synthesis of PDI<sub>X</sub> (X = A to F) derivatives are illustrated in Scheme 4.1. Here, PDI<sub>A</sub>,<sup>10</sup> PDI<sub>B</sub>,<sup>11</sup> PDI<sub>C</sub>,<sup>12</sup> PDI<sub>F</sub>,<sup>13</sup> and, PDI<sub>I</sub><sup>14</sup> were synthesized as described in the literature. PDI<sub>D</sub>, which has a similar chemical structure to that of PDI<sub>C</sub>, was prepared following a modification of the procedure described for PDI<sub>C</sub>.<sup>15</sup> PDI<sub>E</sub> was synthesized in a moderate yield via direct bromination from PDI<sub>A</sub>. It should be noted that monobromo- and dibromo-substituted and unsubstituted PDIs are normally obtained in this bromination reaction, making the purification of PDI<sub>E</sub> tedious. The relative EAs of this PDI<sub>X</sub> (X = A to F) derivatives were estimated using cyclic voltammetry. The potentials determined from the

cyclic voltammograms shown in Figure 4.5 were referenced to the ferrocenium/ferrocene ( $\text{FeCp}_2^{+/0}$ ) redox couple by using ferrocene as an internal standard. The first electrochemical half-wave reduction potentials  $E_{1/2}^{0/-}$  were used to estimate the solid-state EA for the PDIs according to  $\text{EA} = -e(E_{1/2}^{0/-} + 4.8 \text{ V})$  based on the solid-state IP value of 4.8 eV for ferrocene.<sup>16</sup> In all cases, reversible reduction waves for the first and second reduction were observed. The estimated EAs of the PDI acceptors are listed in Table 4.1, and they vary by 140 meV. This estimation of EAs assumes that solid-state polarization energies and solvation effects are constant for all  $\text{PDI}_X$  ( $X = \text{A to F}$ ) in dichloromethane solution, which could be reasonable because of their structural similarities.



**Figure 4.5.** The cyclic voltammograms of  $\text{PDI}_X$  ( $X = \text{A to F}$ ) in  $\text{CH}_2\text{Cl}_2$ , 0.1 M  $[n\text{-Bu}_4\text{N}][\text{PF}_6]$ , with a scan rate =  $50 \text{ mVs}^{-1}$  for each material.  $\text{FeCp}_2$  was used as an internal reference.

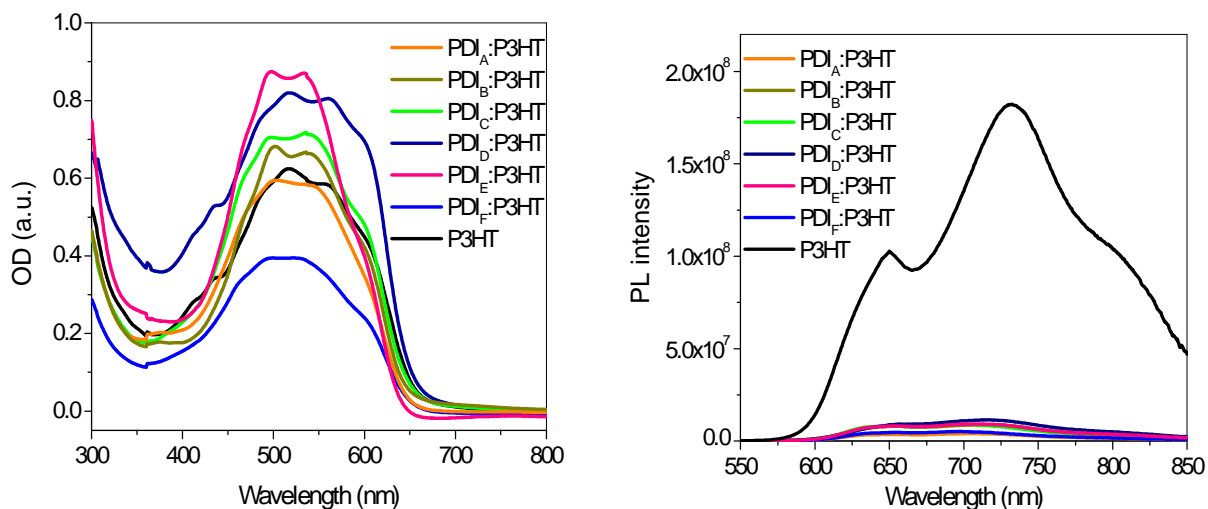


**Scheme 4.1.** The synthetic scheme for the PDI<sub>X</sub> (X = A to F) materials.

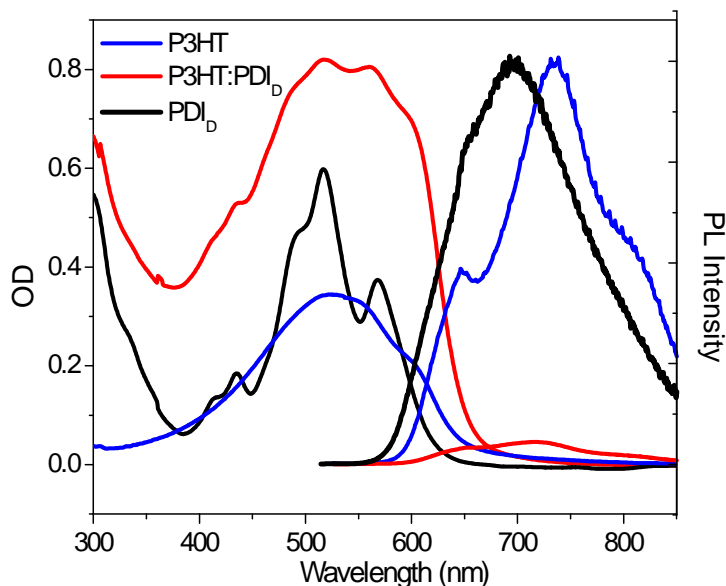
### 4.3 Optical properties of P3HT:PDI<sub>X</sub> (X = A to F) blends

All these PDI<sub>X</sub> (X = A to F) materials showed typical PDI-type UV-Vis absorption in solution with PDI<sub>C</sub> and PDI<sub>D</sub> exhibiting  $\sim 20$  nm red-shift of  $\lambda_{\text{max}}$  compared with the other PDI materials, probably due to the extended conjugation from the two incorporated ethynyl groups in the PDI-bay positions.<sup>15</sup> Furthermore, this series of PDI derivatives were all found to blend readily with P3HT in common organic solvents, such as chloroform and

chlorobenzene, resulting in high, optical quality films obtained by spin-coating a P3HT:PDI<sub>X</sub> (X = A to F) mixture (1:1 weight ratio) from chloroform solutions. The UV-Vis absorption spectra and photoluminescence (PL) spectra of these pristine spin-cast films, measured by Dr. Shaoee in the Durrant group, are quite similar to each other, as shown in Figure 4.6. Typical UV-Vis absorption spectra, from P3HT and PDI<sub>D</sub>, of the pristine materials and blend films are presented in Figure 4.7. It is apparent that the PDI absorption spectra overlap significantly with that of P3HT in films, implying that photo-excitation of the P3HT:PDI<sub>X</sub> (X = A to F) blends could, in principle, generate both P3HT and PDI<sub>X</sub> singlet excitons. Thin-film PL spectra were collected to evaluate the efficiency of exciton quenching for all P3HT:PDI<sub>X</sub> (X = A to F) blends. The absorption and emission spectra indicate that the singlet exciton of P3HT has a smaller bandgap than that of PDI. Consistent with this observation, the PDI-type emission was very strongly quenched (> 99%) for all P3HT:PDI<sub>X</sub> blend films relative to that of pristine films from PDI-based materials, suggesting possible rapid energy-transfer from PDI<sub>X</sub> to P3HT with the formation of PDI-based excitons and polarons following the photo-excitation of P3HT:PDI<sub>X</sub> blends. Hence, charge photo-generation more likely occurs via electron-transfer from P3HT singlet excitons to PDI acceptors. Weak residual P3HT emission was observed in these blend films, corresponding to 70 – 92 % photoluminescence quenching (PLQ) compared to the pristine P3HT films (determined by integration over the emission band with normalization for absorbance variations of the blend films and P3HT film), as detailed in Table 4.1.



**Figure 4.6.** The absorption and photoluminescence spectra measured for the following pristine P3HT film and blend films of PDI<sub>x</sub>:P3HT (X = A to F, 1:1 weight ratio) spin-cast from chloroform solution at 1000 rpm for 1 minute. The PL spectra were measured using 500 nm excitation and adjusted to the same absorbance at the excitation wavelength (These figures were adapted from Dr. Safa Shoaee in the Durrant group).



**Figure 4.7.** The absorption and photoluminescence spectra measured for the following pristine and blend films: PDI<sub>D</sub>, P3HT, and (1:1) P3HT:PDI<sub>D</sub>. The PL spectra were measured using 500 nm excitation, and the intensities were normalized according to the absorbance (This figure was adapted from Dr. Safa Shoaee in the Durrant group).

**Table 4.1. Properties of the P3HT:PDI<sub>x</sub> blends (Some data were collected by Dr. Safa Shaoee in the Durrant group).**

Blend (P3HT:PDI <sub>x</sub> )	E <sub>1/2</sub> <sup>0/-</sup> (V)	EA <sub>A</sub> <sup>a</sup> (eV)	ΔG <sub>CS</sub> <sup>b</sup> (eV)	ΔOD <sup>c</sup>	PLQ <sup>d</sup> (%)	ΔOD/PLQ
PDI <sub>A</sub>	-1.09	-3.71	0.72	4.2 × 10 <sup>-4</sup>	0.86	4.8 × 10 <sup>-4</sup>
PDI <sub>B</sub>	-1.09	-3.71	0.72	5.1 × 10 <sup>-4</sup>	0.92	4.7 × 10 <sup>-4</sup>
PDI <sub>C</sub>	-1.06	-3.74	0.75	3.7 × 10 <sup>-4</sup>	0.70	5.3 × 10 <sup>-4</sup>
PDI <sub>D</sub>	-1.05	-3.75	0.76	5.0 × 10 <sup>-4</sup>	0.90	5.6 × 10 <sup>-4</sup>
PDI <sub>E</sub>	-1.02	-3.78	0.79	5.1 × 10 <sup>-4</sup>	0.83	6.2 × 10 <sup>-4</sup>
PDI <sub>F</sub>	-0.96	-3.84	0.84	3.1 × 10 <sup>-4</sup>	0.88	4.5 × 10 <sup>-4</sup>
PDI <sub>2</sub>	-1.10	-3.70 <sup>14</sup>	0.70	2.9 × 10 <sup>-4</sup>	0.70	4.1 × 10 <sup>-4</sup>

a. Estimated electron affinities evaluated by cyclic voltammetry from the E<sub>1/2</sub><sup>0/-</sup> value. b. ΔG<sub>CS</sub> estimated as E<sub>S</sub> - (IP - EA), where IP is the ionisation potential of the polymer evaluated by an ambient ultraviolet photoelectron spectroscopy technique (4.8 eV for P3HT) and E<sub>S</sub>, the singlet exciton energy of the donor, measured from intercept of the normalized absorption and emission spectra. c. ΔOD evaluated from the amplitude of the transient absorbance at 1 μs decay following photo-excitation (λ<sub>probe</sub> = 700 nm), after correction for ground-state absorbance at the excitation wavelength. d. Steady-state PL quenching of the blend film relative to the corresponding pristine polymer film.

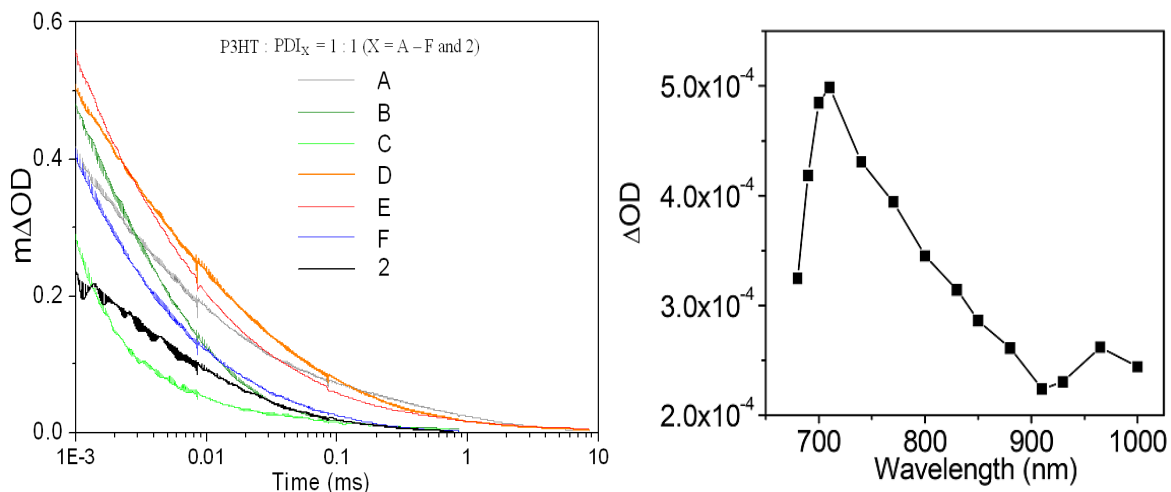
#### 4.4 Transient absorption of P3HT:PDI<sub>x</sub> (X= A to F) blends

Dr. Shaoee in the Durrant group used the transient absorption to monitor the yields of long-lived, dissociated charges on the microsecond timescale in each P3HT:PDI<sub>x</sub> blend film. Power law (ΔOD ∝ t<sup>-α</sup>) absorption transients (with 0.38 < α < 0.50) were observed for all these P3HT:PDI<sub>x</sub> films. The transient absorption spectra of these investigated blends exhibited a well-defined absorption maximum at approximately 700 nm that corresponds to PDI radical anions,<sup>11,17-18</sup> as well as a weaker, broad absorption between 900 and 1000 nm assigned to P3HT polarons.<sup>19-22</sup> The pristine P3HT and PDI films gave negligible transient signals on the same timescales, indicating the transient absorption in the blend films is due to the interaction of the two components. Furthermore, oxygen-independent decays of the transient absorption of all P3HT:PDI<sub>x</sub> (X = A to F) films suggest that these long-lived transient absorption should be assigned to the ion pair absorption rather than possible triplet-state absorption, since triplet state generally could be quenched with O<sub>2</sub>. These ΔOD signal intensities at 700 nm at a time delay of 1 μs, corresponding to the free PDI-based radical

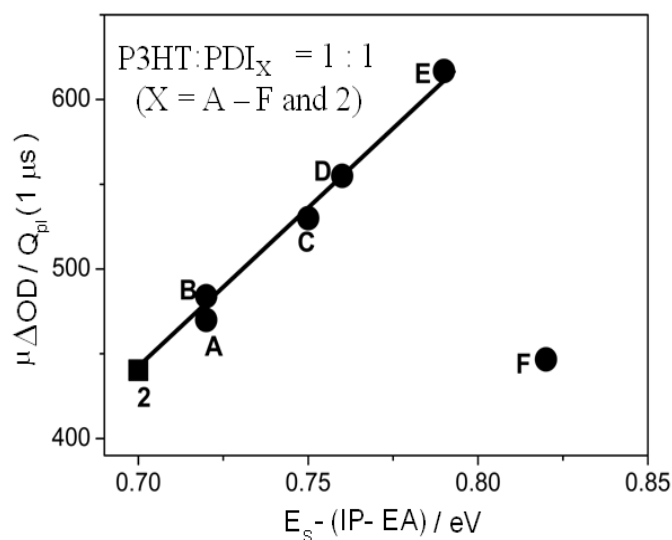
anion absorption, are summarized in Table 4.1 (normalized for variations ( $< \pm 35\%$ ) in the density of absorbed photons due to variations in film optical density at the excitation wavelength). It is worth noting that an increase in the  $\Delta OD$  greater than two-fold (at 1  $\mu\text{s}$  at 700 nm) for P3HT:PDI<sub>D</sub> relative to P3HT:PDI<sub>2</sub> was observed, consistent with the greater PL quenching for P3HT:PDI<sub>D</sub> blend film (as shown in Table 4.1). The increase in yield of long-lived ion-pairs could therefore be partially assigned to more efficient dissociation of initially generated excitons at the D/A interface. Here,  $\Delta OD/PLQ$  was used as a direct indicator, taking into account the small variations in PLQ observed between the blend films to account for changes in the efficiency of charge photo-generation, as described in literature.<sup>6-7,23</sup> Moreover, Figure 4.9 shows a plot of the correlation between the yield of photo-generated charges (estimated from  $\Delta OD/PLQ$ ) and the energetic driving force for charge separation  $\Delta G_{CS} = E_S - (IP_D + EA_A)$ . Estimates were performed using P3HT singlet energies for  $E_S$ , and a remarkably good correlation is observed between  $\Delta G_{CS}$  and  $\Delta OD/PLQ$ , with the exception of PDI<sub>F</sub>, wherein the polaron yield is observed to show a linear dependence with  $\Delta G_{CS}$ , increasing by  $\sim 40\%$  for each 0.1 eV increase in  $\Delta G_{CS}$ . The variation in  $\Delta G_{CS}$  between different blend films results solely from variations in the EAs of the PDIs, as both  $E_S$  and  $IP_D$  correspond to P3HT, which is invariant for this study. It is apparent that P3HT:PDI<sub>F</sub> blend film shows a low polaron yield considering its relatively large  $\Delta G_{CS}$ , which might be attributed to serious distortion of the planarity of the PDI due to the bulky 1,7-dibromo-substituents, causing possible changes in PDI-anion absorption coefficient as well as a lower electron mobility and film morphology in blends.<sup>24-25</sup> It should be noted that such a linear correlation is based on a relatively small variation (140 meV) of the  $\Delta G_{CS}$  compared to some



previously studied systems, and it might not be applicable to other systems. Moreover, there is no obvious dependence using the  $E_S$  of PDIs in estimating the  $\Delta G_{CS}$ .



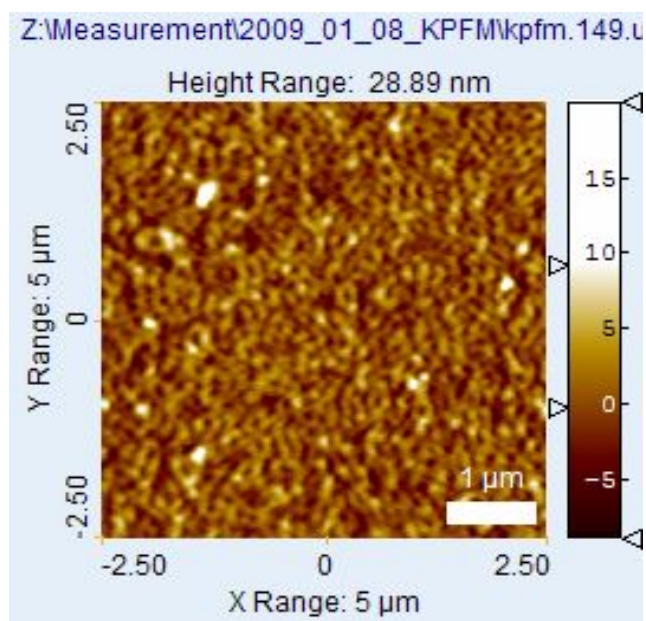
**Figure 4.8.** The transient absorption decay (left) for P3HT:PDI<sub>X</sub> (X = A –F and 2) in a N<sub>2</sub> environment, probed at 700 nm, with  $\lambda_{exc} = 520$  nm at 50  $\mu\text{Jcm}^{-2}$ . Spectrum of P3HT:PDI<sub>D</sub> at 1  $\mu\text{s}$  under N<sub>2</sub> using  $\lambda_{exc} = 520$  nm at 50  $\mu\text{Jcm}^{-2}$  (right) (These figures were adapted from Dr. Safa Shoaee in the Durrant group).



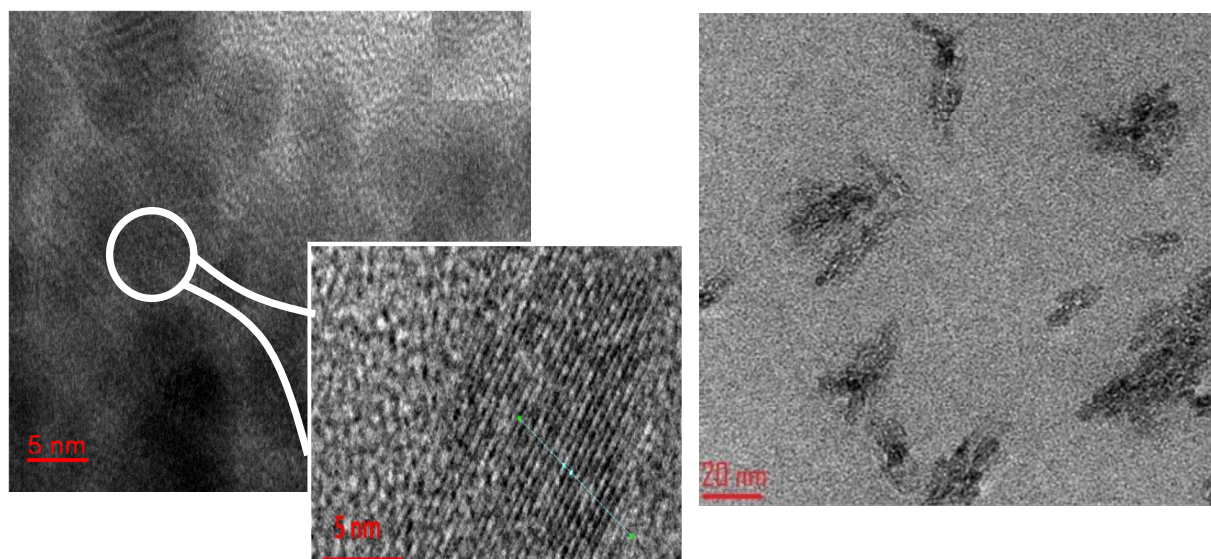
**Figure 4.9.** The transient absorbance signal measured at 1  $\mu\text{s}$  of various P3HT:PDI<sub>X</sub> (1:1 weight ratio) blend films with P3HT plotted against  $-\Delta G_{CS}$ , estimated as  $E_S - (IP_D - EA_A)$ . The transient signal has been corrected for variation in optical absorbance at the excitation wavelength (500 nm) and PL quenching.  $\lambda_{prb} = 700$  nm at 50  $\mu\text{Jcm}^{-2}$  (This figure was adapted from Dr. Safa Shoaee in the Durrant group).

#### 4.5 Morphology study and solar cells of P3HT:PDI<sub>D</sub> blends

The morphology of these blended films was studied using atomic force microscopy (AFM, Figure 4.10) and transmission electron microscopy (TEM, Figure 4.11). As shown in Figure 4.10, the P3HT:PDI<sub>D</sub> blends (on PEDOT/PSS coated ITO, ~ 70 nm in thickness, 1:1 weight ratio, spin-cast from 20 mg/mL chlorobenzene solution) have very smooth surfaces (average roughness = 2.5 nm). In contrast, the P3HT:PDI<sub>2</sub> blend films show phase-segregation on the scale of a few hundreds of nanometres, leading to some features that rise 500 – 600 nm out of the plane of the film (average roughness is 100 nm).<sup>6</sup> These large features were assigned to the PDI aggregates, as described earlier in literature.<sup>6</sup> The much smoother morphology of P3HT:PDI<sub>D</sub> indicates that PDI<sub>D</sub> could disperse within the P3HT phase much better than PDI<sub>2</sub>, which could be advantageous for solar cell applications. Similar morphology was obtained for other P3HT:PDI<sub>x</sub> films, with average roughnesses of several nanometers, consistent with the observation of efficient PDI PLQ and reasonably efficient P3HT PLQ. The TEM data for P3HT:PDI<sub>D</sub> films show clear evidence for the crystallinity of small PDI domains, consistent with the absorption spectra and the well-established tendency of PDIs to  $\pi$ - $\pi$  stack. The lattice spacing of PDI<sub>D</sub> crystallites was determined from these TEM images to be 0.6 nm, which is typically observed for PDI crystallites. The morphology of P3HT:PDI<sub>D</sub> blend is consistent with that observed by Friend's group, where the polymer:PDI blends they studied showed small features on the order of tens of nanometres and some evidence of perylene aggregation in one case of P3HT:PDI blend.

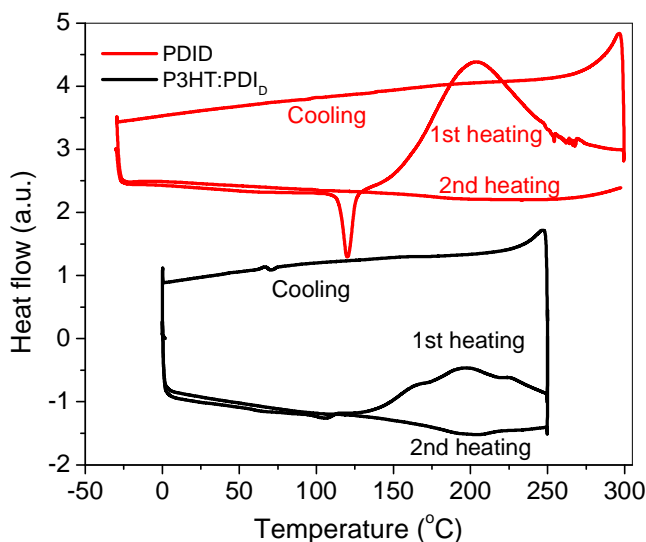


**Figure 4.10.** The AFM images of P3HT:PDI<sub>D</sub> (1:1 weight ratio) blends. The films were prepared via spin-casting from 20 mg/mL chlorobenzene solution on PEDOT:PSS coated ITO with a spin rate of 700 rpm for 1 minute (This figure was adapted from Dr. Debin Wang in the Riedo group).



**Figure 4.11.** The TEM micrographs of P3HT:PDI<sub>D</sub> (left) film (expanded region, centre: crystallisation of PDI<sub>D</sub> lattice) and P3HT:PDI<sub>2</sub> (right).<sup>6</sup> (This figure was adapted from Dr. Safa Shoaee in the Durrant group).

BHJ OPV devices were constructed and characterized by Dr. Cheun in the Kippelen group using P3HT:PDI<sub>D</sub> and P3HT:PDI<sub>2</sub> (1:1 weight ratio of P3HT and PDI acceptor) blends with an average active layer thickness of ~ 70 nm. The P3HT:PDI<sub>D</sub> blend solar cell shows a PCE of ~ 0.001% with a short-circuit current ( $J_{SC}$ ) of 0.040 mA/cm<sup>2</sup> and an open-circuit voltage ( $V_{OC}$ ) of 0.055 V. All parameters are higher than that observed for devices based on the P3HT:PDI<sub>2</sub> blend with PCEs << 0.001%.<sup>6</sup> The poorer device performance of the cells based on P3HT:PDI<sub>2</sub> blend could be attributed to the significant phase-separation and subsequent formation of large PDI<sub>2</sub> aggregates. It should be noted that post-annealing of the pristine P3HT:PDI<sub>D</sub> blend at 175 °C for 15 minutes could result in solar cells with much better performance (PCE = 0.013%,  $V_{OC}$  = 0.34 V and  $J_{SC}$  = 0.13 mA/cm<sup>2</sup>) and much higher yields of charge photo-generation, according to transient absorption at 1μs (~ two folds). However, according to differential scanning calorimetry (DSC) analysis of PDI<sub>D</sub> and P3HT:PDI<sub>D</sub> blend (1:1 weight ratio), there are exothermic processes occurring upon heating at *ca.* 140 °C under nitrogen, as shown in Figure 4.12. Since PDI<sub>D</sub> does not exhibit obvious weight lost until *ca.* 300 °C according to its thermogravimetric analysis (TGA) trace under nitrogen, such an exothermic process might be attributed to thermal-cross-linking, probably on the triple bond in PDI<sub>D</sub>. This observation indicates that the OPV performance increasing upon thermal-annealing might also be attributed to the chemical process, resulting in the formation of new materials in the active layers. Furthermore, there was no dramatic improvement in the overall device PCEs for solar cells with various P3HT:PDI<sub>D</sub> blend ratios (from 1: 1 to 1:4 D/A weight ratio), and all these devices exhibit PCEs lower than 0.002%.

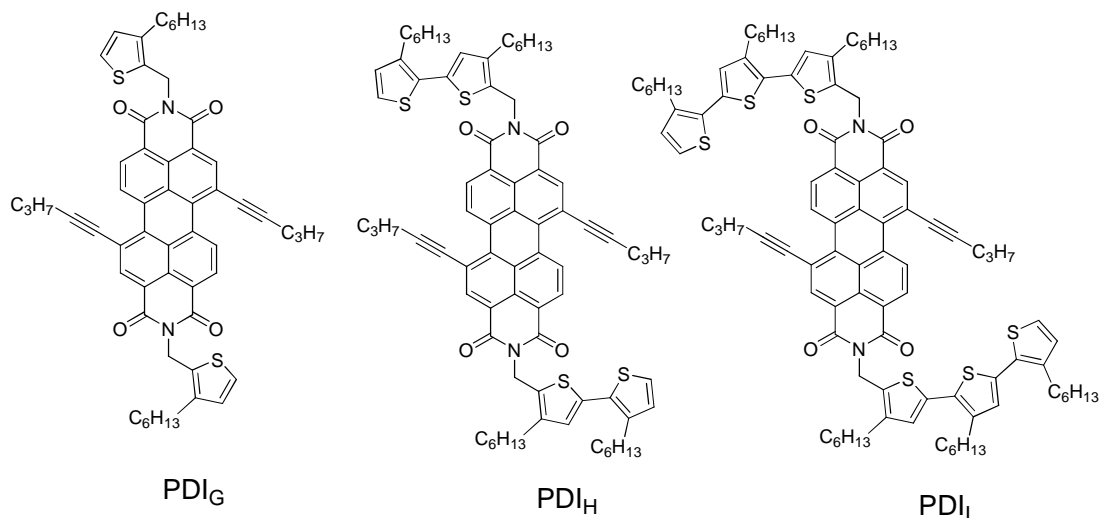


**Figure 4.12.** The DSC traces for PDI<sub>D</sub> and P3HT:PDI<sub>D</sub> (sample prepared from 1:1 weight ratio blend in CHCl<sub>3</sub> solution) under nitrogen.

#### 4.6 Synthesis of new PDI<sub>X</sub> (X= G to I) materials

Although the yield of charge photo-generation as well as the respective solar cell performance for P3HT:PDI<sub>D</sub> blends are much higher than that of the P3HT:PDI<sub>2</sub> blends, the overall PCEs of this system are still considerably smaller than the best state-of-the-art solar cells using fullerene-based acceptors.<sup>4-5,26-28</sup> To better understand the role of the miscibility between P3HT and PDI for the overall solar cell performance, new PDI materials, PDI<sub>X</sub> (X =G to I), with incorporated oligo-3-hexyl-thiophenes on imide positions were synthesized, as shown in Figure 4.13 and Scheme 4.2. The similar PDI-core structure of these new PDI-based materials relative to PDI<sub>D</sub> could ensure them similar electrical and optical properties as well as the promising photo-physics in the blend with P3HT as PDI<sub>D</sub>. The chemical similarity of oligo-3-hexyl-thiophene moieties to P3HT potentially could help to increase the

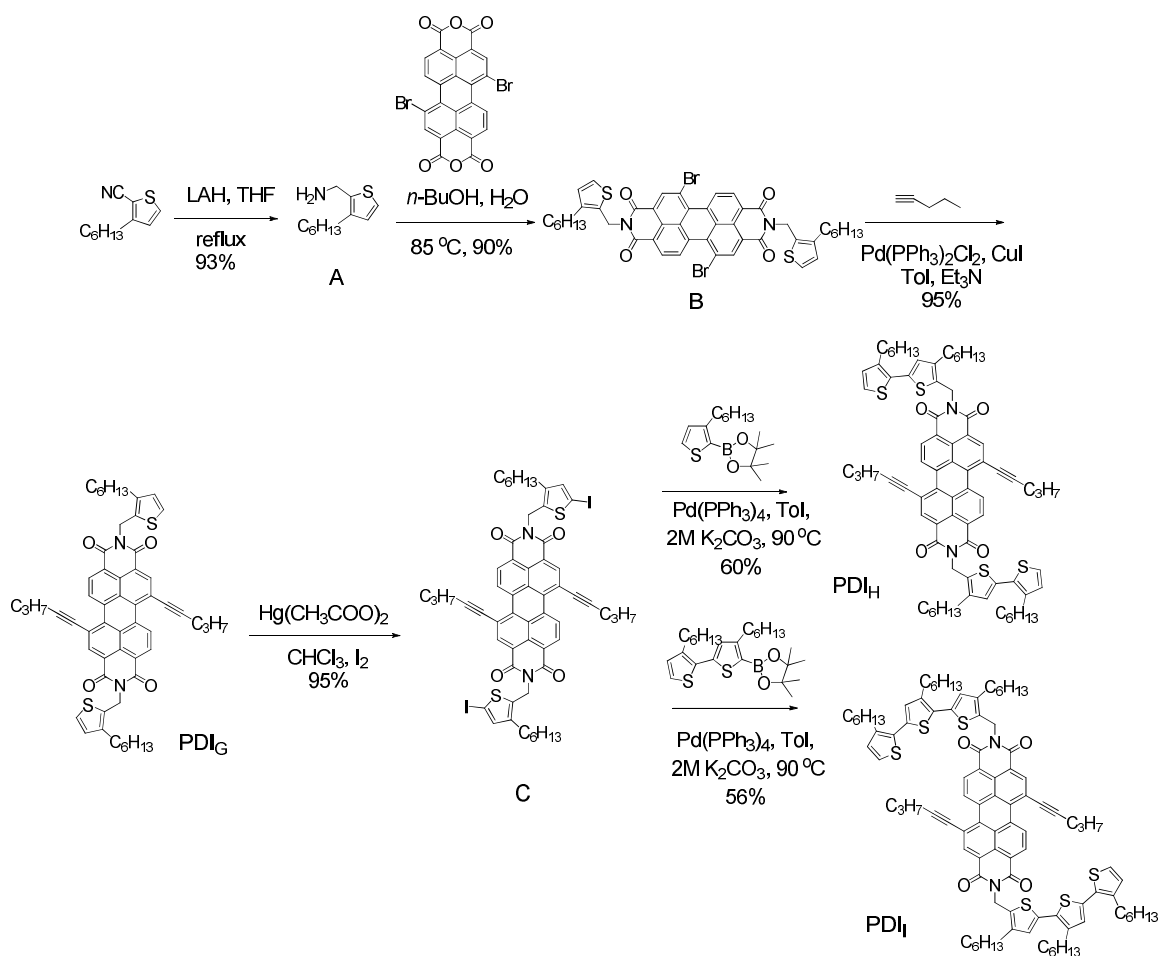
miscibility of these new PDIs with P3HT in films, which might lead to better solar-cell performance.



**Figure 4.13.** The chemical structures of PDI materials with oligo-3-hexyl-thiophene moieties.

As shown in Scheme 4.2, the three new PDI materials, PDI<sub>X</sub> (X = G to I), were synthesized in a straightforward fashion. Compound **B** was synthesized through a condensation reaction<sup>29</sup> between (3-hexylthiophen-2-yl)methanamine and 1,7-dibromoperylene-3,4,9,10-tetracarboxylic acid dianhydride<sup>29</sup> in a good yield via a literature procedure.<sup>11,29-30</sup> Sonogashira coupling between **B** and pent-1-yne afforded PDI<sub>G</sub> in an excellent yield using Pd(PPh<sub>3</sub>)<sub>2</sub>Cl<sub>2</sub> as a catalyst.<sup>17,31</sup> Mercury(II)-mediated iodination of PDI<sub>G</sub> afforded compound **C** in an excellent yield with the iodine group on the 2-position on each 3-hexylthiophene ring; The commonly used NBS-based bromination was avoided due to the possibility of side-reaction on the CH<sub>2</sub> group at the PDI imide positions. It is worth noting only the 2-position on 3-hexylthiophene ring could be iodinated using such a mercury (II) catalyzed reaction.<sup>32</sup> PDI<sub>H</sub> and PDI<sub>I</sub> were then synthesized via Suzuki coupling<sup>33</sup> between compound **C** and 2-(3-hexylthiophen-2-yl)-4,4,5,5-tetramethyl-1,3,2-dioxaborolane<sup>32</sup> or 2-(3',4'-dihexyl-2,2'-bithiophen-5-yl)-4,4,5,5-tetramethyl-1,3,2-

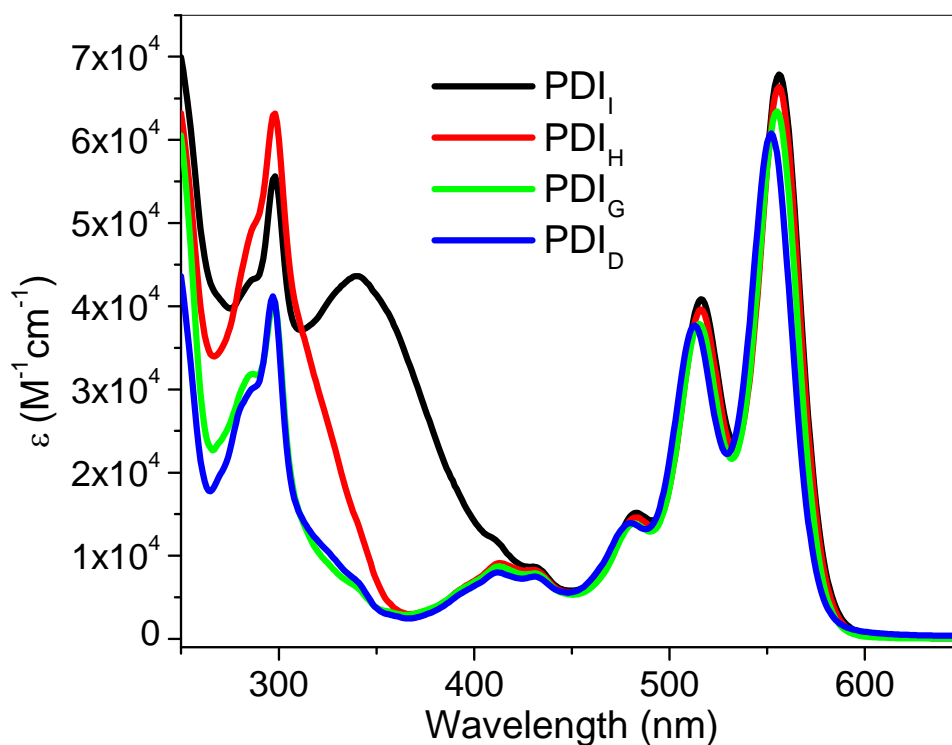
dioxaborolane<sup>32</sup> with *ca.* 60% yields using Pd(PPh<sub>3</sub>)<sub>4</sub> as a catalyst. It should be pointed out that PDI<sub>H</sub> and PDI<sub>I</sub> tended to stick on silica gel or alumina column for unknown reasons, which made their purification challenging using normal chromatography techniques. Size-exclusion chromatography with cross-linked polystyrene beads was used to obtain PDI<sub>H</sub> and PDI<sub>I</sub> with satisfactory purity. Furthermore, it was found that Stille coupling<sup>34</sup> is not suitable for preparing PDI<sub>H</sub> and PDI<sub>I</sub> using compound **C** and respective tin reagents, since less than 10% yields were obtained for both compounds. All three new PDI materials exhibit excellent solubility in common organic solvents, including toluene, chloroform, and chlorobenzene, because of the attached oligothiophene moieties.



**Scheme 4.2.** The synthetic scheme for the three new PDI materials.

#### 4.7 Optical and electrochemical properties of new PDI<sub>X</sub> (X= G to I)

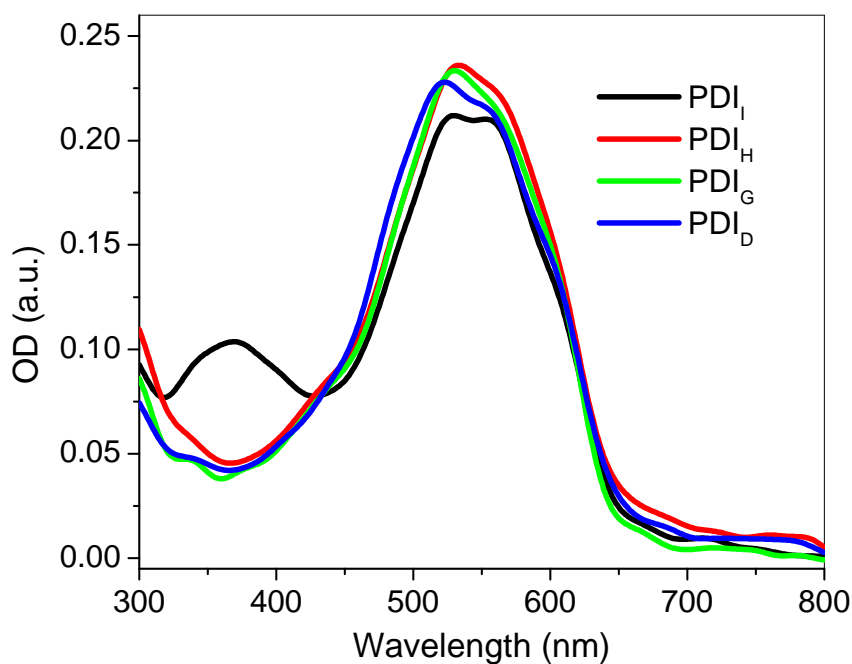
The UV-Vis absorption spectra of PDI<sub>X</sub> (X = G to I) and PDI<sub>D</sub> were shown in Figure 4.14 (*ca.*  $1 \times 10^{-5}$  mol/L in CHCl<sub>3</sub>). The PDI characteristic absorption band of PDI<sub>X</sub> (X = G to I and D) are similar in shape as well as the peak absorption coefficient between 400 – 600 nm as PDI<sub>D</sub>. There is a 2 nm red-shift for the lowest-energy band along with a slight increase of the peak molar absorption coefficient as each 3-hexylthiophene unit is added. The obvious absorption difference, especially for PDI<sub>G</sub> and PDI<sub>I</sub>, on the high energy portion (between 200 – 400 nm) can be attributed to the absorption of the oligo-3-hexylthiophenes on the PDI side-chains.



**Scheme 4.14.** The UV-Vis absorption spectra of PDI<sub>X</sub> (X = G to I) and PDI<sub>D</sub> in dilute chloroform solution with concentration of *ca.*  $1 \times 10^{-5}$  mol/L.



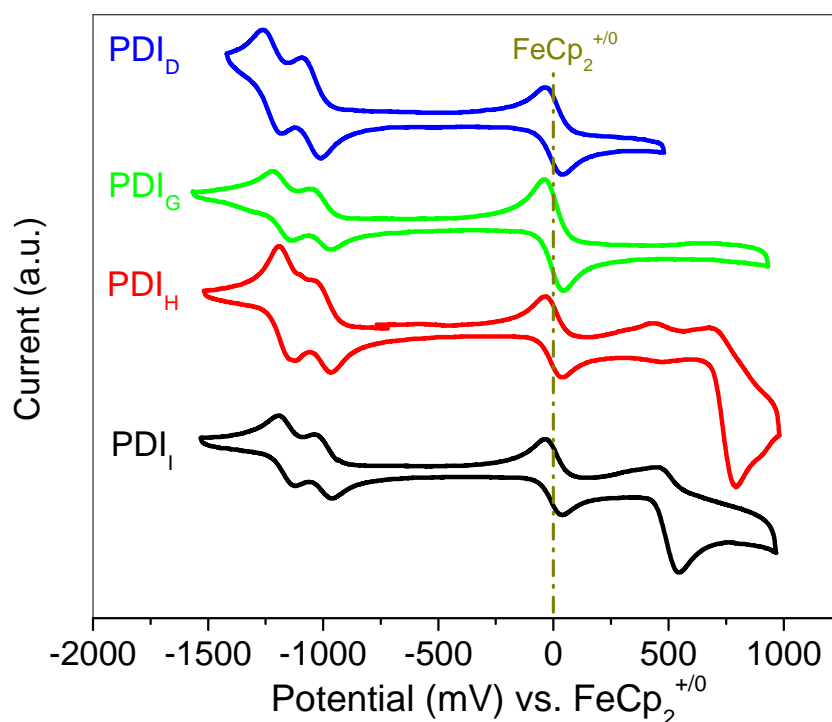
These three new PDI derivatives were all found to blend readily with P3HT, resulting in high quality optical films of P3HT:PDI<sub>X</sub> (X = G to I) blends (1:1 weight ratio) via spin-coating from chlorobenzene solutions. The thin-film UV-Vis absorption spectra of P3HT:PDI<sub>X</sub> (X = G to I, and D) on glass are shown in Figure 4.15. Similar to the solution spectra, the thin-film absorption spectra of the blends are quite similar in shape because of the similar PDI core structures and the use of the same donor polymer, P3HT. The exception is the P3HT:PDI<sub>I</sub> blend. The high energy band, with maximum at *ca.* 380 nm, in the thin film of the P3HT:PDI<sub>I</sub> blend can be attributed to the absorption from the oligo-3-hexylthiophenes, which was also observed in the solution absorption spectrum of PDI<sub>I</sub>.



**Scheme 4.15.** The thin-film UV-Vis absorption of P3HT:PDI<sub>X</sub> (X = G to I, and D, 1:1 weight ratio, 5 mg/mL) on glass, spin-casted from chlorobenzene solution with a rate of 1000 rpm for 1 minute.

As shown in Figure 4.16 and Table 4.2, the redox properties of PDI<sub>X</sub> (X = G to I) and PDI<sub>D</sub> were investigated using cyclic voltammetry (CV) in anhydrous dichloromethane,

using  $\text{FeCp}_2$  as an internal reference. For reduction, the half-wave potential ( $E_{1/2}^{0/-}$  and  $E_{1/2}^{-/2-}$ ) values of  $\text{PDI}_X$  ( $X = \text{G to I}$ ) and  $\text{PDI}_D$ , are *ca.* -1.1 V for the first reduction and *ca.* -1.2 V for the second reduction vs.  $\text{FeCp}_2^{+/0}$  redox couple, respectively. Here,  $\text{PDI}_X$  ( $X = \text{G to I}$ ) are more readily reduced than  $\text{PDI}_D$ , based on their less negative  $E_{1/2}^{0/-}$ , probably due to the inductive effect from the oligo-3-hexylthiophene moieties. Moreover, these PDI derivatives become slightly more readily reduced in dichloromethane with additional 3-hexylthiophene units. The EC type (reverse electron transfer followed by rapid chemical decomposition) molecular oxidation peak observed for  $\text{PDI}_H$  and  $\text{PDI}_I$ , with  $E_{1/2}^{+/0} = 0.73$  and 0.50 V, respectively, can be attributed to the oxidation of oligo-3-hexylthiophene moieties on the PDI imide positions.



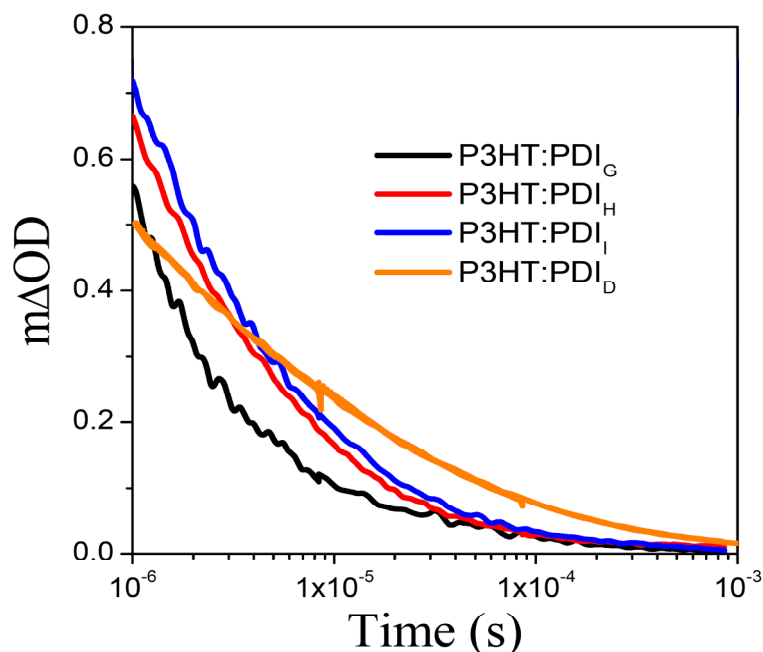
**Figure 4.16.** The cyclic voltammograms of  $\text{PDI}_D$  (blue),  $\text{PDI}_G$  (green),  $\text{PDI}_H$  (red), and  $\text{PDI}_I$  (black) in  $\text{CH}_2\text{Cl}_2$  (0.1 M  $[n\text{-Bu}_4\text{N}][\text{PF}_6]$ ), with scan rate =  $50 \text{ mV s}^{-1}$  for each material using  $\text{FeCp}_2$  as an internal reference.

**Table 4.2. Summary of the redox properties of PDI<sub>X</sub> (X = G – I and D) in CH<sub>2</sub>Cl<sub>2</sub> vs. FeCp<sub>2</sub><sup>+0</sup>**

	$E_{1/2}^{-/-}$ (V)	$E_{1/2}^{-/0}$ (V)	$E_{1/2}^{+/0}$ (V)
<b>PDI<sub>D</sub></b>	-1.22	-1.05	N.A.
<b>PDI<sub>G</sub></b>	-1.18	-1.01	N.A.
<b>PDI<sub>H</sub></b>	-1.16	-1.01	0.73
<b>PDI<sub>I</sub></b>	-1.16	-1.00	0.50

#### 4.8 Transient absorption of the P3HT:PDI<sub>X</sub> (X= G to I) blends

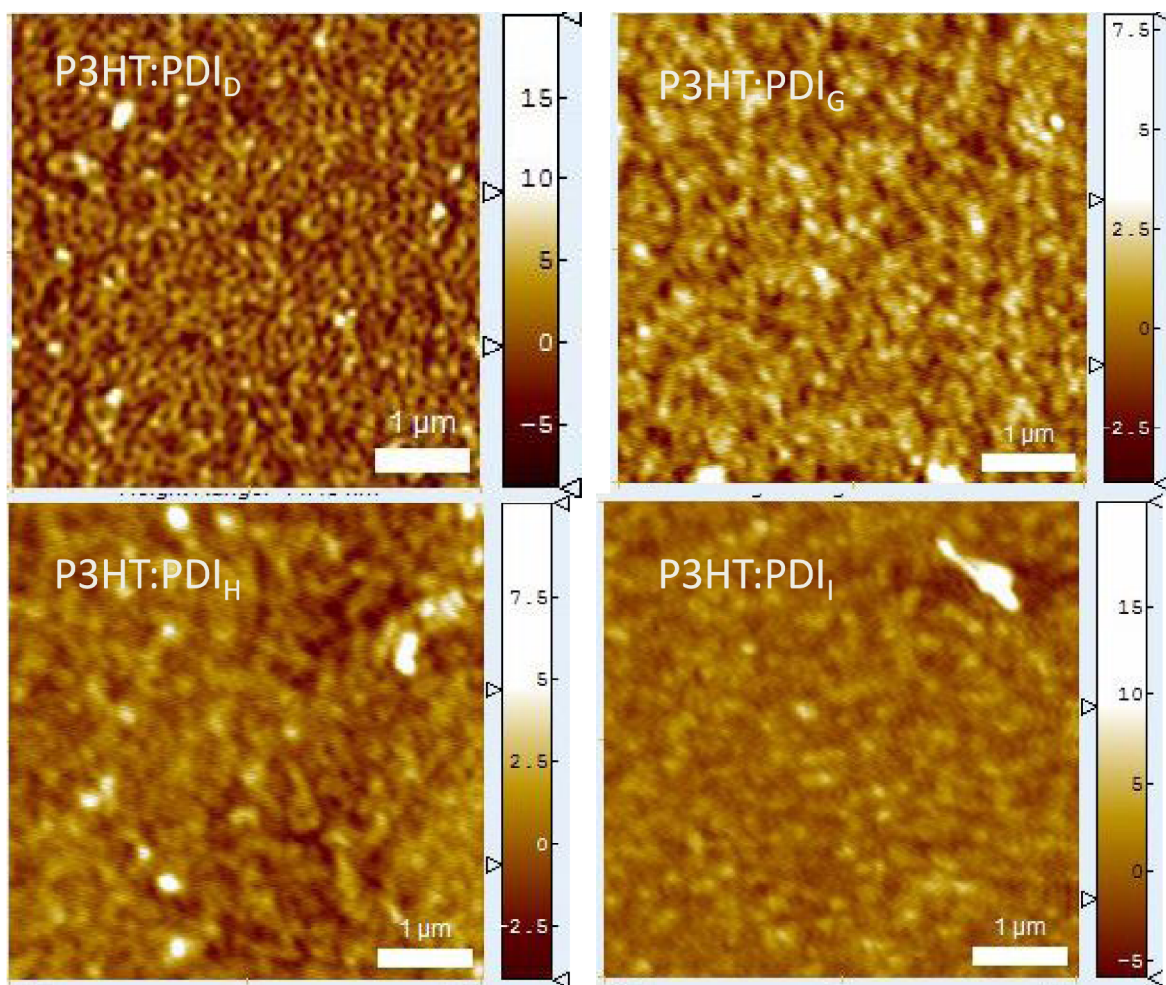
Transient absorption spectroscopy was employed to monitor the long-lived, dissociated charges on the microsecond timescale in these P3HT:PDI<sub>X</sub> blend films (X = G to I) By Dr. Safa Shoaee in the Durrant group. The transient absorption spectra of these P3HT:PDI<sub>X</sub> (X = G to I) films, similar to those of previous P3HT:PDI blend films, exhibited well-defined absorption maxima at approximately 700 nm that can be assigned to PDI radical anions<sup>11,17-18</sup> as well as a weaker, broad absorption between 900 and 1000 nm assigned to P3HT cation.<sup>19-22</sup> The transient absorption decay were shown in Figure 4.17. It is worth noting that there was an obvious increase in  $\Delta OD$  (at 1  $\mu$ s at 700 nm) for P3HT:PDI<sub>X</sub> (X = G to I) relative to P3HT:PDI<sub>D</sub>, although the decay of the absorption is faster compared to that of the P3HT:PDI<sub>D</sub> films. The increase in long-lived polarons (at 1  $\mu$ s) may, therefore, be due to more efficient dissociation of initially generated excitons on the D/A interface, which might because of the better mixing of these new PDI materials with oligo-3-hexylthiophene moieties, although the increase in free energy of charge separation resulting from lower EA might also contribute to the increase in yields of charge photo-generation. However, no linear correlation between the charge photo-generation and  $\Delta G_{CS}$  were observed for these series materials with PDI<sub>D</sub>.



**Figure 4.17.** The transient absorption decay for P3HT:PDI<sub>X</sub> (X = G to I, and D) in N<sub>2</sub> environment, monitored at 700 nm, with  $\lambda_{exc} = 520$  nm at  $50 \mu\text{Jcm}^{-2}$  (This figure was adapted from Dr. Safa Shoaee in the Durrant group).

#### 4.9 Morphology study and solar cells of P3HT:PDI<sub>X</sub> (X = G to I and D) blends

AFM topography images of these blend films, taken by Dr. Debin Wang in the Reido group, are shown in Figure 4.15. The AFM images show no obvious differences between the films. The average film-surface roughness for P3HT:PDI<sub>X</sub> blends (X = G to I and D) are 1.0, 1.2, 1.7, and 2.5 nm, respectively. The smaller surface roughness of the P3HT:PDI<sub>G</sub> blends compared with P3HT:PDI<sub>D</sub> might be attributed to better mixing for PDI<sub>G</sub> with P3HT than PDI<sub>D</sub> because of the chemical similarities between the 3-hexylthiophene moieties in PDI<sub>G</sub> with P3HT. The surface in the P3HT:PDI<sub>G</sub> blend is quite similar to the homopolymer films from P3HT prepared in a similar manner. However, as the number of 3-hexyl-thiophene repeat unit increases in these PDI materials, from PDI<sub>G</sub> to PDI<sub>H</sub> and PDI<sub>I</sub>, the average surface roughness observed in the AFM images also increases. The reason for this is still unclear.



**Figure 4.18.** The AFM (topography) images of P3HT:PDI<sub>x</sub> (X = G to I, and D, 1:1 weight ratio) on ITO substrates. The films were prepared via spin-casting from 20 mg/mL chlorobenzene solution on PEDOT:PSS coated ITOs at the rate of 1000 rpm for 1 minute. (These images were adapted from Dr. Debin Wang in the Riedo group)

BHJ solar cell devices were constructed by Dr. Hyeunseok Cheun in the Kippelen group using P3HT:PDI<sub>x</sub> (X = G to I, 1:1 weight ratio) blends, and the device performances are summarized in Table 4.3. Here, all the devices showed very low performance with PCEs less than 0.1%. One of the reasons for low device performance might be low electron mobilities of the PDI-based materials (electron mobility is in the order of  $10^{-5}$  to  $10^{-6}$  cm<sup>2</sup>V<sup>-1</sup>s<sup>-1</sup> for these materials in OFETs measured by Dr. Shree P. Tiwari in the Kippelen group),

which could result in charge accumulation and inefficient charge collection, with possible unbalanced charge carrier mobilities. For the devices with average active layer thickness of *ca.* 70 nm, P3HT:PDI<sub>G</sub> cells show better performance as compared with the other two blend systems and P3HT:PDI<sub>D</sub>, with short-circuit current ( $J_{SC}$ ) and PCEs of  $0.35 \pm 0.08$  mA/cm<sup>2</sup> and  $0.028 \pm 0.006$  %, respectively. The large increase (more than 20 times) of  $J_{SC}$  and PCEs for devices from P3HT:PDI<sub>G</sub> over P3HT:PDI<sub>D</sub> might be attributable to the better mixing of the donor and acceptor materials, which is consistent with the AFM surface average roughness measurement of the smoother P3HT:PDI<sub>G</sub> blends. Although the devices from P3HT:PDI<sub>H</sub> and P3HT:PDI<sub>I</sub> are both better than that from P3HT:PDI<sub>D</sub>, the improvement is much smaller. The reason for this observation is still unclear.

**Table 4.3. Summary of the solar cell performance of P3HT:PDI<sub>X</sub> (X = G to I and D)**

Devices	$V_{OC}$ (mV)	$J_{SC}$ (mA/cm <sup>2</sup> )	FF	PCEs (%)
<b>P3HT:PDI<sub>D</sub></b>	$55 \pm 3$	$0.040 \pm 0.004$	$0.27 \pm 0.01$	0.001
<b>P3HT:PDI<sub>G</sub></b>	$253 \pm 6$	$0.35 \pm 0.08$	$0.29 \pm 0.01$	$0.028 \pm 0.006$
<b>P3HT:PDI<sub>H</sub></b>	$117 \pm 5$	$0.08 \pm 0.01$	$0.30 \pm 0.01$	0.003
<b>P3HT:PDI<sub>I</sub></b>	$143 \pm 12$	$0.08 \pm 0.02$	$0.32 \pm 0.01$	0.004

#### 4.10 Conclusions

A series of PDI-based acceptors PDI<sub>X</sub> (X = A to F) with different electron affinities have been synthesized, and the films of these materials blended with P3HT (in 1:1 weight ratio) were characterized with transient absorption spectroscopy, which was used to monitor the long-lived free PDI radical anion. The observations in this chapter provide further evidence that a key factor determining the efficiency of charge photo-generation at organic

D/A blend films is the free energy difference, referred to herein as  $\Delta G_{CS}$ . Generally, a larger  $\Delta G_{CS}$  for this series of blends results in a higher yield of charge photo-generation. A good linear correlation between  $\Delta G_{CS}$  and the yield of charge photo-generation was observed for  $PDI_X$  ( $X = A$  to  $E$ , with EA of  $\sim 140$  meV range), where the photo-generated charge yield was observed to show a linear dependence on  $\Delta G_{CS}$ , increasing by  $\sim 40\%$  for a 0.1 eV increase in  $\Delta G_{CS}$ . Furthermore, an increase in yields of the charge photo-generation was observed using blends of P3HT:  $PDI_X$  ( $X = G$  to  $I$ ), where this series of  $PDI_X$  has lower EA as well as attached oligo-3-hexyl-thiophene moieties as compared to  $PDI_D$ . However, no obvious correlation was observed between  $\Delta G_{CS}$  and the yield of charge photo-generation for these films. An approximate 20-fold increase in PCEs was observed for solar cells using P3HT: $PDI_G$  over P3HT:  $PDI_D$ , presumably due to better mixing between P3HT and  $PDI_G$  because of the incorporated 3-hexyl-thiophenes. However, no significant improvement of PCEs was obtained for solar cells with  $PDI_H$  and  $PDI_I$ , which have more oligo-3-hexylthiophene moieties, as compared to those using  $PDI_D$ ; the reason for this is still unclear.

#### 4.11 Experimental section

**General:** Most organic and inorganic chemicals used for the synthesis in this chapter were obtained from Aldrich and Alfa Aesar. Palladium-based catalysts were purchased from Strem Chemicals and used without further purification.  $PDI_A$ ,<sup>10</sup>  $PDI_B$ ,<sup>11</sup>  $PDI_C$ ,<sup>12</sup>  $PDI_F$ ,<sup>13</sup> and,  $PDI_I$ <sup>14</sup> were synthesized as described in the literature.  $^1H$  and  $^{13}C$  NMR spectra were collected on Bruker 400 or 500 MHz spectrometers using tetramethylsilane (TMS;  $\delta = 0$  ppm) as an internal standard. Mass spectra were measured on an Applied Biosystems 4700 Proteomics Analyzer using MALDI mode. Elemental analyses were carried out by Atlantic Microlabs using a LECO 932 CHNS elemental analyzer. Solution and thin film UV-Vis

absorption spectra were recorded on a Varian Cary 500 UV/Vis/near-IR spectrophotometer. Electrochemical measurements were carried out under nitrogen in deoxygenated 0.1 M solutions of tetra-*n*-butylammonium hexafluorophosphate in dry dichloromethane using a computer-controlled BAS 100B electrochemical analyzer, a glassy-carbon working electrode, a platinum-wire auxiliary electrode, and an Ag wire anodized with AgCl as a pseudo-reference electrode. Cyclic voltammetry was performed at a scan rate of 50 mV/s. The potentials were referenced to the  $\text{FeCp}_2^{+/0}$  redox couple by using ferrocene as an internal standard.

Transient absorption decays were measured by Dr. Safa Shaoee in the Durrant group at Imperial College (London) by exciting the sample film, under nitrogen atmosphere, with a dye laser (Photon Technology International Inc., GL-301). The excitation wavelength used was 500 nm for all blends, with pump intensities of  $\sim 30 \mu\text{Jcm}^{-2}$  and a repetition frequency of 4 Hz. A 100 W quartz halogen lamp (Bentham, IL 1) with a stabilized power supply (Bentham, 605) was used as a probe light source, with a typical probe wavelength of 700 nm. The probe light passing through the sample film was detected with a silicon photodiode (Hamamatsu Photonics, S1722-01). Signal from the photodiode was pre-amplified and sent to the main amplification system with an electronic band-pass filter (Costronics Electronics). The amplified signal was collected with a digital oscilloscope (Tektronics, TDS220), which was synchronized with a trigger signal of the pump laser pulse from a photodiode (Thorlabs Inc., DET210). To reduce stray light, scattered light and sample emission, two monochromators and appropriate optical cut-off filters were placed before and after the sample. The TEM examination was also done by Dr. Safa Shaoee in the Durrant group at Imperial College (London). Solutions were spun onto PEDOT:PSS(10 nm)-coated ITO



substrates, retrieved on carbon-coated copper grids after the films were floated on water. The sample film thickness was controlled by solution concentration, typically around 30 nm. The samples were then stained with RuO<sub>4</sub> vapor.

AFM was carried out with a two-pass lift mode procedure using a Veeco Multimode IV AFM by Dr. Debin Wang in the Riedo group. The film was prepared in a way similar to making the active layer of the solar cell devices described later. The surface topography is obtained by a generic tapping mode scan in the first pass. On the first pass (main scan), the cantilever was mechanically vibrated near its resonant frequency by a small piezoelectric oscillator. Nanoworld SCM-PIT probes were selected for the operation. The mechanical properties (force constant  $k = 2.8$  N/m and resonance frequency  $f = 75$  kHz) and the special Pt/Ir-coated probes are optimized for electrostatic force application. The typical tip radius of curvature is less than 25 nm.

BHJ solar cells were fabricated by Dr. Hyeunseok Cheun in the Kippelen group. Solutions of P3HT:PDI<sub>X</sub> (X= G to I and D, 1: 1 weight ratio) were made in chlorobenzene (20 mg/mL) for each blend. ITO-coated glasses (Colorado Concept Coatings LLC) with a sheet resistivity of *ca.* 15  $\Omega$ /sq were used as the substrates for solar cells. The substrates were cleaned in an ultrasonic bath of detergent water, rinsed with deionized water, and then cleaned in sequential ultrasonic baths of deionized water, acetone, and isopropanol. Nitrogen was used to dry the substrates after each of the last three baths. A 300-nm-thick layer of SiO<sub>x</sub> was deposited on the cleaned ITOs by e-beam deposition (AXXIS, Kurt J. Lesker) to pattern the anode. Next, the substrates were ultrasonicated in isopropanol for 15 min, blown dry with nitrogen, and air-plasma treated for 2 min. A hole-conducting layer of PEDOT : PSS (CLEVIOS P VP AI 4083, H. C. Starck) was filtered through a 0.45- $\mu$ m-pore

PVDF filter and spin coated on the substrates at 5000 rpm for 1 min, and the substrates were annealed at 140 °C for 15 min in ambient atmosphere. After loading into a nitrogen-filled glove box, films of the blends were deposited on the substrates by spin coating for 1 min at speed of 700 rpm for the mixture. All solutions were filtered through 0.2-μm-pore PTFE filters prior to spin coating. The substrates were then loaded into a vacuum thermal evaporation system (SPECTROS, Kurt J. Lesker) connected to the glove box, and ~ 200 nm of Al was deposited through a shadow mask at a rate of  $1 - 3 \text{ \AA s}^{-1}$  and a base pressure of  $\sim 7 \times 10^{-8}$  Torr to define the cathodes. The completed devices were transferred in a sealed container to another nitrogen-filled glove box for electrical measurements. Current-voltage characteristics were measured using a source meter (2400, Keithley) controlled by a LabVIEW program. When testing the solar cells under illumination, filtered light from a 175 W Xenon lamp (ASB-XE-175EX, CVI) was used as a broadband light source with an irradiance of  $\sim 90 \text{ mW/cm}^2$  to simulate sunlight.

**PDI<sub>D</sub>**: *N,N'*-Bis(octyl)-1,(6)7-dibromo-3,4,9,10-perylene diimide(mixture of isomer)<sup>35</sup> (0.50 g, 0.65 mmol), CuI (10 mg, 0.052 mmol), and Pd(PPh<sub>3</sub>)<sub>2</sub>Cl<sub>2</sub> (38 mg, 0.052 mmol) were charged to a two-neck round-bottomed flask equipped with a condenser. After evacuating and refilling nitrogen three times, pent-1-yne (0.14 g, 2.8 mmol), toluene (10.0 mL), and triethylamine (3.0 mL) were added by syringe. The mixture was then heated at 80 °C under nitrogen for 12 h. After the mixture was cooled to room temperature, it was passed through a short silica gel plug and eluted with CHCl<sub>3</sub>. After the solvent was removed under reduced pressure, the resultant solid was refluxed in 50 mL CHCl<sub>3</sub>/MeOH (1 : 4) for 2 h. After the mixture was cooled to room temperature, PDI<sub>D</sub> was collected by filtration as a red solid (0.38 g, 74%). <sup>1</sup>H NMR (500 MHz, CDCl<sub>3</sub>):  $\delta$  10.0 (m, 2H), 8.67 (s, 1.66H), 8.62 (s, 0.36H),

8.59 (d,  $J = 8.5$  Hz, 0.39H), 8.54 (d,  $J = 8.5$  Hz, 1.75H), 4.13 (t,  $J = 7.5$  Hz, 4H), 4.04 (t,  $J = 7.0$  Hz, 4H), 1.82–1.71 (m, 8H), 1.49–1.23 (m, 18H), 1.17 (t,  $J = 7.0$  Hz, 6H), 0.88 (t,  $J = 7.0$  Hz, 6H) (1,6-, and 1,7- Isomers are present according to the aromatic proton resonance in  $^1\text{H}$  NMR because the starting material is the mixture of 1,6- and 1,7- isomers<sup>35</sup>).  $^{13}\text{C}\{^1\text{H}\}$  NMR (125 MHz,  $\text{CDCl}_3$ ):  $\delta$  163.1, 162.9, 162.6, 162.4, 137.7, 133.4, 133.2, 133.1, 132.9, 130.0, 126.8, 122.7, 122.4, 121.5, 121.2, 121.1, 120.5, 101.8, 101.7, 82.5, 40.6, 31.8, 29.4, 29.3, 28.0, 27.2, 22.7, 22.3, 21.8, 14.1, 13.9 (The observation of four carbonyl carbon resonances and one more aromatic carbons could be attributed to the presence of the two isomers<sup>35</sup>). HRMS (FAB) Calcd for  $\text{C}_{50}\text{H}_{54}\text{N}_2\text{O}_4$  ( $\text{M}^+$ ) 746.4083. Found: 747.4200 ( $\text{M} + \text{H}$ ). Anal. Calcd for  $\text{C}_{50}\text{H}_{54}\text{N}_2\text{O}_4$ : C, 80.40; H, 7.29; N, 3.75. Found : C, 80.14; H, 7.29; N, 3.77.

3-Hexylthiophen-2-yl-methanamine (compound **A**): 3-Hexylthiophene-2-carbonitrile<sup>36</sup> (3.0 g, 16 mmol) in THF (10 mL) was added to lithium aluminum hydride (2.0 g, 50 mmol) in THF (70 mL) at 0 °C under nitrogen atmosphere by syringe. The mixture was then heated to reflux for 12 h. After the reaction mixture was cooled to 0 °C, water (10 mL) was added to the mixture under nitrogen atmosphere by syringe. The white precipitate was removed via filtration and washed with THF ( $3 \times 20$  mL). The solvent of filtrate was then removed and the resultant residue was dissolved in hexane (300 mL), washed with water ( $3 \times 100$  mL), and dried over anhydrous  $\text{Na}_2\text{SO}_4$ . After the solvent was removed under vacuum, (3-hexylthiophen-2-yl)methanamine was obtained as a colorless oil (2.8 g, 92%).  $^1\text{H}$  NMR (300 MHz,  $\text{CDCl}_3$ ):  $\delta$  7.10 (d,  $J = 5.1$  Hz, 1H), 6.84 (d,  $J = 5.0$  Hz, 1H), 3.96 (s, 2H), 2.56 (t,  $J = 7.5$  Hz, 2H), 1.58 (m, 2H) , 1.4–1.2 (m, 6H), 0.84 (t,  $J = 7.0$  Hz, 3H) (The amine proton does not show up in the  $^1\text{H}$  NMR).  $^{13}\text{C}$  NMR: (75 MHz,  $\text{CDCl}_3$ ),  $\delta$  140.2, 137.9, 129.0, 122.2, 39.1, 31.6, 30.8, 29.0, 28.1, 22.5, 14.0. HRMS (EI) Calcd for  $\text{C}_{11}\text{H}_{19}\text{NS}$ :

197.12382. Found: 197.12309; Anal. Calcd for  $C_{11}H_{19}NS$ : C, 66.95; H, 9.70; N, 7.10. Found: C, 66.55 ; H, 9.71; N, 7.04.

**PDI<sub>E</sub>**: PDI<sub>A</sub><sup>10</sup> (6.0 g, 5.6 mmol),  $K_2CO_3$  (4.0 g, 29 mmol) and chlorobenzene (80 mL) were mixed in a 200 mL round-bottomed flask equipped with condenser. Bromine (4.8 mL, 93 mmol) in chlorobenzene (10 mL) was added dropwise. The reaction mixture was then heated to 60 °C and kept overnight before it was cooled to room temperature and poured into saturated  $Na_2S_2O_3$  solution (500 mL). The mixture was extracted with  $CHCl_3$  ( $2 \times 200$  mL) and the organic phase was washed with water ( $2 \times 100$  mL) and dried over  $Na_2SO_4$ . After the solvent was removed, the residue was purified using column chromatography on silica gel, with  $CHCl_3$  / hexane (1 : 1) as the eluent. After the solvent was removed under reduced pressure, PDI<sub>E</sub> was obtained as a red solid (2.7 g, 42%). <sup>1</sup>H NMR (500 MHz,  $CDCl_3$ ):  $\delta$  9.62 (d,  $J$  = 8.0 Hz, 1H), 8.72 (s, 1H), 8.51 (m, 3H), 8.36 (m, 2H), 4.09 (d,  $J$  = 7.0 Hz, 2H), 4.06 (d,  $J$  = 7.0 Hz, 2H), 1.95 (m, 2H), 1.5–1.1 (m, 80H), 0.82 (m, 12H). <sup>13</sup>C{<sup>1</sup>H} NMR (125 MHz,  $CDCl_3$ ):  $\delta$  163.5, 163.2, 163.1, 162.3, 138.9, 133.5, 133.1, 133.0, 130.8, 130.3, 128.5, 128.3, 127.9, 127.6, 126.6, 123.5, 123.4, 123.3, 122.92, 122.7, 122.5, 120.9, 44.79, 44.72, 36.63, 36.58, 31.9, 31.7, 30.1, 30.0, 29.7, 29.6 (2 close peaks), 29.6, 29.4, 26.5 (2 close peaks), 22.7, 14.1 (Two aromatic carbon peaks and 31 alkyl carbon peaks were not observed, presumably due to overlap). HRMS (MALDI) Calcd for  $C_{72}H_{105}BrN_2O$  ( $M^+$ ): 1140.728. Found: 1140.734. Anal. Calcd for  $C_{72}H_{105}BrN_2O$ : C, 75.69; H, 9.26; N, 2.45. Found : C, 75.77; H, 9.26; N, 2.50.

**Compound B**: 1,(6)7-Dibromoperylene-3,4,9,10-tetracarboxylic acid dianhydride (1.50 g, 2.6 mmol) in <sup>n</sup>BuOH/ $H_2O$  (1:1, 100 mL) was sonicated for 10 min. (3-hexylthiophen-2-yl)methanamine (1.6 g, 8.0 mmol) was added and the reaction mixture was stirred at 80 °C

for 17 h under nitrogen. Concentrated HCl (10 mL) was added and the mixture was stirred at room temperature for 30 min. The mixture was extracted with chloroform ( $2 \times 100$  mL), washed with water ( $2 \times 100$  mL), and dried over anhydrous  $\text{Na}_2\text{SO}_4$ . The solvent was removed and the residue was purified by column chromatography over silica gel eluted with  $\text{CHCl}_3$ /hexane (2 : 1) to give **B** as a red solid (2.5 g, 90%).  $^1\text{H}$  NMR (400 MHz,  $\text{CDCl}_3$  for 1,7-dibromo isomer only):  $\delta$  9.42 (d,  $J = 8.0$  Hz, 2H), 8.91 (s, 2H), 8.68 (d,  $J = 8.0$  Hz, 2H), 7.12 (d,  $J = 5.2$  Hz, 2H), 6.81 (d,  $J = 5.2$  Hz, 2H), 5.50 (s, 4H), 2.91 (t,  $J = 8.0$  Hz, 4H), 1.61 (m, 4H), 1.4–1.3 (m, 12H), 0.84 (t,  $J = 6.8$  Hz, 6H).  $^{13}\text{C}$  NMR: (100 MHz,  $\text{CDCl}_3$ ),  $\delta$  163.0, 162.6, 162.1, 161.8, 142.0, 141.9, 138.3, 138.2, 133.3, 133.1, 132.9, 132.5, 131.8, 131.5, 130.2, 130.1, 129.2, 128.5, 128.4, 128.1, 126.9, 124.5, 123.2, 123.0, 122.6, 122.3, 121.7, 120.8, 36.7, 31.8, 31.3, 29.3, 28.4, 22.7, 14.1. (The observation of four carbonyl carbon resonances is consistent with previous work on perylene diimides using swallow-tailed *N*-substituents, and it has been attributed to restricted rotation about the N—C—thiophene bonds.<sup>37</sup> Eight more aromatic resonances than observed in the pure 1,7-isomer might be due to the presence of 1,6-, and 1,7-isomers and/or restricted rotation about the N—C—thiophene bonds.) HRMS (FAB) Calcd for  $\text{C}_{46}\text{H}_{40}\text{Br}_2\text{N}_2\text{O}_4\text{S}_2$ : 906.080. Found: 906.081. Anal. Calcd for  $\text{C}_{46}\text{H}_{40}\text{Br}_2\text{N}_2\text{O}_4\text{S}_2$ : C, 60.80; H, 4.44; N, 3.08. Found: C, 60.56; H, 4.35; N, 3.10.

**PDI<sub>G</sub>**: Pent-1-yne (0.28 g, 5.6 mmol) was added to a deoxygenated mixture of **B** (1.86 g, 2.00 mmol), copper(I) iodide (0.030 g, 0.15 mmol), and  $\text{Pd}(\text{PPh}_3)_2\text{Cl}_2$  (0.12 g, 0.15 mmol) in toluene (30 mL) and triethylamine (8.0 mL) under nitrogen in a 50 mL 2-neck round-bottomed flask. The reaction mixture was stirred overnight under nitrogen before the solvent was removed by rotary evaporation. The residue was then purified using column chromatography on silica gel, eluted with hexane/dichloromethane (1:4). After the solvent

was removed under vacuum, **PDI<sub>G</sub>** was obtained as a red solid (1.68 g, 95%). <sup>1</sup>H NMR (500 MHz, CDCl<sub>3</sub> for 1,7-isomer only):  $\delta$  9.98 (d,  $J$  = 8.0 Hz, 2H), 8.68 (s, 2H), 8.53 (d,  $J$  = 7.5 Hz, 2H), 7.11 (d,  $J$  = 5.0 Hz, 2H), 6.81 (d,  $J$  = 5.0 Hz, 2H), 5.53 (s, 4H), 2.92 (t,  $J$  = 7.5 Hz, 4H), 2.61 (t,  $J$  = 7.5 Hz, 4H), 1.80 (sextet,  $J$  = 6.0 Hz, 4H), 1.64 (pentet,  $J$  = 7.5 Hz, 4H), 1.4–1.3 (m, 12H), 1.15 (t,  $J$  = 6.5 Hz, 6H), 0.90 (t,  $J$  = 6.5 Hz, 6H). <sup>13</sup>C NMR: (100 MHz, CDCl<sub>3</sub>),  $\delta$  163.2, 163.0, 162.7, 162.5, 141.9, 141.8, 138.2, 134.1, 134.0, 133.8, 133.7, 132.1, 130.4, 130.3, 128.4, 127.3, 127.1, 126.8, 126.5, 124.4, 122.8, 122.6, 121.6, 121.4, 121.0, 101.6, 101.4, 82.4, 82.3, 36.6, 31.8, 31.3, 29.3, 28.4, 22.7, 22.2, 21.8, 14.1, 13.9. (The observation of four carbonyl carbon resonances is consistent with previous work on perylene diimides using swallow-tailed *N*-substituents and it has been attributed to restricted rotation about the N—C—thiophene bonds.<sup>37</sup> Eight more aromatic resonances than observed in the pure 1,7-isomer might be due to the presence of 1,6-, and 1,7-isomers and/or restricted rotation about the N—C—thiophene bonds.) HRMS (FAB) Calcd for C<sub>56</sub>H<sub>54</sub>N<sub>2</sub>O<sub>4</sub>S<sub>2</sub>: 882.3525; Found: 882.3595. Anal. Calcd for C<sub>56</sub>H<sub>54</sub>N<sub>2</sub>O<sub>4</sub>S<sub>2</sub>: C, 76.16; H, 6.16; N, 3.17. Found: C, 75.96; H, 6.24; N, 3.16.

Compound **C**: **PDI<sub>G</sub>** (1.50 g, 1.61 mmol) was dissolved in CHCl<sub>3</sub> (60 mL) and the solution was cooled to 0 °C. Hg(CH<sub>3</sub>COO)<sub>2</sub> (1.13 g, 3.54 mmol) was then added in one portion and the mixture was then warmed up to room temperature slowly and kept stirring overnight. Iodine (0.90 g, 3.54 mmol) was added to the mixture in one portion after it was cooled down to 0 °C. The mixture was warmed up to room temperature and stirred for 1 h before it was passed through a short silica gel plug and eluted with CHCl<sub>3</sub>. After the solvent was removed by rotary evaporation, **C** was obtained as a red solid (1.71 g, 93%). <sup>1</sup>H NMR (500 MHz, CDCl<sub>3</sub> for 1,7-dibromo isomer only):  $\delta$  10.10 (d,  $J$  = 8.5 Hz, 2H), 8.77 (s, 2H), 8.64 (d,  $J$  =

8.5 Hz, 2H), 6.95 (s, 2H), 5.45 (s, 4H), 2.89 (t,  $J = 7.0$  Hz, 4H), 2.62 (m, 4H), 1.80 (sextet,  $J = 7.0$  Hz, 4H), 1.64 (m, 4H), 1.4-1.3 (m, 12H), 1.15 (t,  $J = 6.5$  Hz, 6H), 0.90 (t,  $J = 7.0$  Hz, 6H).  $^{13}\text{C}$  NMR: (125 MHz,  $\text{CDCl}_3$ ),  $\delta$  163.0, 162.9, 162.7, 162.5, 143.9, 138.3, 138.1, 134.2, 133.7, 130.3, 127.3, 127.1, 126.9, 122.5, 121.5, 121.1, 101.8, 101.5, 82.3, 73.2, 36.4, 31.8, 31.2, 29.7, 29.2, 28.1, 22.7, 21.8, 14.1, 13.9. (The observation of four carbonyl carbon resonances is consistent with previous work on perylene diimides using swallow-tailed *N*-substituents and has been attributed to restricted rotation about the N—C—thiophene bonds.<sup>37</sup> Two aromatic carbon resonances are missing, presumably due to overlap) HRMS (MALDI) Calcd for  $\text{C}_{56}\text{H}_{52}\text{I}_2\text{N}_2\text{O}_4\text{S}_2$ : 1134.15. Found: 1134.17. Anal. Calcd for  $\text{C}_{56}\text{H}_{52}\text{I}_2\text{N}_2\text{O}_4\text{S}_2$ : C, 59.26; H, 4.62; N, 2.47. Found: C, 59.40; H, 4.67; N, 2.59.

**PDI<sub>H</sub>**: 2-(3-Hexylthiophen-2-yl)-4,4,5,5-tetramethyl-1,3,2-dioxaborolane<sup>38</sup> (0.34 g, 1.2 mmol) was added to a deoxygenated mixture of **C** (0.36 g, 0.3 mmol), and  $\text{Pd}(\text{PPh}_3)_4$  (0.046 g, 0.040 mmol) in toluene (15 mL) and 2M aqueous  $\text{K}_2\text{CO}_3$  (10 mL) under nitrogen in a 2-neck round-bottomed flask with a reflux condenser attached. The reaction mixture was then heated to 95 °C for 2 h. Toluene (50 mL) was added to the mixture and the resultant mixture was washed with water ( $2 \times 20$  mL). The organic phase was dried with anhydrous  $\text{MgSO}_4$ . After filtration and solvent removal by rotary evaporation, the residue was purified using flash column chromatography on silica gel and eluted with hexane/dichloromethane (1:1). The resultant red solid was further purified using size-exclusion chromatography (1.2 meter long, 5 cm in diameter, with SX1 polystyrene beads) and eluted with fresh-distilled THF to give **PDI<sub>H</sub>** as a red solid (0.218 g, 60%).  $^1\text{H}$  NMR (400 MHz,  $\text{CDCl}_3$  for 1,7-isomer only):  $\delta$  10.03 (d,  $J = 8.4$  Hz, 2H), 8.73 (s, 2H), 8.58 (d,  $J = 8.4$  Hz, 2H), 7.07 (d,  $J = 5.2$  Hz, 2H), 6.85 (d,  $J = 5.2$  Hz, 2H), 6.79 (s, 2H), 5.50 (s, 4H), 2.93 (t,  $J = 7.6$  Hz, 4H), 2.69 (t,  $J = 7.6$

Hz, 4H), 2.62 (t,  $J = 7.2$  Hz, 4H), 1.80 (sextet,  $J = 7.2$  Hz, 4H), 1.65 (m, 4H), 1.4-1.2 (m, 28H), 1.17 (t,  $J = 7.6$  Hz, 6H), 0.91 (t,  $J = 6.8$  Hz, 6H), 0.81 (t,  $J = 6.8$  Hz, 6H).  $^{13}\text{C}$  NMR: (100 MHz,  $\text{CDCl}_3$ ),  $\delta$  163.2, 163.0, 162.8, 162.6, 142.3, 139.4, 138.3, 135.1, 134.2, 134.0, 133.8, 132.2, 132.0, 130.8, 130.4, 129.8, 127.4, 127.2, 127.1, 127.0, 123.4, 122.8, 122.6, 121.7, 121.0, 101.5, 82.3, 36.7, 31.8, 31.6, 31.2, 30.6, 29.3, 29.1(2 close peaks) 28.5, 22.7, 22.6, 22.3 21.8, 14.1, 14.0, 13.9. (The observation of four carbonyl carbon resonances is consistent with previous work on perylene diimides using swallow-tailed *N*-substituents and it has been attributed to restricted rotation about the N—C—thiophene bonds.<sup>37</sup> Three more aromatic resonances than observed in the pure 1,7-isomer might be due to the presence of 1,6-, and 1,7-isomers and/or restricted rotation about the N—C—thiophene bonds.). HRMS (MALDI) Calcd for  $\text{C}_{76}\text{H}_{82}\text{N}_2\text{O}_4\text{S}_4$ : 1214.5157. Found: 1214.5084. Anal. Calcd for  $\text{C}_{76}\text{H}_{82}\text{N}_2\text{O}_4\text{S}_4$ : C, 75.08; H, 6.80; N, 2.30. Found: C, 75.23; H, 7.03; N, 2.38.

**PDI<sub>I</sub>**: 2-(3',4'-dihexyl-2,2'-bithiophen-5-yl)-4,4,5,5-tetramethyl-1,3,2-dioxaborolane<sup>32</sup> (0.42 g, 0.90 mmol) was added to a deoxygenated mixture of **C** (0.36 g, 0.30 mmol), and  $\text{Pd}(\text{PPh}_3)_4$  (0.046 g, 0.040 mmol) in toluene (15 mL) and 2M aqueous  $\text{K}_2\text{CO}_3$  (10 mL) under nitrogen in a 2-neck round-bottomed flask with a reflux condenser attached. The reaction mixture was then heated to 90 °C for 2 h. Toluene (50 mL) was added to the mixture and the resultant mixture was washed with water ( $2 \times 100$  mL). The organic phase was dried with anhydrous  $\text{MgSO}_4$ . After the solid was removed via filtration and the solvent removal by rotary evaporation, the residue was purified using flash column chromatography on silica gel, eluted with chloroform and size-exclusion chromatography (1.2 meter long, 5 cm in diameter, with SX1 polystyrene beads) eluted with fresh-distilled THF to give **PDI<sub>H</sub>** as a red solid (0.26 g, 56%).  $^1\text{H}$  NMR (400 MHz,  $\text{CDCl}_3$  for 1,7-dibromo isomer only):  $\delta$  10.05 (d,  $J = 8.4$  Hz, 2H),



8.73 (s, 2H), 8.58 (d,  $J = 8.4$  Hz, 2H), 7.09 (d,  $J = 5.2$  Hz, 2H), 6.86 (d,  $J = 5.2$  Hz, 2H), 6.84 (s, 2H), 6.82 (s, 2H), 5.51 (s, 4H), 2.93 (t,  $J = 7.6$  Hz, 4H), 2.71 (m, 8H), 2.62 (t,  $J = 6.8$  Hz, 4H), 1.82 (sextet,  $J = 7.2$  Hz, 4H), 1.6-1.2 (m, 48H), 1.17 (t,  $J = 7.6$  Hz, 6H), 0.92 (t,  $J = 7.2$  Hz, 6H), 0.84 (m, 12H).  $^{13}\text{C}$  NMR: (100 MHz,  $\text{CDCl}_3$ ),  $\delta$  163.2, 163.0, 162.8, 162.6, 142.4, 139.5, 139.4, 138.3, 134.8, 133.9 (2peaks), 132.2, 130.6, 130.4, 130.0, 128.5, 127.4, 127.2, 127.0, 123.4, 122.6, 121.7, 121.0, 101.5, 82.3, 36.7, 31.8, 31.6 (2peaks), 31.2, 30.6, 30.5, 29.3, 29.2 (3 peaks), 28.5, 22.7, 22.6, 22.2, 21.8, 14.1, 140.0, 13.9 (The observation of four carbonyl carbon resonances is consistent with previous work on perylene diimides using swallow-tailed *N*-substituents and has been attributed to restricted rotation about the N—C—thiophene bonds.<sup>37</sup> Three more aromatic resonances than observed in the pure 1,7-isomer might due to the presence of 1,6-, and 1,7-isomers and/or restricted rotation about the N—C—thiophene bonds.). HRMS (MALDI) Calcd for  $\text{C}_{96}\text{H}_{110}\text{N}_2\text{O}_4\text{S}_6$ : 1546.679. Found: 1546.765. Anal. Calcd for  $\text{C}_{96}\text{H}_{110}\text{N}_2\text{O}_4\text{S}_6$ : C, 74.47; H, 7.16; N, 1.81. Found: C, 74.49; H, 7.29; N, 1.91.

#### 4.12 References

- (1) Thompson, B. C.; Fréchet, J. M. J. *Angew. Chem. Int. Ed.* **2008**, *47*, 58-77.
- (2) Kippelen, B.; Brédas, J. L. *Energy Environ. Sci.* **2009**, *2*, 251-261.
- (3) Günes, S.; Neugebauer, H.; Sariciftci, N. S. *Chem. Rev.* **2007**, *107*, 1324-1338.
- (4) Liang, Y.; Feng, D.; Wu, Y.; Tsai, S.-T.; Li, G.; Ray, C.; Yu, L. *J. Am. Chem. Soc.* **2009**, *131*, 7792-7799.
- (5) Liang, Y. Y.; Wu, Y.; Feng, D. Q.; Tsai, S. T.; Son, H. J.; Li, G.; Yu, L. P. *J. Am. Chem. Soc.* **2009**, *131*, 56-57.
- (6) Shoaee, S.; An, Z.; Zhang, X.; Barlow, S.; Marder, S. R.; Duffy, W.; Heeney, M.; McCulloch, I.; Durrant, J. R. *Chem. Commun.* **2009**, 5445 - 5447
- (7) Ohkita, H.; Cook, S.; Astuti, Y.; Duffy, W.; Tierney, S.; Zhang, W.; Heeney, M.; McCulloch, I.; Nelson, J.; Bradley, D. D. C.; Durrant, J. R. *J. Am. Chem. Soc.* **2008**, *130*, 3030-3042.
- (8) Ford, T. A.; Avilov, I.; Beljonne, D.; Greenham, N. C. *Phys. Rev. B* **2005**, *71*, 125212.
- (9) MITTAL, J. P. *Pure & Appl. Chem.* **1995**, *67*, 103-110.
- (10) Odom, S. A.; Kelley, R. F.; Ohira, H.; Ensley, T.; Huang, C.; Padilha, L. A.; Webster, S.; Coropceanu, V.; Barlow, S.; Hagan, D. J.; Van Stryland, E. W.; Brédas, J.-L.; Anderson, H. L.; Wasielewski, M. R.; Marder, S. R. *J. Phys. Chem. A* **2009**, *113*, 10826-10831.
- (11) Tauber, M. J.; Kelley, R. F.; Giaimo, J. M.; Rybtchinski, B.; Wasielewski, M. R. *J. Am. Chem. Soc.* **2006**, *128*, 1782-1783.
- (12) Rohr, U.; Kohl, C.; Müllen, K.; Craats, A. v. d.; Warman, J. *J. Mater. Chem.* **2001**, *11*, 1789-1799.
- (13) Zhan, X.; Tan, Z. A.; Domercq, B.; An, Z.; Zhang, X.; Barlow, S.; Li, Y.; Zhu, D.; Kippelen, B.; Marder, S. R. *J. Am. Chem. Soc.* **2007**, *129*, 7246-7247.
- (14) An, Z.; Yu, J.; Jones, S. C.; Barlow, S.; Yoo, S.; Domercq, B.; Prins, P.; Siebbeles, L. D. A.; Kippelen, B.; Marder, S. R. *Adv. Mater* **2005**, *17*, 2580-2583.
- (15) Rohr, U.; Kohl, C.; Müllen, K.; Craats, A. v. d.; Warman, J. *J. Mater. Chem* **2001**, *11*, 1789-1799.
- (16) Thelakkat, M.; Schmidt, H.-W. *Adv. Mater.* **1998**, *10*, 219-223.
- (17) An, Z. S.; Odom, S. A.; Kelley, R. F.; Huang, C.; Zhang, X.; Barlow, S.; Padilha, L. A.; Fu, J.; Webster, S.; Hagan, D. J.; Van Stryland, E. W.; Wasielewski, M. R.; Marder, S. R. *J. Phys. Chem. A* **2009**, *113*, 5585-5593.
- (18) O'Neil, M. P.; Niemczyk, M. P.; Svec, W. A.; Gosztola, D.; L.Gaines, G.; Wasielewski, M. R. *Science* **1992**, *257*, 63-65.
- (19) Korovyanko, O. J.; Österbacka, R.; Jiang, X. M.; Vardeny, Z. V.; Janssen, R. A. J. *Phys. Rev. B* **2001**, *64*, 235122.
- (20) Westerling, M.; Österbacka, R.; Stubb, H. *Phys. Rev. B* **2002**, *66*, 165220.
- (21) Österbacka, R.; An, C. P.; Jiang, X. M.; Vardeny, Z. V. *Science* **2000**, *287*, 839-843.
- (22) Clarke, T. M.; Ballantyne, A. M.; Nelson, J.; Bradley, D. D. C.; Durrant, J. R. *Adv. Funct. Mater.* **2008**, *18*, 4029 - 4035.

- (23) Shuttle, C. G.; O'Regan, B.; Ballantyne, A. M.; J. Nelson; Bradley, D. C.; de Mello, J.; Durrant, J. R. *Appl. Phys. Lett.* **2008**, 92, 093311.
- (24) Würthner, F. *Chem. Commun.* **2004**, 1564-1579.
- (25) Scholz, M.; Schmidt, R.; Krause, S.; Schöll, A.; Reinert, F.; Würthner, F. *Appl. Phys. A: Mater. Sci. Process.* **2009**, 95, 285-290.
- (26) Piliego, C.; Holcombe, T. W.; Douglas, J. D.; Woo, C. H.; Beaujuge, P. M.; Fréchet, J. M. J. *J. Am. Chem. Soc.* **2010**, 132, 7595-7597.
- (27) Zou, Y.; Najari, A.; Berrouard, P.; Beaupr, S.; Aich, B. R.; Tao, Y.; Leclerc, M. *J. Am. Chem. Soc.* **2010**, 132, 5330-5331.
- (28) He, Y.-J.; Chen, H.-Y.; Hou, J.-H.; Li, Y.-F. *J. Am. Chem. Soc.* **2010**, 132, 1377-1382.
- (29) Nagao, Y. *Progress Org. Chem.* **1997**, 31, 43-49.
- (30) Ahrens, M. J.; Fuller, M. J.; Wasielewski, M. R. *Chem. Mater.* **2003**, 15, 2684-2686.
- (31) Chinchilla, R.; Nájera, C. *Chem. Rev.* **2007**, 107, 874-922.
- (32) Cremer, J.; Mena-Osteritz, E.; Pschierer, N. G.; Müllen, K.; Bäuerle, P. *Org. Biomol. Chem.* **2005**, 3, 985-994.
- (33) Miyaura, N.; Suzuki, A. *Chem. Rev.* **1995**, 95, 2457-2483.
- (34) Stille, J. K. *Angew. Chem. Int. Ed.* **1986**, 25, 508-524.
- (35) Ahrens, M. J.; Tauber, M. J.; Wasielewski, M. R. *J. Org. Chem.* **2006**, 71, 2107-2112.
- (36) Dohi, T.; Ito, M.; Yamaoka, N.; Morimoto, K.; Fujioka, H.; Kita, Y. *Tetrahedron* **2009**, 65, 10797-10815.
- (37) Wescott, L. D.; Mattern, D. L. *J. Org. Chem.* **2003**, 68, 10058-10066.
- (38) Pan, H.; Li, Y.; Wu, Y.; Liu, P.; Ong, B. S.; Zhu, S.; Xu, G. *J. Am. Chem. Soc.* **2007**, 129, 4112-4113.

## CHAPTER 5

# PHOTO-INDUCED CHARGE TRANSFER AND OPTICAL LIMITING IN DYADS COMPOSED OF TWO-PHOTON ABSORBING DONORS AND A PERYLENE DIIMIDE ACCEPTOR

### 5.1 Introduction

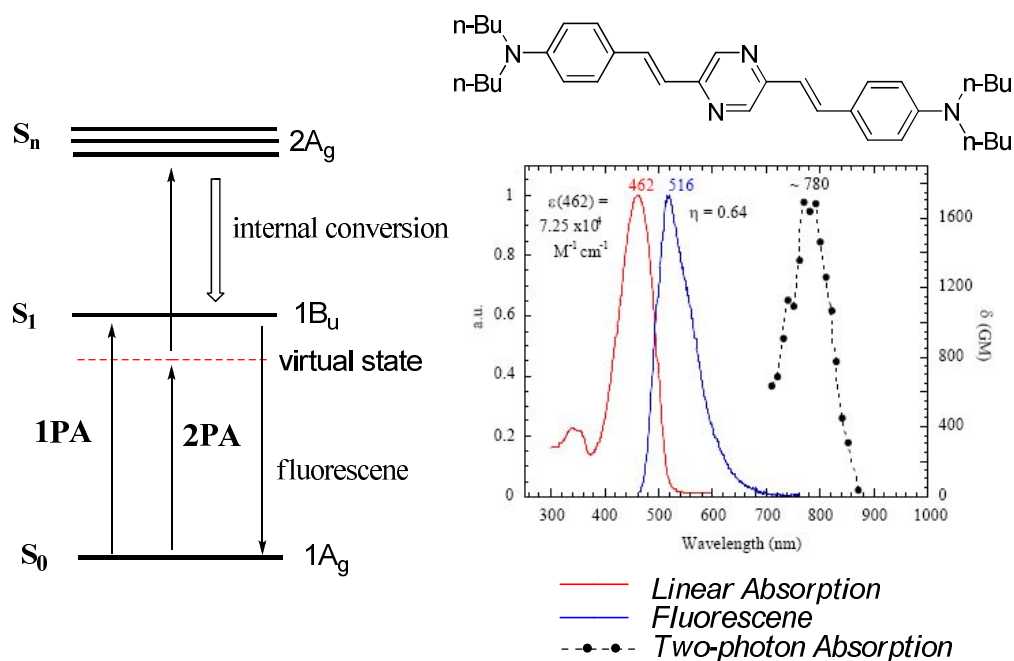
Optical limiters are devices designed to have high transmittance for low intensity inputs, such as ambient light, while at the same time exhibiting dramatically reduced transmittance on an ultrafast (nanosecond or shorter) timescale when exposed to high intensity irradiation (i.e. laser beams).<sup>1-2</sup> Since the development of the first laser in the 1960's, effective optical limiters have been built and tested to protect optical sensors against laser-induced damage. Organic conjugated materials, with delocalized  $\pi$ -electrons in the molecular backbone, are considered to be promising and offer many advantages for optical limiting, such as fast response-time, high damage thresholds, ease of processing, and facile structural modifications, allowing applications at a wide range of wavelengths.<sup>1,3</sup> Over the decades, the use of organic conjugated materials relying on various mechanisms, including reverse saturable absorption (RSA, which will be explained in more detail in Chapter 6)<sup>4-8</sup> and two-photon absorption (2PA, which will be explained in more detail below),<sup>9-11</sup> have been proven to be successful for laser pulse suppression and the use of organic conjugated materials for optical limiting is growing rapidly.

Two-photon absorption, which was first analyzed theoretically in the 1930s by Göppert-Mayer<sup>12</sup> and was first demonstrated experimentally in 1961 soon after the

invention of the laser<sup>13</sup> is a nonlinear optical process in which the simultaneous absorption of two photons of identical or different frequencies to excite a molecule from its ground state ( $S_0$ ) to an excited state.<sup>3,14-15</sup> 2PA is considered as an effective way of accessing a given excited state by using photons of half the energy (or twice the wavelength) of the corresponding one-photon-induced electronic transition, thus enabling a wide range of new applications including photodynamic therapy, 3D-photopolymerization, microfabrication and lithography.<sup>3</sup>

In the case of a centrosymmetric chromophore, the 2PA process is often dominated by the interaction of the ground state with just two excited states. The three “essential” states in such a model have alternating symmetry: both the ground state ( $S_0$ ) and the final state ( $S_n$ ) wave-functions, respectively, are gerade (symmetric with respect to the center of inversion), whereas the lowest excited state ( $S_1$ ) is often ungerade (antisymmetric with respect to the center of inversion).<sup>3</sup> These states could be labeled as  $1A_g$ ,  $1B_{1u}$ , and  $2A_g$  for centrosymmetric molecules as illustrated in Figure 5.1. For one-photon absorption (1PA), electronic transitions are electric-dipole-allowed for both  $1A_g$  to  $1B_{1u}$  and  $1B_{1u}$  to  $2A_g$  according to selection rules.<sup>3</sup> In the case of 2PA, the optical frequency is out of resonance with both these one-photon transitions and it creates a nonstationary state that is a superposition (or mixture) of  $1A_g$  and  $1B_{1u}$ . Such a “virtual state” is illustrated in Figure 5.1 and only exists while the molecule experiences the field of the first photon within a short time-scale (approximately 5 fs).<sup>16</sup> The transient presence of  $1B_{1u}$  with ungerade parity in this superposition allows the second photon at same optical frequency to induce an electric-dipole transition to the final gerade state,  $2A_g$ . The  $1A_g$  to  $2A_g$  transition is, therefore, allowed in 2PA, but forbidden in 1PA.<sup>3</sup> Hence, 1PA and 2PA

might access different excited states (Figure 5.1) from the ground state.<sup>3,14,17</sup> However, according to Kasha's rule,<sup>18</sup> which states that fluorescence and other photo-physical processes almost always occur from the lowest excited state of a molecule because molecules in higher excited states could quickly reach the lowest excited state via internal conversion. This is the reason why two-photon-excitation of a molecule could afford similar following processes as one-photon-excitation of the same molecule, regardless of whether the 2PA excitation of the molecule directly accesses the same excited state as its 1PA. For example, 2PA-induced emission from organic dyes should give similar spectra and fluorescent quantum yields via 1PA excitation. Similarly, 2PA-induced charge-transfer in molecular dyads could give similar charge-transfer and recombination rates as well as the photo-induced charge-transfer efficiency as 1PA, although the photo excitation wavelengths and mechanism are different.



**Figure 5.1.** The Jablonski diagram for two-photon and one-photon absorption and the 1PA, 2PA, and emission spectra of an example 2PA dye.<sup>14,19</sup>

One of the essential differences between 2PA compared with 1PA is that 2PA is typically several orders of magnitude weaker than linear absorption under ambient light intensity and only becomes significant when high intensity irradiation (typically  $10^{20-30}$  photon  $\text{cm}^{-2} \text{s}^{-1}$ ) is applied.<sup>14</sup> The 2PA probability has a quadratic dependency on the intensity of the incident irradiation ( $2\text{PA} \propto I^2$ ) since two photons are absorbed simultaneously while the probability of 1PA depends linearly on the intensity of the incident irradiation ( $1\text{PA} \propto I$ ) according to Beer-Lambert Law.<sup>3,14</sup> This indicates that 2PA is intensity-dependent absorption and would appear to be an ideal mechanism for optical power limiting. For example, 2PA could offer the advantage of high transmission at low incident light intensity for fundamental optical frequencies while the linear transmission for a material composed of RSA process is necessarily significantly less than unity ( $< 90\%$ ).<sup>1,9</sup> However, the 2PA cross-sections of current organic materials ( $< 100000$  GM, Göppert-Mayer, where  $1 \text{ GM} = 10^{-50} \text{ cm}^4 \text{ s photon}^{-1} \text{ molecule}^{-1}$ ) are generally not sufficiently large enough to form effective optical limiters purely by 2PA alone. A more practical strategy is to use the combination of 2PA and subsequent excited-state absorption (ESA) for optical suppression. A small amount of 2PA can generate a population of excited states, which then could absorb much more light through 1PA by cycling between ESA and the respective internal conversion.<sup>20-24</sup> Hence, these materials would potentially exhibit high linear transmission at low intensity light to preserve the detection function of the sensors, while strongly attenuating energetic laser pulses using the ESA absorption following their 2PA excitation of the nanosecond or shorter timescales laser pulse. For this process to be effective, the ESA band should have considerable spectral overlap with the 2PA band of the chromophore as well as a

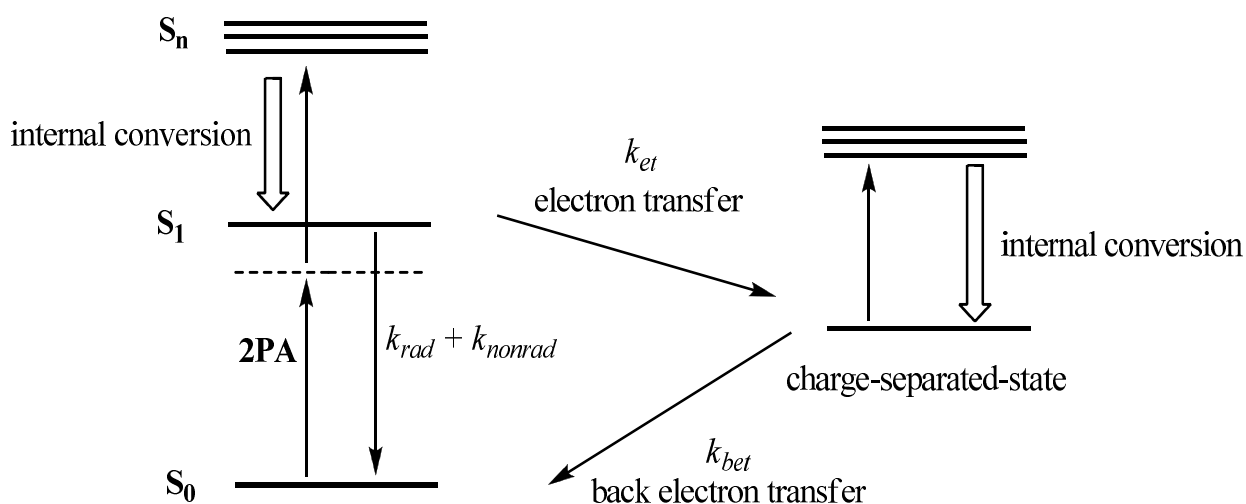
sufficient excited-state lifetime for these states to play an important role in the further light suppression. However, it is rather difficult to independently tune the energies of molecular 2PA and ESA bands of the same molecule for maximum overlap and to optimize the overall nonlinear absorption process. Generally, the 2PA and ESA absorption bands of a 2PA chromophore are fixed by the chemical structures. Moreover, both the strength and wavelengths of the ESA are not easily tuned using common methods. One possible method has been demonstrated by Belfield and coworkers utilizing the energy-transfer between 2PA dyes and a perylene diimide. In this case, the long-lived PDI excited state and the respective ESA at the two-photon excitation wavelength optimize the light suppression at 640 nm.<sup>25</sup> Another effective approach to circumvent this limitation is to exploit the photo-induced charge-transfer states between a 2PA chromophore and an electron acceptor or donor to form strongly absorbing radical ion pairs.<sup>26-28</sup> For example, thick films of a poly[2-methoxy-5-(2-ethylhexyloxy)-1,4-phenylene-vinylene] (MEH-PPV): phenyl-C<sub>61</sub>-butyric-acid-methyl ester (PCBM) blend have been proven to be an effective system for optical limiting in the NIR (700 – 900 nm) range using charge-transfer complexes from MEH-PPV:PCBM blend following the two-photon excitation of MEH-PPV donor and electron transfer from MEH-PPV exciton to PCBM LUMO.<sup>27</sup>

The spectroscopic overlap between the ion absorption band and the 2PA band of the chromophores are expected to significantly enhance the nonlinear absorption for optical suppression at the ion absorption wavelengths. For example, if the 2PA occurs in the electron donor, then the acceptor could be independently tuned to achieve effective spectral overlap between the absorption of its radical anion and the 2PA band of the



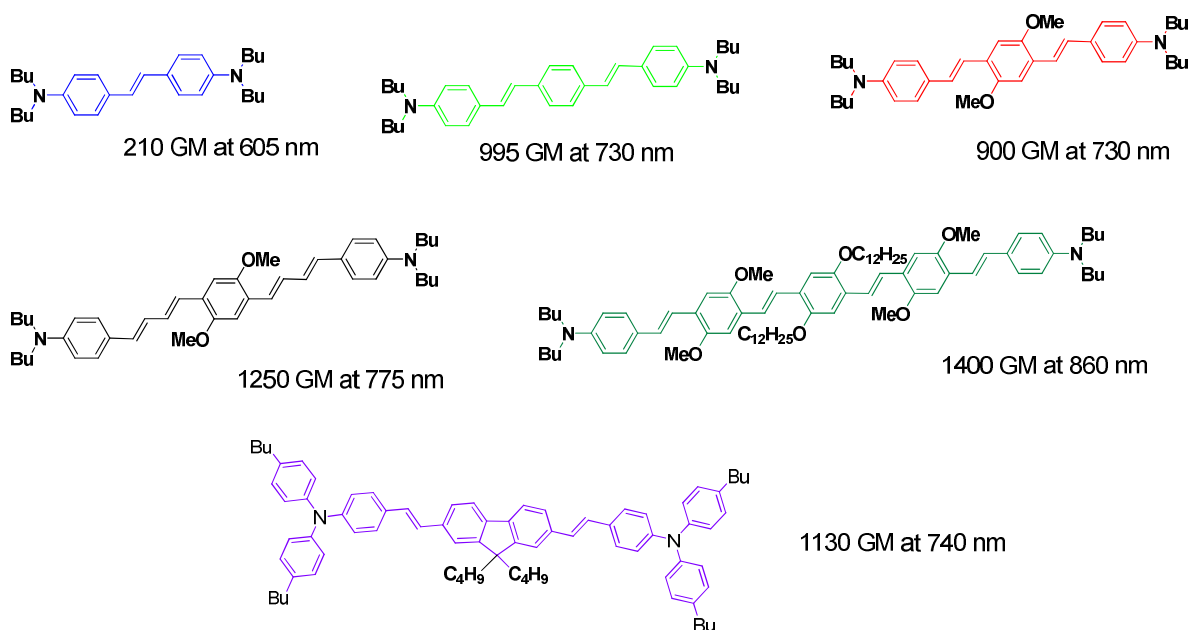
donor. Potentially, both the radical cation and anion bands could have spectral overlap with the 2PA band and are used for optical limiting at particular wavelengths. In addition to favorable spectroscopic overlap between the 2PA and radical ion bands, requirements for intense ion absorption and large 2PA cross section, rapid photo-induced electron-transfer, and relatively slow charge-recombination rate are essential for such optical limiting system to respond effectively against laser pulses.<sup>26</sup>

Furthermore, the 2PA generated radical ion pairs could be similar to those from 1PA process at different photo-excitation wavelengths in lifetime as well as other properties, including absorption coefficient. A proposed state-energy diagram for 2PA-induced electron transfer is shown in Figure 5.2. Two-photon excitation could promote an electron from the ground state ( $S_0$ ) of a 2PA chromophore into an excited state ( $S_n$ ) followed by the internal conversion that allows a fast relaxation back to the first excited state ( $S_1$ ), according to the Kasha's rule described earlier. The efficiency of 2PA-induced electron transfer, similar to the corresponding 1PA process, is determined by the rate constant for electron transfer ( $k_{et}$ ), which competes with the rate constants for radiative and non-radiative decay of  $S_1$  state, while the lifetime of the charge-separated state depends on back-electron-transfer process with rate constant of  $k_{bet}$ . Here, because of the spectroscopic overlap between the radical ion absorption and the chromophore 2PA band, the following 1PA of the charge-separated state is expected to enhance the non-linear absorption for optimizing the light suppression. Furthermore, sufficient population of the charge-separated state, which is related to the 2PA cross section and the lifetime of these states, is necessary for effective optical limiting according to the mechanism,



**Figure 5.2. The Jablonski diagram for 2PA-induced charge transfer.**

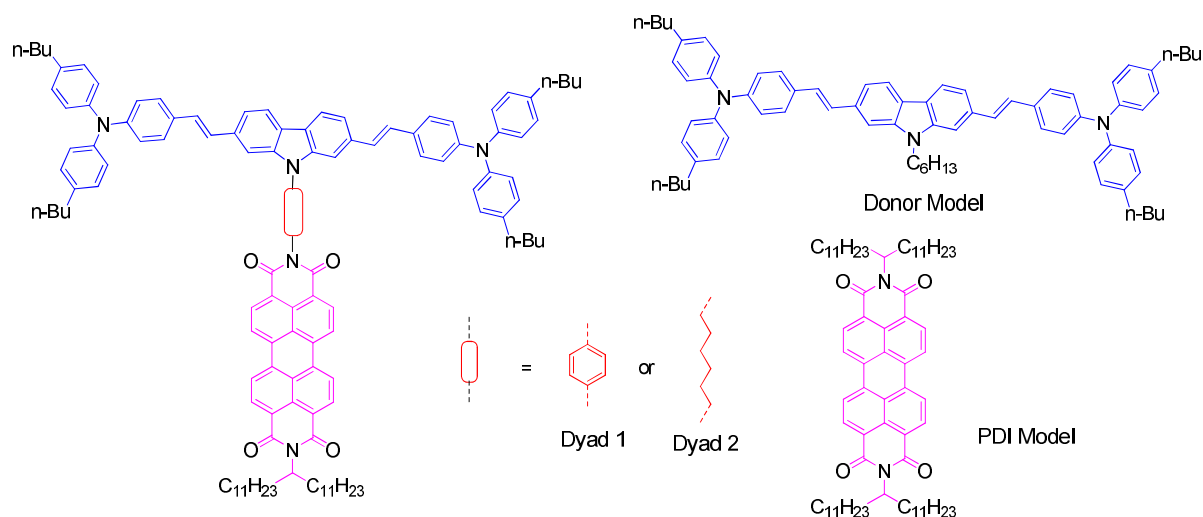
Perylene-3,4,9,10-tetracarboxylic acid diimides (also known as perylene diimides or PDI) have been widely used as acceptors in studies of photo-induced electron-transfer processes in molecular dyads and triads because of their electron-accepting nature and easily identified radical anion absorption spectra, which exhibit a unique absorption with peaks at *ca.* 700, 800, and 1000 nm.<sup>29-30</sup> The characteristic absorption in the visible to NIR range for long-lived photo-generated PDI radical-anions or dianions has been demonstrated in many donor-PDI systems using transient absorption techniques.<sup>29,31-37</sup> The photo-generated PDI radical anions are well suited for optical limiting because of their strong absorption in a spectral region (600 – 1000 nm) where neutral PDI molecules exhibit negligible ground-state absorption. Moreover, the relatively long lifetimes, typically from hundreds of picoseconds to tens of nanoseconds, observed for the photo-generated radical ion pairs for donor-PDI systems<sup>29,31-37</sup> are suitable for optical limiting of long-duration pulses (*e.g.*, on the nanosecond timescale).



**Figure 5.3. 2PA cross-sections of some D- $\pi$ -D type quadrupolar chromophores.**<sup>3,38-39</sup>

Many donor- $\pi$ -donor (D- $\pi$ -D) type quadrupolar chromophores have been shown to exhibit fairly large 2PA cross sections.<sup>3,14</sup> Such D- $\pi$ -D materials, especially for those with terminal triaryl-amine type donor and stilbene type  $\pi$ -spacer, typically exhibit strong 2PA with cross-sections over one thousand GM between 600 and 1000 nm (as illustrated in Figure 5.3) as well as high fluorescence quantum yields and strong electron donating properties (both in the ground state and particularly in the excited-state).<sup>14</sup> There are considerable spectroscopic overlaps between the 2PA band of many of these electron donating D- $\pi$ -D chromophores and the radical-anion absorption of the perylene diimides. Hence, molecular dyads consisting of D- $\pi$ -D 2PA chromophores and PDI-based acceptors potentially could show enhanced optical-limiting response relative to that of the isolated 2PA chromophores using PDI radical anion absorption generated by the electron transfer to PDI following the two-photon excitation of donor moieties. The formation of

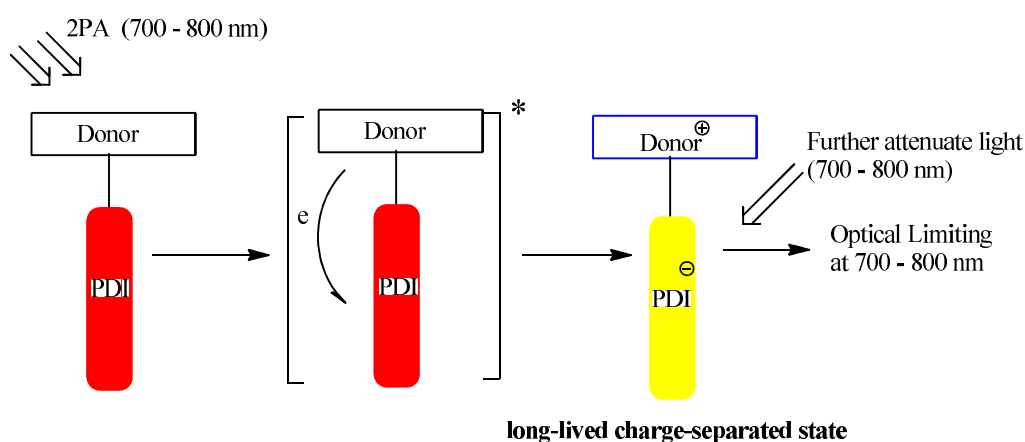
relatively long-lived charge-separated states following rapid electron transfer is another key requirement for effective optical limiting for such systems, which could be tuned by utilizing different spacers between the donor and PDI to control the electron-transfer and back-electron-transfer rate.



**Figure 5.4.** The chemical structures of the phenylene-linked (1) and hexylene-linked (2) dyads and the respective model compounds.

In this chapter, two different molecular donor-spacer-acceptor type molecular dyads were synthesized (as shown in Figure 5.4) for 2PA-induced optical limiting (as illustrated in Figure 5.5) in the wavelength range corresponding to the PDI radical anion absorption (700 – 800 nm). The dyads consist of a PDI moiety linked to a D- $\pi$ -D 2PA chromophore. The donor chromophore, by analogy with similar 2PA chromophores, is expected to have a strong 2PA band in the 600 – 900 nm range.<sup>40-41</sup> Linking the donor and acceptor through the imide position of the PDI minimizes the ground-state electronic coupling between the donor and PDI, because both the HOMO and LUMO of the PDI

has a node on each imide nitrogen.<sup>29</sup> The donor and acceptor chromophores are linked with two different spacers, which are expected to affect the photo-induced charge-transfer and recombination rate in the dyads due to variations in donor-acceptor distance and molecular conformations. For dyad **1**, the 2PA donor is rigidly bound at a fixed distance from the PDI acceptor by a single phenylene group, whereas for dyad **2**, a longer, more flexible *n*-hexylene linker was employed.



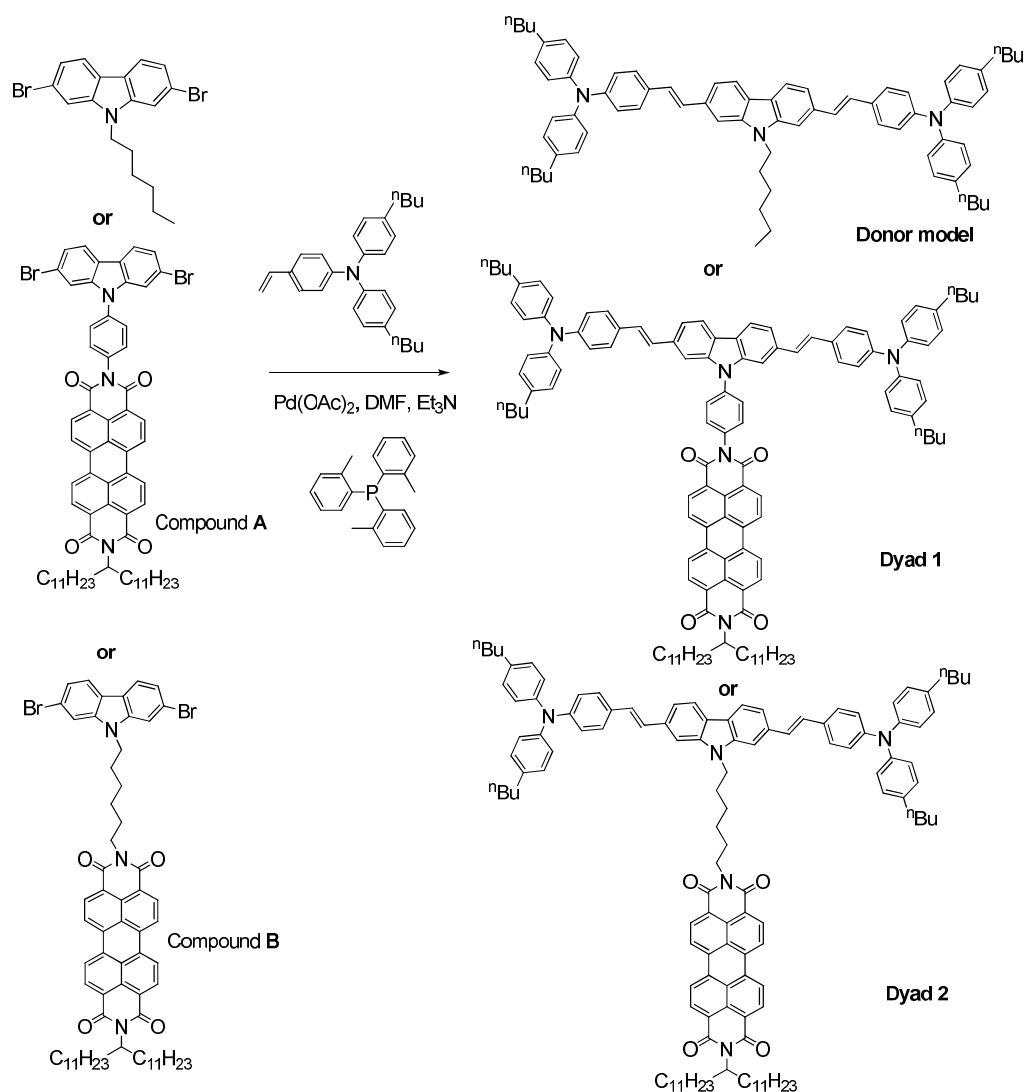
**Figure 5.5. Mechanism for 2PA-induced charge transfer and optical limiting in the dyads.**

## 5.2 Synthesis and thermal properties of the dyads and model compounds

Transition metal-catalyzed cross-coupling reactions have been widely used in synthesizing organic conjugated materials. The palladium-catalyzed C-C coupling between aryl halides or vinyl halides and activated alkenes in the presence of a base is referred as the Heck Reaction, first described by Heck and coworkers in the early 1970s.<sup>42-43</sup> Because of the outstanding *trans* selectivity from the Heck Reaction,<sup>43-44</sup> it was employed in this chapter to afford the dyads and model compound since *trans* stilbene-based 2PA dyes could give higher 2PA cross-sections in general.<sup>45</sup>

As shown in Scheme 5.1 and 5.2, the synthetic strategy involved the preparation of Compound **A** and Compound **B** as well as the Heck coupling reaction<sup>42-43</sup> of these compounds for the respective dyad syntheses. 2,7-Dibromo-9*H*-carbazole<sup>46</sup> and 1,6-dibromohexane were used as the starting materials to prepare 2,7-dibromo-9-(6'-bromohexyl)-carbazole, which was further converted into 2-[6-(2,7-dibromo-9*H*-carbazol-9-yl)hexyl]isoindoline-1,3-dione in a high yield via an S<sub>N</sub>2 reaction using potassium 1,3-dioxoisoindolin-2-ide as the nucleophile in DMF. 6-(2',7'-Dibromo-carbazol-9'-yl)hexan-1-amine was then obtained after the hydrogenation of 2-[6-(2,7-dibromo-9*H*-carbazol-9-yl)hexyl]isoindoline-1,3-dione with hydrazine upon heating in ethanol. This was used for further synthesis without additional purification, because of its limited solubility in common organic solvents. Compound **A** and Compound **B** were synthesized through the condensation reaction between (4-(2',7'-dibromo-carbazol-9'-yl)aniline<sup>46</sup> or 6-(2,7-dibromo-9*H*-carbazol-9-yl)hexan-1-amine) and *N*-(1-undecyl-dodecyl)-perylene-3,4-dicarboxylicmonoanhydride-9,10-dicarboxylicmonoimide<sup>47</sup> at 180 °C in molten imidazole using anhydrous zinc(II) acetate as a catalyst.<sup>29</sup> The yields of these reactions were around 80%, and the purification of the products was straightforward. The formation of the dyads via the Heck coupling reaction was carried out using 4-*n*-butyl-*N*-(4-butylphenyl)-*N*-(4-vinylphenyl)aniline<sup>48</sup> and Compound **A** or Compound **B**, and the yields were between 40 – 60%. The reference compounds, **Donor model** and **PDI model** (*N,N'*-di-undecyl-dodecyl-perylene-3,4,9,10-tetracarboxyldiimide),<sup>47</sup> with similar chemical structures to the donor and PDI moieties in the dyads, were prepared for comparison. <sup>1</sup>H and <sup>13</sup>C NMR spectra, together with mass spectroscopy and elemental analysis, were used to confirm the chemical structures and



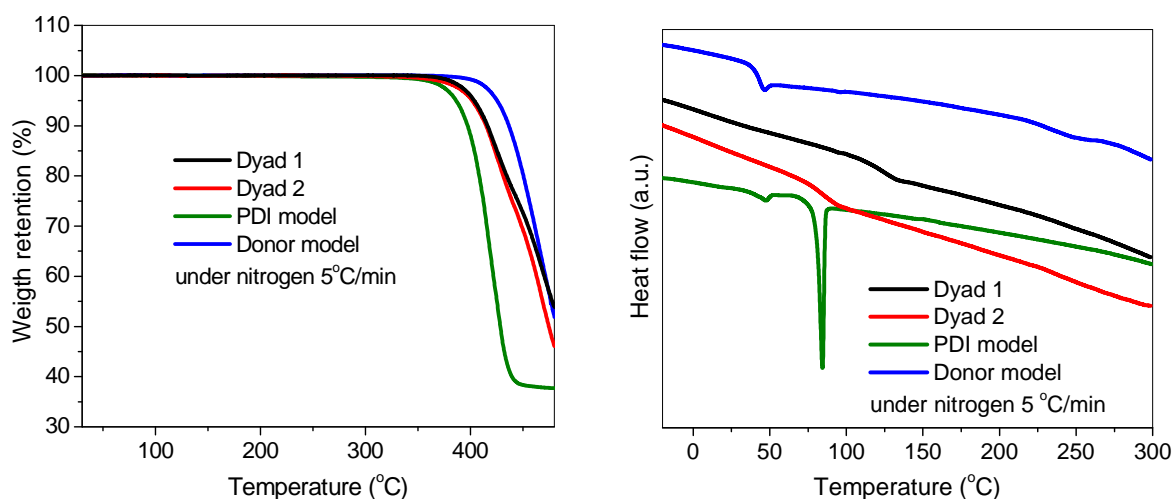


**Scheme 5.2.** The synthetic scheme for the dyads and donor model compound.

As shown in Figure 5.6 and Table 5.1, the dyads and respective model compounds exhibit good thermal stability, with the decomposition temperatures ( $T_d$ ), defined as that at which 5% weight loss is observed, in excess of 380 °C under nitrogen, according to thermogravimetric analysis (TGA) from room temperature to 500 °C. The **Donor model** has  $T_d$  at around 426 °C while that for **PDI model** is 384 °C.  $T_d$  for the dyads is slightly higher than 400 °C. The thermal behavior of these materials was recorded using



differential scanning calorimetry (DSC) in the temperature range from -20 to 300 °C under nitrogen atmosphere with a heating rate of 5 °C/min. The DSC trace for the second heating cycle revealed glass-transition temperatures ( $T_g$ ) of 119, 85, 51, and 40 °C, for Dyad 1, Dyad 2, PDI model, and Donor model, respectively. The lower  $T_g$  of Dyad 2 over Dyad 1 might be attributed to the more flexible linker between the donor moiety and PDI pendant. The first  $T_g$  for Donor model at 40 °C could be assigned to the side-chain  $T_g$ . There is also a small transition for Donor model at *ca.* 220 °C, which might be the glass transition for the aromatic scaffold, as the rigid chemical structure and possible  $\pi$ - $\pi$  stacking would lead to a higher  $T_g$ . In addition, there is a melting transition at 84 °C in the DSC trace of PDI model, while the absence of such a melting transition in the dyads suggests them to be amorphous materials. The good thermal stability and relatively high  $T_g$  for the dyads could be advantageous for some practical applications.

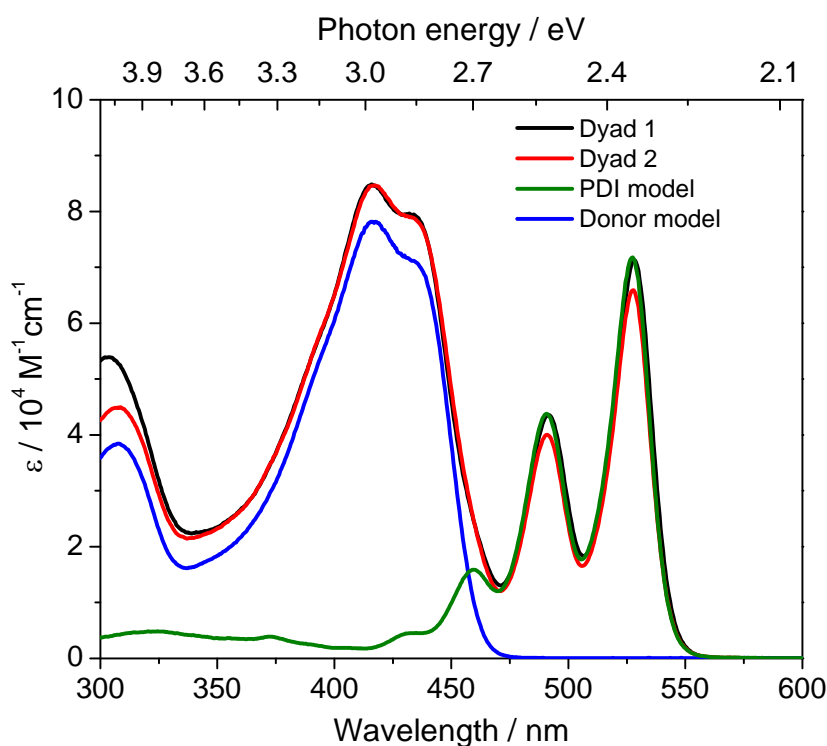


**Figure 5.6.** The TGA traces (left) for Dyad 1 (black), Dyad 2 (red), PDI model (green) and Donor model compound (blue) under N<sub>2</sub> flow with a 5K/min heating rate for each material. DSC (right) curves for Dyad 1 (black), Dyad 2 (red), PDI model (green) and Donor model (blue) with heating rate of 5 K/min under N<sub>2</sub> flow in the second cycle.

### 5.3 Optical properties of the dyads and model compounds

The UV-Vis absorption spectra of the dyads and the model compounds in dilute toluene solution (*ca.*  $1 \times 10^{-5}$  mol/L) are shown in Figure 5.7. The UV-Vis absorption spectra of the dyads are essentially superpositions of the characteristic absorption bands of both **Donor model** ( $\lambda_{\text{max}} = 416$  nm) and **PDI model** ( $\lambda_{\text{max}} = 528$  nm) model compounds. This is consistent with the expectation of limited ground-state electronic coupling between the donor moiety and PDI pendant, at least in dilute toluene solution. The absorbance ratio of the (0,0) and (0,1) transitions ((0,0)/(0,1)) of the PDI moieties in the dyads is *ca.* 1.66 in dilute solution. This indicates free-PDI-type absorption in solution and limited molecular aggregation among the PDI units is present in these dyads as well as the **PDI model**.<sup>49</sup> The emission spectra of these compounds are shown in Figure 5.8. The dyads and **Donor model** were excited at 390 nm, to minimize adventitious emission from the weak, ground-state PDI absorption (5% of that for **Donor model** in absorbance at 390 nm), while **PDI model** was excited at 490 nm. Both dyad compounds show much lower fluorescence quantum yields ( $0.4 \pm 0.1\%$  and  $4 \pm 1\%$  for Dyad **1** and Dyad **2**, respectively), than the **PDI model** ( $83 \pm 5\%$ ) and **Donor model** ( $89 \pm 5\%$ ) in toluene. Strong fluorescence quenching in the dyads suggests the possibility of the efficient electron transfer from the donor moiety and acceptor pendant following the donor excitation. Furthermore, both dyads show dual emission upon excitation at 390 nm (i.e., primary of the donor moiety) with also the PDI-based emission bands being observed, which suggests energy transfer from the excited donor to PDI, as well as the direct excitation of PDI at this wavelength. Excitation spectra of the dyads obtained at the PDI emission wavelength of 579 nm (Figure 5.9) yield a spectrum that matches the

shapes of both the donor and acceptor absorption in the dyads, indicating that the PDI emission observed when exciting the dyads at 390 nm originates from energy transfer. When the donor parts of the excitation spectra are normalized to that of the absorption spectra, the signal from the acceptor is stronger, because the energy transfer from the donor is not 100% efficient, and there is presumably some difference in electron-transfer efficiency between Dyad 1 and Dyad 2. From the emission spectra, it is clear that Dyad 2 exhibits much more efficient energy-transfer than Dyad 1. The linear optical properties of the dyads and model compounds are also summarized in Table 5.1.



**Figure 5.7.** The UV-Vis absorption spectra of the dyads and model compound: Dyad 1 (black), Dyad 2 (red), PDI model (green) and donor model (blue) in toluene with concentration of *ca.*  $1 \times 10^{-5} \text{ mol/L}$ .

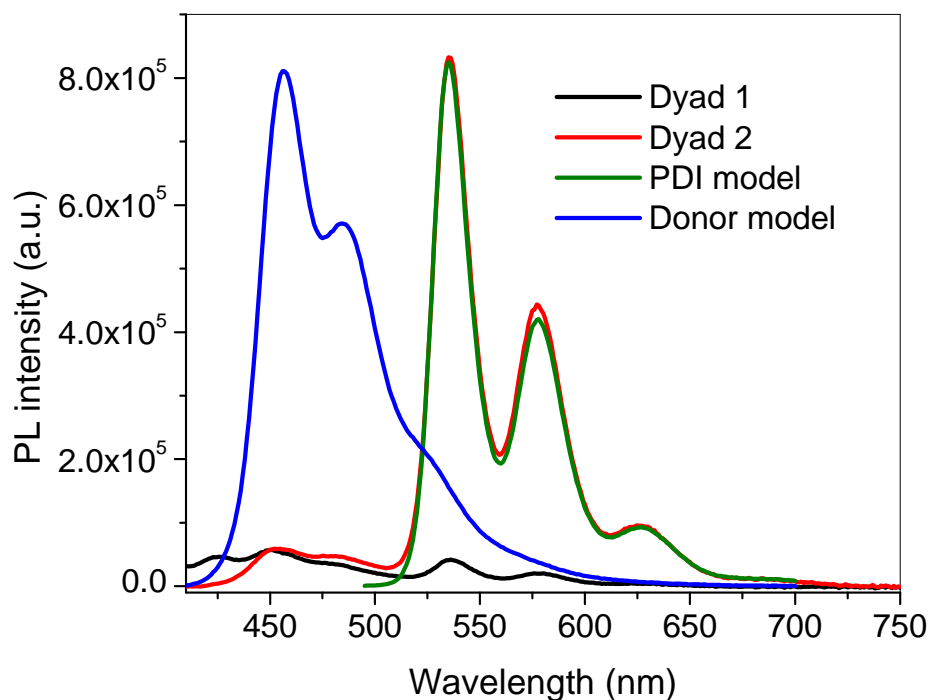


Figure 5.8. The emission spectra of the dyads and model compounds: Dyad 1 (black), Dyad 2 (red), PDI model (green) and donor model (blue) in toluene with concentration of *ca.*  $1 \times 10^{-6}$  mol/L. The Donor model and dyads are excited at 390 nm while the PDI model is excited at 490 nm.

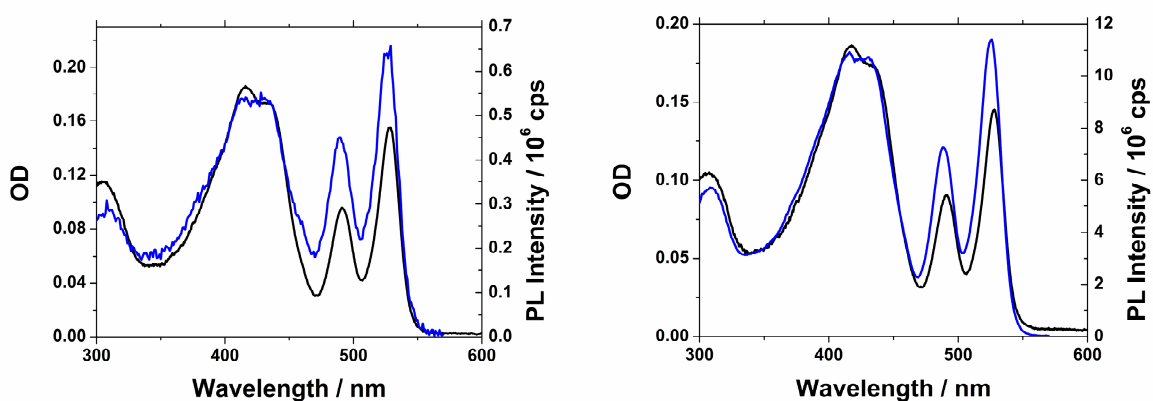


Figure 5.9. The excitation spectra (blue) of 2  $\mu$ M Dyad 1 (left) and Dyad 2 (right) in toluene with a fixed emission wavelength at 579 nm, overlaid with their respective absorption spectra (black) show that the dual emission observed for both dyads in the emission spectra is a result of energy transfer (Excitation spectra were collected by Dr. Matthew Sartin in the Perry group).

**Table 5.1, Summary of the linear optical properties for dyads and models in solution and thermal properties.**

<b>Materials</b>	<b><math>\lambda_{\text{abs}}/\text{nm}</math> (in <math>\text{CHCl}_3</math>)</b>	<b><math>\lambda_{\text{em}}/\text{nm}</math> (in toluene)</b>	<b><math>\eta_{\text{em}}</math> (in toluene)</b>	<b><math>T_d / ^\circ\text{C}</math></b>	<b><math>T_g / ^\circ\text{C}</math></b>
<b>Dyad A</b>	528, 492, 419	450, 537, 580 (Excited at 390 nm)	$0.4 \pm 0.1\%$	404	119
<b>Dyad B</b>	527, 490, 420	451, 535, 576, 620 (Excited at 390 nm)	$4 \pm 1\%$	402	86
<b>PDI model</b>	526, 490, 458	535, 577, 620 (Excited at 490 nm)	$83 \pm 5\%$	N/A	N/A
<b>Donor model</b>	419	456, 484 (Excited at 390 nm)	$89 \pm 5\%$	426	40, 243

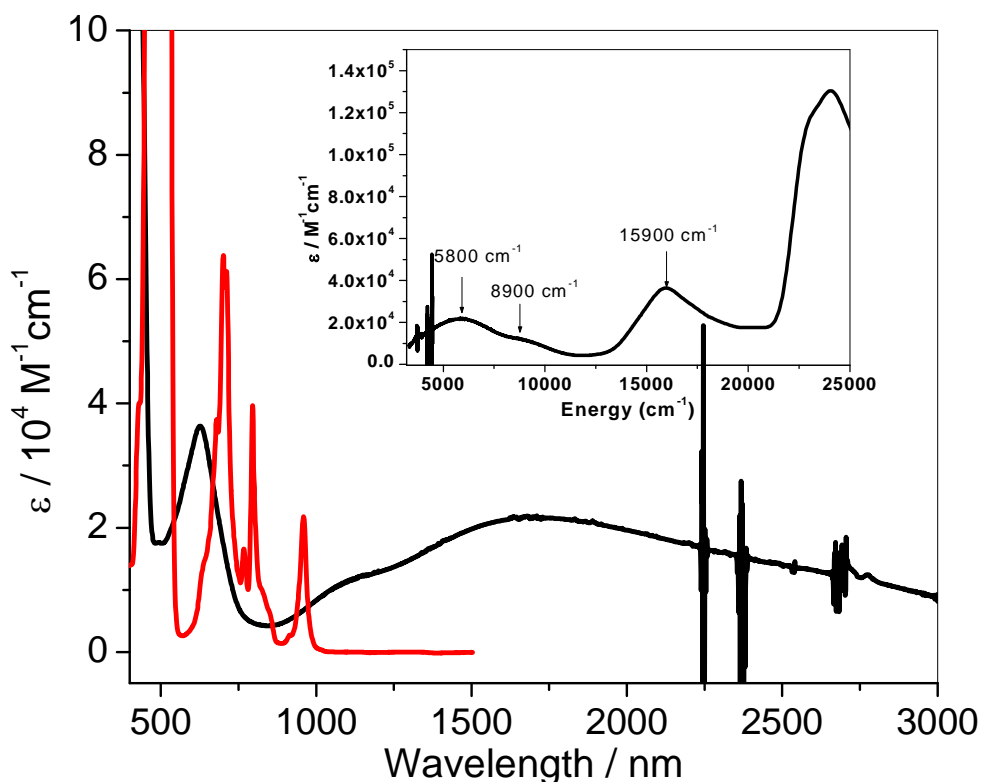
To demonstrate the photo-induced generation of radical ions, transient absorption spectra of the photo-excited dyads are compared with the ground-state absorption spectra of chemically generated radical ions of the model compounds and the dyads. The radical anion of **PDI model** was generated in THF solution by reduction with cobaltocene ( $E_{1/2}^{+/0} = -1.33 \text{ V}$  in  $\text{CH}_2\text{Cl}_2$  vs.  $\text{FeCp}_2^{+/0}$ ),<sup>37,50</sup> and the radical cation of **Donor model** was obtained in dichloromethane after oxidation with tris(*p*-bromophenyl)aminium hexachloroantimonate ( $E_{1/2}^{+/0} = +0.70 \text{ V}$  in  $\text{CH}_2\text{Cl}_2$  vs.  $\text{FeCp}_2^{+/0}$ ).<sup>37,50-51</sup> During the preparation of the radical cation or anion, a large excess of **PDI model** and **Donor model** compounds were used to ensure the generation of only mono-ions. As shown in Figure 5.10, the absorption spectrum of the **PDI model** radical anion is similar to the spectra of other PDI radical anions with similar chemical structures in literature, with peaks at 698, 798, and 958 nm.<sup>30,32,34,37</sup> The oxidation of **Donor model** leads to intense absorption bands in the visible to NIR region, with peaks at 630 and 1680 nm (*ca.* 16000 and 5900  $\text{cm}^{-1}$ , respectively). The rather intense ( $\epsilon_{\text{max}} = \text{ca. } 2.2 \times 10^4 \text{ M}^{-1}\text{cm}^{-1}$ ) absorption band

peaked at *ca.* 5900 cm<sup>-1</sup> within the NIR region could be ascribed to the inter-valence charge-transfer (IVCT) absorptions previously observed for other strongly coupled bis(diarylamino) mixed-valence cations, while the higher energy band peaked at 16000 cm<sup>-1</sup> with  $\epsilon_{\text{max}} = \text{ca. } 4 \times 10^4 \text{ M}^{-1}\text{cm}^{-1}$  is presumably related to the localized triarylamine type radical-cation absorption.<sup>51-52</sup> The observed width of the IVCT absorption band ( $\bar{\nu}_{1/2}[\text{obs}] = \text{ca. } 4000 \text{ cm}^{-1}$ ) is in good agreement with the width expected from Hush theory for class-II compounds ( $\bar{\nu}_{1/2}[\text{Hush}] = \text{ca. } 3660 \text{ cm}^{-1}$  according to Eq 5.1)<sup>53</sup> given in cm<sup>-1</sup> and  $\bar{\nu}_{\text{max}}$  here is also in cm<sup>-1</sup>, suggesting the radical cation of **Donor model** is belonging class-II type IVCT system. In the framework of the Hush model, the electronic coupling N-N distance, between nitrogen redox centers, may be derived from Eq 5.2,<sup>53</sup> where R was estimated to be around 22.1 Å for the intramolecular terminal N-N distance using approximation of B3LYP/6-31G\* in Gaussian 03 program suite. Here, was found to be *ca.* 670 cm<sup>-1</sup> and quite close to the electron coupling in a similar class-II IVCT system with phenylene instead of carbazole-base bridge.<sup>52</sup> It is worth noting the transition seen in the radical cation of **Donor model** at *ca.* 8900 cm<sup>-1</sup> could be attributed to a highest bridge-based orbital to the terminal donor radical cation (B → D<sup>+</sup>), which was also observed previously in other IVCT systems.<sup>52,54</sup> As more than one equivalent oxidation reagent, tris(*p*-bromophenyl)aminium hexachloroantimonate, was added (as shown in Figure 5.11), the absorption peaked at 1680 nm (around 5900 cm<sup>-1</sup>) started to decrease in intensity and a new absorption peaked at 1300 nm (~ 7700 cm<sup>-1</sup>) began to grow, which could be ascribed to the forming of the **Donor model** dications. Here, it should be noted that the formed **Donor model** dications exhibited a very similar higher

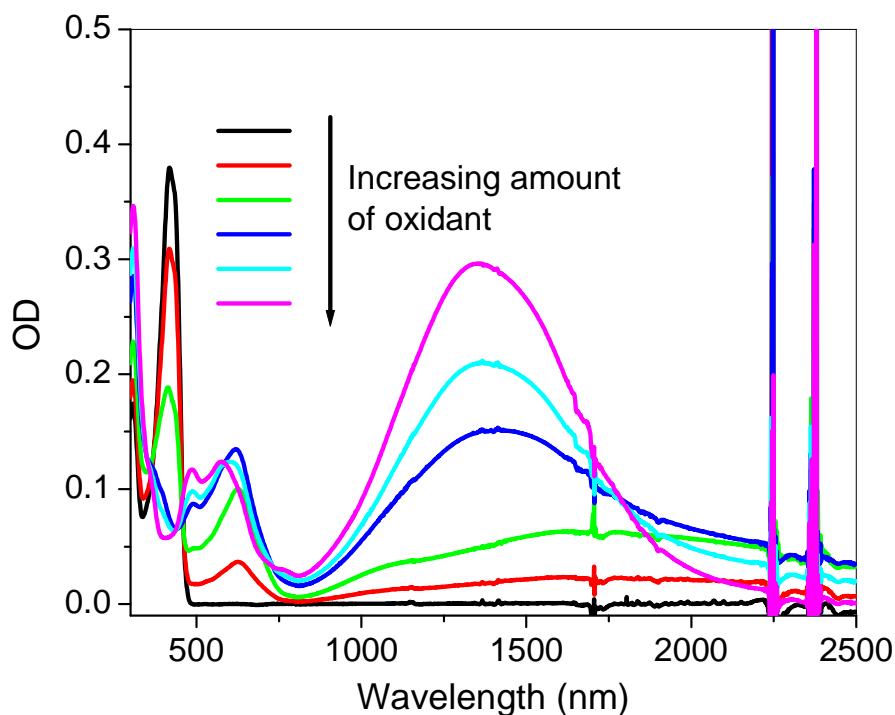
energy band, peaked at  $\sim 620$  nm ( $16100$   $\text{cm}^{-1}$ ), as that for the respective radical cations. It further supports that the argument that the higher energy band peaked at  $630$  nm ( $16000$   $\text{cm}^{-1}$ ) for the radical cation of **Donor model** is from the localized triarylamine type cations, which is expected to be similar to the localized triarylamine type cation in the dication of **Donor model**.

$$\bar{\nu}_{1/2}[\text{Hush}] = \sqrt{2310 \times \bar{\nu}_{\text{max}}} \quad \text{Eq 5.1}$$

$$V = 2.06 \times 10^{-2} \times (\epsilon_{\text{max}} \times \bar{\nu}_{\text{max}} \times \Delta \bar{\nu}_{1/2})^{1/2} / R \quad \text{Eq 5.2}$$



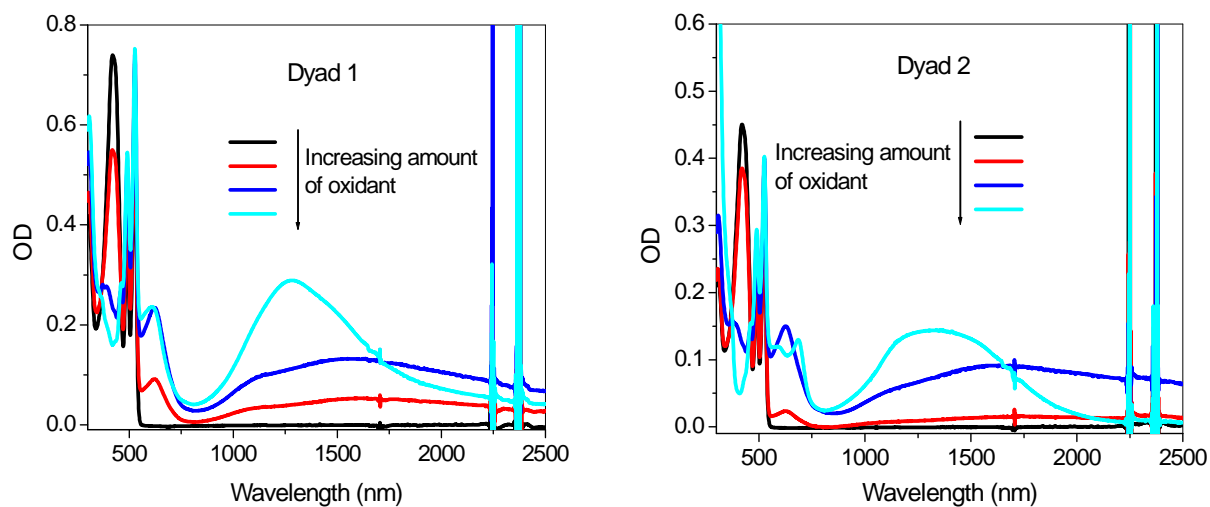
**Figure 5.10.** The radical-ion absorption of the model compounds: cation of **Donor model** in dichloromethane (black) and **PDI model** anion in THF (red). Both spectra were taken under nitrogen atmosphere. The inserted plot is the absorption spectrum of cation of **Donor model** plot in energy form. A large excess **PDI** or **Donor model** was used to ensure the generation of mono ion only.



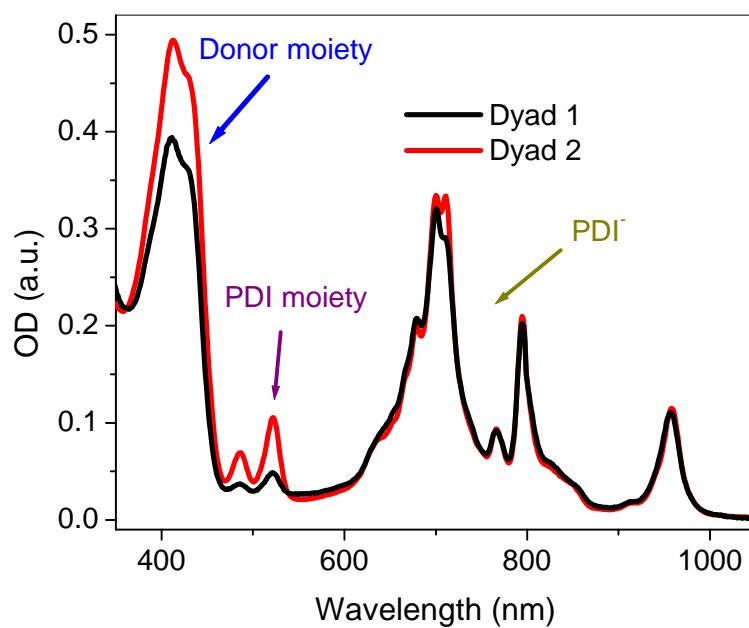
**Figure 5.11.** The neutral Donor model absorption spectrum (black) and the absorption spectra of Donor model with various amount (tris(*p*-bromophenyl)aminium hexachloroantimonate mixture) in CH<sub>2</sub>Cl<sub>2</sub>.

Similar spectra were obtained when the dyads were oxidized with various equivalents of oxidant reagent (tris(*p*-bromophenyl)aminium hexachloroantimonate), as illustrated in Figure 5.12. The PDI characteristic absorption bands remained almost unchanged for both dyads as the more oxidant reagent was added. When the dyads were reduced with cobaltocene in anhydrous THF, PDI radical anion type absorption was observed alongside the **Donor model** characteristic absorption band (Figure 5.13). The similarities of the radical anion and cation absorption spectra of the dyads to those of the **PDI model** or **Donor model**, respectively, suggests limited ground-state electronic coupling between the perylene diimide and donor moieties in the dyads.





**Figure 5.12.** The neutral Dyad 1 (left) and Dyad 2 (right) absorption (black) and the absorption of dyads with different amounts of oxidation reagent (tris(*p*-bromophenyl)aminium hexachloroantimonate mixture) in dichloromethane.



**Figure 5.13.** The radical-anion absorption spectra of the Dyad 1 (black) and Dyad 2 (red) via chemical reduction using cobaltocene in THF. The radical anions were generated in a nitrogen-flow glove-box and the absorption spectra were taken under nitrogen atmosphere.

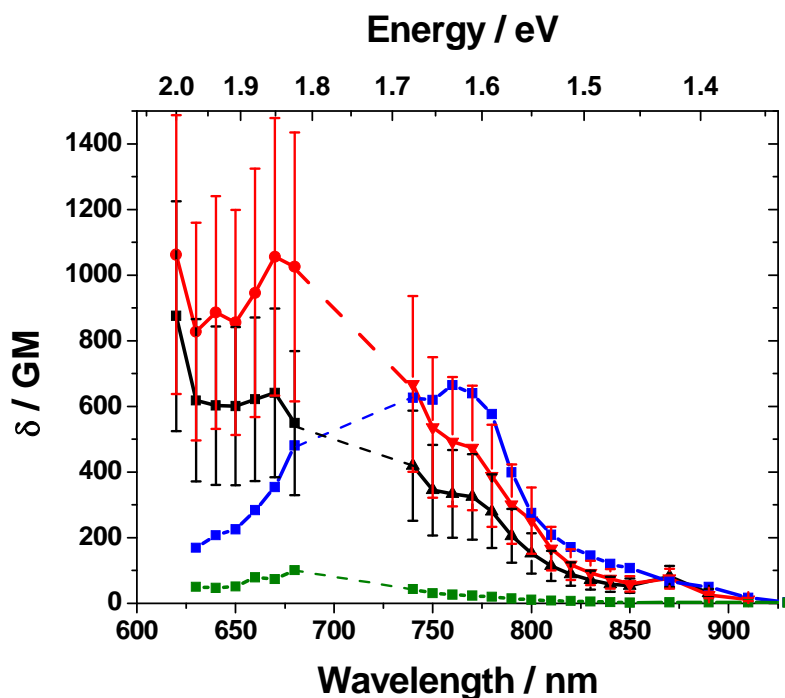


Figure 5.14. The 2PA spectra of Dyad 1 (black), Dyad 2 (red), Donor model (blue), and PDI model (green) prepared at 100  $\mu\text{M}$  in toluene. The difference between the dyad spectra and the 2PA spectrum of the donor and acceptor could result from overestimation of the quantum yield of the dyads, due to direct excitation of the acceptor in the one-photon fluorescence spectra. Additionally, the uncertainty in the dyad cross-section is  $\sim 40\%$ , due to the large uncertainty in dyad quantum yields. The uncertainty in the model compound-cross-section is  $\sim 15\%$  (2PA spectra were collected by Dr. Nisan Siegel in the Perry group).

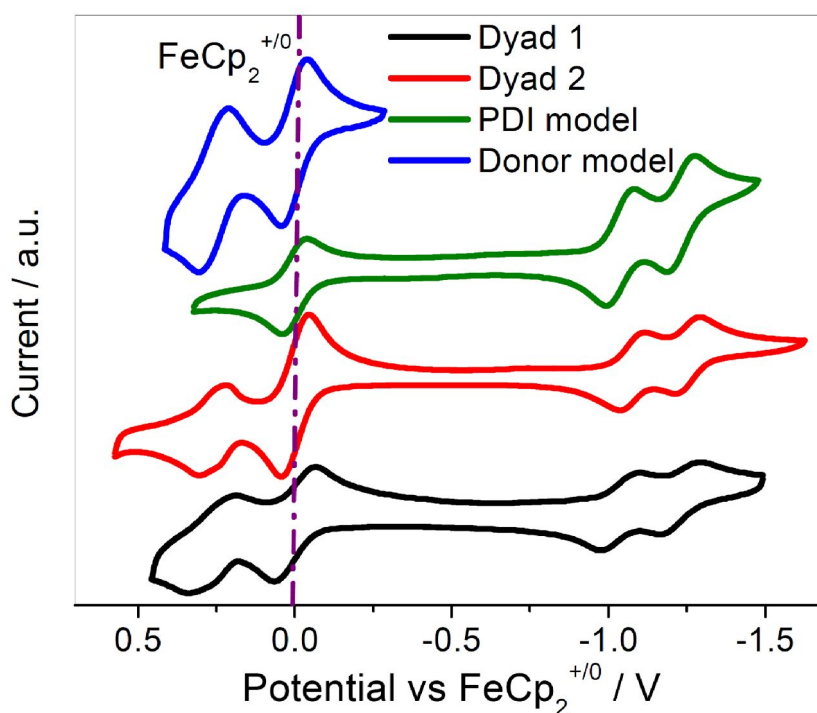
As shown in Figure 5.14, the 2PA spectrum of the **Donor model** has a maximum of *ca.* 750 nm with a 2PA cross-section around 700 GM. The spectrum of the **Donor model** resembles those of previously reported compounds similar in chemical structure with dihydrophenanthrene bridge instead of carbazole bridge.<sup>41</sup> The **PDI model** 2PA spectrum shows a weak absorption with a maximum 2PA cross-section of 100 GM near 680 nm, which is also consistent with previously reported 2PA data for PDIs and PDI-like species.<sup>55</sup> The dyad 2PA spectra resemble those of the model compounds in shape and 2PA cross-sections. The difference between the dyad spectra and the 2PA spectra of

the model compounds could result from the overestimation of the fluorescence quantum yield of the dyads, due to possible direct excitation of the PDI moieties at 390 nm, in the one-photon induced fluorescence spectra. Additionally, the uncertainty in the dyad 2PA cross-section is ~ 40% because of the large uncertainty in dyad emission quantum yields. Regardless of these issues, the data indicate considerable spectroscopic overlap of the donor 2PA band with both the PDI model radical-anion and donor model radical-cation absorptions between 600 – 800 nm. This suggests that the photo-generation of both radical ions following the 2PA excitation could enhance the strength of the nonlinear absorption to realize further optical suppression.

#### 5.4 Redox properties of the dyads and model compounds

As shown in Figure 5.15 and table 5.2, the electrochemical properties of the dyads and model compounds were investigated using cyclic voltammetry (CV) in anhydrous dichloromethane, using ferrocene ( $\text{FeCp}_2$ ) as an internal reference. The half-wave reduction potential ( $E_{1/2}^{0/-}$  and  $E_{1/2}^{-/2-}$ ) values (defined as  $(E_{pa} + E_{pc})/2$ , where  $E_{pa}$  and  $E_{pc}$  are peak oxidation and reduction potentials, respectively) of Dyad **1**, Dyad **2**, and **PDI model**, are around *ca.* -1.1 V for the first reduction and *ca.* -1.2 V for the second reduction vs.  $\text{FeCp}_2^{+/0}$  redox couple, respectively. These peaks correspond to the reduction of the PDI moieties and similar to the reported data for PDIs and PDI-like species.<sup>29</sup> In the oxidation, two close overlapping redox processes were observed for Dyad **1**, Dyad **2**, and **Donor model** all at *ca.* 0.27 V, which could be assigned to the two close oxidation process of the donor moieties. These observations, together with the UV-Vis absorption spectra of the dyads, suggest limited ground-state electronic coupling between chromophores within the dyads. According to these electrochemistry data, there

should be a sufficiently large LUMO offset (*ca.* 1.4 eV) between the PDI moiety and donor moiety in the dyads to promote efficient charge transfer in the dyads following photo-excitation of the donor. This is consistent with the strong fluorescence quenching observed in the dyads.<sup>56-57</sup>



**Figure 5.15.** The cyclic voltammograms of Dyad 1 (black), Dyad 2 (red), PDI model (green) and donor model (blue), in CH<sub>2</sub>Cl<sub>2</sub> (0.1 M [*n*-Bu<sub>4</sub>N][PF<sub>6</sub>]), with a scan rate = 50 mV s<sup>-1</sup> for each material, using FeCp<sub>2</sub> as an internal reference.

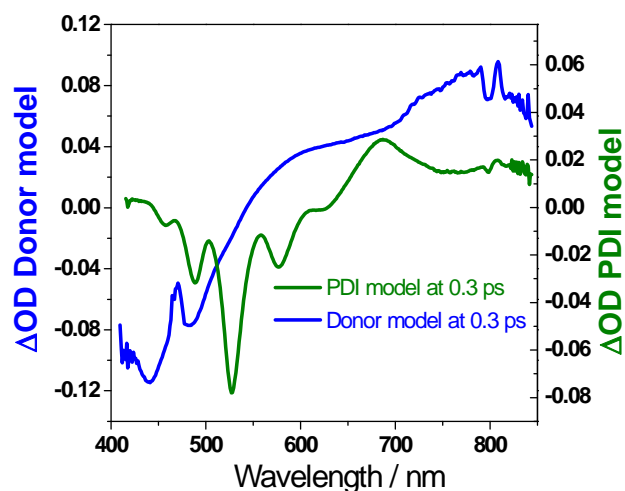
**Table 5.2.** Electrochemical half-wave potentials (V) for dyads and model compounds vs. FeCp<sub>2</sub><sup>+ / 0</sup> in CH<sub>2</sub>Cl<sub>2</sub> (0.1 M [*n*-Bu<sub>4</sub>N][PF<sub>6</sub>]) with a scan rate of 50 mV s<sup>-1</sup> for each material.

Materials	$E_{1/2}^{2+/+}$	$E_{1/2}^{+/0}$	$E_{1/2}^{0/-}$	$E_{1/2}^{-1/2-}$
Dyad 1	+0.27 <sup>a</sup>		-1.04	-1.23
Dyad 2	+0.27 <sup>a</sup>		-1.08	-1.25
PDI model	--		-1.08	-1.27
Donor model	+0.27 <sup>a</sup>		--	--

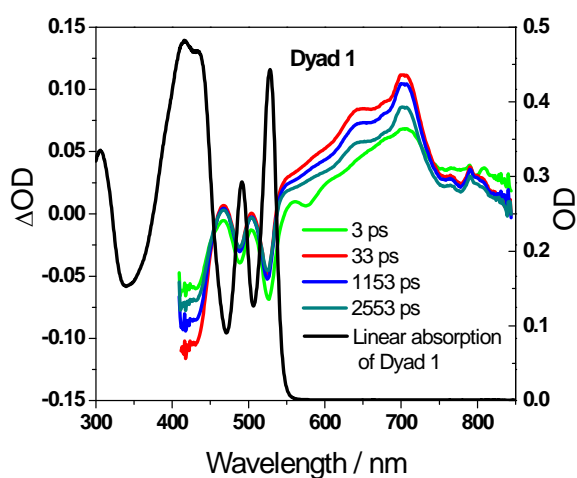
a : Two closely overlapping redox processes.

## 5.5 Transient absorption

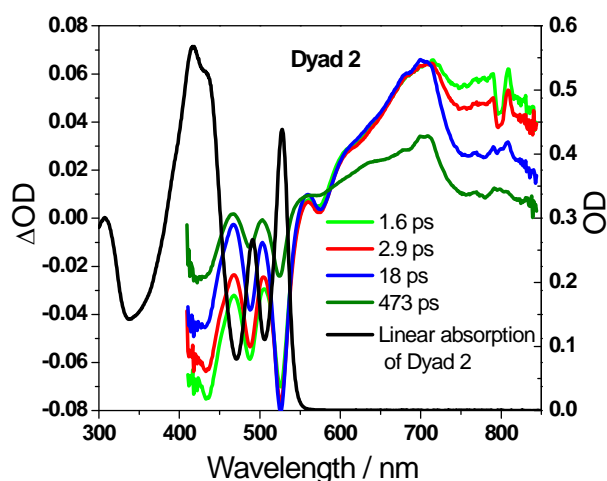
Femtosecond (fs) transient absorption spectroscopy was performed by Dr. Matthew Sartin in the Perry group on solutions of the dyads in order to verify the photo-generation of radical ion-pairs and determine their lifetimes. The transient absorption spectra of Dyad **1** and Dyad **2**, shown in Figure 5.15, were generated by pumping primarily the donor moiety at 390 nm. The transient spectra shortly after the photo-excitation (*ca.* approximately < 3 ps) show the excited-state absorption spectrum for the donor with some contribution of the acceptor assigned according to the transient data for the model compounds (Figure 5.15 a), presumably due to energy transfer. The spectra at later time intervals show the growth of absorption bands with peaks at 630 and 710 nm, as well as ground-state bleaching for both the donor and perylene diimide. The photo-induced absorption band positions match well with the electronic absorption band of the donor radical cation (*ca.* 625 nm in dichloromethane) and the PDI radical anion (*ca.* 700 nm in THF). Furthermore, photo-excitation of the donor also leads to a rapid depletion of the PDI ground-state, which is consistent with electron-transfer quenching of the donor excited state. Much stronger radical-ion absorption is apparent in the fs transient absorption spectra of Dyad **1** than in Dyad **2**, indicating more efficient charge transfer in Dyad **1** after photo-excitation. This is consistent with the lower fluorescence quantum yield and less efficient energy transfer observed for Dyad **1** than Dyad **2**.



(a)



(b)

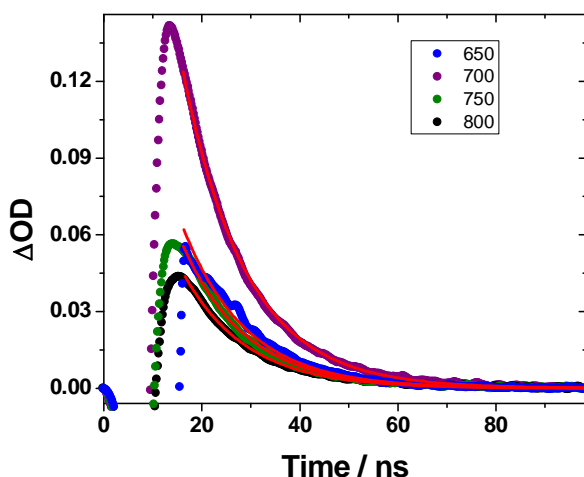


(c)

**Figure 5.16.** The fs-pulse transient absorption spectra for (a) Donor model (blue) and PDI model (green) in toluene with excitation at absorption maximum; (b) 34  $\mu\text{M}$  Dyad 1; and (c) 37  $\mu\text{M}$  Dyad 2 in toluene, at various time after photo-excitation at 390 nm with 2.7  $\mu\text{J}/\text{pulse}$  with OD of the dyads at  $\sim 0.35$  in a 2 mm cuvette under nitrogen atmosphere (The spectra were collected by Dr. Matthew Sartin in the Perry group).

The rise-time of the transient absorption corresponding to the radical ions is 3 ps for Dyad 1, indicates a fast electron transfer following the photo-excitation. The faster rise time of  $\sim 300$  fs of the absorption band peaked at *ca.* 700 nm for Dyad 2 probably

contains a certain amount of ESA absorption of PDI due to significant energy transfer, since the fluorescence data indicate strong energy transfer and significantly reduced the quenching of overall fluorescence compared to Dyad **1**. Moreover, the shape of the transient absorption spectra of Dyad **2** are significantly broader than that of Dyad **1**, especially for spectra in short decay time (ca. < 100 ps). This could indicate a contribution from the PDI excited-state absorption from energy transfer (fs transient absorption of the models are shown in Figure 5.16a), which occurs in the similar wavelength region (peaked at ca. 680 nm according to Figure 5.16a) as the radical ion spectra. Nanosecond transient absorption of Dyad **1** indicates a charge-separated lifetime of 13 ns (Figure 5.17). The charge-separated life-time for Dyad **2** is 600 ps according to the fs transient absorption spectra. The much faster charge-transfer and recombination rate of Dyad **2** in toluene is likely due to the flexibility of the hexylene linker, which allows conformational sampling of shorter donor-acceptor distance.



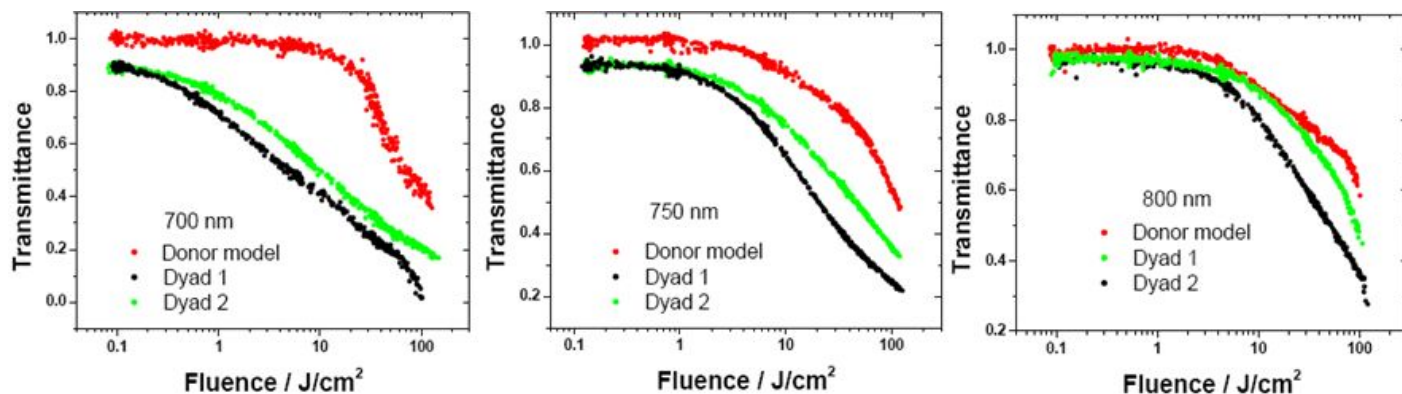
**Figure 5.17.** The Nanosecond pulse transient absorption decay following excitation at 355 nm (OD = 0.11) of 2  $\mu$ M Dyad **1** in toluene using 900  $\mu$ J/pulse. The initial 10 ns “bleach” is due to scattered laser light. The red lines are fit lines (The data were collected by Dr. Matthew Sartin in the Perry group).

## 5.6 Optical limiting

Optical limiting measurements were performed using nanosecond (ns) laser pulses (6 ns) at 700, 750, and 800 nm (Figure 5.18 and Table 5.3) by Dr. Matthew Sartin in the Perry group. The results indicate significantly stronger non-linear optical suppression for dyads **1** and **2**, as compared with **Donor model**, with the response of **1** being somewhat stronger than for **2** at all three wavelengths. The limiting threshold ( $I$  at  $T = T_0/2$ , where  $T_0$  is the linear transmission) of Dyad **1** ( $7.2 \text{ J/cm}^2$ ) is an order of magnitude lower than that of **Donor model** ( $72.4 \text{ J/cm}^2$ ) and just approximately half of that for Dyad **2** ( $14.6 \text{ J/cm}^2$ ) at 700 nm. A similar trend was observed at the other wavelengths (750 nm and 800 nm). The optical limiting response of the **Donor model** is attributed to 2PA, plus some contribution of ESA, particularly at longer wavelengths. The stronger limiting for the dyads is consistent with long-lived 2PA-induced charge-separated species leading to further absorption of incident light by intense absorption from the resultant radical ions. It should be noted that a small, linear absorption between 700 to 800 nm is observable in 2 mM solutions of the dyads, which lowers the linear transparency of the optical limiting samples for the dyads. The concentration-dependent growth of this band implies that it indicates an intermolecular charge-transfer-complex most likely due to the molecular aggregation at high concentration in solution (as shown in Figure 5.19). Excitation of the concentrated dyads (2 mM in toluene) by directly pumping this band at 680 nm resulted in similar charge-separated states as those from higher energy (390 nm) pumping with rapid charge recombination ( $< 40 \text{ ps}$ ). This observation suggests that such ground-state absorption of the charge-transfer-complexes



might have a deleterious contribution on generating long-lived ions for further optical suppression using nanosecond laser pulses.



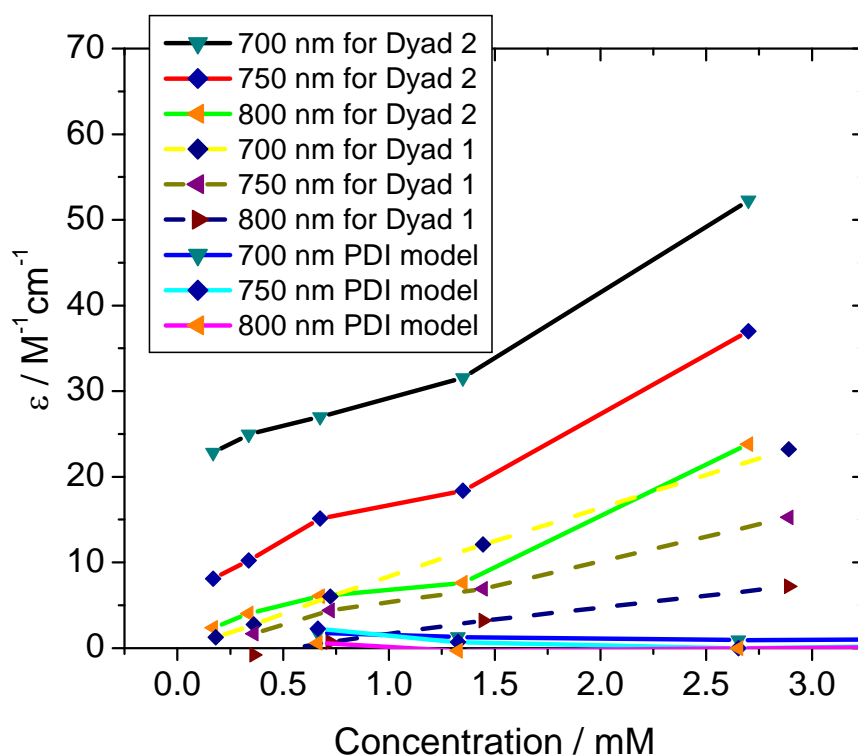
**Figure 5.18.** The nanosecond OL of 2 mM solutions of Dyad 1 (black), Dyad 2 (green), and Donor model (red) in toluene at various pump wavelengths focused in an f/5 geometry onto the middle of a 1 cm pathlength cell: 700 nm (left), 750 nm (center), and 800 nm (right) (The data were collected by Dr. Matthew Sartin in the Perry group).

**Table 5.3.** Summary of the optical limiting performance of the materials lines (The data were collected by Dr. Matthew Sartin in the Perry group).

Materials	Limiting threshold			Figure of Merit		
	(I at T = T <sub>0</sub> /2) J/cm <sup>2</sup>			(FOM = T <sub>0</sub> /T <sub>F</sub> )		
	700 nm	750 nm	800 nm	700 nm	750 nm	800 nm
Dyad 1	7.2	25.2	53.6	17.2	4.3	3.5
Dyad 2	14.6	56.3	94.9	5.4	2.9	2.2
Donor model	72.4	112	N.A.	2.8	2.1	1.7

The stronger optical limiting for Dyad 1 vs. 2 is consistent with the reduced photo-generated radical-ion population in Dyad 2 observed in the fluorescence and transient absorption measurements. The Figures of Merit (FOM = T<sub>0</sub>/T<sub>F</sub>, where T<sub>0</sub> is the linear transmission, and T<sub>F</sub> is the high fluence transmission) for optical limiting of Dyad 1

in toluene are 17.2, 4.2, and 3.5 using 700 nm, 750 nm, and 800 nm excitation, respectively. These FOMs compare favorably with FOM obtained from porphyrinviologen dyads (2.4 at 600 nm) that used one-photon-induced charge-separated state to provide the optical limiting.<sup>58</sup> While higher FOM have recently been reported for a MEH-PPV/fullerene blend-based charge-separated systems,<sup>27</sup> solutions of the present dyads facilitate simple infiltration of microcapillary waveguides,<sup>59</sup> which can lead to dramatically increased interaction length, thereby enhancing the optical limiting (FOM > 37 for Dyad **1** and ~ 17 for Dyad **2** at 750 nm).



**Figure 5.19.** Concentration dependence of peak absorption coefficients at 700, 750, and 800 nm for the Dyads and PDI model.

## 5.7 Conclusions

Two donor-PDI dyads with 2PA D- $\pi$ -D type donor have been synthesized and characterized. Long-lived charge-separated states were demonstrated via transient absorption spectra in the donor-PDI dyads after the photo-excitation on donor moieties in the dyads. The donor-acceptor linker strongly affects the rate of charge transfer and recombination. Dyad **1**, with its rigid, phenylene linker, exhibits lower charge transfer and recombination rates than Dyad **2**, which has a hexylene linker. Furthermore, the stronger fluorescence quenching observed for Dyad **1** indicates more efficient charge photo-generation. In both cases, the strong overlap of the corresponding perylene diimide radical-anion absorption with the 2PA band of the attached D- $\pi$ -D donor leads to strong enhancement of the optical limiting by the dyads over that of the 2PA chromophore itself. This work also illustrates an approach through which donors and acceptors can be independently chosen to maximize optical limiting for a particular spectral range. Moreover, the ability to vary the timescale for recombination by altering the linker groups may allow further optimization of the optical suppression.

## 5.8 Experimental section

**General.** Most organic and inorganic chemicals were obtained from Aldrich and Alfa Aesar. Palladium-based catalysts were purchased from Strem Chemicals and used without further purification. The  $^1\text{H}$  and  $^{13}\text{C}$  NMR spectra were collected on a Bruker 400 MHz or Bruker 500 MHz spectrometer using tetramethylsilane (TMS;  $\delta = 0$  ppm) as an internal standard. Mass spectra were measured on a VG Instruments 70-SE using the electron impact (EI) mode or on an Applied Biosystems 4700 Proteomics Analyzer using

MALDI mode. Elemental analyses were carried out by Atlantic Microlabs using a LECO 932 CHNS elemental analyzer. Solution UV-Vis absorption spectra were recorded on a Varian Cary 5E spectrophotometer. Solution emission and excitation spectra were measured using Fluorolog-2 from Spex (Edison, NJ). Electrochemical measurements were carried out under nitrogen in deoxygenated 0.1 M solutions of tetra-*n*-butylammonium hexafluorophosphate in dry CH<sub>2</sub>Cl<sub>2</sub> using a computer-controlled BAS 100B electrochemical analyzer, a glassy-carbon working electrode, a platinum-wire auxiliary electrode, and Ag wire anodized with AgCl as a pseudo-reference electrode. Potentials were referenced to the ferrocenium/ferrocene (FeCp<sub>2</sub><sup>+/0</sup>) couple by using ferrocene as an internal standard. TGA measurements were performed on an NETZSCH STA 449C analyzer under a nitrogen flow of 40 mL/min with a heating rate of 5 °C /min. DSC measurements were performed on a TA Instruments DSC Q200 analyzer under a nitrogen flow of 50 mL/min with a heating and cooling rate of 5 °C/min.

**Generation of radical ions.** The radical anion of the **PDI model** compound was generated in anhydrous THF solution by reduction with cobaltocene in a nitrogen atmosphere glove box. The radical cation of the **donor model** compound was generated in anhydrous dichloromethane by oxidation with tris(*p*-bromophenyl)aminium hexachloroantimonate. The absorption spectra of the radical ions were recorded a Varian Cary 5E UV-Vis-NIR spectrophotometer using 1.0 cm pathlength cells.

**Two-photon absorption spectroscopy:** Two-photon absorption (2PA) spectra were determined using the reference-based two-photon excited fluorescence (2PEF) method by Dr. Nisan Sigel in the Perry group.<sup>14,60</sup> The source of excitation light was a nanosecond pulsed optical parametric oscillator (Quanta-Ray MOPO 730) pumped by a Q-switched

Nd:YAG laser (Quanta-Ray PRO250). The 2PEF method determines the 2PA spectra of unknowns by measuring the fluorescence emitted by the unknowns under two-photon excitation conditions and comparing it to the fluorescence emitted by a known reference compound under the same conditions. The 2PEF measurements of the model compounds were made in toluene (Sigma-Aldrich spectroscopic grade) solution at chromophore concentrations of 80–110  $\mu\text{M}$ . The data reported here comprise several collections of over 200 pulses at each wavelength. 1,4-Bis(2-methylstyryl)benzene (Sigma-Aldrich, 99%) in cyclohexane (Sigma-Aldrich, spectroscopic grade) and fluorescein<sup>61</sup> (Acros, laser grade) in aqueous NaOH solution (pH 11) were used as references for 630 – 680 nm and 690 – 1040 nm, respectively. The 2PA cross-section values of 1,4-bis(2-methylstyryl)benzene reported by Kennedy<sup>62</sup> were reduced in scale by a factor of 10, as described by Fisher. The uncertainties in the measured cross sections are approximately  $\pm 15\%$  for the model compounds and approximately  $\pm 40\%$  for the dyads.

**Femtosecond transient absorption measurements:** The femtosecond transient absorption spectra were collected by Dr. Matthew M. Sartin in the Perry group. The excitation source for femtosecond transient absorption measurements was generated by an optical parametric amplifier (TOPAS, Newport) pumped by a Ti:Sapphire regenerative amplifier (Spitfire, Newport), operating at 1 kHz repetition rate. The 800 nm Spitfire output could be varied by the TOPAS over 465 – 2900 nm. For wavelengths below 465 nm, the TOPAS output was frequency doubled using a BBO crystal. Approximately 5% of the 800 nm Spitfire output was used to generate the white-light continuum probe beam (420–950 nm) in a sapphire plate. The laser pulse width in this spectral region was 120 fs. Transient data were collected using a commercially available

Helios spectrometer (Ultrafast Systems, Sarasota, FL). The width of the instrument response function was 200 fs, and the maximum time delay was 3.2 ns. At each temporal delay, the signal was averaged for 1 s. The pump beam was chopped at 500 Hz to alternate between signal and reference data. A correction factor for the chirp of the white light was generated using the ultrafast response of toluene. All samples were prepared in 2 mm cuvettes and deaerated with N<sub>2</sub>. The pump wavelengths were 390 nm for Dyad **1** (34  $\mu$ M, OD = 0.35), Dyad **2** (34  $\mu$ M, OD = 0.36), and **Donor model** (30  $\mu$ M, OD = 0.32) and 530 nm for **PDI model** compound (29  $\mu$ M, OD = 0.39). The pump energy for all samples was  $\sim$ 3.3  $\mu$ J/pulse.

**Nanosecond transient absorption measurements:** The nanosecond transient absorption spectra were collected by Dr. Matthew M. Sartin in the Perry group. The excitation source for transient absorbance experiments was an optical parametric oscillator (Newport Spectra-Physics, Irvine, CA) pumped by the third harmonic of a Nd:YAG laser (Newport Spectra-Physics) with a pulse width of 6 ns. A 2  $\mu$ M sample of Dyad **1** in a deaerated, 1 cm cuvette was pumped at 528 nm (OD = 0.33), using  $\sim$ 2 mJ/cm<sup>2</sup>. The probe beam was generated using a 240W tungsten-halogen lamp (Oriel 69931 Radiometric Power Supply, Newport Oriel, Irvine, CA). The pump and probe overlapped at an angle of  $\sim$ 5° in the sample. The white light was focused into an Acton SpectraPro 2150i monochromator (Princeton Instruments, Trenton, NJ) and the transmitted light was collected by a HCA-S-200M-Si photodiode (Femto, Berlin, Germany). The transient signal was digitized using a Tektronix digital oscilloscope (Model 3034B, 300 MHz, 2.5 Gigasamples/sec). The response time of the system was limited by the laser pulse width.

**Nanosecond Optical-Limiting Measurements:** The nanosecond transient optical limiting measurements were performed by Dr. Matthew M. Sartin in the Perry group. The excitation source for optical-limiting (OL) measurements is the same as that for nanosecond transient absorption. A mechanical shutter reduced the pulse repetition rate to 1 Hz to minimize damage to the sample. The dyads were prepared as deaerated, 2 mM solutions in 1 cm cuvettes, with transmittance > 0.9 at the excitation wavelength of 750 nm. The laser was focused into the center of the cuvette using f/5 geometry, and the transmitted light was detected by a New Focus photoreceiver (San Jose, California), sampled using a Stanford Research Systems boxcar averager (Sunnyvale, CA), and recorded using an analog to digital converter and computer. A beam splitter placed before the sample redirected part of each pulse to a reference photoreceiver to normalize for fluctuations in the input energy of each pulse.

**2,7-Dibromo-9-(6-bromohexyl)-9H-carbazole:** 2,7-Dibromo-9H-carbazole<sup>46</sup> (1.62 g, 5.00 mmol) and KOH (0.28 g, 5.0 mmol) were stirred in anhydrous DMF (20 mL) at 0 °C. Then 1,6-dibromohexane (2.5 g, 10 mmol) was added in one portion, and the resultant mixture was stirred overnight at room temperature. The mixture was poured into water (300 mL), and ethyl acetate (200 mL) was used to extract the product. The organic phase was washed with water (6 × 100 mL) and dried over Na<sub>2</sub>SO<sub>4</sub>. After the solvent was removed, the residue was recrystallized from hexane (100 mL) to afford a white solid (1.94 g, 79%). <sup>1</sup>H NMR (500 MHz, CDCl<sub>3</sub>): δ 7.88 (d, *J* = 8.5 Hz, 2H), 7.50 (s, 2H), 7.33 (dd, *J*<sub>1</sub> = 8.5 Hz, *J*<sub>2</sub> = 1.0 Hz, 2H), 4.20 (t, *J* = 7.0 Hz, 2H), 3.38 (t, *J* = 6.5 Hz, 2H), 1.88 (m, 4H), 1.51 (m, 2H), 1.47 (m, 2H). <sup>13</sup>C{<sup>1</sup>H} NMR (125 MHz, CD<sub>2</sub>Cl<sub>2</sub>): δ 141.3, 122.6, 121.5, 121.3, 119.7, 111.9, 43.2, 33.6, 32.5, 28.6, 27.9, 26.4. HRMS (EI) calcd. for

244

$C_{18}H_{18}Br_3N$  ( $M^+$ ): 484.8989, found: 484.8979. Anal. Calcd. for  $C_{18}H_{18}Br_3N$ : C, 44.30; H, 3.72; N, 2.87. Found: C, 44.26; H, 3.67; N, 2.93.

**2-[6-(2,7-Dibromo-9*H*-carbazol-9-yl)hexyl]isoindoline-1,3-dione:** 2,7-Dibromo-9-(6-bromohexyl)-9*H*-carbazole (1.60 g, 3.30 mmol) was dissolved in anhydrous DMF (10 mL) and cooled to 0 °C. Potassium 1,3-dioxoisindolin-2-ide (1.3 g, 7.0 mmol) was then added in one portion. The resultant mixture was stirred overnight at room temperature and then poured into water (200 mL). The white solid was collected by filtration and purified by column chromatography on silica gel, eluted with  $CH_2Cl_2$  / hexane (1:2) to give a white solid (1.64 g, 90%).  $^1H$  NMR (500 MHz,  $CDCl_3$ ):  $\delta$  7.85 (d,  $J$  = 8.0 Hz, 2H), 7.83 (m, 2H), 7.69 (m, 2H), 7.48 (d,  $J$  = 1.5 Hz, 2H), 7.31 (dd,  $J_1$  = 8.0 Hz,  $J_2$  = 1.5 Hz, 2H), 4.19 (t,  $J$  = 7.5 Hz, 2H), 3.68 (t,  $J$  = 7.0 Hz, 2H), 1.84 (m, 2H), 1.66 (m, 2H), 1.42 (m, 4H).  $^{13}C\{^1H\}$  NMR (125 MHz,  $CD_2Cl_2$ ):  $\delta$  168.4, 141.3, 133.9, 132.1, 123.2, 122.5, 121.5, 121.3, 119.7, 111.9, 43.2, 37.7, 28.7, 28.4, 26.7, 26.6. HRMS (EI) calcd. for  $C_{26}H_{22}Br_2N_2O_2$  ( $M^+$ ): 552.0048, found: 552.0023. Anal. Calcd. for  $C_{26}H_{22}Br_2N_2O_2$ : C, 56.34; H, 4.00; N, 5.05. Found: C, 56.37; H, 4.09; N, 5.05.

**6-(2,7-Dibromo-9*H*-carbazol-9-yl)hexan-1-amine:** 2-[6-(2,7-Dibromo-9*H*-carbazol-9-yl)hexyl]isoindoline-1,3-dione (1.67 g, 3.00 mmol) and hydrazine monohydrate (2.2 mL) were heated in refluxing ethanol (60 mL) for 4 h. After the reaction mixture was cooled to -10 °C, the white solid was filtered and washed with cold methanol to give a white solid (1.24 g, 99%) which was used in the synthesis of compound **B** without further purification, due to the poor solubility.



**Compound A:** *N*-(1-Undecyl-dodecyl)-perylene-3,4-dicarboxyanhydride-9,10-dicarboximide<sup>2</sup> (0.356 g, 0.50 mmol), 4-(2,7-dibromo-9*H*-carbazol-9-yl)aniline<sup>46</sup> (0.413 mg, 1.00 mmol), anhydrous zinc (II) acetate (80 mg, 0.44 mmol), and imidazole (3.0 g) were heated under N<sub>2</sub> at 180 °C overnight. The reaction mixture was then allowed to be cooled to *ca.* 130 °C and poured into 4N aqueous HCl (160 mL). The red precipitate was collected by filtration and washed with 2N aqueous HCl (3 × 10 mL), water (3 × 10 mL), and methanol (2 × 10 mL) in a subsequence. The solid was then dissolved in CHCl<sub>3</sub> (5 mL) and a minimum amount of silica gel was added to absorb the liquid. After the solvent was removed under reduced pressure, the dried silica gel was added to the top of a hexane-packed silica gel column, and the column was eluted with CHCl<sub>3</sub> to give a red solid (0.53 g, 89 %). <sup>1</sup>H NMR (500 MHz, CDCl<sub>3</sub>): δ 8.78 (d, *J* = 8.0 Hz, 2H), 8.72–8.662 (m, 6H), 7.95 (d, *J* = 8.5 Hz, 2H), 7.75 (d, *J* = 8.5 Hz, 2H), 7.68 (d, *J* = 1.0 Hz, 2H), 7.65 (d, *J* = 8.5 Hz, 2H), 7.42 (dd, *J*<sub>1</sub> = 8.5 Hz, *J*<sub>2</sub> = 1.0 Hz, 2H), 5.18 (m, 1H), 2.26 (m, 2H), 1.86 (m, 2H), 1.29–1.21 (m, 36H), 0.83 (t, *J* = 6.5 Hz, 6H). <sup>13</sup>C{<sup>1</sup>H} NMR (125 MHz, CDCl<sub>3</sub>): δ 165.0, 164.1, 163.9, 141.8, 137.2, 135.8, 134.9, 134.6, 134.5, 132.4, 132.3, 131.6, 131.2, 130.2, 129.9, 128.9, 128.0, 127.0, 126.7, 124.6, 124.4, 123.9, 123.8, 123.6, 123.5, 123.3, 122.3, 122.0, 121.8, 120.6, 116.4, 113.6, 113.5, 55.3, 32.8, 32.3, 30.2, 30.1 (3 peaks) 30.0, 29.8, 27.5, 23.2, 14.7 (the observation of three carbonyl carbon resonances is consistent with previous work on perylene bis(dicarboxyimide)s using similar swallow-tailed *N*-substituents and it has been attributed to restricted rotation of the N—C<sub>alkyl</sub> bonds.<sup>3</sup> Two aromatic carbon peaks and one alkyl carbon were not observed, presumably due to overlap). HRMS (MALDI) calcd. for C<sub>65</sub>H<sub>65</sub>Br<sub>2</sub>N<sub>3</sub>O<sub>4</sub> (M<sup>+</sup>): 1109.33, found: 1109.35. Anal. Calcd. for C<sub>65</sub>H<sub>65</sub>Br<sub>2</sub>N<sub>3</sub>O<sub>4</sub>: C, 70.20; H, 5.89; N, 3.78. Found: C, 69.99; H, 5.92; N, 3.81

**Compound B:** *N*-(1-Undecyl-dodecyl)-perylene-3,4-dicarboxyanhydride-9,10-dicarboximide<sup>2</sup> (0.713 g, 1.00 mmol), 6-(2,7-dibromo-9*H*-carbazol-9-yl)hexan-1-amine (0.500 g, 1.2 mmol), anhydrous zinc (II) acetate (200 mg, 1.10 mmol), and imidazole (10.0 g) were heated under N<sub>2</sub> at 180 °C overnight. The reaction mixture was allowed to cool to *ca.* 130 °C and poured into 4 N aqueous HCl (160 mL). The red precipitate was collected by filtration and washed with water (3 × 30 mL) and then with methanol (3 × 30 mL). The solid was then dissolved in CHCl<sub>3</sub> (10 mL) and a minimum amount of silica gel was added to absorb the liquid. After the solvent was removed under reduced pressure, the dried silica gel was added to the top of a hexane-packed silica gel column and eluted with CHCl<sub>3</sub> / hexane (3:2 and then 2:1, and finally CHCl<sub>3</sub> / ethyl acetate (20:1). After the solvent was removed, **Compound B** was obtained as a red solid (0.81 g, 72%). <sup>1</sup>H NMR (500 MHz, CDCl<sub>3</sub>): δ 8.65–8.56 (m, 8H), 7.83 (d, *J* = 8.0 Hz, 2H), 7.49 (s, 2H), 7.29 (d, *J* = 8.0 Hz, 2H), 5.16 (m, 1H), 4.19 (m, 4H), 4.16 (t, *J* = 7.5 Hz, 2H), 2.25 (m, 2H), 1.85 (m, 4H), 1.74 (m, 2H), 1.47 (m, 4H), 1.30 – 1.17 (m, 34H) 0.83 (t, *J* = 6.0 Hz, 6H). <sup>13</sup>C{<sup>1</sup>H} NMR (125 MHz, CD<sub>2</sub>Cl<sub>2</sub>): δ 164.6, 163.4 (2 close peaks), 141.3, 134.7, 134.3, 131.8, 131.4, 131.1, 129.5, 129.3, 126.4, 126.3, 124.0, 123.1, 122.9, 122.5, 121.4, 121.2, 119.7, 111.9, 55.0, 43.3, 40.3, 32.4, 31.9, 29.6 (3 peaks), 29.5, 28.6, 27.8, 27.0, 26.9, 26.7, 25.0, 22.6, 14.1. (the observation of three carbonyl carbon resonances is consistent with previous work on perylene bis(dicarboxyimide)s using similar swallow-tailed *N*-substituents and it has been attributed to restricted rotation of the N—C<sub>alkyl</sub> bonds.<sup>3</sup> One alkyl carbon resonance was not observed, presumably due to overlap). HRMS (MALDI) calcd. for C<sub>65</sub>H<sub>73</sub>Br<sub>2</sub>N<sub>3</sub>O<sub>4</sub> (M<sup>+</sup>): 1117.402, found: 1117.379. Anal. Calcd. for C<sub>65</sub>H<sub>73</sub>Br<sub>2</sub>N<sub>3</sub>O<sub>4</sub>: C, 69.70; H, 6.57; N, 3.75. Found: C, 69.86; H, 6.49; N, 3.67.

**Dyad 1:** Compound **A** (0.33 g, 0.30 mmol), *N,N*-di(4-*n*-butylphenyl)-4-vinylaniline (0.77 g, 2.0 mmol), tri-*o*-tolylphosphine (60 mg, 0.20 mmol), and palladium(II) acetate (22 mg, 0.010 mmol) were charged to a two-neck round-bottomed flask equipped with a condenser. After evacuating and refilling the flask with nitrogen three times, DMF (9.0 mL) and triethylamine (3.0 mL) were added by syringe. The resultant mixture was then heated under N<sub>2</sub> at 100 °C for 24 h. After the mixture was allowed to cool to room temperature, it was poured into methanol (100 mL) and the resultant solid was collected by filtration. The solid was then dissolved in toluene and purified using column chromatography on silica gel, with toluene / hexane (3:1) as the eluent. After the solvent was removed under reduced pressure, the resultant solid was heated in refluxing ethanol for 2 h; Dyad **1**, as a red solid, was collected by filtration while the solution was hot (298 mg, 58%). <sup>1</sup>H NMR (500 MHz, CDCl<sub>3</sub>): δ 8.70–8.62 (m, 8H), 8.09 (d, *J* = 8.0 Hz, 2H), 7.88 (d, *J* = 8.5 Hz, 2H), 7.69 (d, *J* = 8.0 Hz, 2H), 7.64 (s, 2H), 7.54 (d, *J* = 8.0 Hz, 2H), 7.41 (d, *J* = 8.5 Hz, 4H), 7.17 (s, 4H), 7.11 (d, *J* = 8.5 Hz, 8H), 7.02 (d, *J* = 8.5 Hz, 8H), 6.98 (d, *J* = 8.5 Hz, 2H), 5.18 (m, 1H), 2.92 (t, *J* = 7.5 Hz, 8H), 2.26 (m, 2H), 1.86 (m, 2H), 4.39 (t, *J* = 6.0 Hz, 2H), 3.63 (m, 2H) 3.03 (t, *J* = 6.0 Hz, 2H), 2.26 (m, 2H), 2.04 (m, 2H), 1.87 (m, 2H), 1.63 (quintet, *J* = 7.5 Hz, 8H), 1.41–1.2 (m, 34H), 0.96 (t, *J* = 7.5 Hz, 12H), 0.84 (t, *J* = 7.5 Hz, 6H). <sup>13</sup>C{<sup>1</sup>H} NMR (125 MHz, CDCl<sub>3</sub>): δ 163.9, 163.0, 162.8, 147.0, 144.5, 141.0, 137.3, 137.0, 135.4, 134.7, 133.5, 133.2, 131.3, 130.1, 129.8, 129.2, 128.9, 128.5, 137.3, 127.2, 126.5, 126.1, 125.8, 123.9, 122.8, 122.5, 122.4, 122.1, 121.9, 119.6, 118.2, 107.1, 54.2, 34.4, 33.0, 31.7, 31.2, 28.9 (4 closely spaced peaks), 28.6, 26.3, 22.0, 21.8, 13.4, 13.3. (the observation of three carbonyl carbon resonances is consistent with previous work on perylene bis(dicarboxyimide)s using similar swallow-tailed *N*-substituents and it has been

attributed to restricted rotation of the N—C<sub>alkyl</sub> bonds.<sup>3</sup> Two aromatic carbon and one alkyl carbon resonance were not observed, presumably due to overlap). HRMS (MALDI) calcd. for C<sub>121</sub>H<sub>129</sub>N<sub>5</sub>O<sub>4</sub> (M<sup>+</sup>): 1717.005, found: 1715.998 ((M-1)<sup>+</sup>). Anal. Calcd. for C<sub>121</sub>H<sub>129</sub>N<sub>5</sub>O<sub>4</sub>: C, 84.62; H, 7.57; N, 4.08; Found: C, 84.53; H, 7.65; N, 4.12.

**Dyad 2:** Compound **B** (0.33 g, 0.30 mmol), *N,N*-di(4-*n*-butylphenyl)-4-vinylaniline (0.77 g, 2.0 mmol), tri-*o*-tolylphosphine (60 mg, 0.20 mmol), and palladium (II) acetate (22 mg, 0.010 mmol) were charged to a two-neck, round-bottomed flask equipped with a condenser. After evacuating and refilling the flask with nitrogen three times, DMF (9 mL) and triethylamine (3 mL) were added by syringe. The mixture was then heated under N<sub>2</sub> at 100 °C for 24 h. After the mixture was allowed to cool to room temperature, the solvent was removed under reduced pressure and the residue was purified by column chromatography on silica gel, eluted with CHCl<sub>3</sub> / hexane (1:1 and then 4:3). After the solvent was removed under reduced pressure, the resulting solid was refluxed in ethanol for 2 h; Dyad **2**, as a red solid, was collected by filtration while the solution was hot (210 mg, 41%). <sup>1</sup>H NMR (500 MHz, CD<sub>2</sub>Cl<sub>2</sub>): δ 8.6–8.4 (m, 8H), 7.94 (d, *J* = 8.0 Hz, 2H), 7.49 (s, 2H), 7.42 (d, *J* = 9.0 Hz, 4H), 7.37 (d, *J* = 8.0 Hz, 2H), 7.19 (s, 4H), 7.08 (d, *J* = 7.0 Hz, 8H), 7.0–6.7 (m, 12H), 5.2–5.1 (m, 1H), 4.35 (t, *J* = 7.0 Hz, 2H), 4.16 (t, *J* = 7.0 Hz, 2H), 2.58 (t, *J* = 7.5 Hz, 8H), 2.3–2.2 (m, 2H), 1.95–1.94 (m, 2H), 1.87–1.83 (m, 2H), 1.77–1.73 (m, 2H), 1.60 (quintet, *J* = 8.0 Hz, 8H), 1.4–1.2 (m, 48H), 0.95 (t, *J* = 7.5 Hz, 12H), 0.84 (t, *J* = 7.0 Hz, 6H). <sup>13</sup>C{<sup>1</sup>H} NMR (125 MHz, CDCl<sub>3</sub>): δ 164.6, 163.5, 163.4, 147.6, 145.2, 141.4, 137.7, 137.6, 135.4, 134.6, 134.4, 131.8, 131.4, 131.1, 130.9, 129.5, 128.3, 129.1, 128.9, 127.7, 127.6, 127.2, 126.4, 126.3, 124.6, 123.9, 123.1, 122.9, 122.5, 122.2, 120.2, 117.5, 106.5, 54.8, 43.0, 40.3, 35.0, 33.7, 32.3, 31.9, 29.6, 29.5, 29.3, 28.8, 27.7,

27.0, 26.9, 26.7, 22.7, 22.4, 14.1, 14.0. (The observation of three carbonyl carbon resonances, along with three additional aromatic resonances, can be attributed to restricted rotation of the N—C<sub>alkyl</sub> bonds.<sup>3</sup> Two alkyl carbon resonances were not observed, presumably due to overlap). HRMS (MALDI) calcd. for C<sub>121</sub>H<sub>137</sub>N<sub>5</sub>O<sub>4</sub> (M<sup>+</sup>): 1724.067, found: 1724.075. Anal. Calcd. for C<sub>121</sub>H<sub>137</sub>N<sub>5</sub>O<sub>4</sub>: C, 84.22; H, 7.95; N, 4.09. Found: C, 84.02; H, 8.08; N, 4.05.

**Donor model:** 2,7-Dibromo-9-*n*-hexyl-9*H*-carbazole<sup>63</sup> (0.41 g, 1.0 mmol), *N,N*-di(4-*n*-butylphenyl)-4-vinylaniline<sup>5</sup> (1.0, 2.6 mmol), tri-*o*-tolylphosphine (60 mg, 0.20 mmol), and palladium (II) acetate (22 mg, 0.010 mmol) were charged to a two-neck round-bottomed flask equipped with a condenser. After evacuating and refilling the flask with nitrogen three times, DMF (12 mL) and triethylamine (4 mL) were added by syringe. The mixture was then heated under N<sub>2</sub> at 100 °C for 12 h. After the mixture was allowed to cool to room temperature, the solvent was removed under reduced pressure and the residue was purified by column chromatography on silica gel, using CHCl<sub>3</sub>/hexane (1:20 and then 1:5) as eluents to give **Donor model** as a yellow solid (0.44 g, 44%). <sup>1</sup>H NMR (500 MHz, CD<sub>2</sub>Cl<sub>2</sub>): δ 8.00 (d, *J* = 8.0 Hz, 2H), 7.38 (s, 2H), 7.43–7.40 (m, 6H), 7.19 (s, 4H), 7.11 (d, *J* = 8.0 Hz, 8H), 7.02–6.99 (m, 12H), 4.35 (t, *J* = 7.0 Hz, 2H), 2.59 (t, *J* = 7.5 Hz, 8H), 1.93 (quintet, *J* = 7.5 Hz, 2H), 1.61 (quintet, *J* = 6.5 Hz, 8H), 1.4–1.2 (m, 14H), 0.95 (t, *J* = 7.0 Hz, 12H), 0.89 (t, *J* = 7.0 Hz, 3H). <sup>13</sup>C{<sup>1</sup>H} NMR (125 MHz, CD<sub>2</sub>Cl<sub>2</sub>): δ 148.2, 145.6, 142.0, 138.4, 135.9, 131.2, 129.6, 127.9, 127.8, 127.5, 125.1, 122.6, 122.5, 120.6, 118.0, 106.8, 43.4, 35.4, 34.1, 32.0, 29.3, 27.3, 22.9, 22.8, 14.2, 14.1. (Two aromatic carbon resonances were not observed, presumably due to overlap). HRMS

(MALDI) calcd. for  $C_{74}H_{83}N_3$  ( $M^+$ ): 1013.659, found: 1013.665. Anal. Calcd. for  $C_{74}H_{83}N_3$ : C, 87.61; H, 8.25; N, 4.14. Found: C, 87.35; H, 8.18; N, 4.11.

**PDI model:** (*N,N'*-Bis(1-undecyl-dodecyl)-perylene-3,4,9,10-tetracarboxylic diimide): A mixture of perylene-3,4,9,10-tetracarboxydianhydride (6.0 g, 15 mmol), 1-undecyl-dodecylamine (12 g, 35 mmol), anhydrous zinc (II) acetate (1.6 g, 8.7 mmol) and imidazole (70 g) were heated at 180 °C for 5 hours before it was allowed to cool to room temperature and treated with 2 N aqueous HCl solution (400 mL). The mixture was then extracted with chloroform (2 × 200 mL). The organic phase was washed with water (3 × 100 mL) and dried over  $MgSO_4$ . The solvent was then removed under reduced pressure and the residue was purified by flash chromatography on silica gel, using  $CHCl_3$  / hexane (1:1 and then 2:1) as eluent to give **PDI model** as a red solid (12 g, 77%).  $^1H$  NMR (500 MHz,  $CDCl_3$ ):  $\delta$  8.64 (m, 8H), 5.18 (m, 2H), 2.22 (m, 4H), 1.86 (m, 4H), 1.4–1.1 (m, 72H), 0.80 (t,  $J$  = 6.6 Hz, 12H). The  $^1H$  NMR spectrum of this product is consistent with that reported in the literature.<sup>34</sup>

## 5.9 References

- (1) Spangler, C. W. *J. Mater. Chem.* **1999**, 9, 2013-2022.
- (2) Zhang, L.; Wang, L. *J. Mater. Sci.* **2008**, 43, 5692-5701.
- (3) Pawlicki, M.; Collins, H. A.; Denning, R. G.; Anderson, H. L. *Angew. Chem. Int. Ed.* **2009**, 48, 3244-3266.
- (4) Perry, J. W.; Mansour, K.; Lee, I.-Y. S.; Wu, X.-L.; Bedworth, P. V.; Chen, C.-T.; Ng, D.; Marder, S. R.; Miles, P.; Wada, T.; Tian, M.; Sasabe, H. *Science* **1996**, 273, 1533-1536.
- (5) Su, X.; Xu, H.; Yang, J.; Lin, N.; Song, Y. *Polymer* **2008**, 29, 3722-2730.
- (6) Zhou, G.-J.; Wong, W.-Y.; Poon, S.-Y.; Ye, C.; Lin, Z. *Adv. Funct. Mater.* **2009**, 19, 531-544.
- (7) Zhou, G.-J.; Wong, W.-Y.; Lin, Z.; Ye, C. *Angew. Chem. Int. Ed.* **2006**, 45, 6189-6193.
- (8) Zhou, G.-J.; Wong, W.-Y.; Ye, C.; Lin, Z. *Adv. Funct. Mater.* **2007**, 17, 963-972.
- (9) Ehrlich, J. E.; Wu, X. L.; Lee, I.-Y. S.; Hu, Z.-Y.; Rockel, H.; Marder, S. R.; Perry, J. W. *Opt. Lett.* **2002**, 25, 1843-1845.
- (10) Charlot, M.; Izard, N.; Mongin, O.; Riehl, D.; Blanchard-Desce, M. *Chem. Phys. Lett.* **2006**, 417, 297-302.
- (11) Bouit, P.-A.; Wetzel, G.; Berginc, G.; Loiseaux, B.; Toupet, L.; Feneyrou, P.; Bretonniere, Y.; Kamada, K.; Maury, O.; Andraud, C. *Chem. Mater.* **2007**, 19, 5325-5335.
- (12) Göppert-Mayer, M. *Ann. Phys.* **1931**, 401, 273-294.
- (13) Kaiser, W.; Garrett, C. G. B. *Phys. Rev. Lett.* **1961**, 7, 229-231.
- (14) Rumi, C.; Barlow, S.; Wang, J.; Perry, J. W.; Marder, S. R. *Adv. Polym. Sci.* **2008**, 213, 1-95.
- (15) He, G. S.; Tan, L.-S.; Zheng, Q.; Prasad, P. N., 108, 1245. *Chem. Rev.* **2008**, 108, 1245-1330.
- (16) Birge, R. R.; Pierce, B. M. *Int. J. Quantum Chem.* **1986**, 29, 639-656.
- (17) Wang, J. *Ph.D thesis* **2007**, University of Arizona.
- (18) Kasha, M. *Discuss. Faraday Soc.* **1950**, 9, 14-19.
- (19) Rumi, M.; Pond, S. J. K.; Meyer-Friedrichsen, T.; Zhang, Q.; Bishop, M.; Zhang, Y.; Barlow, S.; Marder, S. R.; Perry, J. W. *J. Phys. Chem. C* **2008**, 112, 8061-8071.
- (20) Gu, B.; Ji, W.; Patil, P. S.; Dharmaprakash, S. M. *J. Appl. Phys.* **2008**, 103, 103511.
- (21) Gu, B.; Ji, W.; Huang, X. Q.; Patil, P. S.; Dharmaprakash, S. M. *J. Appl. Phys.* **2009**, 033511.
- (22) Silly, M. G.; Porrès, L.; Mongin, O.; Chollet, P.-A.; Blanchard-Desce, M. *Chem. Phys. Lett.* **2003**, 379, 74-8.
- (23) Belfield, K. D.; Bondar, M. V.; Hernandez, F. E.; Przhonska, O. F. *J. Phys. Chem. C* **2008**, 112, 5618-5622.

- (24) Perry, J. W.; Barlow, S.; Ehrlich, J. E.; Heikal, A. A.; Hu, Z.-Y.; Lee, I.-Y. S.; Mansour, K.; Marder, S. R.; Röckel, H.; Rumi, M.; Thayumanavan, S.; Wu, X.-L. *Nonlinear Opt.* **1999**, *21*, 225-230.
- (25) Belfield, K. D.; Bondar, M. V.; Hernandez, F. E.; Przhonska, O. V. *J. Phys. Chem. C* **2008**, *112*, 5618-5622.
- (26) Cha, M.; Sariciftci, N. S.; Heeger, A. J.; Hummelen, J. C.; Wudl, F. *Appl. Phys. Lett.* **1995**, *67*, 3850-3852.
- (27) Chi, S.-H.; Hales, J. M.; Cozzuol, M.; Ochoa, C.; Fitzpatrick, M.; Perry, J. W. *Opt. Express* **2009**, *17*, 22062-22072.
- (28) Gust, D.; Moore, T.; Moore, A. *J. Photochem. Photobiol. B* **2000**, *58*, 63-65.
- (29) Würthner, F. *Chem. Commun.* **2004**, 1564-1579.
- (30) Ford, W. E.; Hiratsuka, H.; Kamat, P. V. *J. Phys. Chem. A* **1989**, *93*, 6692-6696.
- (31) Wasielewski, M. R. *Acc. Chem. Res.* **2009**, *42*, 1910-1921.
- (32) O'Neil, M. P.; Niemczyk, M. P.; Svec, W. A.; Gosztola, D.; L. Gaines, G.; Wasielewski, M. R. *Science* **1992**, *257*, 63-65.
- (33) Jimnez, A. J.; Spnig, F.; Rodriguez-Morgade, M. S.; Ohkubo, K.; Fukuzumi, S.; Guldi, D. M.; Torres, T. *Org. Lett.* **2007**, 2481-2484.
- (34) Kelley, R. F.; Shin, W. S.; Rybtchinski, B.; Sinks, L. E.; Wasielewski, M. R. *J. Am. Chem. Soc.* **2007**, *129*, 3173-3181.
- (35) Bullock, J. E.; Carmieli, R.; Mickley, S. M.; Vura-Weis, J.; Wasielewski, M. R. *J. Am. Chem. Soc.* **2009**, *131*, 11919-11929.
- (36) Kelley, R. F.; Tauber, M. J.; Wasielewski, M. R. *J. Am. Chem. Soc.* **2006**, *128*, 4779-4791.
- (37) An, Z.; Odom, S. A.; Kelley, R. F.; Huang, C.; Zhang, X.; Barlow, S.; Padilha, L. A.; Fu, J.; Webster, S.; Hagan, D. J.; Stryland, E. W. V.; Wasielewski, M. R.; Marder, S. R. *J. Phys. Chem. A* **2009**, *113*, 5585-5593.
- (38) Albota, M.; Beljonne, D.; Brédas, J.-L.; Ehrlich, J. E.; Fu, J.-Y.; Heikal, A. A.; Hess, S. E.; Kogej, T.; Levin, M. D.; Marder, S. R.; McCord-Maughon, D.; Perry, J. W.; Röckel, H.; Rumi, M.; Subramaniam, G.; Webb, W. W.; Wu, X.-L.; Xu, C. *Science* **1998**, *281*, 1653-1656.
- (39) Mongin, O.; Porres, L.; Charlot, M.; Katan, C.; Blanchard-Desce, M. *Chem. Eur. J.* **2007**, *131*, 1481-1498.
- (40) Belfield, K. D.; Bondar, M. V.; Hernandez, F. E.; Przhonska, O. V.; Yao, S. *J. Phys. Chem. B* **2007**, *111*, 12723-12729.
- (41) Ventelon, L.; Blanchard-Desce, M.; Moreaux, L.; Mertz, J. *Chem. Commun.* **1999**, 2055-2056.
- (42) Heck, R. F.; Nolley, J. P. *J. Org. Chem.* **1972**, *37*, 2320-2322.
- (43) Heck, R. F. *Org. React.* **1982**, *27*, 345-390.
- (44) de Meijere, A.; Meyer, F. E. *Angew. Chem. Int. Ed* **1994**, *33*, 2379-2411.
- (45) Belfield, K. D.; Yao, S.; Bondar, M. V. *Adv. Polym. Sci.* **2008**, *213*, 97-156.
- (46) Jian, H.; Tour, J. M. *J. Org. Chem.* **2003**, *68*, 5901-5103.
- (47) Tauber, M. J.; Kelley, R. F.; Giaimo, J. M.; Rybtchinski, B.; Wasielewski, M. R. *J. Am. Chem. Soc.* **2006**, *128*, 1782-1783.



- (48) Behl, M.; Hattemer, E.; Brehmer, M.; Zentel, R. *Macromol. Chem. Phys.* **2002**, *203*, 503-510.
- (49) Gómez, R.; Veldman, D.; Blanco, R.; Seoane, C.; Segura, J. L.; Janssen, R. A. J. *Macromolecules* **2007**, *40*, 2760-2772.
- (50) Connelly, N. G.; Geiger, W. E. *Chem. Rev.* **1996**, *96*, 877-910.
- (51) Odom, S. A.; Lancaster, K.; Beverina, L.; Lefler, K. M.; Thompson, N. J.; Coropceanu, V.; Brédas, J.-L.; Marder, S. R.; Barlow, S. *Chem. Eur. J.* **2007**, *13*, 9637-9646.
- (52) Barlow, S.; Risko, C.; Chung, S.-J.; Tucker, N. M.; Coropceanu, V.; Jones, S. C.; Levi, Z.; Brédas, J. L.; Marder, S. R. *J. Am. Chem. Soc.* **2005**, *127*, 16900-16911.
- (53) Hush, N. S. *Prog. Inorg. Chem.* **1967**, *8*, 391-444.
- (54) Jones, S. C.; Coropceanu, V.; Barlow, S.; Kinnibrugh, T.; Timofeeve, T.; Brédas, J. L.; Marder, S. R. *J. Am. Chem. Soc.* **2004**, *126*, 11782-11783.
- (55) Corrêa, D. S. O., S. L.; Misoguti, L.; Zilio, S. C.; Aroca, R. F.; Constantino, C. J. L.; Mendonça, C. R. *Journal of Physical Chemistry A* **2006**, *110*, 6433-6438.
- (56) Brédas, J.-L.; Beljonne, D.; Coropceanu, V.; Cornil, J. *Chem. Rev.* **2004**, *104*, 4971-5004.
- (57) Thompson, B. C.; Fréchet, J. M. J. *Angew. Chem. Int. Ed.* **2008**, *47*, 58-77.
- (58) Dupuis, B.; Michaut, C.; Jouanin, I.; Delaire, J.; Robin, P.; Feneyrou, P.; Dentan, V. *Chem. Phys. Lett.* **1999**, *300*, 169-176.
- (59) Hales, J. M.; Cozzuol, M.; Screen, T. E. O.; Anderson, H. L.; Perry, J. W. *Opt. Express* **2009**, *17*, 18478-18481.
- (60) Rumi, M.; Ehrlich, J. E.; Heikal, A. A.; Perry, J. W.; Barlow, S.; Hu, Z.; McCord-Maughon, D.; Parker, T. C.; Rockel, H.; Thayumanavan, S.; Marder, S. R.; Beljonne, D.; Brédas, J.-L. *J. Am. Chem. Soc.* **2000**, *122*, 9500-9510.
- (61) Xu, C.; Webb, W. W. *J. Opt. Soc. Am. B* **1996**, *13*, 481-491.
- (62) Kennedy, S. M.; Lytle, F. E. *Anal. Chem.* **1986**, *58*, 2643-2647.
- (63) Tang, W.; Lin, T.; Ke, L.; Chen, Z.-K. *J. Polym. Sci. Part A: Polym. Chem.* **2008**, *46*, 7725-7738.

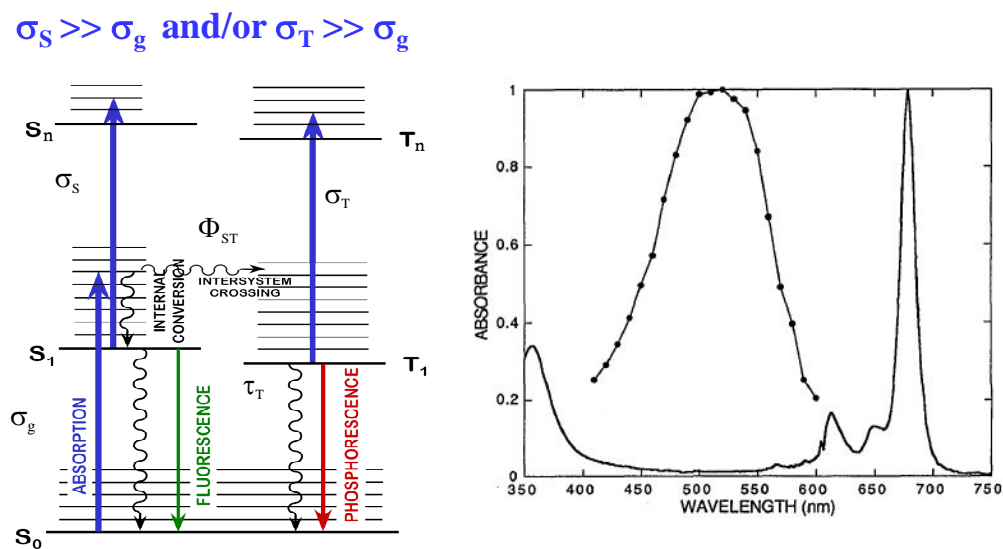
## CHAPTER 6

### PHOTO-INDUCED ELECTRON TRANSFER AND OPTICAL LIMITING IN POLY(CARBAZOLE-ALT-FLUORENE)S BEARING PERYLENE DIIMIDES AS PENDANT ACCEPTOR

#### 6.1 Introduction

As discussed in Chapter 5, the design of effective optical power limiters for use in various wavelength regions has attracted significant research interest due to their potential applications in protecting optical sensors, including human eyes.<sup>1-2</sup> One of the key challenges for effective optical limiting is the development of systems that maintain high transparency under low-intensity irradiation, but that can also instantaneously attenuate an incident laser pulse whose pulse length may vary from femto- to micro-seconds. This requires effective optical limiters in which different absorption mechanisms are involved at different intensities of irradiation and that can provide pulse attenuation over very short to moderate time scales.<sup>1-3</sup> Materials that exhibit reverse saturable absorption (RSA) are currently of interest for optical limiting of highly energetic laser beams. RSA can occur under conditions of intense irradiation when the excited states of the materials, typically the lowest singlet-state ( $S_1$ ) and / or triplet-state ( $T_1$ ), have absorption cross section ( $\sigma_e$ ) considerably in excess of the corresponding ground-state absorption cross section ( $\sigma_g$ ) at the same wavelength. The effectiveness of molecules exhibiting RSA for optical limiting is determined mainly by the ratio of excited-state to ground-state absorption cross sections,  $\sigma_e/\sigma_g$ , which is a function of wavelength, and the populations of the states that evolve in time during the pulse.<sup>1,4</sup> In

general, for a system with sufficient linear absorption and excited-state life-time, the larger of the  $\sigma_e/\sigma_g$ , the better the potential optical limiting response at the certain wavelengths. Fullerene derivatives,<sup>5-6</sup> heavy-atom-substituted phthalocyanines (Pc),<sup>7-10</sup> and oligo- and/or poly-metallayne-based compounds<sup>11-13</sup> are among the most promising RSA-based materials for optical limiting because they exhibit wide wavelength windows of relatively high linear transparency combined with strong excited-state absorption (normally that of  $T_1$ ) in the 450 – 600 nm region, while the strongly absorbing triplet states are formed in high yield via intersystem crossing after photoexcitation.<sup>7</sup> However, the use of these particular materials outside of the 450 – 600 nm region into the near-infrared (NIR) region is limited by relatively small ratios of excited-state to ground-state absorption cross sections or by formation of insufficient populations of the relevant excited states due to limited linear absorption in the NIR.



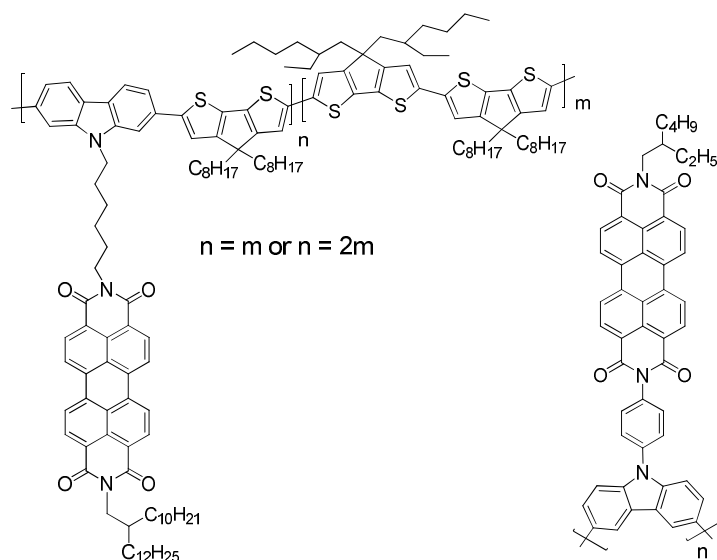
**Figure 6.1.** The Jablonski diagram (left) for RSA-based optical limiting processes through either singlet- or triplet-excited-state absorption. Electronic absorption (right) of bis[tri-(n-hexyl)siloxy]SnPc: ground-state absorption (solid line) and triplet state absorption (data points linked by line).<sup>4</sup>

Another approach for extending RSA-type optical limiting into the NIR that has recently been investigated utilizes species that exhibit strong radical-ion absorptions from following photoinduced electron transfer within or between molecules.<sup>14-17</sup> Blends of polythiophene and fullerene derivatives were among the earliest effective optical limiters relying on this mechanism; the strong optical suppression observed was attributed to the photo-generated polythiophene polaron absorption at *ca.* 750 nm arising from excited-state electron transfer between polythiophene and C<sub>60</sub>.<sup>15</sup> Similar phenomena have been utilized in other polymer blends<sup>16</sup> and in molecular dyads to achieve good optical suppression in NIR range.<sup>14,17</sup> In principle, donor-acceptor (D-A) type “double-cable” conjugated polymers,<sup>18-22</sup> in which electron-accepting moieties are covalently linked to an electron-donating conjugated polymer backbone appear to be promising candidate for optical limiting at certain wavelengths since the occurrence of rapid charge separation and long-lived charge-separated states in such kinds of polymers has been demonstrated in previous solar-energy-conversion research.<sup>18-21</sup> Moreover, because of their homogeneous molecular distribution and constant distance between the donor and acceptor building blocks (in contrast to simple donor / acceptor material blends), “double-cable” polymers of this type could help overcome the phase-separation issues commonly encountered for physical blends and maximize the donor-acceptor interaction in the solid state. This could potentially result in higher-quality films due to better control of film morphology, as well as achievement of a larger population electron-transfer states to absorb strongly following the photoexcitation.

As described in earlier chapters, perylene-3,4,9,10-tetracarboxylic acid diimides (also known as perylene diimides or PDIs) are a group of promising acceptors

extensively used for organic optical and electronic applications.<sup>23-24</sup> An interesting property of PDI-based materials is the tendency of these coplanar dyes to aggregate with neighboring molecules in solution or solid state due to strong  $\pi - \pi$  stacking interactions; these aggregates could extend the low-energy absorption edge of PDI materials beyond 600 nm.<sup>23</sup> On the other hand, the existence of long-lived charge-separated states has been proven in many donor-PDI systems and PDI radical anions are strongly absorbing in the visible to NIR range (*ca.* 600 to 1000 nm).<sup>25-31</sup> Hence, spectroscopic overlap is likely between the weak ground-state absorption in the low-energy tail of the absorption of PDI aggregates and the fairly strong absorption from the PDI radical anions that can be formed following the photo-excitation, suggesting the possibility of RSA-type optical limiting using the photo-generated vis-NIR radical-anion absorption if appropriate donor moieties are incorporated that lead to high populations of long-lived photo-induced charge-separated states. In contrast, carbazole-containing conjugated polymers or oligomers are typically considered as electron donors with hole-transporting character, relatively high-energy HOMOs, and stable radical cations (which are often described as polarons in the context of conjugated polymers). Since the last decade, carbazole-based conjugated materials have been extensively studied for organic electronic applications, resulting in high-performance devices.<sup>32-34</sup> Recently, efficient photo-induced electron-transfer processes has been demonstrated in the PDI/polycarbazole blends or PDI-grafted D–A “double-cable” polycarbazole copolymers, as shown in Figure 6.2, and promising devices have been achieved using these materials as active layers in solution-processed solar cells.<sup>20-22,35</sup> However, there are no reports on using photo-generated radical-ion absorption in PDI/donor polymer blends or PDI-based D–A “double-cable” polymers for

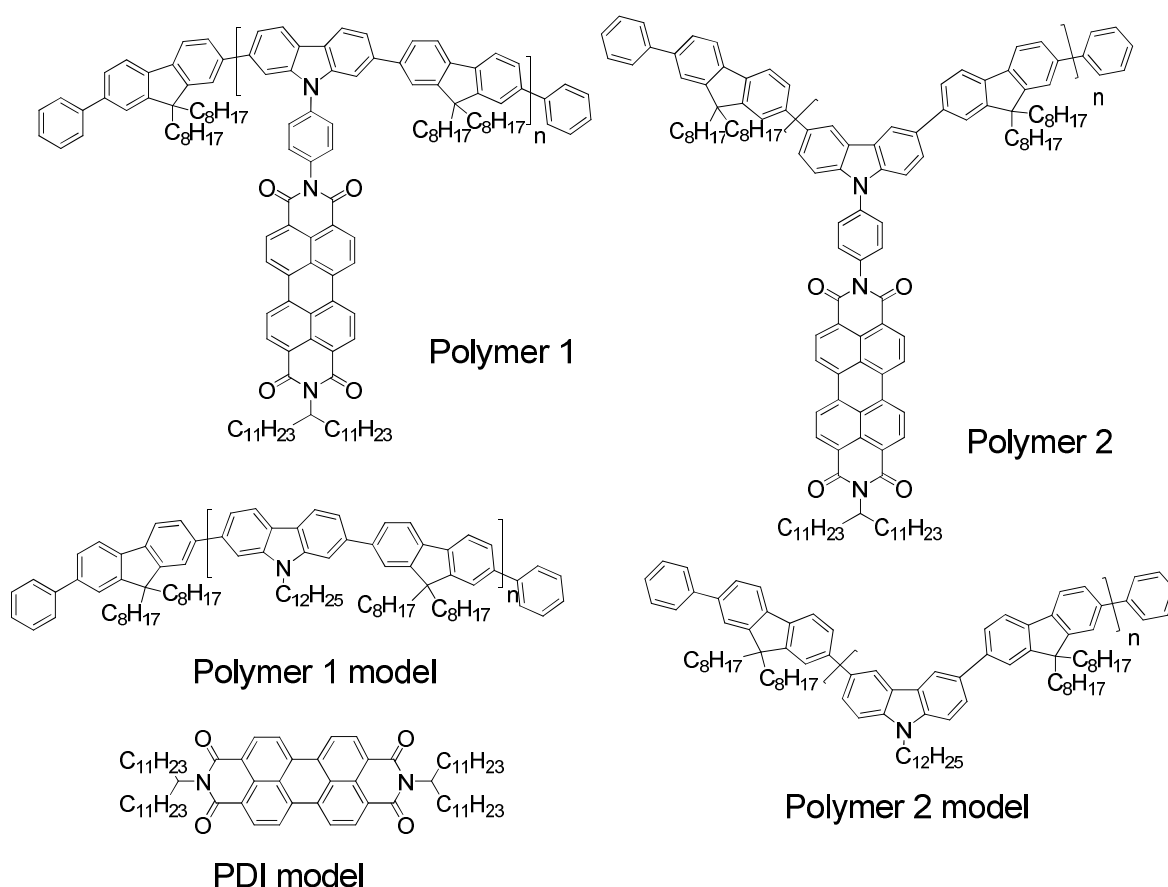
optical-limiting applications, partly due to the challenge of obtaining long-lived charge-separated states ( $> 1$  ns) and sufficient ground-state absorption or two-photon absorption (2PA) in the same spectral range as that in which the photo-generated ion pair absorbs .



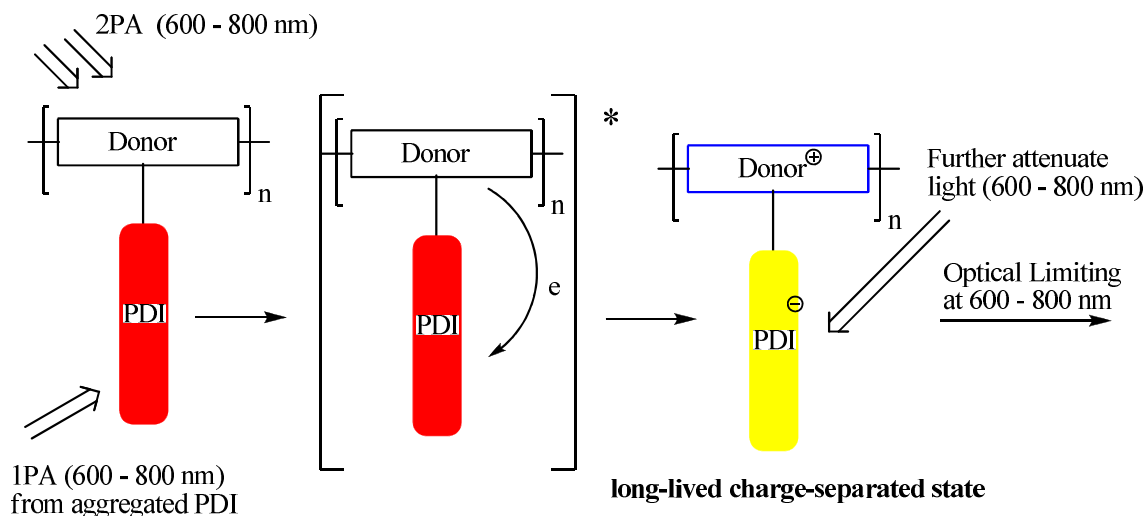
**Figure 6.2.** Two published PDI-based “double-cable” polycarbazole copolymers.<sup>20-21</sup>

In this chapter, the syntheses of two new poly(carbazole-*alt*-2,7-fluorene)s (PCFs), bearing PDIs on the side chains as pendant acceptors are reported. The investigation of their photophysics, other physical properties, and optical-limiting behaviors are also described. As shown in Figure 6.3, the PDI moieties are covalently bound to the electron-donating poly(2,7-carbazole-*alt*-2,7-fluorene) and poly(3,6-carbazole-*alt*-2,7-fluorene) polymeric backbones in the D–A type “double-cable” Polymer **1** and Polymer **2**, respectively. The polymeric architecture is expected to enhance  $\pi$ - $\pi$  stacking interaction<sup>22</sup> between the PDI moieties to provide sufficient ground-state absorption from aggregated PDIs ((PDI)<sub>n</sub>) at wavelengths at which the PDI radical anion absorbs strongly to permit optical limiting via one-photon-induced electron-transfer. In addition, the expected 2PA

bands of the PCF backbones might also contribute to the optical suppression, as illustrated in Figure 6.4. A phenylene linker was chosen to covalently bind the PDI moieties on the polymer side-chain according to previous observations of a long-lived charge-separated state in a PDI-phenylene-donor dyad, as described in Chapter 5. Both PDI-grafted poly(2,7-carbazole-*alt*-2,7-fluorene) and poly(3,6-carbazole-*alt*-2,7-fluorene) were synthesized to investigate effects of the donor polymer on the optical-limiting performance of these materials. As shown in Figure 6.3, model compounds were also synthesized for comparison purposes.

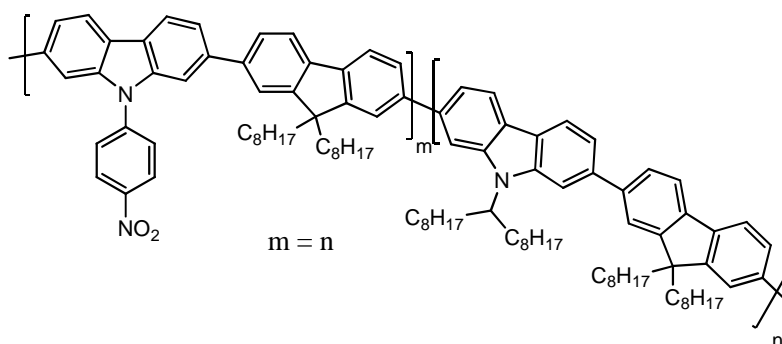


**Figure 6.3.** The chemical structures of PDI grafted polymers and the model compounds.



**Figure 6.4.** The mechanism for optical-limiting response for PDI-grafted PCFs.

At the end of this chapter, a poly(2,7-carbazole-*alt*-2,7-fluorene) substituted with a 4-nitrophenyl acceptor (**Polymer-NO<sub>2</sub>**, as shown in Figure 6.5) is also described: this polymer can perform optical limiting using the photo-generated radical-cation and / or triplet-state absorption in the visible to NIR range. Compared to the PDI grafted polymers, **Polymer-NO<sub>2</sub>** has the advantage of high linear transparency in the visible because of the weak absorption of 4-nitrophenyl acceptors relative to that of PDI moieties between 400 and 700 nm.



**Figure 6.5.** The chemical structure of 4-nitrophenyl grafted polymer.



## 6.2 Syntheses of the PDI-grafted monomers and polymers

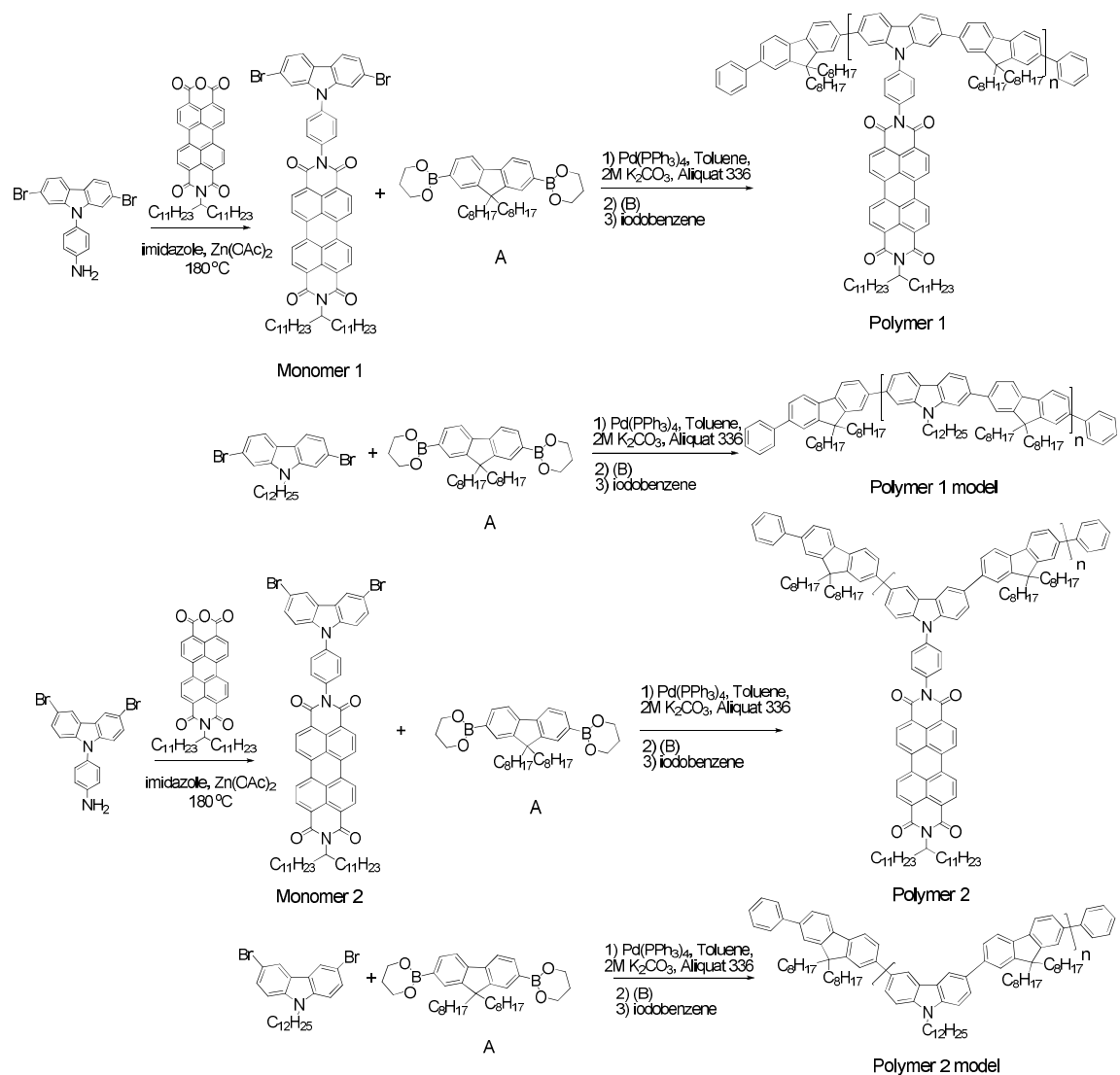
Carbazole- and fluorene-containing conjugated polymers such as poly(carbazole)s,<sup>35-36</sup> poly(2,7-fluorene)s,<sup>37</sup> and poly(3,6-carbazole-*alt*-2,7-fluorene)s<sup>38</sup> has been extensively synthesized for organic electronics applications and methods developed in this work were utilized in our synthesis of the PDI-grafted PCFs. Two new monomers containing dibromo-carbazole and PDI moieties with phenylene linkers were designed, and the desired PDI-grafted polymers were prepared following general Suzuki polymerization procedures.<sup>37-38</sup> Scheme 6.1 outlines the synthesis of the new monomers and respective copolymers. *N*-(1-Undecyl-dodecyl)-perylene-3,4-dicarboxyanhydride-9,10-dicarboximide,<sup>39</sup> 4-(2,7-dibromo-9*H*-carbazol-9-yl)aniline,<sup>40</sup> 4-(3,6-dibromo-9*H*-carbazol-9-yl)aniline,<sup>40</sup> 2,7-dibromo-9-dodecyl-9*H*-carbazole,<sup>36</sup> 3,6-dibromo-9-dodecyl-9*H*-carbazole,<sup>41</sup> and the respective starting materials were prepared as described in the literature. Monomer **1** was readily accessible through a condensation reaction between *N*-(1-undecyl-dodecyl)-perylene-3,4-dicarboxyanhydride-9,10-dicarboximide and 4-(2,7-dibromo-9*H*-carbazol-9-yl)aniline in molten imidazole at 180 °C catalyzed by anhydrous zinc acetate. Monomer **2** was prepared by the same method using 4-(3,6-dibromo-9*H*-carbazol-9-yl)aniline instead of 4-(2,7-dibromo-9*H*-carbazol-9-yl)aniline as the starting material. The yields for these condensation reactions are in the range of 85 – 100%, and silica-gel column chromatography was used to purify the products. The incorporation of long swallow-tail chains in the PDI N-terminus provides the PDI-grafted monomers with excellent solubility for use in polymerizations. The chemical structures and the purity of these monomers were confirmed by <sup>1</sup>H and <sup>13</sup>C NMR spectra, mass spectroscopy, and elemental analysis. High-molecular-weight alternating poly(carbazole-*alt*-2,7-fluorene)s

with grafted PDI pendants were then obtained through palladium-catalyzed Suzuki coupling between 2,2'-(9,9-dioctyl-9*H*-fluorene-2,7-diyl)bis(1,3,2-dioxaborinane) and the appropriate PDI-grafted dibromo-carbazole monomers using Pd(PPh<sub>3</sub>)<sub>4</sub> (1 mol% to the monomer) as the source of catalyst.<sup>38,42</sup> Polymer **1** and Polymer **2** were found to have number-average molecular weights ( $M_n$ ) of 15.4 and 18.1 kD, with polydispersities ( $M_w/M_n$ ) of 3.7 and 1.9, respectively, as determined by gel-permeation chromatography (GPC), using polystyrene as a standard in toluene. Both PDI-grafted polymers show good solubility in toluene, dichloromethane, chloroform, and, tetrahydrofuran (THF), which allows optical-limiting measurements to be performed in high-concentration solutions and gives the potential for fabricating high-quality films for solid-state measurements. The much lower yield in the synthesis of Polymer **2** might be attributable to the high content of low molecular weight materials formed during the Suzuki polycondensations, which were removed in the subsequent purification through Soxhlet extraction with methanol and acetone. It is worth noting that it was found that Ni(COD)<sub>2</sub>-catalyzed Yamamoto polycondensations of Monomers **1** and **2** only lead to oligomers, with only 2 or 3 repeat units, rather than high-molecular-weight polymers (>10 kD), despite similar polymerization conditions being reported by Müllen and coworkers to afford high-molecular-weight poly(*N*-alkyl-2,7-carbazole)s.<sup>35</sup> The model polymers were synthesized through similar procedures and were found to have higher molecular weights and larger polydispersities; values of  $M_n = 61.1$  kD and  $M_w/M_n = 4.0$  and  $M_n = 24.5$  kD and  $M_w/M_n = 3.6$  were estimated according to GPC (toluene) for Polymer **1** model and Polymer **2** model respectively. These model polymers, especially Polymer **2** model, also show high solubility in common organic solvents like toluene, chlorobenzene, THF, and chloroform

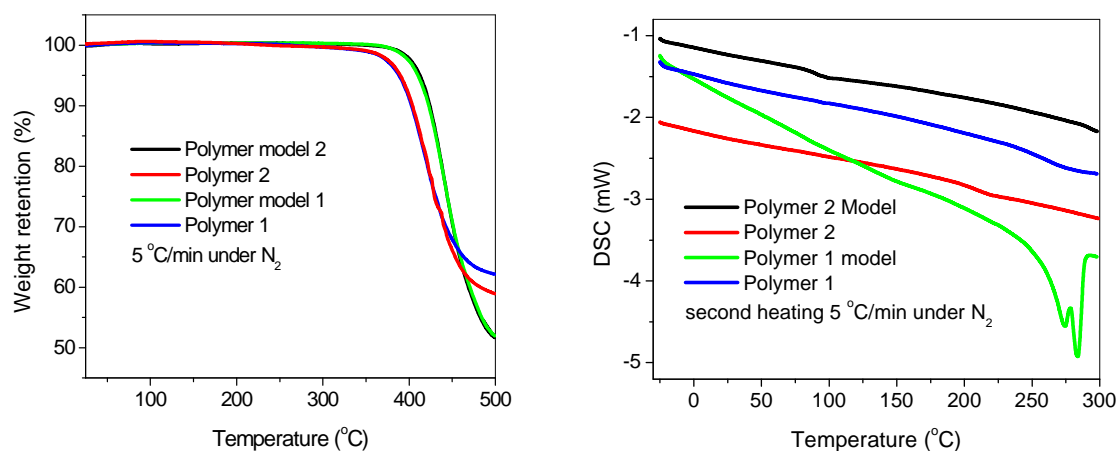
(> 10 mg/mL) at ambient temperature. However, Polymer **1** model shows limited solubility in CH<sub>2</sub>Cl<sub>2</sub> (< 1 mg/mL).

### 6.3 Thermal properties of the materials

As revealed in Figure 6.6, all the polymers exhibited good thermal stability, with the decomposition temperatures ( $T_d$ ), defined as that at which 5% weight loss is observed, in excess of 385 °C under nitrogen, according to thermogravimetric analysis (TGA). The incorporation of the PDI moieties causes values of  $T_d$  to decrease by ca. 20 °C relative to those for the respective model polymers; this may be due to either degradation of the PDI aromatic core or of the swallow-tail side chain. The thermal behavior of these polymers was also investigated by differential scanning calorimetry (DSC) analysis from –25 to 300 °C under nitrogen atmosphere. This analysis revealed that the glass-transition temperatures ( $T_g$ ) for Polymer **1**, Polymer **2**, Polymer **1** model, and, Polymer **2** model were 277, 210, 160, and 95 °C, respectively. Grafting the PDI moieties onto the polymer backbone leads to increases in  $T_g$  of over 110 °C relative to the model polymers; this may be attributable to strong  $\pi$ – $\pi$  interactions between the side-chain PDI segments in the solid state. Polymer **1** model melts at around 280 °C under nitrogen, while no obvious melting transition was observed for the other three polymers. The good thermal stability and high glass-transition temperatures are attractive attributes from the point of view of using these polymers as active materials in organic optical and electronic devices. Table 6.1 summarizes the polydispersities and thermal properties, as well as the isolated yields and molecular-weight data, for the polymers.



**Scheme 6.1.** The synthetic schemes for the PDI-grafted monomers and respective polymers and the model materials.



**Figure 6.6.** The TGA traces (left) and DSC traces (right) of the polymer in nitrogen atmosphere.

**Table 6.1.** Polymerization results and thermal properties of the polymers

Polymer	Yield	$M_n$	$M_w / M_n$	$T_d (^{\circ}\text{C})$	$T_g (^{\circ}\text{C})$	$T_m (^{\circ}\text{C})$
<b>Polymer 1</b>	84%	15.4 k	3.68	388	277	N.A.
<b>Polymer 2</b>	26%	18.1 k	1.91	390	210	N.A.
<b>Polymer 1 model</b>	80%	61.1 k	4.00	409	160	~280
<b>Polymer 2 model</b>	68%	24.5 k	3.55	412	95	N.A.

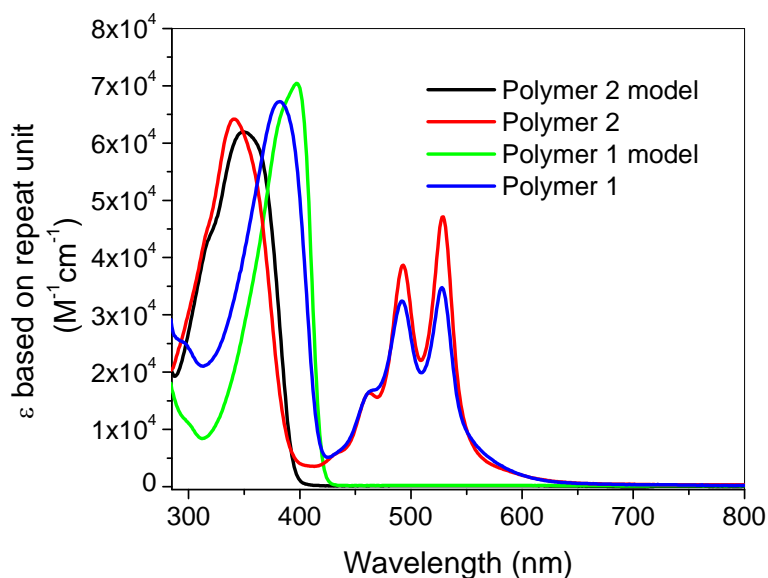
#### 6.4 Linear absorption and emission properties in solution

As shown in Figure 6.7, the solution UV-Vis absorption spectra of Polymer **1** and Polymer **2** in toluene are essentially superpositions of the characteristic absorption bands of the polymer models and of aggregated PDIs (*ca.*  $10^{-5}$  mol/L based on PDI concentration).<sup>23,43</sup> The absorption maximum of the polymer models show a slight red shift relative to the corresponding bands from the analogous PDI-grafted polymers, which may be ascribed to the possible torsion in the PDI-grafted polymer chains due to the PDI pendant, which reduces the effective conjugation length in the polymer backbone. In the

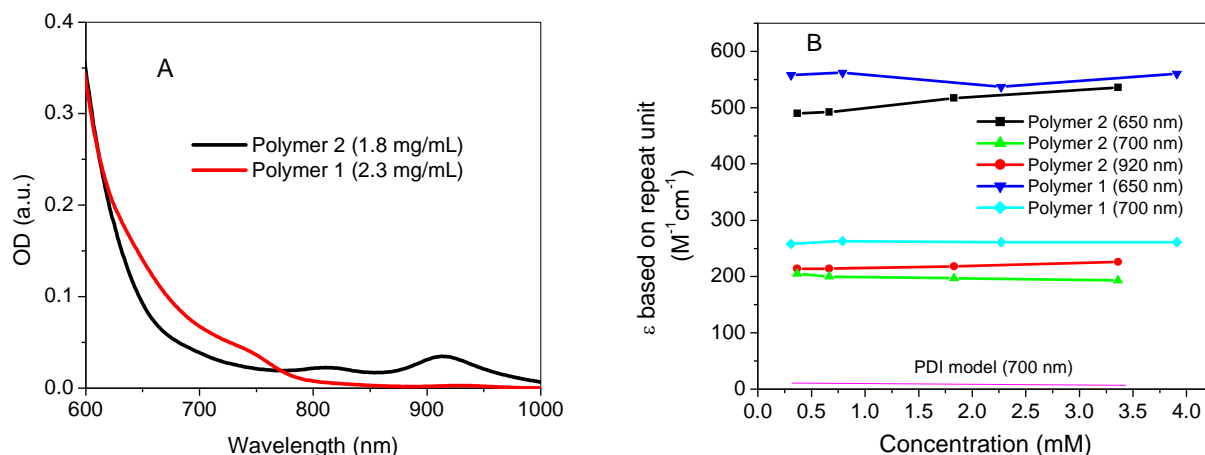
polymers with PDI pendants, the ratio of the intensity of the (0,0) vibronic sub-band of the PDI absorption to the (0,1) sub-band was found to be significantly smaller than the value of 1.66, typical for non-aggregated PDIs (1.23 for Polymer **2** and 1.13 for Polymer **1**), which indicates substantial aggregation of the PDI side-chains, even in dilute toluene solution (*ca.*  $10^{-5}$  mol/L based on polymer repeat unit concentration).<sup>22-23,43</sup> In concentrated toluene solution ( $\sim 10^{-3}$  mol/L based on polymer repeat unit concentration), Polymer **1** and **2** exhibit increased absorption between 600 and 800 nm, as illustrated in Figure 6.8. The molar absorption coefficients for Polymer **1** and **2** are *ca.* 250 and 560  $\text{M}^{-1}\text{cm}^{-1}$  at 700 nm and 650 nm, respectively in toluene, calculated based on the concentration of PDI repeat units, compared with  $< 20 \text{ M}^{-1}\text{cm}^{-1}$  for the PDI model in the same spectral region at similar concentration. This enhanced absorption in NIR range might originate from PDI aggregate absorption on the single polymer side-chain due to the higher local PDI concentration than that were seen in free PDIs. The weak absorption band seen for concentrated solutions of Polymer **2** at  $\sim 920$  nm might be attributed to absorption from an intra- or intermolecular ground-state charge-transfer complex between the PCF backbone and PDI moieties. It is worth noting that the molar extinction coefficients in the NIR range for Polymer **1** and **2** are not significantly dependent on the PDI concentration; this might indicate saturated aggregation in the investigated concentration range for the PDI moieties on the polymer side-chains.

The emission spectra of the PDI grafted polymers and the model compounds in toluene are shown in Figure 6.9. Dual emission consisting of both PDI aggregate and donor polymer emission was observed with much lower fluorescent quantum yields (0.5% and 0.7% for Polymer **1** and Polymer **2**, respectively, excited at 375 nm) being

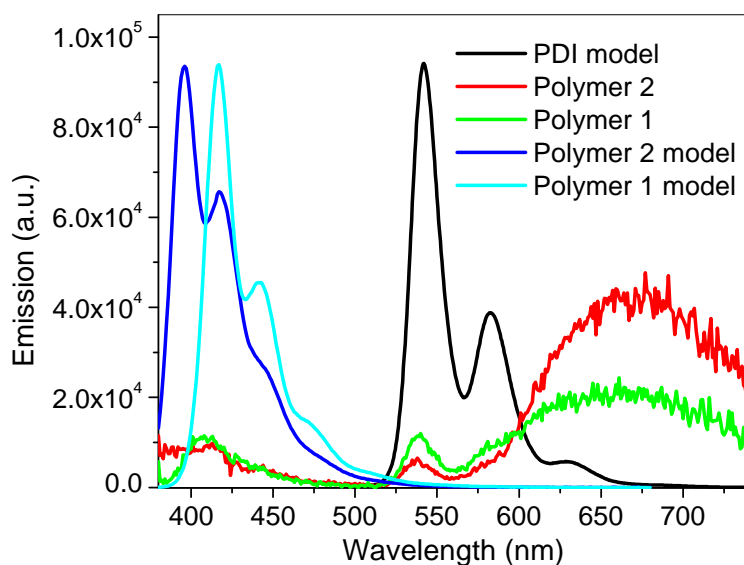
observed for the PDI grafted polymers than for the PDI model (83%, excited at 490 nm), or the polymer models (65% and 56% for Polymer **1** and Polymer **2**, respectively). The extensive fluorescence quenching suggests the possibility of efficient electron transfer occurring from the donor polymer backbones to PDI moieties following donor excitation. Furthermore, clear aggregated PDI type emission (peak at *ca.* 680 nm) was observed in the emission spectra for the PDI grafted polymers, consistent with the aggregated type PDI UV-Vis absorption spectra of these two PDI-grafted polymers. The excitation spectra (with a constant emission wavelength at 620 nm) of Polymer **1** and **2** are shown in Figure 6.10; the excitation spectra consist of the characteristic bands of the donor polymer backbone and PDI aggregates, which indicate that energy transfer from the donor polymer backbone to the PDI/aggregated-PDI (or PDI aggregate) side groups could be the reason for the dual emission observed following donor-polymer-based photo-excitation at 375 nm.



**Figure 6.7.** The linear absorption spectra of the polymers in diluted toluene solution.

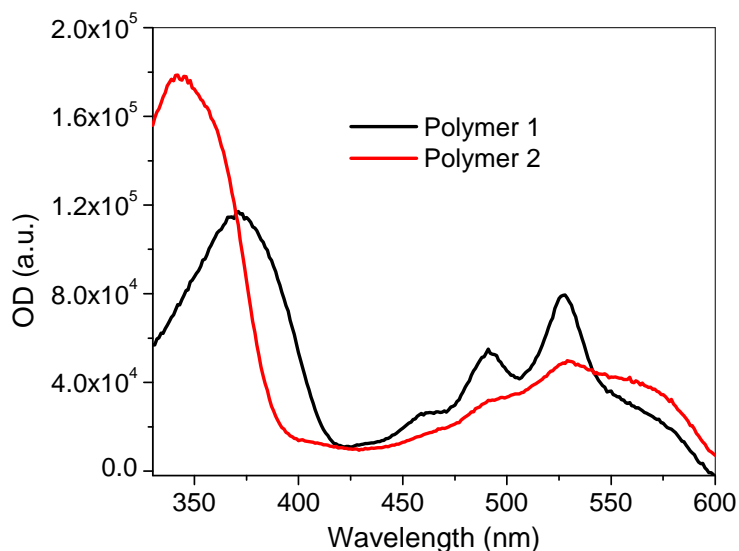


**Figure 6.8.** A) The absorption spectra of the PDI-grafted polymers in highly concentrated toluene solutions. The band peaked at 920 nm for polymer 2 is tentatively attributed to ground-state intermolecular or intramolecular charge-transfer complexes; B) molar absorptivity of the PDI-grafted polymers in highly concentrated toluene solution at different wavelengths.



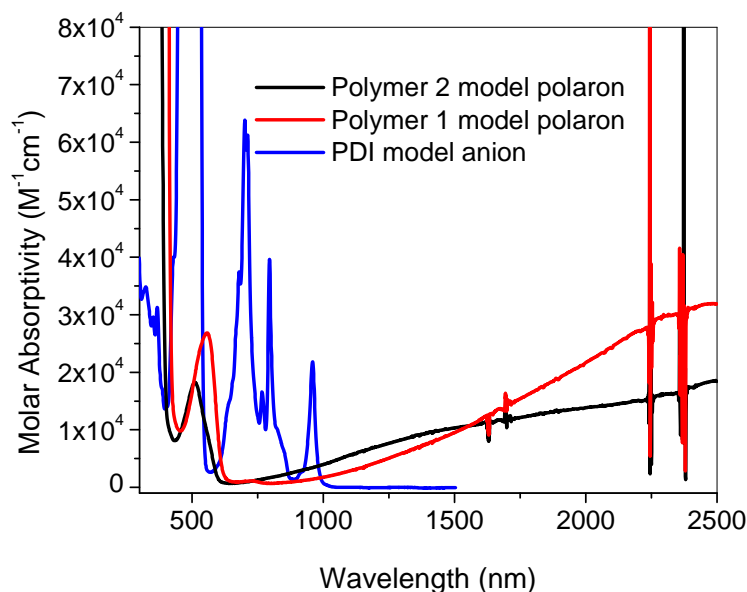
**Figure 6.9.** The emission spectra of the PDI grafted polymers and respective model compounds. Polymer 1 and 2 as well as the respective model polymer were excited at 375 nm. The PDI model emission spectrum was collected using excitation at 490 nm.





**Figure 6.10.** The excitation spectra (blue) of Polymer 1 (black) and (b) Polymer 2 (red) in toluene with a fixed emission wavelength at 620 nm.

Polarons were generated in the model polymers in dichloromethane by addition of an excess of Polymer 1 and 2 models to a dilute solution of tris(4-bromophenyl)aminium hexachloroantimonate.<sup>44</sup> The radical anion of the PDI model was prepared in THF via chemical reduction with cobaltocene.<sup>45</sup> The resulting radical-ion absorption spectra are shown in Figure 6.11. The absorption maximum of the polaron from Polymer 1 model in the UV-Vis range is at around 560 nm; this shows a *ca.* 50 nm red shift compared with the polaron generated from the Polymer 2 model, presumably because of the cross-conjugation in Polymer 2 model backbone. The polarons of Polymer 1 and 2 models also exhibit intense, but broad, absorption bands in the NIR region. These are quite similar in terms of energy and molar absorption extinction coefficient to intervalence charge-transfer (IVCT) absorptions previously observed for bis(diarylamino) cations and to the absorptions of polycarbazole-based polarons.<sup>44,46-47</sup>

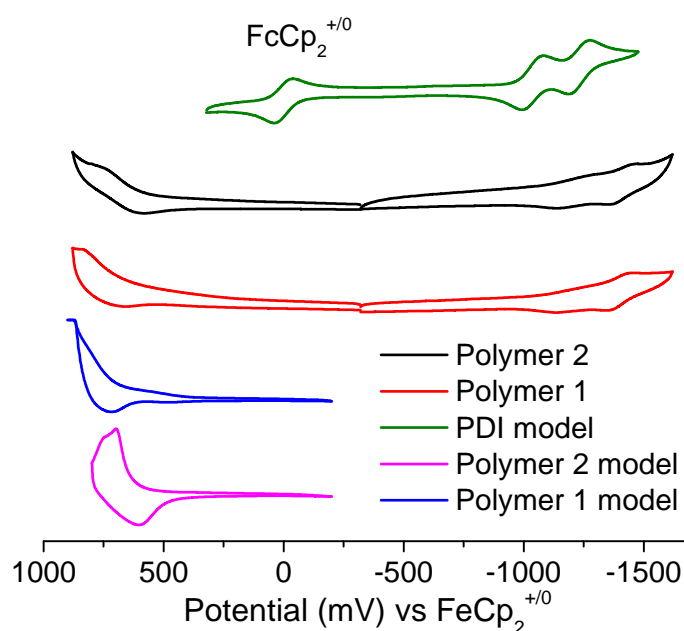


**Figure 6.11.** The polaron absorption of the model polymers, Polymer 1 model (red) and Polymer 2 model (black), in  $\text{CH}_2\text{Cl}_2$  and the PDI model radical-anion absorption (blue) in THF.

### 6.5 Redox properties

The electrochemical behavior of the polymers was investigated by cyclic voltammetry (CV). The measurement was performed under nitrogen, in a solution of tetrabutylammonium hexafluorophosphate (0.10 M) in anhydrous acetonitrile, with a scan rate of 50 mV/s using polymer films drop-cast onto a platinum working electrode from 2 mg/mL polymer solutions in chloroform. Here, oxidative and reductive scans were carried out separately for the polymer film samples. The results are summarized in Table 6.2, and the cyclic voltammograms of the polymers and PDI model are shown in Figure 6.12. The electrochemical oxidation and reduction onsets ( $E_{ox}^{onset}$  and  $E_{red}^{onset}$  vs. ferrocenium/ferrocene ( $\text{FcCp}_2^{+/0}$ )) were also used to estimate the IP and EA values according to  $\text{IP} = (E_{ox}^{onset} + 4.8) \text{ eV}$ ,  $\text{EA} = -(E_{red}^{onset} + 4.8) \text{ eV}$  based on assumption of a

solid state IP value of 4.8 eV for ferrocene.<sup>48</sup> The estimated values of the IP in these polymers are found to be *ca.* 5.2 to 5.4 eV, which are similar to a literature value for poly(carbazole-*alt*-fluorene).<sup>38</sup> The estimated values of the EA for Polymer **1** and Polymer **2** are both of *ca.* -3.8 eV, which are similar to that of the PDI model (for which a CV measurement was performed using a dichloromethane solution). The similarity of the IP and EA values estimated for the PDI grafted polymers to those for the model compounds also suggests weak ground-state electron-coupling between the PDI pendants and donor polymer backbones. The large EA offset (> 1.0 eV) and IP offset (> 0.7 eV) between the PDI model and respective polymer model reveal sufficient driving force for electron transfer in these PDI grafted polymers from either the donor polymer exciton or PDI exciton.<sup>49-50</sup>



**Figure 6.12.** The cyclic voltammograms of polymer films drop-cast from ~ 2 mg/mL  $\text{CHCl}_3$  solution onto a Pt working electrode in acetonitrile with 0.1 M tetra-*n*-butylammonium hexafluorophosphate, except for PDI model, for which the CV was performed in solution. Potential was scanned at a rate of 50 mV/s.

**Table 6.2. Summary of the optical and electrochemical behaviors of the polymers**

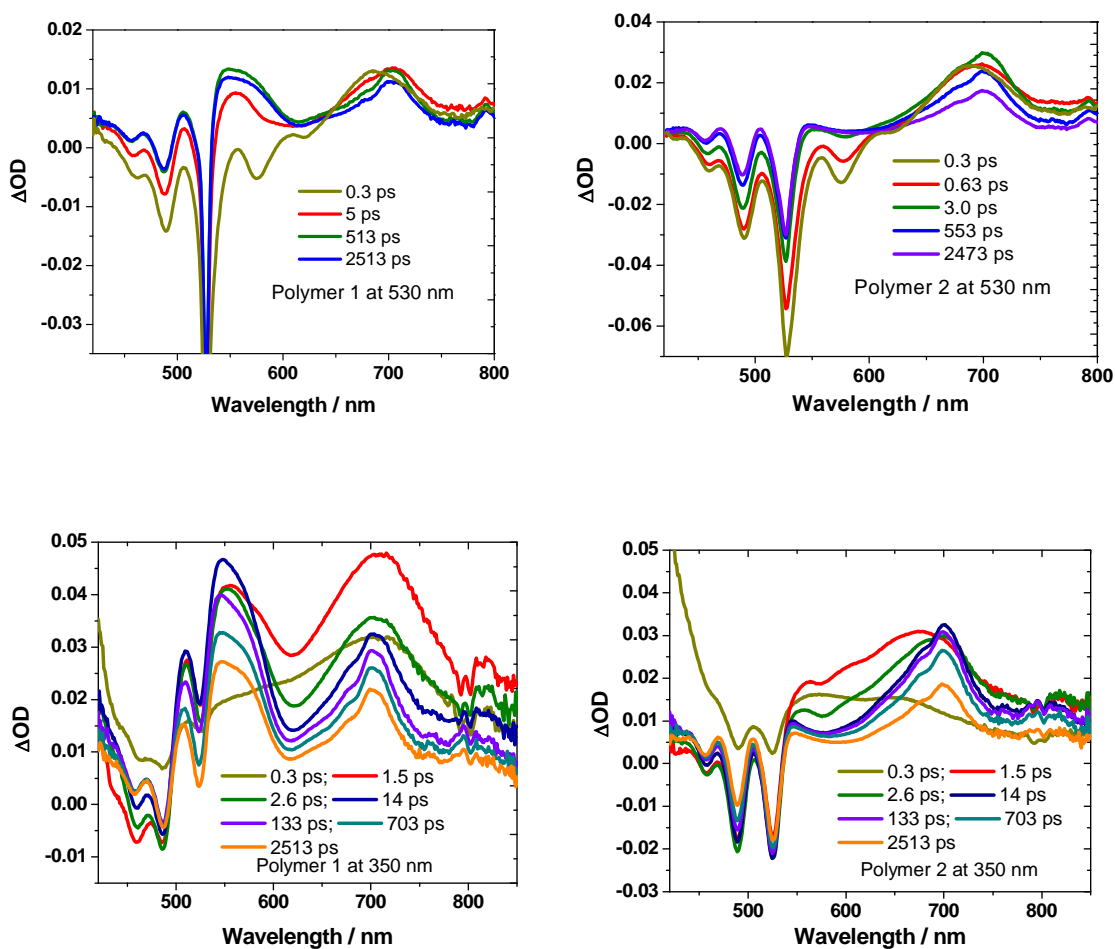
Polymer	$\lambda_{\max}^{\text{abs}}$ (nm)	$E_g$ (optical) (eV)	$E_{ox}^{\text{onset}}$ (V)	$E_{red}^{\text{onset}}$ (V)	EA (eV)	IP (eV)
Polymer 1	381, 491, 528	2.1	0.44	-1.04	-3.8	5.2
Polymer 2	340, 491, 527	2.1	0.55	-1.06	-3.8	5.4
Polymer 1 model	386	2.9	0.40	N.A.	-2.3 <sup>a</sup>	5.2
Polymer 2 model	349	3.1	0.54	N.A.	-2.8 <sup>a</sup>	5.3
PDI model	459, 490, 527	2.2	N.A.	-1.01 <sup>b</sup>	-3.8	6.0 <sup>c</sup>

IP =  $(E_{ox}^{\text{onset}} + 4.8)$  eV and EA =  $-(E_{red}^{\text{onset}} + 4.8)$  eV,  $E_{ox}^{\text{onset}}$  and  $E_{red}^{\text{onset}}$  are respective to  $\text{FeCp}_2^{+/0}$ . a : EA =  $E_g$  (optical) - IP; b: based on  $E_{1/2}^{0/-}$  obtained from solution measurement in  $\text{CH}_2\text{Cl}_2$ ; c: IP = - (EA -  $E_g$  (optical))

## 6.6 Transient absorption of the polymers

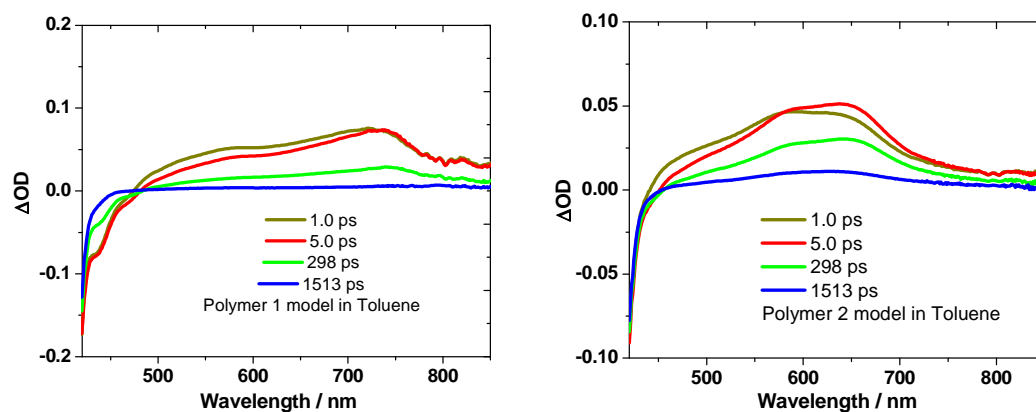
The transient absorption spectra of Polymers **1** and **2** in toluene, generated by pumping the PDI moiety at 530 nm or the donor polymer backbone at 350 nm with femtosecond laser pulses, are shown in Figure 6.13. The transient absorption spectra of Polymer **1** after pumping the PDI pendants showed the growth of absorption bands with peaks at 580 and 710 nm, while only a transient absorption peaked at *ca.* 710 nm was observed for Polymer **2**. The band at 710 nm for both polymers can be assigned to the PDI excited-state absorption which begins within a short period after the photo-excitation (< 5 ps) of the PDI pendants and/or the PDI radical anion absorption formed afterwards. The transient absorption band peaked at *ca.* 580 nm for Polymer **1** could be attributed to the polaron absorption from the oxidized poly(2,7-carbazole-*alt*-2,7-fluorene), which matches well with the cation absorption of the Polymer **1** model in the visible range. The fast rise (< 0.3 ps) of this peak following PDI photo-excitation indicates rapid electron-transfer following the photo-excitation, which is consistent with the strong fluorescence quenching of these PDI-grafted polymers, as compared with that of the model compounds. A similar case was expected in Polymer **2**, since strong fluorescence quenching and a long-lived transient absorption band at 710 nm were also observed.

However, no obvious polaron absorption at *ca.* 500 nm from the oxidized poly(3,6-carbazole-*alt*-2,7-fluorene) backbone was observed, perhaps because the polaron absorption is obscured by the strong ground-state bleach of the PDI pendants in the transient absorption spectra.

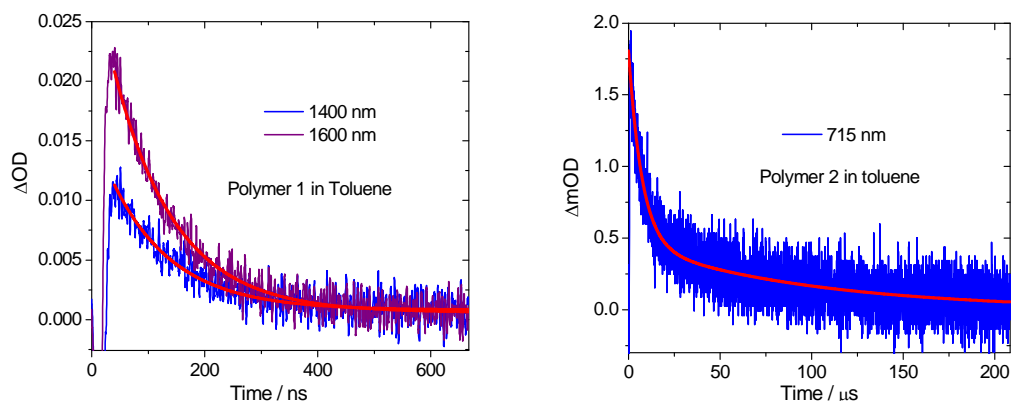


**Figure 6.13.** The femtosecond transient absorption of Polymer 1 (top left) and Polymer 2 (top right) in toluene excited at 530 nm. Transient absorption of Polymer 1 (bottom left) and Polymer 2 (bottom right) in toluene following excitation at 350 nm. All samples were prepared at  $\sim 30 \mu\text{M}$  (in PDI units) in toluene in a 2 mm cuvette to yield an OD near 0.3 at the excitation wavelength (Transient absorption spectra were collected by Dr. Matthew M. Sartin in the Perry group).

Pumping primarily on the donor polymer backbone at 350 nm, with femtosecond laser pulses, yields similar transient absorption spectra as PDI pumping. However, the excited-state absorptions from both donor polymer backbones, which were further confirmed by the transient absorption spectra of the donor polymer models as shown in Figure 6.14, were recorded immediately after photo-excitation at the polymer backbones (0.3 ps). The rapid growth of the 580 nm and 710 nm absorption (< 1.5 ps) for Polymer **1** indicates rapid electron transfer between the donor-polymer excitons and the PDI pendants, while fast energy transfer from the donor polymer backbone to the PDI pendants could possibly also take place. The transient absorption spectra obtained from donor pumping on Polymer **2** is similar to that of Polymer **1**, despite the observation of no donor polymer polaron absorption in the transient absorption spectra of Polymer **2**, presumably due to the spectroscopic overlap between the polaron absorption, peaked at *ca.* 500 nm, and the PDI ground-state bleaching.



**Figure 6.14.** The femtosecond laser pulse transient absorption of Polymer **1** model (left) and Polymer **2** model (right) in toluene excited at 350 nm with OD of *ca.* 0.3. (Transient absorption spectra were collected by Dr. Matthew M. Sartin in the Perry group).

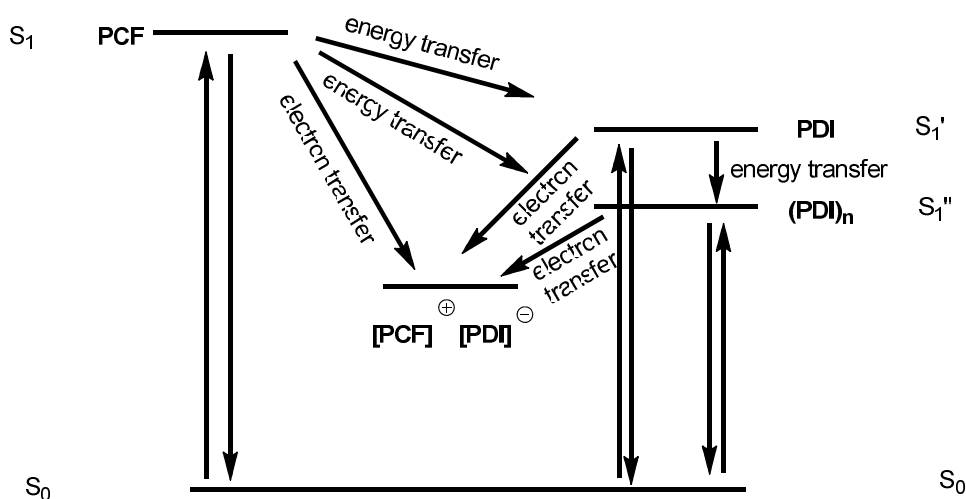


**Figure 6.15.** The nanosecond transient absorption decay of Polymer 1 model (left, probe at NIR) and Polymer 2 model (right, probe at 715 nm) in toluene excited at 355 nm with OD of *ca.* 0.2. (Transient absorption spectra were collected by Dr. Matthew M. Sartin in the Perry group).

Hence, either donor pumping or acceptor pumping on Polymer 1 and 2 could similarly result in short-lived excited-states followed by fast electron transfer to yield relatively long-lived charge-separated states. Nanosecond laser pulse transient absorption spectroscopy was used to analyze the lifetime of the charge-separated states in the polymers. The charge-separated state of Polymer 1 exhibits a lifetime of 130 ns, while that for Polymer 2 is *ca.* 70  $\mu$ s, as shown in Figure 6.15. However, the relatively weak signal of the ion absorption in this nanosecond transient absorption indicates relatively low yields of photo-induced charge-transfer states on the nanosecond time scale, especially for Polymer 2, for which no significant signal correlated to the polymer cation absorption was observed in the NIR. It is also worth noting that direct pumping of the PDI aggregates at 680 nm in highly concentrated polymer solution (4 mg/mL) also results in long-lived charge-separated states and a strong transient absorption band between 600 – 800 nm, which indicates possible optical limiting application at these wavelengths

using these PDI grafted polymers between 600 – 800 nm since PDI aggregates on the polymer side-chain show fairly strong absorption in this range.

The results of the transient absorption measurements in solution can be summarized in a Jablonski diagram (Figure 6.16). After photo-excitation of the donor polymer backbone (PCF), the excited state is largely quenched by energy and electron transfer from the PCF excited-states to PDI or (PDI)<sub>n</sub> leading to low fluorescence quantum yields. The new generated PDI or (PDI)<sub>n</sub> based excitons are quenched predominantly via electron-transfer by accepting an electron from PCF. If PDI or (PDI)<sub>n</sub> is photo-excited directly, these PDI-based excited-states could be quenched in the same way, i.e., by electron-transfer from PCF, forming PDI radical anion and donor polymer polaron (or by other radiative and nonradiative decay mechanisms). Furthermore, the relatively long-lasting transient-states (> 1 ns) and broad and fairly strong ESA (from *ca.* 450 – 800 nm) for both the model polymers indicated their potential use for optical limiting in their whole 2PA band.



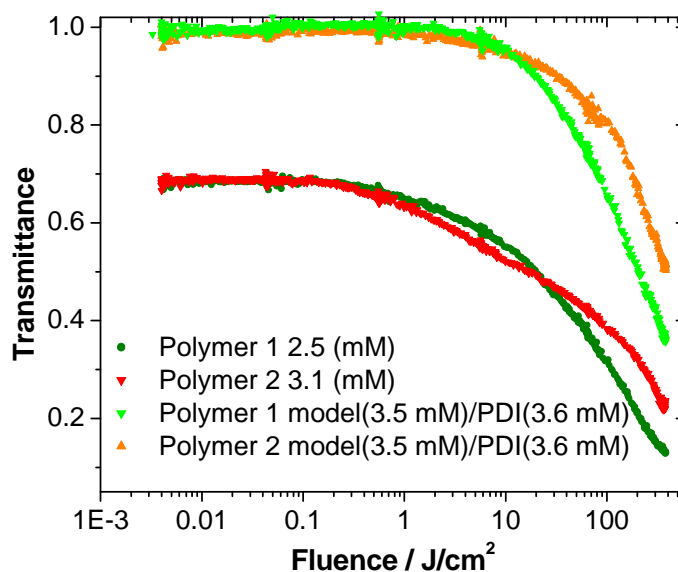
**Figure 6.16.** Proposed energy level diagram showing the lowest excited singlet states of PCF and non-aggregated PDI, of the aggregates (PDI)<sub>n</sub>, and that of the charge-transfer state. The arrows show the processes that might occur upon photo-excitation of PCF or PDI.



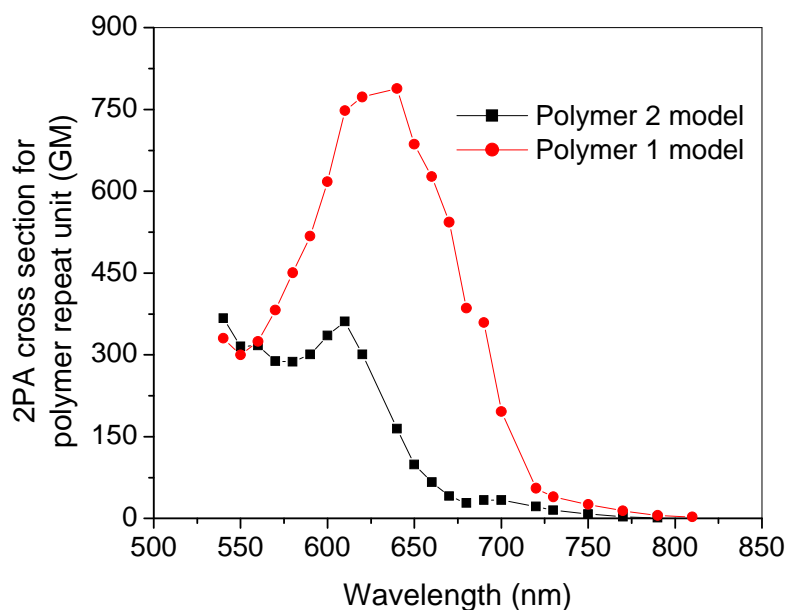
## 6.7 Non-linear absorption and optical limiting

The optical limiting behavior of Polymers **1** and **2** upon photo-excitation with a 680 nm laser pulse (6 ns pulse width) are shown in Figure 6.17, along with those of the blend of [polymer model]/[PDI model] (3.5 mmol/L : 3.5 mmol/L in toluene) solution in a 2 mm cuvette. Polymer **1** and **2** samples were prepared at high concentration (2.5 mmol/L for Polymer **1** and 3.1 mmol/L for Polymer **2** in toluene, based on the repeat unit concentration) to ensure a linear transmittance of the sample at around 70%, so the linear absorption of the PDI aggregates could contribute to one-photon-induced optical limiting. Both-PDI grafted polymers yielded noticeable optical limiting starting at lower fluence as compared to the blend samples, even when the model blend systems have higher material concentration. The optical-limiting phenomena of the model compounds blends at high fluence could be attributed to the 2PA of the model polymers. This is further supported by the 2PA spectra of the two model polymers in toluene using two-photon excited fluorescence (2PEF) method.<sup>51-52</sup> The 2PA spectra of both model polymers are shown in Figure 6.18, with 2PA cross sections (based on polymer repeating units) of 350 and 50 GM for Polymer **1** and Polymer **2** models, respectively, at 680 nm. The much larger 2PA cross section for Polymer **1** model is presumably responsible for its stronger optical-limiting response at 680 nm. Additionally, the short-lived excited-state absorptions of the polymer models may contribute to optical limiting as there are considerable overlap between the 2PA bands and excited-state absorption bands. The optical-limiting behavior of the PDI-grafted polymers may be due to one-photon-induced charge separation of the aggregated PDI/ground-state charge-transfer complexes at low fluence, with additional contribution from the 2PA of the donor polymer backbone at high fluence. The figures-

of-merit ( $\text{FOM} = T_0/T_F$ , where  $T_0$  is the linear transmission, and  $T_F$  is the high fluence transmission) for optical limiting in toluene are 5.8, 3.3, 2.7 and 1.8 for Polymer **1**, Polymer **2**, Polymer **1** model/PDI and Polymer **2** model/PDI, respectively, at 680 nm. The stronger and faster limiting response for the PDI grafted polymers relative to the perspective model polymer/PDI blends is due to the contribution from subsequent photo-generated PDI-radical-ions absorption. The larger FOM for Polymer **1** over Polymer **2** is in agreement with the fact that Polymer **1** model shows much larger 2PA cross-section relative to that for Polymer **2** model at 680 nm, which leads to higher PDI-radical-ion populations via two-photon excitation at 680 nm, presumably due to greater importance of 2PA-induced electron transfer at higher fluence.



**Figure 6.17. Optical limiting of 680 nm, 6 ns pulses focused in f/5 geometry onto samples of Polymer **1** and **2** in toluene, and the respective polymer model compounds mixed with PDI model in toluene, in a nitrogen-purged 2 mm cell (Optical limiting behavior was measured by Dr. Matthew M. Sartin in the Perry group).**

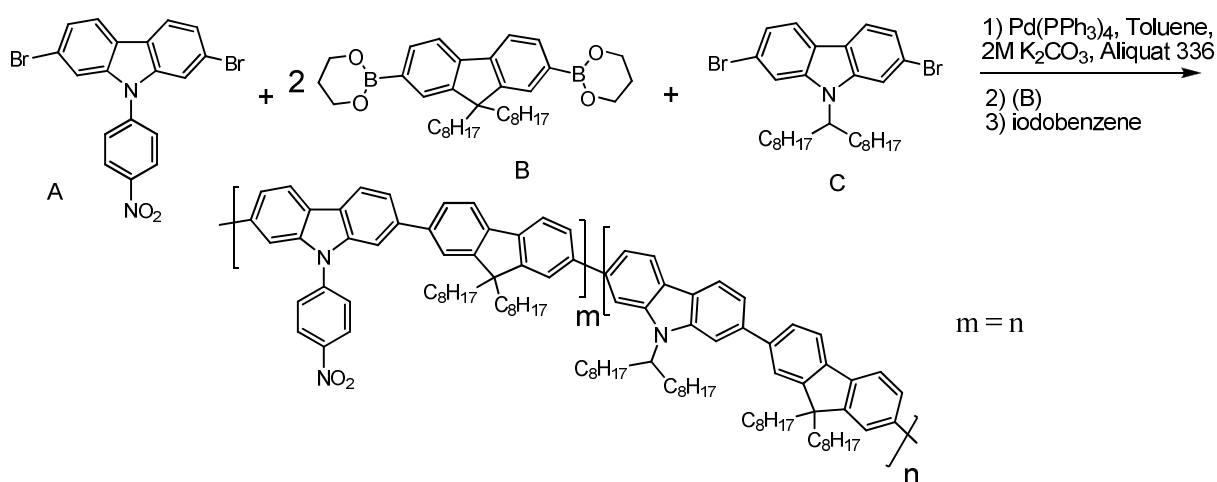


**Figure 6.18.** The 2PA spectra of the Polymer models, Polymer 1 model (red) and Polymer 2 model (black) in 100  $\mu\text{M}$  solution in toluene (2PA spectra were collected by Dr. Nisan Siegel in the Perry group).

#### 6.8 D–A type PCF with 4-nitrophenyl acceptor for optical limiting

It is worth noting that the 2PA band of Polymer 1 model shows significant overlap with its radical-cation absorption band, suggesting its potential use for 2PA-induced optical limiting in the range of 500 – 600 nm, if acceptor(s) with limited ground-state absorption in this region, instead of PDI moieties, are grafted on the polymer side chain. Hence, a new polymer with 4-nitrophenyl pendants was synthesized followed general Suzuki polymerization procedures.<sup>38</sup> Here, the 4-nitrophenyl group was incorporated into the first carbazole-based monomer as the pendant acceptor while a second carbazole-based monomer with long-branching alkyl chain was used in the polymerization to improve the polymer solubility, as shown in scheme 6.2. A high molecular weight ( $M_n = 45$  kD,  $M_w/M_n = 1.9$ , estimated using GPC (THF)) poly(2,7-

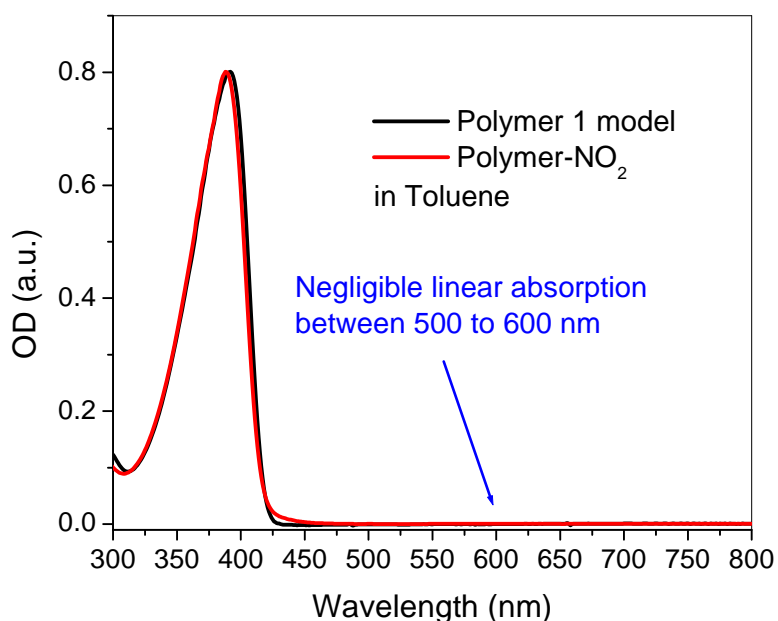
carbazole-*alt*-2,7-fluorene) with 4-nitrophenyl pendants (**Polymer-NO<sub>2</sub>**) was obtained through palladium-catalyzed Suzuki coupling polymerization<sup>38</sup> with the presence of 1 mol% Pd(PPh<sub>3</sub>)<sub>4</sub>. The <sup>1</sup>H NMR spectrum and elemental analysis indicate that the actual molar ratio of each monomer (22 mol% for the 4-phenylnitro substituted carbazole monomer) in the polymer is in good agreement with that expected from corresponding feed ratio used in the polymerization. The good solubility of this polymer (> 20 mg/mL in toluene) make possible further characterization, including optical limiting in high concentration solution, and facilitates thin-film preparation via processes such as drop-casting and spin-casting.



**Scheme 6.2.** The synthetic scheme for a new polymer with 4-nitrophenyl pendants.

The UV-Vis absorption of **Polymer-NO<sub>2</sub>** is similar to that of Polymer **1** model in the UV-Vis range and no obvious absorption between 500 – 650 nm was observed in dilute toluene solution (< 0.1 mg/mL). Furthermore, no obvious PCF-type emission is observed following donor pumping at 370 nm in the new nitro-phenyl substituted D – A

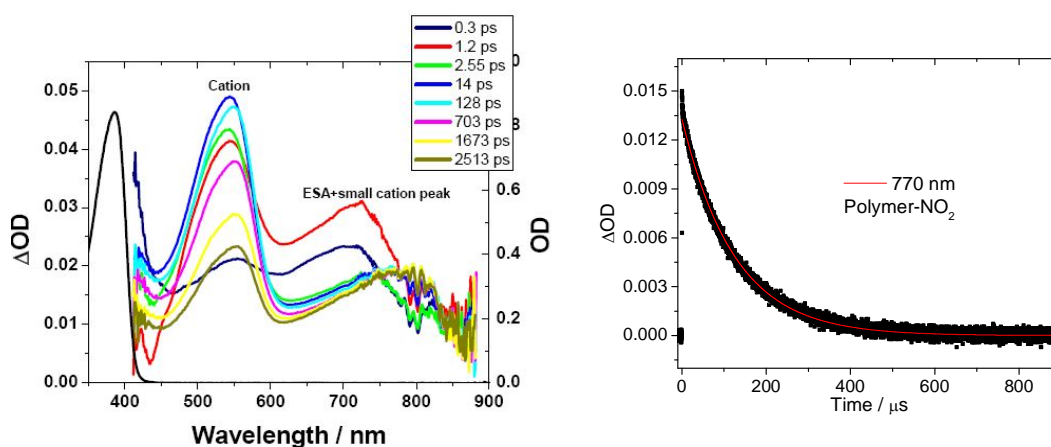
type polymer, which suggests efficient electron transfer quenching of the PCF excited states following the excitation. Because of the analogous polymer backbones, similar 2PA properties as well as electrochemical properties are expected for **Polymer-NO<sub>2</sub>** and Polymer **1** model. **Polymer-NO<sub>2</sub>** is also thermally quite stable with decomposition (5% weight loss, TGA under nitrogen) temperatures ( $T_d$ ) in excess of *ca.* 350 °C, which is around 50 °C lower than the model polymer. However, no obvious glass transition was observed using DSC (heating rate of 5 °C/min) within the temperature range from -30 to 300 °C under nitrogen.



**Figure 6.19.** The linear absorption of **Polymer-NO<sub>2</sub>** in dilute toluene solution.

Femtosecond-pulse transient absorption spectroscopy on **Polymer-NO<sub>2</sub>** solution was performed to investigate the role of electron transfer in the quenching process after

the photo-excitation. The transient absorption spectra, generated by pumping the donor polymer backbone at 355 nm, are shown in Figure 6.20. The spectra show feature attributed to the donor polymer backbone excited-state absorption right after photo-excitation (at 0.3 ps) and the subsequent growth of polymer radical-cation absorption bands peaked at 550 nm (rise within several picoseconds), suggesting rapid electron transfer occurs in the polymer excited state. During the decay of the polymer radical-cation, the growth of an unexpected transient absorption peaked at *ca.* 770 nm was observed. This band was attributed to a triplet-state absorption since nanosecond-pulse transient absorption spectra indicate that the lifetime of this new transient state is over 200  $\mu$ s and that this species is sensitive to oxygen. This broad transient band could potentially expand the optical limiting range of **Polymer-NO<sub>2</sub>** over its whole 2PA band.



**Figure 6.20.** The femtosecond transient absorption spectra of Polymer-NO<sub>2</sub> (left) and Nanosecond transient absorption decay at 770 nm of Polymer-NO<sub>2</sub> (right) in toluene excited at 355 nm (Transient absorption spectra were collected by Dr. Matthew M. Sartin in the Perry group).

The optical limiting behaviors of Polymer **1** model and **Polymer-NO<sub>2</sub>** (solution of ~ 13 mg/mL in toluene) upon excitation with 680, 630, 580, and 532 nm lasers (6 ns

pulse width) are shown in Figure 6.21. Here, slightly better optical limiting response at 680 nm (FOM = 4.4 and 5.9, respectively for Polymer **1** model and **Polymer-NO<sub>2</sub>**) and 630 nm (FOM = 5.5 and 6.3, respectively for Polymer **1** model and **Polymer-NO<sub>2</sub>**) were obtained for **Polymer-NO<sub>2</sub>**. The similar performance of optical limiting for **Polymer-NO<sub>2</sub>** and Polymer **1** model may be due to a larger excited-state absorption cross-section for the Polymer **1** model system in the spectroscopic range, despite the fact that the transient species life time for **Polymer-NO<sub>2</sub>** at 680 nm and 630 nm are several orders of magnitude longer than that for Polymer **1** model. At shorter wavelengths, e.g. *ca.* 580 nm, **Polymer-NO<sub>2</sub>** give a much stronger optical limiting response in comparison to Polymers **1** model and the FOM for **Polymer-NO<sub>2</sub>** is found to be 8.2 while that for Polymers **1** model is  $\sim 2.6$ . The much larger FOM at 580 nm for **Polymer-NO<sub>2</sub>** is attributable to the further absorption from the photo-generated radical-cations. The nanosecond optical-limiting response of both the polymers become weaker at still shorter wavelengths such as 532 nm (the FOMs for both polymers are around 2.3) probably due to the smaller 2PA cross-section as well as weaker subsequent ESA. As compared the model polymer, **Polymer-NO<sub>2</sub>** shows lower linear transparency at all wavelengths examined at similar concentration probably due to possible ground-state charge transfer as the polymer concentration increases ( $\sim 13$  mg/mL in toluene for the samples for optical limiting measurement).

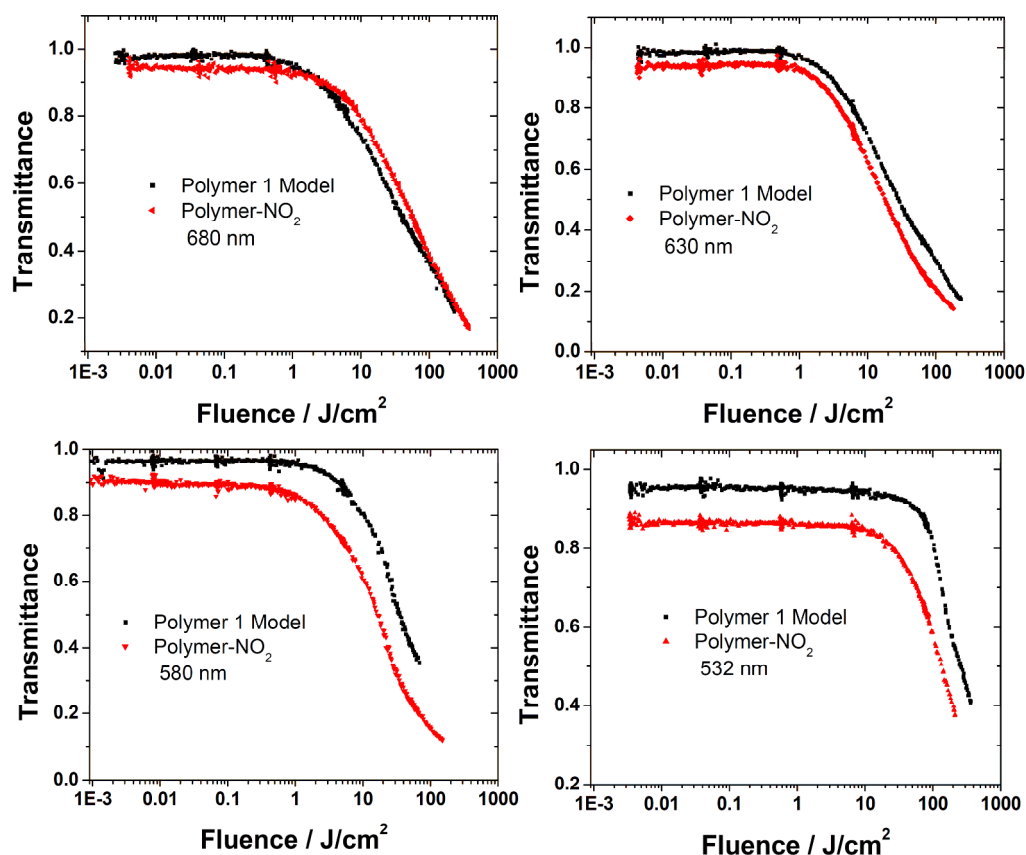


Figure 6.21. Optical limiting for 6 ns pulses focused in an  $f/5$  geometry onto samples of Polymer-NO<sub>2</sub> (red) and Polymer 1 model (black) of 13 mg/mL in toluene in a N<sub>2</sub> purged, 2 mm cell. (Optical limiting behavior was measured by Dr. Matthew M. Sartin in the Perry group).

## 6.9 Conclusions

We have prepared two new D–A “double-cable” conjugated polymers with poly(carbazole-*alt*-2,7-fluorene)s as the electron-donating polymer backbone and electron-deficient PDI moieties incorporated into the side chains as pendant acceptors. Efficient photo-induced charge transfer in these copolymers was confirmed by the strong fluorescence quenching and the transient absorption spectra. Long-lived charge separated states with strong absorption between 600 – 800 nm were observed following the



excitation of either PDI or donor polymer. Furthermore, the PDI-grafted copolymers exhibited strong enhancement of the nonlinear optical absorption compared with blends of the model compounds at 680 nm. This is attributed to the combination of one-photon absorption from the aggregated PDI and 2PA contribution from the polymer backbone. Due the observation of significant overlap between the 2PA band and radical-cation absorption bands of Polymer **1** model, a new nitrophenyl substituted poly(carbazole-*alt*-2,7-fluorene) was synthesized for optical limiting in the polymer radical cation absorption range. When the nitro-phenyl group are incorporated to the poly(2,7-carbazole-*alt*-2,7-fluorene)s, photo-induced charge transfer occurs to form long-lived polymer cations, with strong absorption at *ca.* 580 nm that results in better optical limiting responses than that of the model polymer itself at these wavelengths. Furthermore, because of the formation of a long-lived triplet-state at **Polymer-NO<sub>2</sub>** from its charge-separated-state, broad ESA is obtained for **Polymer-NO<sub>2</sub>** covering the whole UV-Vis range, which gives similar or slightly better optical limiting response for **Polymer-NO<sub>2</sub>** solution in comparison to that for Polymer **1** model at other wavelengths investigated.

### 6.10 Experimental section

**General:** Most organic and inorganic chemicals were obtained from Aldrich and Alfa Aesar. Palladium-based catalysts were purchased from Strem Chemicals and used without further purification. <sup>1</sup>H and <sup>13</sup>C NMR spectra were collected on Bruker 400 or 500 MHz spectrometers using tetramethylsilane (TMS;  $\delta = 0$  ppm) as an internal standard. Mass spectra were measured on an Applied Biosystems 4700 Proteomics Analyzer using MALDI mode. Elemental analyses were carried out by Atlantic Microlabs using a LECO 932 CHNS elemental analyzer. Solution UV-Vis absorption spectra were recorded on a

UV3101PC (Shimadzu, Kyoto, Japan) absorbance spectrophotometer. The solution emission spectra and excitation spectra were taken using a Shimadzu FP-5301PC spectrofluorometer in toluene. For electrochemical measurements, the polymer films were drop-cast onto a platinum disk working electrode from a 2 mg/mL polymer solution in chloroform. A platinum wire served as the auxiliary electrode, and an Ag wire anodized with AgCl served as a pseudo-reference electrode. The experiments were performed deoxygenated 0.1 M solutions of tetra-*n*-butylammonium hexafluorophosphate in dry acetonitrile at a scan rate of 50 mV s<sup>-1</sup>, using a computer-controlled BAS 100B electrochemical analyzer. Potentials were referenced to the ferrocenium/ferrocene (FeCp<sub>2</sub><sup>+/0</sup>) couple by using ferrocene as an internal standard. Thermogravimetric analysis measurements were performed on an NETZSCH STA 449C analyzer under 40 mL/min N<sub>2</sub> flow with a heating rate of 5K/min. Differential scanning calorimetry measurements were performed on a TA Instruments DSC Q200 analyzer under 50 mL/min N<sub>2</sub> flow with heating rate of 5K/min.

**Generation of Radical Ions:** The radical anion of the PDI model compound was generated in anhydrous THF solution by reduction with cobaltocene in a nitrogen atmosphere glove box. The radical cation of the polymer model compounds was generated in anhydrous dichloromethane after oxidation with tris(*p*-bromophenyl)aminium hexachloroantimonate. The spectra of the radical ions were recorded a Varian Cary 5E UV-Vis-NIR spectrophotometer using 1 cm pathlength cells.

**Two-Photon Absorption Spectroscopy:** Two-photon absorption (2PA) spectra were obtained using the reference-based two-photon-excited fluorescence (2PEF) method by Dr. Nisan Sigel in the Perry group.<sup>52-53</sup> The excitation source was an optical parametric

oscillator (Quanta-Ray MOPO 730) pumped by 6 ns pulses from the third harmonic of a Q-switched Nd:YAG laser (Quanta-Ray PRO250). The 2PEF method determines the 2PA spectra of unknowns by measuring the fluorescence emitted by the unknowns under two-photon excitation conditions and comparing it to the fluorescence emitted by a known reference compound under the same conditions. The 2PEF measurements of the model compounds were made in toluene (Sigma-Aldrich spectroscopic grade) solution at chromophore concentrations of 80 – 110  $\mu$ M. The data shown here comprise several collections of over 200 pulses at each wavelength. 1,4-bis(2-methylstyryl)benzene<sup>51,54</sup> (Sigma-Aldrich, 99%) in cyclohexane (Sigma-Aldrich, spectroscopic grade) and fluorescein<sup>52</sup> (Acros, laser grade) in aqueous NaOH solution (pH 11) were used as references for 630 – 680 nm and 690 – 1040 nm, respectively. The 2PA cross-section values of 1,4-bis(2-methylstyryl)benzene reported by Kennedy<sup>54</sup> were reduced in scale by a factor of 10, as described by Fisher.<sup>51</sup> The uncertainties in the measured cross sections are approximately  $\pm 15\%$ .

**Femtosecond transient absorption measurements:** The femtosecond transient absorption spectra were collected by Dr. Matthew M. Sartin in the Perry group. The excitation source for femtosecond transient absorption measurements was generated by an optical parametric amplifier (TOPAS, Newport) pumped by a Ti:Sapphire regenerative amplifier (Spitfire, Newport), operating at 1 kHz repetition rate. The 800 nm Spitfire output could be varied by the TOPAS over 465-2900 nm. Approximately 5% of the 800 nm Spitfire output was used to generate the white light continuum probe beam (420 – 950 nm) in a sapphire plate. Transient data were collected using a commercially available Helios spectrometer (Ultrafast Systems, Sarasota, FL). The time resolution for

this system was 7 fs, and the maximum time delay was 3.2 ns. At each temporal delay, the signal was averaged for 1 s. The pump beam was chopped at 500 Hz to alternate between signal and reference data. A correction factor for the chirp of the white light was generated using the ultrafast response of toluene. All samples were prepared in 2 mm cuvettes and deaerated with N<sub>2</sub>. The pump wavelengths were 530 nm for the PDI-grafted polymers. The pump energy for all samples was ~ 3.3  $\mu$ J/pulse.

**Nanosecond transient absorption measurements:** The nanosecond transient absorption spectra were collected by Dr. Matthew M. Sartin in the Perry group. The excitation source for transient absorbance experiments was the same as for the 2PEF experiments. Polymer 1 was prepared at 6  $\mu$ M in toluene in a deaerated, 1 cm cuvette, with an OD = 0.2. The probe beam was generated using a 240W tungsten-halogen lamp (Oriel 69931 Radiometric Power Supply, Newport Oriel, Irvine, CA). The pump and probe overlapped at an angle of ~5° in the sample. The white light was focused into an Acton SpectraPro 2150i monochromator (Princeton Instruments, Trenton, NJ) and the transmitted light was collected by a HCA-S-200M-IN photodiode (Femto, Berlin, Germany). The transient signal was digitized using a Tektronix digital oscilloscope (Model 3034B, 300 MHz, 2.5 Gigasamples/sec). The response time of the system was limited by the laser pulse width.

**Nanosecond optical limiting measurements:** The nanosecond optical-limiting was measured by Dr. Matthew M. Sartin in the Perry group. The excitation source for optical limiting measurements was the same as for the ns TA measurements. A mechanical shutter reduced the pulse repetition rate to 1 Hz to minimize damage to the sample. The samples were prepared as deaerated solutions in 2 mm cuvettes, with T *ca.* 0.7 at the excitation wavelength of 680 nm. The laser was focused into the center of the cuvette

using an f/5 geometry, and the transmitted light was detected by a New Focus photoreceiver (San Jose, California), sampled using a Stanford Research Systems boxcar average (Sunnyvale, CA), and recorded on a 300 MHz Tektronix oscilloscope (Richardson, Texas). A beam splitter placed before the sample redirected part of each pulse to a reference photoreceiver to determine fluctuations in the input energy of each pulse.

## Synthesis

**Monomer 1:** *N*-(1-Undecyl-dodecyl)-perylene-3,4-dicarboxyanhydride-9,10-dicarboximide<sup>39</sup> (0.356 g, 0.50 mmol), 4-(2,7-dibromo-9*H*-carbazol-9-yl)aniline<sup>40</sup> (0.413 mg, 0.99 mmol), anhydrous zinc acetate (80 mg, 0.44 mmol), and imidazole (3.0 g) were heated under N<sub>2</sub> at 180 °C overnight. The reaction mixture was then allowed to cool to *ca.* 130 °C before being poured into a 4 N aqueous HCl solution (200 mL). The red precipitate was filtered and washed sequentially with 2 N aqueous HCl (3 × 10 mL), water (3 × 10 mL), and MeOH (3 × 10 mL). The solid was then dissolved in CHCl<sub>3</sub> (5 mL), and a minimum amount of silica gel was added to absorb the liquid. After the solvent was removed under reduced pressure, the dried silica gel was added to the top of a hexane-packed silica gel column, and the column was eluted with CHCl<sub>3</sub> to give **Monomer 1** as a red solid (0.53 g, 89 %). <sup>1</sup>H NMR (500 MHz, CDCl<sub>3</sub>): δ 8.78 (d, *J* = 8.0 Hz, 2H), 8.72- 8.66 (m, 6H), 7.95 (d, *J* = 8.5 Hz, 2H), 7.75 (d, *J* = 8.5 Hz, 2H), 7.68 (d, *J* = 1.0 Hz, 2H), 7.65 (d, *J* = 8.5 Hz, 2H), 7.42 (dd, *J* = 8.5, 1.0 Hz, 2H), 5.18 (m, 1H), 2.26 (m, 2H), 1.86 (m, 2H), 1.29-1.21 (m, 36H), 0.83 (t, *J* = 6.5 Hz, 6H). <sup>13</sup>C {<sup>1</sup>H} NMR (125 MHz, CDCl<sub>3</sub>): δ 165.0, 164.1, 163.9, 141.8, 137.2, 135.8, 134.9, 134.6, 134.5, 132.4, 132.3, 131.6, 131.2, 130.2, 129.9, 128.9, 128.0, 127.0, 126.7, 124.6, 124.4, 123.9, 123.8,

123.6, 123.5, 123.3, 122.3, 122.0, 121.8, 120.6, 116.4, 113.6, 113.5, 55.3, 32.8, 32.3, 30.2, 30.1 (3 peaks), 30.0, 29.8, 27.5, 23.2, 14.7 (The observation of three carbonyl carbon resonances is consistent with previous work on perylene bis(dicarboxyimide)s using similar, swallow-tailed *N*-substituents, in which this has been attributed to restricted rotation about the N—C<sub>alkyl</sub> bonds. Two aromatic carbon peaks and one alkyl carbon were not observed, presumably due to overlap). HRMS (MALDI) calcd for C<sub>65</sub>H<sub>65</sub>Br<sub>2</sub>N<sub>3</sub>O<sub>4</sub> (M<sup>+</sup>): 1109.33, found: 1109.35. Anal. Calcd for C<sub>65</sub>H<sub>65</sub>Br<sub>2</sub>N<sub>3</sub>O<sub>4</sub>: C, 70.20; H, 5.89; N, 3.78. Found: C, 69.99; H, 5.92; N, 3.81. for C<sub>65</sub>H<sub>65</sub>Br<sub>2</sub>N<sub>3</sub>O<sub>4</sub>: C, 70.20; H, 5.89; N, 3.78.

**Monomer 2:** *N*-(1-Undecyl-dodecyl)-peryene-3,4-dicarboxyanhydride-9,10-dicarboximide<sup>39</sup> (0.356 g, 0.50 mmol), 4-(3,6-dibromo-9*H*-carbazol-9-yl)aniline<sup>40</sup> (0.450 mg, 1.08 mmol), anhydrous zinc acetate (80 mg, 0.44 mmol), and imidazole (3.5 g) were heated under N<sub>2</sub> at 180 °C overnight. The reaction mixture was then allowed to cool to *ca.* 130 °C and poured into 4 N aqueous HCl (160 mL). The red precipitate was filtered and washed sequentially with 2 N aqueous HCl (3 × 10 mL), water (3 × 10 mL), and MeOH (2 × 10 mL). The solid was then dissolved in CHCl<sub>3</sub> (5 mL) and a minimum amount of silica gel was added to absorb the liquid. After the solvent was removed under reduced pressure, the dried silica gel was added to the top of a hexane-packed silica gel column, and the column was eluted with CHCl<sub>3</sub> to give **Monomer 2** as a red solid (0.58 g, 97 %). <sup>1</sup>H NMR (500 MHz, CDCl<sub>3</sub>): δ 8.76 (d, *J* = 8.0 Hz, 2H), 8.71- 8.66 (m, 6H), 8.17 (d, *J* = 2.0 Hz, 2H), 7.72 (d, *J* = 6.5 Hz, 2H), 7.61 (d, *J* = 6.5 Hz, 2H), 7.53 (dd, *J*<sub>1</sub> = 9.0 Hz, *J*<sub>2</sub> = 2.0 Hz, 2H), 7.42 (dd, *J* = 9.0 Hz, 2H), 5.20 (m, 1H), 2.27 (m, 2H), 1.86 (m, 2H), 1.29-1.21 (m, 36H), 0.84 (t, *J* = 7.0 Hz, 6H). <sup>13</sup>C {<sup>1</sup>H} NMR (125 MHz, CDCl<sub>3</sub>): δ 164.7,

163.7, 163.6, 139.8, 137.2, 135.3, 135.0, 134.1, 134.0, 131.8, 131.2, 129.9, 129.7, 129.6, 127.5, 126.6, 126.3, 124.6, 124.4, 123.8, 123.7, 1231.5, 123.4, 123.1, 113.6, 112.1, 32.7, 32.4, 30.1(3 close peaks), 29.8, 27.5, 23.2, 14.4 (The observation of three carbonyl carbon resonances and one more aromatic carbon peaks is consistent with previous work on perylene bis(dicarboxyimide)s using similar swallow-tailed *N*-substituents and has been attributed to restricted rotation about the N—C<sub>alkyl</sub> bonds. Three alkyl carbons were not observed, presumably due to overlap). HRMS (MALDI) calcd for C<sub>65</sub>H<sub>65</sub>Br<sub>2</sub>N<sub>3</sub>O<sub>4</sub> (M<sup>+</sup>): 1109.33, found: 1110.36 (M + 1). Anal. Calcd for C<sub>65</sub>H<sub>65</sub>Br<sub>2</sub>N<sub>3</sub>O<sub>4</sub>: C, 70.20; H, 5.89; N, 3.78. Found: C, 70.30; H, 6.03; N, 3.76.

**Polymer 1:** 2,2'-(9,9-Dioctyl-9*H*-fluorene-2,7-diyl)bis(1,3,2-dioxaborinane) (0.2336 g, 0.4183 mmol), **Monomer 1** (0.4652 g, 0.4182 mmol), Aliquat 336 (40 mg), and Pd(PPh<sub>3</sub>)<sub>4</sub> (4.8 mg, 0.0040 mmol) were charged to a 25 mL two-neck round-bottomed flask with a condenser. The system was then evacuated and refilled with N<sub>2</sub> 4 times. Toluene (5.0 mL) and 2 N aqueous K<sub>2</sub>CO<sub>3</sub> (3.0 mL) were added before the mixture was heated to 90 °C and kept at that temperature for 3 d. Then, 2,2'-(9,9-dioctyl-9*H*-fluorene-2,7-diyl)bis(1,3,2-dioxaborinane) (100 mg, 0.17 mmol) in toluene (1.0 mL) was added, and the mixture was stirred for another 12 h. Iodobenzene (0.3 mL) was then added to end cap the polymer, and the mixture was kept stirring for another 12 h. After the mixture was cooled to room temperature, it was added dropwise to 125 mL MeOH. The resultant solid was filtered and washed with water and MeOH before drying under vacuum. The solid was washed sequentially with hot MeOH and hot acetone using a Soxhlet apparatus. The residue was then extracted with CHCl<sub>3</sub> in a Soxhlet apparatus. Most of the solvent was then removed, and the residue was passed through a short silica plug, eluting with

CHCl<sub>3</sub>/Et<sub>3</sub>N (100 : 1). The solvent was then removed, and the residue was dissolved in 5 mL CHCl<sub>3</sub>, and added dropwise to 100 mL MeOH. The resulting solid was filtered and washed with water and MeOH before drying under vacuum. The precipitation was repeated, and the resulting solid was then filtered and dried under vacuum to give Polymer **1** as a red solid (0.45 g, 83%). GPC (Toluene):  $M_n = 15.4$  kD,  $M_w/M_n = 3.68$ . <sup>1</sup>H NMR (500 MHz, CDCl<sub>3</sub>):  $\delta$  9.0- 7.0 (m,b, 24nH), 5.18 (sb, 1nH), 2.5-0.1 (m, 80nH). Anal. Calcd for polymer (C<sub>94</sub>H<sub>105</sub>N<sub>3</sub>O<sub>4</sub>)<sub>n</sub>: C, 84.07; H, 8.03; N, 3.13; Found : C, 83.38; H, 7.80; N, 3.09.

**Polymer 2** : 2,2'-(9,9-Dioctyl-9*H*-fluorene-2,7-diyl)bis(1,3,2-dioxaborinane) (0.2337 g, 0.4185 mmol), **Monomer 2** (0.4653 g, 0.4185 mmol), Aliquat 336 (40 mg), and Pd(PPh<sub>3</sub>)<sub>4</sub> (4.8 mg, 0.0040 mmol) were charged to a 25 mL two-neck round-bottomed flask with a condenser. The system was then evacuated and refilled with nitrogen 4 times. Toluene (5.0 mL) and 2 N aqueous K<sub>2</sub>CO<sub>3</sub> (3.0 mL) were added before the mixture was heated to 90 °C and kept at that temperature for 3 d. Then 2,2'-(9,9-dioctyl-9*H*-fluorene-2,7-diyl)bis(1,3,2-dioxaborinane) (100 mg, 0.17 mmol) in toluene (1.0 mL) was added and the mixture was stirred for another 12 h. Iodobenzene (0.5 mL) was then added to end cap the polymer and the mixture was kept stirring for another 12 h. After the mixture was cooled to room temperature, it was added dropwise to 125 mL MeOH. The resulting solid was filtered and washed with water and MeOH before drying under vacuum. The solid was washed sequentially with hot MeOH and hot acetone hot acetone using a Soxhlet apparatus. The residue was then extracted with CHCl<sub>3</sub> in a Soxhlet apparatus. Most of the solvent was then removed, and the residual was run through a short silica plug, eluting with CHCl<sub>3</sub>/Et<sub>3</sub>N (100 : 1). The solvent was then removed, and the residue



was dissolved in  $\text{CHCl}_3$  (5 mL) and added dropwise to 100 mL MeOH. The resulting solid was filtered and washed with water and MeOH before drying under vacuum. The precipitation was repeated, and the resulting solid was then filtered and dried under vacuum to give Polymer 2 as a red solid (0.14 g, 25%) GPC (Toluene):  $M_n = 18.3$  kD,  $M_w/M_n = 1.91$ .  $^1\text{H}$  NMR (500 MHz,  $\text{CDCl}_3$ ):  $\delta$  9.0-7.5 (m,b, 24nH), 5.18 (sb, 1nH), 2.3 - 1.0 (m, 68nH), 1.0 - 0.1 (m, 12nH). Anal. Calcd for polymer  $(\text{C}_{94}\text{H}_{105}\text{N}_3\text{O}_4)_n$ : C, 84.07; H, 8.03; N, 3.13; Found : C, 84.09; H, 7.98; N, 2.90.

**2,7-Dibromo-9-dodecyl-9H-carbazole:**<sup>36</sup> A mixture of 2,7-dibromo-9H-carbazole<sup>40</sup> (7.8 g, 24 mmol), 1-bromododecane (12.5 g, 50 mmol), and NaOH (2.0 g, 50 mmol) in DMF (anhydrous, 50 mL) was stirred overnight under  $\text{N}_2$ . After the reaction, the mixture was poured into water (200 mL). Ethyl acetate ( $2 \times 100$  mL) was used to extract the product. The ethyl acetate solution was washed with water ( $2 \times 100$  mL) and saturated aqueous NaCl (200 mL), dried with  $\text{MgSO}_4$ , and evaporated to dryness *in vacuo*. The residue was recrystallized in 100 mL ethanol to give 2,7-dibromo-9-dodecyl-9H-carbazole as colorless needle crystals (9.9 g, 84%).  $^1\text{H}$  NMR (400 MHz,  $\text{CDCl}_3$ ):  $\delta$  7.83 (d,  $J = 7.6$  Hz, 2H), 7.49 (d,  $J = 2.0$  Hz, 2H), 7.31 (dd,  $J_1 = 7.6$  Hz,  $J_2 = 2.0$  Hz, 2H), 4.13 (t,  $J = 7.2$  Hz, 2H), 1.81 (quintet,  $J = 7.2$  Hz, 2H), 1.18-1.40 (m, 18H), 0.88 (t,  $J = 7.2$  Hz, 3H). The  $^1\text{H}$  NMR spectrum of this compound is consistent with that reported in the literature.

**3,6-Dibromo-9-dodecyl-9H-carbazole:**<sup>41</sup> A mixture of 3,6-dibromo-9H-carbazole (7.8 g, 24 mmol), 1-bromododecane (12.5 g, 50 mmol), and NaOH (2.0 g, 50 mmol) in DMF (anhydrous, 50 mL) was stirred overnight under  $\text{N}_2$ . After the reaction, the mixture was poured into water (200 mL). Ethyl acetate ( $2 \times 100$  mL) was used to extract the product.

The ethyl acetate solution was washed with water ( $2 \times 100\text{mL}$ ) and saturated aqueous NaCl (200 mL), dried with  $\text{MgSO}_4$ , and evaporated to dryness *in vacuo*. The residue was recrystallized from ethanol (100 mL) to give 3,6-dibromo-9-dodecyl-9*H*-carbazole as colorless needle crystals (10.1 g, 85%).  $^1\text{H}$  NMR (400 MHz,  $\text{CDCl}_3$ ):  $\delta$  8.08 (d,  $J = 2.0$  Hz, 2H), 7.52 (d,  $J = 2.0$  Hz, 2H), 7.31 (d,  $J = 8.8$  Hz, 2H), 4.18 (t,  $J = 7.2$  Hz, 2H), 1.80 (quintet,  $J = 7.2$  Hz, 2H), 1.18-1.44 (m, 18H), 0.86 (t,  $J = 7.2$  Hz, 3H). The  $^1\text{H}$  NMR spectrum of this compound is consistent with that reported in the literature.

**Polymer 1 model:** 2,2'-(9,9-Dioctyl-9*H*-fluorene-2,7-diyl)bis(1,3,2-dioxaborinane) (0.4648 g, 0.8324 mmol), 2,7-dibromo-9-dodecyl-9*H*-carbazole (0.4104 g, 0.8324 mmol), Aliquat 336 (40 mg), and  $\text{Pd}(\text{PPh}_3)_4$  (9.5 mg, 0.0080 mmol) were charged to a 25 mL, two-neck, round-bottomed flask with a condenser. The system was then evacuated and refilled with  $\text{N}_2$  4 times. Toluene (8.0 mL) and 2 N aqueous  $\text{K}_2\text{CO}_3$  (4.0 mL) were added before the mixture was heated to  $90^\circ\text{C}$  and kept for 3 d. Then 2,2'-(9,9-dioctyl-9*H*-fluorene-2,7-diyl)bis(1,3,2-dioxaborinane) (100 mg, 0.17 mmol) in toluene (1.0 mL) was added, and the mixture was kept stirring for another 12 h. Iodobenzene (0.3 mL) was then added to end cap the polymer, and the reaction was kept stirring for another 6 h. After the mixture was cooled to room temperature, it was added dropwise to 125 mL MeOH. The formed solid was filtered and washed with water and MeOH before drying under vacuum. The solid was washed sequentially with hot MeOH and hot acetone using a Soxhlet apparatus. The residue was then extracted with  $\text{CHCl}_3$  using a Soxhlet apparatus. Most of the solvent was then removed, and the residual was run through a short silica plug, eluting with  $\text{CHCl}_3$  and then with THF. The solvent was then removed under reduced pressure; the residue was then dissolved in 20 mL  $\text{CHCl}_3$ , and the solution was added

dropwise to 200 mL MeOH. The resulting solid was filtered and washed with water and MeOH before drying under vacuum. Polymer **1** model was then obtained as a pale yellow solid (0.41 g, 80%). GPC (Toluene):  $M_n = 61.1$  kD,  $M_w/M_n = 4.00$ .  $^1\text{H}$  NMR (500 MHz,  $\text{CDCl}_3$ )  $\delta$  8.32 (sb, 2nH), 8.0-7.6 (mb, 10nH), 4.50 (sb, 2nH), 2.18 (sb, 4nH), 1.90 (sb, 2H), 1.6 -1.0 (mb, 42 nH), 0.9 -0.3 (mb, 9nH). Anal. Calcd for polymer  $(\text{C}_{53}\text{H}_{71}\text{N})_n$ : C, 88.15; H, 9.91; N, 1.94; Found : C, 88.00; H, 10.02; N, 1.87.

**Polymer 2 model:** 2,2'-(9,9-Dioctyl-9*H*-fluorene-2,7-diyl)bis(1,3,2-dioxaborinane) (0.4650 g, 0.8327 mmol), 2,7-dibromo-9-dodecyl-9*H*-carbazole (0.4106 g, 0.8324 mmol), Aliquat 336 (40 mg), and  $\text{Pd}(\text{PPh}_3)_4$  (9.5 mg, 0.0080 mmol) were charged to a 25 mL two-neck round-bottomed flask with condenser. The system was then evacuated and refilled with  $\text{N}_2$  4 times. Toluene (8.0 mL) and 2 N  $\text{K}_2\text{CO}_3$  aqueous solution (4.0 mL) were added before the mixture was heated to 90 °C and kept at this temperature for 3 d. Then, 2,2'-(9,9-dioctyl-9*H*-fluorene-2,7-diyl)bis(1,3,2-dioxaborinane) (100 mg, 0.17 mmol) in toluene (1.0 mL) was added, and the mixture was kept stirring for another 12 h. Iodobenzene (0.3 mL) was then added to end cap the polymer, and the mixture was kept stirring for another 12 h. After the mixture was cooled to room temperature, it was added dropwise to 125 mL MeOH. The formed solid was filtered and washed with water and MeOH before drying under vacuum. The solid was washed sequentially with hot MeOH and hot acetone using a Soxhlet apparatus. The residue was then extracted with  $\text{CHCl}_3$  in a Soxhlet apparatus. Most of the solvent was then removed, and the residue was run through a short silica plug, eluting with  $\text{CHCl}_3$  and then with THF. The solvent was removed, and the residue was dissolved in 10 mL  $\text{CHCl}_3$  before precipitating in 125 mL MeOH. The resulting solid was filtered and washed with water and MeOH before drying

under vacuum. The precipitation was repeated, and the resulting solid was then filtered and dried to give Polymer **2** model as a white solid (0.34 g, 68%). GPC (Toluene):  $M_n$  = 24.6 kD,  $M_w/M_n$  = 3.55.  $^1\text{H}$  NMR (500 MHz,  $\text{CDCl}_3$ ):  $\delta$  8.53 (s, 2nH), 7.8-7.6 (mb, 8nH), 7.56 (sb, 2nH) 4.39 (sb, 2nH), 2.17 (sb, 4nH), 1.94 (sb, 2nH), 1.58 (sb, 2nH) 1.4 -1.0 (mb, 40 nH), 0.9 -0.2 (mb, 9nH). Anal. Calcd for polymer  $(\text{C}_{53}\text{H}_{71}\text{N})_n$ : C, 88.15; H, 9.91; N, 1.94; Found : C, 87.94; H, 9.99; N, 1.90.

**2,7-Dibromo-9-(4-nitrophenyl)-9H-carbazole:**<sup>40</sup> A mixture of 2,7-dibromocabazole<sup>40</sup> (5.00 g, 15.3 mmol),  $\text{K}_2\text{CO}_3$  (10.56 g, 76.52 mmol) and DMF (50 mL) was stirred under nitrogen for 20 min before the addition of 4-fluoronitrobenzene (9.9 g, 70 mmol). The reaction mixture was stirred overnight at room temperature and then poured into water (500 mL). The yellow solid was collected by filtration. The crude material was recrystallized from benzene to afford the product as a light yellow solid (5.9 g, 86%).  $^1\text{H}$  NMR (400 MHz,  $\text{CDCl}_3$ ):  $\delta$  8.56 (d,  $J$  = 8.9 Hz, 2H), 7.99 (d,  $J$  = 8.3 Hz, 2H), 7.77 (d,  $J$  = 9.0 Hz, 2H), 7.60 (d,  $J$  = 1.5 Hz, 2H), 7.50 (dd,  $J_1$  = 8.3 Hz,  $J_2$  = 1.6 Hz, 2H). The  $^1\text{H}$  NMR spectrum of this compound is consistent with that reported in the literature.<sup>40</sup>

**2,7-dibromo-9-(heptadecan-9-yl)-9H-carbazole:**<sup>32</sup> To the mixture of powdered potassium hydroxide (5.71 g, 102 mmol) and 2,7-dibromo-9H-carbazole (6.67 g, 20.4 mmol) in a three-neck round-bottomed flask, a solution of heptadecan-9-yl-4-methylbenzenesulfonate (10.9 g, 26.6 mmol) in dimethyl sulfoxide (32 mL) was added at room temperature. The reaction was stirred overnight at room temperature under nitrogen. It was then separated with water and hexane using a separatory funnel. The product in the hexane layer was washed twice with water and dried over  $\text{Na}_2\text{SO}_4$ . The solvent was then removed under reduced pressure and purified by silica gel column chromatography,

eluting with hexanes. 2,7-Dibromo-9-(heptadecan-9-yl)-9H-carbazole was then obtained as a white solid (6.2 g, 93%).  $^1\text{H}$  NMR ( $\text{CDCl}_3$ , 300 MHz):  $\delta$  7.91 (br, 2H), 7.65 (br, 1H), 7.55 (br, 1H), 7.30 (d,  $J = 5.3$  Hz, 2H), 4.40 (m, 1H), 2.19 (m, 2H), 1.90 (m, 2H), 1.17 (m, 22H), 0.95 (m, 2H), 0.87 (t,  $J = 6.0$  Hz, 6H) The  $^1\text{H}$  NMR spectrum of this compound is consistent with that reported in the literature.<sup>32</sup>

**Polymer-NO<sub>2</sub>**: 2,2'-(9,9-Dioctyl-9H-fluorene-2,7-diyl)bis(1,3,2-dioxaborinane) (0.4648 g, 0.8324 mmol), 2,7-dibromo-9-(heptadecan-9-yl)-9H-carbazole (0.2344 g, 0.4161 mmol), 2,7-dibromo-9-(4-nitrophenyl)-9H-carbazole (0.1860 g, 0.4166 mmol), Aliquat 336 (40 mg), and  $\text{Pd}(\text{PPh}_3)_4$  (9.6 mg, 0.0081 mmol) were charged to a 25 mL two-neck round-bottomed flask with a condenser. The system was then evacuated and refilled with nitrogen 4 times. Toluene (15.0 mL) and 2 N aqueous  $\text{K}_2\text{CO}_3$  (10.0 mL) were added before the mixture was heated to 90 °C and kept at that temperature for 2 d. Then 2,2'-(9,9-dioctyl-9H-fluorene-2,7-diyl)bis(1,3,2-dioxaborinane) (100 mg, 0.17 mmol) in toluene (1.0 mL) was added, and the mixture was kept stirring for another 2 h. Iodobenzene (0.3 mL) was then added to end cap the polymer, and the reaction was kept stirring for another 3 h. After the mixture was cooled to room temperature, it was added dropwise to 125 mL MeOH. The formed solid was filtered and washed with water and MeOH before drying under vacuum. The solid was washed sequentially with hot MeOH and hot acetone using a Soxhlet apparatus. The residue was then extracted with  $\text{CHCl}_3$  with a Soxhlet apparatus. Solvent was then removed under reduced pressure; the residue was dissolved in 20 mL  $\text{CHCl}_3$ , and added dropwise to 200 mL MeOH. The resulting solid was filtered and washed with water and MeOH before drying under vacuum. **Polymer-NO<sub>2</sub>** was then obtained as a pale yellow solid (0.37 g, 54%). GPC (THF):  $M_n =$

45 kD,  $M_w/M_n = 1.9$ .  $^1\text{H}$  NMR ( $\text{CDCl}_3$ , 500 MHz):  $\delta$  8.57 (sb, 2nH), 8.2 – 7.5 (mb, 26nH), 4.72 (sb, nH), 2.4 – 2.0 (mb, 12nH), 1.90 (sb, 72nH), 0.8 (mb, 18 nH). Anal. Calcd for polymer  $(\text{C}_{105}\text{H}_{131}\text{N}_3\text{O}_2)_n$ : C, 85.96; H, 9.00; N, 2.86; Found : C, 85.94; H, 9.02; N, 2.84.

## 6.11 References

- (1) Spangler, C. W. *J. Mater. Chem.* **1999**, 9, 2013-2022.
- (2) Pawlicki, M.; Collins, H. A.; Denning, R. G.; Anderson, H. L. *Angew. Chem. Int. Ed.* **2009**, 48, 3244-3266.
- (3) Ehrlich, J. E.; Wu, X. L.; Lee, I.-Y. S.; Hu, Z.-Y.; Rockel, H.; Marder, S. R.; Perry, J. W. *Opt. Lett.* **2002**, 25, 1843-1845.
- (4) Perry, J. W.; Mansour, K.; Marder, S. R.; Perry, K. J.; Alvarez, D.; Choong, I. *Opt. Express* **1994**, 19, 625-627.
- (5) Tutt, L. W.; Kost, A. *Nature* **1992**, 356, 225-229.
- (6) Sun, Y. P.; Riggs, J. E.; Liu, B. *Chem. Mater.* **1997**, 9, 1268-1272.
- (7) Yu, C.; Hanack, M.; Blau, W. J.; Dini, D.; Liu, Y.; Bai, Y. L. *J. Mater. Sci.* **2005**, 41, 2169-2185.
- (8) Zhang, L.; Wag, L. *J. Mater. Sci.* **2008**, 43, 5692-5701.
- (9) Perry, J. W.; Mansour, K.; Lee, I.-Y. S.; Wu, X.-L.; Bedworth, P. V.; Chen, C.-T.; Ng, D.; Marder, S. R.; Miles, P.; Wada, T.; Tian, M.; Sasabe, H. *Science* **1996**, 273, 1533-1536.
- (10) de la Torre, G.; Vaquez, P.; Agullo-Lopez, F.; Torres, T. *Chem. Rev.* **2004**, 104, 3723-3750.
- (11) Zhou, G.-J.; Wong, W.-Y.; Lin, Z.; Ye, C. *Angew. Chem. Int. Ed.* **2006**, 45, 6189-6193.
- (12) Zhou, G.; Wong, W.-Y.; Poon, S.-Y.; Ye, C.; Lin, Z. *Adv. Funct. Mater.* **2009**, 19, 531-544.
- (13) Zhou, G.-J.; Wong, W.-Y.; Ye, C.; Lin, Z. *Adv. Funct. Mater.* **2007**, 17, 963-972.
- (14) Dupuis, B.; Michaut, C.; Jouanin, I.; Delaire, J.; Robin, P.; Feneyrou, P.; Dentan, V. *Chem. Phys. Lett.* **1999**, 300, 169-176.
- (15) Cha, M.; Sariciftci, N. S.; Heeger, A. J.; Hummelen, J. C.; Wudl, F. *Appl. Phys. Lett.* **1995**, 67, 3850-3852.
- (16) Chi, S.-H.; Hales, J. M.; Cozzuol, M.; Ochoa, C.; Fitzpatrick, M.; Perry, J. W. *Opt. Express* **2009**, 17, 22062-22072.
- (17) Huang, C.; Sartin, M. M.; Siegel, N.; Cozzuol, M.; Stephen Barlow; Perry, J. W.; Marder, S. R., *Submitted*.
- (18) Cravino, A.; Sariciftci, N. S. *J. Mater. Chem.* **2002**, 12, 1931-1943.
- (19) Tan, Z.; Hou, J.; He, Y.; Zhou, E.; Yang, C.; Li, Y. *Macromolecules* **2007**, 40, 1868-1873.
- (20) Koyuncu, S.; Zafer, C.; Koyuncu, F. B.; Aydin, B.; Can, M.; Sefer, E.; Ozdemir, E.; Icli, S. *J. Polym. Sci. Part A: Polym. Chem.* **2009**, 47, 6280-6291.
- (21) Yuan, M.-C.; Su, M.-H.; Chiu, M.-Y.; Wei, K.-H. *J. Polym. Sci. Part A: Polym. Chem.* **2010**, 48, 1298-1309.
- (22) Gómez, R.; Veldman, D.; Blanco, R.; Seoane, C.; Segura, J. L.; Janssen, R. A. J. *Macromolecules* **2007**, 40, 2760-2772.
- (23) Würthner, F. *Chem. Commun.* **2004**, 1564-1579.
- (24) Zhan, X.; Tan, Z.; Domercq, B.; An, Z.; Zhang, X.; Barlow, S.; Li, Y.; Zhu, D.; Kippelen, B.; Marder, S. R. *J. Am. Chem. Soc.* **2007**, 129, 7246-7247.
- (25) Wasielewski, M. R. *Acc. Chem. Res.* **2009**, 42, 1910-1921.

- (26) Bullock, J. E.; Carmieli, R.; Mickley, S. M.; Vura-Weis, J.; Wasielewski, M. R. *J. Am. Chem. Soc.* **2009**, *131*, 11919-11929.
- (27) Kelley, R. F.; Tauber, M. J.; Wasielewski, M. R. *J. Am. Chem. Soc.* **2006**, *128*, 4779-4791.
- (28) Kelley, R. F.; Shin, W. S.; Rybtchinski, B.; Sinks, L. E.; Wasielewski, M. R. *J. Am. Chem. Soc.* **2007**, *129*, 3173-3181.
- (29) O'Neil, M. P.; Niemczyk, M. P.; Svec, W. A.; Gosztola, D.; L.Gaines, G.; Wasielewski, M. R. *Science* **1992**, *257*, 63-65.
- (30) Muthukumar, K.; Loewe, R. S.; Kirmaier, C.; Hindin, E.; Schwartz, J. K.; Sazanovich, I. V.; Diers, J. R.; Bocian, D. F.; Holten, D.; Lindsey, J. S. *J. Phys. Chem. B* **2004**, *107*, 3431-3442.
- (31) Kirmaier, C.; Hindin, E. K., J.; Schwartz; Sazanovich, I. V.; Diers, J. R.; Muthukumar, K.; Taniguchi, M.; Bocian, D. F.; Lindsey, J. S.; Holten, D. *J. Phys. Chem. B* **2003**, *107*, 3443-3454.
- (32) Morin, J.-F.; Drolet, N.; Tao, Y.; Leclerc, M. *Chem. Mater.* **2004**, *16*, 4619-4626.
- (33) Walkim, S.; Aich, B.-R.; Tao, Y.; Leclerc, M. *Polym. Rev.* **2008**, *48*, 432-462.
- (34) Park, S. H.; Roy, A.; Beaupre, S.; Cho, S.; Coates, N.; Moon, J. S.; Moses, D.; Leclerc, M.; Lee, K.; Heeger, A. J. *Nat. Photonics.* **2009**, *3*, 297-302.
- (35) Li, J. L.; Dierschke, F.; Wu, J. S.; Grimsdale, A. C.; Müllen, K. *J. Mater. Chem.* **2006**, *16*, 96-100.
- (36) Iraqi, A.; Wataru, I. *Chem. Mater.* **2004**, *16*, 442-448.
- (37) Ranger, M.; Rondeau, D.; Leclerc, M. *Macromolecules* **1997**, *30*, 7686-7691.
- (38) Liu, B.; Yu, W.-L.; Lai, Y.-H.; Huang, W. *Chem. Mater.* **2001**, *13*, 1984-1991.
- (39) Tauber, M. J.; Kelley, R. F.; Giaimo, J. M.; Rybtchinski, B.; Wasielewski, M. R. *J. Am. Chem. Soc.* **2006**, *128*, 1782-1783.
- (40) Jian, H.; Tour, J. M. *J. Org. Chem.* **2003**, *68*, 5901-5103.
- (41) Iraqi, A.; Wataru, I. *J. Polym. Sci. Part A: Polym. Chem.* **2004**, *42*, 6041-6051.
- (42) Yu, W. L.; Pei, J.; Huang, W.; Heeger, A. J. *Adv. Mater.* **2000**, *12*, 828-831.
- (43) Würthner, F.; Thalacker, C.; Diele, S.; Tschierske, C. *Chem. Eur. J.* **2001**, *7*, 2245-2253.
- (44) Odom, S. A.; Lancaster, K.; Beverina, L.; Lefler, K. M.; Thompson, N. J.; Coropceanu, V.; Brédas, J.-L.; Marder, S. R.; Barlow, S. *Chem. Eur. J.* **2007**, *13*, 9637-9646.
- (45) An, Z. S.; Odom, S. A.; Kelley, R. F.; Huang, C.; Zhang, X.; Barlow, S.; Padilha, L. A.; Fu, J.; Webster, S.; Hagan, D. J.; Van Stryland, E. W.; Wasielewski, M. R.; Marder, S. R. *J. Phys. Chem. A* **2009**, *113*, 5585-5593.
- (46) Barlow, S.; Risko, C.; Chung, S. J.; Tucker, N. M.; Coropceanu, V.; Jones, S. C.; Levi, Z.; Bredas, J. L.; Marder, S. R. *J. Am. Chem. Soc.* **2005**, *127*, 16900-16911.



- (47) Lévesque, I.; Bertrand, P.-O.; Blouin, N.; Leclerc, M.; Zecchin, S.; Zotti, G.; Ratcliffe, C. I.; Dennis D. Klug; Gao, X.; Gao, F.; Tse, J. S. *Chem. Mater.* **2007**, *19*, 2128-2138.
- (48) Thelakkat, M.; Schmidt, H.-W. *Adv. Mater.* **1998**, *10*, 219-223.
- (49) Brédas, J.-L.; Beljonne, D.; Coropceanu, V.; Cornil, J. *Chem. Rev.* **2004**, *104*, 4971-5004.
- (50) Thompson, B. C.; Fréchet, J. M. J. *Angew. Chem. Int. Ed.* **2008**, *47*, 58-77.
- (51) Fisher, W. G.; Wachter, E. A.; Lytle, F. E.; Armas, M. *Appl. Spectrosc.* **1998**, *52*, 536-545.
- (52) Xu, C.; Webb, W. W. *J. Opt. Soc. Am. B* **1996**, *13*, 481-491.
- (53) Rumi, M.; Ehrlich, J. E.; Heikal, A. A.; Perry, J. W.; Barlow, S.; Hu, Z.; McCord-Maughon, D.; Parker, T. C.; Rockel, H.; Thayumanavan, S.; Marder, S. R.; Beljonne, D.; Brédas, J.-L. *J. Am. Chem. Soc.* **2000**, *122*, 9500-9510.
- (54) Kennedy, S. M.; Lytle, F. E. *Anal. Chem.* **1986**, *58*, 2643-2647.

## **CHAPTER 7**

### **CONCLUSIONS AND OUTLOOK**

#### **7.1 Conclusions and outlook**

This dissertation described the investigation of the synthesis and characterization of new perylene diimide (PDI)-based photonic and electronic materials. Chapter 1 provided a general introduction to PDI-based materials and their applications in organic electronics. In Chapter 2, the main goal was to develop solution-processable PDIs for organic electronic devices, particularly for organic field-effect transistors (OFETs) and organic photovoltaics (OPVs). Chapter 3 described the use of diblock copolymers with oligothiophene donors and PDI pendants for OPV applications. Chapter 4 was concerned with PDI-based acceptors in which EA and miscibility with P3HT are varied through the substituents to influence the yields of charge photo-generation in organic donor/acceptor blends. Chapter 5 and 6 discussed photo-induced process in new D–A type PDIs and their application to optical limiting using photo-generated ion-pairs.

The first scientific part of this thesis, including Chapters 2 and 3, was concerned with developing PDI-based polymers as alternative acceptors for fullerene derivatives in organic solar cells. In Chapter 2, a series of PDI-grafted homopolynorbornenes had been synthesized, characterized, and investigated as solution-processable electron-transport materials in OFETs and acceptors in solar cells. ROMP was found to be an effective method for synthesizing the PDI-grafted polymers with high molecular-weight and sufficient solubility for solution-process devices. For the PDI-grafted homopolymers,

UV-Vis absorption and X-ray evidence suggested that the PDI pendants on the side-chain of **C11PDI HP** and **C7PDI HP** tended to  $\pi$ - $\pi$  stack with nearby PDI moieties. Organic solar cells using P3HT/**C11PDI HP** blend showed PCEs of up to  $0.38 \pm 0.01\%$  without optimization. These are among the best reported PCEs for PDI/P3HT blends. The poorer photovoltaic performance based on blends of P3HT/**C7PDI HP**, which had shorter N-terminal side-chain compared to **C11PDI HP**, might be attributed to poor miscibility with P3HT. This was further confirmed by Kelvin probe force microscopy (KPFM), in which large domains (larger than 1  $\mu\text{m}$ ) corresponding to PDI aggregates were observed. The  $\pi$ - $\pi$  stacking of PDI moieties on polymer side-chains could be largely suppressed by incorporation of functional groups at the bay position of **N-PDI HP**, which led to much poorer OPV performance, despite the fact that **N-PDI HP** showed a broader and more red-shifted absorption spectrum, with an EA similar to that of normal PDI materials

Future research for such PDI-based polymers could include studies of:

- 1) The side-chain effect in improving the miscibility of PDI-based polymers with donor polymers in physical blends using various alkyls or other types of substituents, like oligothiophenes, on the imide positions. The increased miscibility of these PDI-based materials may provide opportunities for improving thin-film nano-morphology for better OPVs.
- 2) Improving the light-harvesting ability of the PDI/donor blends. Another reason for the poor PCEs and short-circuit current for PDI-based devices is relatively poor light-harvesting. In general, spin-cast films of PDI/donor (1:1 weight ratio) based solar cells show absorbance lower than 0.4 at the absorption maximum,

while that for PCBM/P3HT prepared in similar conditions could be over 1.0. Different solvent systems, together with various additives, should be tried for optimization.

- 3) PDI-based homopolymers with bay-substituents of limited steric hindrance could be of interest for organic electronic applications. The PDI electronic properties could be modified for a specific purpose, while the  $\pi$ - $\pi$  interaction between neighboring PDI moieties can still facilitate charge transport.
- 4) Using these polymers for other possible applications. For example, the blend of PDI HP/MEH PPV potentially could be used for 2PA-induced optical limiting between 700 – 900 nm using the 2PA of MEH-PPV, the radical anion absorption of PDI, and the polaron absorption of MEH-PPV in this range.

Chapter 3 extended the study of the PDI-based polymers by incorporating oligothiophenes (OTs) and the **C11PDI** as pendants into a diblock copolynorbornene framework for OPVs. These **PDI-OT** copolymers exhibit broad absorption spectra from 300 to 600 nm, with both characteristic **OT** and **PDI** bands. Moreover, strong PL quenching (> 95 %) of the copolymer films compared to films of pure **C11PDI HP** or **5T/6T HP** suggests that efficient electron transfer occurs following photoexcitation. Among the copolymers, **PDI-5T CPA** showed much higher PCEs and  $J_{SC}$  (PCE = 0.15%, and  $J_{SC}$  = 0.42 mA/cm<sup>2</sup>) than the other two copolymers and respective homopolymer blends, which is consistent with the greater yield of charge photo-generation determined from the transient absorption decays. Furthermore, the lower yield of charge photo-generation (5 to 10 times lower than typical P3HT/PDI blend) might be a key reason for

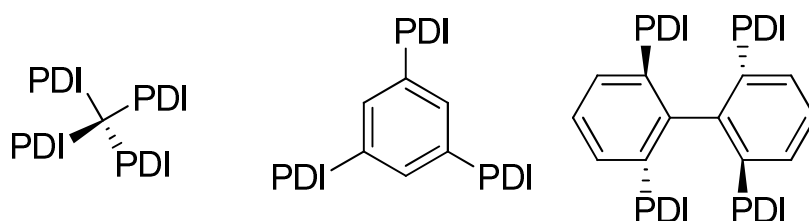
the poor device performance. These observations suggest that thin-films from **PDI-5T CPA** might exhibit more favourable micro-phase-segregation, although no obvious surface morphology differences were observed in the TEM images.

Future research for such PDI-OT-based diblock polymers could include studies of:

- 1) The bulk-morphology of these thin-films, such as the TEM images of film-cross-sections, which might be valuable for providing better understanding of the relationship between the morphology and device performance.
- 2) The use of such diblock copolymers as compatibilizers for donor/acceptor blends in solar cells may be worth trying, as the presence of these OT/PDI BCP might help to direct and stabilize the thin-film morphology in order to achieve phase-segregation with an appropriate length scale.
- 3) New diblock copolymers with PDI and two-photon absorption (2PA) donor pendants are of interest for optical limiting application if the donors show 2PA band overlap with PDI radical anion absorption between 700 – 1000 nm. The aggregation of PDIs on the polymer side-chains, in principle, could stabilize the PDI radical anion after the 2PA-induced electron transfer, resulting in a low charge-recombination rate.<sup>1-2</sup>

It should also be noted that the solar cell performance based on the PDI-grafted polynorbornenes in Chapters 2 and 3 are relatively low, like most solar cells using PDI acceptors. One of the major reasons for the poor performance could be the challenge in controlling the molecular alignment of the PDI-based materials, which leads to much

lower electron mobility in films compared to devices with fullerene-based acceptors. This is an important issue to be addressed before any big breakthrough PDI-based solution-processed solar cells can be constructed. “3D-PDI” type materials, as shown in Figure 7.1, could be a candidate for taking advantage of the three-dimensional charge transport observed in fullerene-type acceptors. Such “3D-PDI” materials might show fewer molecular alignment issues as normal PDIs do because of the possible isotropy-charge-transport abilities of such 3-D materials.



**Figure 7.1.** Some possible “3D-PDI” type materials.

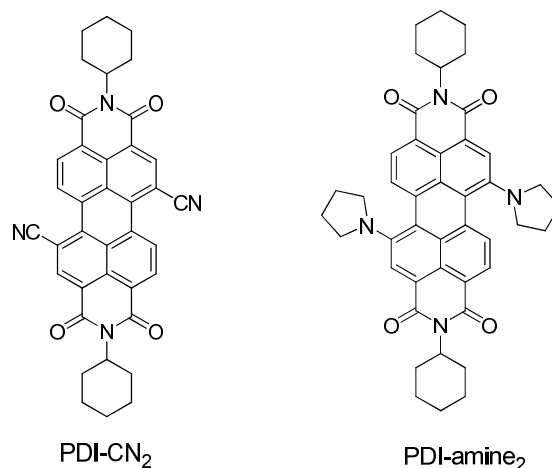
Chapter 4 reported on studies of the efficiency of charge photo-generation in the blend of P3HT and a series PDI-based acceptors PDI<sub>X</sub> (X = A to F) with various electron affinities. It was further confirmed that  $\Delta G_{CS}$  (the free energy difference between the first singlet excited state and final charge-separated states) is a key factor in determining the efficiency of charge photo-generation at organic D/A blend films. Typically, in our research, blends with larger  $\Delta G_{CS}$  gave higher yields of charge photo-generation, and a clear correlation between  $\Delta G_{CS}$  and the yield of charge photo-generation was observed for P3HT:PDI<sub>X</sub> (X = A to E, with EA of *ca.* 140 meV), where the photo-generated charge yield was observed to increase by *ca.* 40% for every 0.1 eV increase in  $\Delta G_{CS}$ . Further increases in charge photo-generation yields were observed when using blends of

P3HT:PDI<sub>X</sub> (X = G to I), where this series of PDI materials with oligo-3-hexyl-thiophene moieties at the imide position have lower EA. An increase in PCEs of a factor of *ca.* 20 was observed for solar cells using P3HT:PDI<sub>G</sub> over P3HT:PDI<sub>D</sub>, probably due to better mixing between P3HT and PDI<sub>G</sub>, because of the structural similarities between the incorporated 3-hexyl-thiophenes. However, no significant improvement in PCEs was obtained for solar cells with PDI<sub>H</sub> and PDI<sub>I</sub>, which have more oligo-3-hexylthiophenes moieties, as compared to those using PDI<sub>D</sub>. Although large improvements in solar cell PCEs have been obtained, the overall performance for the devices in this chapter still fall far below the state-of-the-art values for OPVs in general. The poor device performances, despite the promising photo-physics, are similar to those PDI materials described in earlier chapters, presumably for similar reasons. Although an almost linear dependence of the yield of charge photo-generation on  $\Delta G_{CS}$  was observed for P3HT:PDI<sub>X</sub> (X = A to E) blends, such observation is limited to a small range of PDI EA (*ca.* 140 meV).

Future research could include studies of:

- 1) The photo-physics of blends of P3HT:PDI using other PDIs such as PDI-CN<sub>2</sub> and PDI-amine<sub>2</sub>, as shown in Figure 7.2,<sup>3-5</sup> with lower and higher EA respectively, to extend the correlation range.
- 2) Single-carrier time-of-flight (TOF) measurements based on analysis of such blend films could provide the relationship between the yield of charge photo-generation and respective charge carriers mobility in the blends. This study might give us a direct reason for the poor performance of solar cells with such promising photophysics.

- 3) The photophysics of the blend films of the P3HT and PDI-grafted polymers are worth studying, and this could give insight into the relationship between the morphology-photophysics and the device performance, since the electronic properties of **C11PDI HP** and **C7PDI HP** are similar.



**Figure 7.2, Other PDI-based materials whose blend photophysics should be investigated.**

The last part of this thesis, including Chapters 5 and 6, explored the photo-induced electron transfer of PDI-donor systems and the use of the photo-generated PDI radical-anion absorption in realizing optical power limiting in the NIR (600 – 800 nm). In Chapter 5, an effective approach for 2PA-induced optical limiting through which donors and acceptors can be independently chosen to maximize optical suppression for a particular wavelength has been demonstrated. In this chapter, PDI-based dyads with a D- $\pi$ -D type two-photon dye were synthesized and characterized. Long-lived charge-separated states in the dyads were demonstrated according to their transient absorption spectra via photo-excitation of the donor moieties. Furthermore, the D-PDI linkers can strongly affect the charge-transfer and recombination rates. Dyad **1**, with its rigid,



phenylene linker, exhibits a lower charge separation and recombination rate than Dyad **2**, which has a hexylene linker. In both cases, significant overlap of the corresponding PDI radical-anion absorption with the 2PA band of the attached D- $\pi$ -D donor leads to strong enhancement of optical suppression of the dyads with respect to the 2PA chromophore.

In Chapter 6, D-A “double-cable” conjugated polymers with poly(carbazole-*alt*-2,7-fluorene)s as the electron-donating polymer backbones and electron-deficient PDI moieties incorporated into the side chains as pendant acceptors were investigated as optical limiters. Efficient photo-induced charge-transfer in these polymers was confirmed by transient absorption spectra, and long-lived charge-separated states with strong PDI anion absorption between 600 – 800 nm were observed via either donor or acceptor pumping. Because the PDI radical anion can be generated via PDI aggregate excitation and/or 2PA from the polymer backbone, these copolymers show strong enhancement of the nonlinear optical absorption compared with blends of the model materials at 680 nm. Moreover, **Polymer-NO<sub>2</sub>**, in which 4-nitrophenyl groups were incorporated in poly(2,7-carbazole-*alt*-2,7-fluorene) as acceptors, showed stronger optical limiting compared with poly(2,7-carbazole-*alt*-2,7-fluorene) itself, using photo-generated polaron absorption at 580 nm. Furthermore, **Polymer-NO<sub>2</sub>** also exhibit slightly better optical limiting response than poly(2,7-carbazole-*alt*-2,7-fluorene) at wavelengths other than 580 nm because of the broad long-lived triplet state absorption following charge-transfer after photo-excitation.

Future research could include studies of:

- 1) Further efforts on varying the timescale for recombination by using other linker groups in the donor-PDI dyads. For example, the using of linkers such as

biphenylene or fluorenylene might lead to longer charge-separated life-times because of the longer donor-acceptor distance. Such compounds could be used in optical limiters for long pulses if the electronic coupling between the donor and PDI moieties is strong enough to drive efficient and fast charge separation.

- 2) Donor chromophores with larger 2PA cross section between 600 – 800 nm, like squaraine dyes, could be incorporated to PDIs for better 2PA-induced charge-separation-type optical limiting in the PDI radical-anion absorbing region, as stronger 2PA could, in principle, generate more PDI radical anions. A similar concept could be applied to the polymer system by using donor polymers, like MEH-PPV, with larger 2PA cross sections between 600 – 800 nm.
- 3) Optical limiting could be extended to other wavelengths using the dyad approach with other D/A systems. Acceptors other than PDIs or donors, in principle, could be used for optical limiting at other wavelengths using this approach so long as (a) the ions exhibit much stronger absorption compared to the ground state absorption at the wavelength of photo-generation, and (b) the photo-generated ion pair has sufficient population and life-time.
- 4) The nitro-phenyl group or similar derivatives seems to be good candidates for incorporation into donor-conjugated polymers, which show significant overlap between their 2PA band and respective polaron absorptions for 2PA-induced charge-separation-based OL at particular wavelengths.

In conclusion, this thesis provided insightful research into charge-transfer processes in PDI materials or donor:PDI blends and their use in OPVs and optical limiting. From what has been observed, although PDI might not be a promising acceptor

for OPV applications, the studies on donor:PDI systems could offer better understanding of overall photovoltaic process, which might guide research in other D/A system and lead to better solar cells. Moreover, the use of photo-generated PDI anion absorption for optical limiting was demonstrated and found to give good optical suppression for laser pulses between 650 – 800 nm. Further optimization of these D/A systems is expected to improve the optical limiting performance. Similar research, in principle, could be extended to lasers at other wavelengths, using other photo-generated ion pair absorption.

## 7.2 References

- (1) Kelley, R. F.; Shin, W. S.; Rybtchinski, B.; Sinks, L. E.; Wasielewski, M. R. *J. Am. Chem. Soc.* **2007**, *129*, 3173-3181.
- (2) Haque, S. A.; Handa, S.; Peter, K.; Palomares, E.; Thelakkat, M.; Durrant, J. M. *Angew. Chem. Int. Ed.* **2005**, 5740-5744.
- (3) Jones, B. A.; Facchetti, A.; Wasielewski, M. R.; Marks, T. J. *J. Am. Chem. Soc.* **2007**, *129*, 15259-15278.
- (4) Jones, B. A.; Ahrens, M. J.; Yoon, M.-H.; Facchetti, A.; Marks, T. J.; Wasielewski, M. R. *Angew. Chem. Int. Ed.* **2004**, *43*, 6363-6366.
- (5) Zhao, Y.; Wasielewski, M. R. *Tetrahedron Lett.* **1999**, *40*, 7047-7050.